THE UNIVERSITY OF CHICAGO

TWO-DIMENSIONAL OPTOMECHANICAL RESONATORS IN GALLIUM ARSENIDE

A DISSERTATION SUBMITTED TO
THE FACULTY OF THE DIVISION OF THE PHYSICAL SCIENCES
IN CANDIDACY FOR THE DEGREE OF
DOCTOR OF PHILOSOPHY

DEPARTMENT OF PHYSICS

BY
RHYS GEOFFREY POVEY

CHICAGO, ILLINOIS
AUGUST 2023

Table of Contents

List of Figures

List of Tables

Acknowledgments

Without people, the secrets of the universe are worth shit.

Mathew Ackerman, Anchita Addya, Ankur Agrawal, Santiago Aguilar, Colin Aitken, Felipe Alamos, Ben Allen, Chris Anderson, Gustav Anderson, Henry Ando, Alexander Anferov, Evan Angelico, Jenni Antane, Greg Anthony, Adam Antoszewski, Natasha Antropova, Yuta Asano, Alexandra Asbah, Andrew Ascott, Ahmad Awais, Nora Bailey, Elizabeth Bain, Yasmine Baktash, Alissa Bans, Saeid Barati, Ben Barber, Rach Barbour, Joshua Barker, Edward Barry, Claire Baum, Lucas Beaufore, Paula Begne, Kathleen Beilsmith, Asher Berlin, Carly Bertrand, Lauren Beversluis, Alexandra Beyrouthy, Moiz Bharmal, Sharba Bhattacharjee, Audrey Bienfait, Tim Black, Jennifer Blanc, Carlos Blanco, Lindsey Bleem, Alexander Bogatskiy, Simon Boron, Alexandre Bourassa, Rufus Boyack, Benjamin Boyd, Koen Breyne, Antoine Brillant, Maddie Brooker, Kings Brooks, Alex Brown, Sarah Brown, Oliver Browne, Andrea Bryant, Patrick Bryant, Arad Bulka, Thomas Burhani, Mary Burkey, Zily Burstein, Olivia Bussone, Clark Butler, Aleksander Durumeriç, João Caldeira, Nathalie Callaert, Tankut Can, Lauryn Carver, Cody Castle, Karla Cavalli, Ross Cawthon, Hugo Ceccato, Laura Cespedes, Javier Chacon, Romit Chakraboty, Srivatsan Chakram, Sara Chamberlin, Hung-Shen Chang, Melissa Chansy, Huanqing Chen, Jingyuan Chen, Mandy Chen, Yangyang Cheng, Wen Han Chiu, Theresa Chmiel, Jungmin Cho, Subhadip Chodhury, Ming-Han Chou, Mriga Chowdhary, Kasey Christiansen, Ula Cichon, Logan Clark, Andrew

Cleland, Mat Cloutier, Katy Colleton, Monika Collins, Sarah Collins, Christopher Conner, Rosemary Cook, Sara Corley, Davi Costa, Delphine Coursault, Annette Crabbe, Janette Crabbe, Peter Crabbe, Steven Crabbe, Sam Craig, Daniel Creedon, Timothy Cronin, Alex Crook, Julian Cuevas, Patrick Cunningham, Jonas Dalmazzo, Jeff Dandoy, Joseph Dang, Daine Danielson, Andrea Daru, Hollie Davis, Julian Day-Cooney, Pratiti Deb, Rachel Dec, Jary Delgado, Tanvi Deshmukh, Craig DeValk, Karia Dibert, Rebecca Diesing, Luisella Difalcis, Chunyang Ding, Mark DiTusa, Pranathi Diwakar, Akash Dixit, Katie Dixon, Zoheyr Doctor, Kristin Dona, Justin Douglas, Peter Duda, Nick Dulchinos, Étienne Dumur, Ryan Duncombe, Maddy Duretete, Daniel Dutcher, Tomasz Ślęàak, Nate Earnest, Maria Łęcka, Alex Edelman, Tahra Eissa, Sebastian Ellis, Silvia Ellis, Jake Ellowitz, Reed Essick, Francesca Falzon, Lisa Fan, Amanda Farah, Kavon Farvardin, Michael Fedderke, Jacob Feder, Adina Feinstein, Hannah Fejzic, Melissa Fender, Nicole Fields, Peter Fields, Patrick Figliozzi, Heidi Finnane, Maya Fishbach, Michael Florian, Will Foreman, Caris Fox, Chiara Fratto, Andrea Frazier, Julian Freed-Brown, Max Freedman, Erin Fry, Joel Fuentes, Nicholas Fuhrmann, Victor Gai, Fraol Galan, Joey Gamblin, Jill Gandhi, Lou Gar, Samantha Gartner, Annabeth Gellman, Alex Georgakopoulos, Akhil Ghanta, Indranil Ghosh, Kyle Gibson, Emily Gilbert, Elena Glen, Simas Glinskis, Pranav Gokhale, Joseph Golec, Sam Gonzalez, Graeme Gossel, Timothy Grabnic, Pierre Gratia, Joel Grebel, David Grossnickle, Daniel Grzenda, Eyjólfur Guðmundsson, Cesar Guerrero, Spencer Guo, Lipi Gupta, Shobit Gupta, Katie Hadida, Haley Hager, Steve Hammersmark, Ian Hammock, Joshua Hampton, Ryo Hanai, Patrick Hanley, Alex Hanselman, Chris Hansen, Grace Hansen, Richard Hansen, Andrew Hard, Reid Harris, John Hartnett, Matt Hawes, Kevin He, Lancelot Henry, Daniel Herbst, James Higgie, Jake Higgins, Pieter Hoekstra, Alex Hoffman, Daniel Holz, Lesya Horyn, Rei Hoshi, Sean Howe, Alec Hryciuk, Wei-Han Hsaio, Kaeli Hughes, Suzy Hur, Maxwell Hutchinson, Christopher Iacovetti, Connor Imes, Ram Itani, Hannah Jackson, Sonia Jaffe, Marta Jamrozik, Zack Jarin, Kate Jesse, Aniket Joglekar, Russell Johnson, Wesley Jolley,

Mike Jones, Anita Joshi, Yash Joshi, Olivia Junell, Yu Kambe, Judith Kamm, Anastasia Kannis, Michael Kardas, Jonathan Karsch, Yael Katz, Will Kay, Ulysses Keevan-Lynch, Maggie Kelty, Jordan Kemp, Megan Kennedy, Alexandra Khoo, Kavia Khosla, Gourav Khullar, Adam Kline, Paulina Knight, Anna Kolarzyk, Gerwin Koolstra, Samuel Kopfinger, Will Koval, Karol Krizka, Martin Kruit, Lindsay Kruse, Kasia Krysztofiak, Nikita Kuklev, Matt Kurley, Putri Kusumo, Kevin Labe, Grace Lacy-Hansell, Sean Laguna, Jonathan Lam, Kara Lamb, Bahareh Lampert, Phil Landry, Samantha Lapp, James Lasker, Misha Laskin, Denise Lau, Bethany Lavelle, Louise Leadbitter, Pablo Lechon, Abhimanyu Lele, Paula Lemos-Costa, Giovani Leone, Hayden Lewis, Mark Lewis, Coco Li, Zimu Li, Armun Liaghat, Chloe Lindeman, Sasha Lindskog, Peter Littlewood, Kimberly Liu, Richard Liu, Lawson Lloyd, Ihar Lobach, Katie Long, Yanan Long, Christian Lopac, Nick Lorenz, Mathew Low, Leah Luben, Andrew Ludwig, Evan Lynch, Adam Maccora, Alexandre Machado, Shae Machlus, Rhea Mahanta, Glenn Mahon, Edward Malachosky, Philip Mansfield, Andrew Mao, Joseph Mastron, Ariel Matalon, Charles Mathews, Chitavi Maulloo, Katrina Maxcy, Travis Maxfield, Erica May, Vivian May, Luigi Mazzenga, Conor Mccaffrey, David McCowan, Lee McCuller, Mary Pat McCullough, Sarah McCusker, Alexander McDonald, Stewart McDonald, Shehan McFadden, Ryan McGeehan, Chris McGilligan, Tim McGilligan, Kaitlin McLean, Cameron McLendon, Nobuko McNeill, Emma McPike, Jonathan Medrano, Sam Meehan, Nikita Mehta, Umang Mehta, Constantinos Melachrinos, Shankar Menon, Jonathan Merker, Aaron Meyer, Chris Meyer, Kevin Miao, Marissa Michelle, Daniel Micheroni, Sanja Miklin, Andrew Miller, Jacob Miller, Lisa Miller, Mary Miller, Myles Minter, Peter Mintun, Omar Mirza, Mark Miskin, Noah Mitchell, Christina Mo, Joseph Mohr, Drew Moore, Wynton Moore, Peter Morfe, Jessy Morgan, Josh Morris-Levenson, Robert Morton, Michael Moses, Brian Moths, Anna Movsheva, Aaron Mowitz, Carson Muir, Sravan Munagavalasa, Julia Murphy, Kieran Murphy, Michael van der Naald, Saispoorthi Nagasamudram, Ravi Naik, Darshana Nair, Lisa Nash, Amruta Nayak, Caner Nazaroglu, Andrew Neil, Alex Nepon,

Andrii Neshchadin, David Newsom, Sam Nichols, Shannon Nicholson, Lisa Noble, Ra'idah Noohu, Will Notini, Torben Noto, Johannes de Nova, Terry O'Brien, Jan Offermann, Dan O'Hanlon, Victoria Okuneye, Joakim Olsson, Kristóf Oltvai, Krisztina Orban, Mark Oreglia, Andrew Oriani, Hannah Orland, Rodrigo Ortiz, Boleszek Osinski, Maddy Oswald, John Otto, Clai Owens, Lukas Palm, Bipul Pandey, Meg Panetta, Stephen Parker, Vivak Patel, Jonty Paul, Gregory Peairs, Ellen Pen, Susan Pen, Sean Pepper, Susana Pérez, Meghan Perez, Stéphane Perrard, Ryan Peters, Annie Phan, Jim Pilcher, Marissa Pioso, Gustaf Piper-Downs, Jason Poh, Jess Pontis, Ben Povey, Geoffrey Povey, Margitta Povey, Nikki Povey, Ross Povey, Sally Povey, Travis Povey, Kartik Prabhu, Ananta Prayitno, Rohail Premjee, Aleksander Promiński, André Pulcherio, Olivia Pura, Hong Qiao, Dylan Quintana, Sony Rain, Karthik Ramanathan, Guillermina Ramirez, Daniel Ramirez-Raftree, Bharat Reddy, Steven Redford, Toby Redman, Huw Rees, Suhail Rehman, David Reid, Omar Reus, Matt Reyer, Abby Reynolds, Gabrielle Roberts, Duncan Rocha, Mathew Rocklin, Anne Ruelle, Dana Russo, Amanda Rynes, Hibiki Sakai, Michael Sala, Jean Salac, Andrew Saldana, Claudio Sansone, Ned Sasamoto, Gautam Satishchandran, Kevin Satzinger, John Savage, Brendan Saxberg, Michael Scaffidi, Karl Schaefer, Martin Scheeler, Colin Scheibner, Jordan Scherer, Nathan Schine, Desiree Schippers, Anthony Schlimgen, Joseph Schneider, Matt Schulte, Eric Schultz, David Schuster, Taryn Sermano, Jack Le Serve, Scott Le Serve, Savdeep Sethi, Emma Severn, Vishy Sharma, Alan Shen, Steven Shenton, Nora Shipp, Sergei Shmakov, Carlos Sierra, Julian Silva, Rachel Silvert, Kevin Singh, Kartik Singhal, Daniel Smith, Emily Smith, Rebecca Smith, Siddhartha Sohoni, William Sokolowsky, Pearl Somboonsong, Vishal Soni, Daniel Southall, Chris Stamper, Giordon Stark, Mark Stone, Dustin Stuart, Brad Studnitzer, Erica Sturm, Aziza Suleymanzade, Shreya Sutariya, James Swann, Kirk Swanson, Miranda Swanson, Dean Swimmer, Toka Tarek, Noah Taylor, Golnar Teimouri, Savannah Thais, Vaidehee Thatte, Alexis Thomas, Ryan Thomas, Lena Thomer, Rebecca Thompson, Grace Thornton, Michael Tobar, Jonathan Trisnadi, Syrian Truong,

Luke Tucker, Lynn Tung, Phil Turski, Michal Ugarenko, Trevor Ung, Amit Vainsencher, Andrew Valentine, Lisa VanAusdall, Bodhi Vani, Louis Varriano, Darren Veit, Ilana Ventura, Mohit Verma, Thoams Videbaek, Abigail Vieregg, Erzsebet Vincent, Yau Wah, Peyton Walker, Sally Walker, Robin Walters, Yifan Wang, Billy Warner, Sasha Warren, Noah Wasserman, Elyse Watkins, Laura Watkins, Andrea Watson, Kristin Watson, Simon Watson, Jordan Webster, Kuang Wei, Gabriel Weiderpass, Robert Weinbaum, Cheyne Weis, Adam Weiss, Lauren Weiss, Leah Weiss, Erica Westerman, Vance Wheeler, Andrew White, Samuel Whiteley, Damien Wilkie, Gareth Williams, Jason Williams, Lauren Williams, Nicholas Williams, Olivia Wine, Ryan Wood, June Wu, Miles Wu, Xuntao Wu, Zach Wziontka, Huan Xu, Jian Xu, Rachana Yajur, Haoxiong Yan, Ge Yang, Alyson Yee, Hannah Yi, Jake Zappala, Katarzyna Zawieracz, Cyrus Zeledon, Ben Zhang, Jerry Zhang, Walter Zhang, Youpeng Zhong, Kat Ziegler, Tracey Ziev, Johnny Zimmerman.

Abstract

Quantum technology is pivotal to the future of physics, whether through quantum computing and simulation, or quantum sensing and measurement. All sorts of systems exhibit quantum phenomena and many different platforms are being developed for quantum information processing. Connecting these disparate quantum systems together is key to exploiting the advantages of each and growing the potential applications of quantum hardware.

One of the most popular quantum computing platforms is superconducting qubits, using microwave-frequency electronics at cryogenic temperatures, which have promising results but are confined to operating within dilution refrigerators. In order to communicate through ambient environments, the ability to convert quantum signals between microwave electronics and infra-red fiber optics is highly sought after. Of the various approaches to this challenge, a promising candidate is optomechanical crystal resonators that use simultaneous photonic and phononic crystals to create a co-localized cavity coupling infra-red electromagnetic modes to microwave-frequency acoustic modes, which then via electromechanical interactions can undergo direct transduction to electronics. The majority of work in this area has been on one-dimensional nanobeam resonators which provide strong optomechanical couplings of $g_{\mathrm{om}} \sim 1\,\mathrm{MHz}$ but, due to their geometry, suffer from an inability to dissipate heat produced by the laser pumping required for operation.

Here we explore two-dimensional optomechanical crystal resonators, as structures with improved heat conduction properties, for their potential application in quantum microwave-electronic to infra-red optic transduction. Gallium arsenide is used as our material of choice due to its native piezoelectricity and favourable mechanical resonance frequencies. We conclude by adapting the vertebrae quasi-two-dimensional optomechanical resonator design to gallium arsenide and demonstrating a device with $\not{g}_{\mathrm{om}} \approx 650\,\mathrm{kHz}$.

This thesis is structured with a succinct main matter, that tells the story of developing a two-dimensional optomechanical crystal resonator, and a library of appendices that provide more elaborate details. Throughout, Einstein notation is generally assumed where appropriate.

CHAPTER 1

Introduction

The development of technology exploiting the features of quantum mechanics has gathered great momentum over the past couple of decades, spurred on by the promise of applications in quantum computing [1, 2] and quantum communication [3, 4]. Science towards these goals have lead to improved control over quantum phenomena, including macroscopic quantum objects [5–7], quantum limited noise [8–12], and quantum sensing [13, 14]. Indeed the future of high precision measurement and detection in physics will need to take place at the quantum limit and take advantage of quantum effects.

1.1 Quantum mechanics

Whilst now a century old [15], the theory of quantum mechanics has only recently been able to be probed and manipulated at macroscopic scales. The basic premise of quantum mechanics is that the state of a system is described by a unit vector in a complex Hilbert space and observables are self-adjoint operators [16]. These operators can be non-commuting, leading to a discretization of possible states and quantized values, hence the name quantum mechanics. As a result of this formulation, outcomes of observations are described by probability distributions, and states can be a linear combination of other states (superposition). Additionally, when combining quantum systems, the subsystem states can be correlated in a way that classical systems can not (entanglement). This leads to a truly magical theory of how the universe works, allowing objects to go through walls, where without determinism free will can exist, and despite extremely low odds[1] water can be turned into wine.

1. Clearly not a problem for a divine being.

1.2 Quantum computing

Quantum computing entails the development of a computer architecture where the fundamental bits, and operations between them, are quantum in nature. At large scales, a quantum computer has the potential to solve problems and perform algorithms beyond the reach of classical computers [2, 17]. Famously this includes Shor's algorithm [18] to factor a product of two prime numbers and break the widespread cryptography system of RSA [19]. Of particular interest to academic and industrial communities, however, is their ability to better simulate systems that are fundamentally quantum mechanical in nature such as complicated chemical structures [20–22].

Many different platforms for quantum computing are being developed by various research groups around the world. These include ion traps [23, 24], neutral atoms [25–28], silicon quantum dots [29–36], floating electrons [37–39], topological braids [40, 41], and superconducting circuits [42–46].

Superconducting circuits represents one of the most developed archetypes [47, 48], garnering significant investments from major technology companies [49–52]. The basic building block of this approach is a superconducting (no resistive loss) electrical resonator (capacitor, inductor) in which the inductor has been replaced by a Josephson junction [53–55] that exhibits non-linear inductance. This non-linearity produces anharmonicity in the energy levels, allowing the first two to be uniquely addressed as quantum bit (qubit) [56, 57]. To interface with current high-frequency electronic technology, and sit above thermal noise backgrounds, these qubits are typically built in the microwave C band of $[4, 8]\,\mathrm{GHz}$, and housed in dilution refrigerators at $\sim 10\,\mathrm{mK}$.

Whilst microwave frequencies are suitable for quantum signal processing within a dilution refrigerator, quantum state transfer to the outside at ambient temperatures requires frequen-

cies $\gtrsim 10\,\mathrm{THz}$ to avoid being swamped by thermal noise. To this end, and in the interest of being able to connect more quantum systems together, we are interested in quantum transduction between vastly different frequencies. In this thesis we are particularly looking at conversion between $\sim 4\,\mathrm{GHz}$ microwave electronics and $\sim 195\,\mathrm{THz}$ infra-red electromagnetic waves in fiber optics.

1.3 Quantum transduction

The goal of quantum transduction is to transfer a quantum state between systems, often at vastly different frequencies. A common intermediary for frequency conversion are mechanical acoustic modes due to their ability to couple to most everything. For microwaves to infra-red there are a variety of approaches being investigated [58–61], these include the direct but weak electro-optic effect [62–70], membrane in the middle [9, 71–82], magnomechanics [83–87], quantum dots in surface acoustic waves resonators [88–92], quantum dots in electric resonators [93–95], high overtone bulk acoustic resonators [96–100], spin defects [101–104], erbium ions [105–108], optomechanical scattering tracks [109–114], and optomechanical crystal resonators[115–137].

Optomechanical crystal resonators work by using a simultaneous photonic and phononic crystal to create a cavity with both optic and acoustic modes which can couple via an optomechanical interaction [138–142]. The acoustic mode is made to be at microwave frequencies, and piezoelectric materials are used to convert this to an electrical excitation. Here we investigate two-dimensional optomechanical crystals in a natively piezoelectric material as a candidate system for quantum microwave electronic to infra-red transduction.

CHAPTER 2

Physics

In this chapter we introduce physics theory applicable to the operation of a two-dimensional optomechanical crystal quantum electro-opto-mechanical transducer. Detailed derivations can be found in corresponding appendices.

2.1 Electro-opto-mechanical transfer

Quantum state transfer between an infra-red optical resonator and microwave frequency electronic resonator can be carried out with a mechanical intermediary that couples to both. The Hamiltonian describing this interaction is summarized by

$$\hat{H} \ni \underbrace{\hbar\,\omega_{\mathrm{o}}\,\hat{a}^{\dagger}\,\hat{a}}_{\substack{\text{optical}\\ \text{resonator}}} + \underbrace{\hbar\,\omega_{\mathrm{m}}\,\hat{b}^{\dagger}\,\hat{b}}_{\substack{\text{mechanical}\\ \text{resonator}}} + \underbrace{\hbar\,\omega_{\mathrm{e}}\,\hat{c}^{\dagger}\,\hat{c}}_{\substack{\text{electrical}\\ \text{resonator}}} + \underbrace{\hbar\,g_{\mathrm{om}}\,\hat{a}^{\dagger}\,\hat{a}\,\left(\hat{b}^{\dagger}+\hat{b}\right)}_{\substack{\text{optomechanical}\\ \text{interaction}}} + \underbrace{\hbar\,g_{\mathrm{em}}\,\left(\hat{b}^{\dagger}+\hat{b}\right)\,\left(\hat{c}^{\dagger}+\hat{c}\right)}_{\substack{\text{electromechanical}\\ \text{interaction}}},$$

ignoring constant shifts and external couplings.

The optomechanical Hamiltonian is derived in App. C but can be easily conceptualized as a Fabry-Pérot cavity which has one side connected to a spring. Mechanical oscillations in displacement change the length of the cavity and hence resonant frequency, then linearizing this interaction gives the above expression. It should be noted therefore, this form is only valid when the displacement oscillations are small compared to the total length of the cavity. The electromechanical interaction is derived in App. K, where an additional electric field produced by piezoelectricity drives the electric resonator circuit.

With the addition of a strong optical pump $\hbar\,\hat{a}^{\dagger}\,L\,\exp[-\mathrm{i}\,\omega_{\mathrm{L}}\,t]$ and cold mechanics, the

optomechanical interaction can be linearized. Then, if the optical pump frequency is red-detuned away from the optical resonance by the mechanical resonance frequency, $\omega_{\mathrm{L}} = \omega_{\mathrm{o}} - \omega_{\mathrm{m}}$, we can select for an optomechanical swapping interaction. Furthermore, if the electronics and mechanics are matched in frequency, the electromechanical interaction will likewise provide swap terms under the rotating wave approximation. Rotating the optics into the frame of the laser pump, our Hamiltonian can now be surmised as

$$\hat{H}_{\substack{\mathrm{rot}\\\mathrm{lvl}}} \ni \underbrace{\hbar\,\Delta_{\mathrm{om}}\,\hat{a}^{\dagger}\,\hat{a}}_{\substack{\text{(rotated) optical}\\\text{resonator}}} + \underbrace{\hbar\,\omega_{\mathrm{m}}\,\hat{b}^{\dagger}\,\hat{b}}_{\substack{\text{mechanical}\\\text{resonator}}} + \underbrace{\hbar\,\omega_{\mathrm{e}}\,\hat{c}^{\dagger}\,\hat{c}}_{\substack{\text{electrical}\\\text{resonator}}} + \underbrace{\hbar\,g_{\mathrm{om}}\left(\bar{a}^{*}\,\hat{a}\,\hat{b}^{\dagger} + \bar{a}\,\hat{a}^{\dagger}\,\hat{b}\right)}_{\substack{\text{optomechanical}\\\text{swap}}} + \underbrace{\hbar\,g_{\mathrm{em}}\left(\hat{b}^{\dagger}\,\hat{c} + \hat{b}\,\hat{c}^{\dagger}\right)}_{\substack{\text{electromechanical}\\\text{swap}}} ,$$

where

$$\Delta_{\mathrm{om}} = \omega_{\mathrm{o}} - \omega_{\mathrm{L}} + g_{\mathrm{om}}\left(\bar{b}^{*} + \bar{b}\right) \approx \omega_{\mathrm{m}} \approx \omega_{\mathrm{e}} ,$$

and $\bar{a}$, $\bar{b}$, $\bar{c}$ are the linearized-around averages which scale with optical pump strength L,

$$\bar{a} = \frac{-\mathrm{i}\,L}{\mathrm{i}\,\Delta_{\mathrm{om}} + \frac{\gamma_{\mathrm{o}}}{2}} , \qquad \bar{b} \approx \frac{-\mathrm{i}\,g_{\mathrm{om}}\,|\bar{a}|^{2} - \mathrm{i}\,g_{\mathrm{em}}\,\bar{c}}{\mathrm{i}\,\omega_{\mathrm{m}} + \frac{\gamma_{\mathrm{m}}}{2}} , \qquad \bar{c} = \frac{-\mathrm{i}\,g_{\mathrm{em}}\,\bar{b}}{\mathrm{i}\,\omega_{\mathrm{e}} + \frac{\gamma_{\mathrm{e}}}{2}} .$$

Full details and derivations can be found in App. J and App. K. In this form it is straightforward to see how an optical or electronic excitation can be swapped through the mechanics with couplings $\bar{a}\,g_{\mathrm{om}}$ and g_{em}.

Adding baths (see App. I), denoting internal losses as γ^{int}, coupling the optics to a symmetric bi-directional waveguide, each side $\gamma_{\mathrm{o}}^{\mathrm{wg}}$, and connecting an electronic transmission line, $\gamma_{\mathrm{e}}^{\mathrm{tx}}$, we obtain the system given in Fig. 2.1 with full input-output equations of motion given in App. K. With

$$\gamma_{\mathrm{o}} = \gamma_{\mathrm{o}}^{\mathrm{int}} + 2\,\gamma_{\mathrm{o}}^{\mathrm{wg}} , \qquad \gamma_{\mathrm{m}} = \gamma_{\mathrm{m}}^{\mathrm{int}} , \qquad \gamma_{\mathrm{e}} = \gamma_{\mathrm{e}}^{\mathrm{int}} + \gamma_{\mathrm{e}}^{\mathrm{tx}} ,$$

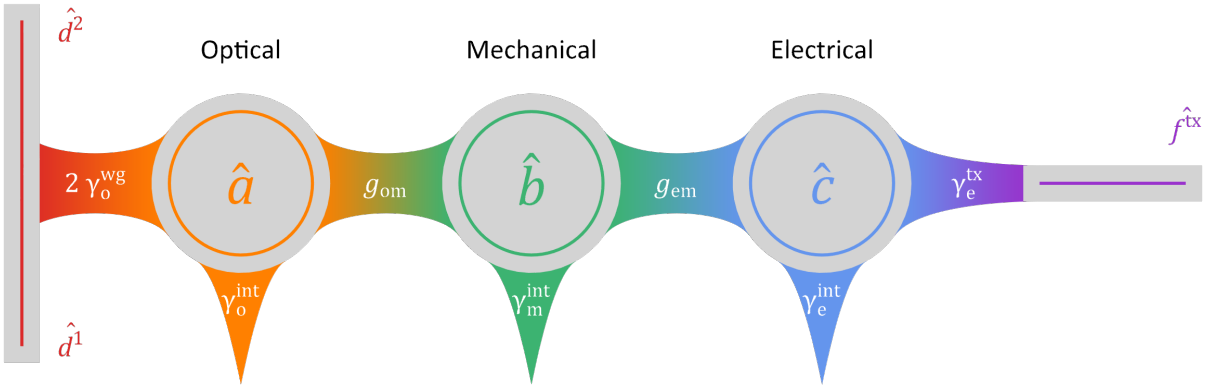

Figure 2.1: Schematic of the electro-opto-mechanical system. Operators $\hat{a}$, $\hat{b}$, $\hat{c}$ represent our optical, mechanical, and electrical resonators, whilst $\hat{d}$ are our optical input-output ports and $\hat{f}$ is our electrical transmission line port.

we can define cooperativities

$$\mathcal{C}_{\mathrm{om}} = \frac{4\,{g_{\mathrm{om}}}^2\,|\bar{a}|^2}{\gamma_{\mathrm{o}}\,\gamma_{\mathrm{m}}}\,, \qquad\qquad \mathcal{C}_{\mathrm{em}} = \frac{4\,{g_{\mathrm{em}}}^2}{\gamma_{\mathrm{e}}\,\gamma_{\mathrm{m}}}\,,$$

which serve as figures of merit for transduction performance. The optic to microwave transmission (either direction), worked out in App. K, is then

$$T_{\mathrm{o}\leftrightarrow\mathrm{e}} = \frac{4\,\frac{\gamma_{\mathrm{o}}^{\mathrm{wg}}}{\gamma_{\mathrm{o}}}\,\frac{\gamma_{\mathrm{e}}^{\mathrm{tx}}}{\gamma_{\mathrm{e}}}\,\mathcal{C}_{\mathrm{om}}\,\mathcal{C}_{\mathrm{em}}}{\left(1+\mathcal{C}_{\mathrm{om}}+\mathcal{C}_{\mathrm{em}}\right)^2}\,. \tag{2.1}$$

In order to have the detuned pump provide the appropriate three wave mixing, $\omega_{\mathrm{o}} = \omega_{\mathrm{L}} + \omega_{\mathrm{m}}$, for this transmission, our optomechanical system should ideally be sideband resolved. That is, the optical resonance width is less than the mechanical frequency so that the pump can be outside the optical resonance, $\frac{\gamma_{\mathrm{o}}}{2} < \omega_{\mathrm{m}}$.

This transmission represents the output when all other inputs, including internal thermal baths are zero. In a real experiment, thermal population of the mechanical and electrical resonators will add noise to the output. For this reason, being below microwave frequencies or

outside of a dilution refrigerator makes low-noise conversion difficult. An effective transducer will have less than one added noise quantum during the swap process.

Inspecting (2.1) we see that transmission increases toward $\frac{\gamma_{\mathrm{o}}^{\mathrm{wg}}}{\gamma_{\mathrm{o}}}\frac{\gamma_{\mathrm{e}}^{\mathrm{tx}}}{\gamma_{\mathrm{e}}}$ as $\mathcal{C}_{\mathrm{om}}$ and $\mathcal{C}_{\mathrm{em}}$ are increased together. Of particular importance, $\mathcal{C}_{\mathrm{om}}$ is proportional to optical pump power, and thus whilst $\mathcal{C}_{\mathrm{om}} < \mathcal{C}_{\mathrm{em}} + 1$ transmission can be improved by driving the pump harder. In practice however, heating and non-linear effects from excessive pump powers can quickly create problems. Setups more able to dissipate unwanted heat are thus beneficial by allowing stronger optical pumping. In some situations, pulsed pumping can be employed to help mitigate heat build-up [143].

An alternative method for state transfer involves blue-detuning the optical pump to provide a pair generation term with $\bar{a}\,\hat{a}^{\dagger}\,\hat{b}^{\dagger}$, and create entangled optical photon, mechanical phonon pairs. A teleportation scheme can then be used to transfer states between the optical and electronic sides [144–147]. This method however requires $g_{\mathrm{em}} > \bar{a}\,g_{\mathrm{om}}$ which, depending on device properties, may be less efficient.

2.2 Optomechanical crystals

An optomechanical crystal is a periodically structured material that is simultaneously both a phononic crystal and photonic crystal [148]. In each case, the translational symmetry of the medium impacts the dispersion relations for propagating waves at wavelengths on the order of the periodic crystal lattice distance, leading to phenomena not present in homogeneous media. Of particular interest is the realization of band gaps: intervals of frequency where wave propagation is forbidden. For nanofabricated devices, these periodic structures are typically etched holes in a suspended beam or plate, such that we are considering a two-dimensional patterned plane.

The translational symmetry present within a crystal is characterized by a set of linearly independent lattice vectors (primitive vectors) $\{\vec{a_i}\}_{i=1}^{n}$ such that material properties, M, satisfy

$$M\big(\vec{x} + \textstyle\sum_{i=1}^{n} c_i\,\vec{a_i}\big) = M(\vec{x}) \quad : \quad \{c_i\}_{i=1}^{n} \subset \mathbb{Z}\,.$$

For photonic crystals, the material properties are permittivity and permeability, whilst for phononic crystals it's density, stiffness-compliance, and piezoelectric couplings, or perhaps the existence of solid material at all. The infinite set of discrete points $\sum_{i=1}^{n} c_i\,\vec{a_i}$ is called the Bravais lattice, and a fundamental repeating region is called a unit cell. The number of independent lattice vectors, n, is the dimension of the crystal.

Propagating plane waves through the crystal obey 'translational' symmetry of wavevectors according to the reciprocal lattice. If $\{\vec{a_i}\}_{i=1}^{n}$ are the primitive lattice vectors, then the primitive reciprocal lattice vectors are $\{\vec{b_i}\}_{i=1}^{n}$ and must satisfy $\vec{a_i} \cdot \vec{b_j} = 2\,\pi\,\delta_{i\,j}$. In matrix form we can write this as

$$\underline{\underline{A}}^{\mathsf{T}} \cdot \underline{\underline{B}} = 2\,\pi\,\underline{\underline{\mathbb{I}_n}} \quad : \quad \begin{array}{l} \underline{\underline{A}} = \big[\vec{a_1}\big|\vec{a_2}\big|\ldots\big|\vec{a_n}\big]\,, \quad A_{i\,j} = \big(\vec{a_j}\big)_i \\ \\ \underline{\underline{B}} = \big[\vec{b_1}\big|\vec{b_2}\big|\ldots\big|\vec{b_n}\big]\,, \quad B_{i\,j} = \big(\vec{b_j}\big)_i \end{array}\,,$$

which has the simple solution $\underline{\underline{B}}^{\mathsf{T}} = 2\,\pi\,\underline{\underline{A}}^{-1}$.

Photonic crystal behaviour is described by classical electrodynamics (Maxwell's equations) in a medium with Floquet (periodic) boundary conditions. For completeness, governing equations are given in App. A. Phononic crystal behaviour is described by continuum solid mechanics for elastic media (Hooke's law), with piezoelectricity included as needed, and similar Floquet boundary conditions. The mathematical description is outlined in App. B.

A one-dimensional repeating pattern over a two-dimensional plane can be described by one of seven frieze groups. Of these, the 'most symmetric' is p2mm which includes translation and two mirror reflections. For a two-dimensional repeating pattern over a two-dimensional plane, there are seventeen wallpaper groups. The crystallographic restriction theorem limits the smallest angle of rotational symmetry to be $\pi/3$ (i.e. order 6), and the 'most symmetric' group which also includes mirror reflections is then p6m. In terms of the reciprocal lattice space, the more symmetries that exist the more restricted the unique fundamental domain becomes, and the less (inverse) area the dispersion relations cover. One might expect then that greater symmetric patterns lead to more and wider band gaps appearing.

2.2.1 Wallpaper group p6m lattice

With full crystallographic name p6mm, this wallpaper group forms a hexagonal (or double triangular) tiling of the plane with $\pi/3$ rotational symmetry and mirror symmetries parallel, perpendicular, and between the two primitive lattice vectors. The fundamental region for this pattern is half an equilateral triangle that is then translated and flipped to cover the plane. For a lattice spacing length a, the primitive lattice vectors are[1]

$$\vec{a_1} = \begin{pmatrix} a \\ 0 \end{pmatrix}, \qquad \vec{a_2} = \begin{pmatrix} \frac{a}{2} \\ \frac{\sqrt{3}\,a}{2} \end{pmatrix}.$$

The reciprocal lattice vectors are thus

$$\vec{b_1} = \begin{pmatrix} \frac{2\,\pi}{a} \\ \frac{-2\,\pi}{\sqrt{3}\,a} \end{pmatrix}, \qquad \vec{b_2} = \begin{pmatrix} 0 \\ \frac{4\,\pi}{\sqrt{3}\,a} \end{pmatrix}.$$

1. By convention, other choices are allowed.

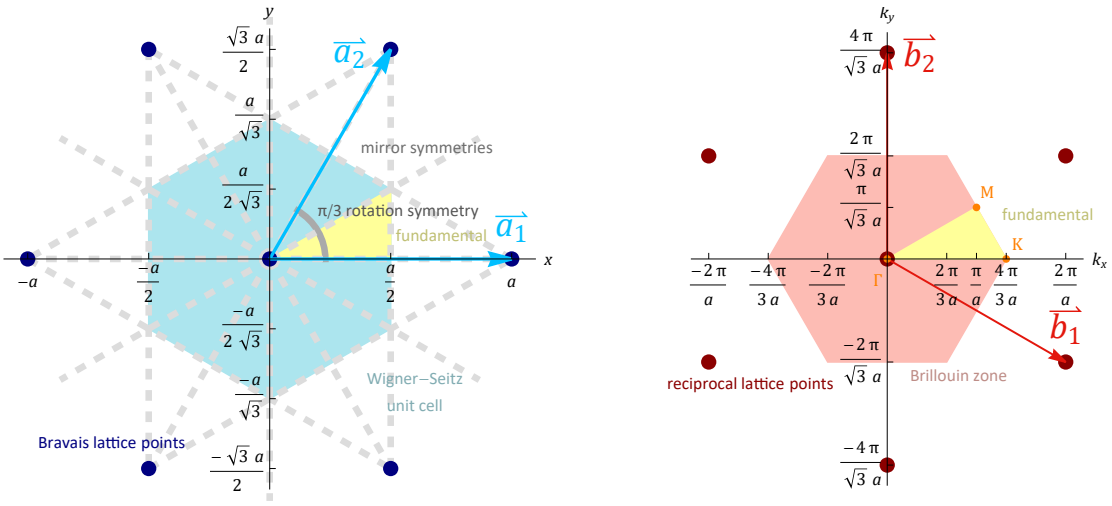

Figure 2.2: Wallpaper group p6m (left) lattice and (right) reciprocal lattice.

Reciprocal lattices inherit the same symmetries and thus there is a similar fundamental reciprocal region that is repeated. The corners of this region are given special names

$$\Gamma = \begin{pmatrix} 0 \\ 0 \end{pmatrix}, \qquad \mathrm{M} = \begin{pmatrix} \frac{\pi}{a} \\ \frac{\pi}{\sqrt{3}\,a} \end{pmatrix}, \qquad \mathrm{K} = \begin{pmatrix} \frac{4\,\pi}{3\,a} \\ 0 \end{pmatrix}.$$

A diagram of the lattice, and its reciprocal, along with unit cells and named points is given in Fig. 2.2

If the third dimension, which we will call z, is a finite thickness, e.g. a suspended membrane with straight side-wall holes, there exists is a mirror symmetry in the z axis about the central plane of the slab. Electromagnetic or acoustic modes in the slab can then, following Ap D, be classified as either z mirror symmetric ($\overset{+}{z}$) or z mirror antisymmetric ($\overset{-}{z}$). With the right pattern it's possible to achieve complete phononic band gaps that do not permit any acoustics, and $\overset{+}{z}$ photonic band gaps that prohibit z mirror symmetric electromagnetic modes. Whilst a complete photonic band gap would be desirable, it is difficult to achieve. Fortunately the fiber optic modes, optical grating couplers (see App. V), and suspended

beams (see App. S) select for $\overset{+}{z}$ modes.

Simulations of specific optomechanical crystals, their dispersion plots, and band gaps are available in App. U.

2.2.2 Defect cavities

A defect in an optomechanical crystal with band gaps will create a region where waves of those otherwise gapped frequencies can locally exist, with the surrounding crystal acting as a wall. If the size and shape of the defect is appropriate then constructive interference can occur for particular gapped frequencies, giving rise to resonators. Should the cavity support co-localized acoustic and electromagnetic resonances, then optomechanical coupling can occur between them.

Given a geometry with material properties, acoustic displacement mode profile $\vec{Q}(\vec{x})$, and electric mode profile $\vec{E}(\vec{x})$, the optomechanical coupling g_{om} appearing in Sec. 2.1 can be calculated following the derivation in App. C. The two major contributions to the optomechanical coupling come from the moving boundary effect and photo-elastic effect. Moving boundary is the process described by the example in Sec. 2.1 where the acoustic oscillations, happening on a much slower time scale than electromagnetic oscillations, deform the resonator's shape affecting the electromagnetic resonance. In the reverse direction, photon pressure/scattering exerts force on the acoustic resonator's boundaries. For infinitesimal displacements, the effect can be linearized, and computed with a surface integral of the fields over the resonator's boundary, given by (C.14). The photo-elastic effect is the change in electric permittivity in response to mechanical strain. Acoustic oscillations cause local oscillations in strain and in turn local oscillations in permittivity that influence the electromagnetic resonance. In the reverse direction, photon propagation through the internal

material, via a series of scattering events, can impart local strain. At first order the interaction is characterized by the photo-elastic tensor (property of the material), and the effect computed with a volume integral over the resonator, given by (C.19). Both effects can be generalized to changes in electric permittivity from displacements, whether that be by moving the boundaries (medium interfaces) or internal material couplings.

Symmetries

If the optomechanical cavity resonator has mirror symmetries then the resonator modes can be categorized by those symmetries as detailed in App. D. Proved in App. E, if the acoustic mode has any mirror antisymmetry, there will be no optomechanical coupling. As such, we require mechanical resonance displacement fields to be mirror symmetric (when possible) to see any coupling to electromagnetic fields.

In addition to the symmetries provided by the optomechanical crystal pattern and cavity shape, we also need to consider orientation with respect the solid material atomic lattice and symmetries therein. Mirror symmetries in the cavity need to be lined up with mirror symmetries in the material.

CHAPTER 3

Design

In this chapter we go over the various design choices for our optomechanical crystal devices.

3.1 Dimensionality

Whilst one-dimensional optomechanical crystals have proved very successful (see App. Δ) with demonstrated couplings of $g_{\mathrm{om}} \sim 1\,\mathrm{MHz}$, they suffer from their poor ability to dissipate heat. As discussed in Sec. 2.1, this limits the optical pump power that can be used and hence the optomechanical coupling rate. One approach to improve heat dissipation is to use a two-dimensional optomechanical crystal which can support acoustic propagation in all planar directions, as well as simply provide a greater cross-sectional area for heat conductance. To this end, we explored two-dimensional optomechanical crystal system for transduction.

Additionally, two-dimensional optomechanical crystals allow the possibility of waveguides being crafted through them, as has been demonstrated with photonic crystals [149–151]. With careful design, waveguides can be engineered to only allow mechanics or optics to pass. One major drawback of this functionality, however, is the difficulty in tuning extrinsic couplings between waveguides and defect cavity resonators. The waveguide size, and cavity distance, are locked to the crystal lattice.

Unfortunately, it was found that full two-dimensional optomechanical crystal resonator designs seemed to exhibit less optomechanical coupling and lower quality factors than their one-dimensional counterparts. This has lead to quasi-two-dimensional resonators being developed [152] where the design is essentially a one-dimensional optomechanical crystal resonator embedded in a two-dimensional crystal waveguide.

3.2 Material

The electromechanical coupling is most easily carried out with a piezoelectric material, however the optomechanical element can be different. In Ref. [122] silicon is used as the base material with aluminium nitride deposited to create localized regions for piezoelectric interaction. This additional interface is a source of loss, so it was decided to use a single piezoelectric material for the entire device.

Commonly available piezoelectric substrates are aluminium nitride (AlN), gallium arsenide (GaAs), and lithium niobate ($LiNbO_3$). Based on previous work [120, 121], aluminium nitride was found to be sub-optimal for optomechanical coupling. Lithium niobate has a significantly greater piezoelectric coupling than gallium arsenide, but is a physically harder material with fabrication challenges for etching smooth straight holes. Gallium arsenide, however, has a strong history of use in optomechanical devices [77, 114, 123, 125, 128, 153–158].

Importantly, gallium arsenide has a favourable speed of sound such that, for two-dimensional optomechanical crystal patterns, when photonic band gaps are covering 194 THz, the phononic band gap is in the $[3, 5]$ GHz region where we would like to interface with microwave electronics. For this and the above reasons, gallium arsenide was the material of choice. Full details on relevant material properties for gallium arsenide are available in Sec. M.1.

There are non-idealities to working with gallium arsenide, however. Firstly, some reaction between the aluminium gallium arsenide sacrificial layer, the chlorine etch, and hydrofluoric acid release produced debris that was difficult to clear. Secondly, gallium arsenide is comparatively an atomically heavy substrate that produces significant electron back scatter during electron beam lithography. Thirdly, the piezoelectric coupling tensor for gallium arsenide is composed of 'twist' elements that are not optimal for interdigitated transducers [124].

3.3 Crystal pattern

Our optomechanical crystal pattern is created by patterning air holes through a suspended slab of material. The effectiveness of an optomechanical pattern is discerned through its acoustic and electromagnetic dispersion relations. A useful pattern will exhibit large band gaps around the desired frequencies, allowing resonances in defects to be trapped.

On the phononic side, the resonant frequency will need to match the piezoelectric element and microwave electronic components, in particular a superconducting qubit. Interdigitated transducers can be fabricated for any particular frequency $\lesssim 8\,\mathrm{GHz}$ (although matching the resonance of two mechanical elements through fabrication only can be challenging), and superconducting qubits are typically in the region of $[2, 8]\,\mathrm{GHz}$.

On the photonic side, we wish to interface with telecom fiber optic components, i.e. the infrared C band[1] $\lambda \in [1530, 1565]\,\mathrm{nm}$, or approximately $f \in [191, 196]\,\mathrm{THz}$. Comparatively, this is a much smaller relative target and will dictate fine tuning of the optomechanical pattern. As complete band gaps are difficult to come by in photonic crystals, we are primarily interested in z mirror symmetric band gaps, matching the mode type used by grating coupler optical connections (see App. V).

Following the design of photonic crystal resonators [159–164], early two-dimensional optomechanical crystal designs utilized circular holes with a defect cavity [165–173] or slot [73, 174, 175]. Although much harder to fabricate, the snowflake pattern is now commonly used [152, 176–178]. Other shapes such as crosses [179] and shamrocks [180] have been used for phononic crystals.

Deciding to explore other shape possibilities, a wide variety of optomechanical crystal pat-

1. This region has low fiber absorption, atmospheric transmission, and works with erbium doped fiber amplifiers.

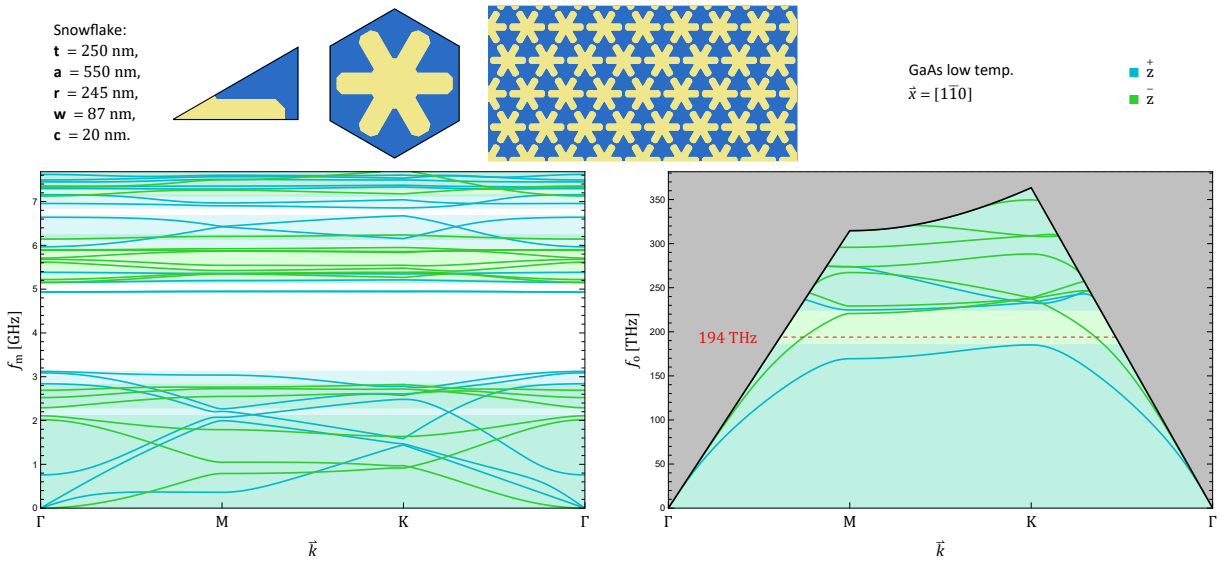

Figure 3.1: Snowflake (parametrized in Sec. U.2.1) in GaAs, (left) acoustic and (right) electromagnetic dispersion plots from finite element simulations.

terns were investigated and are detailed in App. U. Following arguments in Sec. 2.2, wallpaper group $p6m$ was the primary focus for patterns. Some care needs to be taken that the pattern can actually be fabricated. Based on electron beam lithography trials, critical dimensions need to be $\gtrsim 50\,\mathrm{nm}$ and radii of curvature $\gtrsim 15\,\mathrm{nm}$. Obviously, the holes also need to be made such that the solid material is connected and can actually be suspended. Patterns that result in 'drums' and 'bridges' create a more defined separation of acoustic vibrations [139, 176] and lead to wider mechanical band gaps.

Due to its large band gaps, the final choice was the snowflake shaped pattern, as also favoured in other work. A geometric description of the snowflake is given in Sec. U.2.1, and dispersion plots are shown in Fig. 3.1.

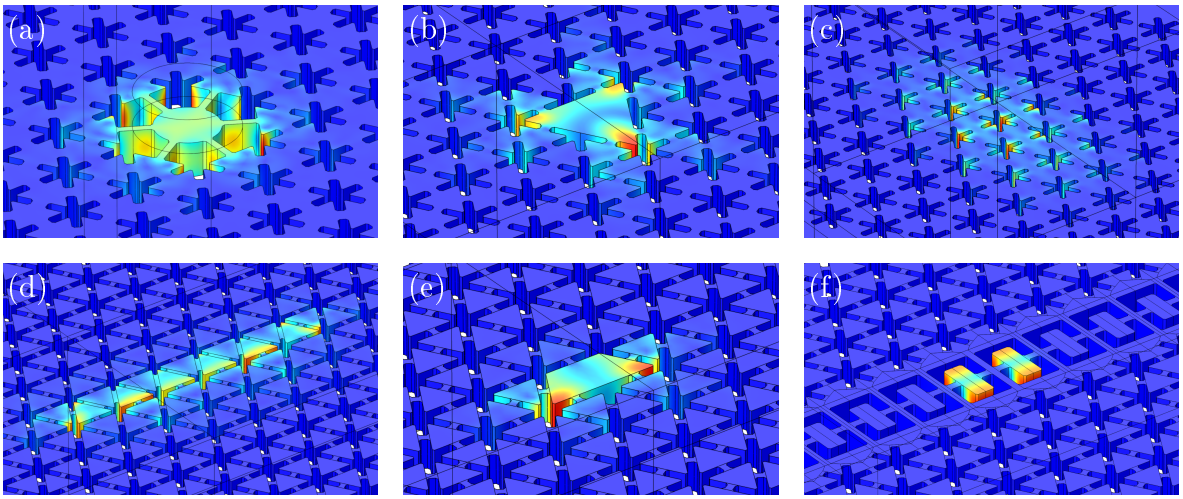

Figure 3.2: Simulations of various two-dimensional optomechanical crystal resonators that were explored. Colour depicts mechanical displacement $|\vec{Q}|$.

3.4 Resonator

Various resonator designs, a selection depicted in Fig. 3.2, were simulated with finite element modelling software [181] using eigenfrequency studies to find resonant modes. Knowledge of the appropriate band gap lets us set limits on the frequency search range. Perfectly matched layers are used for boundaries that extend to infinity and restrictions on the imaginary part of the complex frequency (loss) are implemented to avoid spurious eigenmodes that are not trapped in our resonator. Symmetry planes are used when possible. The self-piezoelectric influence on mechanical modes is small, so violations to enforcing symmetries based on piezoelectric couplings were ignored. Models were generally constructed using scripts [182] to trial a wide range of parameters and designs.

Optomechanical couplings for simulated modes were calculated using the formulas derived in App. C for the moving boundary effect, photo-elastic effect, and electro-optic effect. This involved solving the acoustic and electromagnetic eigenmodes on the same mesh and combining results. Based on (C.11), ideal optomechanical resonators have low mode volumes and concentrate the overlap of electromagnetic and displacement fields.

Early resonator designs attempted to disconnect the tuning of resonator dimensions from that of the crystal pattern by carving out a rather large hole in the crystal and suspending a disc, Fig. 3.2(a). The radius of the disc could then be varied to achieve the desired optical resonance frequency near 194 THz. Some examples and simulations of these resonators are available in App. X, with the best optomechanical couplings calculated to be $g_{\mathrm{om}} \sim 400\,\mathrm{kHz}$. However, far from the whispering gallery mode regime, the simulated optical quality factors of these disc resonators were extremely poor and they were deemed unusable.

Subsequent designs leaned toward minor defects in the crystal pattern and hence resonators whose geometric dimensions were closely tied to that of the optomechanical crystal pattern. To aid designs and simulation, a wide survey of band gaps for different snowflake dimensions were carried out, with some of the results available in Sec. U.6.

One type of design following this approach is a gradient defect, Fig. 3.2(c), where over some region snowflakes with allowed modes at the resonance frequency are used, and a gradient is made to the regular crystal pattern. This style is more analogous to the resonators seen in nanobeams (see App. Δ) where the optomechanical pattern goes through a gradient to a defect region. Compared to the one-dimensional case, in two dimensions this leads to modes that occupy a larger volume and inherently have weaker optomechanical coupling.

The dominant resonator shape that was pursued, however, was that of a small trapezium formed by joining three triangles together within the snowflake crystal pattern, Fig. 3.2(e). These had better simulated quality factors and optomechanical couplings ($g_{\mathrm{om}} \sim 600\,\mathrm{kHz}$) than any other two-dimensional design. Unfortunately, despite relentless fabrication attempts and optimizations, the best resonators had internal quality factors of $Q_{\mathrm{o}}^{0} \sim 2500$, much lower than the estimated 5 k to 10 k minimum needed to have a chance at seeing any optomechanics. Extensive details on these resonators are covered in App. Y.

Recent work from other groups has been in the direction of quasi-2D optomechanical cavity resonators [152, 178, 183], where the cavity resides within a waveguide through the optomechanical crystal and operates in a Fabry-Pérot fashion. Currently, these 'vertebrae' style resonators embedded in snowflakes, Fig. 3.2(f), have only been realized in silicon. Adaptations of this style were carried out to suit gallium arsenide, producing favourable results with simulated $g_{\mathrm{om}} \sim 750\,\mathrm{kHz}$ and large optical quality factors limited by simulation size. Furthermore, gallium arsenide generated acoustic modes at $\sim 4.5\,\mathrm{GHz}$ near the operating frequency of conventional superconducting qubits. Specifics of these designs are detailed in App. Z. Optomechanical crystal resonators of this style were successfully able to be fabricated and measured.

3.5 Waveguides

Basic waveguides can be created within the snowflake crystal pattern by removing a line of snowflakes and/or truncating snowflakes on either side. Unfortunately these waveguides had to be kept straight as angled turns ($2\,\pi/3$) through the lattice did not produce good transmission. Straight waveguides, however, are able to accommodate continuously variable widths, breaking the crystal lattice into two separate regions. This variability proved crucial for controlling coupling to hanger resonators or the design parameters of an in-waveguide resonator.

An alternative variety of waveguide is that of partial waveguides where the snowflake dimensions are slightly varied so that only acoustics or electromagnetic modes are gapped out, allowing the other to propagate. Extensive surveys of snowflake crystal band gaps, Sec. U.6, can be used to help design such structures. An important consideration with partial waveguides is the ability to make a path from the starting snowflake dimensions to a zero-sized snowflake without gapping out the propagating mode. Otherwise it is impossible

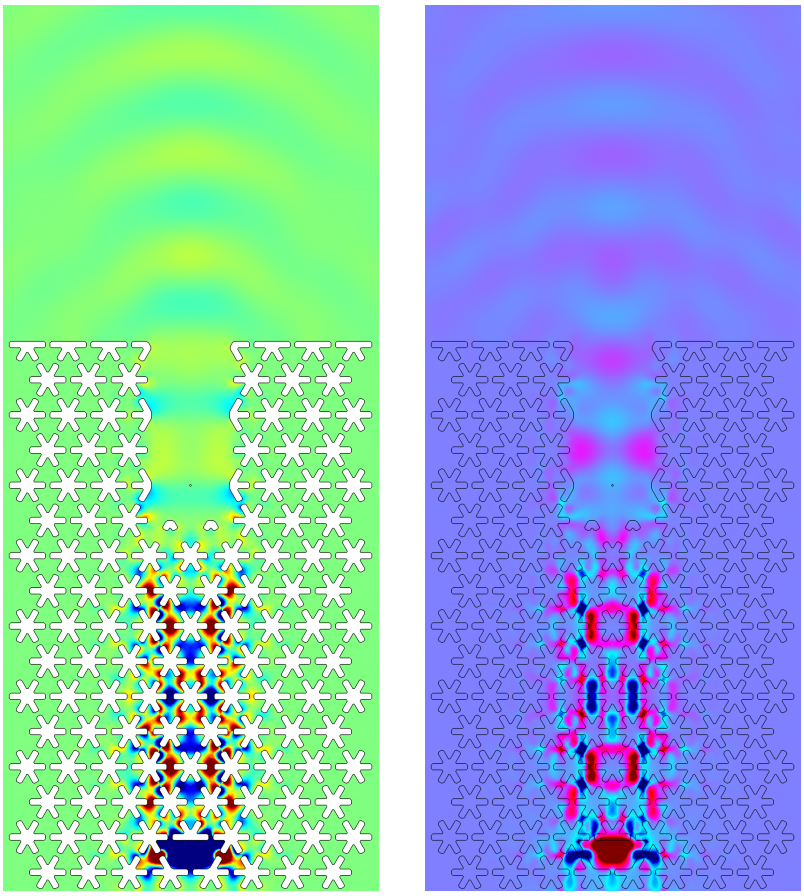

Figure 3.3: Finite element simulation of an acoustic partial waveguide connected to a resonator, showing (left) Q_z and (right) V. The snowflakes that make up the waveguide have slightly shorter r and are transitioned away.

to transition the partial waveguide to an empty one for connecting to other device elements.

Example simulations of partial waveguides are given in Fig. 3.3 and Fig. 3.4. Unfortunately for snowflake dimensions used, the partial optic-only waveguide involved feature sizes that were too small to reliably fabricate.

For acoustic waves that intend to be mapped to electric waves through the piezoelectric interaction, the direction of travel with respect to the gallium arsenide material crystal is critical. Due to the differing symmetry of the piezoelectric coupling tensor, as derived in App. F, the joint mechanical-electric wave must travel in the [110] (or equivalent $\pi/2$

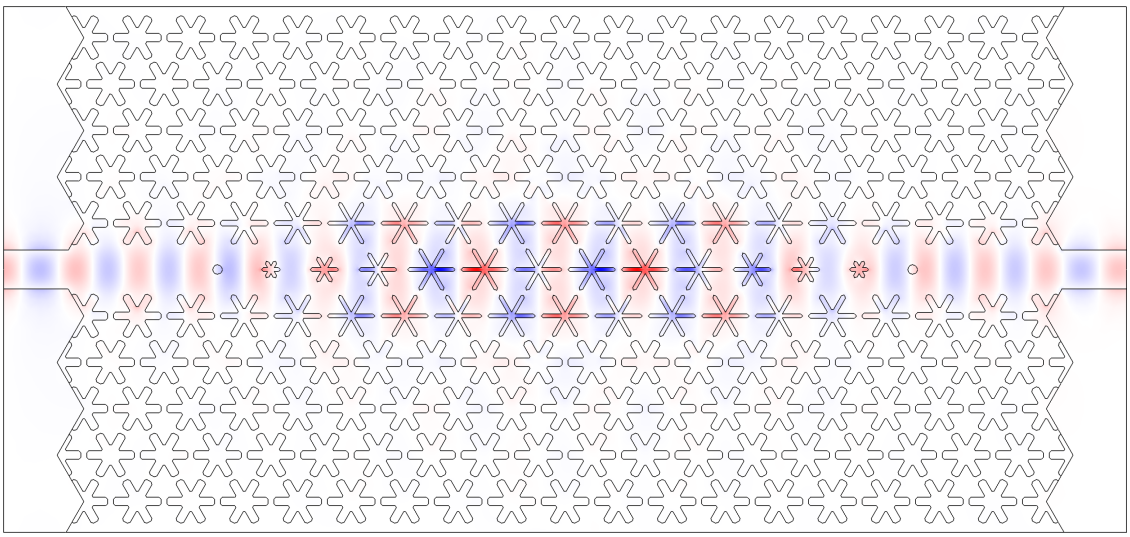

Figure 3.4: Finite element simulation of an electromagnetic partial waveguide, showing E_y. The snowflakes that make up the waveguide have narrower w and gradient to a blank waveguide.

rotations) crystal direction to share the same symmetry properties.

3.6 Optical coupling

Coupling light in and out of our devices is done through grating couplers. These work by creating a Bragg diffraction grating to deflect light into and out of the plane. Whilst these have a poorer efficiency than edge couplers, they make for easier development cycles by allowing many devices to be probed on the central surface area of a chip. Because aluminium gallium arsenide has a similar index of refraction to gallium arsenide our optical couplers had to be suspended, requiring large release undercuts. Simulations of grating couplers were performed to optimize design parameters, and then refined over fabrication runs. A complete description of how they work and their design is provided in App. V.

3.7 Electrical coupling

Whilst electrical coupling was not implemented on devices described in this thesis, the future integration of an electrical connection was an element of design. Using a partial acoustic waveguide described above, mechanical modes can be coupled to a region with electrodes that utilize the piezoelectric effect to convert displacements into voltages and drive a circuit (or vice-versa). Following previous designs, interdigitated transducers can be used with surface acoustic waves [120, 128, 184–190] or membrane Lamb waves [121, 122, 191], however these require large areas for efficient coupling. Alternatively, more compact approaches [124, 131, 132, 192–194] could be viable but might suffer with gallium arsenide's comparatively weak piezoelectric coupling.

CHAPTER 4

Fabrication

Fabrication was carried out at the Pritzker Nanofabrication (PNF) facility at the University of Chicago. Whilst gallium arsenide (GaAs) is not an uncommon material in the semiconductor industry, its use in the PNF was unique to this project and many recipes had to be developed. This chapter will detail the main fabrication procedures involved and provide the method used for device fabrication. Step by step procedure tables are given in App. Ω.

4.1 Wafer

Heterostructure wafers of 250 nm GaAs, 1 µm $Al_{0.9}Ga_{0.1}As$, on bulk GaAs were procured from IQE. The top surface of the GaAs is a (100) crystal plane, and using a counter clockwise (US) specification has the major flat (OF) perpendicular to $[01\bar{1}]$. Gallium arsenide has $\pi/2$ rotation symmetry about its cardinal axes (see Sec. M.1), thus the (100) surface is equivalent to a (001) $\vec{z}$ crystal axis orientation.

The thin AlGaAs sacrificial layer helps the growth of the top substrate layer during manufacturing but, with our infra-red wavelength $\lambda \approx 1.5\,\mu m > 1\,\mu m$, a larger gap could be beneficial to optical properties. Furthermore, a lower fraction of aluminium in the sacrificial layer, whilst slowing down the release chemistry, might produce less unwanted by-products.

Wafers were diced into 1 cm × 1 cm squares using AZ 1518 resist to protect the top surface. The underside of the two-side-polished chips were then marked by light scratching. Various process steps for the $1\,cm^2$ chip utilized custom made plastic bowl holders detailed in App. Ↄ.

4.2 Plasma etching

Patterned holes in the gallium arsenide are made through inductively coupled plasma (ICP) reactive ion etching (RIE), a process that involves bombarding the substrate with ions which attack the material both physically and chemically. A resist mask defined through lithography is used to limit the etching to only designated regions, and the etching process needs to be selective enough such that the desired material etch depth is reached before the resist succumbs to the etch. The etching is primarily controlled through the chemical composition, maintained pressure, radio frequency power that creates the plasma, bias power for accelerating ions into the substrate, and time duration. Additional factors such as the size of etching regions and the total exposed area can also influence the etch.

A good etching recipe balances isotropic chemical processes with directional physical processes to achieve vertical sidewalls perpendicular to the substrate. Characterization of the sidewall angle was performed using a scanning electron microscope (SEM) looking at either cleaved cross-sections or perspective angle analysis.

Cleaved cross-sections are the most direct, albeit destructive, method for investigating the sidewall angle. This approach involves etching a pattern of long lines into the substrate, then breaking the chip perpendicular to the lines, such that their profile can be seen when looking at the cleaved face. Angles in the SEM image can be found by doing edge detection and fitting the pixels, an example is shown in Fig. 4.1. Averaging between opposing corners can help reduce the systematic errors from non-perpendicular cleaves and viewing angles.

The second approach involves taking an SEM image of an etched periodic structure with known distances and angles. By measuring the image angles of the periodic pattern, the viewing vector can be determined, allowing image sidewall angles to be interpreted, details of this process are outlined in App. Q. Due to the lower edge contrast of the perspective

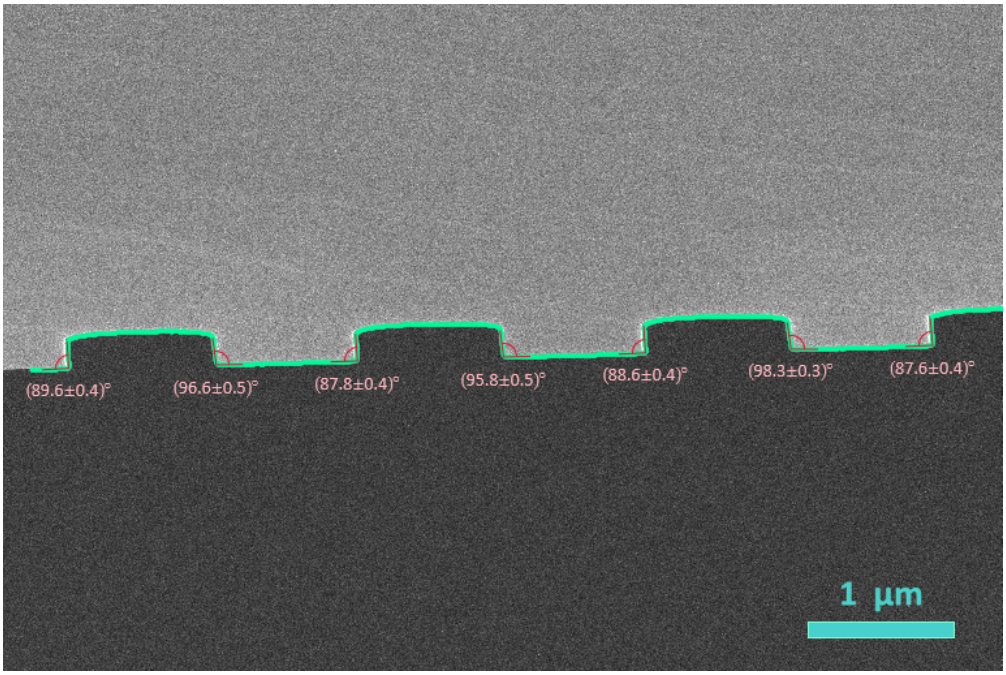

Figure 4.1: SEM image looking at the cleaved face of etched parallel lines, the upper light grey is GaAs. Edge detected pixels are shown in blue, and fits to each corner are depicted with red lines. Uncertainties are from the fit only.

view, measuring angles is more difficult and more uncertain, which is further compounded by the angle computation chain, making this method imprecise.

Approximately 70 etch tests were carried out, resulting in the following recipe,

ICP	50 W
Bias	300 W
Pressure	3 mTorr
Cl_2	2 sccm
Ar	13 sccm

with etch rate $\sim$ 250 nm/min over large open regions, and half that for small holes. For etching through regions with small holes, the Cl_2 flow was increased to 3 sccm.

The system used in the PNF was a Plasma-Therm ICP Chlorine etcher. Chips were adhered

onto a silicon carrier wafer using a small amount of Santovac 5 diffusion pump oil, ensuring none was exposed beyond the edge of the chip. Excess oil protruding the chip seemed to hinder ICP ignition.

There appeared to be some reaction of the chlorine etch with the AlGaAs layer when it broke though producing a brown substance (possibly some aluminium chloride) that was difficult to remove. Transferring the chip to a water bath, upside down, immediately after etching (before any photoresist stripping) helped reduce the amount of by-product. Keeping the chip cool during the etch is also rumoured to help.

4.3 Electron beam lithography

Electron beam (ebeam) lithography is a revolutionary fabrication process that allows patterning on nanometer scales. The basic principle involves applying a charge sensitive resist to the substrate, precision shooting high energy electrons at it, then using a chemical developer to remove or leave only the affected regions. The electron beam writer used in the PNF is a Raith EBPG5000, operating at 100 kV.

The ebeam resist should be optimized to produce the highest resolution patterns, whilst being able to withstand the etching process. For the the 2D snowflake optomechanic crystal devices we use 14%[1] hydrogen silsesquioxane (HSQ) in a ~ 300 nm layer which is resistant to chlorine used for etching GaAs. Thinner resist layers (such as those using 6% HSQ) produce better resolutions, but our GaAs etching process involves a significant physical component that needs a thicker resist. HSQ must be stored cold (but only opened at room temperature to avoid condensation) in plastic bottles, is easily spoiled by prolonged exposure to air [195], and will deteriorate over six months to a year [196].

1. By weight in methyl isobutyl ketone (MIBK).

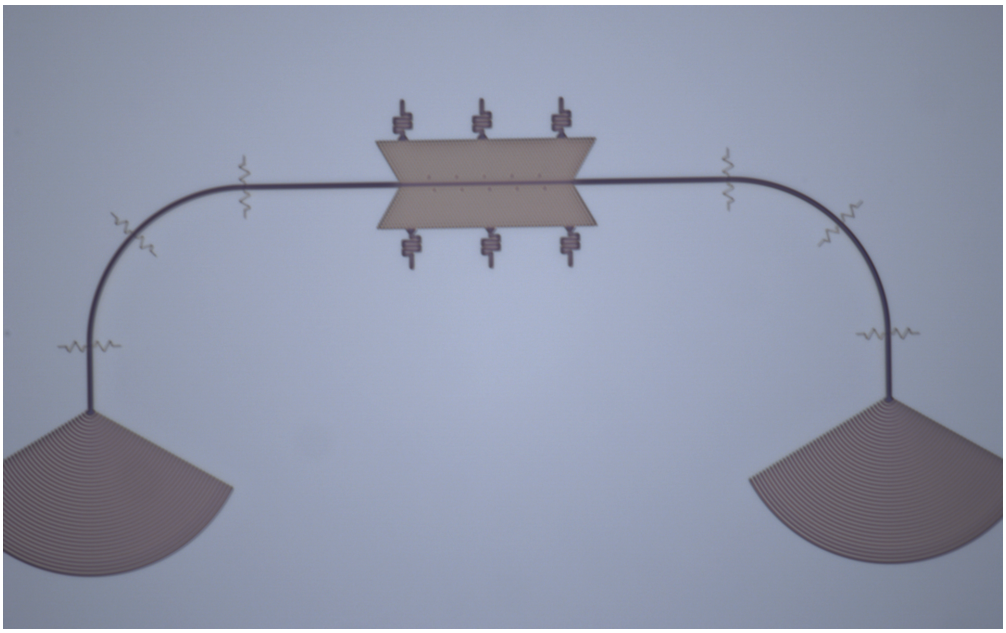

Figure 4.2: Optical microscope image of a HSQ layer.

The 14% HSQ is spun at 6000 rpm for 1 min before a 3 min 115°C pre-bake, the vacuum chuck was unable to hold at higher spin speeds. As HSQ is a negative resist, we expose regions we want kept with electrons. Unexposed regions are removed by development in 25% Tetramethylammonium hydroxide (TMAH) for 75 sec, followed by a series of water baths. Remaining resist is hardened with a 15 min 300°C hard-bake. HSQ has a sensitivity to air that requires the spinning, exposing, and developing to be carried out promptly. Fig. 4.2 depicts a typical completed HSQ layer.

A substantial challenge with ebeam lithography is proximity errors from electron back scatter, this is particularly prevalent in gallium arsenide which is made from much heavier atoms than other common substrates like silicon or sapphire. Accounting for this in the exposure pattern is called proximity effect correction (PEC), and is described in App. N. In addition to long range electron back scatter, HSQ is known to suffer from a hydrogen diffusion process when exposed to electrons, contributing to a diffusion term in the point spread function that is not captured in electron scattering simulations. Furthermore this diffusion is a

time-ordered effect in that exposed areas will affect nearby subsequent exposures. To help mitigate this, and provide some smoothing, the pattern is exposed in $\times 2$ multi-pass.

Various long range ($> 1\mu$m) PEC schemes were tested by varying parameters of a point spread function of the form, from Sec. N.2,

$$\mathrm{PSF}[r] = \frac{\eta_a \, f_{\mathrm{G}}[\sigma_a; r] + \eta_b \, f_{\mathrm{G}}[\sigma_b; r] + f_{\mathrm{GP}}[\sigma_c, \gamma_c, \nu_c; r]}{1 + \eta_a + \eta_b} \, ,$$

starting with parameters based on simulations from TRACER [197], CASINO [198], and CHARIOT [199, 200]. Results were analyzed by capturing large high resolution SEM images of the snowflake pattern over a region of the device spanning the central waveguide to the edge, then performing edge detection and snowflake fitting as a function of location, as described in App. P. PEC parameters were tuned to give constant snowflake dimensions. The PEC was implemented using BEAMER [201] software, setting the short range correction cut-off to 0.1 μm. Including medium range corrections on the order of pattern features helps scaling for the overall pattern filling density. A comparison of PECs demonstrating the necessity is shown in Fig. 4.3.

In addition to medium-long range PEC, manual dosage scaling is applied to snowflake inner and outer corners to improve corner sharpness. Details of this are included in App. O.

Based on the minimal dosages required (including PEC range and multi-pass) and beam current for a small spot size, the pattern grid is chosen to satisfy the maximal exposure frequency,

$$\text{exposure frequency} = \frac{(\text{beam current})}{(\text{dose})\,(\text{step length})^2} \leqslant 125\,\mathrm{MHz} \, .$$

With a beam current of 0.2 nA, the grid step size used was 1 nm.

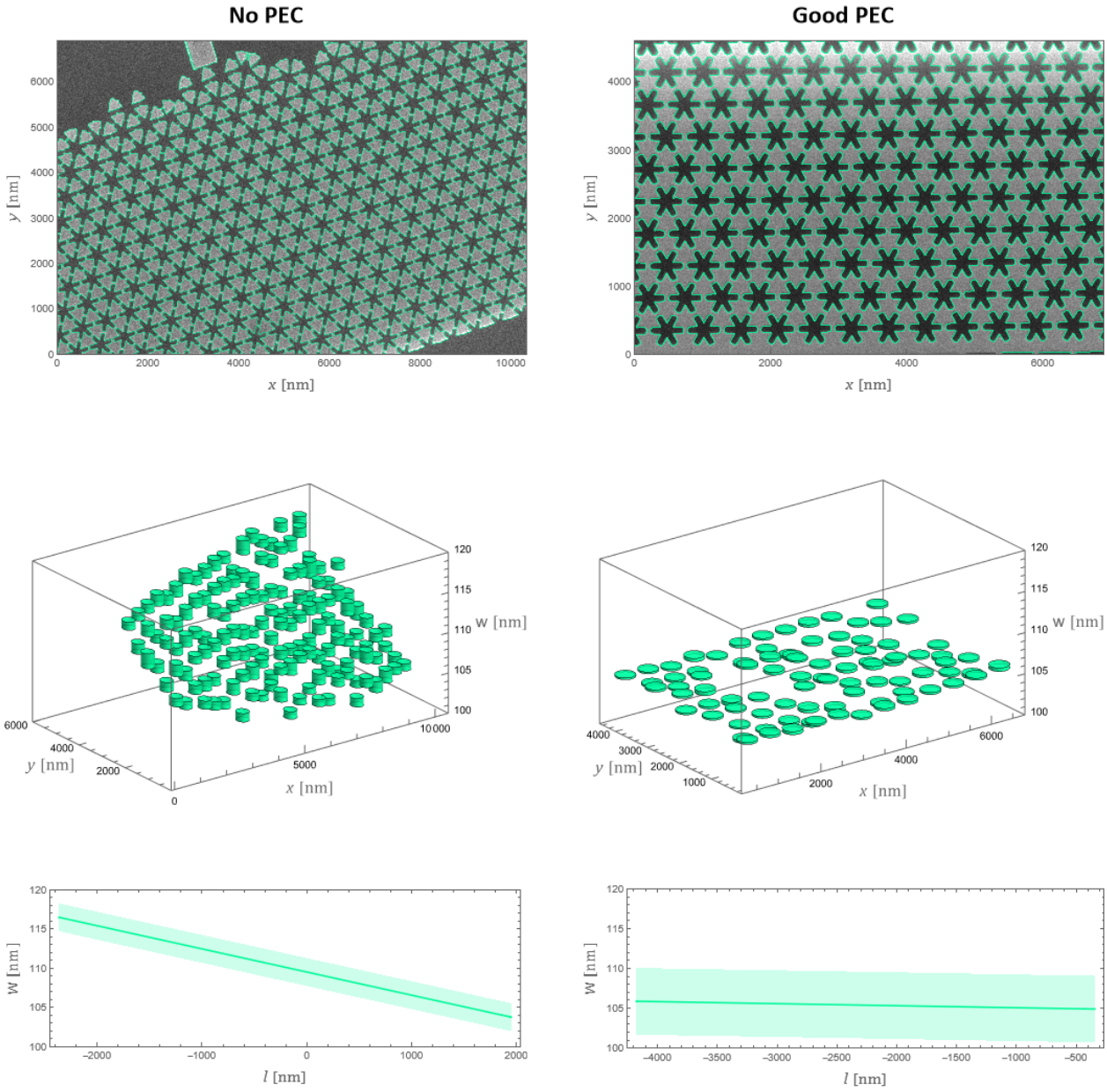

Figure 4.3: Comparison of snowflake w (left) no proximity effect correction to (right) proximity effect correction using point spread function (N.3).

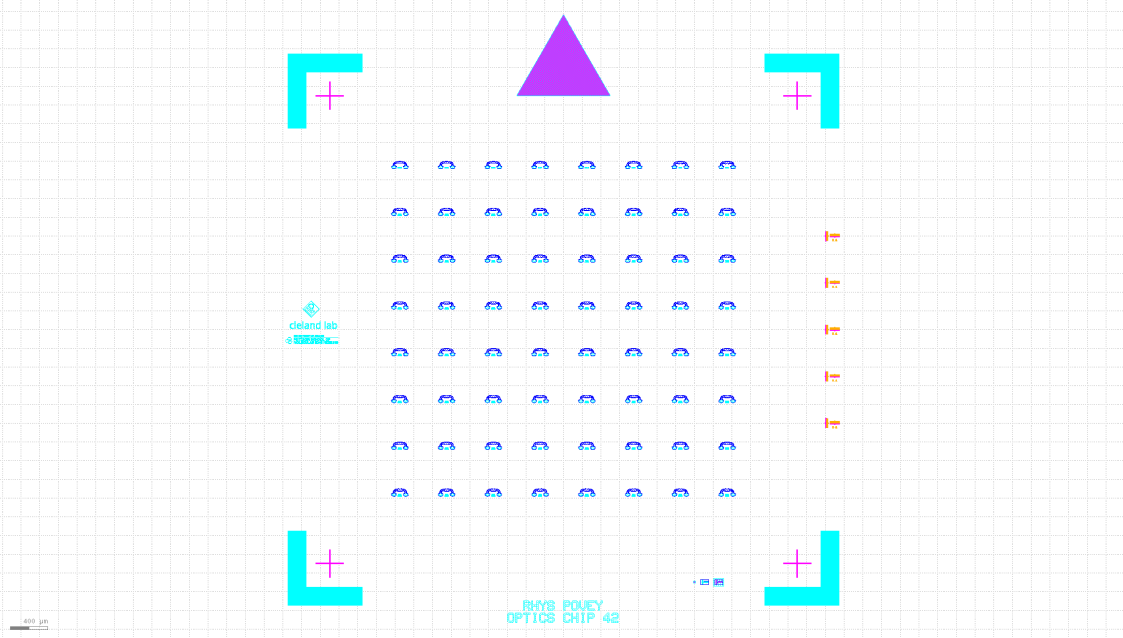

Figure 4.4: A typical chip layout with device waveguides aligned to $[1\bar{1}0]$. In magenta are ebeam HSQ markings for alignment crosses and directional arrow, these are removed during the HF release. In cyan is the partial etch mask, and in blue is the full etch mask. On the side, in orange, are test exposure regions for doing manual alignment. This square working region is 5 mm × 5 mm, sitting in the middle of a 1 cm × 1 cm chip.

The ebeam layer additionally includes cross-shaped alignment markers and a directional 'up' arrow for following photolithography steps. These larger scale features are written with a larger step size of 25 nm, a higher current beam of 100 na, and in a single pass at 1100 μC cm^{-2}. An example chip layout is shown in Fig. 4.4.

4.4 Photolithography

Because a negative resist is used to for masking the main features, we need an accompanying positive resist mask to designate the etching region and protect the rest of the chip. The larger scales involved, $\gtrsim 1\,\mu$m, allow photolithography to be used. Exposures were carried out using a Heidelberg MLA150 Direct Write with a 375 nm laser. AZ MiR 703 photoresist was used, spun at 4500 rpm for 45 sec to give a $\sim$ 600 nm layer, with a 1 min 90°C pre-bake

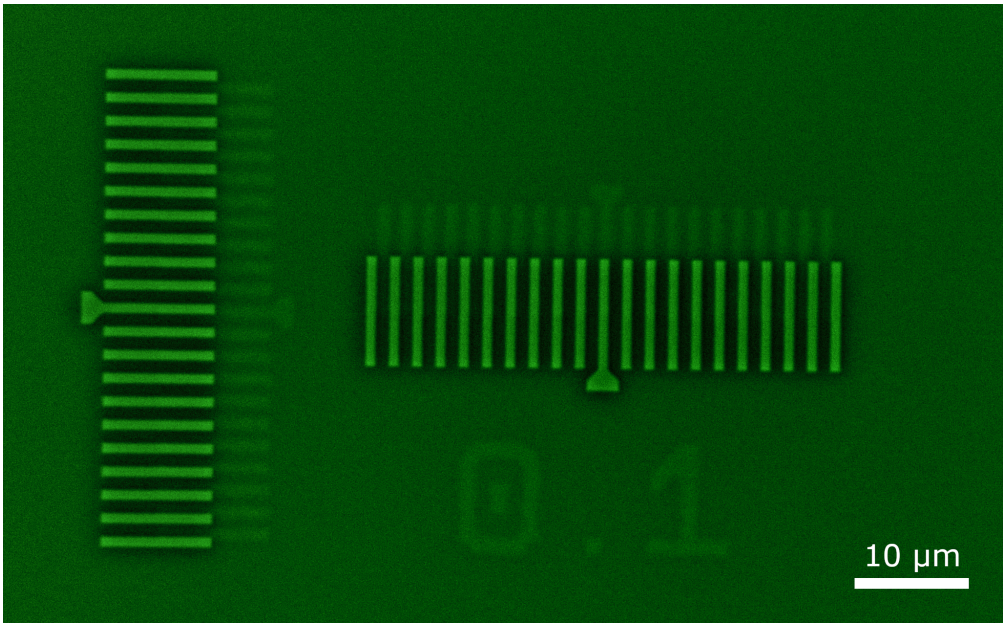

Figure 4.5: Microscope image with green filter and polarizer looking at a vernier scale between developed HSQ and exposed photoresist. The contrast has been adjusted for better visibility.

and 1 min 115°C post-bake. Development was done in AZ 300 MIF for 75 sec. To smooth the resist sidewalls, an oxygen plasma downstream asher 'descum' process is carried out.

Photolithographic exposures are aligned to the ebeam layer through four cross-shaped patterns in the corners of the chip working area that are written as part of the ebeam step. The Heidelberg's alignment to these is not super accurate so to achieve sub-micron alignment a manual correction process is used. A 0.1 µm vernier scale half is printed on the chip with the ebeam resist, and a matching vernier scale half is exposed in the covering photoresist typically at double the normal dosage. Using a green filter and polarizer, the completed vernier scale can be seen with an optical microscope without any development, as demonstrated in Fig. 4.5. From this the misalignment can be measured and corrected in the optical exposure pattern before returning the chip to the direct write tool.

After etching, the photoresist is removed through oxygen plasma ashing, acetone, and *N*-methyl-2-pyrrolidone (NMP). The first step is a 'decrust' ashing process to remove the top

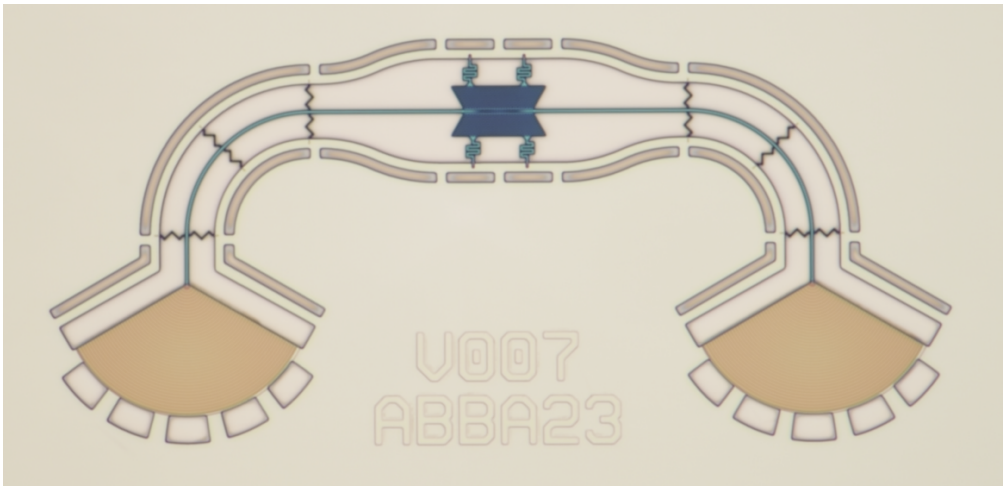

Figure 4.6: Optical microscope image of a device after HSQ and two photolithography-etch-strip steps.

layer of burnt and hardened photoresist. Second is an acetone bath to remove the bulk of the photoresist. Third is a hot 80°C NMP bath, without sonification (which was found to damage delicate features). Acetone and NMP are incompatible chemicals so a couple of IPA baths are used between them. Finally the NMP is rinsed off in an IPA then water bath and a stronger ashing process is applied to remove any stubborn pieces of photoresist. The liquid stripping steps were typically carried out with the chip upside-down.

Typically two photolithography and etching steps are required, first for a partial etch only $\sim 100\,\text{nm}$ deep to create the grating couplers, and then a second etch that goes all the way through. Fig. 4.6 depicts a device that has gone through both photolithography, etching, stripping steps. Additional chip markings and labels are included in the partial etch lithography step.

4.5 Release

The final step in the fabrication process is the release of the top GaAs layer by etching out the AlGaAs sacrificial layer from underneath, nominally carried out with hydrofluoric acid

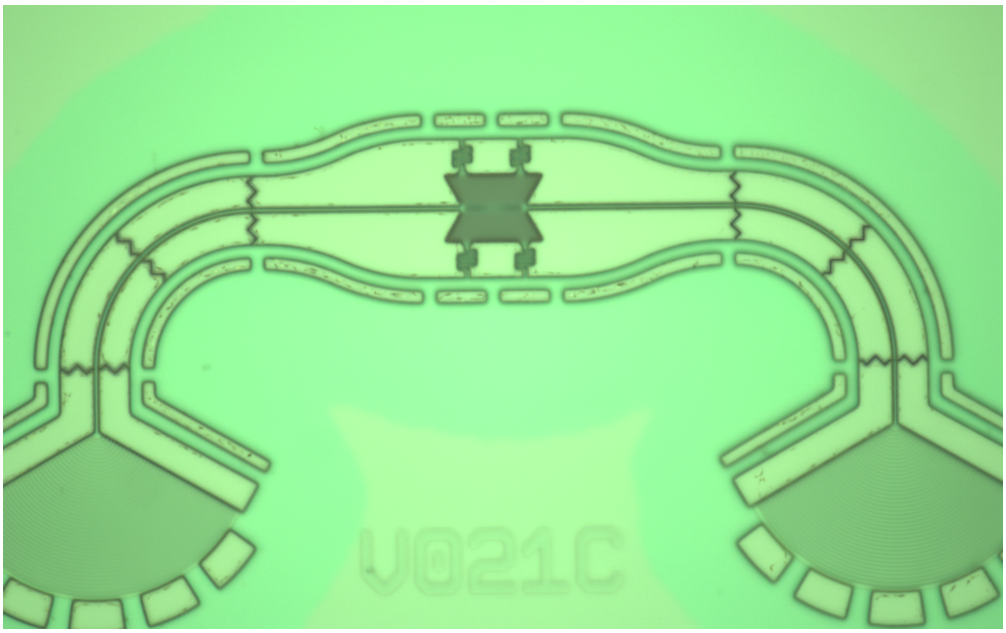

Figure 4.7: Optical microscope image of a device with debris after releasing.

(HF) [202–205]. Conveniently, the HF simultaneously strips the HSQ mask. Releasing the top layer is the most delicate fabrication step as the suspended GaAs is fragile and prone to breaks, fractures, collapses, or being blown out if the etching reaction is too violent. Lattice mismatch between the AlGaAs and GaAs provides a source of stress that can easily cause fatal damage during the release. A mixture of 1 49% HF (by weight) to 4 water is used to create a $\sim$ 10% HF solution that the chip is placed in for 1 min. This is followed by a '5C homeopathy' series of water baths to purge the acid.

The etch produces by-products AlF_3 which dissolves in water, and $Al(OH)_3$ which can be cleaned with KOH [77, 161, 206, 207]. A bath of 1 30% KOH (by weight) to 2 water, to get a $\sim$ 20% KOH (by weight) solution[2], for 1 min was used for cleaning. This was again followed by series of water baths. The overall usefulness of this step was questionable, however.

Through some interaction of the aluminium gallium arsenide, chlorine etch, and/or hydrofluoric acid, some unknown brown debris often persisted in open regions or along edges as seen

2. KOH has about double the density of water.

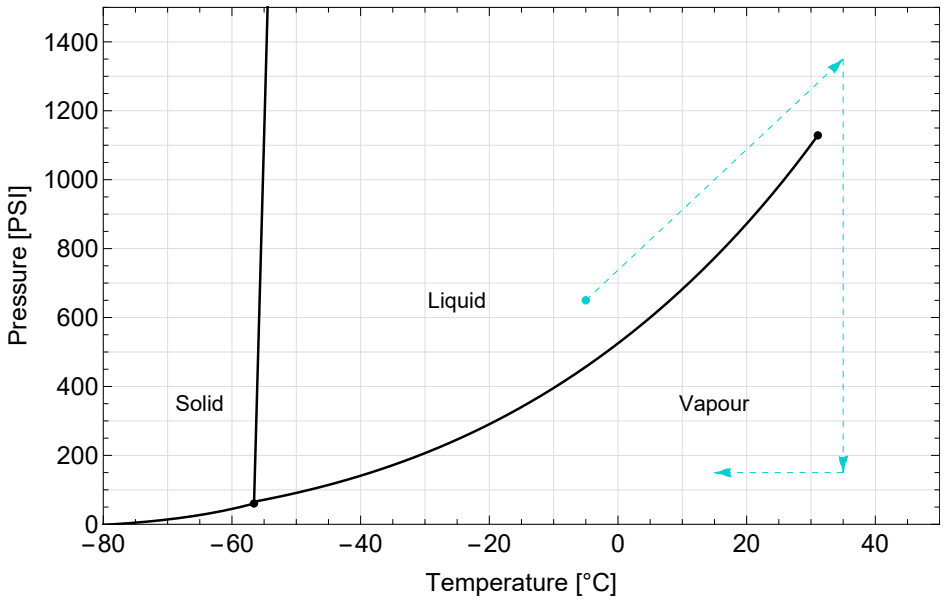

Figure 4.8: Carbon dioxide phase diagram [210] with drying pathway shown going around the critical point.

in Fig. 4.7. This waste product, possibly aluminium or gallium oxides, can be cleaned up with a hydrogen peroxide (H_2O_2) followed by potassium hydroxide (KOH) bath [208, 209] but this also eats in to the GaAs causing an extra $\sim$ 20 nm of damage and thus was not performed. Lower concentrations or durations might be able to make this cleaning work but it's unlikely as the etch is digital based on the H_2O_2 penetration into KOH. A solvent based clean of toluene, acetone, methanol, and isopropanol provided negligible cleaning.

Perforated regions of GaAs were found to exhibit cracking from stresses encountered during the release process. To remedy this, perforated regions (e.g. snowflakes) to be released were surrounded by open areas and connected with bridges. These bridges, with a zigzag or serpentine spring-like design, provided some flex for the plate as it underwent release, mitigating the formation of cracks. Additionally a secondary release trench surrounding the released areas proved to be effective in limiting cracks and flaking in the outer top layer.

Throughout the release process, the sample must remain submerged in liquid as surface tension forces from evaporation is enough to collapse the suspended layer.[211] To take the

chip out of liquid it goes through a carbon dioxide (CO_2) critical point dryer (CPD). This process involves replacing the liquid with cooled liquid CO_2, and then heating under pressure to put it in a superfluid state, which can then be vented. By going around the carbon dioxide critical point (304 K, 7.88 MPa) there is no destructive evaporative phase transition. The phase diagram for carbon dioxide and the drying pathway are shown in Fig. 4.8. When using the CPD, it is important to have a long enough hold time at the peak temperature to ensure the fluid comes into thermal equilibrium above the critical point, out of an abundance of safety, 12 minutes was used for this hold. If using an apparatus to hold the chip in the chamber, it needs to allow for drainage. Additionally, bowls were sometimes observed to collect carbon dioxide clouds.

Throughout the whole release, cleaning, and drying process, some chips were held upside down in the bowls with the goal to avoid any suspended particulates from falling on the surface. It is unclear if this actually provided any benefits.

Further cleaning can be done with a strong, hot oxygen plasma ash to which the suspended GaAs is resistant. This is particularly useful for removing small dust-like particles that can be deposited by the CPD. A completed fabricated chip is shown in Fig. 4.9.

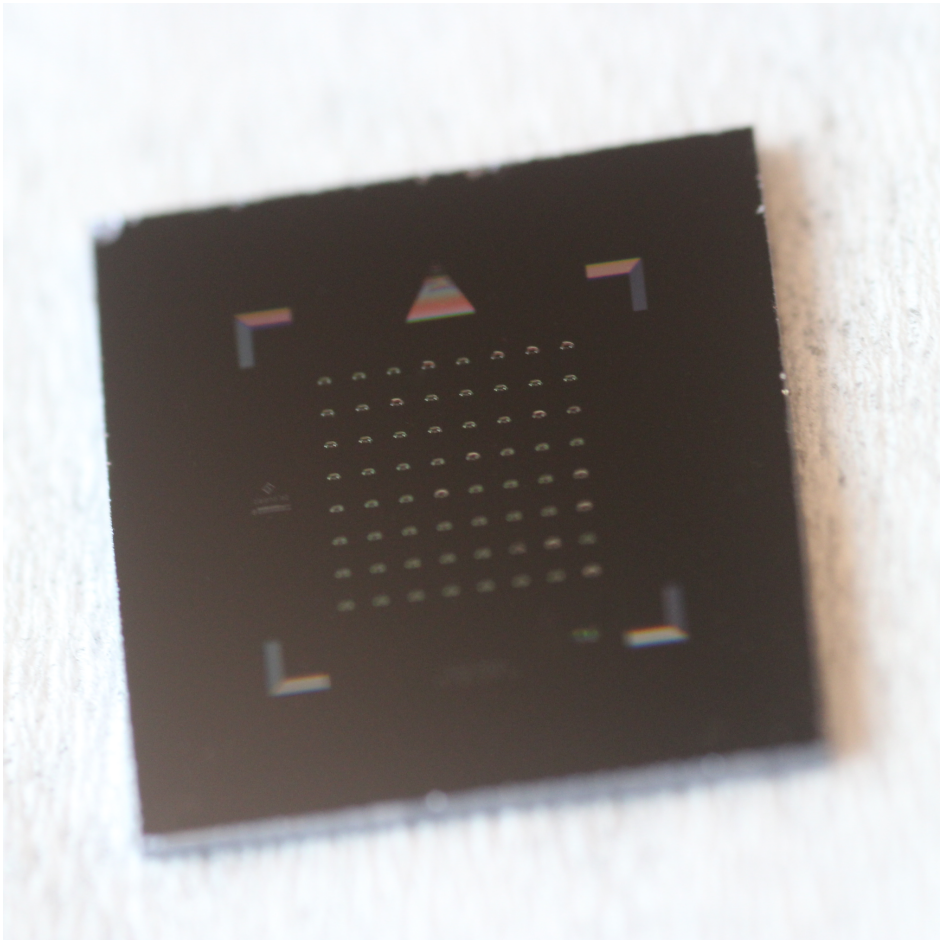

Figure 4.9: Photograph of a finished chip.

CHAPTER 5

Measurement

This chapter covers the optical measurements carried out on optomechanical crystal resonators in order to determine their optomechanical coupling rate. Upgrades were made to the existing setup to better lock and track resonances, and calculations updated to remove approximations and use more accurate spectral densities rather than idealized powers.

5.1 Thermal optomechanical signal

At room temperatures, microwave frequency mechanical resonators have ~ 1000 phonons. Through the optomechanical effect, this ambient vibration oscillates the optical resonance frequency, and if the side of this resonance is probed by a laser, the transmission will exhibit a modulation at the mechanical resonance frequency that can be detected using a spectrum analyzer, illustrated in Fig. 5.1. The full derivation of this effect is carried out in App. L and leads to the mechanical thermal spectrum being captured in the spectral density output of a photodetector,

$$S_{XX}(\omega) \ni \underbrace{\mathfrak{T}(\omega_{\mathrm{L}};\omega)}_{\substack{\text{optical}\\ \text{transmission}}} \; {g_{\mathrm{om}}}^2 \; \underbrace{\frac{\bar{n}_{\mathrm{m}}\,\gamma_{\mathrm{m}}}{\left(\omega-\omega_{\mathrm{m}}\right)^2+\left(\frac{\gamma_{\mathrm{m}}}{2}\right)^2}}_{\text{thermal mechanics}} ,$$

where $\mathfrak{T}(\omega_{\mathrm{L}};\omega)$ is a complicated transmission function that incorporates the entire optical setup and optical resonance itself.

In order to determine the optical transmission factor, we can use a calibrated phase modulated signal (see Sec. Λ.10.1). Conveniently, if we weakly phase modulate our laser with frequency f_Φ and amplitude A_Φ, the resulting signal picked up by the spectrum analyzer

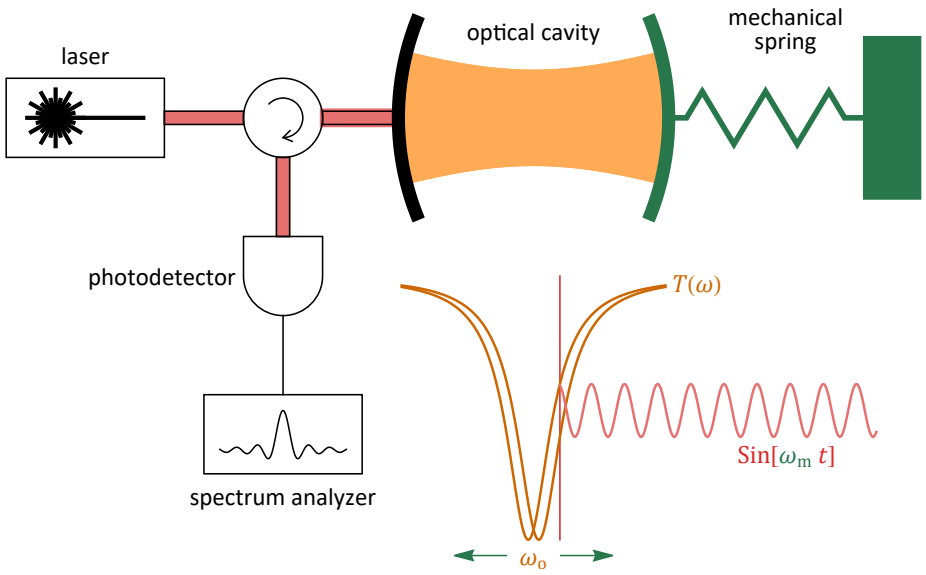

Figure 5.1: Diagram depicting the influence and measurement of a mechanical resonance on an optical cavity. The mechanical mode vibrations alter the optical cavity length and hence optical resonance frequency. Probing the steepest part of the transmission curve reveals oscillations at the mechanical resonance frequency. A fast photodetector and spectrum analyzer is able to resolve this signal.

contains the same transmission factor to leading order in A_Φ. Also worked out in detail in App. L, the measured power is

$$P_{\omega_\Phi} = \mathfrak{T}(\omega_L;\omega_\Phi)\,\frac{{\omega_\Phi}^2\,{A_\Phi}^2}{2}\ .$$

Given a phase modulation drive power, the resulting A_Φ can be calibrated as described in Sec. Σ.1.2. Choosing ω_Φ near ω_m such that $\mathfrak{T}(\omega_L;\omega_\Phi) \approx \mathfrak{T}(\omega_L;\omega_m)$ we're able to substitute out the optical transmission factor and determine g_{om} by fitting the spectrum.

Following the math in Sec. L.5, if we fit our measured power spectral density[1] (with quadratic

1. PSD_1 refers to the one-sided power spectral density (see App. Λ).

background as needed) to

$$\mathrm{PSD}_1(f \sim f_\mathrm{m}) = \frac{\mathcal{A}}{(f-f_\mathrm{m})^2 + (\Gamma_\mathrm{m})^2} + \mathcal{C}_\mathrm{m}^0 + \mathcal{C}_\mathrm{m}^1 (f - f_\mathrm{m}) + \mathcal{C}_\mathrm{m}^2 (f - f_\mathrm{m})^2 \,,$$

the optomechanical coupling is then

$$g_\mathrm{om} = \frac{g_\mathrm{om}}{2\,\pi} = \sqrt{\frac{\mathcal{A}\,\pi\,{f_\Phi}^2\,{A_\Phi}^2}{4\,\bar{n}_\mathrm{m}\,\Gamma_\mathrm{m}\,P_{f_\Phi}}} \,.$$

One difficulty with this calculation is estimating the acoustic mode population $\bar{n}_\mathrm{m}$, in particular because the cavity temperature will be slightly above ambient temperature due to laser heating. At room temperature, however, this should be a marginal effect.

5.2 Optical setup

The optical setup, described thoroughly in App. Σ, uses an infra-red laser and fiber optic components with free space coupling vertically down to the chip that lines up with fabricated grating couplers (see App. V). An intensity feedback system on the input side keeps delivered power stable, and a phase modulator hooked up to a microwave signal generator provides the calibration signal. On the output side, an erbium doped fiber amplifier and tunable filter take the optical signal to a high bandwidth photodetector that can resolve microwave frequency signals, passing them to a spectrum analyzer.

Taking place in an ambient room environment, the device under test and entire optical setup are prone to thermal drifts. This leads to both the optical resonance drifting in frequency, and the overall transmission varying. For prolonged measurements we need to be able to track the optical resonance whilst we probe its edge. To do this whilst compensating for varying transmission, a second harmonic dither lock system was implemented. Described in

App. Υ, this method oscillates the laser frequency at some rate ω_{dither} such that

$$\omega_{\text{L}} = \omega_0 + \underset{\text{amp}}{\omega_{\text{dither}}} \sin[\omega_{\text{dither}}\, t] \ ,$$

and interrogates the transmitted signal at $2\,\omega_{\text{dither}}$. At the resonance inflection points, i.e. the edges we wish to probe, the 2nd derivative, and hence this signal, should be zero. Using a feedback system to adjust the laser frequency until this signal is zero allows the inflection points to be tracked regardless of any transmission fluctuations.

Whilst the dither lock is able to adequately track the optical resonance, varying transmissions and hence measured powers at the spectrum analyzer makes long scans unreliable. Thus we generally want to take reasonably quick single scans ($\sim 1\,\text{min}$) that capture both the phase modulation signal and thermal mechanics, and then do any averaging or statistics ourselves. To make an accurate measurement of the monotone phase modulation signal, we use a resolution bandwidth much greater than the frequency step size such that the signal convolves with the spectrum analyzer windowing and can be fit to the window function. This method, detailed in Sec. Λ.12, uses more data to determine the signal power and avoids the imprecision of a single bin measurement with unknown window location systematics. As the optomechanical signal is thermal, it doesn't suffer a signal-to-noise hit by increasing the resolution bandwidth.

An extra complication with faster spectrum scans is that the time dependent dithering becomes resolved. In particular, when measuring the phase modulated signal with a single scan, oscillations at $\omega_{\text{dither}}/v_{\text{scan}}$, where v_{scan} is the scan speed in Hz/s, can be observed. For any individual sweep the relative start time and hence phase of this oscillation is random, so averaging will suppress its effect. For analyzing single scans however, we can account for this in our fitting. If the spectrum analyzer frequency bin $f_{\text{SA}} = f_1 + v_{\text{scan}}\, t$ and $\underset{\text{amp}}{\omega_{\text{dither}}}$ is

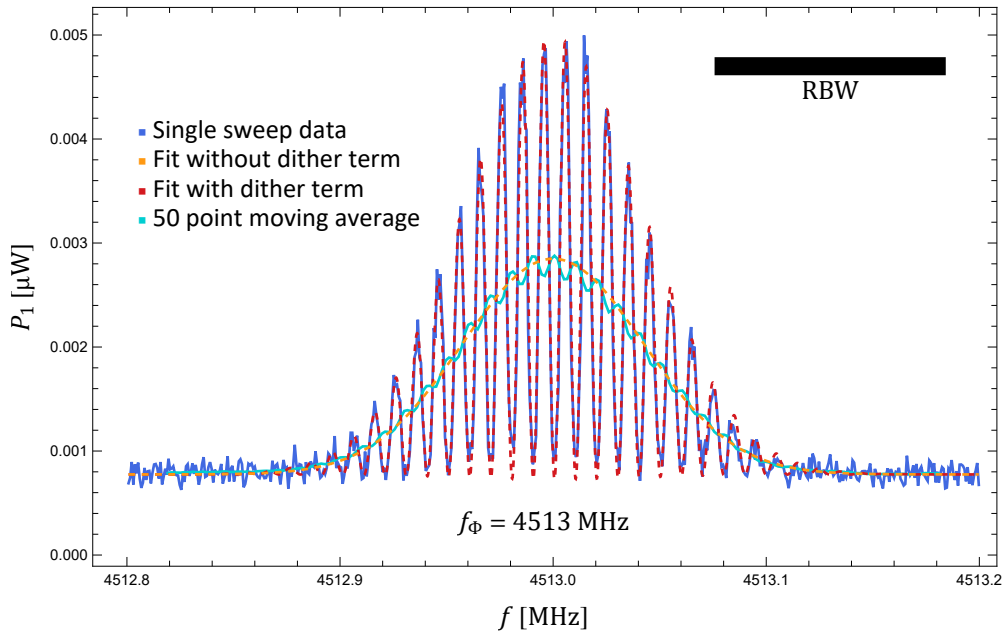

Figure 5.2: Dithering imprint on a single spectrum analyzer sweep over the phase modulated signal expressed by the windowing function. Both fits give the same value $P_{f_\Phi} = 2.21124\,\mathrm{nW}$.

small, we can perform a linear expansion

$$
\begin{aligned}
P_1(f_{\mathrm{SA}}) = {} & \left(P_{f_\Phi}\big|_{\omega_\mathrm{L}=\omega_0}\right) w(f_{\mathrm{SA}}; f_\Phi) \\
& + \left(\frac{\mathrm{d}\,P_{f_\Phi}}{\mathrm{d}\,\omega_\mathrm{L}}\Big|_{\omega_\mathrm{L}=\omega_0}\right) \underset{\mathrm{amp}}{\omega_{\mathrm{dither}}}\, w(f_{\mathrm{SA}}; f_\Phi)\, \sin\!\left[\frac{\omega_{\mathrm{dither}}}{v_{\mathrm{scan}}}\, f_{\mathrm{SA}} + \theta\right] \\
& + \mathrm{bg}(f_{\mathrm{SA}}) + \mathcal{O}\left[\underset{\mathrm{amp}}{\omega_{\mathrm{dither}}}\right]^2
\end{aligned}
$$

$$
\begin{aligned}
= {} & P_{f_\Phi}\, \sqrt{L} \sqrt{\frac{2\,\log[10]}{5\,\pi}}\, \exp\!\left[-(f_\Phi - f_{\mathrm{SA}})^2\, L\, \frac{2\,\log[10]}{5\,\mathrm{RBW}^2}\right] \\
& + \mathcal{B}_\Phi\, \sqrt{L} \sqrt{\frac{2\,\log[10]}{5\,\pi}}\, \exp\!\left[-(f_\Phi - f_{\mathrm{SA}})^2\, L\, \frac{2\,\log[10]}{5\,\mathrm{RBW}^2}\right]\, \sin[2\pi\,\mathcal{T}\, f_{\mathrm{SA}} + \theta] \\
& + \mathcal{C}^0_\Phi + \mathcal{C}^1_\Phi\, (f_{\mathrm{SA}} - f_\Phi)\,,
\end{aligned}
$$

for a Gaussian window, where $\mathcal{B}_\Phi, \mathcal{C}^0_\Phi, \mathcal{C}^1_\Phi, \mathcal{T}, \theta, P_{f_\Phi}$ are fit parameters with $\tilde{\mathcal{T}} = f_{\mathrm{dither}}/v_{\mathrm{scan}}$. The scan start relative to dither phase is random so θ will be a random phase for each scan,

averaging over scans will then take $\sin \to 0$. An example wide-RBW spectrum analyzer scan over the phase modulated signal with dithering, along with fits, is given in Fig. 5.2.

To resolve the thermal spectrum in a single scan, we capture the maximal amount of frequency bins (40 000) and perform a moving average of 100 or 200 points in offsets of half that.

With a large number of individual scans and measurements, we generate enough statistics to make an estimate of the optomechanical coupling. Assuming it has a fixed 'true' value across a set of measurements we can perform a weighed mean (see App. Φ). This statistical process can account for unknown uncertainties inherent in the measurement process. To separate systematic uncertainties from statistical uncertainties when combining measurements we express the optomechanical coupling in the form

$$g_{\mathrm{om}} = \frac{f_\Phi \, A_\Phi}{\sqrt{k_\mathrm{B} \, \mathbb{T}/h}} \underbrace{\sqrt{\frac{\mathcal{A} \, \pi \, f_\mathrm{m}}{4 \, \alpha_\mathrm{m} \, P_{f_\Phi}}}}_{\mathcal{D}} \, .$$

The second factor, $\mathcal{D}$, contains all the parameters from fits on an individual scan and each scan is an independent measurement. Thus, this factor can be combined in a weighted mean over all the scans in the run and will contain all the statistical uncertainty. Temperature, $\mathbb{T}$, and phase modulation strength, A_Φ, have systematic uncertainties that are correlated across all scans in a run, and are included once to ascertain g_{om}.

The data taking process is highly automated with a series of scripts that set power levels, find the optical resonance, calibrate and engage the dither lock, align the optical filter, adjust the amplifier pumps, and take spectrum scans.

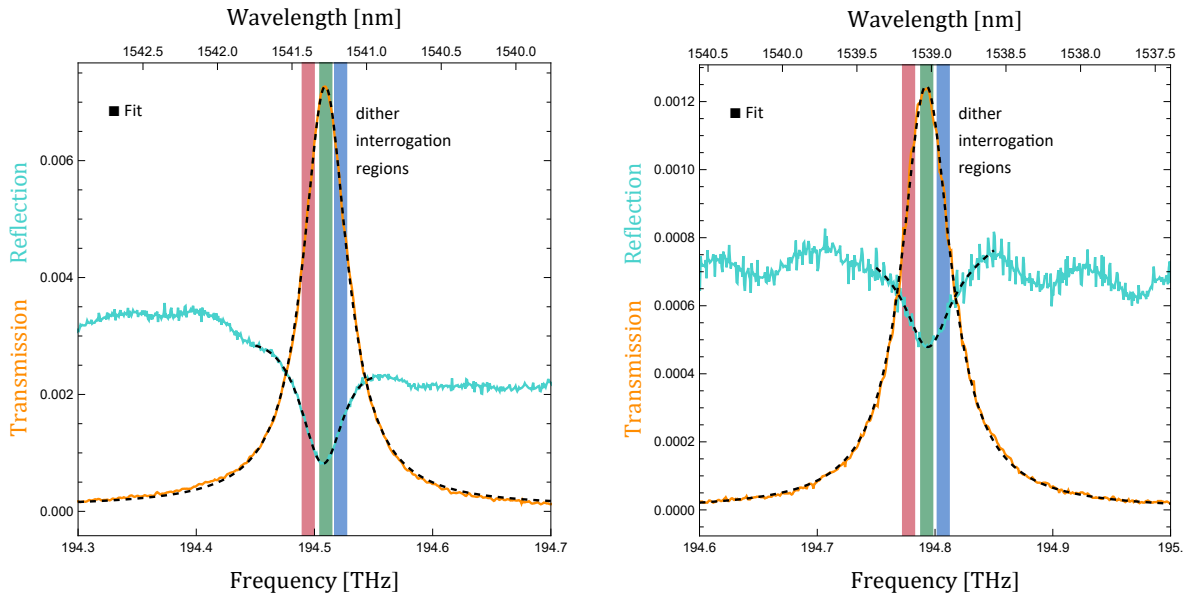

Figure 5.3: Transmission and reflection plots through (left) device A and (right) device B. The highlighted dither interrogation regions, colour coded to the red inflection, peak, and blue inflection, are estimates of the dithering regions covered during optomechanical measurements. Device A has $f_{\mathrm{o}} = 194.5\,\mathrm{THz}$, $Q_{\mathrm{o}}^{\mathrm{L}} \approx 4300$, $\beta_{\mathrm{o}}^{1} \approx 0.50$, $Q_{\mathrm{o}}^{0} \approx 8600$. Device B has $f_{\mathrm{o}} = 194.8\,\mathrm{THz}$, $Q_{\mathrm{o}}^{\mathrm{L}} \approx 3900$, $\beta_{\mathrm{o}}^{1} \approx 0.15$, $Q_{\mathrm{o}}^{0} \approx 5100$.

5.3 Nanobeam resonators

Preliminary tests of optical setup and optomechanical measurement process were carried out on gallium arsenide nanobeam resonators. These one-dimensional optomechanical crystals are much simpler to make and have proven results; with minimal optimization, couplings comparable to others' work were able to be achieved [122, 123, 157]. A complete description of the nanobeam design and measurement is available in App. Δ, the optomechnical coupling rate was $\mathscr{g}_{\mathrm{om}} \approx 600\,\mathrm{kHz}$.

5.4 Vertebrae resonators

Two particularly good $\mathsf{n}_{\mathrm{defect}} = 1$ vertebrae resonator devices, as described in App. Z, with loaded optical quality factors $Q_{\mathrm{o}}^{\mathrm{L}} > 3500$ were extensively measured. Ironically, their

favourable optical properties were attributed to rupturing during the release process that contorted the suspended optomechanical crystal plates out of the plane. This put the resonators vertically higher above the bulk substrate than usual, contributing to lower loss. Their optical profiles are given in Fig. 5.3.

Optomechanical coupling measurements were made from the thermal mechanical spectrum with plots in Fig. 5.4 and Fig. 5.5. Spectrum analyzer data were assumed to be precise measurements of a noisy source signal with distribution (see Sec. Φ.3.4). The coupling rates measured were $g_{\mathrm{om}} = (649 \pm 8)\,\mathrm{kHz}$ and $g_{\mathrm{om}} = (441 \pm 6)\,\mathrm{kHz}$, comparable to nanobeam resonators fabricated. Determination of these values is dependent on the mechanical mode population $\bar{n}_{\mathrm{m}}$ which was calculated from an estimation of temperature $\mathbb{T} = (295 \pm 3)\,\mathrm{K}$ based on ambient conditions.

Monitoring of the optical setup is carried out over the course of the scans. Fig. 5.6 plots experimental parameters during the scans presented in Fig. 5.4.

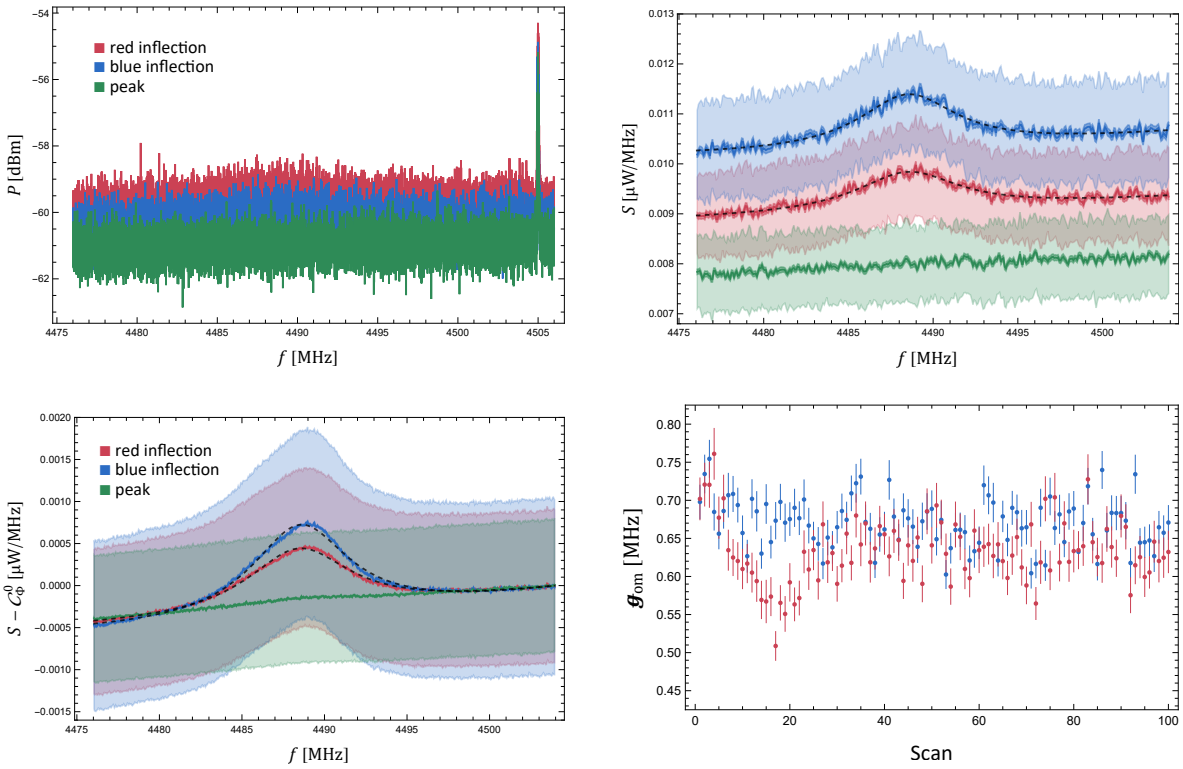

Figure 5.4: Device A measurements. (Top left) full power spectrum measured during a single scan. (Top right) a single power spectrum with 200 point moving average showing the thermal mechanical spectrum. Dark shading around the trace represents uncertainty in the averaged value, light shading represents the scatter standard deviation of the source. (Bottom left) power average of 100 scans with baseline adjustment and 100 point moving average. Uncertainty in mean is imperceptible, and the light shading shows source scatter. Fitting to this produces $\vartheta_{\mathrm{om}} = (629 \pm 9)\,\mathrm{kHz}$ for the red inflection, and $\vartheta_{\mathrm{om}} = (668 \pm 9)\,\mathrm{kHz}$ for the blue inflection, with $Q_{\mathrm{m}} = 600 \pm 4$. (Bottom right) optomechanical coupling measured from each individual scan. The weighted means are $\vartheta_{\mathrm{om}} = (625 \pm 8)\,\mathrm{kHz}$ for red inflection points, and $\vartheta_{\mathrm{om}} = (665 \pm 9)\,\mathrm{kHz}$ for blue inflection points.

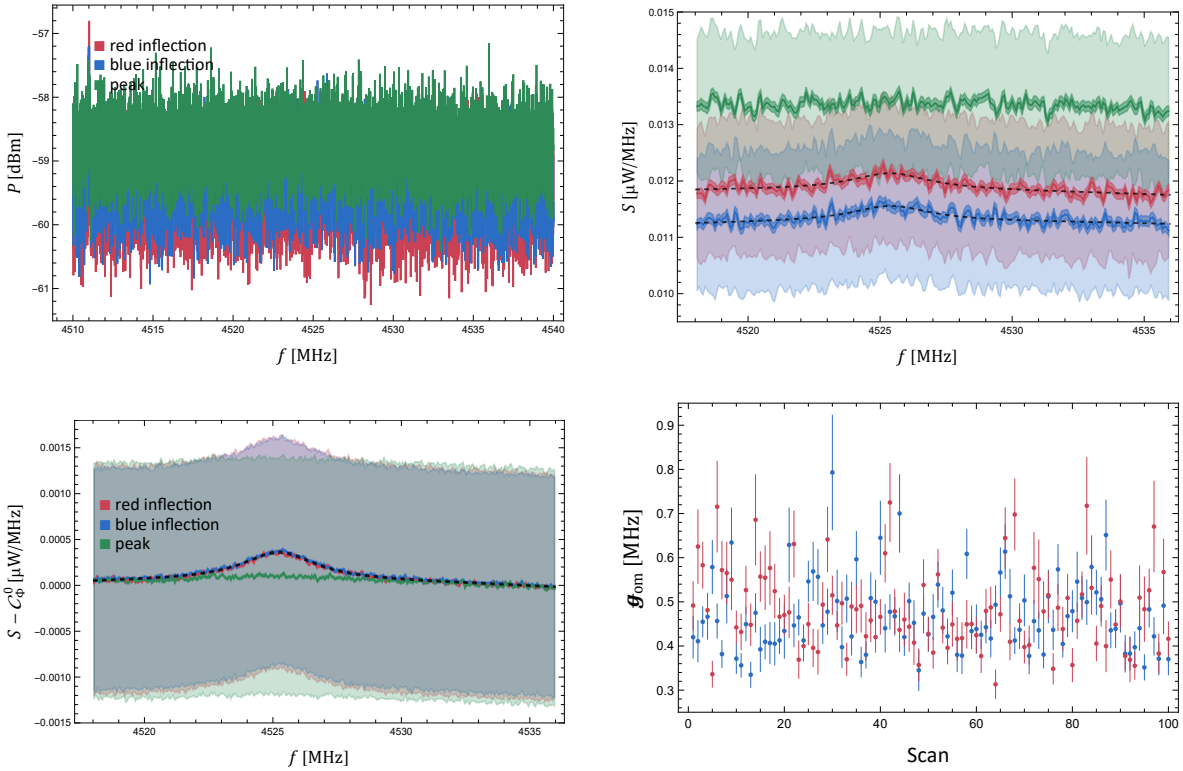

Figure 5.5: Device B measurements. (Top left) full power spectrum measured during a single scan. (Top right) a single power spectrum with 200 point moving average showing the thermal mechanical spectrum. Dark shading around the trace represents uncertainty in the averaged value, light shading represents the scatter standard deviation of the source. (Bottom left) power average of 100 scans with baseline adjustment and 100 point moving average. Uncertainty in mean is imperceptible, and the light shading shows source scatter. Fitting to this produces $g_{\mathrm{om}} = (471 \pm 9)\,\mathrm{kHz}$ for the red inflection, and $g_{\mathrm{om}} = (461 \pm 8)\,\mathrm{kHz}$ for the blue inflection, with $Q_{\mathrm{m}} = 1279 \pm 18$. (Bottom right) optomechanical coupling measured from each individual scan. The weighted means are $g_{\mathrm{om}} = (445 \pm 7)\,\mathrm{kHz}$ for red inflection points, and $g_{\mathrm{om}} = (438 \pm 7)\,\mathrm{kHz}$ for blue inflection points.

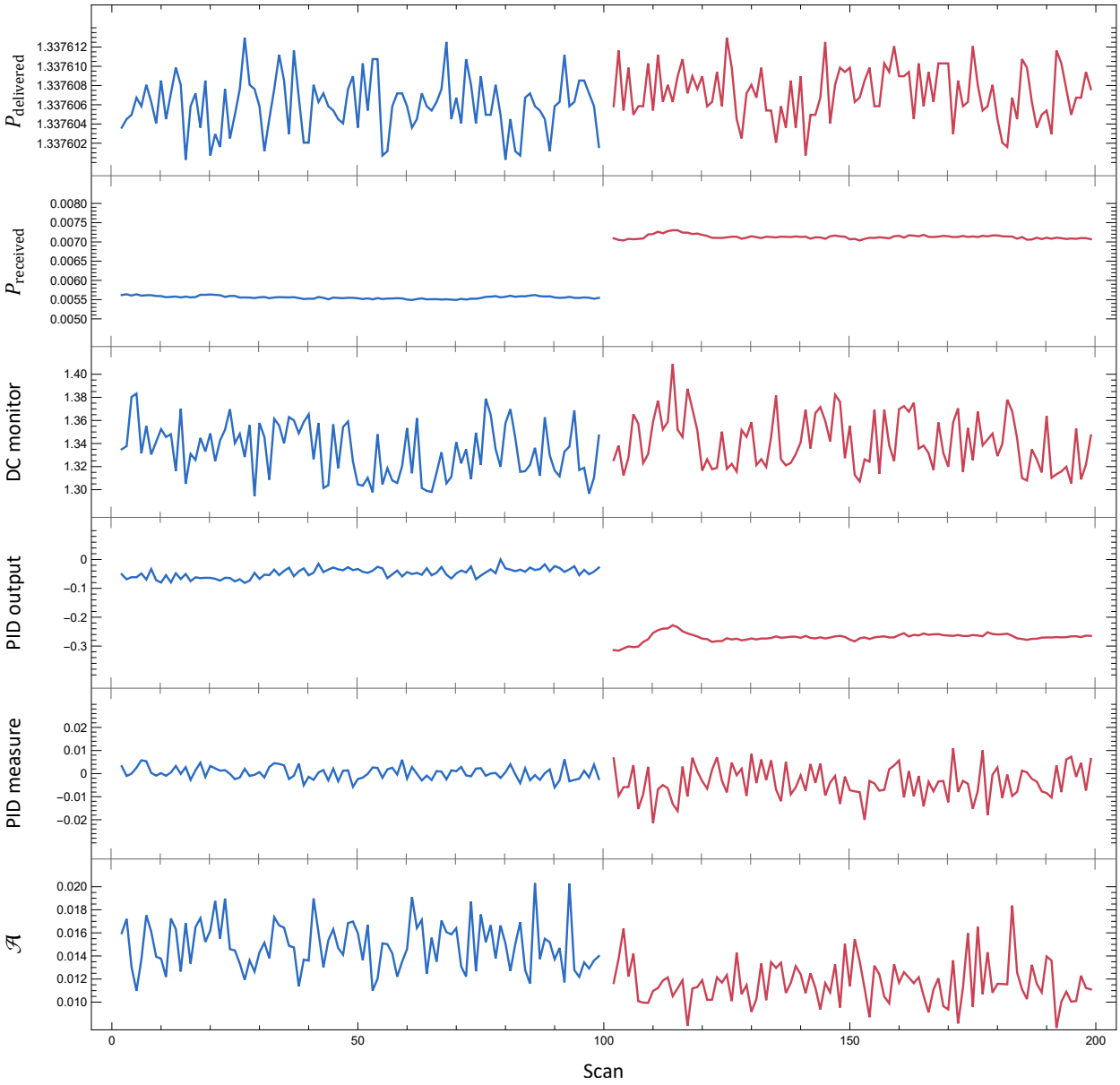

Figure 5.6: Monitoring the feedback control systems (see App. Σ) during the series of scans for device A.

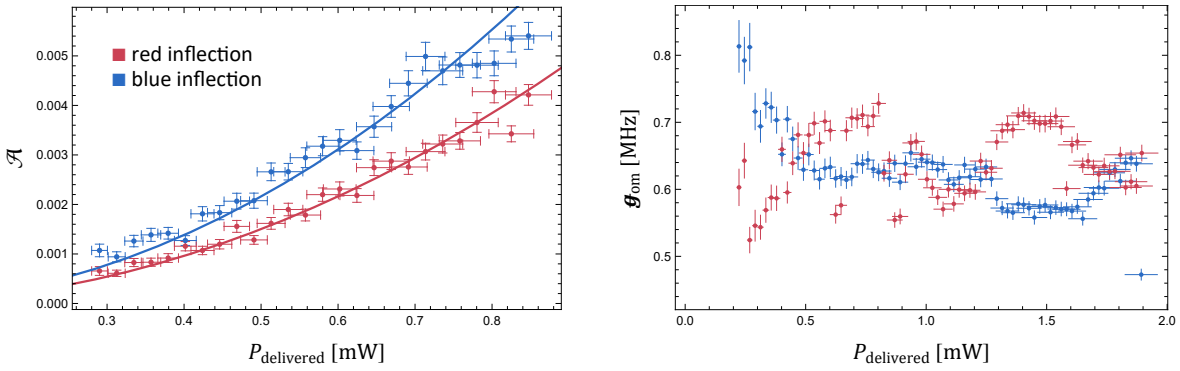

Figure 5.7: (Left) Spectrum fit $\mathcal{A}$ for different powers measured at the blue and red inflection points over the linear operating regime of the fast photodetector. Solid line is a fit to ${P_{\text{delivered}}}^2$. (Right) optomechanical couplings calculated for each individual scan. The weighted average produces $g_{\text{om}} = (620 \pm 8)\,\text{kHz}$. Delivered power is an estimate of the power leaving the V-groove to the chip based on the input power feedback control setting and includes systematic uncertainty.

5.4.1 Power dependence

Extensive power dependent measurements were made of device A and are plotted in Fig. 5.8.

From App. L we expect the thermal spectrum 'height' $\mathcal{A}$ to be proportional to ${P_{\text{delivered}}}^2$.

Plots of $\mathcal{A}$ and g_{om} are given in Fig. 5.7.

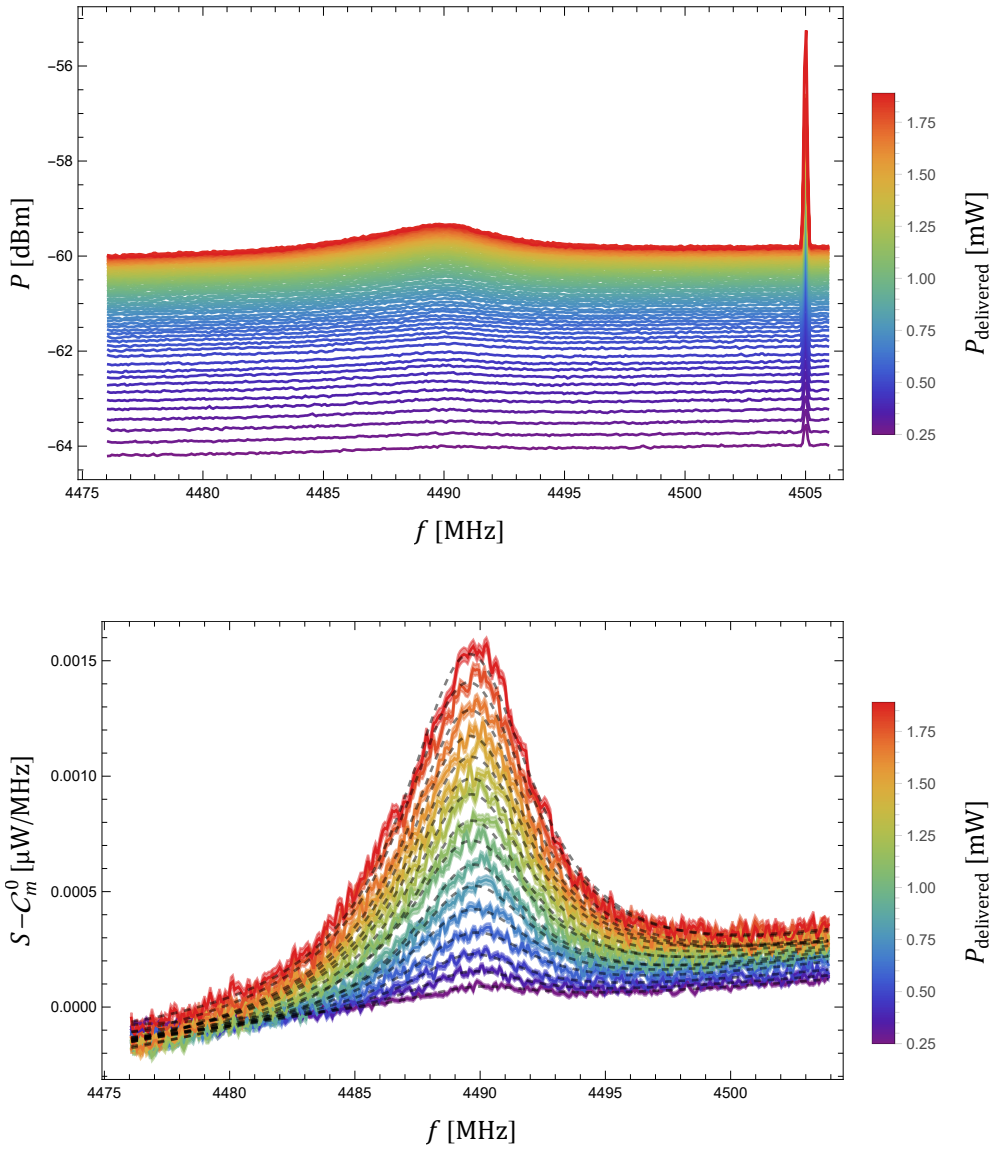

Figure 5.8: (Top) measured power spectrums from varied input powers with a 200 point moving average. The phase modulated signal is visible at 4505 MHz. (Bottom) spectral densities for a selection of input powers, plotted with background subtraction to be overlaid, and with a 200 point moving average. Shading around the traces represents mean uncertainty. Fits to the power spectral densities are shown in black dashing.

5.4.2 Double paddle

A double paddle, $\mathsf{n}_{\text{defect}} = 2$, vertebrae device with mechanical mode splitting of 13 MHz was also measured with results given in Fig. 5.9.

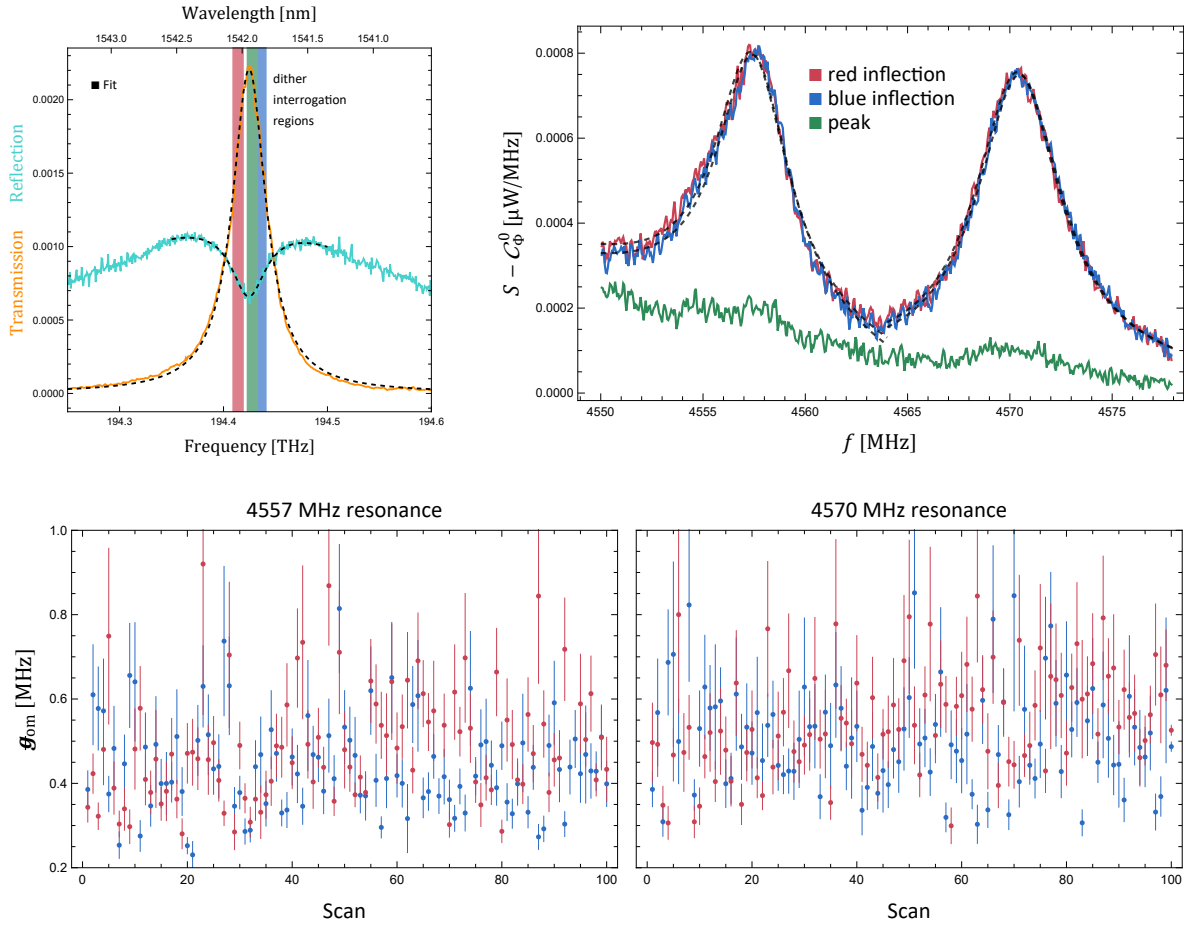

Figure 5.9: Double paddle device measurements. (Top left) optical transmission and reflection. Fits produce $f_o = 194.4\,\mathrm{THz}$, $Q_o^L \approx 4950$, $\beta_o^1 \approx 0.16$, $Q_o^0 \approx 6500$. (Top right) power average of 100 scans with baseline adjustment and 100 point moving average. Fitting gives $\mathcal{g}_{om} = (444 \pm 10)\,\mathrm{kHz}$ and $Q_m = 1037 \pm 25$ for the lower frequency peak, and $\mathcal{g}_{om} = (505 \pm 8)\,\mathrm{kHz}$ and $Q_m = 905 \pm 13$ for higher frequency peak. (Bottom) optomechanical coupling measured from each individual scan. The weighted means are $\mathcal{g}_{om} = (379 \pm 6)\,\mathrm{kHz}$ for the lower frequency resonance, and $\mathcal{g}_{om} = (445 \pm 7)\,\mathrm{kHz}$ for the higher frequency peak.

CHAPTER 6

Conclusion

Here we discuss our findings and propose future steps for development.

6.1 Results

After much toil, a quasi-two-dimensional optomechanical crystal resonator was made in gallium arsenide using the vertebrae cavity design [152]. Optomechanical couplings exceeding 500 kHz were measured, making them as good as one-dimensional nanobeam resonators tested. Further optimizations to the design and fabrication process can likely improve on this value.

While a rigorous assessment of the two-dimensional heat conductance properties of our devices would require cryogenic temperatures, the advantages of two dimensions were confirmed in the silicon vertebrae device of Ref. [152]. It's worth noting that power dependent non-linearities that warped the optical resonance of the one-dimensional nanobeams at high powers, thought to be attributed to having separate waveguide and cavity structures, were not observed in the two-dimensional vertebrae resonators.

The most encouraging result of this work is the frequencies that a gallium arsenide two-dimensional optomechanical resonator can target. Whilst supporting an optical resonance frequency of 194 THz for infra-red fiber connections, the mechanical mode resonance frequency is ~ 4.5 GHz, ideal for interfacing with superconducting qubits [212]. Silicon two-dimensional optomechanical resonators have mechanical resonances ~ 10 GHz [152, 178].

Whilst it's impossible to make a quantitative statement, it seems likely that a 1 μm suspen-

sion clearance (less than our vacuum wavelength $\sim 1.5\,\mu m$) is too low and contributes to significant optical loss.

6.2 Next steps

Clearly quantum microwave-electronic to infra-red optic transduction did not occur so there is still much to do. The three major milestones down that road are: improved optical quality factor to enter the sideband resolved regime, electromechanical integration, and cryogenic operation.

6.2.1 Design optimization

There are a lot of dimensional design parameters and geometric tweaks that can be made in the vertebrae design. With our computing architecture, simulations of a vertebrae resonator take $\sim 1\,hour$. Many possibilities described in App. Z received only cursory attention. A thorough optimization would require significant computational resources but could potentially improve the optomechanical coupling by tens of percent.

Furthermore there is plenty of room to get creative with the design, perhaps some way to have the cavity paddles more connected to avoid mode splitting. Or an entirely different quasi-two-dimensional design.

6.2.2 Fabrication

Gallium arsenide is a challenging material to work with when it comes to electron beam lithography. An alternative resist or excruciating HSQ handling requirements will be needed

to achieve nanometer level consistency. Meticulous fine tuning will be required for $\mathsf{n}_{\mathrm{defect}} > 1$ single resonance multi-paddle vertebrae devices.

Wafers with a thicker sacrificial aluminium gallium arsenide layer should be tried. Furthermore, a lower aluminium concentration, down to 70%, may produce less by-product and slow down the release to be more gentle. Recent gallium arsenide nanobeam optomechanical crystal experiments used 3 µm of $Al_{0.7}Ga_{0.3}As$ and achieve $Q_o^L = 3.3 \times 10^4$ [128]. With a gentler release, the serpentine tethers can be removed for more thermal conductivity between the optomechanical crystal plate and remainder of the chip.

6.2.3 Edge optic coupling

Grating couplers and transmission through the device are convenient for development, but transitioning to edge coupling and a reflection based measurement setup will eventually be needed. Described briefly in App. V, tapered beam waveguides to tapered optical fibers provide superior optical coupling.

This approach also allows excess suspended beam waveguides to be removed, and in particular the tethers holding them up that can be a source of both optical and mechanical loss. If the acoustic cavity can be supported only through strongly impeding phononic crystals, such as the cross shielding [179], very high mechanical quality factors are obtainable. It might, however, still be preferable to have a long suspended beam waveguide to keep the main cavity out of the direct path of the laser [117].

Additionally, a one-sided optical coupling allows the other side of the vertebrae waveguide to be used for electromechanical coupling. This would avoid the need to go through the snowflakes with the partial waveguides mentioned in Ch. 3.

A significant downside is the number of accessible devices on a chip. Improvements in fabrication reliability will mitigate this problem, however.

6.2.4 Cryogenics

Temperatures below $\sim 100\,\mathrm{mK}$ are needed to put the acoustic resonator in to its ground state. Moreover, everything should be better at cryogenic temperatures, particularly quality factors. Vacuum and thermal stability will also help with measurement precision.

The major challenge for cryogenics is optical coupling. Dilution refrigerators with optical fiber ports are now commonplace but aligning the fiber with the device is difficult. That being said, cryogenic optical coupling is now routine for many labs [213]. Its likely desirable to develop edge coupling first so as to avoid future re-engineering.

At cryogenic temperatures we expect gallium arsenide to contract by about 1 part in 1000 (see Sec. M.1.6). This will shift resonances around but not enough to be problematic. It does, however, limit the amount of pre-cool-down alignment that can be done.

6.2.5 Electromechanics

Transduction of the acoustic vibrations into an electrical signal is a fundamental component of the full device. Assuming that one-sided optical reflection measurements are successful, it will likely be preferable to have the acoustics use the other side of the vertebrae waveguide. A leaky mechanical partial waveguide [122] can connect the resonator to either a small electrode pad or large interdigitated transducer array.

One complication will be the choice of electrode metal. Aluminium is often used for its superconductivity and simple fabrication techniques but is attacked by hydrofluoric acid

and thus incompatible with our release process.

Once there is an electric connection, a superconducting qubit can be fabricated on a separate substrate and integrated with a flip-chip architecture [214].

6.2.6 Multi-mode

Defect cavity paddles with slightly different resonances could potentially be a feature. It might be possible to create a broadband transducer, investigate dual mode behaviour [215, 216] or implement a chiral network [217].

6.2.7 Other

If optical quality factors remain mediocre, a secondary optical cavity, e.g. a gallium arsenide micro-disc, can be used to create effective sideband resolved dynamics [218].

One could also try alternative optomechanical coupling measurements using Hopf Bifurcation that avoids thermal population uncertainty [219].

APPENDIX A

Electromagnetics

A.1 Maxwell's equations

The infra-red optical field occupying our cavity and traversing the photonic crystal is described by standard electrodynamics. With the following field definitions over position $\vec{x}$,

$\vec{E}$	$\vec{D}$	$\vec{H}$	$\vec{B}$
electric	electric displacement	magnetic	magnetic flux density

þ	$\vec{J}$
free charge density	free current density

we have Maxwell's equations in matter [220],

$$\vec{\nabla} \cdot \vec{D} = \text{þ} \, , \qquad \vec{\nabla} \cdot \vec{B} = 0 \, ,$$

$$\vec{\nabla} \times \vec{E} = -\frac{\partial}{\partial t}\vec{B} \, , \qquad \vec{\nabla} \times \vec{H} = \frac{\partial}{\partial t}\vec{D} + \vec{J} \, .$$

The fields are related via material properties

ε_{ij}	μ_{ij}
permittivity	permeability

in non-cross coupling materials[1] by

$$D_i = \varepsilon_{i\,j}\, E^j \ , \qquad\qquad B_i = \mu_{i\,j}\, H^j \ .$$

If the material is piezoelectric (see App. B) these are modified to include fields generated by strain.

With space-time metric $g_{\mu\,\nu} = \mathrm{diag}[1,-1,-1,-1]$, we can write Maxwell's equations in terms of the electromagnetic field strength tensor, and its Hodge dual[2],

$$(F^{\alpha\,\beta}) = \begin{pmatrix} 0 & -E_x/c & -E_y/c & -E_z/c \\ E_x/c & 0 & -B_z & B_y \\ E_y/c & B_z & 0 & -B_x \\ E_z/c & -B_y & B_x & 0 \end{pmatrix} , \qquad G^{\alpha\,\beta} = (\star F)^{\alpha\,\beta} = \tfrac{1}{2}\,\epsilon^{\alpha\,\beta\,\gamma\,\delta}\, F_{\gamma\,\delta} \ ,$$

as

$$\partial_\alpha\, F^{\alpha\,\beta} = \ \mu_0\, J^\beta \ , \qquad\qquad \partial_\alpha\, G^{\alpha\,\beta} = \ 0 \ .$$

A.2 Wave equations of motion

In an isotropic ($\varepsilon_{i\,j} = \varepsilon\,\delta_{i\,j}$, $\mu_{i\,j} = \mu\,\delta_{i\,j}$), homogeneous ($\partial_i\,\varepsilon = 0$, $\partial_i\,\mu = 0$), non-dispersive ($\Im[\varepsilon] = 0$, $\Im[\mu] = 0$), non-conducting ($J^i = 0$), source free ($\mathfrak{p} = 0$) material, we can

1. Media that are bi-isotropic or bi-anisotropic have additional cross couplings between electric and magnetic fields.

2. Here, ϵ is the Levi-Civita symbol.

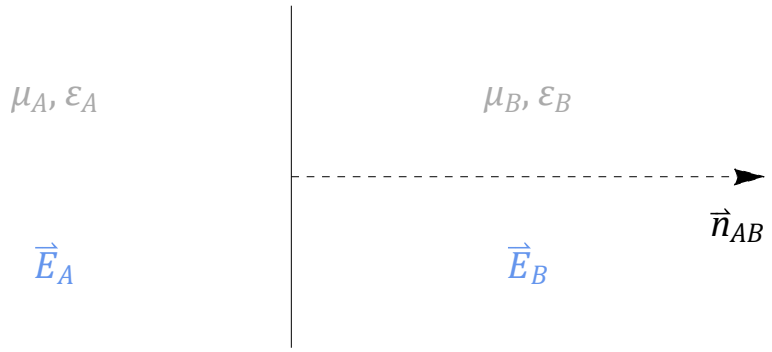

Figure A.1: Interface between materials A and B.

substitute within Maxwell's equations to obtain [220]

$$\frac{\partial}{\partial x^j}\frac{\partial}{\partial x^j}E^i - \mu\,\varepsilon\,\frac{\partial^2}{\partial t^2}E^i = 0\,,$$

$$\frac{\partial}{\partial x^j}\frac{\partial}{\partial x^j}H^i - \mu\,\varepsilon\,\frac{\partial^2}{\partial t^2}H^i = 0\,.$$

For a harmonic oscillation, $E^i(\vec{x},t) = \Re\big[E(\vec{x})\,\mathrm{e}^{-\mathrm{i}\,\omega\,t}\big]$, we get

$$\frac{\partial}{\partial x^j}\frac{\partial}{\partial x^j}E^i(\vec{x}) + \mu\,\varepsilon\,\omega^2 E^i(\vec{x}) = 0\,,$$

$$\frac{\partial}{\partial x^j}\frac{\partial}{\partial x^j}H^i(\vec{x}) + \mu\,\varepsilon\,\omega^2 H^i(\vec{x}) = 0\,,$$

with complex fields over position $\vec{x}$.

A.3 Interfaces

At the interface between two materials A and B, with normal vector $\vec{n}_{AB}$ defined to be going from A to B as depicted in Fig. A.1, the electric and magnetic fields must obey the

following boundary conditions

$$\vec{n}_{AB} \times \left(\vec{E}_B - \vec{E}_A\right) = 0 \,, \qquad\qquad \vec{n}_{AB} \cdot \left(\vec{D}_B - \vec{D}_A\right) = \text{þ}_S \,,$$

$$\vec{n}_{AB} \times \left(\vec{H}_B - \vec{H}_A\right) = \vec{J}_S \,, \qquad\qquad \vec{n}_{AB} \cdot \left(\vec{B}_B - \vec{B}_A\right) = 0 \,,$$

where þ_S is the free surface charge density and $\vec{J}_S$ is the free surface current density.

A.4 Conductor symmetries

The symmetry condition for electromagnetic fields is (see Sec. D.6)

$$\underline{\underline{S}} \cdot \vec{E}\big[\vec{r}\big] = s\, \vec{E}\big[\underline{\underline{S}} \cdot \vec{r}\big] \,, \qquad\qquad \underline{\underline{S}} \cdot \vec{H}\big[\vec{r}\big] = -s\, \vec{H}\big[\underline{\underline{S}} \cdot \vec{r}\big] \,.$$

At the origin of the symmetry, the fields must be eigenvectors of the symmetry matrix $\underline{\underline{S}}$ with the corresponding eigenvalue,

$$\underline{\underline{S}} \cdot \vec{E}[0] = s\, \vec{E}[0] \,, \qquad\qquad \underline{\underline{S}} \cdot \vec{H}[0] = -s\, \vec{H}[0] \,.$$

For a x mirror, $\underline{\underline{S}} = \text{diag}[-1, 1, 1]$, the eigenvalues are ± 1 with eigenvectors spaces

$$V_1 = \left\{\hat{\vec{y}}, \hat{\vec{z}}\right\} \,, \qquad\qquad V_{-1} = \left\{\hat{\vec{x}}\right\} \,.$$

In general, for a $\vec{n}$ mirror symmetry, at the mirror we find

$$s = 1 \quad \Rightarrow \quad \begin{cases} \vec{E} \perp \vec{n} \\ \vec{H} \parallel \vec{n} \end{cases} \quad \Rightarrow \quad \begin{cases} \vec{E} \cdot \vec{n} = 0 \\ \vec{H} \times \vec{n} = 0 \end{cases} ,$$

$$s = -1 \quad \Rightarrow \quad \begin{cases} \vec{E} \parallel \vec{n} \\ \vec{H} \perp \vec{n} \end{cases} \quad \Rightarrow \quad \begin{cases} \vec{E} \times \vec{n} = 0 \\ \vec{H} \cdot \vec{n} = 0 \end{cases} .$$

Comparing this to our interface conditions, $s = -1$ corresponds to $\vec{E}_B = 0$ and $\vec{B}_B = 0$, i.e. an electrical conductor, and thus this boundary condition can be used to enforce mirror antisymmetry. For the other situation of $s = 1$, the mirror symmetry is enforced by a theoretical magnetic conductor.

A.5 Periodic boundaries

The infinite repeating pattern of a photonic crystal can be reduced to a single unit cell with periodic boundary conditions following Floquet's theorem. For a lattice vector $\vec{a}$, which will go between the boundaries, and a particular wavevector $\vec{k}$, the fields obey

$$\vec{E}(\vec{x} + \vec{a}) = \vec{E}(\vec{x})\, \mathrm{e}^{-\mathrm{i}\, \vec{k} \cdot \vec{a}} , \qquad \vec{H}(\vec{x} + \vec{a}) = \vec{H}(\vec{x})\, \mathrm{e}^{-\mathrm{i}\, \vec{k} \cdot \vec{a}} .$$

Note that applying a change of coordinate system $\vec{x} \mapsto \vec{x} - \vec{a}$ to the wave equations, following Sec D.3, yields

$$\frac{\partial}{\partial x^j} \frac{\partial}{\partial x^j} E^i(\vec{x} + \vec{a}) + \mu(\vec{x} + \vec{a})\, \varepsilon(\vec{x} + \vec{a})\, \omega^2 E^i(\vec{x} + \vec{a}) = 0 ,$$

and for a periodic material $\mu(\vec{x}+\vec{a}) = \mu(\vec{x})$, $\varepsilon(\vec{x}+\vec{a}) = \varepsilon(\vec{x})$,

$$\frac{\partial}{\partial x^j}\frac{\partial}{\partial x^j}E^i(\vec{x}+\vec{a}) + \mu(\vec{x})\,\varepsilon(\vec{x})\,\omega^2 E^i(\vec{x}+\vec{a}) = 0\ ,$$

implying $\vec{E}(\vec{x}+\vec{a}) \propto \vec{E}(\vec{x})$ and likewise $\vec{H}(\vec{x}+\vec{a}) \propto \vec{H}(\vec{x})$.

APPENDIX B

Piezoelectrics

B.1 Piezoelectric equations

Various crystalline solid materials without inversion symmetry exhibit piezoelectric behaviour, where strains in the material generate electric fields and vice-versa. The relationship between these quantities are given by material property coupling tensors. In the context of continuum solid mechanics and electromagnetics, we have the following field definitions over position x^i,

$$\underset{\text{displacement}}{Q^i} \qquad \underset{\text{strain}}{\epsilon_{ij}} = \frac{1}{2}\left(\frac{\partial Q_i}{\partial x^j} + \frac{\partial Q_j}{\partial x^i}\right) \qquad \underset{\text{stress}}{\sigma^{ij}}$$

$$\underset{\text{electric}}{E^i} \qquad \underset{\substack{\text{electric}\\ \text{displacement}}}{D^i} \quad ,$$

and material properties

$$\underset{\text{stiffness}}{c^{ijkl}} \qquad \underset{\text{compliance}}{s_{ijkl}} \qquad \underset{\text{permittivity}}{\varepsilon_{ij}} \qquad \underset{\substack{\text{piezoelectric}\\ \text{stress}}}{e^{ijk}} \qquad \underset{\substack{\text{piezoelectric}\\ \text{strain}}}{d_{ijk}} \quad .$$

Piezoelectricity provides an extension to Hooke's Law. Using Einstein summation notation,

the relations in stress-charge form are [221]

$$\sigma^{ij} = c^{ijkl}\,\epsilon_{kl} - e^{kij}\,E_k\,, \qquad\qquad D^k = e^{kij}\,\epsilon_{ij} + \varepsilon^{kl}\,E_l\,,$$

where the compliance is defined for constant electric field and the permittivity is defined for constant strain. In strain-charge form,

$$\epsilon_{ij} = s_{ijkl}\,\sigma^{kl} + d_{kij}\,E^k\,, \qquad\qquad D_k = d_{kij}\,\sigma^{ij} + \varepsilon_{kl}\,E^l\,,$$

where stiffness is defined for constant electric field and the permittivity is defined for constant stress. The two forms are related by

$$c^{abij}\,s_{ijcd} = \frac{1}{2}\left(\delta^a_{\ c}\,\delta^b_{\ d} + \delta^a_{\ d}\,\delta^b_{\ c}\right)\,, \qquad c^{ijkl}\,s_{ijkl} = 6\,, \qquad e^{kij} = d^k_{\ ab}\,c^{abij}\,.$$

The material property tensors exhibit symmetries

$$c^{((ij)(kl))}\,, \qquad s_{((ij)(kl))}\,, \qquad e^{k\,(ij)}\,, \qquad d_{k\,(ij)}\,,$$

and thus can be written as matrices using Voigt notation (see App. G). The stress-charge form is then

$$\underline{\tilde{\sigma}} = \underline{\underline{\tilde{c}}} \cdot \underline{\tilde{\epsilon}} - \underline{\underline{\tilde{e}}}^{\mathsf{T}} \cdot \underline{E}\,, \qquad\qquad \underline{D} = \underline{\underline{\tilde{e}}} \cdot \underline{\tilde{\epsilon}} + \underline{\underline{\varepsilon}} \cdot \underline{E}\,,$$

and the strain-charge form is

$$\underline{\tilde{\epsilon}} = \underline{\underline{\tilde{s}}} \cdot \underline{\tilde{\sigma}} + \underline{\underline{\tilde{d}}}^{\mathsf{T}} \cdot \underline{E}\,, \qquad\qquad \underline{D} = \underline{\underline{\tilde{d}}} \cdot \underline{\tilde{\sigma}} + \underline{\underline{\varepsilon}} \cdot \underline{E}\,,$$

with relations

$$\underline{\underline{\tilde{c}}} \cdot \underline{\underline{\tilde{s}}} = \underline{\underline{\mathbb{I}_6}} \,, \qquad \underline{\underline{\tilde{e}}} = \underline{\underline{\tilde{d}}} \cdot \underline{\underline{\tilde{c}}} \,, \qquad \underline{\underline{\tilde{c}}}^{\mathsf{T}} = \underline{\underline{\tilde{c}}} \,, \qquad \underline{\underline{\tilde{s}}}^{\mathsf{T}} = \underline{\underline{\tilde{s}}} \,.$$

B.2 Isotropic materials

Isotropic materials have only two independent quantities, with various names for different combinations of them.

$$\underset{\substack{\text{Young's}\\ \text{modulus}}}{E} = \frac{1}{\tilde{s}_{1\,1}} \,, \qquad \underset{\substack{\text{Poisson's}\\ \text{ratio}}}{\nu} = -\frac{\tilde{s}_{1\,2}}{\tilde{s}_{1\,1}} \,,$$

$$\underset{\substack{\text{shear}\\ \text{modulus}}}{\mu} = \frac{1}{\tilde{s}_{4\,4}} = \tilde{c}^{4\,4} \,, \qquad \underset{\substack{\text{pressure}\\ \text{modulus}}}{M} = \tilde{c}^{1\,1} \,,$$

$$\underset{\substack{\text{1st Lamé}\\ \text{parameter}}}{\lambda} = \tilde{c}^{1\,2} \,, \qquad \underset{\substack{\text{bulk}\\ \text{modulus}}}{K} = \frac{\tilde{c}^{1\,1} + 2\,\tilde{c}^{1\,2}}{3} \,,$$

and some example relations are

$$E = 3\,K\,(1 - 2\,\nu) = 2\,\mu\,(1 + \nu) \,, \qquad M = \lambda + 2\,\mu \,.$$

For acoustic waves, some speeds are

$$\underset{\substack{\text{acoustic}\\ \text{gas}}}{v} = \sqrt{K/\rho} \,, \qquad \underset{\substack{\text{longitudinal wave}\\ \text{phase velocity}}}{v} = \sqrt{M/\rho} \,, \qquad \underset{\substack{\text{transverse wave}\\ \text{phase velocity}}}{v} = \sqrt{\mu/\rho} \,,$$

where ρ is material density.

For cubic crystals, such as GaAs, one can define an anisotropy factor

$$\underset{\substack{\text{anisotropy}\\ \text{factor}}}{A} = \frac{2\,\tilde{c}^{4\,4}}{\tilde{c}^{1\,1} - \tilde{c}^{1\,2}} \ ,$$

which is equal to one for true isotropic materials.

B.3 Vibration equation of motion

The equation of motion for a vibrating solid is [222]

$$\rho\,\frac{\partial^2}{\partial t^2} Q^i - \frac{\partial}{\partial x^j}\sigma^{i\,j} = F^i \ ,$$

where F^i is external force.

For a harmonic oscillation with no external forces, $Q^i(\vec{x},t) = \Re\big[Q(\vec{x})\,\mathrm{e}^{-\mathrm{i}\,\omega\,t}\big]$, we get

$$-\rho\,\omega^2\,Q^i(\vec{x}) - c^{i\,j\,k\,l}\,\frac{1}{2}\left(\frac{\partial}{\partial x^j}\frac{\partial}{\partial x^k}Q_l(\vec{x}) + \frac{\partial}{\partial x^j}\frac{\partial}{\partial x^l}Q_k(\vec{x})\right) + e^{k\,i\,j}\,\frac{\partial}{\partial x^j}E_k(\vec{x}) = 0 \ ,$$

with complex fields over position $\vec{x}$.

APPENDIX C

Optomechanical coupling

C.1 Origin

The optomechanical system Hamiltonian can be formulated as the combination of an optical simple harmonic oscillator of angular frequency ω_{o} and a mechanical simple harmonic oscillator of angular frequency ω_{m} [138],

$$\hat{H}_{\mathrm{unc}} = \hbar\,\omega_{\mathrm{o}}\left(\hat{a}^{\dagger}\,\hat{a} + \frac{1}{2}\right) + \hbar\,\omega_{\mathrm{m}}\left(\hat{b}^{\dagger}\,\hat{b} + \frac{1}{2}\right)\ , \tag{C.1}$$

where $\hat{a}$ and $\hat{b}$ are the annihilation operators for photons and phonons respectively.

This system is most basically modeled as a one-dimensional Fabry-Pérot cavity with one mirror attached to a spring (Fig. C.2). For a mechanical harmonic oscillator in one dimension, the phonon creation and annihilation operators are related to the displacement (from equilibrium), x, and momentum, p, operators by

$$\hat{x} = \sqrt{\frac{\hbar}{2\,m_{\mathrm{eff}}\,\omega_{\mathrm{m}}}}\left(\hat{b}^{\dagger} + \hat{b}\right)\ , \qquad\qquad \hat{p} = i\sqrt{\frac{\hbar\,m_{\mathrm{eff}}\,\omega_{\mathrm{m}}}{2}}\left(\hat{b}^{\dagger} - \hat{b}\right)\ ,$$

where m_{eff} is the effective mass. The factor appearing in $\hat{x}$ is often called the zero point fluctuation,

$$x_{\mathrm{zpf}} = \sqrt{\frac{\hbar}{2\,m_{\mathrm{eff}}\,\omega_{\mathrm{m}}}}\ . \tag{C.2}$$

The resonance frequency of the optical Fabry-Pérot cavity depends on the length, which in

turn depends on the displacement of the spring-mirror. For a small perturbation we can make the Taylor expansion

$$\omega_{\mathrm{o}}(x) = \omega_{\mathrm{o}}(0) + x \left.\frac{\mathrm{d}\,\omega_{\mathrm{o}}(x')}{\mathrm{d}\,x'}\right|_{x'=0} + \mathcal{O}\,[x]^2$$

$$= \approx \omega_{\mathrm{o}}(0) + x \left(\frac{\Delta\omega_o(x)}{x}\right) .$$

Using this first order expansion we can make the substitution into (C.1)

$$\omega_{\mathrm{o}} \mapsto \omega_{\mathrm{o}} + \left(\frac{\Delta\omega_o(x)}{x}\right) \hat{x} = \omega_{\mathrm{o}} + \sqrt{\frac{\hbar}{2\,m_{\mathrm{eff}}\,\omega_{\mathrm{m}}}}\,\frac{\Delta\omega_o(x)}{x}\,\left(\hat{b}^\dagger + \hat{b}\right)$$

where the new $\omega_{\mathrm{o}} = \omega_{\mathrm{o}}(0)$ is the equilibrium-position optical angular frequency.

Our first order coupled Hamiltonian is now

$$\hat{H} = \hbar\,\omega_{\mathrm{o}}\,\left(\hat{a}^\dagger\,\hat{a} + \frac{1}{2}\right) + \hbar\,\omega_{\mathrm{m}}\,\left(\hat{b}^\dagger\,\hat{b} + \frac{1}{2}\right) + \hbar\,g_{\mathrm{om}}\,\left(\hat{a}^\dagger\,\hat{a} + \frac{1}{2}\right)\,\left(\hat{b}^\dagger + \hat{b}\right)\,, \tag{C.3}$$

where the optomechanical coupling between $\hat{a}$ and $\hat{b}$ is

$$g_{\mathrm{om}} = \sqrt{\frac{\hbar}{2\,m_{\mathrm{eff}}\,\omega_{\mathrm{m}}}}\,\frac{\Delta\omega_o(x)}{x}\,. \tag{C.4}$$

For a one-dimensional system such as the Fabry-Pérot cavity, where $\omega_{\mathrm{o}} \propto 1/\text{length}$, this approximation is valid for $x \ll \text{length}$. In this regime we find $\Delta\omega_{\mathrm{o}}(x) \propto x$.

C.2 Phasors

When using the frequency domain it is helpful to work with phasors. For our one-dimensional mechanical simple harmonic oscillator

$$x(t) = \Re\left[X\,\mathrm{e}^{-\mathrm{i}\,\omega_\mathrm{m}\,t}\right] = \Re[X]\cos[\omega_\mathrm{m}\,t] + \Im[X]\sin[\omega_\mathrm{m}\,t] \quad : \quad X \in \mathbb{C}\,,$$

noting that $\max[x(t)] = |X|$.

For a vector field such as solid displacement

$$Q_i(\vec{r},t) = \Re\left[Q_i(\vec{r})\,\mathrm{e}^{-\mathrm{i}\,\omega_\mathrm{m}\,t}\right] \quad : \quad Q_i(\vec{r}) \in \mathbb{C}\,.$$

C.3 Bra-ket notation

To simplify equations we use the following bra-ket notation. For a vector field $\vec{v}(\vec{r}) \in \mathbb{C}^3$ over $\vec{r} \in \mathbb{R}^3$, and scalar field $s(\vec{r})$ or 2-tensor field $t(\vec{r})$,

$$\langle \vec{v}\,|\,s\,|\,\vec{v}\rangle = \iiint_V v_i(\vec{r})^*\,s(\vec{r})\,v_i(\vec{r})\,\mathrm{d}^3\vec{r}\,,$$
$$\langle \vec{v}\,|\,t\,|\,\vec{v}\rangle = \iiint_V v_i(\vec{r})^*\,t_{i\,j}(\vec{r})\,v_j(\vec{r})\,\mathrm{d}^3\vec{r}\,.$$

C.4 Effective mass

For a simple one-dimensional system such as the Fabry-Pérot cavity with a spring-mirror as described above, the effective mass is just the mass of the moving mirror. When dealing with

a three-dimensional acoustic resonance of a solid object we need to derive what the effective mass is. The mechanical system Hamiltonian is

$$\hat{H}_{\mathrm{m}} = \hbar\,\omega_{\mathrm{m}}\,\hat{b}^{\dagger}\,\hat{b} + \frac{\hbar\,\omega_{\mathrm{m}}}{2} = \frac{\hat{p}^2}{2\,m_{\mathrm{eff}}} + \frac{m_{\mathrm{eff}}\,{\omega_{\mathrm{m}}}^2\,\hat{x}^2}{2} + \frac{\hbar\,\omega_{\mathrm{m}}}{2}\ .$$

Classically, the potential energy is

$$U(t) = \frac{m_{\mathrm{eff}}\,{\omega_{\mathrm{m}}}^2}{2}\,x(t)^2\ ,$$

with a peak value of

$$U_{\mathrm{m}} = \max[U(t)] = \frac{m_{\mathrm{eff}}\,{\omega_{\mathrm{m}}}^2}{2}\,|X|^2\ . \tag{C.5}$$

For a solid acoustic resonance, the peak potential energy is [222]

$$U_{\mathrm{m}} = \frac{{\omega_{\mathrm{m}}}^2}{2}\iiint_V \rho(\vec{r})\,Q_i(\vec{r})^*\,Q_i(\vec{r})\,\mathrm{d}^3\vec{r} = \frac{{\omega_{\mathrm{m}}}^2}{2}\left\langle \vec{Q}\,\middle|\,\rho\,\middle|\,\vec{Q}\right\rangle\ . \tag{C.6}$$

Equating the single particle (C.5) and solid (C.6) potential energies, we find

$$m_{\mathrm{eff}} = \frac{\langle\vec{Q}|\rho|\vec{Q}\rangle}{|X|^2}\ ,$$

or using (C.2),

$$x_{\mathrm{zpf}} = \frac{\sqrt{\frac{\hbar}{2\,\omega_{\mathrm{m}}}}\,|X|}{\sqrt{\langle\vec{Q}|\rho|\vec{Q}\rangle}}\ . \tag{C.7}$$

C.5 Three-dimensional mechanics

To go between our one-dimensional quantum mechanical SHO, x, and three-dimensional time harmonic acoustic resonance, with displacement field $\vec{Q}$, we make the parameterization

$$Q_i(\vec{r},t) = q_i(\vec{r})\, x(t)\ . \tag{C.8}$$

We can extend this to the phasors representation via

$$\Re\left[Q_i(\vec{r})\, \mathrm{e}^{-\mathrm{i}\,\omega_\mathrm{m}\, t}\right] = q_i(\vec{r})\, \Re\left[X\, \mathrm{e}^{-\mathrm{i}\,\omega_\mathrm{m}\, t}\right]\ ,$$

$$\Rightarrow \quad |Q_i(\vec{r})|\, \cos\left[\arg[Q_i(\vec{r})] - \omega_\mathrm{m}\, t\right] = q_i(\vec{r})\, |X|\, \cos\left[\arg[X] - \omega_\mathrm{m}\, t\right]\ ,$$

$$\begin{aligned}\Rightarrow \quad & |Q_i(\vec{r})|\, \left(\cos\left[\arg[Q_i(\vec{r})]\right]\, \cos[\omega_\mathrm{m}\, t] + \sin\left[\arg[Q_i(\vec{r})]\right]\, \sin[\omega_\mathrm{m}\, t]\right) \\ & \qquad = q_i(\vec{r})\, |X|\, \left(\cos\left[\arg[X]\right]\, \cos[\omega_\mathrm{m}\, t] + \sin\left[\arg[X]\right]\, \sin[\omega_\mathrm{m}\, t]\right)\ ,\end{aligned}$$

$$\begin{aligned}\Rightarrow \quad & \Big(|Q_i(\vec{r})|\, \cos\left[\arg[Q_i(\vec{r})]\right] - q_i(\vec{r})\, |X|\, \cos\left[\arg[X]\right]\Big) \\ & \qquad = -\Big(|Q_i(\vec{r})|\, \sin\left[\arg[Q_i(\vec{r})]\right] - q_i(\vec{r})\, |X|\, \sin\left[\arg[X]\right]\Big)\, \tan(\omega_\mathrm{m}\, t)\ .\end{aligned}$$

By separation of variables this would give us $\tan(\omega_\mathrm{m}\, t)$ is constant but this is obviously not true, instead our only other option is

$$\begin{aligned}|Q_i(\vec{r})|\, \cos\left[\arg[Q_i(\vec{r})]\right] &= q_i(\vec{r})\, |X|\, \cos\left[\arg[X]\right] \\ |Q_i(\vec{r})|\, \sin\left[\arg[Q_i(\vec{r})]\right] &= q_i(\vec{r})\, |X|\, \sin\left[\arg[X]\right]\ .\end{aligned}$$

And, if we take the first equation and add the second equation multiplied by i, we arrive at

$$Q_i(\vec{r}) = q_i(\vec{r})\, X \quad : \quad Q_i(\vec{r}) \in \mathbb{C},\ X \in \mathbb{C},\ q_i(\vec{r}) \in \mathbb{R}\ . \tag{C.9}$$

The linear approximation requirement of $x \ll$ length is now equivalent to $|\vec{Q}| \ll$ acoustic solid length scales.

C.6 Three-dimensional optics

If an optical cavity $\{\varepsilon(\vec{r}), \mu(\vec{r})\}$ with resonance $\{\vec{E}(\vec{r}), \vec{H}(\vec{r}), \omega_{\mathrm{o}}\}$ undergoes a material perturbation to $\{\varepsilon'(\vec{r}), \mu'(\vec{r})\}$ with new resonance $\{\vec{E}'(\vec{r}), \vec{H}'(\vec{r}), {\omega_{\mathrm{o}}}'\}$, the change in frequency is [220, 223]

$$\begin{aligned}
\frac{\Delta\omega_{\mathrm{o}}}{{\omega_{\mathrm{o}}}'} &= -\frac{\iiint_V \left(E_i(\vec{r})^*\, \Delta\varepsilon_{i\,j}(\vec{r})\, E'_j(\vec{r}) + H_i(\vec{r})^*\, \Delta\mu_{i\,j}(\vec{r})\, H'_j(\vec{r}) \right) \mathrm{d}^3\vec{r}}{\iiint_V \left(E_i(\vec{r})^*\, \varepsilon_{i\,j}(\vec{r})\, E'_j(\vec{r}) + H_i(\vec{r})^*\, \mu_{i\,j}(\vec{r})\, H'_j(\vec{r}) \right) \mathrm{d}^3\vec{r}} \\
&= -\frac{\langle \vec{E}|\Delta\varepsilon|\vec{E}'\rangle + \langle \vec{H}|\Delta\mu|\vec{H}'\rangle}{\langle \vec{E}|\varepsilon|\vec{E}'\rangle + \langle \vec{H}|\mu|\vec{H}'\rangle}\ ,
\end{aligned}$$

where $\Delta\omega_{\mathrm{o}} = {\omega_{\mathrm{o}}}' - \omega_{\mathrm{o}}$, $\Delta\varepsilon(\vec{r}) = \varepsilon'(\vec{r}) - \varepsilon(\vec{r})$, and $\Delta\mu(\vec{r}) = \mu'(\vec{r}) - \mu(\vec{r})$.

We now consider a small perturbation with $\Delta\mu(\vec{r}) = 0$, $\vec{H}'(\vec{r}) = \vec{H}(\vec{r})$, and ${\omega_{\mathrm{o}}}' \approx \omega_{\mathrm{o}}$. We can decompose $\vec{E}(\vec{r})$ into two orthogonal vector fields, $\vec{E}(\vec{r}) = \vec{E}^{\parallel}(\vec{r}) + \vec{E}^{\perp}(\vec{r})$, such that $\vec{E}^{\parallel}(\vec{r})$ and $\vec{D}^{\perp}(\vec{r}) = \varepsilon(\vec{r}) \cdot \vec{E}^{\perp}(\vec{r})$ are smooth everywhere, in patricular over the material boundary.

For a small perturbation then, $\vec{E}'^{\parallel}(\vec{r}) \approx \vec{E}^{\parallel}(\vec{r})$ and $\vec{D}'^{\perp}(\vec{r}) \approx \vec{D}^{\perp}(\vec{r})$, and we get

$$\begin{aligned}
\frac{\Delta\omega_{\mathrm{o}}}{\omega_{\mathrm{o}}} &\approx -\frac{\langle\vec{E}|\varepsilon'|\vec{E}'\rangle - \langle\vec{E}|\varepsilon|\vec{E}'\rangle}{\langle\vec{E}|\varepsilon|\vec{E}'\rangle + \langle\vec{H}|\mu|\vec{H}\rangle} \\
&= -\frac{\langle\vec{E}^{\parallel}|\varepsilon'|\vec{E}'^{\parallel}\rangle + \langle\vec{D}^{\perp}|\varepsilon^{-1}|\vec{D}'^{\perp}\rangle - \langle\vec{E}^{\parallel}|\varepsilon|\vec{E}'^{\parallel}\rangle - \langle\vec{D}^{\perp}|\varepsilon'^{-1}|\vec{D}'^{\perp}\rangle}{\langle\vec{E}^{\parallel}|\varepsilon|\vec{E}'^{\parallel}\rangle + \langle\vec{D}^{\perp}|\varepsilon'^{-1}|\vec{D}'^{\perp}\rangle + \langle\vec{H}|\mu|\vec{H}\rangle} \\
&\approx -\frac{\langle\vec{E}^{\parallel}|\varepsilon'|\vec{E}^{\parallel}\rangle + \langle\vec{D}^{\perp}|\varepsilon^{-1}|\vec{D}^{\perp}\rangle - \langle\vec{E}^{\parallel}|\varepsilon|\vec{E}^{\parallel}\rangle - \langle\vec{D}^{\perp}|\varepsilon'^{-1}|\vec{D}^{\perp}\rangle}{\langle\vec{E}^{\parallel}|\varepsilon|\vec{E}^{\parallel}\rangle + \langle\vec{D}^{\perp}|\varepsilon'^{-1}|\vec{D}^{\perp}\rangle + \langle\vec{H}|\mu|\vec{H}\rangle} \\
&= -\frac{\langle\vec{E}^{\parallel}|\Delta\varepsilon|\vec{E}^{\parallel}\rangle - \langle\vec{D}^{\perp}|\Delta\varepsilon^{-1}|\vec{D}^{\perp}\rangle}{\langle\vec{D}^{\perp}|\Delta\varepsilon^{-1}|\vec{D}^{\perp}\rangle + \langle\vec{E}|\varepsilon|\vec{E}\rangle + \langle\vec{H}|\mu|\vec{H}\rangle} \,.
\end{aligned}$$

Now

$$\left\langle\vec{E}\,\middle|\,\varepsilon\,\middle|\,\vec{E}\right\rangle = \left\langle\vec{H}\,\middle|\,\mu\,\middle|\,\vec{H}\right\rangle \gg \langle\vec{D}^{\perp}|\Delta\varepsilon^{-1}|\vec{D}^{\perp}\rangle \,,$$

Thus

$$\Delta\omega_{\mathrm{o}} \approx \frac{-\omega_{\mathrm{o}}}{2}\left(\frac{\langle\vec{E}^{\parallel}|\Delta\varepsilon|\vec{E}^{\parallel}\rangle - \langle\vec{D}^{\perp}|\Delta\varepsilon^{-1}|\vec{D}^{\perp}\rangle}{\langle\vec{E}|\varepsilon|\vec{E}\rangle}\right) \,. \tag{C.10}$$

C.7 Optomechanical coupling

Substituting (C.7) and (C.10) into (C.4), we get

$$g_{\mathrm{om}} = -\frac{\frac{\omega_{\mathrm{o}}}{2}\sqrt{\frac{\hbar}{2\,\omega_{\mathrm{m}}}}\,|X|}{\sqrt{\langle\vec{Q}|\rho|\vec{Q}\rangle}\,\langle\vec{E}|\varepsilon|\vec{E}\rangle}\left(\left\langle\vec{E}^{\parallel}\,\middle|\,\frac{\Delta\varepsilon(t)}{x(t)}\,\middle|\,\vec{E}^{\parallel}\right\rangle - \left\langle\vec{D}^{\perp}\,\middle|\,\frac{\Delta\varepsilon^{-1}(t)}{x(t)}\,\middle|\,\vec{D}^{\perp}\right\rangle\right) \,. \tag{C.11}$$

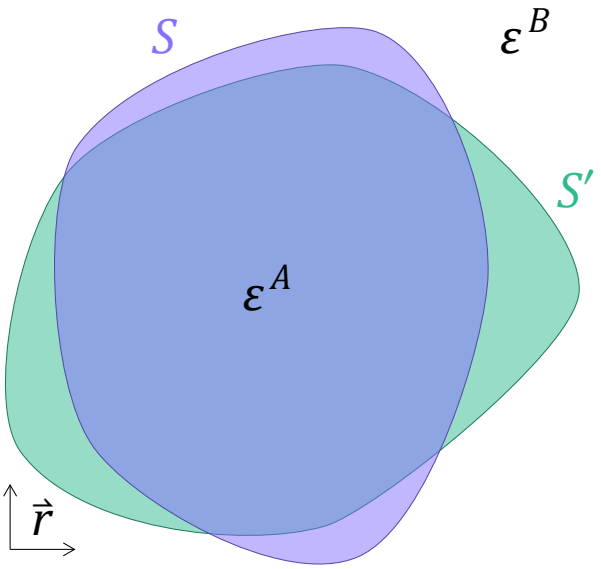

Figure C.1: Moving boundary of an acoustic solid volume.

Here we've used V to denote all three-dimensional space, but note that ρ is only defined over the solid domain $S \subset V$. It should also be mentioned that the optomechanical coupling g_{om} is an angular frequency, the optomechanical coupling rate is typically quoted as $\frac{g_{\text{om}}}{2\pi}$.

C.8 Moving boundary effect

The most obvious cause of changing permittivity in an acoustic resonance is the moving boundary of the solid. At optical frequencies much higher than the mechanical frequencies this shifted boundary can be treated quasi-statically. If we have a volume, the acoustic solid S, with uniform permittivity inside of ε^A and a uniform permittivity outside of ε^B, which

shifts to a new volume S', as depcited in Fig. C.1, the change in permittivity is

$$\Delta\varepsilon(\vec{r}) = \begin{cases} 0 & : \quad (\vec{r} \in S) \wedge \left(\vec{r} \in S'\right) \\ 0 & : \quad (\vec{r} \notin S) \wedge \left(\vec{r} \notin S'\right) \\ \varepsilon^A - \varepsilon^B & : \quad (\vec{r} \notin S) \wedge \left(\vec{r} \in S'\right) \\ \varepsilon^B - \varepsilon^A & : \quad (\vec{r} \in S) \wedge \left(\vec{r} \notin S'\right) \end{cases} .$$

Putting this into an integral over the whole space V,

$$\begin{aligned} \iiint_V \Delta\varepsilon(\vec{r})\, f(\vec{r})\, \mathrm{d}^3\vec{r} &= \left(\iiint_{S'} \varepsilon^A - \iiint_S \varepsilon^A + \iiint_{V\setminus S'} \varepsilon^B - \iiint_{V\setminus S} \varepsilon^B \right) f(\vec{r})\, \mathrm{d}^3\vec{r} \\ &= \left(\iiint_{S'} \varepsilon^A - \iiint_S \varepsilon^A + \iiint_V \varepsilon^B - \iiint_{S'} \varepsilon^B - \iiint_V \varepsilon^B + \iiint_S \varepsilon^B \right) f(\vec{r})\, \mathrm{d}^3\vec{r} \\ &= \left(\iiint_{S'} (\varepsilon^A - \varepsilon^B) - \iiint_S (\varepsilon^A - \varepsilon^B) \right) f(\vec{r})\, \mathrm{d}^3\vec{r} \,. \end{aligned}$$

The volume S' at any point in time is defined from the displacement field of the acoustic solid,

$$S'(t) = \left\{ \vec{r} + \vec{Q}(\vec{r}, t) : \vec{r} \in S \right\} ,$$

thus an integral over S' can be mapped to an integral over S using the Jacobian $J(\vec{r}, t)$,

$$\iiint_{S'(t)} f(\vec{r})\, \mathrm{d}^3\vec{r} = \iiint_S f\left(\vec{r} + \vec{Q}(\vec{r}, t)\right) \, |J(\vec{r}, t)|\, \mathrm{d}^3\vec{r} \,, \qquad |J(\vec{r}, t)| = \det\left[\frac{\partial\left(\vec{r} + \vec{Q}(\vec{r}, t)\right)}{\partial\, \vec{r}} \right] .$$

Hence

$$\iiint_V \Delta\varepsilon(\vec{r})\, f(\vec{r})\, \mathrm{d}^3\vec{r} = \iint_S \left(\varepsilon^A - \varepsilon^B\right) \left(f\left(\vec{r} + \vec{Q}(\vec{r},t)\right)\, |J(\vec{r},t)| - f(\vec{r}) \right) \mathrm{d}^3\vec{r}\,. \tag{C.12}$$

We now want to take $Q_i(\vec{r},t) = q_i(\vec{r})\, x(t)$ and expand out for small x. The elements of the Jacobian matrix are

$$J_{i\,j}(\vec{r},t) = \frac{\partial\left(r_i + q_i(\vec{r})\, x(t)\right)}{\partial\, r_j} = \delta_{i\,j} + x(t)\, \frac{\partial\, q_i(\vec{r})}{\partial\, r_j}\ ,$$

thus

$$J(\vec{r},t) = \mathbb{I} + x(t) \left(\frac{\partial\, \vec{q}(\vec{r})}{\partial\, \vec{r}} \right)\ .$$

For small $x(t)$, the determinant can be expanded out as

$$|J(\vec{r},t)| = \det\left[\mathbb{I} + x(t) \left(\frac{\partial\, \vec{q}(\vec{r})}{\partial\, \vec{r}} \right) \right] = 1 + x(t)\ \mathrm{tr}\left[\frac{\partial\, \vec{q}(\vec{r})}{\partial\, \vec{r}} \right] + \mathcal{O}\left[x(t)\right]^2\ .$$

For an arbitrary function f, the expansion for small x is

$$f\left(\vec{r} + \vec{q}(\vec{r})\, x(t)\right) = f(\vec{r}) + x(t)\, q_k(\vec{r})\, \frac{\partial\, f(\vec{r})}{\partial\, r_k} + \mathcal{O}\left[x(t)\right]^2\ .$$

Substituting these expressions into (C.12) and keeping only terms up to first order in x,

$$\iiint_V \Delta\varepsilon(\vec{r})\, f(\vec{r})\, \mathrm{d}^3\vec{r} \approx \iint_S \left(\varepsilon^A - \varepsilon^B\right) x(t) \left(q_k(\vec{r})\, \frac{\partial\, f(\vec{r})}{\partial\, r_k} + \frac{\partial\, q_k(\vec{r})}{\partial\, r_k}\, f(\vec{r}) \right) \mathrm{d}^3\vec{r}\,. \tag{C.13}$$

By the Divergence Theorem, this is equivalent to

$$\oint\!\!\!\!\!\!\diagup_{\partial S} \left(\varepsilon^A - \varepsilon^B\right) x(t)\, f(\vec{r})\, q_k(\vec{r})\, n_k(\vec{r})\, \mathrm{d}^2\vec{r}\,,$$

where $\vec{n}$ is the normal vector to the surface of the solid, and f is continuously differentiable over the neighbourhood of S.

Replacing $f(\vec{r}) = E_i^{\parallel}(\vec{r})^*\, E_j^{\parallel}(\vec{r})/x(t)$, restoring ε to a tensor, and using (C.9), we find

$$\left\langle \vec{E}^{\parallel} \,\middle|\, \frac{\Delta\varepsilon(t)}{x(t)} \,\middle|\, \vec{E}^{\parallel} \right\rangle = \frac{1}{X} \oint\!\!\!\!\!\!\diagup_{\partial S} E_i^{\parallel}(\vec{r})^* \left(\varepsilon^A_{i\,j} - \varepsilon^B_{i\,j}\right) E_j^{\parallel}(\vec{r})\, Q_k(\vec{r})\, n_k(\vec{r})\, \mathrm{d}^2\vec{r}\,,$$

and likewise with $f(\vec{r}) = D_i^{\perp}(\vec{r})^*\, D_j^{\perp}(\vec{r})/x(t)$ carrying out this process with ε^{-1},

$$\left\langle \vec{D}^{\perp} \,\middle|\, \frac{\Delta\varepsilon^{-1}(t)}{x(t)} \,\middle|\, \vec{D}^{\perp} \right\rangle = \frac{1}{X} \oint\!\!\!\!\!\!\diagup_{\partial S} D_i^{\perp}(\vec{r})^* \left((\varepsilon^A)^{-1}{}_{i\,j} - (\varepsilon^B)^{-1}{}_{i\,j}\right) D_j^{\perp}(\vec{r})\, Q_k(\vec{r})\, n_k(\vec{r})\, \mathrm{d}^2\vec{r}\,.$$

Putting this in to (C.11),

$$g_{\mathrm{MB}}^{\mathrm{om}} = -\frac{\omega_{\mathrm{o}}}{2}\sqrt{\frac{\hbar}{2\,\omega_{\mathrm{m}}}}\,\frac{|X|}{X} \frac{\displaystyle\oint\!\!\!\!\!\!\diagup_{\partial S} Q_k(\vec{r})\, n_k(\vec{r}) \left(E_i^{\parallel}(\vec{r})^* \left(\varepsilon^A_{i\,j} - \varepsilon^B_{i\,j}\right) E_j^{\parallel}(\vec{r}) - D_i^{\perp}(\vec{r})^* \left((\varepsilon^A)^{-1}{}_{i\,j} - (\varepsilon^B)^{-1}{}_{i\,j}\right) D_j^{\perp}(\vec{r})\right) \mathrm{d}^2\vec{r}}{\sqrt{\displaystyle\oint\!\!\!\!\!\!\diagup_{V} Q_i(\vec{r})^*\, \rho(\vec{r})\, Q_i(\vec{r})\, \mathrm{d}^3\vec{r} \quad \oint\!\!\!\!\!\!\diagup_{V} E_i(\vec{r})^*\, \varepsilon_{i\,j}(\vec{r})\, E_j(\vec{r})\, \mathrm{d}^3\vec{r}}}\,. \tag{C.14}$$

The factor $|X|/X = \exp[-\mathrm{i}\,\arg[X]]$ ensures $g_{0\mathrm{MB}} \in \mathbb{R}$. In this formulation $\vec{E}^{\parallel}$ and $\vec{D}^{\perp}$ are only calculated over the boundary of S where they are well defined and continuous.

C.8.1 Moving boundary alternative derivation

An equivalent form for $\Delta\varepsilon/x$ is

$$\varepsilon(x) = \varepsilon(0) + x \left.\frac{\mathrm{d}\,\varepsilon(x')}{\mathrm{d}\,x'}\right|_{x'=0} + \mathcal{O}\left[x\right]^2$$

$$\Rightarrow \quad \Delta\varepsilon(x) = \varepsilon(x) - \varepsilon(0) \approx x \left.\frac{\mathrm{d}\,\varepsilon(x')}{\mathrm{d}\,x'}\right|_{x'=0} ,$$

$$\Rightarrow \quad \frac{\Delta\varepsilon_{i\,j}(\vec{r},t)}{x(t)} \approx \left.\frac{\mathrm{d}\,\varepsilon_{i\,j}(\vec{r},t)}{\mathrm{d}\,x(t)}\right|_{x(t)=0} .$$

Expanding this derivative

$$\left.\frac{\mathrm{d}\,\varepsilon_{i\,j}(\vec{r},t)}{\mathrm{d}\,x(t)}\right|_{x(t)=0} = \left.\frac{\mathrm{d}\,\varepsilon_{i\,j}(\vec{r},t)}{\mathrm{d}\,Q_k(\vec{r},t)}\right|_{x(t)=0} \frac{\partial\,Q_k(\vec{r},t)}{\partial\,x(t)} ,$$

$$\overset{(C.8)}{=} \left.\frac{\mathrm{d}\,\varepsilon_{i\,j}(\vec{r},t)}{\mathrm{d}\,Q_k(\vec{r},t)}\right|_{x(t)=0} q_k(\vec{r}) ,$$

$$\overset{(C.9)}{=} \left.\frac{\mathrm{d}\,\varepsilon_{i\,j}(\vec{r},t)}{\mathrm{d}\,Q_k(\vec{r},t)}\right|_{x(t)=0} \frac{Q_k(\vec{r})}{X} .$$

Consider the interface of two permittivities (the boudnary of the solid), given by the set $\partial S = \{\vec{r}_S\}$, with ε^A on one side and ε^B on the other, and with a normal vector (perpendicular to the boundary) $\vec{n}(\vec{r}_S)$ pointing from side A to side B, then

$$\left.\frac{\mathrm{d}\,\varepsilon_{i\,j}(\vec{r},t)}{\mathrm{d}\,Q_k(\vec{r},t)}\right|_{x(t)=0} = \left(\varepsilon^A_{i\,j} - \varepsilon^B_{i\,j}\right) \delta\left[\vec{r} - \vec{r}_S\right] n_k(\vec{r}) ,$$

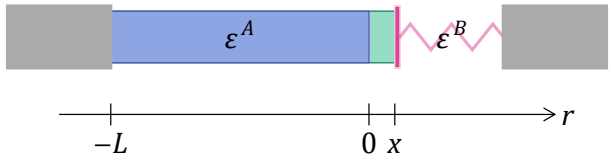

Figure C.2: A one-dimensional optomechanical system.

where $x(t) = 0$ is satisfied by taking $\vec{r}_S$ to be the equilibrium surface.

Following the same procedure for ε^{-1} and putting everything into (C.11) we arrive at (C.14) as expected.

C.8.2 One-dimensional equivalence

Consider the one-dimensional Fabry-Pérot optomechanical system Fig. C.2, of length L and spring-mirror displacement x about $r = 0$, with permittivity ε^A inside the cavity and ε^B outside. We wish to ensure

$$\int_{-\infty}^{\infty} \frac{\Delta\varepsilon(r,x)}{x} f(r)\,\mathrm{d}r = \int_{-\infty}^{\infty} \left.\frac{\mathrm{d}\,\varepsilon(r,x')}{\mathrm{d}\,x'}\right|_{x'=0} f(r)\,\mathrm{d}r$$

is equivalent when using the method of (C.13).

Following the traditional calculation, the permittivity is

$$\varepsilon(r,x) = \begin{cases} \varepsilon^A & : \quad r < x \\ \varepsilon^B & : \quad r > x \end{cases} = \varepsilon^B + \left(\varepsilon^A - \varepsilon^B\right)\left(\Theta\left[r+L\right] - \Theta\left[r-x\right]\right) \ ,$$

and taking the derivative with respect to x,

$$\frac{\mathrm{d}\,\varepsilon(r,x)}{\mathrm{d}\,x} = \left(\varepsilon^A - \varepsilon^B\right)\,\delta\left[r-x\right] \ .$$

Thus

$$\int_{-\infty}^{\infty} \left.\frac{\mathrm{d}\,\varepsilon(r,x')}{\mathrm{d}\,x'}\right|_{x'=0} f(r)\,\mathrm{d}r = \int_{-\infty}^{\infty} \left(\varepsilon^A - \varepsilon^B\right)\,\delta\,[r]\;f(r)\,\mathrm{d}r = \left(\varepsilon^A - \varepsilon^B\right)\;f(0)\;. \qquad \text{(C.15)}$$

To use the method of the previous section, we first need to define an appropriate $Q(r,x)$ that captures the mechanics,

$$Q(x): \quad S = [-L,0] \quad \rightarrow \quad S'(x) = [-L,x]$$

$$\begin{array}{ccc} 0 & \mapsto & x \\ -L & \mapsto & 0 \\ r & \mapsto & x + \frac{r\,x}{L} \end{array}$$

that is, $Q(r,x) = x\,\left(\frac{L+r}{L}\right)$, and hence $q(r) = \frac{L+r}{L}$. Using this in (C.13),

$$\begin{aligned} \int_{-\infty}^{\infty} \frac{\Delta\varepsilon(r,x)}{x}\,f(r)\,\mathrm{d}r &= \int_{-L}^{0} \left(\varepsilon^A - \varepsilon^B\right)\left(\left(\frac{L+r}{L}\right)\frac{\partial\,f(r)}{\partial\,r} + \frac{1}{L}\,f(r)\right)\mathrm{d}r \\ &= \left(\varepsilon^A - \varepsilon^B\right)\left(\int_{-L}^{0} \frac{\partial\,f(r)}{\partial\,r}\,\mathrm{d}r + \frac{1}{L}\int_{-L}^{0}\left(f(r) + r\,\frac{\partial\,f(r)}{\partial\,r}\right)\mathrm{d}r\right) \\ &= \left(\varepsilon^A - \varepsilon^B\right)\left(\int_{-L}^{0} \frac{\partial\,f(r)}{\partial\,r}\,\mathrm{d}r + \frac{1}{L}\int_{-L}^{0} \frac{\partial\,(r\,f(r))}{\partial\,r}\,\mathrm{d}r\right) \\ &= \left(\varepsilon^A - \varepsilon^B\right)\left(\Big(f(0) - f(-L)\Big) + \frac{1}{L}\Big(0\,f(0) - (-L)\,f(-L)\Big)\right) \\ &= \left(\varepsilon^A - \varepsilon^B\right)\;f(0)\;, \end{aligned}$$

the same as (C.15).

C.9 Photo-elastic effect

The strain induced from the deformation of a solid object causes the electric permittivity to change slightly [224],

$$\Delta\left(\varepsilon_r^{-1}\right)_{i\,j} = p_{i\,j\,k\,l}\,\epsilon_{k\,l}\ , \tag{C.16}$$

where p is the photo-elastic tensor and ϵ is strain. To use this expression we need to expand out $[\varepsilon_r + \Delta\varepsilon_r]^{-1}$ but this not straightforward as ε_r and $\Delta\varepsilon_r$ might not commute. Instead we use $f(A+B) = f(\mathbb{I} + A^{-1}B)f(A)$ to get

$$[\varepsilon_r + \Delta\varepsilon_r]^{-1} = \left[\mathbb{I} + \varepsilon_r^{-1}\cdot\Delta\varepsilon_r\right]^{-1}\cdot\varepsilon_r^{-1}\ , \tag{C.17}$$

where we can expand out $[\mathbb{I} + \varepsilon_r^{-1}\cdot\Delta\varepsilon_r]^{-1}$ in a Taylor expansion for small $\varepsilon_r^{-1}\cdot\Delta\varepsilon_r$ as it commutes with $\mathbb{I}$,

$$\left[\mathbb{I} + \varepsilon_r^{-1}\cdot\Delta\varepsilon_r\right]^{-1} = \mathbb{I} + \left(\left.\frac{\mathrm{d}\left[\mathbb{I}+s\,\mathbb{I}\right]^{-1}}{\mathrm{d}\,s}\right|_{s=0}\right)\cdot\left(\varepsilon_r^{-1}\cdot\Delta\varepsilon_r\right) + \mathcal{O}\left[\varepsilon_r^{-1}\cdot\Delta\varepsilon_r\right]^2\ ,$$

and evaluate the matrix inverse derivative

$$\left.\frac{\mathrm{d}\left[\mathbb{I}+s\,\mathbb{I}\right]^{-1}}{\mathrm{d}\,s}\right|_{s=0} = -\left[\mathbb{I}+s\,\mathbb{I}\right]^{-1}\cdot\frac{\mathrm{d}\left(\mathbb{I}+s\,\mathbb{I}\right)}{\mathrm{d}\,s}\cdot\left[\mathbb{I}+s\,\mathbb{I}\right]^{-1}\Big|_{s=0} = -\mathbb{I}\ .$$

Putting this all back together into (C.17),

$$[\varepsilon_r + \Delta\varepsilon_r]^{-1} \approx \left(\mathbb{I} - \varepsilon_r^{-1}\cdot\Delta\varepsilon_r\right)\cdot\varepsilon_r^{-1} = \varepsilon_r^{-1} - \varepsilon_r^{-1}\cdot\Delta\varepsilon_r\cdot\varepsilon_r^{-1}\ , \tag{C.18}$$

$$\Rightarrow \quad [\varepsilon_r + \Delta\varepsilon_r]^{-1} - \varepsilon_r^{-1} = \Delta\left(\varepsilon_r^{-1}\right) \approx -\varepsilon_r^{-1} \cdot \Delta\varepsilon_r \cdot \varepsilon_r^{-1} \ ,$$

$$\Rightarrow \quad \Delta\varepsilon \approx -\frac{\varepsilon \cdot \Delta\left(\varepsilon_r^{-1}\right) \cdot \varepsilon}{\varepsilon_0} \ ,$$

and substituting in the photo-elastic effect (C.16)

$$\Delta\varepsilon_{i\,j} = \frac{-\varepsilon_{i\,a}\, p_{a\,b\,c\,d}\, \epsilon_{c\,d}\, \varepsilon_{b\,j}}{\varepsilon_0} \ .$$

Thus

$$\frac{\Delta\varepsilon_{i\,j}(\vec{r},t)}{x(t)} = \frac{-\varepsilon_{i\,a}(\vec{r})\, \varepsilon_{b\,j}(\vec{r})\, p_{a\,b\,c\,d}(\vec{r})}{\varepsilon_0}\, \frac{\epsilon_{c\,d}(\vec{r},t)}{x(t)} \ .$$

Now, the strain can be converted into frequency domain form,

$$\frac{\epsilon_{c\,d}(\vec{r},t)}{x(t)} = \frac{1}{2}\left(\frac{\partial\left(\frac{Q_c(\vec{r},t)}{x(t)}\right)}{\partial\, r_d} + \frac{\partial\left(\frac{Q_d(\vec{r},t)}{x(t)}\right)}{\partial\, r_c}\right)$$

$$= \frac{1}{2}\left(\frac{\partial\, q_c(\vec{r})}{\partial\, r_d} + \frac{\partial\, q_d(\vec{r})}{\partial\, r_c}\right)$$

$$= \frac{1}{X}\,\frac{1}{2}\left(\frac{\partial\, Q_c(\vec{r})}{\partial\, r_d} + \frac{\partial\, Q_d(\vec{r})}{\partial\, r_c}\right)$$

$$= \frac{\epsilon_{c\,d}(\vec{r})}{X} \ .$$

Thus

$$\left\langle \vec{E}^{\parallel} \,\middle|\, \frac{\Delta\varepsilon(t)}{x(t)} \,\middle|\, \vec{E}^{\parallel} \right\rangle = \frac{-1}{X\,\varepsilon_0} \left\langle \vec{E}^{\parallel} \,\middle|\, \varepsilon \cdot (p:\epsilon) \cdot \varepsilon \,\middle|\, \vec{E}^{\parallel} \right\rangle$$

$$= \frac{-1}{X\,\varepsilon_0} \left\langle \vec{D}^{\parallel} \,\middle|\, (p:\epsilon) \,\middle|\, \vec{D}^{\parallel} \right\rangle \ .$$

The $\vec{D}^{\perp}$ piece is much simpler, using (C.16) directly,

$$\left\langle \vec{D}^{\perp} \,\middle|\, \frac{\Delta\varepsilon^{-1}(t)}{x(t)} \,\middle|\, \vec{D}^{\perp} \right\rangle = \frac{1}{X\,\varepsilon_0} \left\langle \vec{D}^{\perp} \,\middle|\, (p:\epsilon) \,\middle|\, \vec{D}^{\perp} \right\rangle \ .$$

Putting this all together into (C.11),

$$g_{\mathrm{PE}}^{\mathrm{om}} = \frac{\omega_{\mathrm{o}}}{2} \sqrt{\frac{\hbar}{2\,\omega_{\mathrm{m}}}}\, \frac{|X|}{X}\, \frac{\dfrac{1}{\varepsilon_0} \left\langle \vec{D} \,\middle|\, (p:\epsilon) \,\middle|\, \vec{D} \right\rangle}{\sqrt{\langle \vec{Q}|\rho|\vec{Q}\rangle}\, \langle \vec{E}|\varepsilon|\vec{E}\rangle}$$

$$= \frac{\omega_{\mathrm{o}}}{2} \sqrt{\frac{\hbar}{2\,\omega_{\mathrm{m}}}}\, \frac{|X|}{X}\, \frac{\dfrac{1}{\varepsilon_0} \iiint_V E_i(\vec{r})^*\, \varepsilon_{i\,a}(\vec{r})\, p_{a\,b\,c\,d}(\vec{r})\, \epsilon_{c\,d}(\vec{r})\, \varepsilon_{b\,j}(\vec{r})\, E_j(\vec{r})\, \mathrm{d}^3\vec{r}}{\sqrt{\iiint_V Q_i(\vec{r})^*\, \rho(\vec{r})\, Q_i(\vec{r})\, \mathrm{d}^3\vec{r} \quad \iiint_V E_i(\vec{r})^*\, \varepsilon_{i\,j}(\vec{r})\, E_j(\vec{r})\, \mathrm{d}^3\vec{r}}} \ ,$$

noting that p is only non-zero over the mechanical solid so the top integral is only over the domain S. If we assume the electric permittivity of our solid, ε^A, is uniform and isotropic,

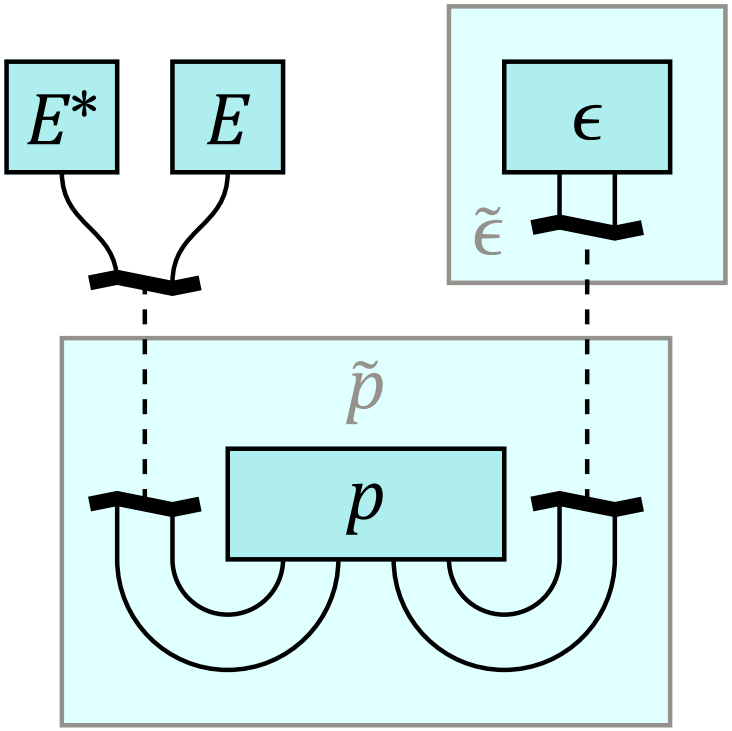

Figure C.3: Penrose tensor diagram of $E_i^* \, p_{i\,j\,k\,l} \, \epsilon_{k\,l} \, E_j$ evaluation.

we get

$$g_{\mathrm{PE}}^{\mathrm{om}} = \frac{\omega_{\mathrm{o}}}{2} \sqrt{\frac{\hbar}{2\,\omega_{\mathrm{m}}}} \, \frac{|X|}{X} \, \frac{\dfrac{\left(\varepsilon^A\right)^2}{\varepsilon_0} \oiint\limits_S E_i(\vec{r})^* \, p_{i\,j\,c\,d}(\vec{r}) \, \epsilon_{c\,d}(\vec{r}) \, E_j(\vec{r}) \, \mathrm{d}^3\vec{r}}{\sqrt{\oiint\limits_V Q_i(\vec{r})^* \, \rho(\vec{r}) \, Q_i(\vec{r}) \, \mathrm{d}^3\vec{r} \quad \oiint\limits_V E_i(\vec{r})^* \, \varepsilon_{i\,j}(\vec{r}) \, E_j(\vec{r}) \, \mathrm{d}^3\vec{r}}} \, . \tag{C.19}$$

C.9.1 Cubic(3) photo-elastic tensor expansion

For a Cubic(3) crystal (point groups 432, $\bar{4}$3m, m$\bar{3}$m)[1], the photo-elastic tensor, in conventional solid mechanics Voigt notation (Sec. G.5), has the form [224]

$$\underline{\underline{\tilde{p}}} = \left(\tilde{p}^{\tilde{i}\,\tilde{j}}\right) = \begin{pmatrix} \tilde{p}^{1\,1} & \tilde{p}^{1\,2} & \tilde{p}^{1\,2} & 0 & 0 & 0 \\ \tilde{p}^{1\,2} & \tilde{p}^{1\,1} & \tilde{p}^{1\,2} & 0 & 0 & 0 \\ \tilde{p}^{1\,2} & \tilde{p}^{1\,2} & \tilde{p}^{1\,1} & 0 & 0 & 0 \\ 0 & 0 & 0 & \tilde{p}^{4\,4} & 0 & 0 \\ 0 & 0 & 0 & 0 & \tilde{p}^{4\,4} & 0 \\ 0 & 0 & 0 & 0 & 0 & \tilde{p}^{4\,4} \end{pmatrix},$$

in a coordinate system aligned with the crystal. We can contract this with the strain Voigt vector to get

$$\left(\tilde{p}^{\tilde{i}\,\tilde{j}}\,\tilde{\epsilon}_{\tilde{j}}\right) = \begin{pmatrix} \tilde{p}^{1\,1} & \tilde{p}^{1\,2} & \tilde{p}^{1\,2} & 0 & 0 & 0 \\ \tilde{p}^{1\,2} & \tilde{p}^{1\,1} & \tilde{p}^{1\,2} & 0 & 0 & 0 \\ \tilde{p}^{1\,2} & \tilde{p}^{1\,2} & \tilde{p}^{1\,1} & 0 & 0 & 0 \\ 0 & 0 & 0 & \tilde{p}^{4\,4} & 0 & 0 \\ 0 & 0 & 0 & 0 & \tilde{p}^{4\,4} & 0 \\ 0 & 0 & 0 & 0 & 0 & \tilde{p}^{4\,4} \end{pmatrix} \cdot \begin{pmatrix} \epsilon_{1\,1} \\ \epsilon_{2\,2} \\ \epsilon_{3\,3} \\ 2\,\epsilon_{2\,3} \\ 2\,\epsilon_{1\,3} \\ 2\,\epsilon_{1\,2} \end{pmatrix} = \begin{pmatrix} \tilde{p}^{1\,1}\,\epsilon_{1\,1} + \tilde{p}^{1\,2}\,\epsilon_{2\,2} + \tilde{p}^{1\,2}\,\epsilon_{3\,3} \\ \tilde{p}^{1\,2}\,\epsilon_{1\,1} + \tilde{p}^{1\,1}\,\epsilon_{2\,2} + \tilde{p}^{1\,2}\,\epsilon_{3\,3} \\ \tilde{p}^{1\,2}\,\epsilon_{1\,1} + \tilde{p}^{1\,2}\,\epsilon_{2\,2} + \tilde{p}^{1\,1}\,\epsilon_{3\,3} \\ 2\,\tilde{p}^{4\,4}\,\epsilon_{2\,3} \\ 2\,\tilde{p}^{4\,4}\,\epsilon_{1\,3} \\ 2\,\tilde{p}^{4\,4}\,\epsilon_{1\,2} \end{pmatrix},$$

1. GaAs is F$\bar{4}$3m in $\bar{4}$3m. Si is Fd$\bar{3}$m in m$\bar{3}$m.

which is a contravariant (stress-like) Voigt vector. Applying an inverse contravariant Voigt, i.e. stress-like, transformation

$$
(p_{a\,b\,c\,d}\,\epsilon_{c\,d}) =
\begin{pmatrix}
\tilde{p}^{1\,1}\,\epsilon_{1\,1} + \tilde{p}^{1\,2}\,(\epsilon_{2\,2} + \epsilon_{3\,3}) & 2\,\tilde{p}^{4\,4}\,\epsilon_{1\,2} & 2\,\tilde{p}^{4\,4}\,\epsilon_{1\,3} \\
2\,\tilde{p}^{4\,4}\,\epsilon_{1\,2} & \tilde{p}^{1\,1}\,\epsilon_{2\,2} + \tilde{p}^{1\,2}\,(\epsilon_{1\,1} + \epsilon_{3\,3}) & 2\,\tilde{p}^{4\,4}\,\epsilon_{2\,3} \\
2\,\tilde{p}^{4\,4}\,\epsilon_{1\,3} & 2\,\tilde{p}^{4\,4}\,\epsilon_{2\,3} & \tilde{p}^{1\,1}\,\epsilon_{3\,3} + \tilde{p}^{1\,2}\,(\epsilon_{1\,1} + \epsilon_{2\,2})
\end{pmatrix}.
$$

Thus, when dealing with isotropic permittivities,

$$
\begin{aligned}
E_a{}^*\,p_{a\,b\,c\,d}\,\epsilon_{c\,d}\,E_b = {} & E_1{}^*\,E_1\left(\tilde{p}^{1\,1}\,\epsilon_{1\,1} + \tilde{p}^{1\,2}\,\epsilon_{2\,2} + \tilde{p}^{1\,2}\,\epsilon_{3\,3}\right) \\
& + E_2{}^*\,E_2\left(\tilde{p}^{1\,2}\,\epsilon_{1\,1} + \tilde{p}^{1\,1}\,\epsilon_{2\,2} + \tilde{p}^{1\,2}\,\epsilon_{3\,3}\right) \\
& + E_3{}^*\,E_3\left(\tilde{p}^{1\,2}\,\epsilon_{1\,1} + \tilde{p}^{1\,2}\,\epsilon_{2\,2} + \tilde{p}^{1\,1}\,\epsilon_{3\,3}\right) \\
& + 2\,E_2{}^*\,E_3\,\tilde{p}^{4\,4}\,\epsilon_{2\,3} + 2\,E_3{}^*\,E_2\,\tilde{p}^{4\,4}\,\epsilon_{2\,3} \\
& + 2\,E_1{}^*\,E_3\,\tilde{p}^{4\,4}\,\epsilon_{1\,3} + 2\,E_3{}^*\,E_1\,\tilde{p}^{4\,4}\,\epsilon_{1\,3} \\
& + 2\,E_1{}^*\,E_2\,\tilde{p}^{4\,4}\,\epsilon_{1\,2} + 2\,E_2{}^*\,E_1\,\tilde{p}^{4\,4}\,\epsilon_{1\,2}
\end{aligned}
$$

$$
\begin{aligned}
= {} & |E_1|^2\left(\tilde{p}^{1\,1}\,\epsilon_{1\,1} + \tilde{p}^{1\,2}\,\epsilon_{2\,2} + \tilde{p}^{1\,2}\,\epsilon_{3\,3}\right) \\
& + |E_2|^2\left(\tilde{p}^{1\,2}\,\epsilon_{1\,1} + \tilde{p}^{1\,1}\,\epsilon_{2\,2} + \tilde{p}^{1\,2}\,\epsilon_{3\,3}\right) \\
& + |E_3|^2\left(\tilde{p}^{1\,2}\,\epsilon_{1\,1} + \tilde{p}^{1\,2}\,\epsilon_{2\,2} + \tilde{p}^{1\,1}\,\epsilon_{3\,3}\right) \\
& + 4\,\Re[E_2{}^*\,E_3]\,\tilde{p}^{4\,4}\,\epsilon_{2\,3} \\
& + 4\,\Re[E_1{}^*\,E_3]\,\tilde{p}^{4\,4}\,\epsilon_{1\,3} \\
& + 4\,\Re[E_1{}^*\,E_2]\,\tilde{p}^{4\,4}\,\epsilon_{1\,2}\,.
\end{aligned}
$$

A Penrose diagram of this evaluation is shown in Fig. C.3. This result differs from that of Chan [225, 226], and its citations [167, 227], where they incorrectly apply an inverse covariant Voigt transformation to get $(p_{a\,b\,c\,d}\,\epsilon_{c\,d})$.

C.9.2 Rotated photo-elastic tensor

If our material is not aligned with our coordinate system we need a more general expansion. Whilst $\left(E_i{}^*\,E_j\right)$ is not symmetric (it's Hermitian), its contracted with symmetric p, thus we can write

$$E_a{}^*\,p_{a\,b\,c\,d}\,\epsilon_{c\,d}\,E_b = (\tilde{E^2})_{\tilde{\imath}}\,\tilde{p}^{\tilde{\imath}\,\tilde{\jmath}}\,\tilde{\epsilon}_{\tilde{\jmath}}\,,$$

where

$$\underline{\tilde{E^2}} = \begin{pmatrix} |E_1|^2 \\ |E_2|^2 \\ |E_3|^2 \\ 2\,\Re[E_2{}^*\,E_3] \\ 2\,\Re[E_1{}^*\,E_3] \\ 2\,\Re[E_1{}^*\,E_2] \end{pmatrix}$$

is a covariant (strain-like) Voigt vector.

C.10 Electro-optic effect

Similar to the photo-elastic effect, the electric permittivity also responds to applied static electric fields. At optical frequencies, for piezoelectric materials, this is the quasi-static

piezoelectric electric field induced by the solid deformation. Denoting the static electric field[2] as $\vec{E}^S$, the electro-optic effect is [224]

$$\Delta\left(\varepsilon_r^{-1}\right)_{ij} = r_{ijk}\,E_k^S + s_{ijkl}\,E_k^S\,E_l^S\ ,$$

where r is the linear electro-optic tensor, and s is the quadratic electro-optic tensor which from here on will be ignored. Following the same procedure as the photo-elastic effect,

$$\Delta\varepsilon_{ij} = \frac{-\varepsilon_{ia}\,r_{abc}\,E_c^S\,\varepsilon_{bj}}{\varepsilon_0}\ .$$

For a piezoelectric material, if we assume $\vec{E}^S \propto \vec{Q}$ then $E_c^S(\vec{r},t)/x(t) = E_c^S(\vec{r})/X$, and again following the same procedure as the photo-elastic effect,

$$g_{\text{EO}}^{\text{om}} = \frac{\omega_\text{o}}{2}\sqrt{\frac{\hbar}{2\,\omega_\text{m}}}\,\frac{|X|}{X}\,\frac{\frac{1}{\varepsilon_0}\left\langle\vec{D}\,\middle|\,\left(r\cdot E^S\right)\,\middle|\,\vec{D}\right\rangle}{\sqrt{\langle\vec{Q}|\rho|\vec{Q}\rangle}\,\langle\vec{E}|\varepsilon|\vec{E}\rangle}$$

$$= \frac{\omega_\text{o}}{2}\sqrt{\frac{\hbar}{2\,\omega_\text{m}}}\,\frac{|X|}{X}\,\frac{\frac{1}{\varepsilon_0}\oiint_V E_i(\vec{r})^*\,\varepsilon_{ia}(\vec{r})\,r_{abc}(\vec{r})\,E_c^S(\vec{r})\,\varepsilon_{bj}(\vec{r})\,E_j(\vec{r})\,\mathrm{d}^3\vec{r}}{\sqrt{\oiint_V Q_i(\vec{r})^*\,\rho(\vec{r})\,Q_i(\vec{r})\,\mathrm{d}^3\vec{r}\quad\oiint_V E_i(\vec{r})^*\,\varepsilon_{ij}(\vec{r})\,E_j(\vec{r})\,\mathrm{d}^3\vec{r}}}\ ,$$

where r is only non-zero over the solid.

In practice, the electro-optic effect from piezoelectric materials is orders of magnitude smaller than the other contributions to g_om and can be ignored.

2. The electric field appearing in the piezoelectric equations of Ap B.

APPENDIX D

Symmetry condition

D.1 Origin

The symmetry condition equation occurs whenever a tensor field, F obeys the Helmholtz equation[1]

$$\Delta_{\vec{r}}\, F[\vec{r}] + k[\vec{r}]^2\, F[\vec{r}] = 0 \ ,$$

and there exists a symmetry operation $\underline{\underline{S}} \in O(3)$ such that

$$k\left[\underline{\underline{S}} \cdot \vec{r}\right] = k[\vec{r}] \ . \tag{D.1}$$

D.2 Change of basis

Before proceeding, we'll need a quick summary of basis changes in a linear vector space. Consider a vector space V with two basis sets,

$$A = \{\vec{A}_i\}_i \ , \qquad\qquad B = \{\vec{B}_i\}_i \ ,$$

such that for any vector $\vec{r} \in V$,

$$\vec{r} = {}_A r^i\, \vec{A}_i = {}_B r^i\, \vec{B}_i \ . \tag{D.2}$$

1. $\Delta_{\vec{r}} = \nabla^2_{\vec{r}}$ is the Laplacian operator.

We can define the transformation between A and B as $\underline{\underline{C}}$ such that the vector $\vec{B}_j$ in basis A is

$$\vec{B}_i = C^j_{\ i}\, \vec{A}_j \ ,$$

and relating this to (D.2)

$$\underbrace{{}_B r(\vec{B}_i)^j}_{\delta^j_{\ i}}\ \vec{B}_j = \vec{B}_i = {}_A r(\vec{B}_i)^j\ \vec{A}_j = C^k_{\ i}\ \underbrace{{}_A r(\vec{A}_k)^j}_{\delta^j_{\ k}}\ \vec{A}_j = C^j_{\ i}\, \vec{A}_j \ .$$

Thus for any $\vec{r} \in V$,

$$\vec{r} = {}_A r^i\, \vec{A}_i = {}_B r^i\, \vec{B}_i = {}_B r^i\, C^j_{\ i}\, \vec{A}_j \ ,$$

which tells us

$${}_A r^i = C^i_{\ j}\, {}_B r^j \ , \qquad\qquad {}_B r^i = (C^{-1})^i_{\ j}\, {}_A r^j \ .$$

For the dual vector space we have

$$\vec{A}^i(\vec{r}) = {}_A r^i \ , \qquad\qquad \vec{B}^i(\vec{r}) = {}_B r^i = (C^{-1})^i_{\ j}\, {}_A r^j \ ,$$

$$\Rightarrow \quad \vec{B}^i = (C^{-1})^i_{\ j}\, \vec{A}^i \ .$$

Then for any $\vec{r}^* \in V^*$,

$$\vec{r}^* = {}_A r_i\, \vec{A}^i = {}_B r_i\, \vec{B}^i = {}_B r_i\, (C^{-1})^i_{\ j}\, \vec{A}^j \ ,$$

$$ {}_A r_i = {}_B r_j \, (C^{-1})^j_{\ i} \, , \qquad\qquad {}_B r_i = {}_A r_j \, C^j_{\ i} \, . $$

Extending this to a tensor of rank (P, Q)

$$ {}_B T^{i_1 \cdots i_P}_{j_1 \cdots j_Q} = \left(\prod_{n=1}^{P} (C^{-1})^{i_n}_{\ k_n} \right) \left(\prod_{m=1}^{Q} C^{l_m}_{\ j_m} \right) {}_A T^{k_1 \cdots k_P}_{l_1 \cdots l_Q} \, . \tag{D.3} $$

Note that if A and B have a cartesian metric, requiring $\underline{\underline{C}} \in O(\dim[V])$, then $(C^{-1})^{i_n}_{\ k_n} = (C^{\mathrm{T}})_{i_n \, k_n} = C_{k_n \, i_n}$ and the use of contravariant or covariant indecies is irrelevant.

D.3 Change of coordinate system

We will also need a summary of coordinate system changes and the induced bases of their tangent spaces. Given a space M, with a coordinate system $\{a^i\}_i$, we can define the transformation to a new coordinate system on M as

$$ b^i = D^i\big(\{a^k\}_k\big) \, , \qquad\qquad a^i = (D^{-1})^i\big(\{b^k\}_k\big) \, , $$

where D is some function of the original coordinates. The metric for the new coordinate system is easily calculated from

$$ \mathrm{d}a^i \, {}_a g_{i\,j} \, \mathrm{d}a^j = \mathrm{d}D^i\big(\{a^k\}_k\big) \, {}_a g_{i\,j} \, \mathrm{d}D^j\big(\{a^k\}_k\big) = \mathrm{d}b^i \, {}_b g_{i\,j} \, \mathrm{d}b^j \, . $$

A point $p \in M$, can be expressed in terms of $\{{}_a p^i\}_i$ or $\{{}_b p^i\}_i$, and has a tangent space $T_p M$.

For each coordinate system, the tangent vector space has a natural basis

$$\vec{A}_i = \left.\frac{\partial}{\partial a^i}\right|_p , \qquad \vec{B}_i = \left.\frac{\partial}{\partial b^i}\right|_p .$$

Following the transformation above and the chain rule, we find

$$\vec{B}_i = \left.\frac{\partial}{\partial b^i}\right|_p = \left.\frac{\partial}{\partial D^i(\{a^k\}_k)}\right|_p = \left.\frac{\partial a^j}{\partial b^i}\right|_p \left.\frac{\partial}{\partial a^j}\right|_p = \left.\frac{\partial (D^{-1})^j(\{b^k\}_k)}{\partial b^i}\right|_p \vec{A}_j .$$

Combining this with a tensor field F of rank (P,Q) over M, using (D.3),

$${}_BF^{i_1\cdots i_P}_{j_1\cdots j_Q}\left[\{{}_bp^k\}_k\right] = \left(\prod_{n=1}^{P}\left.\frac{\partial b^{i_n}}{\partial a^{k_n}}\right|_p\right)\left(\prod_{m=1}^{Q}\left.\frac{\partial a^{l_m}}{\partial b^{j_m}}\right|_p\right){}_AF^{k_1\cdots k_P}_{l_1\cdots l_Q}\left[\{{}_ap^k\}_k\right] ,$$

or if we denote

$$C^j_{\ i}\left[\{{}_bp^k\}_k\right] = \left.\frac{\partial (D^{-1})^j(\{b^k\}_k)}{\partial b^i}\right|_{b^k={}_bp^k} ,$$

then

$${}_BF^{i_1\cdots i_P}_{j_1\cdots j_Q}\left[\{{}_bp^k\}_k\right] = \left(\prod_{n=1}^{P}(C^{-1})^{i_n}_{\ k_n}\left[\{{}_bp^k\}_k\right]\right)\left(\prod_{m=1}^{Q}C^{l_m}_{\ j_m}\left[\{{}_bp^k\}_k\right]\right){}_AF^{k_1\cdots k_P}_{l_1\cdots l_Q}\left[\{(D^{-1})^k(\{{}_bp^l\}_l)\}_k\right] .$$

If a is a Cartesian coordinate system, and the transform $D \in E(\dim[M])$ is a Euclidean transformation (also known as rigid or affine), then the coordinate system b will also be

Cartesian. Furthermore we can write

$$b^i = D^i\big(\{a^k\}_k\big) = R^i{}_j\, a^j + \lambda^i \ ,$$

where $\underline{\underline{R}} \in O(\dim[M])$, and determine

$$\frac{\partial b^i}{\partial a^j} = (C^{-1})^i{}_j = R^i{}_j \ , \qquad\qquad \frac{\partial a^i}{\partial b^j} = C^i{}_j = (R^{-1})^i{}_j \ .$$

This then gives us

$${}_B F^{i_1 \cdots i_P}\Big[\{{}_b p^k\}_k\Big] = \left(\prod_{n=1}^{P} R^{i_n}_{k_n}\right)\ {}_A F^{k_1 \cdots k_P}\Big[\{(R^{-1})^k_l\, {}_b p^l - (R^{-1})^k_l\, \lambda^l\}_k\Big] \ .$$

D.4 Derivation

For simplicity, we'll consider a Cartesian coordinate system on $\mathbb{R}^3$. Starting with the Helmholtz equation,

$$\frac{\partial}{\partial r^i}\frac{\partial}{\partial r^i}\, F^{j_1 \cdots j_N}\Big[\{r^p\}_p\Big] + k\Big[\{r^p\}_p\Big]^2\ F^{j_1 \cdots j_N}\Big[\{r^p\}_p\Big] = 0 \ , \tag{D.4}$$

if we make a change of coordinate system and basis, $\underline{\underline{S}}$, we get[2]

$$\frac{\partial}{\partial(S^i_a\, r^a)}\,\frac{\partial}{\partial(S^i_b\, r^b)}\left(\prod_{n=1}^{N} S^{j_n}_{l_n}\right)\ F^{l_1 \cdots l_N}\Big[\{(S^{-1})^p_q\, r^q\}_p\Big] \\ + k\Big[\{(S^{-1})^p_q\, r^q\}_p\Big]^2\left(\prod_{n=1}^{N} S^{j_n}_{l_n}\right)\ F^{l_1 \cdots l_N}\Big[\{(S^{-1})^p_q\, r^q\}_p\Big] = 0 \ .$$

2. This change of coordinate system also applies to boundary conditions.

Now by the chain rule,

$$\frac{\partial}{\partial(S^i_{\ j}\, r^j)} = (S^{-1})^j_{\ i}\, \frac{\partial}{\partial r^j} \ ,$$

and using (D.1),

$$(S^{-1})^a_{\ i}\, \frac{\partial}{\partial r^a}\, (S^{-1})^b_{\ i}\, \frac{\partial}{\partial r^b} \left(\prod_{n=1}^{N} S^{j_n}_{\ \ l_n} \right) F^{\,l_1 \cdots l_N} \left[\{ (S^{-1})^p_{\ q}\, r^q \}_p \right] + k \left[\{ r^p \}_p \right]^2 \left(\prod_{n=1}^{N} S^{j_n}_{\ \ l_n} \right) F^{\,l_1 \cdots l_N} \left[\{ (S^{-1})^p_{\ q}\, r^q \}_p \right] = 0 \ .$$

For $\underline{\underline{S}} \in O(3)$, i.e. $\underline{\underline{S}}^{-1} = \underline{\underline{S}}^{\mathrm{T}}$, we also have

$$(S^{-1})^a_{\ i}\, (S^{-1})^b_{\ i} = (S^{-1})^a_{\ i}\, S_i^{\ b} = \delta^{a\,b} \ ,$$

which gives us

$$\frac{\partial}{\partial r^i}\, \frac{\partial}{\partial r^i} \left(\prod_{n=1}^{N} S^{j_n}_{\ \ l_n} \right) F^{\,l_1 \cdots l_N} \left[\{ (S^{-1})^p_{\ q}\, r^q \}_p \right] + k \left[\{ r^p \}_p \right]^2 \left(\prod_{n=1}^{N} S^{j_n}_{\ \ l_n} \right) F^{\,l_1 \cdots l_N} \left[\{ (S^{-1})^p_{\ q}\, r^q \}_p \right] = 0 \ ,$$

or in some compacted notation

$$\nabla^2 \left(\underline{\underline{S}}^N \cdot F[\underline{\underline{S}}^{-1} \cdot \vec{r}] \right) + k [\vec{r}]^2 \left(\underline{\underline{S}}^N \cdot F[\underline{\underline{S}}^{-1} \cdot \vec{r}] \right) = 0 \ .$$

Comparing this to the original Helmholtz equation (D.4), we infer that if $F^{\,j_1 \cdots j_N} \left[\{ r^p \}_p \right]$ is a solution, then $\left(\prod_{n=1}^{N} S^{j_n}_{\ \ l_n} \right) F^{\,l_1 \cdots l_N} \left[\{ (S^{-1})^p_{\ q}\, r^q \}_p \right]$ is also a solution. If there are no

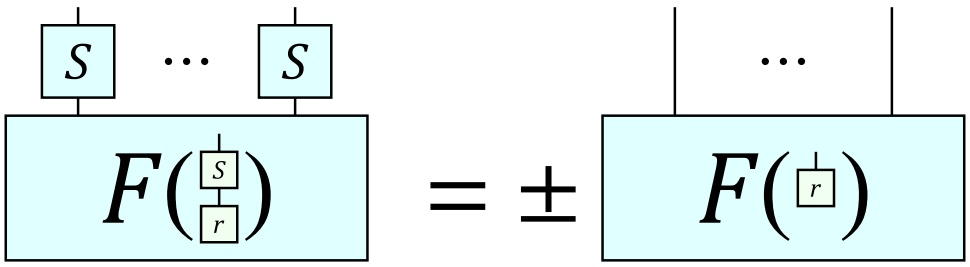

Figure D.1: Penrose tensor diagram for an involutory symmetry operator S with value ± 1.

degenerate solutions for the particular k in (D.4) we must have

$$\underline{\underline{S}}^N \cdot F[\underline{\underline{S}}^{-1} \cdot \vec{r}] = s\, F[\vec{r}] \,,$$

$$\Rightarrow \quad \underline{\underline{S}}^N \cdot F[\vec{r}] = s\, F[\underline{\underline{S}} \cdot \vec{r}] \,.$$

If $\underline{\underline{S}}$ is an involutory matrix, i.e. $\underline{\underline{S}}^{-1} = \underline{\underline{S}}$, then

$$F[\vec{r}] = s\, \underline{\underline{S}}^N \cdot F[\underline{\underline{S}} \cdot \vec{r}] = s^2\, F[\vec{r}] \,,$$

and $s \in \{-1, 1\}$.

D.5 Result

For an involutory symmetry operator $\underline{\underline{S}}$, that is $\underline{\underline{S}} \cdot \underline{\underline{S}} = \underline{\underline{\mathbb{I}}}$, the symmetry condition on a tensor field, F, of rank N that satisfies the Helmholtz equation with $k\left[\underline{\underline{S}} \cdot \vec{r}\right] = k[\vec{r}]$, is

$$\underline{\underline{S}}^N \cdot F\left[\underline{\underline{S}} \cdot \vec{r}\right] = \pm\, F\left[\vec{r}\right] \,.$$

In Cartesian coordinates, this is

$$\left(\prod_{n=1}^{N} S^{i_n}{}_{j_n}\right) F^{j_1 \cdots j_N}\left[\{S^k{}_l\, r^l\}_k\right] = \pm\, F^{i_1 \cdots i_N}\left[\{r^k\}_k\right] \ ,$$

and a Penrose tensor diagram is depicted in Fig. D.1.

Note that for a scalar field,

$$f[\underline{\underline{S}} \cdot \vec{r}] = \pm\, f[\vec{r}] \ .$$

D.6 Electromagnetic mirror symmetries

The symmetry equation for the electromagnetic field tensor (see App. A) is

$$S^{\mu}{}_{\alpha}\, S^{\mu}{}_{\beta}\, F^{\alpha\,\beta}\left[\{r^{\lambda}\}_{\lambda}\right] = s\, F^{\mu\,\nu}\left[\{S^{\lambda}{}_{\gamma}\, r^{\gamma}\}_{\lambda}\right] \ ,$$

$$\begin{aligned} \Rightarrow \quad S^{\mu}{}_{\alpha}\, E^{\alpha}\left[\{r^{\lambda}\}_{\lambda}\right] &= s\, E^{\mu}\left[\{S^{\lambda}{}_{\gamma}\, r^{\gamma}\}_{\lambda}\right] \ , \\ S^{\mu}{}_{\alpha}\, H^{\alpha}\left[\{r^{\lambda}\}_{\lambda}\right] &= -\, s\, H^{\mu}\left[\{S^{\lambda}{}_{\gamma}\, r^{\gamma}\}_{\lambda}\right] \ . \end{aligned}$$

For mirror symmetries about the spatial cardinal axes,

$$\underline{\underline{P\left[\hat{\vec{x}}\right]}} = \begin{pmatrix} -1 & 0 & 0 \\ 0 & 1 & 0 \\ 0 & 0 & 1 \end{pmatrix} , \qquad \underline{\underline{P\left[\hat{\vec{y}}\right]}} = \begin{pmatrix} 1 & 0 & 0 \\ 0 & -1 & 0 \\ 0 & 0 & 1 \end{pmatrix} , \qquad \underline{\underline{P\left[\hat{\vec{z}}\right]}} = \begin{pmatrix} 1 & 0 & 0 \\ 0 & 1 & 0 \\ 0 & 0 & -1 \end{pmatrix} ,$$

and we'll employ the notation $\overset{\pm}{r_i}$ to denote the presence of a symmetry along with its value s_i. For example, about the x axis,

$$\overset{+}{x} \quad \begin{array}{c} x \text{ mirror symmetry} \\ (y\text{-}z \text{ magnetic conductor}) \end{array} \quad s_x = 1 \qquad \begin{array}{rcl} E_x[-x,y,z] &=& -E_x[x,y,z] \\ E_y[-x,y,z] &=& E_y[x,y,z] \\ E_z[-x,y,z] &=& E_z[x,y,z] \end{array} ,$$

$$\overset{-}{x} \quad \begin{array}{c} x \text{ mirror antisymmetry} \\ (y\text{-}z \text{ electric conductor}) \end{array} \quad s_x = -1 \qquad \begin{array}{rcl} E_x[-x,y,z] &=& E_x[x,y,z] \\ E_y[-x,y,z] &=& -E_y[x,y,z] \\ E_z[-x,y,z] &=& -E_z[x,y,z] \end{array} .$$

Note that the 'scalar symmetry values' for the individual components follow

$$\begin{aligned} E_j[-r_i] &= -s_i\,(2\,\delta_{i\,j} - 1)\,E_j[r_i] \,, \\ H_j[-r_i] &= s_i\,(2\,\delta_{i\,j} - 1)\,H_j[r_i] \,. \end{aligned}$$

The magnetic field is actually a 2-form, and H_i is thus a pseudovector (Hodge dual) giving it the 'opposite' symmetry values to E_i. This can be seen by studying the electromagnetic field tensor or connecting $H_x \to H_{y\,z}$.

APPENDIX E

Symmetry in optomechanical coupling

The geometric design of the optomechanical resonator can exhibit various symmetries that will influence which mechanical and electromagnetic modes provide good optomechanical coupling.

E.1 Electromagnetism

Following Maxwell's equations (see App. A) in a source-free, polarization-free, magnetization-free, time harmonic setting, the electric field $\underline{E}$ obeys a Helmholtz equation,

$$\nabla^2_{\vec{r}}\,\underline{E}[\vec{r}] + \omega^2\,\mu\,\varepsilon[\vec{r}]\,\underline{E}[\vec{r}] = 0\ ,$$

where μ is the permeability (assumed constant), ε is the permittivity, and ω is the angular frequency. If there exists a geometric involutory, i.e. mirror or π-rotation, symmetry $\underline{\underline{S}}$ such that $\varepsilon[\underline{\underline{S}}\cdot\vec{r}] = \varepsilon[\vec{r}]$, then, from App. D, $\underline{E}$ obeys

$$\underline{\underline{S}}\cdot\underline{E}\left[\underline{\underline{S}}\cdot\vec{r}\right] = \pm_E\,\underline{E}[\vec{r}]\ ,$$

for any non-degenerate mode.

E.2 Solid mechanics

For a isotropic and homogeneous material, the time harmonic elastodynamic equation (see App. B) for the displacement field $\underline{Q}$ is

$$\mu \nabla^2_{\vec{r}} \underline{Q}[\vec{r}] + (\mu + \lambda) \underline{\nabla_{\vec{r}}} \left(\underline{\nabla_{\vec{r}}} \cdot \underline{Q}[\vec{r}] \right) + \omega^2 \rho[\vec{r}] \underline{Q}[\vec{r}] = 0 \, ,$$

where μ and λ are Lamé parameters, ρ in density, and ω is angular frequency. Using some vector calculus identities we can rewrite this as

$$M \nabla^2_{\vec{r}} \underline{Q}[\vec{r}] + (\mu + \lambda) \underline{\nabla_{\vec{r}}} \times \left(\underline{\nabla_{\vec{r}}} \times \underline{Q}[\vec{r}] \right) + \omega^2 \rho[\vec{r}] \underline{Q}[\vec{r}] = 0 \, ,$$

where $M = 2\,\mu + \lambda$ is the pressure modulus.

If we have a mirror symmetry transform $\underline{\underline{S}}$, such that $\rho[\underline{\underline{S}} \cdot \vec{r}] = \rho[\vec{r}]$, and do a change of coordinates and basis, we get

$$M \nabla^2_{\vec{r}} \left(\underline{\underline{S}} \cdot \underline{Q} \left[\underline{\underline{S}} \cdot \vec{r} \right] \right) + (\mu + \lambda) \left(\underline{\underline{S}} \cdot \underline{\nabla_{\vec{r}}} \right) \times \left(\underline{\nabla_{\vec{r}}} \times \underline{Q} \left[\underline{\underline{S}} \cdot \vec{r} \right] \right) + \omega^2 \rho[\vec{r}] \left(\underline{\underline{S}} \cdot \underline{Q} \left[\underline{\underline{S}} \cdot \vec{r} \right] \right) = 0 \, ,$$

which unfortunately does not take the form of the original equation and hence does not enforce a mirror solution. However, if the displacement field is curl free, $\underline{\nabla} \times \underline{Q} = 0$, the problematic middle term disappears, and the symmetry condition is recovered

$$\underline{\underline{S}} \cdot \underline{Q} \left[\underline{\underline{S}} \cdot \vec{r} \right] = \pm \underline{Q}[\vec{r}] \quad : \quad \underline{\nabla_{\vec{r}}} \times \underline{Q}[\vec{r}] = 0 \, ,$$

for non-degenerate modes.

E.3 Strain

If we have a symmetry condition on the displacement $\underline{Q}$, then this will extend to the strain $\underline{\underline{\epsilon}}$, defined as

$$\epsilon_{i\,j}\left[\{r^k\}_k\right] = \frac{1}{2}\left(\frac{\partial}{\partial r^i}Q_j\left[\{r^k\}_k\right] + \frac{\partial}{\partial r^j}Q_i\left[\{r^k\}_k\right]\right) \ .$$

Starting with

$$(S^{-1})^j_{\ i}\,Q_j\left[\{(S^{-1})^k_{\ l}\,r^l\}_k\right] = s\,Q_i\left[\{r^k\}_k\right] \ ,$$

we derive following,

$$
\begin{aligned}
&(S^{-1})^a_{\ i}\,(S^{-1})^b_{\ j}\,\epsilon_{a\,b}\left[\{(S^{-1})^k_{\ l}\,r^l\}_k\right] \\
&\qquad = (S^{-1})^a_{\ i}\,(S^{-1})^b_{\ j}\,\frac{1}{2}\left(\frac{\partial\,Q_b\left[\{(S^{-1})^k_{\ l}\,r^l\}_k\right]}{\partial\left((S^{-1})^a_{\ c}\,r^c\right)}+\frac{\partial\,Q_a\left[\{(S^{-1})^k_{\ l}\,r^l\}_k\right]}{\partial\left((S^{-1})^b_{\ c}\,r^c\right)}\right) \\
&\qquad = \frac{1}{2}\,(S^{-1})^a_{\ i}\,(S^{-1})^b_{\ j}\,S^c_{\ a}\,\frac{\partial}{\partial r^c}Q_b\left[\{(S^{-1})^k_{\ l}\,r^l\}_k\right] \\
&\qquad\quad + \frac{1}{2}\,(S^{-1})^a_{\ i}\,(S^{-1})^b_{\ j}\,S^c_{\ b}\,\frac{\partial}{\partial r^c}Q_a\left[\{(S^{-1})^k_{\ l}\,r^l\}_k\right] \\
&\qquad = \frac{1}{2}\delta^c_{\ i}\,\frac{\partial}{\partial r^c}(S^{-1})^b_{\ j}\,Q_b\left[\{(S^{-1})^k_{\ l}\,r^l\}_k\right] \\
&\qquad\quad + \frac{1}{2}\delta^c_{\ j}\,\frac{\partial}{\partial r^c}(S^{-1})^a_{\ i}\,Q_a\left[\{(S^{-1})^k_{\ l}\,r^l\}_k\right] \\
&\qquad = \frac{1}{2}\left(s\,\frac{\partial}{\partial r^i}Q_j\left[\{r^k\}_k\right]+s\,\frac{\partial}{\partial r^j}Q_i\left[\{r^k\}_k\right]\right) \\
&\qquad = s\,\epsilon_{i\,j}\left[\{r^k\}_k\right]\ .
\end{aligned}
$$

E.4 Moving boundary

The moving boundary effect contribution to the optopmechanical coupling (C.14) contains

$$
\begin{aligned}
g_{0\mathrm{MB}} \propto \oint\!\!\!\!\!\!\diagup_{\partial\mathrm{Solid}} & \mathrm{d}^2\vec{r}\,Q_k(\vec{r})\,n_k(\vec{r}) \\
& \left(E^{\parallel}_i(\vec{r})^*\,\left(\varepsilon^A_{i\,j}-\varepsilon^B_{i\,j}\right)\,E^{\parallel}_j(\vec{r})-D^{\perp}_i(\vec{r})^*\left((\varepsilon^A)^{-1}{}_{i\,j}-(\varepsilon^B)^{-1}{}_{i\,j}\right)D^{\perp}_j(\vec{r})\right)\ .
\end{aligned}
$$

If there exists an involutory symmetry $\underline{\underline{S}}$ then we can take only half of the integral and add opposing points together; normal vectors following $\underline{\underline{S}} \cdot \underline{n}[\underline{\underline{S}} \cdot \vec{r}] = \underline{n}[\vec{r}]$. The electric field must obey the symmetry condition and because it only appears in terms like $\underline{E}^* \cdot \underline{\underline{\varepsilon}} \cdot \underline{E}$ there will be constructive addition between opposing points. If the displacement field exhibits a symmetry condition we have for opposing points

$$Q_k[\underline{\underline{S}} \cdot \vec{r}]\, n^k[\underline{\underline{S}} \cdot \vec{r}] = \pm_Q\, (S^{-1})^i{}_k\, Q_i[\vec{r}]\, (S^{-1})^k_j\, n^j[\vec{r}] = \pm_Q\, Q_k[\vec{r}]\, n^k[\vec{r}]\,.$$

Thus if the displacement field is antisymmetric (in any direction), the contribution to the integral from opposing points will cancel out and we get $g_{0\mathrm{MB}} = 0$. Intuitively we can think of these mechanical mirror antisymmetric modes as not changing the total volume of the solid (opposite sides move together) and hence not affecting the electromagnetic resonance frequency.

E.5 Photo-elastic

The photo-elastic effect contribution to the optopmechanical coupling (C.19) contains

$$g_{0\mathrm{PE}} \propto \iiint_{\mathrm{Solid}} E_i(\vec{r})^*\, p_{i\,j\,k\,l}(\vec{r})\, \epsilon_{k\,l}(\vec{r})\, E_j(\vec{r})\, \mathrm{d}^3\vec{r}\,.$$

If there exists an involutory symmetry $\underline{\underline{S}}$, with $p_{i\,j\,k\,l}[\underline{\underline{S}} \cdot \vec{r}] = p_{i\,j\,k\,l}[\vec{r}]$, then we can again take half of the integral and add opposing points together. The electric field will obey the symmetry condition with value $\pm_E$, and if the displacement field obeys a symmetry condition

with value $\pm_Q$, we find for mirrored points

$$\begin{aligned} & E_i[\underline{S}\cdot\vec{r}]^*\, p_{i\,j\,k\,l}[\underline{S}\cdot\vec{r}]\,\epsilon_{k\,l}[\underline{S}\cdot\vec{r}]\,E_j[\underline{S}\cdot\vec{r}] \\ & \qquad = (\pm_E)\,S_{a\,i}\,E_a[\vec{r}]^*\,p_{i\,j\,k\,l}[\vec{r}]\,(\pm_Q)\,S_{c\,k}\,S_{d\,l}\,\epsilon_{c\,d}[\vec{r}]\,(\pm_E)\,S_{b\,j}\,E_b[\vec{r}] \\ & \qquad = \pm_Q\; E_a[\vec{r}]^*\,S_{a\,i}\,S_{b\,j}\,S_{c\,k}\,S_{d\,l}\,p_{i\,j\,k\,l}[\vec{r}]\,\epsilon_{c\,d}[\vec{r}]\,E_b[\vec{r}]\,. \end{aligned}$$

Now for a cubic crystal, such as GaAs, the photoelastic tensor, p, has a particular form (see App. C and App. M) such that

$$S_{a\,i}\,S_{b\,j}\,S_{c\,k}\,S_{d\,l}\,p_{i\,j\,k\,l} = p_{a\,b\,c\,d}\,,$$

if $\underline{S}$ is an involutory transform. Thus we again see that if the displacement field is antisymmetric, i.e. $\pm_Q = -1$, the contribution to the integral for mirrored points will cancel out leaving us with $g_{0\mathrm{PE}} = 0$.

E.6 Result

We conclude that to have optomechanical coupling, we can't use a mechanical resonance with any involutory (mirror or π-rotation) antisymmetries.

APPENDIX F

Symmetry in piezoelectricity

F.1 Derivation

Given a mechanical mode symmetry, $S \in O(3)$,

$$(S^{-1})^{j}_{\ i}\, Q_j \left[\underline{\underline{S}}^{-1} \cdot \vec{r}\right] = s_Q\, Q_i\left[\vec{r}\right] \ ,$$

with symmetry value s_Q, we would like to know what symmetry value the piezoelectric voltage response exhibits.

The governing equation for electric fields in a piezoelectric material is (see App. B)

$$\underline{D} = \underline{\underline{\tilde{e}}} \cdot \underline{\tilde{\epsilon}} + \underline{\underline{\varepsilon}} \cdot \underline{E} \ , \qquad\qquad D^i = e^{i\,j\,k}\,\epsilon_{j\,k} + \varepsilon_{i\,j}\,E^j \ ,$$

and if we ignore external fields, the piezoelectric response is simply

$$D^i\left[\vec{r}\right] = e^{i\,j\,k}\left[\vec{r}\right]\,\epsilon_{j\,k}\left[\vec{r}\right] \ .$$

To determine the piezoelectric symmetry value we start with

$$D^i\left[\underline{\underline{S}}^{-1} \cdot \vec{r}\right] = e^{i\,j\,k}\left[\underline{\underline{S}}^{-1} \cdot \vec{r}\right]\,\epsilon_{j\,k}\left[\underline{\underline{S}}^{-1} \cdot \vec{r}\right] \ . \tag{F.1}$$

The piezoelectric coupling tensor e is a material property that obeys the geometric symmetry,

$$e^{i\,j\,k}\left[\underline{\underline{S}}^{-1} \cdot \vec{r}\right] = e^{i\,j\,k}\left[\vec{r}\right] \ ,$$

typically being constant everywhere. From Sec. E.3 we have that the strain symmetry value matches that of the displacement field, hence

$$\epsilon_{j\,k}\left[\underline{\underline{S}}^{-1}\cdot\vec{r}\right]=s_Q\,S^a_{\ j}\,S^b_{\ k}\,\epsilon_{a\,b}\left[\vec{r}\right]\ .$$

Putting this into (F.1),

$$D^i\left[\underline{\underline{S}}^{-1}\cdot\vec{r}\right]=s_Q\,e^{i\,j\,k}\left[\vec{r}\right]\,S^a_{\ j}\,S^b_{\ k}\,\epsilon_{a\,b}\left[\vec{r}\right]\ ,$$

and applying the symmetry operator to both sides,

$$S^i_{\ l}\,D^l\left[\underline{\underline{S}}^{-1}\cdot\vec{r}\right]=s_Q\,S^i_{\ l}\,S^a_{\ j}\,S^b_{\ k}\,e^{l\,j\,k}\left[\vec{r}\right]\,\epsilon_{a\,b}\left[\vec{r}\right]\ . \tag{F.2}$$

Thus the value of the symmetry value for D, defined by

$$S^i_{\ j}\,D^j\left[\underline{\underline{S}}^{-1}\cdot\vec{r}\right]=s_{\text{Piezo}}\,D^i\left[\vec{r}\right]\ ,$$

is dependent on the symmetry operation in question and the piezoelectric coupling tensor.

Once found, the symmetry value for D will match that of E through $\underline{D}=\underline{\underline{\varepsilon}}\cdot\underline{E}$ where ε obeys the geometric symmetry. Relating this to voltage,

$$E_i\left[\vec{r}\right]=-\frac{\partial}{\partial r^i}V\left[\vec{r}\right]\ ,$$

and using the chain rule we have

$$-\frac{\partial}{\partial r^i}V\left[\underline{\underline{S}}^{-1}\cdot\vec{r}\right]=-\frac{\partial\left(S^{-1}\right)^j_{\ k}\,r^k}{\partial r^i}\,\frac{\partial}{\partial\left(\left(S^{-1}\right)^j_{\ l}\,r^l\right)}V\left[\underline{\underline{S}}^{-1}\cdot\vec{r}\right]=\left(S^{-1}\right)^j_{\ i}\,E_j\left[\underline{\underline{S}}^{-1}\cdot\vec{r}\right]\ .$$

Thus given a symmetry condition on E,

$$(S^{-1})^{j}_{\ i}\, E_j \left[\underline{\underline{S}}^{-1} \cdot \vec{r}\right] = s_{\text{Piezo}}\, E_i \left[\vec{r}\right] \ ,$$

we obtain

$$-\frac{\partial}{\partial r^i} V \left[\underline{\underline{S}}^{-1} \cdot \vec{r}\right] = -s_{\text{Piezo}}\, \frac{\partial}{\partial r^i} V \left[\vec{r}\right] \ ,$$

$$\Rightarrow \quad V \left[\underline{\underline{S}}^{-1} \cdot \vec{r}\right] + \text{const}_1 = s_{\text{Piezo}}\, \left(V \left[\vec{r}\right] + \text{const}_2\right) \ .$$

Denoting

$$V_0 = V \left[\underline{\underline{S}}^{-1} \cdot \vec{r} = \vec{r}\right] \ ,$$

and solving for $s_{\text{Piezo}} \in \{-1, 1\}$, we get the symmetry condition on piezoelectric voltage

$$\left(V \left[\underline{\underline{S}}^{-1} \cdot \vec{r}\right] - V_0\right) = s_{\text{Piezo}}\, \left(V \left[\vec{r}\right] - V_0\right) \ .$$

F.2 GaAs

Gallium arsenide's piezoelectric coupling tensor contains only (see App. M)

$$e_{1\,2\,3} = e_{2\,3\,1} = e_{3\,1\,2} = e_{3\,2\,1} = e_{2\,1\,3} = e_{1\,3\,2} = e \ ,$$

with other elements equal to zero.

F.2.1 [100] mirror symmetry

For a x mirror symmetry,

$$\underline{\underline{S_x}} = \begin{pmatrix} -1 & 0 & 0 \\ 0 & 1 & 0 \\ 0 & 0 & 1 \end{pmatrix} ,$$

with GaAs, we can calculate

$$(S_x)^i_{\ l}\,(S_x)^a_{\ j}\,(S_x)^b_{\ k}\,e^{l\,j\,k} = -e^{l\,j\,k} .$$

Putting this into (F.2) means that

$$s_{\text{Piezo}} = -s_Q ,$$

i.e. the piezoelectric response shows the opposite symmetry to mechanical displacement across a (100) mirror. As GaAs is unchanged under $\pi/2$ rotations, this is also true for [010] and [001].

F.2.2 [110] mirror symmetry

For a $x - y$ mirror symmetry,

$$\underline{\underline{S_{x-y}}} = \begin{pmatrix} 0 & 1 & 0 \\ 1 & 0 & 0 \\ 0 & 0 & 1 \end{pmatrix} ,$$

with GaAs, we can calculate

$$(S_{x-y})^{i}_{\ l}\,(S_{x-y})^{a}_{\ j}\,(S_{x-y})^{b}_{\ k}\,e^{l\,j\,k} = e^{l\,j\,k}\ .$$

Putting this into (F.2) means that

$$s_{\text{Piezo}} = s_{Q}\ ,$$

i.e. the piezoelectric response shows the same symmetry as mechanical displacement across a (110) mirror.

APPENDIX G

Voigt transforms

Voigt notation is a common method, particularly in solid mechanics, of expressing symmetric tensors as a lower rank tensor [228].

G.1 Tensors

First, let us quickly review tensors. Starting with a vector space V of dimension n over field $\mathbb{F}$ with basis $\{\vec{e}_1, \ldots, \vec{e}_n\}$, and its dual space V^* with basis $\{\vec{e}^1, \ldots, \vec{e}^n\}$, we define the tensor space $\mathcal{T}^p_q(V)$ of contravariant order p and covariant order q as the set of tensors (multilinear maps)

$$\mathbf{T} : \underbrace{V^* \times V^* \times \cdots}_{p} \times \underbrace{V \times V \times \cdots}_{q} \longrightarrow \mathbb{F} \ ,$$

$$\mathbf{T} = \sum_{i_1=1}^{n} \cdots \sum_{i_p=1}^{n} \sum_{j_1=1}^{n} \cdots \sum_{j_q=1}^{n} T^{i_1 \ldots i_p}_{j_1 \ldots j_q} \, \vec{e}_{i_1} \otimes \cdots \otimes \vec{e}_{i_n} \otimes \vec{e}^{\, j_1} \otimes \cdots \otimes \vec{e}^{\, j_n} \ .$$

We define the metric for V as

$$\mathbf{g} = \sum_{i=1}^{n} \sum_{j=1}^{n} g_{i\,j} \, \vec{e}^{\, i} \otimes \vec{e}^{\, j} \ ,$$

so that $T_i = \sum_{j=1}^{n} g_{i\,j} \, T^j$.

G.2 Voigt transform

A Voigt transform on a pair of symmetric tensor indices reduces it to a single index,

$$\left(\mathbf{T} : \cdots \times V \times V \times \cdots \to \mathbb{F}\right) \mapsto \left(\tilde{\mathbf{T}} : \cdots \times W \times \cdots \to \mathbb{F}\right)$$
$$T_{\cdots (i\,j) \cdots} \mapsto \tilde{T}_{\cdots\, a \,\cdots}$$

where W, of dimension $\frac{n^2+n}{2}$, is a linear subspace of $V \otimes V$, has basis $\{\vec{f}_1, \ldots, \vec{f}_{n\,(n-1)}\}$, and metric $\mathbf{h}$. Parentheses denote symmetrization $T_{(i\,j)} = \frac{1}{2}(T_{i\,j} + T_{j\,i})$, which is simply $T_{i\,j}$ if already symmetric. A complete Voigt transform on a tensor, with all pairs of indices symmetric, maps $\mathcal{T}^p(V) \to \mathcal{T}^{p/2}(W)$. For a faithful Voigt representation, we require that the tensors provide an equivalent mapping,

$$\sum_{i=1}^{n}\sum_{j=1}^{n} T^{\cdots (i\,j) \cdots} \vec{e}_i \otimes \vec{e}_j \;\cdots = \mathbf{T} = \tilde{\mathbf{T}} = \sum_{a=1}^{n\,(n-1)} \tilde{T}^{\cdots\, a \,\cdots} \vec{f}_a \;\cdots \,. \tag{G.1}$$

In order to proceed we define a general relationship between $\vec{f}_a$ and $\vec{e}_i$,

$$\begin{aligned} &\vec{f}_a = \vec{e}_a \otimes \vec{e}_a && \text{for } a \in \{1, \ldots, n\}\,, \\ &\vec{f}_a = \alpha\left(\vec{e}_{i_a} \otimes \vec{e}_{j_a} + \vec{e}_{j_a} \otimes \vec{e}_{i_a}\right) && \text{for } a \in \{n+1, \ldots, n\,(n-1)\} \text{ and } i_a \neq j_a\,. \end{aligned}$$

In the case of $n = 3$ and using standard Voigt ordering $(2\,3, 1\,3, 1\,2)$,

$$\begin{aligned} \vec{f}_1 &= \vec{e}_1 \otimes \vec{e}_1\,, & \vec{f}_4 &= \alpha\left(\vec{e}_2 \otimes \vec{e}_3 + \vec{e}_3 \otimes \vec{e}_2\right)\,, \\ \vec{f}_2 &= \vec{e}_2 \otimes \vec{e}_2\,, & \vec{f}_5 &= \alpha\left(\vec{e}_1 \otimes \vec{e}_3 + \vec{e}_3 \otimes \vec{e}_1\right)\,, \\ \vec{f}_3 &= \vec{e}_3 \otimes \vec{e}_3\,, & \vec{f}_6 &= \alpha\left(\vec{e}_1 \otimes \vec{e}_2 + \vec{e}_2 \otimes \vec{e}_1\right)\,. \end{aligned}$$

Putting this into (G.1) we find the contravariant Voigt transform rules

$$\begin{aligned} \tilde{T}^1 &= T^{1\,1}\,, & \tilde{T}^4 &= \tfrac{1}{\alpha}\,T^{2\,3}\,, \\ \tilde{T}^2 &= T^{2\,2}\,, & \tilde{T}^5 &= \tfrac{1}{\alpha}\,T^{1\,3}\,, \\ \tilde{T}^3 &= T^{3\,3}\,, & \tilde{T}^6 &= \tfrac{1}{\alpha}\,T^{1\,2}\,. \end{aligned}$$

We now wish to impose that contractions behave properly in Voigt notation, i.e.

$$\sum_{i=1}^{n}\sum_{j=1}^{n}\sum_{k=1}^{n}\sum_{l=1}^{n} A^{i\,j}\,g_{i\,k}\,g_{j\,l}\,B^{k\,l} = \sum_{a=1}^{n\,(n-1)}\sum_{b=1}^{n\,(n-1)} \tilde{A}^a\,h_{a\,b}\,\tilde{B}^b\,,$$

and in the case of $n = 3$ this gives the metric on W to be

$$(h_{a\,b}) = \begin{pmatrix} {g_{1\,1}}^2 & {g_{1\,2}}^2 & {g_{1\,3}}^2 & 2\,\alpha\,g_{1\,1}\,g_{1\,3} & 2\,\alpha\,g_{1\,2}\,g_{2\,3} & 2\,\alpha\,g_{1\,3}\,g_{3\,3} \\ {g_{1\,2}}^2 & {g_{2\,2}}^2 & {g_{2\,3}}^2 & 2\,\alpha\,g_{1\,2}\,g_{2\,3} & 2\,\alpha\,g_{2\,2}\,g_{2\,3} & 2\,\alpha\,g_{3\,3}\,g_{2\,3} \\ {g_{1\,3}}^2 & {g_{2\,3}}^2 & {g_{3\,3}}^2 & 2\,\alpha\,g_{1\,3}\,g_{3\,3} & 2\,\alpha\,g_{2\,3}\,g_{3\,3} & 2\,\alpha\,g_{3\,3}\,g_{3\,3} \\ 2\,\alpha\,g_{1\,2}\,g_{1\,3} & 2\,\alpha\,g_{2\,2}\,g_{2\,3} & 2\,\alpha\,g_{3\,3}\,g_{3\,3} & 2\,\alpha^2\,({g_{2\,3}}^2 + g_{2\,2}\,g_{3\,3}) & 2\,\alpha^2\,(g_{1\,3}\,g_{2\,3} + g_{1\,2}\,g_{3\,3}) & 2\,\alpha^2\,(g_{1\,3}\,g_{2\,2} + g_{1\,2}\,g_{2\,3}) \\ 2\,\alpha\,g_{1\,1}\,g_{1\,3} & 2\,\alpha\,g_{1\,2}\,g_{2\,3} & 2\,\alpha\,g_{1\,3}\,g_{3\,3} & 2\,\alpha^2\,(g_{1\,3}\,g_{2\,3} + g_{1\,2}\,g_{3\,3}) & 2\,\alpha^2\,({g_{1\,3}}^2 + g_{1\,1}\,g_{3\,3}) & 2\,\alpha^2\,(g_{1\,2}\,g_{1\,3} + g_{1\,1}\,g_{2\,3}) \\ 2\,\alpha\,g_{1\,1}\,g_{1\,2} & 2\,\alpha\,g_{1\,2}\,g_{2\,2} & 2\,\alpha\,g_{1\,3}\,g_{2\,3} & 2\,\alpha^2\,(g_{1\,3}\,g_{2\,2} + g_{1\,2}\,g_{2\,3}) & 2\,\alpha^2\,(g_{1\,2}\,g_{1\,3} + g_{1\,1}\,g_{2\,3}) & 2\,\alpha^2\,({g_{1\,2}}^2 + g_{1\,1}\,g_{2\,2}) \end{pmatrix}.$$

This also gives us the dual basis vectors, $\vec{f}^{\,a} = \sum_{b=1}^{n\,(n-1)} h^{a\,b}\,\vec{f}_b$, using $(h^{a\,b}) = (h_{a\,b})^{-1}$,

$$\begin{aligned}
\vec{f}^{\,1} &= \vec{e}^{\,1} \otimes \vec{e}^{\,1}\ , & \vec{f}^{\,4} &= \tfrac{1}{2\,\alpha}\left(\vec{e}^{\,2} \otimes \vec{e}^{\,3} + \vec{e}^{\,3} \otimes \vec{e}^{\,2}\right)\ , \\
\vec{f}^{\,2} &= \vec{e}^{\,2} \otimes \vec{e}^{\,2}\ , & \vec{f}^{\,5} &= \tfrac{1}{2\,\alpha}\left(\vec{e}^{\,1} \otimes \vec{e}^{\,3} + \vec{e}^{\,3} \otimes \vec{e}^{\,1}\right)\ , \\
\vec{f}^{\,3} &= \vec{e}^{\,3} \otimes \vec{e}^{\,3}\ , & \vec{f}^{\,6} &= \tfrac{1}{2\,\alpha}\left(\vec{e}^{\,1} \otimes \vec{e}^{\,2} + \vec{e}^{\,2} \otimes \vec{e}^{\,1}\right)\ .
\end{aligned}$$

We also obtain the covariant Voigt transform rules

$$\begin{aligned}
\tilde{T}_1 &= T_{1\,1}\ , & \tilde{T}_4 &= 2\,\alpha\,T_{2\,3}\ , \\
\tilde{T}_2 &= T_{2\,2}\ , & \tilde{T}_5 &= 2\,\alpha\,T_{1\,3}\ , \\
\tilde{T}_3 &= T_{3\,3}\ , & \tilde{T}_6 &= 2\,\alpha\,T_{1\,2}\ .
\end{aligned}$$

For the common case of $V = \mathbb{R}^3$ and $(g_{i\,j}) = \mathbb{I}_3$, we get

$$(h_{a\,b}) = \begin{pmatrix}
1 & 0 & 0 & 0 & 0 & 0 \\
0 & 1 & 0 & 0 & 0 & 0 \\
0 & 0 & 1 & 0 & 0 & 0 \\
0 & 0 & 0 & 2\,\alpha^2 & 0 & 0 \\
0 & 0 & 0 & 0 & 2\,\alpha^2 & 0 \\
0 & 0 & 0 & 0 & 0 & 2\,\alpha^2
\end{pmatrix},$$

which in general is not equal to $\mathbb{I}_6$. Thus whilst indices on T can be raised or lowered 'freely', the same is not true for $\tilde{T}$ and care must be taken to ensure only covariant and contravariant indices are contracted together.

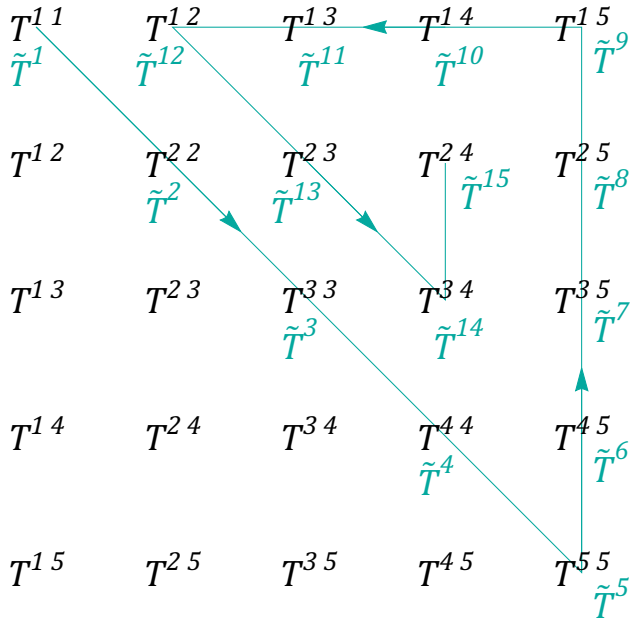

Figure G.1: Voigt ordering for a 5×5 symmetric tensor.

G.3 Voigt order

The matching of tensor indices to their Voigt counterpart follows a spiral pattern, starting along the diagonal, then going around the upper right triangle of the symmetric tensor. An example for $n = 5$ is given in Fig. G.1.

G.4 Multiple Voigt transforms

Tensors with multiple pairs of symmetric indices can have each Voigt transformed, as an example the transformation rules for $T_{(ij)(kl)} \mapsto \tilde{T}_{ab}$, $n = 3$ are

$$\tilde{T}^{11} = T^{1111} \qquad \tilde{T}^{14} = \tfrac{1}{\alpha} T^{1123} \qquad \tilde{T}^{41} = \tfrac{1}{\alpha} T^{2311} \qquad \tilde{T}^{44} = \tfrac{1}{\alpha^2} T^{2323}$$

$$\tilde{T}_{11} = T_{1111} \qquad \tilde{T}_{14} = 2\,\alpha\, T_{1123} \qquad \tilde{T}_{41} = 2\,\alpha\, T_{2311} \qquad \tilde{T}_{44} = 4\,\alpha^2\, T_{2323}$$

G.5 Solid mechanics convention

In solid mechanics it is typical to take $\alpha = 1$, denote the contravariant Voigt transform as 'stress-like', and the covariant Voigt transform as 'strain-like'. In this setting many authors do not properly keep track of raised/lowered indices and instead ensure that any contractions in Voigt notation take place between a stress-like transformed tensor and a strain-like transformed tensor. As such, stress $\sigma_{(i\,j)}$, stiffness $c_{(i\,j)\,(k\,l)}$, photoelasticity $p_{(i\,j)\,(k\,l)}$, all transform stress-like; whilst strain $\epsilon_{(i\,j)}$, compliance $s_{(i\,j)\,(k\,l)}$, transform strain-like. The strain is defined as $\epsilon_{i\,j} = \partial_{(i}\,Q_{j)} = \frac{1}{2}(\partial_i\,Q_j + \partial_j\,Q_i)$.

For reference,

$$\begin{pmatrix} \tilde{\sigma}^1 \\ \tilde{\sigma}^2 \\ \tilde{\sigma}^3 \\ \tilde{\sigma}^4 \\ \tilde{\sigma}^5 \\ \tilde{\sigma}^6 \end{pmatrix} \underset{\text{like}}{\overset{\text{stress}}{=}} \begin{pmatrix} \sigma^{1\,1} \\ \sigma^{2\,2} \\ \sigma^{3\,3} \\ \sigma^{2\,3} \\ \sigma^{1\,3} \\ \sigma^{1\,2} \end{pmatrix}, \qquad \begin{pmatrix} \tilde{\epsilon}_1 \\ \tilde{\epsilon}_2 \\ \tilde{\epsilon}_3 \\ \tilde{\epsilon}_4 \\ \tilde{\epsilon}_5 \\ \tilde{\epsilon}_6 \end{pmatrix} \underset{\text{like}}{\overset{\text{strain}}{=}} \begin{pmatrix} \epsilon_{1\,1} \\ \epsilon_{2\,2} \\ \epsilon_{3\,3} \\ 2\,\epsilon_{2\,3} \\ 2\,\epsilon_{1\,3} \\ 2\,\epsilon_{1\,2} \end{pmatrix},$$

$$\begin{pmatrix} \tilde{c}^{11} & \tilde{c}^{12} & \tilde{c}^{13} & \tilde{c}^{14} & \tilde{c}^{15} & \tilde{c}^{16} \\ \tilde{c}^{21} & \tilde{c}^{22} & \tilde{c}^{23} & \tilde{c}^{24} & \tilde{c}^{25} & \tilde{c}^{26} \\ \tilde{c}^{31} & \tilde{c}^{32} & \tilde{c}^{33} & \tilde{c}^{34} & \tilde{c}^{35} & \tilde{c}^{36} \\ \tilde{c}^{41} & \tilde{c}^{42} & \tilde{c}^{43} & \tilde{c}^{44} & \tilde{c}^{45} & \tilde{c}^{46} \\ \tilde{c}^{51} & \tilde{c}^{52} & \tilde{c}^{53} & \tilde{c}^{54} & \tilde{c}^{55} & \tilde{c}^{56} \\ \tilde{c}^{61} & \tilde{c}^{62} & \tilde{c}^{63} & \tilde{c}^{64} & \tilde{c}^{65} & \tilde{c}^{66} \end{pmatrix} \begin{matrix} \\ \\ \\ = \\ \text{stress} \\ \text{like} \\ \\ \\ \end{matrix} \begin{pmatrix} c^{1111} & c^{1122} & c^{1133} & c^{1123} & c^{1113} & c^{1112} \\ c^{2211} & c^{2222} & c^{2233} & c^{2223} & c^{2213} & c^{2212} \\ c^{3311} & c^{3322} & c^{3333} & c^{3323} & c^{3313} & c^{3312} \\ c^{2311} & c^{2322} & c^{2333} & c^{2323} & c^{2313} & c^{2312} \\ c^{1311} & c^{1322} & c^{1333} & c^{1323} & c^{1313} & c^{1312} \\ c^{1211} & c^{1222} & c^{1233} & c^{1223} & c^{1213} & c^{1212} \end{pmatrix},$$

$$\begin{pmatrix} \tilde{s}_{11} & \tilde{s}_{12} & \tilde{s}_{13} & \tilde{s}_{14} & \tilde{s}_{15} & \tilde{s}_{16} \\ \tilde{s}_{21} & \tilde{s}_{22} & \tilde{s}_{23} & \tilde{s}_{24} & \tilde{s}_{25} & \tilde{s}_{26} \\ \tilde{s}_{31} & \tilde{s}_{32} & \tilde{s}_{33} & \tilde{s}_{34} & \tilde{s}_{35} & \tilde{s}_{36} \\ \tilde{s}_{41} & \tilde{s}_{42} & \tilde{s}_{43} & \tilde{s}_{44} & \tilde{s}_{45} & \tilde{s}_{46} \\ \tilde{s}_{51} & \tilde{s}_{52} & \tilde{s}_{53} & \tilde{s}_{54} & \tilde{s}_{55} & \tilde{s}_{56} \\ \tilde{s}_{61} & \tilde{s}_{62} & \tilde{s}_{63} & \tilde{s}_{64} & \tilde{s}_{65} & \tilde{s}_{66} \end{pmatrix} \begin{matrix} \\ \\ \\ = \\ \text{strain} \\ \text{like} \\ \\ \\ \end{matrix} \begin{pmatrix} s_{1111} & s_{1122} & s_{1133} & 2\,s_{1123} & 2\,s_{1113} & 2\,s_{1112} \\ s_{2211} & s_{2222} & s_{2233} & 2\,s_{2223} & 2\,s_{2213} & 2\,s_{2212} \\ s_{3311} & s_{3322} & s_{3333} & 2\,s_{3323} & 2\,s_{3313} & 2\,s_{3312} \\ 2\,s_{2311} & 2\,s_{2322} & 2\,s_{2333} & 4\,s_{2323} & 4\,s_{2313} & 4\,s_{2312} \\ 2\,s_{1311} & 2\,s_{1322} & 2\,s_{1333} & 4\,s_{1323} & 4\,s_{1313} & 4\,s_{1312} \\ 2\,s_{1211} & 2\,s_{1222} & 2\,s_{1233} & 4\,s_{1223} & 4\,s_{1213} & 4\,s_{1212} \end{pmatrix},$$

$$\begin{pmatrix} \tilde{e}^{11} & \tilde{e}^{12} & \tilde{e}^{13} & \tilde{e}^{14} & \tilde{e}^{15} & \tilde{e}^{16} \\ \tilde{e}^{21} & \tilde{e}^{22} & \tilde{e}^{23} & \tilde{e}^{24} & \tilde{e}^{25} & \tilde{e}^{26} \\ \tilde{e}^{31} & \tilde{e}^{32} & \tilde{e}^{33} & \tilde{e}^{34} & \tilde{e}^{35} & \tilde{e}^{36} \end{pmatrix} \begin{matrix} \\ = \\ \text{stress} \\ \text{like} \end{matrix} \begin{pmatrix} e^{111} & e^{122} & e^{133} & e^{123} & e^{113} & e^{112} \\ e^{211} & e^{222} & e^{233} & e^{223} & e^{213} & e^{212} \\ e^{311} & e^{322} & e^{333} & e^{323} & e^{313} & e^{312} \end{pmatrix},$$

$$\begin{pmatrix} \tilde{d}_{11} & \tilde{d}_{12} & \tilde{d}_{13} & \tilde{d}_{14} & \tilde{d}_{15} & \tilde{d}_{16} \\ \tilde{d}_{21} & \tilde{d}_{22} & \tilde{d}_{23} & \tilde{d}_{24} & \tilde{d}_{25} & \tilde{d}_{26} \\ \tilde{d}_{31} & \tilde{d}_{32} & \tilde{d}_{33} & \tilde{d}_{34} & \tilde{d}_{35} & \tilde{d}_{36} \end{pmatrix} \begin{matrix} \\ = \\ \text{strain} \\ \text{like} \end{matrix} \begin{pmatrix} d_{111} & d_{122} & d_{133} & 2\,d_{123} & 2\,d_{113} & 2\,d_{112} \\ d_{211} & d_{222} & d_{233} & 2\,d_{223} & 2\,d_{213} & 2\,d_{212} \\ d_{311} & d_{322} & d_{333} & 2\,d_{323} & 2\,d_{313} & 2\,d_{312} \end{pmatrix},$$

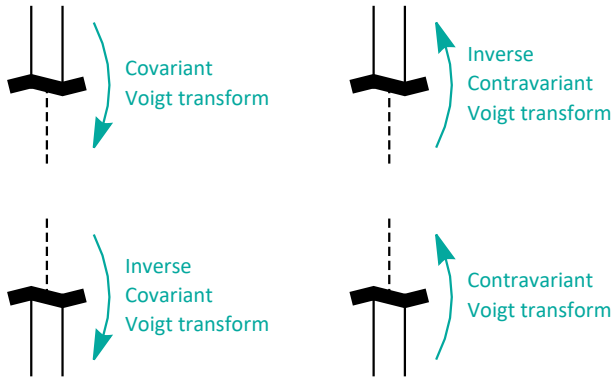

Figure G.2: Voigt transforms in Penrose tensor diagrams.

G.6 Mandel notation

In Mandel notation, or ortho-normal representation, $\alpha = 1/\sqrt{2}$ and $(h_{i\,j}) = \mathbb{I}_{n\,(n-1)}$ with covariant and contravariant transforms identical.

G.7 Penrose diagrams

Voigt transforms can be depicted in Penrose tensor diagrams with the junctions given in Fig.G.2, with an example of stress and strain contraction in Fig. G.3.

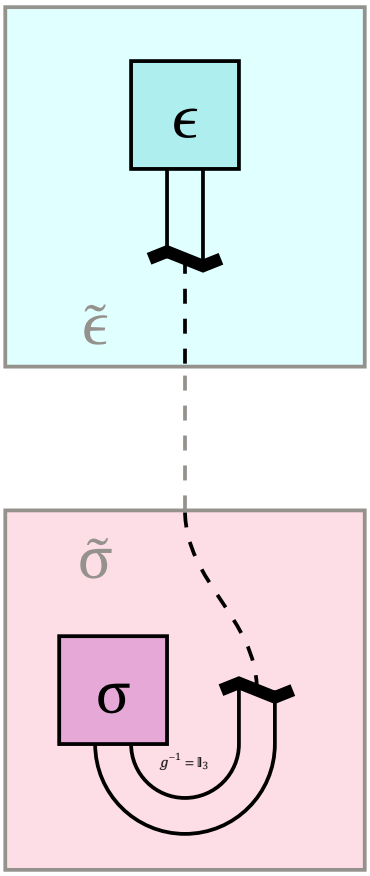

Figure G.3: Voigt transform and contraction $\sum_{i=1}^{3} \tilde{\sigma}^i \, \tilde{\epsilon}_i$.

APPENDIX H

Fourier transforms

H.1 Definition

Throughout this thesis, we will define Fourier transforms for f as

$$\mathcal{F}[f][\omega] = f(\omega) = \frac{1}{\sqrt{2\,\pi}} \int_{-\infty}^{\infty} \mathrm{e}^{\mathrm{i}\,\omega\,t}\, f(t)\,\mathrm{d}t\ ,$$
$$\mathcal{F}^{-1}\big[\mathcal{F}[f]\big][t] = f(t) = \frac{1}{\sqrt{2\,\pi}} \int_{-\infty}^{\infty} \mathrm{e}^{-\mathrm{i}\,\omega\,t}\, f(\omega)\,\mathrm{d}\omega\ ,$$

and

$$f(t)^* = f^*(t)\ , \qquad\qquad f(\omega)^* = f^*(-\omega)\ .$$

H.2 Dirac delta

The Dirac delta distribution obeys

$$\int_{-\infty}^{\infty} \mathrm{e}^{-\mathrm{i}\,x\,y}\,\mathrm{d}x = 2\,\pi\,\delta(y)\ , \tag{H.1}$$
$$\int_{x_1<y}^{x_2>y} \delta(x-y)\,f(x)\,\mathrm{d}x = f(y)\ , \tag{H.2}$$
$$\int_{x_1<y}^{y} \delta(x-y)\,f(x)\,\mathrm{d}x = f(y)/2\ . \tag{H.3}$$

Dirac delta has units inverse to its argument.

H.3 Heaviside step

The Heaviside step function is

$$\Theta(x) = \begin{cases} 1 & : \ x > 0 \\ & \\ 0 & : \ x < 0 \end{cases} ,$$

such that

$$\frac{\mathrm{d}}{\mathrm{d}x}\Theta(x) = \delta(x) \ , \qquad\qquad \Theta(x) = \int_{-\infty}^{x} \delta(y)\,\mathrm{d}y \ .$$

H.4 Convolution

The convolution of f with g is

$$\big(f * g\big)(x) = \int_{-\infty}^{\infty} f(x-y)\,g(y)\,\mathrm{d}y \ .$$

H.5 Identities

$$\mathcal{F}\Big[t \mapsto \mathrm{e}^{-\mathrm{i}\,\Omega\,t}\Big] = \omega \mapsto \sqrt{2\,\pi}\,\delta[\omega - \Omega] \quad : \quad \Omega \in \mathbb{R}$$

$$\mathcal{F}\Big[t \mapsto f[t]\,\mathrm{e}^{-\mathrm{i}\,\Omega\,t}\Big] = \omega \mapsto \mathcal{F}[f][\omega - \Omega] \quad : \quad \Omega \in \mathbb{R}$$

$$\mathcal{F}\Big[t \mapsto \Theta[t]\,\mathrm{e}^{-z\,t}\Big] = \omega \mapsto \frac{1}{\sqrt{2\,\pi}}\,\frac{1}{z - \mathrm{i}\,\omega} \quad : \quad \Re[z] > 0$$

$$\mathcal{F}\Big[t \mapsto \big(f * g\big)[t]\Big] = \omega \mapsto \sqrt{2\,\pi}\,\mathcal{F}[f][\omega]\,\mathcal{F}[g][\omega]$$

APPENDIX I

Quantum input-output

In this appendix we cover coupling a quantum resonator to thermal environments and drives.

I.1 Quantum harmonic oscillator

The Hamiltonian for a quantum simple harmonic oscillator is

$$\hat{H} = \hbar\,\omega\,\left(\hat{a}^\dagger\,\hat{a} + \frac{1}{2}\right) = \frac{\hat{p}^2}{2\,m} + \frac{m\,\omega^2\,\hat{x}^2}{2}\,, \tag{I.1}$$

with

m , mass

ω , resonance frequency

$\hat{x} = \sqrt{\frac{\hbar}{2\,m\,\omega}}\left(\hat{a}^\dagger + \hat{a}\right)$, position

$\hat{a} = \sqrt{\frac{m\,\omega}{2\,\hbar}}\left(\hat{x} + \frac{\mathrm{i}}{m\,\omega}\hat{p}\right)$, annihilation

$\hat{p} = \mathrm{i}\sqrt{\frac{\hbar\,m\,\omega}{2}}\left(\hat{a}^\dagger - \hat{a}\right)$, momentum

$\hat{a}^\dagger = \sqrt{\frac{m\,\omega}{2\,\hbar}}\left(\hat{x} - \frac{\mathrm{i}}{m\,\omega}\hat{p}\right)$, creation

$$[\hat{x}, \hat{p}] = \mathrm{i}\,\hbar\,, \qquad \left[\hat{a}, \hat{a}^\dagger\right] = 1\,,$$

and

$$|n\rangle = \frac{1}{\sqrt{n!}} \left(\hat{a}^\dagger\right)^n |0\rangle \ , \tag{I.2}$$

$$(\hat{a})^m |n\rangle = \sqrt{\frac{n!}{(n-m)!}} \ |n-m\rangle \ , \tag{I.3}$$

$$\left(\hat{a}^\dagger\right)^m |n\rangle = \sqrt{\frac{(n+m)!}{n!}} \ |n+m\rangle \ . \tag{I.4}$$

In opposing bases we have

$$\hat{x}^\dagger = \hat{x} = \mathrm{i}\,\hbar \frac{\partial}{\partial p} \ , \qquad\qquad \hat{p}^\dagger = \hat{p} = -\mathrm{i}\,\hbar \frac{\partial}{\partial x} \ ,$$

noting that

$$\left(\frac{\partial}{\partial x}\right)^\dagger = -\frac{\partial}{\partial x} \ , \qquad\qquad \left(\frac{\partial}{\partial p}\right)^\dagger = -\frac{\partial}{\partial p} \ .$$

I.1.1 Commutator relations

$$\left[\hat{A}, \hat{B}\right]^\dagger = \left[\hat{B}^\dagger, \hat{A}^\dagger\right] = -\left[\hat{A}^\dagger, \hat{B}^\dagger\right] \ ,$$

$$\left[\hat{A}\,\hat{B}, \hat{C}\right] = \hat{A}\,\left[\hat{B}, \hat{C}\right] + \left[\hat{A}, \hat{C}\right]\,\hat{B} \ ,$$

$$\left[\hat{a}^\dagger\,\hat{a}, \hat{a}^\dagger\right] = \hat{a}^\dagger \ , \qquad\qquad \left[\hat{a}^\dagger\,\hat{a}, \hat{a}\right] = \ -\hat{a} \ . \tag{I.5}$$

$$\begin{aligned}\left[\hat{a},(\hat{a}^\dagger)^n\right] &= (\hat{a}^\dagger)^{n-1} + \hat{a}^\dagger \left[\hat{a},(\hat{a}^\dagger)^{n-1}\right] \\ &= \sum_{i=1}^{n} (\hat{a}^\dagger)^{n-1} \\ &= n\,(\hat{a}^\dagger)^{n-1}\ , \end{aligned} \tag{I.6}$$

$$\begin{aligned}\left[\hat{a}^\dagger,\hat{a}^n\right] &= -\,\hat{a}^{n-1} + \hat{a}\,\left[\hat{a}^\dagger,\hat{a}^{n-1}\right] \\ &= -\sum_{i=1}^{n} \hat{a}^{n-1} \\ &= -\,n\,\hat{a}^{n-1}\ , \end{aligned} \tag{I.7}$$

$$\begin{aligned}\left[\hat{a},\mathrm{e}^{\alpha\,\hat{a}^\dagger}\right] &= \sum_{i=0}^{\infty} \frac{\alpha^i}{i!}\left[\hat{a},(\hat{a}^\dagger)^i\right] \\ &\overset{\text{(I.6)}}{=} \sum_{i=0}^{\infty} \frac{\alpha^i\,i}{i!}(\hat{a}^\dagger)^{i-1} \\ &= \alpha\,\sum_{i=1}^{\infty} \frac{\alpha^{i-1}}{(i-1)!}(\hat{a}^\dagger)^{i-1} \\ &= \alpha\,\sum_{j=0}^{\infty} \frac{\alpha^j}{j!}(\hat{a}^\dagger)^{j} \\ &= \alpha\,\mathrm{e}^{\alpha\,\hat{a}^\dagger} \end{aligned} \tag{I.8}$$

$$\begin{aligned}
\left[\hat{a}^\dagger, \mathrm{e}^{-\alpha^* \hat{a}}\right] &= \sum_{i=0}^{\infty} \frac{(-\alpha^*)^i}{i!} \left[\hat{a}^\dagger, \hat{a}^i\right] \\
&\overset{\text{(I.7)}}{=} \sum_{i=0}^{\infty} \frac{(-\alpha^*)^i \, (-i)}{i!} \, \hat{a}^{i-1} \\
&= \alpha^* \sum_{i=1}^{\infty} \frac{(-\alpha^*)^{i-1}}{(i-1)!} \, \hat{a}^{i-1} \\
&= \alpha^* \sum_{j=0}^{\infty} \frac{(-\alpha^*)^j}{j!} \, \hat{a}^j \\
&= \alpha^* \, \mathrm{e}^{-\alpha^* \hat{a}} \qquad \text{(I.9)}
\end{aligned}$$

I.1.2 Baker-Campbell-Hausdorff relations

For $\hat{U} = \mathrm{e}^{\hat{G}}$ and $\hat{U}^\dagger = \hat{U}^{-1} \Leftrightarrow \hat{G}^\dagger = -\hat{G}$,

$$\begin{aligned}
\hat{U}^\dagger \, \hat{A} \, \hat{U} &= \mathrm{e}^{-\hat{G}} \, \hat{A} \, \mathrm{e}^{\hat{G}} \\
&= \hat{A} + \left[\hat{A}, \hat{G}\right] + \frac{1}{2}\left[\left[\hat{A}, \hat{G}\right], \hat{G}\right] + \frac{1}{6}\left[\left[\left[\hat{A}, \hat{G}\right], \hat{G}\right], \hat{G}\right] + \cdots \\
&= \sum_{i=0}^{\infty} \frac{1}{i!} \Big[\cdots \Big[\Big[\hat{A}, \underbrace{\hat{G}\Big], \hat{G}\Big], \cdots, \hat{G}\Big]}_{i} \, . \qquad \text{(I.10)}
\end{aligned}$$

If $\hat{G}$ is infinitesimal, $\Delta\hat{A} = \left[\hat{A}, \hat{G}\right] + \mathcal{O}[\hat{G}^2]$.

For the special case of $\hat{G} \propto -\mathrm{i}\,\hat{a}^\dagger\,\hat{a}$,

$$\begin{aligned}
\mathrm{e}^{\mathrm{i}\,k\,\hat{a}^\dagger\,\hat{a}}\,\hat{a}\,\mathrm{e}^{-\mathrm{i}\,k\,\hat{a}^\dagger\,\hat{a}} &\overset{\text{(I.10)}}{=} \hat{a} + (-\mathrm{i}\,k)\left[\hat{a}, \hat{a}^\dagger\,\hat{a}\right] + \frac{(-\mathrm{i}\,k)^2}{2}\left[\left[\hat{a}, \hat{a}^\dagger\,\hat{a}\right], \hat{a}^\dagger\,\hat{a}\right] + \cdots \\
&\overset{\text{(I.5)}}{=} \hat{a} + (-\mathrm{i}\,k)\,\hat{a} + \frac{(-\mathrm{i}\,k)^2}{2}\,\hat{a} + \cdots \\
&= \hat{a}\,\mathrm{e}^{-\mathrm{i}\,k}
\end{aligned} \tag{I.11}$$

$$\mathrm{e}^{\mathrm{i}\,k\,\hat{a}^\dagger\,\hat{a}}\,\hat{a}^\dagger\,\mathrm{e}^{-\mathrm{i}\,k\,\hat{a}^\dagger\,\hat{a}} = \hat{a}^\dagger\,\mathrm{e}^{\mathrm{i}\,k} \tag{I.12}$$

I.1.3 Displaced quantum harmonic oscillator

We can transform the harmonic oscillator into a coherent state by applying the unitary displacement operator

$$\hat{D}(\alpha) = \mathrm{e}^{\alpha\,\hat{a}^\dagger - \alpha^*\,\hat{a}} = \mathrm{e}^{\alpha\,\hat{a}^\dagger}\,\mathrm{e}^{-\alpha^*\,\hat{a}}\,\mathrm{e}^{-|\alpha|/2}\ .$$

Utilizing Baker-Campbell-Hausdorff relation (I.10) and various commutator relations,

$$\begin{aligned}
\hat{D}(\alpha)^\dagger\,\hat{a}^\dagger\,\hat{a}\,\hat{D}(\alpha) &= \hat{a}^\dagger\,\hat{a} + \alpha\,\hat{a}^\dagger + \alpha^*\,\hat{a} + |\alpha| \\
&= \left(\hat{a}^\dagger + \alpha^*\right)\left(\hat{a} + \alpha\right)\ ,
\end{aligned}$$

$$\hat{D}(\alpha)^\dagger\,\hat{a}\,\hat{D}(\alpha) = \hat{a} + \alpha\ ,$$

$$\hat{D}(\alpha)^\dagger\,\hat{a}^\dagger\,\hat{D}(\alpha) = \hat{a}^\dagger + \alpha^*\ .$$

I.2 Laser drive

A forced harmonic oscillator can be realized be adding a term $F(t)\,\hat{x}$ to the Hamiltonian. In ladder operator formalism the most general expression is

$$f(t)\,\hat{a}^\dagger + f(t)^*\,\hat{a}\ .$$

If our drive is a coherent laser, $f(t) \propto \mathrm{e}^{-\mathrm{i}\,\omega_\mathrm{L}\,t}$ and our Hamiltonian is

$$\hat{H} = \hbar\,\omega_\mathrm{o}\left(\hat{a}^\dagger\,\hat{a} + \frac{1}{2}\right) + \hbar\,L\,\hat{a}^\dagger\,\mathrm{e}^{-\mathrm{i}\,\omega_\mathrm{L}\,t} + \hbar\,L^*\,\hat{a}\,\mathrm{e}^{\mathrm{i}\,\omega_\mathrm{L}\,t}\ .$$

The equation of motion for this is

$$\frac{\mathrm{d}}{\mathrm{d}t}\hat{a}(t) = \left[\hat{a}(t), -\frac{\mathrm{i}}{\hbar}\hat{H}\right] = -\mathrm{i}\,\omega_\mathrm{o}\,\hat{a}(t) - \mathrm{i}\,L\,\mathrm{e}^{-\mathrm{i}\,\omega_\mathrm{L}\,t}\ ,$$

with Fourier transform

$$\hat{a}(\omega) = \frac{-\mathrm{i}\,L\,\sqrt{2\,\pi}\,\delta(\omega - \omega_\mathrm{L})}{\mathrm{i}\,(\omega_\mathrm{o} - \omega)}\ .$$

I.2.1 Rotating frame

To remove the time dependence from this Hamiltonian we can transform to a rotating frame,

$$|\psi_\mathrm{rot}(t)\rangle = \hat{U}_\mathrm{rot}(t)^\dagger\ |\psi(t)\rangle \qquad\qquad \hat{U}_\mathrm{rot}(t) = \mathrm{e}^{-\mathrm{i}\,\omega_\mathrm{L}\,\left(\hat{a}^\dagger\,\hat{a} + \frac{1}{2}\right)\,t}$$

$$
\begin{aligned}
\Rightarrow \quad \hat{H}_{\mathrm{rot}} &= \hat{U}_{\mathrm{rot}}(t)^{\dagger}\left(\hat{H} - \mathrm{i}\,\hbar\,\frac{\partial}{\partial t}\right)\hat{U}_{\mathrm{rot}}(t) \\
&= \hbar\,\omega_{\mathrm{o}}\left(\hat{a}^{\dagger}\,\hat{a} + \frac{1}{2}\right) + \hbar\,L\,\hat{a}^{\dagger}\,\mathrm{e}^{-\mathrm{i}\,\omega_{\mathrm{L}}\,t}\,\mathrm{e}^{\mathrm{i}\,\omega_{\mathrm{L}}\,t} + \hbar\,L^{*}\,\hat{a}\,\mathrm{e}^{\mathrm{i}\,\omega_{\mathrm{L}}\,t}\,\mathrm{e}^{-\mathrm{i}\,\omega_{\mathrm{L}}\,t} - \hbar\,\omega_{\mathrm{L}}\left(\hat{a}^{\dagger}\,\hat{a} + \frac{1}{2}\right) \\
&= \hbar\,\omega_{\mathrm{o}}\left(\hat{a}^{\dagger}\,\hat{a} + \frac{1}{2}\right) + \hbar\,L\,\hat{a}^{\dagger} + \hbar\,L^{*}\,\hat{a} - \hbar\,\omega_{\mathrm{L}}\left(\hat{a}^{\dagger}\,\hat{a} + \frac{1}{2}\right) \\
&= \hbar\,\Delta_{\mathrm{o}}\left(\hat{a}^{\dagger}\,\hat{a} + \frac{1}{2}\right) + \hbar\,L\,\hat{a}^{\dagger} + \hbar\,L^{*}\,\hat{a}\;, \qquad \text{(I.13)}
\end{aligned}
$$

with $\Delta_{\mathrm{o}} = \omega_{\mathrm{o}} - \omega_{\mathrm{L}}$. This rotation is equivalent to the mapping

$$
\hat{a} \mapsto \hat{a}\,\mathrm{e}^{-\mathrm{i}\,\omega_{\mathrm{L}}\,t}\;,
$$

in both the Hamiltonian and equation of motion.

The equation of motion in the rotating frame is

$$
\frac{\mathrm{d}}{\mathrm{d}t}\hat{a}(t) = \left[\hat{a}(t), -\frac{\mathrm{i}}{\hbar}\hat{H}\right] = -\mathrm{i}\,\Delta_{\mathrm{o}}\,\hat{a}(t) - \mathrm{i}\,L\;,
$$

with Fourier transform

$$
\hat{a}(\omega) = \frac{-\mathrm{i}\,L\,\sqrt{2\,\pi}\,\delta(\omega)}{\mathrm{i}\,(\Delta_{\mathrm{o}} - \omega)}\;.
$$

Mapping this result back to the original non-rotating frame takes some care as the rotation is applied to the $\hat{a}$ operator rather than frequency-space, i.e. there is no such relation $\omega_{\mathrm{rot}} = \omega - \omega_{\mathrm{L}}$. Instead we have

$$
\hat{a}(t) = \hat{a}_{\mathrm{rot}}(t)\,\mathrm{e}^{-\mathrm{i}\,\omega_{\mathrm{L}}\,t} \quad \Rightarrow \quad \hat{a}_{\mathrm{rot}}(t) = \hat{a}(t)\,\mathrm{e}^{\mathrm{i}\,\omega_{\mathrm{L}}\,t}\;,
$$

with Fourier transform

$$\hat{a}_{\mathrm{rot}}(\omega) = \hat{a}(\omega + \omega_{\mathrm{L}}) \ ,$$
$$\hat{a}^{\dagger}_{\mathrm{rot}}(\omega) = \hat{a}^{\dagger}(\omega - \omega_{\mathrm{L}}) \ .$$

I.3 Coupling to heat bath

Following that of [225, 229–232]. Begin with an idealized bath as a set of independent harmonic oscillators,

$$\hat{H}_{\mathrm{bath}} = \sum_{q} \hbar\, \omega_q\, \hat{d}^{\dagger}_q\, \hat{d}_q \ , \qquad\qquad \left[\hat{d}_q, \hat{d}^{\dagger}_{q'}\right] = \delta_{q\,q'} \ ,$$

and assume it couples linearly to our resonator $\hat{H}_{\mathrm{sys}}$ (I.1) via

$$\hat{H}^{\mathrm{bath}}_{\mathrm{int}} = \sum_{q} \hbar \left(\kappa_q\, \hat{a}^{\dagger} + \kappa^{*}_q\, \hat{a}\right)\left(\hat{d}^{\dagger}_q + \hat{d}_q\right) \ ,$$

where κ_q has units of s^{-1}. The full Hamiltonian is then

$$\hat{H} = \hat{H}_{\mathrm{sys}} + \hat{H}_{\mathrm{bath}} + \hat{H}^{\mathrm{bath}}_{\mathrm{int}} \ .$$

Moving to the interaction picture with $\hat{U}(t) = \exp\left[-\frac{\mathrm{i}}{\hbar}(\hat{H}_{\mathrm{sys}} + \hat{H}_{\mathrm{bath}})\,t\right]$,

$$\begin{aligned}
\hat{H}^{\mathrm{I}}_{\substack{\mathrm{bath}\\\mathrm{int}}}(t) &= \hat{U}(t)^{\dagger}\,\hat{H}_{\substack{\mathrm{bath}\\\mathrm{int}}}\,\hat{U}(t) \\
&= \sum_q \hbar\,\mathrm{e}^{\frac{\mathrm{i}}{\hbar}\hat{H}_{\mathrm{sys}}\,t}\,\left(\kappa_q\,\hat{a}^{\dagger} + \kappa_q^{*}\,\hat{a}\right)\,\mathrm{e}^{-\frac{\mathrm{i}}{\hbar}\hat{H}_{\mathrm{sys}}\,t}\,\mathrm{e}^{\frac{\mathrm{i}}{\hbar}\hat{H}_{\mathrm{bath}}\,t}\,\left(\hat{d}_q^{\dagger} + \hat{d}_q\right)\,\mathrm{e}^{-\frac{\mathrm{i}}{\hbar}\hat{H}_{\mathrm{bath}}\,t} \\
&\overset{\text{(I.11)}}{=} \sum_q \hbar\left(\kappa_q\,\hat{a}^{\dagger}\,\mathrm{e}^{\mathrm{i}\,\omega_{\mathrm{o}}\,t} + \kappa_q^{*}\,\hat{a}\,\mathrm{e}^{-\mathrm{i}\,\omega_{\mathrm{o}}\,t}\right)\left(\hat{d}_q^{\dagger}\,\mathrm{e}^{\mathrm{i}\,\omega_q\,t} + \hat{d}_q\,\mathrm{e}^{-\mathrm{i}\,\omega_q\,t}\right) \\
&= \sum_q \hbar\Big(\kappa_q^{*}\,\hat{a}\,\hat{d}_q\,\mathrm{e}^{-\mathrm{i}\,(\omega_{\mathrm{o}}+\omega_q)t} + \kappa_q^{*}\,\hat{a}\,\hat{d}_q^{\dagger}\,\mathrm{e}^{-\mathrm{i}\,(\omega_{\mathrm{o}}-\omega_q)t} \\
&\qquad\qquad + \kappa_q\,\hat{a}^{\dagger}\,\hat{d}_q\,\mathrm{e}^{\mathrm{i}\,(\omega_{\mathrm{o}}-\omega_q)t} + \kappa_q\,\hat{a}^{\dagger}\,\hat{d}_q^{\dagger}\,\mathrm{e}^{\mathrm{i}\,(\omega_{\mathrm{o}}+\omega_q)t}\Big)\,,
\end{aligned}$$

with $\hat{H}_{\mathrm{sys}} = \hbar\,\omega_{\mathrm{o}}\left(\hat{a}^{\dagger}\,\hat{a} + \frac{1}{2}\right)$.

Making the rotating wave approximation, averaging over timescales $T \sim \frac{1}{\omega_{\mathrm{o}}+\omega_q} < \frac{1}{\omega_{\mathrm{o}}-\omega_q}$,

$$\hat{H}^{\mathrm{I}}_{\substack{\mathrm{bath}\\\mathrm{int}}}(t) \approx \sum_q \hbar\left(\kappa_q^{*}\,\hat{a}\,\hat{d}_q^{\dagger}\,\mathrm{e}^{-\mathrm{i}\,(\omega_{\mathrm{o}}-\omega_q)t} + \kappa_q\,\hat{a}^{\dagger}\,\hat{d}_q\,\mathrm{e}^{\mathrm{i}\,(\omega_{\mathrm{o}}-\omega_q)t}\right)\,,$$

meaning

$$\hat{H}_{\substack{\mathrm{bath}\\\mathrm{int}}} \approx \sum_q \hbar\left(\kappa_q^{*}\,\hat{a}\,\hat{d}_q^{\dagger} + \kappa_q\,\hat{a}^{\dagger}\,\hat{d}_q\right)\,.$$

I.3.1 Laser driven

In the laser driven scenario we keep $\hat{H}_{\mathrm{sys}} = \hbar\,\omega_{\mathrm{o}}\left(\hat{a}^{\dagger}\,\hat{a} + \frac{1}{2}\right)$ but also include

$$\hat{H}_{\substack{\mathrm{laser}\\\mathrm{int}}} = \hbar\,L\,\hat{a}^{\dagger}\,\mathrm{e}^{-\mathrm{i}\,\omega_{\mathrm{L}}\,t} + \hbar\,L^{*}\,\hat{a}\,\mathrm{e}^{\mathrm{i}\,\omega_{\mathrm{L}}\,t}\,.$$

Then

$$\begin{aligned}\hat{H}^{\mathrm{I}}_{\substack{\mathrm{laser}\\\mathrm{int}}}(t) &= \hat{U}^{\dagger}(t)\,\hat{H}_{\substack{\mathrm{laser}\\\mathrm{int}}}\,\hat{U}(t) \\ &= \hbar\,\mathrm{e}^{\frac{\mathrm{i}}{\hbar}\hat{H}_{\mathrm{sys}}\,t}\,\left(L\,\hat{a}^{\dagger}\,\mathrm{e}^{-\mathrm{i}\,\omega_{\mathrm{L}}\,t} + L^{*}\,\hat{a}\,\mathrm{e}^{\mathrm{i}\,\omega_{\mathrm{L}}\,t}\right)\,\mathrm{e}^{-\frac{\mathrm{i}}{\hbar}\hat{H}_{\mathrm{sys}}\,t} \\ &\overset{\text{(I.11)}}{=} \hbar\left(L\,\hat{a}^{\dagger}\,\mathrm{e}^{\mathrm{i}\,(\omega_{\mathrm{o}}-\omega_{\mathrm{L}})\,t} + L^{*}\,\hat{a}\,\mathrm{e}^{-\mathrm{i}\,(\omega_{\mathrm{o}}-\omega_{\mathrm{L}})\,t}\right)\,,\end{aligned}$$

which we keep in the rotating wave approximation.

I.3.2 Equations of motion

The Heisenberg equation of motion for an operator $\hat{O}(t)$ is

$$\frac{\mathrm{d}}{\mathrm{d}t}\hat{O}(t) = \left[\hat{O}(t), -\frac{\mathrm{i}}{\hbar}\hat{H}\right] + \left(\mathrm{e}^{\frac{\mathrm{i}}{\hbar}\hat{H}\,t}\,\frac{\mathrm{d}\hat{O}}{\mathrm{d}t}\,\mathrm{e}^{-\frac{\mathrm{i}}{\hbar}\hat{H}\,t}\right)\,,$$

where $\hat{O}(t) = \mathrm{e}^{\frac{\mathrm{i}}{\hbar}\hat{H}\,t}\,\hat{O}\,\mathrm{e}^{-\frac{\mathrm{i}}{\hbar}\hat{H}\,t}$ is the Heisenberg picture operator, $\hat{O}$ is the Schrodinger picture operator, and $\hat{H}(t) = \hat{H}$. For the common situation of $\frac{\mathrm{d}}{\mathrm{d}t}\hat{O} = 0$,

$$\frac{\mathrm{d}}{\mathrm{d}t}\hat{O}(t) = \left[\hat{O}(t), -\frac{\mathrm{i}}{\hbar}\hat{H}\right] = \mathrm{e}^{\frac{\mathrm{i}}{\hbar}\hat{H}\,t}\,\left[\hat{O}, -\frac{\mathrm{i}}{\hbar}\hat{H}\right]\,\mathrm{e}^{-\frac{\mathrm{i}}{\hbar}\hat{H}\,t}\,.$$

Consider Hamiltonian

$$\hat{H} = \hat{H}_{\mathrm{sys}}(\hat{a}, \hat{a}^{\dagger}) + \underbrace{\sum_{q}\hbar\,\omega_q\,\hat{d}_q^{\dagger}\,\hat{d}_q}_{\hat{H}_{\mathrm{bath}}} + \underbrace{\sum_{q}\hbar\left(\kappa_q^{*}\,\hat{a}\,\hat{d}_q^{\dagger} + \kappa_q\,\hat{a}^{\dagger}\,\hat{d}_q\right)}_{\hat{H}_{\substack{\mathrm{bath}\\\mathrm{int}}}}\,.$$

The time derivative of $\hat{d}_q(t)$ is

$$\begin{aligned}
\frac{\mathrm{d}}{\mathrm{d}t}\hat{d}_q(t) &= \mathrm{e}^{\frac{\mathrm{i}}{\hbar}\hat{H}\,t}\,\left[\hat{d}_q, -\frac{\mathrm{i}}{\hbar}\hat{H}\right]\,\mathrm{e}^{-\frac{\mathrm{i}}{\hbar}\hat{H}\,t} \\
&= \mathrm{e}^{\frac{\mathrm{i}}{\hbar}\hat{H}\,t}\,\left[\hat{d}_q, -\frac{\mathrm{i}}{\hbar}\left(\hat{H}_{\mathrm{bath}} + \hat{H}_{\substack{\mathrm{bath}\\\mathrm{int}}}\right)\right]\,\mathrm{e}^{-\frac{\mathrm{i}}{\hbar}\hat{H}\,t} \\
&= \mathrm{e}^{\frac{\mathrm{i}}{\hbar}\hat{H}\,t}\,\left(-\frac{\mathrm{i}}{\hbar}\right)\left(\sum_{q'}\hbar\,\omega_{q'}\left[\hat{d}_q, \hat{d}^\dagger_{q'}\,\hat{d}_{q'}\right]\right. \\
&\qquad\qquad \left. + \sum_{q'}\hbar\,\left(\kappa^*_{q'}\,\hat{a}\left[\hat{d}_q, \hat{d}^\dagger_{q'}\right] + \kappa_{q'}\,\hat{a}^\dagger\left[\hat{d}_q, \hat{d}_{q'}\right]\right)\right)\mathrm{e}^{-\frac{\mathrm{i}}{\hbar}\hat{H}\,t} \\
&= \mathrm{e}^{\frac{\mathrm{i}}{\hbar}\hat{H}\,t}\,\left(-\mathrm{i}\,\omega_q\,\hat{d}_q - \mathrm{i}\,\kappa^*_q\,\hat{a}\right)\,\mathrm{e}^{-\frac{\mathrm{i}}{\hbar}\hat{H}\,t} \\
&= -\,\mathrm{i}\,\omega_q\,\hat{d}_q(t) - \mathrm{i}\,\kappa^*_q\,\hat{a}(t)\;.
\end{aligned}$$

This first order differential equation has solution

$$\begin{aligned}
\hat{d}_q(t) &= -\,\mathrm{i}\,\kappa^*_q\,\mathrm{e}^{-\mathrm{i}\,\omega_q\,t}\int^t \mathrm{e}^{\mathrm{i}\,\omega_q\,t'}\,\hat{a}(t')\,\mathrm{d}t' \\
&= -\,\mathrm{i}\,\kappa^*_q\int_{t_0}^t \mathrm{e}^{-\mathrm{i}\,\omega_q\,(t-t')}\,\hat{a}(t')\,\mathrm{d}t' + \mathrm{e}^{-\mathrm{i}\,\omega_q\,(t-t_0)}\,\hat{d}_q(t_0)\;. \qquad \text{(I.14)}
\end{aligned}$$

For $\hat{a}$,

$$\begin{aligned}
\frac{\mathrm{d}}{\mathrm{d}t}\hat{a}(t) &= \mathrm{e}^{\frac{\mathrm{i}}{\hbar}\hat{H}\,t}\left[\hat{a}, -\frac{\mathrm{i}}{\hbar}\hat{H}_{\mathrm{sys}}\right]\mathrm{e}^{-\frac{\mathrm{i}}{\hbar}\hat{H}\,t} + \mathrm{e}^{\frac{\mathrm{i}}{\hbar}\hat{H}\,t}\left[\hat{a}, -\frac{\mathrm{i}}{\hbar}\hat{H}_{\substack{\mathrm{bath}\\\mathrm{int}}}\right]\mathrm{e}^{-\frac{\mathrm{i}}{\hbar}\hat{H}\,t} \\
&= \mathrm{e}^{\frac{\mathrm{i}}{\hbar}\hat{H}\,t}\left[\hat{a}, -\frac{\mathrm{i}}{\hbar}\hat{H}_{\mathrm{sys}}\right]\mathrm{e}^{-\frac{\mathrm{i}}{\hbar}\hat{H}\,t} \\
&\qquad + \mathrm{e}^{\frac{\mathrm{i}}{\hbar}\hat{H}\,t}\left(-\frac{\mathrm{i}}{\hbar}\right)\left(\sum_q \hbar\left(\kappa_q^*\left[\hat{a},\hat{a}\right]\hat{d}_q^\dagger + \kappa_q\left[\hat{a},\hat{a}^\dagger\right]\hat{d}_q\right)\right)\mathrm{e}^{-\frac{\mathrm{i}}{\hbar}\hat{H}\,t} \\
&= \mathrm{e}^{\frac{\mathrm{i}}{\hbar}\hat{H}\,t}\left[\hat{a}, -\frac{\mathrm{i}}{\hbar}\hat{H}_{\mathrm{sys}}\right]\mathrm{e}^{-\frac{\mathrm{i}}{\hbar}\hat{H}\,t} - \sum_q \mathrm{i}\,\kappa_q\,\hat{d}_q(t) \\
&\overset{\text{(I.14)}}{=} \mathrm{e}^{\frac{\mathrm{i}}{\hbar}\hat{H}\,t}\left[\hat{a}, -\frac{\mathrm{i}}{\hbar}\hat{H}_{\mathrm{sys}}\right]\mathrm{e}^{-\frac{\mathrm{i}}{\hbar}\hat{H}\,t} \\
&\qquad - \sum_q |\kappa_q|^2 \int_{t_0}^{t} \mathrm{e}^{-\mathrm{i}\,\omega_q\,(t-t')}\,\hat{a}(t')\,\mathrm{d}t' - \sum_q \mathrm{i}\,\kappa_q\,\mathrm{e}^{-\mathrm{i}\,\omega_q\,(t-t_0)}\,\hat{d}_q(t_0)\;.
\end{aligned}$$

Making the continuum approximation in frequency, $\sum_q \mapsto \int_0^\infty \mathrm{d}\omega$ with $\kappa(\omega_q) = \kappa_q\sqrt{\mathrm{s}}$ and $\hat{d}(\omega_q, t) = \hat{d}_q(t)\sqrt{\mathrm{s}}$,

$$\begin{aligned}
\frac{\mathrm{d}}{\mathrm{d}t}\hat{a}(t) &= \mathrm{e}^{\frac{\mathrm{i}}{\hbar}\hat{H}\,t}\left[\hat{a}, -\frac{\mathrm{i}}{\hbar}\hat{H}_{\mathrm{sys}}\right]\mathrm{e}^{-\frac{\mathrm{i}}{\hbar}\hat{H}\,t} \\
&\qquad - \int_0^\infty |\kappa(\omega)|^2 \int_{t_0}^{t} \mathrm{e}^{-\mathrm{i}\,\omega\,(t-t')}\,\hat{a}(t')\,\mathrm{d}t'\,\mathrm{d}\omega - \int_0^\infty \mathrm{i}\,\kappa(\omega)\,\mathrm{e}^{-\mathrm{i}\,\omega\,(t-t_0)}\,\hat{d}(\omega, t_0)\,\mathrm{d}\omega\;.
\end{aligned}$$

At this point we need to make some approximations to continue. We will assume that our heat bath is Markovian, that is the correlation time between the bath and system τ_B is much less than the system's relxation time, for a resonator this means

$$\tau_B \sim \frac{2\,\pi}{\omega_{\mathrm{o}}} \ll \frac{2\,Q}{\omega_{\mathrm{o}}} = \tau_{\mathrm{decay}}\;,$$

which will be true for a sufficiently high quality factor resonator. In this case coupling to the bath is only important over a narrow bandwidth around ω_{o}, over which κ is approximately

constant, and we can use a Markovian effective spectrum,

$$\int_0^\infty \mathrm{d}\omega \mapsto \int_{-\infty}^\infty \mathrm{d}\omega \qquad\qquad \kappa(\omega) = \kappa = \kappa(\omega_\mathrm{o}) \; .$$

Thus

$$\begin{aligned}\frac{\mathrm{d}}{\mathrm{d}t}\hat{a}(t) \approx \mathrm{e}^{\frac{\mathrm{i}}{\hbar}\hat{H}\,t} \left[\hat{a}, -\frac{\mathrm{i}}{\hbar}\hat{H}_\mathrm{sys}\right] \mathrm{e}^{-\frac{\mathrm{i}}{\hbar}\hat{H}\,t} \\ - |\kappa|^2 \int_{t_0}^t \left(\int_{-\infty}^\infty \mathrm{e}^{-\mathrm{i}\,\omega\,(t-t')}\,\mathrm{d}\omega\right) \hat{a}(t')\,\mathrm{d}t' - \mathrm{i}\,\kappa \int_{-\infty}^\infty \mathrm{e}^{-\mathrm{i}\,\omega\,(t-t_0)}\,\hat{d}(\omega,t_0)\,\mathrm{d}\omega \; .\end{aligned}$$

Using Dirac Delta relations given in App. H,this gives us

$$\begin{aligned}\frac{\mathrm{d}}{\mathrm{d}t}\hat{a}(t) \overset{(\mathrm{H.1})}{=} \mathrm{e}^{\frac{\mathrm{i}}{\hbar}\hat{H}\,t} \left[\hat{a}, -\frac{\mathrm{i}}{\hbar}\hat{H}_\mathrm{sys}\right] \mathrm{e}^{-\frac{\mathrm{i}}{\hbar}\hat{H}\,t} \\ - 2\,\pi\,|\kappa|^2 \int_{t_0}^t \delta(t-t')\,\hat{a}(t')\,\mathrm{d}t' - \mathrm{i}\,\kappa \int_{-\infty}^\infty \mathrm{e}^{-\mathrm{i}\,\omega\,(t-t_0)}\,\hat{d}(\omega,t_0)\,\mathrm{d}\omega \; ,\end{aligned}$$

where the Markovian approximation has introduced $\delta(t-t')$, removing the dependence of $\hat{a}(t)$ on earlier times from the bath interaction. Continuing this through,

$$\begin{aligned}\frac{\mathrm{d}}{\mathrm{d}t}\hat{a}(t) &\overset{(\mathrm{H.3})}{=} \mathrm{e}^{\frac{\mathrm{i}}{\hbar}\hat{H}\,t} \left[\hat{a}, -\frac{\mathrm{i}}{\hbar}\hat{H}_\mathrm{sys}\right] \mathrm{e}^{-\frac{\mathrm{i}}{\hbar}\hat{H}\,t} - \pi\,|\kappa|^2\,\hat{a}(t) - \mathrm{i}\,\kappa \int_{-\infty}^\infty \mathrm{e}^{-\mathrm{i}\,\omega\,(t-t_0)}\,\hat{d}(\omega,t_0)\,\mathrm{d}\omega \\ &= \mathrm{e}^{\frac{\mathrm{i}}{\hbar}\hat{H}\,t} \left[\hat{a}, -\frac{\mathrm{i}}{\hbar}\hat{H}_\mathrm{sys}\right] \mathrm{e}^{-\frac{\mathrm{i}}{\hbar}\hat{H}\,t} - \pi\,|\kappa|^2\,\hat{a}(t) - \sqrt{2\,\pi}\,\mathrm{i}\,\kappa\,\hat{d}_\mathrm{in}(t) \; ,\end{aligned}$$

where we have defined

$$\hat{d}_\mathrm{in}(t) = \frac{1}{\sqrt{2\,\pi}} \int_{-\infty}^\infty \mathrm{e}^{-\mathrm{i}\,\omega\,(t-t_0)}\,\hat{d}(\omega,t_0)\,\mathrm{d}\omega \; , \tag{I.15}$$

such that

$$\begin{aligned}\left[\hat{d}_{\mathrm{in}}(t),\hat{d}_{\mathrm{in}}(t')^{\dagger}\right] &= \frac{1}{2\,\pi}\int_{-\infty}^{\infty}\int_{-\infty}^{\infty}\mathrm{e}^{-\mathrm{i}\,\omega\,(t-t_0)}\,\mathrm{e}^{\mathrm{i}\,\omega'\,(t'-t_0)}\,\left[\hat{d}(\omega,t_0),\hat{d}(\omega',t_0)^{\dagger}\right]\,\mathrm{d}\omega\,\mathrm{d}\omega' \\ &= \frac{1}{2\,\pi}\int_{-\infty}^{\infty}\int_{-\infty}^{\infty}\mathrm{e}^{-\mathrm{i}\,\omega\,(t-t_0)+\mathrm{i}\,\omega'\,(t'-t_0)}\,\delta(\omega-\omega')\,\mathrm{d}\omega\,\mathrm{d}\omega' \\ &= \frac{1}{2\,\pi}\int_{-\infty}^{\infty}\mathrm{e}^{-\mathrm{i}\,\omega\,(t-t')}\,\mathrm{d}\omega \\ &\overset{\text{(H.1)}}{=} \delta(t-t')\;,\end{aligned}$$

noting that $\hat{d}_{\mathrm{in}}(t)$ has units of $\sqrt{\mathrm{number/s}}$.

Defining $\gamma = -2\,\pi\,\kappa^2$, such that γ has units of s^{-1}, we get the quantum Langevin equation

$$\frac{\mathrm{d}}{\mathrm{d}t}\hat{a}(t) = \mathrm{e}^{\frac{\mathrm{i}}{\hbar}\hat{H}\,t}\,\left[\hat{a},-\frac{\mathrm{i}}{\hbar}\hat{H}_{\mathrm{sys}}\right]\,\mathrm{e}^{-\frac{\mathrm{i}}{\hbar}\hat{H}\,t} - \frac{|\gamma|}{2}\hat{a}(t) - \sqrt{\gamma}\,\hat{d}_{\mathrm{in}}(t)\;, \tag{I.16}$$

If we consider some $t_1 > t$, then (I.14) can be reformulated as

$$\hat{d}_q(t) = \mathrm{i}\,\kappa_q^*\int_t^{t_1}\mathrm{e}^{-\mathrm{i}\,\omega_q\,(t-t')}\,\hat{a}(t')\,\mathrm{d}t' + \mathrm{e}^{\mathrm{i}\,\omega_q\,(t_1-t)}\,\hat{d}_q(t_1)\;,$$

and the time reversed quantum Langevin equation is

$$\frac{\mathrm{d}}{\mathrm{d}t}\hat{a}(t) = \mathrm{e}^{\frac{\mathrm{i}}{\hbar}\hat{H}\,t}\,\left[\hat{a},-\frac{\mathrm{i}}{\hbar}\hat{H}_{\mathrm{sys}}\right]\,\mathrm{e}^{-\frac{\mathrm{i}}{\hbar}\hat{H}\,t} + \frac{|\gamma|}{2}\hat{a}(t) - \sqrt{\gamma}\,\hat{d}_{\mathrm{out}}(t)\;, \tag{I.17}$$

with

$$\hat{d}_{\mathrm{out}}(t) = \frac{1}{\sqrt{2\,\pi}}\int_{-\infty}^{\infty}\mathrm{e}^{\mathrm{i}\,\omega\,(t_1-t)}\,\hat{d}(\omega,t_1)\,\mathrm{d}\omega\;.$$

Comparing (I.16) with (I.17) we obtain

$$\hat{d}_{\rm out}(t) - \hat{d}_{\rm in}(t) = \sqrt{\gamma^*}\,\hat{a}(t)\ .$$

I.4 SHO coupled to heat bath

Completing (I.16) with $\hat{H}_{\rm sys} = \hbar\,\omega_{\rm o}\left(\hat{a}^\dagger\,\hat{a} + \frac{1}{2}\right)$,

$$\frac{\rm d}{{\rm d}t}\hat{a}(t) = -{\rm i}\,\omega_{\rm o}\,\hat{a}(t) - \frac{|\gamma|}{2}\hat{a}(t) - \sqrt{\gamma}\,\hat{d}_{\rm in}(t)\ . \tag{I.18}$$

Define a t_0 shifted Fourier transform,

$$\begin{aligned}\hat{a}(\omega) &= \frac{1}{\sqrt{2\,\pi}}\int_{-\infty}^{\infty} {\rm e}^{{\rm i}\,\omega\,(t-t_0)}\,\hat{a}(t)\,{\rm d}t\ ,\\ \hat{a}(t) &= \frac{1}{\sqrt{2\,\pi}}\int_{-\infty}^{\infty} {\rm e}^{-{\rm i}\,\omega\,(t-t_0)}\,\hat{a}(\omega)\,{\rm d}\omega\ .\end{aligned}$$

Note that $\hat{a}(t)$ has units 1 (or $\sqrt{\rm number}$), and $\hat{a}(\omega)$ has units s. We will also define the notation $\hat{a}(t)^\dagger = \hat{a}^\dagger(t)$, $\hat{a}(\omega)^\dagger = \hat{a}^\dagger(-\omega)$.

Applying $\frac{1}{\sqrt{2\,\pi}}\int_{-\infty}^{\infty}{\rm d}t\,{\rm e}^{{\rm i}\,\omega\,(t-t_0)}$ to (I.18),

$$\begin{aligned}\frac{1}{\sqrt{2\,\pi}}\int_{-\infty}^{\infty} {\rm e}^{{\rm i}\,\omega\,(t-t_0)}\left(\frac{\rm d}{{\rm d}t}\hat{a}(t)\right){\rm d}t &= -\frac{{\rm i}\,\omega_{\rm o}}{\sqrt{2\,\pi}}\int_{-\infty}^{\infty} {\rm e}^{{\rm i}\,\omega\,(t-t_0)}\,\hat{a}(t)\,{\rm d}t\\ &\quad - \frac{\gamma}{2\,\sqrt{2\,\pi}}\int_{-\infty}^{\infty} {\rm e}^{{\rm i}\,\omega\,(t-t_0)}\,\hat{a}(t)\,{\rm d}t\\ &\quad - \frac{\sqrt{\gamma}}{2\,\pi}\int_{-\infty}^{\infty}\int_{-\infty}^{\infty} {\rm e}^{{\rm i}\,\omega\,(t-t_0)}\,{\rm e}^{-{\rm i}\,\omega'\,(t-t_0)}\,\hat{d}(\omega',t_0)\,{\rm d}\omega'\,{\rm d}t\ .\end{aligned}$$

Now

$$\int_{-\infty}^{\infty} \mathrm{e}^{\mathrm{i}\,\omega\,(t-t_0)} \left(\frac{\mathrm{d}}{\mathrm{d}t}\hat{a}(t)\right) \mathrm{d}t = \int_{-\infty}^{\infty} \frac{\mathrm{d}}{\mathrm{d}t}\Big(\mathrm{e}^{\mathrm{i}\,\omega\,(t-t_0)}\,\hat{a}(t)\Big)\mathrm{d}t - \int_{-\infty}^{\infty} \mathrm{i}\,\omega\,\mathrm{e}^{\mathrm{i}\,\omega\,(t-t_0)}\,\hat{a}(t)\,\mathrm{d}t$$
$$= \Big[\mathrm{e}^{\mathrm{i}\,\omega\,(t-t_0)}\,\hat{a}(t)\Big]_{t=-\infty}^{t=\infty} - \sqrt{2\,\pi}\,\mathrm{i}\,\omega\,\hat{a}(\omega)\ ,$$

and assuming our oscillator has a finite bandwidth, and thus $\hat{a}(\omega)$ is integrable, by the Riemann-Lebesgue lemma $\hat{a}(t) \to 0$ as $t \to \pm\infty$, so

$$\frac{1}{\sqrt{2\,\pi}} \int_{-\infty}^{\infty} \mathrm{e}^{\mathrm{i}\,\omega\,(t-t_0)} \left(\frac{\mathrm{d}}{\mathrm{d}t}\hat{a}(t)\right) \mathrm{d}t = -\mathrm{i}\,\omega\,\hat{a}(\omega)\ .$$

We also have

$$\frac{1}{2\,\pi} \int_{-\infty}^{\infty}\int_{-\infty}^{\infty} \mathrm{e}^{\mathrm{i}\,\omega\,(t-t_0)}\,\mathrm{e}^{-\mathrm{i}\,\omega'\,(t-t_0)}\,\hat{d}(\omega',t_0)\,\mathrm{d}\omega'\,\mathrm{d}t$$
$$= \frac{1}{2\,\pi} \int_{-\infty}^{\infty}\int_{-\infty}^{\infty} \mathrm{e}^{\mathrm{i}\,(\omega-\omega')(t-t_0)}\,\mathrm{d}t\,\hat{d}(\omega',t_0)\,\mathrm{d}\omega'$$
$$= \int_{-\infty}^{\infty} \delta(\omega-\omega')\,\hat{d}(\omega',t_0)\,\mathrm{d}\omega'$$
$$= \hat{d}(\omega,t_0)\ .$$

Thus the fourier transformed version of (I.18) is

$$\hat{a}(\omega) = \frac{\sqrt{\gamma}}{\mathrm{i}(\omega-\omega_\mathrm{o}) - \frac{|\gamma|}{2}}\,\hat{d}(\omega,t_0)\ , \tag{I.19}$$

which gives us the Lorentzian-like function

$$\hat{a}(\omega)^\dagger\,\hat{a}(\omega) = \frac{|\gamma|}{(\omega-\omega_\mathrm{o})^2 + \frac{|\gamma|^2}{4}}\,\hat{d}(\omega,t_0)^\dagger\,\hat{d}(\omega,t_0)\ ,$$

with width $\gamma/2$. If γ is sufficiently small then our Markovian approximation is valid as this

response function tends to 0 for ω away from $\omega_{\rm o}$.

In the time reversed case

$$\hat{a}(\omega) = \frac{\sqrt{\gamma}}{\mathrm{i}(\omega - \omega_{\rm o}) + \frac{|\gamma|}{2}}\, \hat{d}(\omega, t_1) \ ,$$

giving us

$$\hat{d}(\omega, t_1) = \frac{\mathrm{i}(\omega - \omega_{\rm o}) + \frac{|\gamma|}{2}}{\mathrm{i}(\omega - \omega_{\rm o}) - \frac{|\gamma|}{2}}\, \hat{d}(\omega, t_0) \ .$$

Completing the Fourier transform on $\hat{d}_{\rm in}(t)$ and $\hat{d}_{\rm out}(t)$ tells us

$$\begin{aligned} \hat{d}_{\rm in}(\omega) &= \hat{d}(\omega, t_0) \ , \\ \hat{d}_{\rm out}(\omega) &= \hat{d}(\omega, t_1)\, \mathrm{e}^{\mathrm{i}\,\omega\,(t_1 - t_0)} \ , \end{aligned}$$

and

$$|\hat{d}_{\rm out}(\omega)|^2 = |\hat{d}_{\rm in}(\omega)|^2 \ .$$

I.4.1 Laser driven

Let us now consider Hamiltonian

$$\hat{H} = \hbar\,\omega_{\rm o}\left(\hat{a}^\dagger\,\hat{a} + \tfrac{1}{2}\right) + \underbrace{\hbar\,L\,\hat{a}^\dagger\,{\rm e}^{-{\rm i}\,\omega_{\rm L}\,t} + \hbar\,L^*\,\hat{a}\,{\rm e}^{{\rm i}\,\omega_{\rm L}\,t}}_{\hat{H}_{\substack{\rm laser\\ \rm int}}}$$

$$+ \underbrace{\sum_q \hbar\,\omega_q\,\hat{d}_q^\dagger\,\hat{d}_q}_{\hat{H}_{\rm bath}} + \underbrace{\sum_q \hbar\left(\kappa_q^*\,\hat{a}\,\hat{d}_q^\dagger + \kappa_q\,\hat{a}^\dagger\,\hat{d}_q\right)}_{\hat{H}_{\substack{\rm bath\\ \rm int}}} .$$

We can rotate both the resonator and heat bath with

$$\hat{U}_{\rm rot}(t) = {\rm e}^{-{\rm i}\,\omega_{\rm L}\,(\hat{a}^\dagger\,\hat{a} + \frac{1}{2})\,t}\,{\rm e}^{-{\rm i}\,\omega_{\rm L}\,\hat{d}^\dagger\,\hat{d}\,t} ,$$

to obtain

$$\hat{H}_{\rm rot} = \underbrace{\hbar\,\Delta_{\rm o}\,\left(\hat{a}^\dagger\,\hat{a} + \tfrac{1}{2}\right) + \hbar\,L\,\hat{a}^\dagger + \hbar\,L^*\,\hat{a}}_{\hat{H}_{\rm sys}} + \underbrace{\sum_q \hbar\,\Delta_q\,\hat{d}_q^\dagger\,\hat{d}_q}_{\hat{H}_{\rm bath}} + \underbrace{\sum_q \hbar\left(\kappa_q^*\,\hat{a}\,\hat{d}_q^\dagger + \kappa_q\,\hat{a}^\dagger\,\hat{d}_q\right)}_{\hat{H}_{\substack{\rm bath\\ \rm int}}} ,$$

where

$$\Delta_{\rm o} = \omega_{\rm o} - \omega_{\rm L} , \qquad\qquad \Delta_q = \omega_q - \omega_{\rm L} .$$

Going through the same steps, our continuum approximation is now $\sum_q \mapsto \int_{-\omega_{\rm L}}^{\infty} {\rm d}\Delta$, and

the Langevin equation (I.16) is

$$\frac{\mathrm{d}}{\mathrm{d}t}\hat{a}(t) = -\mathrm{i}\,\Delta_\mathrm{o}\,\hat{a}(t) - \mathrm{i}\,L - \frac{|\gamma|}{2}\hat{a}(t) - \sqrt{\gamma}\,\hat{d}_\mathrm{in}(t)\ . \tag{I.20}$$

We also have

$$\frac{\mathrm{d}}{\mathrm{d}t}\hat{a}^\dagger(t) = \mathrm{i}\,\Delta_\mathrm{o}\,\hat{a}^\dagger(t) + \mathrm{i}\,L^* - \frac{|\gamma|}{2}\hat{a}^\dagger(t) - \sqrt{\gamma^*}\,\hat{d}^\dagger_\mathrm{in}(t)\ .$$

The steady state values can be found by taking $\frac{\mathrm{d}}{\mathrm{d}t}\hat{a}(t) = 0$,

$$\hat{a}(t_\mathrm{s}) = \frac{-\mathrm{i}\,L - \sqrt{\gamma}\,\hat{d}_\mathrm{in}(t_\mathrm{s})}{\mathrm{i}\,\Delta_\mathrm{o} + \frac{|\gamma|}{2}}\ , \tag{I.21}$$

$$\hat{a}^\dagger(t_\mathrm{s}) = \frac{\mathrm{i}\,L^* - \sqrt{\gamma^*}\,\hat{d}^\dagger_\mathrm{in}(t_\mathrm{s})}{-\mathrm{i}\,\Delta_\mathrm{o} + \frac{|\gamma|}{2}}\ , \tag{I.22}$$

which gives us

$$\hat{a}^\dagger(t_\mathrm{s})\,\hat{a}(t_\mathrm{s}) = \frac{|L|^2 + |\gamma|\,\hat{d}^\dagger_\mathrm{in}(t_\mathrm{s})\,\hat{d}_\mathrm{in}(t_\mathrm{s}) + \mathrm{i}\,L\sqrt{\gamma^*}\,\hat{d}^\dagger_\mathrm{in}(t_\mathrm{s}) - \mathrm{i}\,L^*\sqrt{\gamma}\,\hat{d}_\mathrm{in}(t_\mathrm{s})}{{\Delta_\mathrm{o}}^2 + \frac{|\gamma|^2}{4}}\ .$$

Note that in the absence of either the heat bath or laser, this is

$$\hat{a}^\dagger(t_\mathrm{s})\,\hat{a}(t_\mathrm{s}) \overset{\gamma=0}{=} \frac{|L|^2}{{\Delta_\mathrm{o}}^2}\ ,$$

$$\hat{a}^\dagger(t_\mathrm{s})\,\hat{a}(t_\mathrm{s}) \overset{L=0}{=} \frac{|\gamma|}{{\Delta_\mathrm{o}}^2 + \frac{|\gamma|^2}{4}}\ \hat{d}^\dagger_\mathrm{in}(t_\mathrm{s})\,\hat{d}_\mathrm{in}(t_\mathrm{s})$$

Taking the Fourier transform of (I.20),

$$\hat{a}(\omega) = \frac{\sqrt{\gamma}\,\hat{d}(\omega, t_0) + \mathrm{i}\,L\,\sqrt{2\,\pi}\,\delta(\omega)}{\mathrm{i}(\omega - \Delta_\mathrm{o}) - \frac{|\gamma|}{2}} \ ,$$

we see an additional spike at $\omega = 0$, i.e. the laser frequency (in this rotated frame).

Background leveled

Given that a steady background level for $\hat{a}$ exists, we may want to transform into a background leveled frame and look at operators as fluctuations on the background. Taking the steady state to be coherent we want to transform $|\bar{a}\rangle \mapsto |0\rangle$, we do this by

$$|\psi\rangle \mapsto \hat{D}(\bar{a})^\dagger\ |\psi\rangle \ , \qquad\qquad \hat{D}(\bar{a}) = \mathrm{e}^{\bar{a}\,\hat{a}^\dagger - \bar{a}^*\,\hat{a}} \ ,$$

$$\Rightarrow \hat{H}_\mathrm{lvl} = \hat{D}(\bar{a})^\dagger \left(\hat{H} - \mathrm{i}\,\hbar\,\frac{\partial}{\partial t}\right) \hat{D}(\bar{a}) = \hat{D}(\bar{a})^\dagger\,\hat{H}\,\hat{D}(\bar{a}) \ ,$$

$$\Rightarrow \hat{a} \mapsto \hat{a} + \bar{a} \ ,$$

with $\bar{a} \in \mathbb{C}$.

Doing this directly to the equation of motion (I.20) we get

$$\frac{\mathrm{d}}{\mathrm{d}t}\hat{a}(t) = -\mathrm{i}\,\Delta_\mathrm{o}\,\hat{a}(t) - \mathrm{i}\,\Delta_\mathrm{o}\,\bar{a} - \mathrm{i}\,L - \frac{|\gamma|}{2}\hat{a}(t) - \frac{|\gamma|}{2}\bar{a} - \sqrt{\gamma}\,\hat{d}_\mathrm{in}(t) \ .$$

Following (I.21), define

$$\bar{a} = \frac{-\mathrm{i}\,L}{\mathrm{i}\,\Delta_\mathrm{o} + \frac{|\gamma|}{2}} \,, \tag{I.23}$$

to arrive at

$$\frac{\mathrm{d}}{\mathrm{d}t}\hat{a}(t) = -\mathrm{i}\,\Delta_\mathrm{o}\,\hat{a}(t) - \frac{|\gamma|}{2}\hat{a}(t) - \sqrt{\gamma}\,\hat{d}_\mathrm{in}(t) \,.$$

Making this transform to the Hamiltonian,

$$\begin{aligned}
\hat{H}_{\substack{\mathrm{rot}\\\mathrm{lvl}}} &= \hat{D}(\bar{a})^\dagger\,\hat{H}_\mathrm{rot}\,\hat{D}(\bar{a}) \\
&= \hbar\,\Delta_\mathrm{o}\left(\hat{a}^\dagger\,\hat{a} + \tfrac{1}{2}\right) + \hbar\,\Delta_\mathrm{o}\,\bar{a}\,\hat{a}^\dagger + \hbar\,\Delta_\mathrm{o}\,\bar{a}^*\,\hat{a} + \hbar\,\Delta_\mathrm{o}\,|\bar{a}|^2 \\
&\quad + \hbar\,L\,\hat{a}^\dagger + \hbar\,L^*\,\hat{a} + \hbar\,L\,\bar{a}^* + \hbar\,L^*\,\bar{a} \\
&\quad + \sum_q \hbar\,\Delta_q\,\hat{d}_q^\dagger\,\hat{d}_q + \sum_q \hbar\left(\kappa_q^*\,\hat{a}\,\hat{d}_q^\dagger + \kappa_q\,\hat{a}^\dagger\,\hat{d}_q\right) + \sum_q \hbar\left(\kappa_q^*\,\bar{a}\,\hat{d}_q^\dagger + \kappa_q\,\bar{a}^*\,\hat{d}_q\right) \,.
\end{aligned}$$

Proceeding with a derivation of the Langevin equation,

$$\begin{aligned}
\frac{\mathrm{d}}{\mathrm{d}t}\hat{d}_q(t) &= -\mathrm{i}\,\omega_q\,\hat{d}_q(t) - \mathrm{i}\,\kappa_q^*\,\hat{a}(t) - \mathrm{i}\,\kappa_q^*\,\bar{a} \,, \\
\Rightarrow \quad \hat{d}_q(t) &= -\mathrm{i}\,\kappa_q^* \int_{t_0}^{t} \mathrm{e}^{-\mathrm{i}\,\omega_q\,(t-t')}\,\left(\hat{a}(t') + \bar{a}\right)\,\mathrm{d}t' + \mathrm{e}^{-\mathrm{i}\,\omega_q\,(t-t_0)}\,\hat{d}_q(t_0) \,,
\end{aligned}$$

$$\begin{aligned}
\frac{\mathrm{d}}{\mathrm{d}t}\hat{a}(t) &= -\mathrm{i}\,\Delta_\mathrm{o}\,\hat{a}(t) - \mathrm{i}\,\Delta_\mathrm{o}\,\bar{a} - \mathrm{i}\,L - \pi\,|\kappa|^2\,\left(\hat{a}(t) + \bar{a}\right) - \sqrt{2\,\pi}\,\mathrm{i}\,\kappa\,\hat{d}_\mathrm{in}(t) \\
&= -\mathrm{i}\,\Delta_\mathrm{o}\,\hat{a}(t) - \frac{|\gamma|}{2}\hat{a}(t) - \sqrt{\gamma}\,\hat{d}_\mathrm{in}(t) \,,
\end{aligned}$$

where we've used the value of $\bar{a}$ to cancel terms.

The quantity $|\bar{a}|^2$ gives the average number of photons in the cavity, and is equal to

$$\underbrace{\left\langle \hat{a}^\dagger \, \hat{a} \right\rangle}_{\text{unleveled}} = |\bar{a}|^2 = \frac{|L|^2}{\left(\frac{|\gamma|}{2}\right)^2 + {\Delta_\text{o}}^2} \, .$$

I.4.2 Thermal bath

If our bath is thermal and the resonator is in equilibrium with it, we can determine its thermal spectrum. In thermal equilibrium the resonator will be exchanging quanta with the bath but maintaining an average occupation level, we will need to analyze this interaction to proceed [140].

Our Hamiltonian is

$$\hat{H} = \underbrace{\hbar \, \omega_\text{o} \left(\hat{a}^\dagger \, \hat{a} + \tfrac{1}{2} \right) + \sum_q \hbar \, \omega_q \, \hat{d}_q^\dagger \, \hat{d}_q}_{\hat{H}_0} + \underbrace{\sum_q \hbar \left(\kappa_q^* \, \hat{a} \, \hat{d}_q^\dagger + \kappa_q \, \hat{a}^\dagger \, \hat{d}_q \right)}_{\hat{H}_\text{int}} \, ,$$

and we can move to the interaction picture with

$$\underbrace{\mathrm{e}^{-\frac{\mathrm{i}}{\hbar}\hat{H}\,t}}_{\hat{U}(t)} = \underbrace{\mathrm{e}^{-\frac{\mathrm{i}}{\hbar}\hat{H}_0\,t}}_{\hat{U}_0(t)} \; \underbrace{\mathrm{e}^{-\frac{\mathrm{i}}{\hbar}\hat{H}_\text{int}\,t}}_{\hat{U}_\text{I}(t)} \, ,$$

and

$$\left| \psi_\text{I}(t) \right\rangle = \hat{U}_\text{I}(t - t_0) \left| \psi(t_0) \right\rangle = \hat{U}_0^\dagger(t - t_0) \left| \psi(t) \right\rangle \, .$$

The state $\left| \psi_\text{I}(t) \right\rangle$ evolves under the Schrödinger equation with interaction picture Hamilto-

nian $\hat{H}_{\rm I}(t) = \hat{U}_0^\dagger(t)\,\hat{H}_{\rm int}\,\hat{U}_0(t)$, such that

$$\mathrm{i}\,\hbar\,\frac{\mathrm{d}}{\mathrm{d}t}\hat{U}_{\rm I}(t) = \hat{H}_{\rm I}(t)\,\hat{U}_{\rm I}(t)\ ,$$

which can be integrated to give

$$\hat{U}_{\rm I}(t) = 1 - \frac{\mathrm{i}}{\hbar}\int_{t_0}^{t} \hat{H}_{\rm I}(t_1)\,\hat{U}_{\rm I}(t_1)\,\mathrm{d}t_1\ .$$

Applying this to $\big|\psi(t_0)\big\rangle$ we can create a Dyson expansion

$$\begin{aligned}
\big|\psi_{\rm I}(t)\big\rangle &= \big|\psi(t_0)\big\rangle - \frac{\mathrm{i}}{\hbar}\int_{t_0}^{t} \hat{H}_{\rm I}(t_1)\,\big|\psi_{\rm I}(t_1)\big\rangle\,\mathrm{d}t_1 \\
&= \big|\psi(t_0)\big\rangle - \frac{\mathrm{i}}{\hbar}\int_{t_0}^{t} \hat{H}_{\rm I}(t_1)\,\big|\psi_{\rm I}(t_0)\big\rangle\,\mathrm{d}t_1 + \left(\frac{\mathrm{i}}{\hbar}\right)^2\int_{t_0}^{t}\int_{t_0}^{t_1} \hat{H}_{\rm I}(t_1)\,\hat{H}_{\rm I}(t_2)\,\big|\psi_{\rm I}(t_2)\big\rangle\,\mathrm{d}t_2\,\mathrm{d}t_1 \\
&= \cdots
\end{aligned}$$

and for extremely short times get away with only using the first two terms in the second expansion.

Let us now split $\big|\psi\big\rangle = \big|\psi_{\rm SHO}, \psi_{\rm bath}\big\rangle$, and let $\big|\psi(t_0)\big\rangle = \big|n, \psi_{\rm bath}\big\rangle$ where the oscillator has occupation n and the bath is in some state. The probability amplitude of the oscillator gaining, or losing, a quanta (and the bath being in an arbitrary state) over some short time

period t is

$$\left\langle n \pm 1, \psi'_{\rm bath} \,\middle|\, \hat{U}_{\rm I}(t) \,\middle|\, n, \psi_{\rm bath} \right\rangle = -\frac{\mathrm{i}}{\hbar} \int_{t_0}^{t} \left\langle n \pm 1, \psi'_{\rm bath} \,\middle|\, \hat{H}_{\rm I}(t_1) \,\middle|\, n, \psi_{\rm bath} \right\rangle \mathrm{d}t_1$$

$$= -\frac{\mathrm{i}}{\hbar} \int_{t_0}^{t} \left\langle n \pm 1, \psi'_{\rm bath} \,\middle|\, \hat{U}_0^\dagger(t_1) \sum_q \hbar \left(\kappa_q^* \, \hat{a} \, \hat{d}_q^\dagger + \kappa_q \, \hat{a}^\dagger \, \hat{d}_q \right) \hat{U}_0(t_1) \,\middle|\, n, \psi_{\rm bath} \right\rangle \mathrm{d}t_1 \ .$$

We have $\hat{U}_0(t) = \mathrm{e}^{-\mathrm{i}\,\omega_{\rm o}\,(\hat{a}^\dagger\,\hat{a} + \frac{1}{2})\,t} \prod_q \mathrm{e}^{-\mathrm{i}\,\omega_q\,\hat{d}_q^\dagger\,\hat{d}_q\,t}$ and from (I.11), (I.12),

$$\hat{U}_0^\dagger(t)\,\hat{a}\,\hat{U}_0(t) = \hat{a}\,\mathrm{e}^{-\mathrm{i}\,\omega_{\rm o}\,t} \ , \qquad \hat{U}_0^\dagger(t)\,\hat{d}_q\,\hat{U}_0(t) = \hat{d}_q\,\mathrm{e}^{-\mathrm{i}\,\omega_q\,t} \ ,$$
$$\hat{U}_0^\dagger(t)\,\hat{a}^\dagger\,\hat{U}_0(t) = \hat{a}^\dagger\,\mathrm{e}^{\mathrm{i}\,\omega_{\rm o}\,t} \ , \qquad \hat{U}_0^\dagger(t)\,\hat{d}_q^\dagger\,\hat{U}_0(t) = \hat{d}_q^\dagger\,\mathrm{e}^{\mathrm{i}\,\omega_q\,t} \ .$$

Putting these in,

$$\begin{aligned}
&\left\langle n \pm 1, \psi'_{\rm bath} \,\middle|\, \hat{U}_{\rm I}(t) \,\middle|\, n, \psi_{\rm bath} \right\rangle = \\
&\quad -\mathrm{i} \int_{t_0}^{t} \mathrm{e}^{-\mathrm{i}\,\omega_{\rm o}\,t_1} \left\langle n \pm 1 \,\middle|\, \hat{a} \,\middle|\, n \right\rangle \left\langle \psi'_{\rm bath} \,\middle|\, \sum_q \kappa_q^* \,\mathrm{e}^{\mathrm{i}\,\omega_q\,t_1}\, \hat{d}_q^\dagger \,\middle|\, \psi_{\rm bath} \right\rangle \mathrm{d}t_1 \\
&\quad -\mathrm{i} \int_{t_0}^{t} \mathrm{e}^{\mathrm{i}\,\omega_{\rm o}\,t_1} \left\langle n \pm 1 \,\middle|\, \hat{a}^\dagger \,\middle|\, n \right\rangle \left\langle \psi'_{\rm bath} \,\middle|\, \sum_q \kappa_q \,\mathrm{e}^{-\mathrm{i}\,\omega_q\,t_1}\, \hat{d}_q \,\middle|\, \psi_{\rm bath} \right\rangle \mathrm{d}t_1 \ .
\end{aligned}$$

Using the continuum approximation, $\kappa_q = \kappa = \frac{\mathrm{i}\sqrt{\gamma}}{\sqrt{2\,\pi}}$, and (I.15) from the previous section,

$$\sum_q \kappa_q \,\mathrm{e}^{-\mathrm{i}\,\omega_q\,t}\,\hat{d}_q = \mathrm{i}\,\sqrt{\gamma}\,\hat{d}_{\rm in}(t) \ ,$$

giving

$$\left\langle n \pm 1, \psi'_{\text{bath}} \,\middle|\, \hat{U}_{\text{I}}(t) \,\middle|\, n, \psi_{\text{bath}} \right\rangle = \left\langle n \pm 1 \,\middle|\, \hat{a} \,\middle|\, n \right\rangle \sqrt{\gamma^*} \int_{t_0}^{t} \mathrm{e}^{-\mathrm{i}\,\omega_{\text{o}}\,t_1} \left\langle \psi'_{\text{bath}} \,\middle|\, \hat{d}^{\dagger}_{\text{in}}(t_1) \,\middle|\, \psi_{\text{bath}} \right\rangle \mathrm{d}t_1 + \left\langle n \pm 1 \,\middle|\, \hat{a}^{\dagger} \,\middle|\, n \right\rangle \sqrt{\gamma} \int_{t_0}^{t} \mathrm{e}^{\mathrm{i}\,\omega_{\text{o}}\,t_1} \left\langle \psi'_{\text{bath}} \,\middle|\, \hat{d}_{\text{in}}(t_1) \,\middle|\, \psi_{\text{bath}} \right\rangle \mathrm{d}t_1 \ .$$

The probability of the oscillator gaining a quanta (and the bath being in any state) is thus

$$\begin{aligned}
\mathbb{P}_{n\to n+1} &= \left| \left\langle n+1 \,\middle|\, \hat{U}_{\text{I}}(t) \,\middle|\, n \right\rangle \right|^2 \\
&= \sum_{\psi'_{\text{bath}}} \left| \left\langle n+1, \psi'_{\text{bath}} \,\middle|\, \hat{U}_{\text{I}}(t) \,\middle|\, n, \psi_{\text{bath}} \right\rangle \right|^2 \\
&= (n+1)\,|\gamma| \int_{t_0}^{t} \int_{t_0}^{t} \mathrm{e}^{\mathrm{i}\,\omega_{\text{o}}\,(t_2-t_1)} \\
&\qquad \times \sum_{\psi'_{\text{bath}}} \left\langle \psi_{\text{bath}} \,\middle|\, \hat{d}^{\dagger}_{\text{in}}(t_1) \,\middle|\, \psi'_{\text{bath}} \right\rangle \left\langle \psi'_{\text{bath}} \,\middle|\, \hat{d}_{\text{in}}(t_2) \,\middle|\, \psi_{\text{bath}} \right\rangle \mathrm{d}t_1\,\mathrm{d}t_2 \\
&= (n+1)\,|\gamma| \int_{t_0}^{t} \int_{t_0}^{t} \mathrm{e}^{\mathrm{i}\,\omega_{\text{o}}\,(t_2-t_1)} \left\langle \hat{d}^{\dagger}_{\text{in}}(t_1)\,\hat{d}_{\text{in}}(t_2) \right\rangle \mathrm{d}t_1\,\mathrm{d}t_2 \ .
\end{aligned}$$

Likewise the probability of the oscillator losing a quanta is

$$\begin{aligned}
\mathbb{P}_{n\to n-1} &= \left| \left\langle n-1 \,\middle|\, \hat{U}_{\text{I}}(t) \,\middle|\, n \right\rangle \right|^2 \\
&= n\,|\gamma| \int_{t_0}^{t} \int_{t_0}^{t} \mathrm{e}^{-\mathrm{i}\,\omega_{\text{o}}\,(t_2-t_1)} \left\langle \hat{d}_{\text{in}}(t_1)\,\hat{d}^{\dagger}_{\text{in}}(t_2) \right\rangle \mathrm{d}t_1\,\mathrm{d}t_2 \ .
\end{aligned}$$

To reorder $\hat{d}_{\rm in}$, $\hat{d}^\dagger_{\rm in}$ we need

$$\begin{aligned}\left[\hat{d}_{\rm in}(t_1),\hat{d}^\dagger_{\rm in}(t_2)\right] &= \frac{1}{2\,\pi}\int_{-\infty}^{\infty}\int_{-\infty}^{\infty} \mathrm{e}^{-\mathrm{i}\,\omega_1\,(t_1-t_0)}\,\mathrm{e}^{\mathrm{i}\,\omega_2\,(t_2-t_0)}\left[\hat{d}(\omega_1,t_0),\hat{d}^\dagger(\omega_2,t_0)\right]\mathrm{d}\omega_1\,\mathrm{d}\omega_2\\ &= \frac{1}{2\,\pi}\int_{-\infty}^{\infty}\int_{-\infty}^{\infty} \mathrm{e}^{-\mathrm{i}\,\omega_1\,(t_1-t_0)}\,\mathrm{e}^{\mathrm{i}\,\omega_2\,(t_2-t_0)}\,\delta(\omega_1-\omega_2)\,\mathrm{d}\omega_1\,\mathrm{d}\omega_2\\ &= \frac{1}{2\,\pi}\int_{-\infty}^{\infty} \mathrm{e}^{-\mathrm{i}\,\omega_1\,(t_1-t_2)}\,\mathrm{d}\omega_1\\ &= \delta(t_1-t_2)\;.\end{aligned}$$

Thus

$$\mathbb{P}_{n\to n-1} = n\,|\gamma|\int_{t_0}^{t}\int_{t_0}^{t}\mathrm{e}^{\mathrm{i}\,\omega_{\rm o}\,(t_2-t_1)}\left\langle\hat{d}^\dagger_{\rm in}(t_1)\,\hat{d}_{\rm in}(t_2)\right\rangle\mathrm{d}t_1\,\mathrm{d}t_2 + n\,|\gamma|\int_{t_0}^{t}\mathrm{d}t_1\;.$$

If we take $t_2 = t_1+\tau$ we get the integral

$$\int_{t_0-t_1}^{t-t_1}\mathrm{e}^{\mathrm{i}\,\omega_{\rm o}\,\tau}\left\langle\hat{d}^\dagger_{\rm in}(t_1)\,\hat{d}_{\rm in}(t_1+\tau)\right\rangle\mathrm{d}\tau \approx S_{\hat{d}_{\rm in}\hat{d}_{\rm in}}(\omega_{\rm o})$$

where we have applied the Markovian approximation (assuming $\hat{d}_{\rm in}$ auto-correlation is extremely short) to take the integral bounds to $(-\infty,\infty)$, and used the definition of S from Sec. Λ.1. This gives us

$$\begin{aligned}\mathbb{P}_{n\to n+1} &= (n+1)\,|\gamma|\,t\,S_{\hat{d}_{\rm in}\hat{d}_{\rm in}}(\omega_{\rm o})\\ \mathbb{P}_{n\to n-1} &= n\,|\gamma|\,t\left(S_{\hat{d}_{\rm in}\hat{d}_{\rm in}}(\omega_{\rm o})+1\right),\end{aligned}$$

and the rates of increase/decrease are

$$\begin{aligned}&\nu_{n\to n+1} = \tfrac{\mathrm{d}}{\mathrm{d}t}\mathbb{P}_{n\to n+1} = (n+1)\,|\gamma|\,S_{\hat{d}_{\rm in}\hat{d}_{\rm in}}(\omega_{\rm o}) = (n+1)\,\Gamma_\uparrow\;, \quad \Gamma_\uparrow = |\gamma|\,S_{\hat{d}_{\rm in}\hat{d}_{\rm in}}(\omega_{\rm o})\;,\\ &\nu_{n\to n-1} = \tfrac{\mathrm{d}}{\mathrm{d}t}\mathbb{P}_{n\to n-1} = n\,|\gamma|\left(S_{\hat{d}_{\rm in}\hat{d}_{\rm in}}(\omega_{\rm o})+1\right) = n\,\Gamma_\downarrow\;, \qquad \Gamma_\downarrow = |\gamma|\left(S_{\hat{d}_{\rm in}\hat{d}_{\rm in}}(\omega_{\rm o})+1\right).\end{aligned}$$

The probability flux for a certain occupation level is

$$\begin{aligned}\frac{\mathrm{d}}{\mathrm{d}t}\mathbb{P}_n &= \nu_{n-1\to n}\,\mathbb{P}_{n-1} + \nu_{n+1\to n}\,\mathbb{P}_{n+1} - \nu_{n\to n-1}\,\mathbb{P}_n - \nu_{n\to n+1}\,\mathbb{P}_n \\ &= n\,\Gamma_\uparrow\,\mathbb{P}_{n-1} + (n+1)\,\Gamma_\downarrow\,\mathbb{P}_{n+1} - n\,\Gamma_\downarrow\,\mathbb{P}_n - (n+1)\,\Gamma_\uparrow\,\mathbb{P}_n\ .\end{aligned}$$

The average occupation level is

$$\bar{n} = \sum_{n=0}^{\infty} n\,\mathbb{P}_n\ ,$$

with rate of change

$$\frac{\mathrm{d}}{\mathrm{d}t}\bar{n} = \sum_{n=0}^{\infty} n\,\frac{\mathrm{d}}{\mathrm{d}t}\mathbb{P}_n = \Gamma_\uparrow - (\Gamma_\downarrow - \Gamma_\uparrow)\,\bar{n}\ .$$

We note that $\Gamma_\downarrow - \Gamma_\uparrow = |\gamma|$ which we expect from

$$\frac{\mathrm{d}}{\mathrm{d}t}\Big(\hat{a}^\dagger(t)\,\hat{a}(t)\Big) = -|\gamma|\,\hat{a}^\dagger(t)\,\hat{a}(t) - \sqrt{\gamma}\,\hat{a}^\dagger(t)\,\hat{d}_{\mathrm{in}}(t) - \sqrt{\gamma^*}\,\hat{a}(t)\,\hat{d}^\dagger_{\mathrm{in}}(t)\ .$$

In thermal equilibrium we have

$$\frac{\mathrm{d}}{\mathrm{d}t}\bar{n} = 0 \quad\Rightarrow\quad \frac{\Gamma_\downarrow}{\Gamma_\uparrow} = \frac{\bar{n}+1}{\bar{n}} \quad\Rightarrow\quad S_{\hat{d}_{\mathrm{in}}\hat{d}_{\mathrm{in}}}(\omega_{\mathrm{o}}) = \bar{n}\ ,$$

Or equivalently we have detailed balance

$$\mathbb{P}_n\,\nu_{n\to n+1} = \mathbb{P}_{n+1}\,\nu_{n+1\to n} \quad\Rightarrow\quad \frac{\Gamma_\downarrow}{\Gamma_\uparrow} = \frac{\mathbb{P}_n}{\mathbb{P}_{n+1}}\ .$$

This also tells us

$$\mathbb{P}_n = \mathbb{P}_0 \left(\frac{\Gamma_\uparrow}{\Gamma_\downarrow}\right)^n \,, \qquad\qquad \mathbb{P}_0 = 1 - \frac{\Gamma_\uparrow}{\Gamma_\downarrow} \,.$$

We also expect our resonator to obey Bose-Einstein statistics at thermal equilibrium,

$$\mathbb{P}_n = \frac{\mathrm{e}^{-\frac{\hbar\,\omega_\mathrm{o}\,n}{k_\mathrm{B}\,\mathbb{T}}}}{Z} \,, \qquad Z = \frac{1}{1-\mathrm{e}^{-\frac{\hbar\,\omega_\mathrm{o}}{k_\mathrm{B}\,\mathbb{T}}}} \,, \qquad \bar{n} = \frac{1}{\mathrm{e}^{\frac{\hbar\,\omega_\mathrm{o}}{k_\mathrm{B}\,\mathbb{T}}}-1} \,.$$

Thus

$$S_{\hat{d}_\mathrm{in}\hat{d}_\mathrm{in}}(\omega_\mathrm{o}) = \frac{1}{\mathrm{e}^{\frac{\hbar\,\omega_\mathrm{o}}{k_\mathrm{B}\,\mathbb{T}}}-1} \,,$$

and using (I.19),

$$S_{\hat{a}\hat{a}}(\omega) = \frac{|\gamma|\, S_{\hat{d}_\mathrm{in}\hat{d}_\mathrm{in}}(\omega)}{\frac{|\gamma|^2}{4}+(\omega-\omega_\mathrm{o})^2} \approx \frac{|\gamma|\, S_{\hat{d}_\mathrm{in}\hat{d}_\mathrm{in}}(\omega_\mathrm{o})}{\frac{|\gamma|^2}{4}+(\omega-\omega_\mathrm{o})^2} = \frac{|\gamma|}{\frac{|\gamma|^2}{4}+(\omega-\omega_\mathrm{o})^2}\,\frac{1}{\mathrm{e}^{\frac{\hbar\,\omega_\mathrm{o}}{k_\mathrm{B}\,\mathbb{T}}}-1} \,,$$

when γ is sufficiently narrow such that $S_{\hat{d}_\mathrm{in}\hat{d}_\mathrm{in}}(\omega)$ is approximately constant near $\omega = \omega_\mathrm{o}$. The total 'power' is

$$|\bar{a}|^2 = \frac{1}{2\,\pi}\int_{-\infty}^{\infty} S_{\hat{a}\hat{a}}(\omega)\,\mathrm{d}\omega = \frac{1}{\mathrm{e}^{\frac{\hbar\,\omega_\mathrm{o}}{k_\mathrm{B}\,\mathbb{T}}}-1} = \bar{n} \,.$$

At high temperatures,

$$\frac{1}{\mathrm{e}^{\frac{\hbar\,\omega_\mathrm{o}}{k_\mathrm{B}\,\mathbb{T}}}-1} \overset{k_\mathrm{B}\,\mathbb{T}\gg\hbar\,\omega_\mathrm{o}}{\approx} \frac{k_\mathrm{B}\,\mathbb{T}}{\hbar\,\omega_\mathrm{o}} \,.$$

The Markovian approximation for our heat bath dictates

$$R_{\hat{d}_{\rm in}\hat{d}_{\rm in}}(\tau) = \delta(\tau)\,\sigma^2_{\hat{d}_{\rm in}} \ ,$$

where $\sigma^2_{\hat{d}_{\rm in}}$ is some constant. Additionally,

$$\begin{aligned}
R_{\hat{d}^\dagger_{\rm in}\hat{d}^\dagger_{\rm in}}(\tau) &= \delta(\tau)\,\sigma^2_{\hat{d}^\dagger_{\rm in}} \\
&= \big\langle \hat{d}_{\rm in}(t)\,\hat{d}^\dagger_{\rm in}(t+\tau)\big\rangle_t \\
&= \big\langle \big[\hat{d}_{\rm in}(t), \hat{d}^\dagger_{\rm in}(t+\tau)\big]\big\rangle_t + \big\langle \hat{d}^\dagger_{\rm in}(t)\,\hat{d}_{\rm in}(t+\tau)\big\rangle_t \\
&= \delta(\tau) + R_{\hat{d}_{\rm in}\hat{d}_{\rm in}}(\tau) \\
&= \delta(\tau)\,\left(\sigma^2_{\hat{d}_{\rm in}} + 1\right) \ .
\end{aligned}$$

This assumption implies the spectral density is constant and symmetric

$$S_{\hat{d}_{\rm in}\hat{d}_{\rm in}}(\omega) = \int_{-\infty}^{\infty} \delta(\tau)\,\sigma^2_{\hat{d}_{\rm in}}\,\mathrm{e}^{\mathrm{i}\,\omega\,\tau}\mathrm{d}\tau = \sigma^2_{\hat{d}_{\rm in}} = \bar{n} \ ,$$

which is tied directly to $\omega_{\rm o}$. This global dependence of the heat bath on $\omega_{\rm o}$ tells us the thermal spectrum results from this analysis only make sense in the vicinity of $\omega \approx \omega_{\rm o}$. We

can also find

$$
\begin{aligned}
S_{\hat{d}_{\rm in}^\dagger \hat{d}_{\rm in}^\dagger}(\omega) &= \lim_{T\to\infty} \left\langle \hat{d}_{{\rm in}\,T}(-\omega)\, \hat{d}_{{\rm in}\,T}^\dagger(\omega) \right\rangle \\
&= \lim_{T\to\infty} \frac{1}{T} \int_0^T \int_0^T \left\langle \hat{d}_{\rm in}(t_1)\, \hat{d}_{\rm in}^\dagger(t_2) \right\rangle \mathrm{e}^{\mathrm{i}\,\omega(t_2-t_1)}\, \mathrm{d}t_1\, \mathrm{d}t_2 \\
&= \lim_{T\to\infty} \frac{1}{T} \int_0^T \int_0^T \left\langle \left[\hat{d}_{\rm in}(t_1), \hat{d}_{\rm in}^\dagger(t_2) \right] \right\rangle \mathrm{e}^{\mathrm{i}\,\omega(t_2-t_1)}\, \mathrm{d}t_1\, \mathrm{d}t_2 \\
&\quad + \lim_{T\to\infty} \frac{1}{T} \int_0^T \int_0^T \left\langle \hat{d}_{\rm in}^\dagger(t_1)\, \hat{d}_{\rm in}(t_2) \right\rangle \mathrm{e}^{\mathrm{i}\,\omega(t_1-t_2)}\, \mathrm{d}t_1\, \mathrm{d}t_2 \\
&= \lim_{T\to\infty} \frac{1}{T} \int_0^T \int_0^T \delta(t_1-t_2)\, \mathrm{e}^{\mathrm{i}\,\omega(t_2-t_1)}\, \mathrm{d}t_1\, \mathrm{d}t_2 + \lim_{T\to\infty} \left\langle \hat{d}_{{\rm in}\,T}^\dagger(\omega)\, \hat{d}_{{\rm in}\,T}(-\omega) \right\rangle \\
&= \lim_{T\to\infty} \frac{1}{T} \int_0^T \mathrm{d}t_1 + S_{\hat{d}_{\rm in}\hat{d}_{\rm in}}(-\omega) \\
&= 1 + S_{\hat{d}_{\rm in}\hat{d}_{\rm in}}(-\omega)\ ,
\end{aligned}
$$

which naively from above is $\bar{n}+1$ although this might be outside the valid bounds of our approximation. Note that if we carry out the previous analysis of thermal equilibrium and detailed balance on $\hat{d}_{\rm in}^\dagger$ we obtain $S_{\hat{d}_{\rm in}^\dagger \hat{d}_{\rm in}^\dagger}(-\omega_{\rm o}) = \bar{n}+1$.

We might also be interested in

$$S_{(\hat{a}^\dagger+\hat{a})(\hat{a}^\dagger+\hat{a})}(\omega) = \lim_{T\to\infty}\Big(\big\langle \hat{a}_T(-\omega)\,\hat{a}_T^\dagger(\omega)\big\rangle + \big\langle \hat{a}_T^\dagger(-\omega)\,\hat{a}_T(\omega)\big\rangle + \big\langle \hat{a}_T(-\omega)\,\hat{a}_T(\omega)\big\rangle + \big\langle \hat{a}_T^\dagger(-\omega)\,\hat{a}_T^\dagger(\omega)\big\rangle\Big)$$

$$= \frac{|\gamma| \lim_{T\to\infty}\big\langle \hat{d}_{\mathrm{in}\,T}(-\omega)\,\hat{d}_{\mathrm{in}\,T}^\dagger(\omega)\big\rangle}{(\omega+\omega_\mathrm{o})^2+\frac{|\gamma|^2}{4}} + \frac{|\gamma| \lim_{T\to\infty}\big\langle \hat{d}_{\mathrm{in}\,T}^\dagger(-\omega)\,\hat{d}_{\mathrm{in}\,T}(\omega)\big\rangle}{(\omega-\omega_\mathrm{o})^2+\frac{|\gamma|^2}{4}} + \frac{\gamma \lim_{T\to\infty}\big\langle \hat{d}_{\mathrm{in}\,T}(-\omega)\,\hat{d}_{\mathrm{in}\,T}(\omega)\big\rangle}{\Big(\mathrm{i}\,(-\omega-\omega_\mathrm{o})-\frac{|\gamma|}{2}\Big)\,\Big(\mathrm{i}\,(\omega-\omega_\mathrm{o})-\frac{|\gamma|}{2}\Big)} + \frac{\gamma^* \lim_{T\to\infty}\big\langle \hat{d}_{\mathrm{in}\,T}^\dagger(-\omega)\,\hat{d}_{\mathrm{in}\,T}^\dagger(\omega)\big\rangle}{\Big(-\mathrm{i}\,(-\omega-\omega_\mathrm{o})-\frac{|\gamma|}{2}\Big)\,\Big(-\mathrm{i}\,(\omega-\omega_\mathrm{o})-\frac{|\gamma|}{2}\Big)}$$

$$= \frac{|\gamma|\,S_{\hat{d}_\mathrm{in}^\dagger\hat{d}_\mathrm{in}^\dagger}(\omega)}{(\omega+\omega_\mathrm{o})^2+\frac{|\gamma|^2}{4}} + \frac{|\gamma|\,S_{\hat{d}_\mathrm{in}\hat{d}_\mathrm{in}}(\omega)}{(\omega-\omega_\mathrm{o})^2+\frac{|\gamma|^2}{4}}$$

$$= \frac{|\gamma|\,\big(S_{\hat{d}_\mathrm{in}\hat{d}_\mathrm{in}}(-\omega)+1\big)}{(\omega+\omega_\mathrm{o})^2+\frac{|\gamma|^2}{4}} + \frac{|\gamma|\,S_{\hat{d}_\mathrm{in}\hat{d}_\mathrm{in}}(\omega)}{(\omega-\omega_\mathrm{o})^2+\frac{|\gamma|^2}{4}}\,,$$

and at $\omega \approx \omega_\mathrm{o}$

$$S_{(\hat{a}^\dagger+\hat{a})(\hat{a}^\dagger+\hat{a})}(\omega\approx\omega_\mathrm{o}) \approx \frac{|\gamma|\,S_{\hat{d}_\mathrm{in}\hat{d}_\mathrm{in}}(\omega_\mathrm{o})}{(\omega-\omega_\mathrm{o})^2+\frac{|\gamma|^2}{4}}\,,$$

$$\bar{S}_{(\hat{a}^\dagger+\hat{a})(\hat{a}^\dagger+\hat{a})}(\omega\approx\omega_\mathrm{o}) \approx \frac{|\gamma|\,\big(S_{\hat{d}_\mathrm{in}\hat{d}_\mathrm{in}}(\omega_\mathrm{o})+\frac{1}{2}\big)}{(\omega-\omega_\mathrm{o})^2+\frac{|\gamma|^2}{4}}\,,$$

where $\bar{S}$ is the symmetrized spectral density. For the position operator, this gives

$$\begin{aligned}
\bar{S}_{\hat{x}\hat{x}}(\omega \approx \omega_{\mathrm{o}}) &\approx \frac{\hbar}{2\,m\,\omega_{\mathrm{o}}}\,\frac{|\gamma|\ \left(\bar{n}+\frac{1}{2}\right)}{(\omega-\omega_{\mathrm{o}})^2+\frac{|\gamma|^2}{4}} \\
&= \frac{\hbar}{2\,m\,\omega_{\mathrm{o}}}\,\frac{|\gamma|\,\frac{1}{2}\,\coth\!\left[\frac{k_{\mathrm{B}}\,\mathbb{T}}{2\,\hbar\,\omega_{\mathrm{o}}}\right]}{(\omega-\omega_{\mathrm{o}})^2+\frac{|\gamma|^2}{4}} \\
&\overset{k_{\mathrm{B}}\,\mathbb{T}\gg\hbar\,\omega_{\mathrm{o}}}{\approx} \frac{k_{\mathrm{B}}\,\mathbb{T}}{2\,m\,{\omega_{\mathrm{o}}}^2}\,\frac{|\gamma|}{(\omega-\omega_{\mathrm{o}})^2+\frac{|\gamma|^2}{4}}
\end{aligned}$$

Note that this formalism uses random fluctuations in cavity amplitude (occupation) rather than random fluctuations in a driving force as is common by other authors [12, 138–140, 233].

I.5 Adding ports

We can add ports to our system by creating additional heat baths that each individually couple to our system. Following the form of (I.16) we have

$$\frac{\mathrm{d}}{\mathrm{d}t}\hat{a}(t) = \mathrm{e}^{\frac{\mathrm{i}}{\hbar}\hat{H}\,t}\,\left[\hat{a},-\frac{\mathrm{i}}{\hbar}\hat{H}_{\mathrm{sys}}\right]\,\mathrm{e}^{-\frac{\mathrm{i}}{\hbar}\hat{H}\,t} - \frac{|\gamma|}{2}\hat{a}(t) - \sum_i \sqrt{\gamma^i}\,\hat{d}^i_{\mathrm{in}}(t)\ ,$$

$$\hat{d}^i_{\mathrm{out}}(t) = \hat{d}^i_{\mathrm{in}}(t) + \sqrt{\gamma^{i\,*}}\,\hat{a}(t)\ ,$$

with

$$\gamma = \sum_i \gamma^i\ .$$

For a simple harmonic oscillator this is the same form as derived classically in App. Θ.

I.5.1 Laser drive input correspondence

It's possible to instead consider our laser drive as an input port. This corresponds to

$$\kappa_{\mathrm{L}}\,\hat{d}_{\mathrm{L}}(t) = L\,\mathrm{e}^{-\mathrm{i}\,\omega_{\mathrm{L}}\,t}\ ,$$

with

$$\kappa_{\mathrm{L}}(\omega_{\mathrm{L}}) = \kappa_{\mathrm{L}}\,\sqrt{\mathrm{s}} \quad \Rightarrow \quad \sqrt{\gamma_{\mathrm{L}}} = \mathrm{i}\,\sqrt{2\,\pi}\,\kappa_{\mathrm{L}}\,\sqrt{\mathrm{s}}$$

to give

$$\begin{array}{ccc} \sqrt{\gamma_{\mathrm{L}}}\,\hat{d}_{\mathrm{L\,in}}(t) & = & \mathrm{i}\,L\,\mathrm{e}^{-\mathrm{i}\,\omega_{\mathrm{L}}\,t} \\ \wr\,\mathrm{FT} & & \wr\,\mathrm{FT} \\ \sqrt{\gamma_{\mathrm{L}}}\,\hat{d}_{\mathrm{L\,in}}(\omega) & = & \mathrm{i}\,L\,\sqrt{2\,\pi}\,\mathrm{e}^{-\mathrm{i}\,\omega_{\mathrm{L}}\,t_0}\,\delta(\omega-\omega_{\mathrm{L}}) \end{array}$$

where we have

$$\hat{d}_{\mathrm{L\,in}}(t) = \frac{\hat{d}_{\mathrm{L}}(t)}{\sqrt{2\,\pi}\,\sqrt{\mathrm{s}}} = \frac{\mathrm{e}^{-\mathrm{i}\,\omega_{\mathrm{L}}\,(t-t_0)}\,\hat{d}_{\mathrm{L}}(t_0)}{\sqrt{2\,\pi}\,\sqrt{\mathrm{s}}} = \frac{\mathrm{i}\,L}{\sqrt{\gamma_L}}\,\mathrm{e}^{-\mathrm{i}\,\omega_L\,t}\ ,$$

$$\hat{d}_{\mathrm{L\,in}}(\omega) = \hat{d}_{\mathrm{L}}(\omega,t_0) = \delta(\omega-\omega_{\mathrm{L}})\,\hat{d}_{\mathrm{L}}(t_0)\,\sqrt{\mathrm{s}^{-1}} = \delta(\omega-\omega_L)\,\frac{\mathrm{i}\,L\,\sqrt{2\,\pi}}{\sqrt{\gamma_L}}\ ,$$

$$\hat{d}_L(t_0) = \frac{\mathrm{i}\,L\,\sqrt{2\,\pi}\,\sqrt{\mathrm{s}}}{\sqrt{\gamma_L}}\,\mathrm{e}^{-\mathrm{i}\,\omega_L\,t_0}\ .$$

Note that in the rotating frame we have $\omega_{\mathrm{L}} \mapsto 0$.

The laser input power is

$$P_{\mathrm{L}} = \hbar\,\omega_{\mathrm{L}} \left\langle \hat{d}^{\dagger}_{\mathrm{L\,in}}\,\hat{d}_{\mathrm{L\,in}} \right\rangle \quad \Rightarrow \quad |L|^2 = |\gamma_{\mathrm{L}}|\,\frac{P_{\mathrm{L}}}{\hbar\,\omega_{\mathrm{L}}}\;,$$

and γ_{L} represents a coupling efficiency between the laser input and resonator. This gives

$$\hat{d}_{\mathrm{L\,in}}(t) = \sqrt{\frac{P_{\mathrm{L}}}{\hbar\,\omega_{\mathrm{L}}}}\,\mathrm{e}^{-\mathrm{i}\,\omega_L\,t}\;.$$

In this sense, a bath can describe a monotone drive by

$$\hat{d}_{\mathrm{L}}(\omega) = \frac{\mathrm{i}\,L}{\sqrt{\gamma_L}}\,\sqrt{2\,\pi}\,\delta(\omega-\omega_L)\;.$$

I.5.2 Bath drive approximation

If γ is sufficiently small we can approximate a bath input by a resonant drive with $\hat{d}(\omega) = \hat{d}(\omega_{\mathrm{o}})$ constant. We can find the equivalent drive strength by comparing the resonator response.

For a constant bath input,

$$\hat{d}(\omega) = \hat{d}(\omega_{\mathrm{o}}) \ ,$$

$$\Rightarrow \quad \hat{a}(\omega) = \frac{\sqrt{\gamma}\,\hat{d}(\omega_{\mathrm{o}})}{\mathrm{i}\,(\omega - \omega_{\mathrm{o}}) - \frac{\gamma}{2}} \ ,$$

$$\begin{aligned} \Rightarrow \quad \int_{-\infty}^{\infty} \hat{a}(\omega)^{\dagger}\,\hat{a}(\omega)\,\mathrm{d}\omega &= \hat{d}(\omega_{\mathrm{o}})^{\dagger}\,\hat{d}(\omega_{\mathrm{o}}) \int_{\infty}^{\infty} \frac{\gamma}{(\omega - \omega_{\mathrm{o}})^2 + \left(\frac{\gamma}{2}\right)^2}\,\mathrm{d}\omega \\ &= 2\,\pi\,\hat{d}(\omega_{\mathrm{o}})^{\dagger}\,\hat{d}(\omega_{\mathrm{o}}) \ . \end{aligned}$$

For a monotone drive,

$$\hat{d}(\omega) = \frac{\mathrm{i}\,L_d}{\sqrt{\gamma}}\,\sqrt{2\,\pi}\,\delta(\omega - \omega_{\mathrm{o}}) \ ,$$

$$\Rightarrow \quad \hat{a}(\omega) = \frac{\mathrm{i}\,L_d\,\sqrt{2\,\pi}\,\delta(\omega - \omega_{\mathrm{o}})}{\mathrm{i}\,(\omega - \omega_{\mathrm{o}}) - \frac{\gamma}{2}} \ ,$$

$$\begin{aligned} \Rightarrow \quad \int_{-\infty}^{\infty} \hat{a}(\omega)^{\dagger}\,\hat{a}(\omega)\,\mathrm{d}\omega &= 2\,\pi\,|\mathrm{i}\,L_d|^2 \int_{\infty}^{\infty} \frac{\delta(\omega - \omega_{\mathrm{o}})\,\mathrm{s}}{(\omega - \omega_{\mathrm{o}})^2 + \left(\frac{\gamma}{2}\right)^2}\,\mathrm{d}\omega \\ &= \frac{2\,\pi\,|\mathrm{i}\,L_d|^2}{\left(\frac{\gamma}{2}\right)^2}\,\mathrm{s} \ . \end{aligned}$$

Thus we can approximate a bath by resonant drive

$$\mathrm{i}\,L_d = \frac{\gamma}{2}\,\hat{d}(\omega_{\mathrm{o}})\,\sqrt{\mathrm{s}^{-1}} \ .$$

I.6 Non-rotating frame

If we have multiple laser drives there is no way to rotate out the time dependence in the Hamiltonian, and we forced to stay in the non-rotating frame. Working with a time dependent Hamiltonian creates additional complications but equivalent results can be recovered.

In the non-rotating frame, our (multiple) driven and bath coupled harmonic oscillator Hamiltonian is

$$\hat{H} = \hbar\,\omega_{\rm o}\left(\hat{a}^\dagger\,\hat{a} + \tfrac{1}{2}\right) + \underbrace{\sum_l \hbar\left(L_l\,\hat{a}^\dagger\,{\rm e}^{-{\rm i}\,\omega_{\rm l}\,t} + L_l^*\,\hat{a}\,{\rm e}^{{\rm i}\,\omega_{\rm l}\,t}\right)}_{\hat{H}^{\rm laser}_{\rm int}}$$

$$+ \underbrace{\sum_q \hbar\,\omega_q\,\hat{d}_q^\dagger\,\hat{d}_q}_{\hat{H}_{\rm bath}} + \underbrace{\sum_q \hbar\left(\kappa_q^*\,\hat{a}\,\hat{d}_q^\dagger + \kappa_q\,\hat{a}^\dagger\,\hat{d}_q\right)}_{\hat{H}^{\rm bath}_{\rm int}}\ .$$

The Langevin equation of motion (I.16) is then

$$\frac{\rm d}{{\rm d}t}\hat{a}(t) = -{\rm i}\,\omega_{\rm o}\,\hat{a}(t) - \frac{|\gamma|}{2}\hat{a}(t) + \sum_l -{\rm i}\,L_l\,{\rm e}^{-{\rm i}\,\omega_l\,t} - \sqrt{\gamma}\,\hat{d}_{\rm in}(t)\ . \tag{I.24}$$

For $\hat{d}_{\rm in}(t) = 0$, this has solution

$$\hat{a}(t) = \sum_l \left(\frac{-{\rm i}\,L_l\,{\rm e}^{-{\rm i}\,\omega_l\,t}}{{\rm i}\,(\omega_o - \omega_l) + \frac{|\gamma|}{2}}\right) + C\,{\rm e}^{-\left({\rm i}\,\omega_o + \frac{|\gamma|}{2}\right)t}\ , \tag{I.25}$$

where C is some constant. Inspired by (I.23), we'll define

$$\bar{a}_l = \frac{-{\rm i}\,L_l}{{\rm i}\,(\omega_o - \omega_l) + \frac{|\gamma|}{2}} = \frac{-{\rm i}\,L_l}{{\rm i}\,\Delta_{o\,l} + \frac{|\gamma|}{2}}\ , \tag{I.26}$$

noting that

$$|\bar{a}_l \, \mathrm{e}^{-\mathrm{i}\,\omega_l \, t}| = |\bar{a}_l| \; .$$

If we choose to phase match everything at $t = 0$, such that $\hat{a}(0) = \sum_l \bar{a}_l$, we enforce $C = 0$.

From here, we can do leveling on all or a subset of the laser drives,

$$\hat{H}_{\mathrm{lvl}} = \left(\prod_{j=1}^{n} \hat{D}(\bar{a}_j \, \mathrm{e}^{-\mathrm{i}\,\omega_j \, t}) \right)^{\dagger} \left(\hat{H} - \mathrm{i}\,\hbar \, \frac{\partial}{\partial t} \right) \left(\prod_{j=1}^{n} \hat{D}(\bar{a}_j \, \mathrm{e}^{-\mathrm{i}\,\omega_j \, t}) \right) .$$

Defining

$$\hat{A}_j(t) = \bar{a}_j \, \mathrm{e}^{-\mathrm{i}\,\omega_j \, t} \, \hat{a}^{\dagger} - \bar{a}_j^{*} \, \mathrm{e}^{\mathrm{i}\,\omega_j \, t} \, \hat{a} \; ,$$

we have

$$\hat{D}(\bar{a}_j \, \mathrm{e}^{-\mathrm{i}\,\omega_j \, t}) = \mathrm{e}^{\hat{A}_j(t)} \; , \qquad\qquad \hat{D}(\bar{a}_j \, \mathrm{e}^{-\mathrm{i}\,\omega_j \, t})^{\dagger} = \mathrm{e}^{-\hat{A}_j(t)} \; ,$$

and it will be useful to evaluate

$$\frac{\partial}{\partial t} \hat{A}_j(t) = \hat{A}_j'(t) = \left(-\mathrm{i}\,\omega_j \right) \left(\bar{a}_j \, \mathrm{e}^{-\mathrm{i}\,\omega_j \, t} \, \hat{a}^{\dagger} + \bar{a}_j^{*} \, \mathrm{e}^{\mathrm{i}\,\omega_j \, t} \, \hat{a} \right) \; ,$$

$$\left[\frac{\partial}{\partial t}, \hat{A}_j(t)\right] f = \frac{\partial}{\partial t}\hat{A}_j(t)\, f - \hat{A}_j(t)\, \frac{\partial}{\partial t} f$$
$$= \left(\frac{\partial}{\partial t}\hat{A}_j(t)\right) f + \hat{A}_j(t)\, \frac{\partial}{\partial t} f - \hat{A}_j(t)\, \frac{\partial}{\partial t} f$$
$$= \hat{A}'_j(t)\, f$$

$$\Rightarrow \quad \left[\frac{\partial}{\partial t}, \hat{A}_j(t)\right] = \hat{A}'_j(t)\ ,$$

$$\left[\hat{A}'_j(t), \hat{A}_j(t)\right] = \left(-\mathrm{i}\,\omega_j\right) \left(\bar{a}_j\, \mathrm{e}^{-\mathrm{i}\omega_j t}\, \bar{a}^*_j\, \mathrm{e}^{\mathrm{i}\omega_j t} \left[\hat{a}^\dagger, \hat{a}\right] - \bar{a}^*_j\, \mathrm{e}^{\mathrm{i}\omega_j t}\, \bar{a}_j\, \mathrm{e}^{-\mathrm{i}\omega_j t} \left[\hat{a}, \hat{a}^\dagger\right]\right)$$
$$= 2\,\mathrm{i}\,\omega_j\, |\bar{a}_j|^2\ .$$

Using (I.10),

$$\hat{D}(\bar{a}_j\, \mathrm{e}^{-\mathrm{i}\omega_j t})^\dagger \left(-\mathrm{i}\,\hbar\,\frac{\partial}{\partial t}\right) \hat{D}(\bar{a}_j\, \mathrm{e}^{-\mathrm{i}\omega_j t}) =$$

$$= -\mathrm{i}\,\hbar\,\frac{\partial}{\partial t} - \mathrm{i}\,\hbar \left[\frac{\partial}{\partial t}, \hat{A}_j(t)\right] - \mathrm{i}\,\hbar\,\frac{1}{2} \left[\left[\frac{\partial}{\partial t}, \hat{A}_j(t)\right], \hat{A}_j(t)\right]$$
$$- \mathrm{i}\,\hbar\,\frac{1}{6} \left[\left[\left[\frac{\partial}{\partial t}, \hat{A}_j(t)\right], \hat{A}_j(t)\right], \hat{A}_j(t)\right] + \ldots$$

$$= -\mathrm{i}\,\hbar\,\frac{\partial}{\partial t} - \mathrm{i}\,\hbar\,\hat{A}'_j(t) - \hbar\,\omega_j\,|\bar{a}_j|^2 + 0$$

$$= -\mathrm{i}\,\hbar\,\frac{\partial}{\partial t} - \hbar\,\omega_j \left(\bar{a}_j\, \mathrm{e}^{-\mathrm{i}\omega_j t}\, \hat{a}^\dagger + \bar{a}^*_j\, \mathrm{e}^{\mathrm{i}\omega_j t}\, \hat{a} + |\bar{a}_j|^2\right)\ ,$$

and for multiple displacement operators,

$$\left(\prod_{j=1}^{n}\hat{D}(\bar{a}_j\,\mathrm{e}^{-\mathrm{i}\,\omega_j\,t})\right)^{\dagger}\left(-\mathrm{i}\,\hbar\,\frac{\partial}{\partial t}\right)\left(\prod_{j=1}^{n}\hat{D}(\bar{a}_j\,\mathrm{e}^{-\mathrm{i}\,\omega_j\,t})\right) =$$

$$\begin{aligned}
&= \left(\prod_{j=2}^{n}\hat{D}(\bar{a}_j\,\mathrm{e}^{-\mathrm{i}\,\omega_j\,t})\right)^{\dagger}\left(-\hbar\,\omega_1\,\left(\bar{a}_1\,\mathrm{e}^{-\mathrm{i}\,\omega_1\,t}\,\hat{a}^{\dagger}+\bar{a}_1^{*}\,\mathrm{e}^{\mathrm{i}\,\omega_1\,t}\,\hat{a}+|\bar{a}_1|^2\right)\right)\left(\prod_{j=2}^{n}\hat{D}(\bar{a}_j\,\mathrm{e}^{-\mathrm{i}\,\omega_j\,t})\right)\\
&\quad+\left(\prod_{j=2}^{n}\hat{D}(\bar{a}_j\,\mathrm{e}^{-\mathrm{i}\,\omega_j\,t})\right)^{\dagger}\left(-\mathrm{i}\,\hbar\,\frac{\partial}{\partial t}\right)\left(\prod_{j=2}^{n}\hat{D}(\bar{a}_j\,\mathrm{e}^{-\mathrm{i}\,\omega_j\,t})\right)
\end{aligned}$$

$$\begin{aligned}
&= -\hbar\,\omega_1\,\left(\bar{a}_1\,\mathrm{e}^{-\mathrm{i}\,\omega_1\,t}\,\left(\hat{a}^{\dagger}+\sum_{j=2}^{n}\bar{a}_j^{*}\,\mathrm{e}^{\mathrm{i}\,\omega_j\,t}\right)+\bar{a}_1^{*}\,\mathrm{e}^{\mathrm{i}\,\omega_1\,t}\,\left(\hat{a}+\sum_{j=2}^{n}\bar{a}_j\,\mathrm{e}^{-\mathrm{i}\,\omega_j\,t}\right)+|\bar{a}_1|^2\right)\\
&\quad+\left(\prod_{j=2}^{n}\hat{D}(\bar{a}_j\,\mathrm{e}^{-\mathrm{i}\,\omega_j\,t})\right)^{\dagger}\left(-\mathrm{i}\,\hbar\,\frac{\partial}{\partial t}\right)\left(\prod_{j=2}^{n}\hat{D}(\bar{a}_j\,\mathrm{e}^{-\mathrm{i}\,\omega_j\,t})\right)
\end{aligned}$$

$$= \sum_{j=1}^{n}-\hbar\,\omega_j\,\left(\bar{a}_j\,\mathrm{e}^{-\mathrm{i}\,\omega_j\,t}\,\left(\hat{a}^{\dagger}+\sum_{k=j+1}^{n}\bar{a}_k^{*}\,\mathrm{e}^{\mathrm{i}\,\omega_k\,t}\right)+\bar{a}_j^{*}\,\mathrm{e}^{\mathrm{i}\,\omega_j\,t}\,\left(\hat{a}+\sum_{k=j+1}^{n}\bar{a}_k\,\mathrm{e}^{-\mathrm{i}\,\omega_k\,t}\right)+|\bar{a}_j|^2\right)\,.$$

The full displaced Hamiltonian is thus

$$\hat{H}_{\mathrm{lvl}} = \left(\prod_{j=1}^{n} \hat{D}(\bar{a}_j\,\mathrm{e}^{-\mathrm{i}\,\omega_j\,t})\right)^{\dagger} \left(\hat{H} - \mathrm{i}\,\hbar\,\frac{\partial}{\partial t}\right) \left(\prod_{j=1}^{n} \hat{D}(\bar{a}_j\,\mathrm{e}^{-\mathrm{i}\,\omega_j\,t})\right)$$

$$\begin{aligned}
&= \hbar\,\omega_{\mathrm{o}} \left(\hat{a}^{\dagger}\,\hat{a} + \frac{1}{2}\right) + \sum_{j=1}^{n} \hbar\,\omega_{\mathrm{o}}\,\hat{a}^{\dagger}\,\bar{a}_j\,\mathrm{e}^{-\mathrm{i}\,\omega_j\,t} + \sum_{j=1}^{n} \hbar\,\omega_{\mathrm{o}}\,\hat{a}\,\bar{a}_j^{*}\,\mathrm{e}^{\mathrm{i}\,\omega_j\,t} \\
&\quad + \hbar\,\omega_{\mathrm{o}} \left(\sum_{j=1}^{n} \bar{a}_j^{*}\,\mathrm{e}^{\mathrm{i}\,\omega_j\,t}\right) \left(\sum_{j=1}^{n} \bar{a}_j\,\mathrm{e}^{-\mathrm{i}\,\omega_j\,t}\right) \\
&\quad + \underbrace{\sum_{l} \hbar\,L_l\,\mathrm{e}^{-\mathrm{i}\,\omega_l\,t} \left(\hat{a}^{\dagger} + \sum_{j=1}^{n} \bar{a}_j^{*}\,\mathrm{e}^{\mathrm{i}\,\omega_j\,t}\right) + \sum_{l} \hbar\,L_l^{*}\,\mathrm{e}^{\mathrm{i}\,\omega_l\,t} \left(\hat{a} + \sum_{j=1}^{n} \bar{a}_j\,\mathrm{e}^{-\mathrm{i}\,\omega_j\,t}\right)}_{\text{laser interaction}} \\
&\quad + \underbrace{\sum_{q} \hbar\,\omega_q\,\hat{d}_q^{\dagger}\,\hat{d}_q}_{\text{bath}} \\
&\quad + \underbrace{\sum_{q} \hbar\,\kappa_q^{*}\,\hat{d}_q^{\dagger} \left(\hat{a} + \sum_{j=1}^{n} \bar{a}_j\,\mathrm{e}^{-\mathrm{i}\,\omega_j\,t}\right) + \sum_{q} \hbar\,\kappa_q\,\hat{d}_q \left(\hat{a}^{\dagger} + \sum_{j=1}^{n} \bar{a}_j^{*}\,\mathrm{e}^{\mathrm{i}\,\omega_j\,t}\right)}_{\text{bath interaction}} \\
&\quad + \underbrace{\sum_{j=1}^{n} -\hbar\,\omega_j \left(\bar{a}_j\,\mathrm{e}^{-\mathrm{i}\,\omega_j\,t} \left(\hat{a}^{\dagger} + \sum_{k=j+1}^{n} \bar{a}_k^{*}\,\mathrm{e}^{\mathrm{i}\,\omega_k\,t}\right) + \bar{a}_j^{*}\,\mathrm{e}^{\mathrm{i}\,\omega_j\,t} \left(\hat{a} + \sum_{k=j+1}^{n} \bar{a}_k\,\mathrm{e}^{-\mathrm{i}\,\omega_k\,t}\right) + |\bar{a}_j|^2\right)}_{\text{time derivative}} .
\end{aligned}$$

Now,

$$\frac{\mathrm{d}}{\mathrm{d}t}\hat{d}_q(t) = \left[\hat{d}_q(t), -\frac{\mathrm{i}}{\hbar}\hat{H}\right] = -\mathrm{i}\,\omega_q\,\hat{d}_q(t) - \mathrm{i}\,\kappa_q^{*} \left(\hat{a}(t) + \sum_{j=1}^{n} \bar{a}_j\,\mathrm{e}^{-\mathrm{i}\,\omega_j\,t}\right) ,$$

which has solution

$$\begin{aligned}
\hat{d}_q(t) = & -\mathrm{i}\,\kappa_q^*\,\mathrm{e}^{-\mathrm{i}\,\omega_q\,t}\int^t \mathrm{e}^{\mathrm{i}\,\omega_q\,t'}\left(\hat{a}(t') + \sum_{j=1}^{n}\bar{a}_j\,\mathrm{e}^{-\mathrm{i}\,\omega_j\,t'}\right)\mathrm{d}t' \\
= & -\mathrm{i}\,\kappa_q^*\int_{t_0}^{t}\mathrm{e}^{-\mathrm{i}\,\omega_q\,(t-t')}\,\hat{a}(t')\,\mathrm{d}t' \\
& + \sum_{j=1}^{n} -\mathrm{i}\,\kappa_q^*\,\bar{a}_j\int_{t_0}^{t}\mathrm{e}^{-\mathrm{i}\,\omega_q\,(t-t')-\mathrm{i}\,\omega_j\,t'}\,\mathrm{d}t' + \mathrm{e}^{-\mathrm{i}\,\omega_q\,(t-t_0)}\,\hat{d}_q(t_0)\;.
\end{aligned}$$

Focusing on the integral in the summed term,

$$\begin{aligned}
\int_{t_0}^{t}\mathrm{e}^{-\mathrm{i}\,\omega_q\,(t-t')-\mathrm{i}\,\omega_j\,t'}\,\mathrm{d}t' &= \mathrm{e}^{-\mathrm{i}\,\omega_q\,t}\int_{t_0}^{t}\mathrm{e}^{\mathrm{i}\,(\omega_q-\omega_j)\,t'}\,\mathrm{d}t' \\
&= \mathrm{e}^{-\mathrm{i}\,\omega_q\,t}\left(\frac{-\mathrm{i}}{\omega_q-\omega_j}\right)\left(\mathrm{e}^{\mathrm{i}\,(\omega_q-\omega_j)\,t} - \mathrm{e}^{\mathrm{i}\,(\omega_q-\omega_j)\,t_0}\right) \\
&= \frac{-\mathrm{i}\,\mathrm{e}^{-\mathrm{i}\,\omega_j\,t}}{\omega_q-\omega_j}\left(1-\mathrm{e}^{-\mathrm{i}\,(t-t_0)\,(\omega_q-\omega_j)}\right)\;,
\end{aligned}$$

and putting this back into $\hat{d}_q(t)$,

$$\begin{aligned}
\hat{d}_q(t) = & -\mathrm{i}\,\kappa_q^*\int_{t_0}^{t}\mathrm{e}^{-\mathrm{i}\,\omega_q\,(t-t')}\,\hat{a}(t')\,\mathrm{d}t' + \sum_{j=1}^{n}\frac{-\kappa_q^*\,\bar{a}_j\,\mathrm{e}^{-\mathrm{i}\,\omega_j\,t}}{\omega_q-\omega_j}\left(1-\mathrm{e}^{-\mathrm{i}\,(t-t_0)\,(\omega_q-\omega_j)}\right) \\
& + \mathrm{e}^{-\mathrm{i}\,\omega_q\,(t-t_0)}\,\hat{d}_q(t_0)\;.
\end{aligned}$$

Proceeding to $\hat{a}(t)$,

$$\begin{aligned}
\frac{\mathrm{d}}{\mathrm{d}t}\hat{a}(t) &= \left[\hat{a}(t), -\frac{\mathrm{i}}{\hbar}\hat{H}\right] \\
&= -\mathrm{i}\,\omega_{\mathrm{o}}\,\hat{a}(t) + \sum_{j=1}^{n} -\mathrm{i}\,\omega_{\mathrm{o}}\,\bar{a}_j\,\mathrm{e}^{-\mathrm{i}\,\omega_j\,t} \\
&\quad + \underbrace{\sum_{l} -\mathrm{i}\,L_l\,\mathrm{e}^{-\mathrm{i}\,\omega_l\,t}}_{\text{laser int}} + \underbrace{\sum_{q} -\mathrm{i}\,\kappa_q\,\hat{d}_q(t)}_{\text{bath int}} + \underbrace{\sum_{j=1}^{n} \mathrm{i}\,\omega_j\,\bar{a}_j\,\mathrm{e}^{-\mathrm{i}\,\omega_j\,t}}_{\text{time deriv}} .
\end{aligned}$$

Substituting in $\hat{d}_q(t)$ and applying the continuum and Markovian approximations to the bath interaction term, as in Sec. I.3.2,

$$\begin{aligned}
\sum_{q} -\mathrm{i}\,\kappa_q\,\hat{d}_q(t) \approx\ & -|\kappa|^2 \int_{t_0}^{t} \left(\int_{-\infty}^{\infty} \mathrm{e}^{-\mathrm{i}\,\omega\,(t-t')}\,\mathrm{d}\omega \right) \hat{a}(t')\,\mathrm{d}t' \\
& + \sum_{j=1}^{n} \mathrm{i}\,|\kappa|^2\,\bar{a}_j\,\mathrm{e}^{-\mathrm{i}\,\omega_j\,t} \int_{-\infty}^{\infty} \frac{1-\mathrm{e}^{-\mathrm{i}\,(t-t_0)\,(\omega-\omega_j)}}{\omega-\omega_j}\,\mathrm{d}\omega \\
& - \mathrm{i}\,\kappa \int_{-\infty}^{\infty} \mathrm{e}^{-\mathrm{i}\,\omega\,(t-t_0)}\,\hat{d}(\omega,t_0)\,\mathrm{d}\omega \\
\\
=\ & -\pi\,|\kappa|^2\,\hat{a}(t) + \sum_{j=1}^{n} \mathrm{i}\,|\kappa|^2\,\bar{a}_j\,\mathrm{e}^{-\mathrm{i}\,\omega_j\,t} \int_{-\infty}^{\infty} \frac{1-\mathrm{e}^{-\mathrm{i}\,(t-t_0)\,(\omega-\omega_j)}}{\omega-\omega_j}\,\mathrm{d}\omega \\
& - \sqrt{2\,\pi}\,\mathrm{i}\,\kappa\,\hat{d}_{\mathrm{in}}(t) .
\end{aligned}$$

The integral in the summed term can be evaluated as follows,

$$\begin{aligned}
\int_{-\infty}^{\infty} \frac{1-\mathrm{e}^{-\mathrm{i}\,(t-t_0)\,(\omega-\omega_j)}}{\omega-\omega_j}\,\mathrm{d}\omega &= \lim_{x\to\infty} \int_{-x}^{x} \frac{1-\mathrm{e}^{\mathrm{i}\,\theta}}{\theta}\,\mathrm{d}\theta \quad : \quad \theta = -(t-t_0)\,(\omega-\omega_j) \\
&= \lim_{x\to\infty} \int_{-x}^{x} \frac{1-\cos[\theta]}{\theta}\,\mathrm{d}\theta + \lim_{x\to\infty} \mathrm{i} \int_{-x}^{x} \frac{\sin[\theta]}{\theta}\,\mathrm{d}\theta
\end{aligned}$$

and

$$\frac{1-\cos[(-\theta)]}{(-\theta)} = -\frac{1-\cos[\theta]}{\theta} \quad \Rightarrow \quad \int_{-x}^{x} \frac{1-\cos[\theta]}{\theta}\,\mathrm{d}\theta = 0 \;,$$

$$\frac{\sin[(-\theta)]}{(-\theta)} = \frac{\sin[\theta]}{\theta} \quad \Rightarrow \quad \int_{-x}^{x} \frac{\sin[\theta]}{\theta}\,\mathrm{d}\theta = 2\int_{0}^{x} \frac{\sin[\theta]}{\theta}\,\mathrm{d}\theta \;.$$

This non-zero integral is the Sine Integral,

$$\int_{0}^{x} \frac{\sin[\theta]}{\theta}\,\mathrm{d}\theta = \mathrm{Si}[x] \;,$$

which has known limit

$$\lim_{x\to\infty} \mathrm{Si}[x] = \frac{\pi}{2} \;.$$

Putting this all together, we find

$$\int_{-\infty}^{\infty} \frac{1-\mathrm{e}^{-\mathrm{i}\,(t-t_0)\,(\omega-\omega_j)}}{\omega-\omega_j}\,\mathrm{d}\omega = \mathrm{i}\,\pi \;,$$

and

$$\sum_{q} -\mathrm{i}\,\kappa_q\,\hat{d}_q(t) \approx \; -\pi\,|\kappa|^2\,\hat{a}(t) + \sum_{j=1}^{n} -\pi\,|\kappa|^2\,\bar{a}_j\,\mathrm{e}^{-\mathrm{i}\,\omega_j\,t} - \sqrt{2\,\pi}\,\mathrm{i}\,\kappa\,\hat{d}_{\mathrm{in}}(t) \;.$$

Putting this into our equation of motion for $\hat{a}(t)$ and combining terms,

$$\begin{aligned}\frac{\mathrm{d}}{\mathrm{d}t}\hat{a}(t) = & -\mathrm{i}\,\omega_{\mathrm{o}}\,\hat{a}(t) - \frac{|\gamma|}{2}\,\hat{a}(t) - \sqrt{\gamma}\,\hat{d}_{\mathrm{in}}(t) \\ & + \sum_{l} -\mathrm{i}\,L_l\,\mathrm{e}^{-\mathrm{i}\,\omega_l\,t} + \sum_{j=1}^{n} -\left(\mathrm{i}\,\left(\omega_{\mathrm{o}} - \omega_j\right) + \frac{|\gamma|}{2}\right)\,\bar{a}_j\,\mathrm{e}^{-\mathrm{i}\,\omega_j\,t}\end{aligned}$$

$$\begin{aligned}\overset{\text{(I.26)}}{=} & -\mathrm{i}\,\omega_{\mathrm{o}}\,\hat{a}(t) - \frac{|\gamma|}{2}\,\hat{a}(t) - \sqrt{\gamma}\,\hat{d}_{\mathrm{in}}(t) + \sum_{l} -\mathrm{i}\,L_l\,\mathrm{e}^{-\mathrm{i}\,\omega_l\,t} + \sum_{j=1}^{n} \mathrm{i}\,L_j\,\mathrm{e}^{-\mathrm{i}\,\omega_j\,t}\end{aligned}$$

$$= -\mathrm{i}\,\omega_{\mathrm{o}}\,\hat{a}(t) - \frac{|\gamma|}{2}\,\hat{a}(t) - \sqrt{\gamma}\,\hat{d}_{\mathrm{in}}(t) + \sum_{l>n} -\mathrm{i}\,L_l\,\mathrm{e}^{-\mathrm{i}\,\omega_l\,t}\ ,$$

where the sum is now only over laser drives that were not leveled out by displacement transformations.

Note that the same result is obtained by making the mapping $\hat{a} \mapsto \hat{a} + \sum_{j=1}^{n} \bar{a}_j\,\mathrm{e}^{-\mathrm{i}\,\omega_j\,t}$ to (I.24)

$$\begin{aligned}\frac{\mathrm{d}}{\mathrm{d}t}\left(\hat{a}(t) + \sum_{j=1}^{n} \bar{a}_j\,\mathrm{e}^{-\mathrm{i}\,\omega_j\,t}\right) = & -\mathrm{i}\,\omega_{\mathrm{o}}\,\left(\hat{a}(t) + \sum_{j=1}^{n} \bar{a}_j\,\mathrm{e}^{-\mathrm{i}\,\omega_j\,t}\right) - \frac{|\gamma|}{2}\,\left(\hat{a}(t) + \sum_{j=1}^{n} \bar{a}_j\,\mathrm{e}^{-\mathrm{i}\,\omega_j\,t}\right) \\ & + \sum_{l} -\mathrm{i}\,L_l\,\mathrm{e}^{-\mathrm{i}\,\omega_l\,t} - \sqrt{\gamma}\,\hat{d}_{\mathrm{in}}(t)\ ,\end{aligned}$$

$$\begin{aligned}\Rightarrow \quad \frac{\mathrm{d}}{\mathrm{d}t}\hat{a}(t) = & -\mathrm{i}\,\omega_{\mathrm{o}}\,\hat{a}(t) - \frac{|\gamma|}{2}\,\hat{a}(t) - \sqrt{\gamma}\,\hat{d}_{\mathrm{in}}(t) \\ & + \sum_{l} -\mathrm{i}\,L_l\,\mathrm{e}^{-\mathrm{i}\,\omega_l\,t} + \sum_{j=1}^{n} -\left(\mathrm{i}\,\left(\omega_{\mathrm{o}} - \omega_j\right) + \frac{|\gamma|}{2}\right)\,\bar{a}_j\,\mathrm{e}^{-\mathrm{i}\,\omega_j\,t}\ .\end{aligned}$$

I.6.1 Number operator

We can also explore some properties of the number operator $\hat{a}^\dagger\,\hat{a}$ in the non-rotating frame. The time derivative is

$$\frac{\mathrm{d}}{\mathrm{d}t}\hat{a}^\dagger(t)\,\hat{a}(t) = \left(\frac{\mathrm{d}}{\mathrm{d}t}\hat{a}^\dagger(t)\right)\,\hat{a}(t) + \hat{a}^\dagger\,\left(\frac{\mathrm{d}}{\mathrm{d}t}\hat{a}(t)\right) = \mathrm{e}^{\frac{\mathrm{i}}{\hbar}\hat{H}\,t}\,\left[\hat{a}^\dagger\,\hat{a}, -\frac{\mathrm{i}}{\hbar}\hat{H}\right]\,\mathrm{e}^{-\frac{\mathrm{i}}{\hbar}\hat{H}\,t}$$

$$= \sum_l \Big(-\mathrm{i}\,L_l\,\mathrm{e}^{-\mathrm{i}\,\omega_l\,t}\,\hat{a}^\dagger(t) + \mathrm{i}\,L_l^*\,\mathrm{e}^{\mathrm{i}\,\omega_l\,t}\,\hat{a}(t)\Big)$$
$$- |\gamma|\,\hat{a}^\dagger(t)\,\hat{a}(t) - \sqrt{\gamma}\,\hat{a}^\dagger(t)\,\hat{d}_{\mathrm{in}}(t) - \sqrt{\gamma^*}\,\hat{a}(t)\,\hat{d}_{\mathrm{in}}^\dagger(t)\ .$$

Using (I.25) we have, for $\hat{d}_{\mathrm{in}} = 0$ and $C = 0$,

$$\hat{a}^\dagger(t)\,\hat{a}(t) = \sum_l \frac{|L_l|^2}{(\omega_{\mathrm{o}} - \omega_l)^2 + \frac{|\gamma|^2}{4}} + \sum_l \sum_{k\neq l} \frac{L_l^*\,L_k\,\mathrm{e}^{\mathrm{i}\,(\omega_l - \omega_k)\,t}}{\left(-\mathrm{i}\,(\omega_{\mathrm{o}} - \omega_l)\,\frac{|\gamma|}{2}\right)\,\left(\mathrm{i}\,(\omega_{\mathrm{o}} - \omega_k)\,\frac{|\gamma|}{2}\right)}\ .$$

If there is only one laser drive, there is a steady state solution with $\frac{\mathrm{d}}{\mathrm{d}t}\hat{a}^\dagger(t)\,\hat{a}(t) = 0$.

I.7 Coupled baths

Consider the case of two coupled baths, perhaps representing two coupled ports,

$$\hat{H} = \sum_i \hbar\,\omega_i\,\hat{d}_i^\dagger\,\hat{d}_i + \sum_j \hbar\,\omega_j\,\hat{e}_j^\dagger\,\hat{e}_j + \sum_{i,j} \hbar\,\left(\kappa\,\hat{d}_i\,\hat{e}_j^\dagger + \kappa^*\,\hat{d}_i^\dagger\,\hat{e}_j\right)\ ,$$

we have

$$\frac{\mathrm{d}}{\mathrm{d}t}\hat{d}_i(t) = \mathrm{e}^{\frac{\mathrm{i}}{\hbar}\hat{H}\,t}\,\left[\hat{d}_i, -\frac{\mathrm{i}}{\hbar}\hat{H}\right]\,\mathrm{e}^{-\frac{\mathrm{i}}{\hbar}\hat{H}\,t} = -\mathrm{i}\,\omega_i\,\hat{d}_i(t) - \mathrm{i}\,\kappa^*\,\sum_j \hat{e}_j(t)\ ,$$

$$\frac{\mathrm{d}}{\mathrm{d}t}\hat{e}_i(t) = \mathrm{e}^{\frac{\mathrm{i}}{\hbar}\hat{H}\,t}\,\left[\hat{e}_i, -\frac{\mathrm{i}}{\hbar}\hat{H}\right]\,\mathrm{e}^{-\frac{\mathrm{i}}{\hbar}\hat{H}\,t} = -\mathrm{i}\,\omega_i\,\hat{e}_i(t) - \mathrm{i}\,\kappa\,\sum_j \hat{d}_j(t)\ .$$

In the continuum limit this becomes

$$\frac{\mathrm{d}}{\mathrm{d}t}\hat{d}(\omega,t) = -\,\mathrm{i}\,\omega\,\hat{d}(\omega,t) - \mathrm{i}\,\kappa^*\,\int_{-\infty}^{\infty}\hat{e}(\Omega,t)\,\mathrm{d}\Omega\ ,$$

$$\frac{\mathrm{d}}{\mathrm{d}t}\hat{e}(\omega,t) = -\,\mathrm{i}\,\omega\,\hat{e}(\omega,t) - \mathrm{i}\,\kappa\,\int_{-\infty}^{\infty}\hat{d}(\Omega,t)\,\mathrm{d}\Omega\ ,$$

with solutions

$$\hat{d}(\omega,t) = -\,\mathrm{i}\,\kappa^*\,\int_{t_0}^{t}\mathrm{e}^{-\mathrm{i}\,\omega\,(t-t')}\left(\int_{-\infty}^{\infty}\hat{e}(\Omega,t')\,\mathrm{d}\Omega\right)\mathrm{d}\,t' + \mathrm{e}^{-\mathrm{i}\,\omega\,(t-t_0)}\,\hat{d}(\omega,t_0)\ ,$$

$$\hat{e}(\omega,t) = -\,\mathrm{i}\,\kappa\,\int_{t_0}^{t}\mathrm{e}^{-\mathrm{i}\,\omega\,(t-t')}\left(\int_{-\infty}^{\infty}\hat{d}(\Omega,t')\,\mathrm{d}\Omega\right)\mathrm{d}\,t' + \mathrm{e}^{-\mathrm{i}\,\omega\,(t-t_0)}\,\hat{e}(\omega,t_0)\ .$$

As before we define,

$$\hat{d}_{\rm in}(t) = \frac{1}{\sqrt{2\,\pi}} \int_{-\infty}^{\infty} {\rm e}^{{\rm i}\,\omega\,(t-t_0)}\,\hat{d}(\omega,t_0)\,{\rm d}\omega\ , \qquad \hat{d}_{\rm out}(t) = \frac{1}{\sqrt{2\,\pi}} \int_{-\infty}^{\infty} {\rm e}^{{\rm i}\,\omega\,(t_1-t)}\,\hat{d}(\omega,t_1)\,{\rm d}\omega\ ,$$

$$\hat{e}_{\rm in}(t) = \frac{1}{\sqrt{2\,\pi}} \int_{-\infty}^{\infty} {\rm e}^{{\rm i}\,\omega\,(t-t_0)}\,\hat{e}(\omega,t_0)\,{\rm d}\omega\ , \qquad \hat{e}_{\rm out}(t) = \frac{1}{\sqrt{2\,\pi}} \int_{-\infty}^{\infty} {\rm e}^{{\rm i}\,\omega\,(t_1-t)}\,\hat{e}(\omega,t_1)\,{\rm d}\omega\ .$$

Substituting in our solutions we find

$$\hat{d}_{\rm out}(t) - \hat{d}_{\rm in}(t) = -\,{\rm i}\,\kappa^*\,\sqrt{2\,\pi}\,\int_{-\infty}^{\infty} \hat{e}(\Omega,t)\,{\rm d}\Omega\ ,$$

$$\hat{e}_{\rm out}(t) - \hat{e}_{\rm in}(t) = -\,{\rm i}\,\kappa\,\sqrt{2\,\pi}\,\int_{-\infty}^{\infty} \hat{d}(\Omega,t)\,{\rm d}\Omega\ ,$$

$$\int_{-\infty}^{\infty} \hat{d}(\Omega,t)\,{\rm d}\Omega = -\,{\rm i}\,\kappa^*\,\pi\,\int_{-\infty}^{\infty} \hat{e}(\Omega,t)\,{\rm d}\Omega + \hat{d}_{\rm in}(t)\ ,$$

$$\int_{-\infty}^{\infty} \hat{e}(\Omega,t)\,{\rm d}\Omega = -\,{\rm i}\,\kappa\,\pi\,\int_{-\infty}^{\infty} \hat{d}(\Omega,t)\,{\rm d}\Omega + \hat{e}_{\rm in}(t)\ ,$$

and combining everything we have

$$\hat{d}_{\rm out}(t) - \hat{d}_{\rm in}(t) = -\,{\rm i}\,\kappa^*\,\pi\,\Big(\hat{e}_{\rm out}(t) + \hat{e}_{\rm in}(t)\Big)\ ,$$

$$\hat{e}_{\rm out}(t) - \hat{e}_{\rm in}(t) = -\,{\rm i}\,\kappa\,\pi\,\Big(\hat{d}_{\rm out}(t) + \hat{d}_{\rm in}(t)\Big)\ .$$

I.7.1 Single input

If we have only a single input, $\hat{e}_{\rm in}(t) = 0$, we find

$$\hat{d}_{\rm out}(t) = \frac{1 - |\kappa|^2\,\pi^2}{1 + |\kappa|^2\,\pi^2}\,\hat{d}_{\rm in}(t)\ ,$$

$$\hat{e}_{\rm out}(t) = \frac{-{\rm i}\,\kappa\,2\,\pi}{1 + |\kappa|^2\,\pi^2}\,\hat{d}_{\rm in}(t)\ ,$$

with perfect transfer happening at $|\kappa| = 1/\pi$.

APPENDIX J

Quantum optomechanics

This appendix goes through optomechanical interactions providing various derivations [11, 12, 138, 139, 225, 230, 231, 234, 235].

J.1 Optomechanic hamiltonian

The first order coupled optomechanical Hamiltonian is (C.3)

$$\hat{H}_{\rm sys} = \hbar\,\omega_{\rm o}\left(\hat{a}^\dagger\,\hat{a} + \frac{1}{2}\right) + \hbar\,\omega_{\rm m}\left(\hat{b}^\dagger\,\hat{b} + \frac{1}{2}\right) + \hbar\,g_{\rm om}\left(\hat{a}^\dagger\,\hat{a} + \frac{1}{2}\right)\left(\hat{b}^\dagger + \hat{b}\right)\,. \tag{J.1}$$

J.2 Coupling to heat bath

Following the same procedure as App. I, we have heat baths for optics and mechanics,

$$\hat{H}_{\substack{\rm optic\\ \rm bath}} = \sum_q \hbar\,\omega_q\,\hat{d}_q^\dagger\,\hat{d}_q\,, \qquad \hat{H}_{\substack{\rm mech\\ \rm bath}} = \sum_q \hbar\,\omega_q\,\hat{e}_q^\dagger\,\hat{e}_q\,,$$

$$\hat{H}_{\substack{\rm optic\\ \rm bath\\ \rm int}} = \sum_q \hbar\left(\kappa_q\,\hat{a}^\dagger + \kappa_q^*\,\hat{a}\right)\left(\hat{d}_q^\dagger + \hat{d}_q\right)\,, \qquad \hat{H}_{\substack{\rm mech\\ \rm bath\\ \rm int}} = \sum_q \hbar\left(\lambda_q\,\hat{b}^\dagger + \lambda_q^*\,\hat{b}\right)\left(\hat{e}_q^\dagger + \hat{e}_q\right)\,.$$

The full Hamiltonian is

$$\hat{H} = \hat{H}_{\rm sys} + \underbrace{\hat{H}_{\substack{\rm optic\\ \rm bath}} + \hat{H}_{\substack{\rm mech\\ \rm bath}}}_{\hat{H}_{\rm bath}} + \underbrace{\hat{H}_{\substack{\rm optic\\ \rm bath\\ \rm int}} + \hat{H}_{\substack{\rm mech\\ \rm bath\\ \rm int}}}_{\hat{H}_{\rm bath\,int}}\,,$$

noting that

$$\left[\hat{H}_{\rm sys}, \hat{H}_{\rm bath}\right] = 0 \,, \qquad\qquad \left[\hat{H}_{\substack{\rm optic \\ \rm bath}}, \hat{H}_{\substack{\rm mech \\ \rm bath}}\right] = 0 \,.$$

J.2.1 Rotating wave approximation

Move to the interaction picture with $\hat{U}(t) = \exp\left[-\frac{\rm i}{\hbar}(\hat{H}_{\rm sys} + \hat{H}_{\rm bath})\,t\right]$,

$$\begin{aligned}
\hat{H}^{\rm I}_{\substack{\rm bath \\ \rm int}}(t) &= \hat{U}^\dagger(t)\,\hat{H}_{\substack{\rm bath \\ \rm int}}\,\hat{U}(t) \\
&= \sum_q \hbar\,{\rm e}^{\frac{\rm i}{\hbar}\hat{H}_{\rm sys}\,t}\,\left(\kappa_q\,\hat{a}^\dagger + \kappa_q^*\,\hat{a}\right)\,{\rm e}^{-\frac{\rm i}{\hbar}\hat{H}_{\rm sys}\,t}\,{\rm e}^{\frac{\rm i}{\hbar}\hat{H}_{\rm ob}\,t}\,\left(\hat{d}_q^\dagger + \hat{d}_q\right)\,{\rm e}^{-\frac{\rm i}{\hbar}\hat{H}_{\rm ob}\,t} \\
&\quad + \sum_q \hbar\,{\rm e}^{\frac{\rm i}{\hbar}\hat{H}_{\rm sys}\,t}\,\left(\lambda_q\,\hat{b}^\dagger + \lambda_q^*\,\hat{b}\right)\,{\rm e}^{-\frac{\rm i}{\hbar}\hat{H}_{\rm sys}\,t}\,{\rm e}^{\frac{\rm i}{\hbar}\hat{H}_{\rm mb}\,t}\,\left(\hat{e}_q^\dagger + \hat{e}_q\right)\,{\rm e}^{-\frac{\rm i}{\hbar}\hat{H}_{\rm mb}\,t} \,.
\end{aligned}$$

Following BCH,

$$\begin{aligned}
{\rm e}^{\frac{\rm i}{\hbar}\hat{H}_{\rm sys}\,t}\,\hat{a}\,{\rm e}^{-\frac{\rm i}{\hbar}\hat{H}_{\rm sys}\,t} &= \hat{a} + \left[\hat{a}, -\frac{\rm i}{\hbar}\hat{H}_{\rm sys}\,t\right] + \frac{1}{2}\left[\left[\hat{a}, -\frac{\rm i}{\hbar}\hat{H}_{\rm sys}\,t\right], -\frac{\rm i}{\hbar}\hat{H}_{\rm sys}\,t\right] + \cdots \\
&= \hat{a} + \left[\hat{a}, {\rm i}\,t\,\hat{a}^\dagger\,\hat{a}\,\left(-\omega_{\rm o} - g_{\rm om}\,\left(\hat{b}^\dagger + \hat{b}\right)\right)\right] + \cdots \\
&= \hat{a} + \hat{a}\,{\rm i}\,t\,\left(-\omega_{\rm o} - g_{\rm om}\,\left(\hat{b}^\dagger + \hat{b}\right)\right) + \hat{a}\frac{({\rm i}\,t)^2}{2}\,\left(-\omega_{\rm o} - g_{\rm om}\,\left(\hat{b}^\dagger + \hat{b}\right)\right)^2 + \cdots \\
&= \hat{a}\,{\rm e}^{-{\rm i}\,\omega_{\rm o}\,t - {\rm i}\,g_{\rm om}\,\left(\hat{b}^\dagger + \hat{b}\right)t} \,,
\end{aligned}$$

$$\begin{aligned}
{\rm e}^{\frac{\rm i}{\hbar}\hat{H}_{\rm sys}\,t}\,\hat{b}\,{\rm e}^{-\frac{\rm i}{\hbar}\hat{H}_{\rm sys}\,t} &= \hat{b} + \left[\hat{b}, -\frac{\rm i}{\hbar}\hat{H}_{\rm sys}\,t\right] + \frac{1}{2}\left[\left[\hat{b}, -\frac{\rm i}{\hbar}\hat{H}_{\rm sys}\,t\right], -\frac{\rm i}{\hbar}\hat{H}_{\rm sys}\,t\right] + \cdots \\
&= \hat{b} + \left[\hat{b}, -{\rm i}\,\omega_{\rm m}\,t\,\hat{b}^\dagger\,\hat{b} - {\rm i}\,g_{\rm om}\,t\,\hat{a}^\dagger\,\hat{a}\,\left(\hat{b}^\dagger + \hat{b}\right)\right] + \cdots \\
&= \hat{b} + \hat{b}\,(-{\rm i}\,\omega_{\rm m}\,t) - {\rm i}\,g_{\rm om}\,t\,\hat{a}^\dagger\,\hat{a} + \frac{\hat{b}}{2}(-{\rm i}\,\omega_{\rm m}\,t)^2 - {\rm i}\,g_{\rm om}\,t\,\hat{a}^\dagger\,\hat{a}\,(-{\rm i}\,\omega_{\rm m}\,t) + \cdots \\
&= \left(\hat{b} - {\rm i}\,g_{\rm om}\,t\,\hat{a}^\dagger\,\hat{a}\right)\,{\rm e}^{-{\rm i}\,\omega_{\rm m}\,t} \,,
\end{aligned}$$

$$
\begin{aligned}
\mathrm{e}^{\frac{\mathrm{i}}{\hbar}\hat{H}_{\mathrm{sys}}\,t}\,\hat{b}^\dagger\,\mathrm{e}^{-\frac{\mathrm{i}}{\hbar}\hat{H}_{\mathrm{sys}}\,t} &= \hat{b}^\dagger + \left[\hat{b}^\dagger, -\mathrm{i}\,\omega_{\mathrm{m}}\,t\,\hat{b}^\dagger\,\hat{b} - \mathrm{i}\,g_{\mathrm{om}}\,t\,\hat{a}^\dagger\,\hat{a}\,\left(\hat{b}^\dagger + \hat{b}\right)\right] + \cdots \\
&= \hat{b}^\dagger + \hat{b}^\dagger\,(\mathrm{i}\,\omega_{\mathrm{m}}\,t) + \mathrm{i}\,g_{\mathrm{om}}\,t\,\hat{a}^\dagger\,\hat{a} + \frac{\hat{b}}{2}(\mathrm{i}\,\omega_{\mathrm{m}}\,t)^2 + \mathrm{i}\,g_{\mathrm{om}}\,t\,\hat{a}^\dagger\,\hat{a}\,(\mathrm{i}\,\omega_{\mathrm{m}}\,t) + \cdots \\
&= \left(\hat{b}^\dagger + \mathrm{i}\,g_{\mathrm{om}}\,t\,\hat{a}^\dagger\,\hat{a}\right)\,\mathrm{e}^{\mathrm{i}\,\omega_{\mathrm{m}}\,t}\ ,
\end{aligned}
$$

gives us

$$
\begin{aligned}
\hat{H}^{\mathrm{I}}_{\substack{\mathrm{bath}\\\mathrm{int}}}(t) = \sum_q \hbar \Bigg(& \kappa_q\,\hat{a}^\dagger\,\mathrm{e}^{\,\mathrm{i}\,\omega_{\mathrm{o}}\,t + \mathrm{i}\,g_{\mathrm{om}}\left(\hat{b}^\dagger + \hat{b}\right)t} + \kappa_q^*\,\hat{a}\,\mathrm{e}^{\,-\mathrm{i}\,\omega_{\mathrm{o}}\,t - \mathrm{i}\,g_{\mathrm{om}}\left(\hat{b}^\dagger + \hat{b}\right)t}\Bigg) \\
& \times \left(\hat{d}_q^\dagger\,\mathrm{e}^{\mathrm{i}\,\omega_q\,t} + \hat{d}_q\,\mathrm{e}^{-\mathrm{i}\,\omega_q\,t}\right) \\
& + \sum_q \hbar \left(\lambda_q \left(\hat{b}^\dagger + \mathrm{i}\,g_{\mathrm{om}}\,t\,\hat{a}^\dagger\,\hat{a}\right)\,\mathrm{e}^{\mathrm{i}\,\omega_{\mathrm{m}}\,t} + \lambda_q^* \left(\hat{b} - \mathrm{i}\,g_{\mathrm{om}}\,t\,\hat{a}^\dagger\,\hat{a}\right)\,\mathrm{e}^{-\mathrm{i}\,\omega_{\mathrm{m}}\,t}\right) \\
& \times \left(\hat{e}_q^\dagger\,\mathrm{e}^{\mathrm{i}\,\omega_q\,t} + \hat{e}_q\,\mathrm{e}^{-\mathrm{i}\,\omega_q\,t}\right)\ .
\end{aligned}
$$

Using the rotating wave approximation,

$$
\begin{aligned}
\hat{H}^{\mathrm{I}}_{\substack{\mathrm{bath}\\\mathrm{int}}}(t) \approx & \sum_q \hbar \Bigg(\kappa_q\,\hat{a}^\dagger\,\hat{d}_q\,\mathrm{e}^{\,\mathrm{i}\,(\omega_{\mathrm{o}} - \omega_q)\,t + \mathrm{i}\,g_{\mathrm{om}}\left(\hat{b}^\dagger + \hat{b}\right)t} + \kappa_q^*\,\hat{a}\,\hat{d}_q^\dagger\,\mathrm{e}^{\,-\mathrm{i}\,(\omega_{\mathrm{o}} - \omega_q)\,t - \mathrm{i}\,g_{\mathrm{om}}\left(\hat{b}^\dagger + \hat{b}\right)t}\Bigg) \\
& + \sum_q \hbar \Bigg(\lambda_q \left(\hat{b}^\dagger + \mathrm{i}\,g_{\mathrm{om}}\,t\,\hat{a}^\dagger\,\hat{a}\right)\,\hat{e}_q\,\mathrm{e}^{\mathrm{i}\,(\omega_{\mathrm{m}} - \omega_q)\,t} \\
& \qquad + \lambda_q^* \left(\hat{b} - \mathrm{i}\,g_{\mathrm{om}}\,t\,\hat{a}^\dagger\,\hat{a}\right)\,\hat{e}_q^\dagger\,\mathrm{e}^{-\mathrm{i}\,(\omega_{\mathrm{m}} - \omega_q)\,t}\Bigg)\ .
\end{aligned}
$$

This is equivalent to

$$
\hat{H}_{\substack{\mathrm{optic}\\\mathrm{bath}\\\mathrm{int}}} \approx \sum_q \hbar \left(\kappa_q\,\hat{a}^\dagger\,\hat{d}_q + \kappa_q^*\,\hat{a}\,\hat{d}_q^\dagger\right)\ , \qquad \hat{H}_{\substack{\mathrm{mech}\\\mathrm{bath}\\\mathrm{int}}} \approx \sum_q \hbar \left(\lambda_q\,\hat{b}^\dagger\,\hat{e}_q + \lambda_q^*\,\hat{b}\,\hat{e}_q^\dagger\right)\ .
$$

J.2.2 Equations of motion

With the standard approximated bath interaction, and $\gamma_{\rm o} = -2\,\pi\,\kappa^2$, $\gamma_{\rm m} = -2\,\pi\,\lambda^2$, the quantum Langevin equations are

$$\frac{\mathrm{d}}{\mathrm{d}t}\hat{a}(t) = \mathrm{e}^{\frac{\mathrm{i}}{\hbar}\hat{H}\,t}\,\left[\hat{a}, -\frac{\mathrm{i}}{\hbar}\hat{H}_{\rm sys}\right]\,\mathrm{e}^{-\frac{\mathrm{i}}{\hbar}\hat{H}\,t} - \frac{|\gamma_{\rm o}|}{2}\hat{a}(t) - \sqrt{\gamma_{\rm o}}\,\hat{d}_{\rm in}(t)\;,$$

$$\frac{\mathrm{d}}{\mathrm{d}t}\hat{b}(t) = \mathrm{e}^{\frac{\mathrm{i}}{\hbar}\hat{H}\,t}\,\left[\hat{b}, -\frac{\mathrm{i}}{\hbar}\hat{H}_{\rm sys}\right]\,\mathrm{e}^{-\frac{\mathrm{i}}{\hbar}\hat{H}\,t} - \frac{|\gamma_{\rm m}|}{2}\hat{b}(t) - \sqrt{\gamma_{\rm m}}\,\hat{e}_{\rm in}(t)\;.$$

Now

$$\begin{aligned}\left[\hat{a}, -\frac{\mathrm{i}}{\hbar}\hat{H}_{\rm sys}\right] &= \left[\hat{a}, -\mathrm{i}\,\omega_{\rm o}\,\hat{a}^\dagger\,\hat{a} - \mathrm{i}\,g_{\rm om}\,\hat{a}^\dagger\,\hat{a}\,\left(\hat{b}^\dagger + \hat{b}\right)\right]\\ &= -\,\mathrm{i}\,\omega_{\rm o}\,\hat{a} - \mathrm{i}\,g_{\rm om}\,\hat{a}\,\left(\hat{b}^\dagger + \hat{b}\right)\;,\end{aligned}$$

$$\begin{aligned}\left[\hat{b}, -\frac{\mathrm{i}}{\hbar}\hat{H}_{\rm sys}\right] &= \left[\hat{b}, -\mathrm{i}\,\omega_{\rm m}\,\hat{b}^\dagger\,\hat{b} - \mathrm{i}\,g_{\rm om}\,\left(\hat{a}^\dagger\,\hat{a} + \frac{1}{2}\right)\left(\hat{b}^\dagger + \hat{b}\right)\right]\\ &= -\,\mathrm{i}\,\omega_{\rm m}\,\hat{b} - \mathrm{i}\,g_{\rm om}\left(\hat{a}^\dagger\,\hat{a} + \frac{1}{2}\right)\;,\end{aligned}$$

thus

$$\frac{\mathrm{d}}{\mathrm{d}t}\hat{a}(t) = -\,\mathrm{i}\,\omega_{\rm o}\,\hat{a}(t) - \mathrm{i}\,g_{\rm om}\,\hat{a}(t)\,\left(\hat{b}^\dagger(t) + \hat{b}(t)\right) - \frac{|\gamma_{\rm o}|}{2}\hat{a}(t) - \sqrt{\gamma_{\rm o}}\,\hat{d}_{\rm in}(t)\;, \tag{J.2}$$

$$\frac{\mathrm{d}}{\mathrm{d}t}\hat{b}(t) = -\,\mathrm{i}\,\omega_{\rm m}\,\hat{b}(t) - \mathrm{i}\,g_{\rm om}\left(\hat{a}^\dagger\,\hat{a} + \frac{1}{2}\right) - \frac{|\gamma_{\rm m}|}{2}\hat{b}(t) - \sqrt{\gamma_{\rm m}}\,\hat{e}_{\rm in}(t)\;. \tag{J.3}$$

J.2.3 Laser driven

Including a laser drive adds terms $\hbar\, L\, \hat{a}^\dagger\, \mathrm{e}^{-\mathrm{i}\,\omega_\mathrm{L}\, t} + \hbar\, L^*\, \hat{a}\, \mathrm{e}^{\mathrm{i}\,\omega_\mathrm{L}\, t}$ to the Hamiltonian. Performing a rotation as in Sec. I.4.1,

$$\hat{U}_\mathrm{rot}(t) = \mathrm{e}^{-\mathrm{i}\,\omega_\mathrm{L}\,(\hat{a}^\dagger\,\hat{a} + \frac{1}{2})\,t}\, \mathrm{e}^{-\mathrm{i}\,\omega_\mathrm{L}\,\hat{d}^\dagger\,\hat{d}\,t}\ ,$$

the rotated full Hamiltonian is

$$\begin{aligned}
\hat{H}_\mathrm{rot} = \overbrace{\underbrace{\hbar\,\Delta_\mathrm{o}\,\left(\hat{a}^\dagger\,\hat{a} + \tfrac{1}{2}\right)}_{\hat{H}_\mathrm{optic}} + \underbrace{\hbar\, L\, \hat{a}^\dagger + \hbar\, L^*\, \hat{a}}_{\hat{H}_\mathrm{laser}} + \underbrace{\hbar\,\omega_\mathrm{m}\left(\hat{b}^\dagger\,\hat{b} + \tfrac{1}{2}\right)}_{\hat{H}_\mathrm{mech}} + \underbrace{\hbar\, g_\mathrm{om}\left(\hat{a}^\dagger\,\hat{a} + \tfrac{1}{2}\right)\left(\hat{b}^\dagger + \hat{b}\right)}_{\hat{H}_\mathrm{optomech}}}^{\hat{H}_\mathrm{sys}} \\
+ \underbrace{\sum_q \hbar\,\Delta_q\,\hat{d}_q^\dagger\,\hat{d}_q}_{\substack{\hat{H}_\mathrm{optic} \\ \mathrm{bath}}} + \underbrace{\sum_q \hbar\left(\kappa_q\,\hat{a}^\dagger\,\hat{d}_q + \kappa_q^*\,\hat{a}\,\hat{d}_q^\dagger\right)}_{\substack{\hat{H}_\mathrm{optic} \\ \mathrm{bath} \\ \mathrm{int}}} \\
+ \underbrace{\sum_q \hbar\,\omega_q\,\hat{e}_q^\dagger\,\hat{e}_q}_{\substack{\hat{H}_\mathrm{mech} \\ \mathrm{bath}}} + \underbrace{\sum_q \hbar\left(\lambda_q\,\hat{b}^\dagger\,\hat{e}_q + \lambda_q^*\,\hat{b}\,\hat{e}_q^\dagger\right)}_{\substack{\hat{H}_\mathrm{mech} \\ \mathrm{bath} \\ \mathrm{int}}}\ ,
\end{aligned}$$

where

$$\Delta_\mathrm{o} = \omega_\mathrm{o} - \omega_\mathrm{L}\ , \qquad\qquad \Delta_q = \omega_q - \omega_\mathrm{L}\ .$$

It is important to note that this rotation only affects the operators $\hat{a}$ and $\hat{d}$, it does not provide a relation of the sort $\omega_\mathrm{rot} = \omega - \omega_\mathrm{L}$ in frequency space.

The equations of motion are then

$$\frac{\mathrm{d}}{\mathrm{d}t}\hat{a}(t) = -\mathrm{i}\,\Delta_\mathrm{o}\,\hat{a}(t) - \mathrm{i}\,L - \mathrm{i}\,g_\mathrm{om}\,\hat{a}(t)\left(\hat{b}^\dagger(t) + \hat{b}(t)\right) - \frac{|\gamma_\mathrm{o}|}{2}\hat{a}(t) - \sqrt{\gamma_\mathrm{o}}\,\hat{d}_\mathrm{in}(t)\ ,$$

$$\frac{\mathrm{d}}{\mathrm{d}t}\hat{b}(t) = -\mathrm{i}\,\omega_\mathrm{m}\,\hat{b}(t) - \mathrm{i}\,g_\mathrm{om}\left(\hat{a}^\dagger(t)\,\hat{a}(t) + \frac{1}{2}\right) - \frac{|\gamma_\mathrm{m}|}{2}\hat{b}(t) - \sqrt{\gamma_\mathrm{m}}\,\hat{e}_\mathrm{in}(t)\ .$$

We can find the steady state values where $\frac{\mathrm{d}}{\mathrm{d}t}\hat{a}(t) = \frac{\mathrm{d}}{\mathrm{d}t}\hat{b}(t) = 0$,

$$\hat{a}(t_\mathrm{s}) = \frac{-\mathrm{i}\,L - \sqrt{\gamma_\mathrm{o}}\,\hat{d}_\mathrm{in}(t_\mathrm{s})}{\mathrm{i}\,\Delta_\mathrm{o} + \frac{|\gamma_\mathrm{o}|}{2} + \mathrm{i}\,g_\mathrm{om}\left(\hat{b}^\dagger(t_\mathrm{s}) + \hat{b}(t_\mathrm{s})\right)}\ ,$$

$$\hat{b}(t_\mathrm{s}) = \frac{-\mathrm{i}\,g_\mathrm{om}\left(\hat{a}^\dagger(t_\mathrm{s})\,\hat{a}(t_\mathrm{s}) + \frac{1}{2}\right) - \sqrt{\gamma_\mathrm{m}}\,\hat{e}_\mathrm{in}(t_\mathrm{s})}{\mathrm{i}\,\omega_\mathrm{m} + \frac{|\gamma_\mathrm{m}|}{2}}\ .$$

Given that we have a steady state occupancy, let's backward transform from the coherent states (i.e. $|\bar{a}\rangle \mapsto |0\rangle$),

$$|\psi\rangle \mapsto \hat{D}_{\hat{a}}(\bar{a})^\dagger\,\hat{D}_{\hat{b}}(\bar{b})^\dagger\ |\psi\rangle\ , \qquad \hat{D}_{\hat{a}}(\bar{a}) = \mathrm{e}^{\bar{a}\,\hat{a}^\dagger - \bar{a}^*\,\hat{a}}\ , \qquad \hat{D}_{\hat{b}}(\bar{b}) = \mathrm{e}^{\bar{b}\,\hat{b}^\dagger - \bar{b}^*\,\hat{b}}\ ,$$

$$\begin{aligned}\Rightarrow \hat{H} &\mapsto \hat{D}_{\hat{b}}(\bar{b})^\dagger\,\hat{D}_{\hat{a}}(\bar{a})^\dagger\left(\hat{H} - \mathrm{i}\,\hbar\,\frac{\partial}{\partial t}\right)\hat{D}_{\hat{a}}(\bar{a})\,\hat{D}_{\hat{b}}(\bar{b}) \\ &\mapsto \hat{D}_{\hat{a}}(\bar{a})^\dagger\,\hat{D}_{\hat{b}}(\bar{b})^\dagger\,\hat{H}\,\hat{D}_{\hat{a}}(\bar{a})\,\hat{D}_{\hat{b}}(\bar{b})\ ,\end{aligned}$$

$$\Rightarrow \quad \hat{a} \mapsto \hat{a} + \bar{a}\ , \qquad\qquad \hat{b} \mapsto \hat{b} + \bar{b}\ ,$$

where $\hat{a}$ and $\hat{b}$ are now fluctuations on a background $\bar{a}, \bar{b} \in \mathbb{C}$.

Applying this transform to our equations of motion,

$$\frac{\mathrm{d}}{\mathrm{d}t}\hat{a}(t) = \left(-\mathrm{i}\,\Delta_\mathrm{o} - \frac{|\gamma_\mathrm{o}|}{2} - \mathrm{i}\,g_\mathrm{om}\left(\hat{b}^\dagger(t) + \hat{b}(t) + \bar{b} + \bar{b}^*\right)\right)\left(\hat{a}(t) + \bar{a}\right) - \mathrm{i}\,L - \sqrt{\gamma_\mathrm{o}}\,\hat{d}_\mathrm{in}(t)\ ,$$

$$\frac{\mathrm{d}}{\mathrm{d}t}\hat{b}(t) = \left(-\mathrm{i}\,\omega_\mathrm{m} - \frac{|\gamma_\mathrm{m}|}{2}\right)\left(\hat{b}(t) + \bar{b}\right) - \mathrm{i}\,g_\mathrm{om}\left(\hat{a}^\dagger(t) + \bar{a}^*\right)\left(\hat{a}(t) + \bar{a}\right) - \frac{\mathrm{i}\,g_\mathrm{om}}{2} - \sqrt{\gamma_\mathrm{m}}\,\hat{e}_\mathrm{in}(t)\ .$$

For a large background (strong laser drive) and thus small $\hat{a}(t) \ll \bar{a}$ and $\hat{b}(t) \ll \bar{b}$, we can linearize to first order in $\hat{a}(t)$, $\hat{b}(t)$,

$$\begin{aligned}\frac{\mathrm{d}}{\mathrm{d}t}\hat{a}(t) = {} & \left(-\mathrm{i}\,\Delta_\mathrm{o} - \frac{|\gamma_\mathrm{o}|}{2} - \mathrm{i}\,g_\mathrm{om}\left(\bar{b} + \bar{b}^*\right)\right)\hat{a}(t) - \mathrm{i}\,g_\mathrm{om}\,\bar{a}\left(\hat{b}^\dagger(t) + \hat{b}(t)\right) - \sqrt{\gamma_\mathrm{o}}\,\hat{d}_\mathrm{in}(t) \\ & + \left(-\mathrm{i}\,\Delta_\mathrm{o} - \frac{|\gamma_\mathrm{o}|}{2} - \mathrm{i}\,g_\mathrm{om}\left(\bar{b} + \bar{b}^*\right)\right)\bar{a} - \mathrm{i}\,L + \mathcal{O}\left[\hat{a}(t)\,\hat{b}(t)\right]\ ,\end{aligned}$$

$$\begin{aligned}\frac{\mathrm{d}}{\mathrm{d}t}\hat{b}(t) = {} & \left(-\mathrm{i}\,\omega_\mathrm{m} - \frac{|\gamma_\mathrm{m}|}{2}\right)\hat{b}(t) - \mathrm{i}\,g_\mathrm{om}\left(\bar{a}\,\hat{a}^\dagger(t) + \bar{a}^*\,\hat{a}(t)\right) - \sqrt{\gamma_\mathrm{m}}\,\hat{e}_\mathrm{in}(t) \\ & + \left(-\mathrm{i}\,\omega_\mathrm{m} - \frac{|\gamma_\mathrm{m}|}{2}\right)\bar{b} - \mathrm{i}\,g_\mathrm{om}\,|\bar{a}|^2 - \frac{\mathrm{i}\,g_\mathrm{om}}{2} + \mathcal{O}\left[\hat{a}\dagger(t)\,\hat{a}(t)\right]\ .\end{aligned}$$

Doing the same transform to our steady state equations, we can define

$$\bar{a} = \frac{-\mathrm{i}\,L}{\mathrm{i}\,\Delta_\mathrm{o} + \frac{|\gamma_\mathrm{o}|}{2} + \mathrm{i}\,g_\mathrm{om}\left(\bar{b}^* + \bar{b}\right)}\ , \tag{J.4}$$

$$\bar{b} = \frac{-\mathrm{i}\,g_\mathrm{om}\left(|\bar{a}|^2 + \frac{1}{2}\right)}{\mathrm{i}\,\omega_\mathrm{m} + \frac{|\gamma_\mathrm{m}|}{2}}\ , \tag{J.5}$$

for $\langle\hat{a}(t)\rangle = \langle\hat{b}(t)\rangle = \langle\hat{d}_\mathrm{in}(t)\rangle = \langle\hat{e}_\mathrm{in}(t)\rangle = 0$. This pair of equations generates a third order polynomial with complicated solutions.

This leaves us with

$$\frac{\mathrm{d}}{\mathrm{d}t}\hat{a}(t) = \left(-\mathrm{i}\,\Delta_\mathrm{o} - \frac{|\gamma_\mathrm{o}|}{2} - \mathrm{i}\,g_\mathrm{om}\left(\bar{b} + \bar{b}^*\right)\right)\hat{a}(t) - \mathrm{i}\,g_\mathrm{om}\,\bar{a}\left(\hat{b}^\dagger(t) + \hat{b}(t)\right) - \sqrt{\gamma_\mathrm{o}}\,\hat{d}_\mathrm{in}(t)$$

$$\frac{\mathrm{d}}{\mathrm{d}t}\hat{b}(t) = \left(-\mathrm{i}\,\omega_\mathrm{m} - \frac{|\gamma_\mathrm{m}|}{2}\right)\hat{b}(t) - \mathrm{i}\,g_\mathrm{om}\left(\bar{a}\,\hat{a}^\dagger(t) + \bar{a}^*\,\hat{a}(t)\right) - \sqrt{\gamma_\mathrm{m}}\,\hat{e}_\mathrm{in}(t)\ .$$

Taking the fourier transform we find

$$\hat{a}(\omega) = \frac{-\mathrm{i}\,g_\mathrm{om}\,\bar{a}\left(\hat{b}^\dagger(\omega) + \hat{b}(\omega)\right) - \sqrt{\gamma_\mathrm{o}}\,\hat{d}(\omega, t_0)}{\mathrm{i}\,(\Delta_\mathrm{om} - \omega) + \frac{|\gamma_\mathrm{o}|}{2}}\ , \tag{J.6}$$

$$\hat{b}(\omega) = \frac{-\mathrm{i}\,g_\mathrm{om}\left(\bar{a}\,\hat{a}^\dagger(\omega) + \bar{a}^*\,\hat{a}(\omega)\right) - \sqrt{\gamma_\mathrm{m}}\,\hat{e}(\omega, t_0)}{\mathrm{i}\,(\omega_\mathrm{m} - \omega) + \frac{|\gamma_\mathrm{m}|}{2}}\ , \tag{J.7}$$

where

$$\Delta_\mathrm{om} = \Delta_\mathrm{o} + g_\mathrm{om}\left(\bar{b}^* + \bar{b}\right) \approx \Delta_\mathrm{o}\ ,$$
$$\omega_\mathrm{om} = \omega_\mathrm{o} + g_\mathrm{om}\left(\bar{b}^* + \bar{b}\right) \approx \omega_\mathrm{o}\ .$$

These equations show us that a strong background optical field enhances the effective optomechanic coupling to be $\bar{a}\,g_\mathrm{om}$.

J.3 Optical spring

From (J.7), we can see that $\hat{b}(\omega)$ is peaked around $\omega = \omega_\mathrm{m}$, whilst $\hat{b}^\dagger(\omega) = \hat{b}(-\omega)^\dagger$ is peaked around $\omega = -\omega_\mathrm{m}$, thus if our mechanical oscillator is sufficiently high quality ($|\gamma_\mathrm{m}| \ll \omega_\mathrm{m}$),

we need only consider one of $\hat{b}(\omega)$ and $\hat{b}^\dagger(\omega)$. From (J.11), we see that $\hat{a}(\omega)$ is peaked around $\omega = \Delta_{\rm om}$ and $\hat{a}^\dagger(\omega) = \hat{a}(-\omega)^\dagger$ is peaked around $\omega = -\Delta_{\rm om}$, but for $\omega \sim \pm\omega_{\rm m}$ (in order to address the mechanics), $|\gamma_{\rm o}| \not\ll |\Delta_{\rm om}|$ and we cannot separately resolve $\hat{a}(\omega)$ and $\hat{a}^\dagger(\omega)$. A high quality optical resonator only ensures $|\gamma_{\rm o}| \ll \omega_{\rm o}$.

Let us first consider $\omega \sim \omega_{\rm m}$, we find from (J.11)

$$\hat{a}(\omega \sim \omega_{\rm m}) = \frac{-{\rm i}\, g_{\rm om}\, \bar{a}\, \hat{b}(\omega) - \sqrt{\gamma_{\rm o}}\, \hat{d}(\omega, t_0)}{{\rm i}\,(\Delta_{\rm om} - \omega) + \frac{|\gamma_{\rm o}|}{2}} \,,$$

$$\hat{a}^\dagger(\omega \sim \omega_{\rm m}) = \frac{{\rm i}\, g_{\rm om}\, \bar{a}^*\, \hat{b}(\omega) - \sqrt{\gamma_{\rm o}^*}\, \hat{d}^\dagger(\omega, t_0)}{-{\rm i}\,(\Delta_{\rm om} + \omega) + \frac{|\gamma_{\rm o}|}{2}} \,.$$

Substituting this into (J.7) we find

$$\left({\rm i}\,(\omega_{\rm m} - \omega) + \frac{|\gamma_{\rm m}|}{2} + \frac{{g_{\rm om}}^2\, |\bar{a}|^2}{{\rm i}\,(\Delta_{\rm om} - \omega) + \frac{|\gamma_{\rm o}|}{2}} - \frac{{g_{\rm om}}^2\, |\bar{a}|^2}{-{\rm i}\,(\Delta_{\rm om} + \omega) + \frac{|\gamma_{\rm o}|}{2}} \right) \hat{b}(\omega \sim \omega_{\rm m})$$
$$= -\sqrt{\gamma_{\rm m}}\, \hat{e}(\omega, t_0) + \frac{{\rm i}\, g_{\rm om}\, \bar{a}^*\, \sqrt{\gamma_{\rm o}}\, \hat{d}(\omega, t_0)}{{\rm i}\,(\Delta_{\rm om} - \omega) + \frac{|\gamma_{\rm o}|}{2}} + \frac{{\rm i}\, g_{\rm om}\, \bar{a}\, \sqrt{\gamma_{\rm o}^*}\, \hat{d}^\dagger(\omega, t_0)}{-{\rm i}\,(\Delta_{\rm om} + \omega) + \frac{|\gamma_{\rm o}|}{2}} \,.$$

Making the following definitions

$$\delta\omega_{\rm m}(\omega) = {g_{\rm om}}^2\,|\bar{a}|^2\,\Im\left[\frac{1}{{\rm i}\,(\Delta_{\rm om}-\omega)+\frac{|\gamma_{\rm o}|}{2}}-\frac{1}{-{\rm i}\,(\Delta_{\rm om}+\omega)+\frac{|\gamma_{\rm o}|}{2}}\right]\,,$$

$$\gamma_{\rm om}(\omega) = 2\,{g_{\rm om}}^2\,|\bar{a}|^2\,\Re\left[\frac{1}{{\rm i}\,(\Delta_{\rm om}-\omega)+\frac{|\gamma_{\rm o}|}{2}}-\frac{1}{-{\rm i}\,(\Delta_{\rm om}+\omega)+\frac{|\gamma_{\rm o}|}{2}}\right]$$

$$= {g_{\rm om}}^2\,|\bar{a}|^2\,\left(\frac{|\gamma_{\rm o}|}{(\Delta_{\rm om}-\omega)^2+\left(\frac{|\gamma_{\rm o}|}{2}\right)^2}-\frac{|\gamma_{\rm o}|}{(\Delta_{\rm om}+\omega)^2+\left(\frac{|\gamma_{\rm o}|}{2}\right)^2}\right)$$

$$= \frac{{g_{\rm om}}^2\,|\bar{a}|^2\,4\,|\gamma_{\rm o}|\,\Delta_{\rm om}\,\omega}{\left((\Delta_{\rm om}-\omega)^2+\left(\frac{|\gamma_{\rm o}|}{2}\right)^2\right)\left((\Delta_{\rm om}+\omega)^2+\left(\frac{|\gamma_{\rm o}|}{2}\right)^2\right)}\,,$$

we can write

$$\hat{b}(\omega\sim\omega_{\rm m}) = \frac{{\rm i}\,g_{\rm om}\left(\frac{\bar{a}^*\,\sqrt{\gamma_{\rm o}}\,\hat{d}(\omega,t_0)}{{\rm i}\,(\Delta_{\rm om}-\omega)+\frac{|\gamma_{\rm o}|}{2}}+\frac{\bar{a}\,\sqrt{\gamma_{\rm o}^*}\,\hat{d}^\dagger(\omega,t_0)}{-{\rm i}\,(\Delta_{\rm om}+\omega)+\frac{|\gamma_{\rm o}|}{2}}\right)-\sqrt{\gamma_{\rm m}}\,\hat{e}(\omega,t_0)}{{\rm i}\,(\omega_{\rm m}+\delta\omega_{\rm m}(\omega)-\omega)+\frac{|\gamma_{\rm m}|+\gamma_{\rm om}(\omega)}{2}}\,.$$

The functions $\delta\omega_{\rm m}$ and $\gamma_{\rm om}$ are purely real and have following the properties,

$$\delta\omega_{\rm m}(-\omega) = \delta\omega_{\rm m}(\omega)\,, \qquad\qquad \gamma_{\rm om}(-\omega) = -\gamma_{\rm om}(\omega)\,.$$

For $\Delta_{\rm om}\gg\gamma_{\rm o}$, $\gamma_{\rm om}(\omega)$ is positively peaked around $\omega=\Delta_{\rm om}$, and negatively peaked around

$\omega = -\Delta_{\mathrm{om}}$, with a full width at half maximum of $2\,\gamma_{\mathrm{o}}$. So at $\omega = \omega_{\mathrm{m}}$ we have

$$\gamma_{\mathrm{om}}(\omega_{\mathrm{m}}) > 0 \;\; : \omega_{\mathrm{L}} = \omega_{\mathrm{om}} - \omega_{\mathrm{m}} \; ,$$
$$\gamma_{\mathrm{om}}(\omega_{\mathrm{m}}) < 0 \;\; : \omega_{\mathrm{L}} = \omega_{\mathrm{om}} + \omega_{\mathrm{m}} \; ,$$
$$\gamma_{\mathrm{om}}(\omega_{\mathrm{m}}) = 0 \;\; : \omega_{\mathrm{L}} = \omega_{\mathrm{om}} \; .$$

The increased phononic loss γ_{om} for red detuning corresponds to photon conversion.

Doing the same for $\omega \sim -\omega_{\mathrm{m}}$,

$$\hat{b}^{\dagger}(\omega \sim -\omega_{\mathrm{m}}) = \frac{-\mathrm{i}\, g_{\mathrm{om}} \left(\dfrac{\bar{a}^{*}\sqrt{\gamma_{\mathrm{o}}}\,\hat{d}(\omega, t_0)}{\mathrm{i}\,(\Delta_{\mathrm{om}} - \omega) + \frac{|\gamma_{\mathrm{o}}|}{2}} + \dfrac{\bar{a}\sqrt{\gamma_{\mathrm{o}}^{*}}\,\hat{d}^{\dagger}(\omega, t_0)}{-\mathrm{i}\,(\Delta_{\mathrm{om}} + \omega) + \frac{|\gamma_{\mathrm{o}}|}{2}} \right) - \sqrt{\gamma_{\mathrm{m}}^{*}}\,\hat{e}^{\dagger}(\omega, t_0)}{-\mathrm{i}\,(\omega_{\mathrm{m}} + \delta\omega_{\mathrm{m}}(\omega) + \omega) + \frac{|\gamma_{\mathrm{m}}| - \gamma_{\mathrm{om}}(\omega)}{2}} \; .$$

In blue detuned laser pumping regime ($\Delta_{\mathrm{om}} = -\omega_{\mathrm{m}}$), and probing the optical cavity ($\omega \sim -\omega_{\mathrm{m}}$), this equation has a subtle limitation. When $\omega = -\omega_{\mathrm{m}} - \delta\omega_{\mathrm{m}}(\omega)$, the denominator is simply $|\gamma_{\mathrm{m}}| - \gamma_{\mathrm{om}}(\omega)$ with $\gamma_{\mathrm{om}}(\omega) > 0$, meaning if $\gamma_{\mathrm{om}}(\omega) \sim |\gamma_{\mathrm{m}}|$ then $\hat{b}^{\dagger}$ diverges. Recalling the original optomechanical Hamiltonian in App. C, $\hat{x} \propto \left(\hat{b}^{\dagger} + \hat{b}\right)$ must be small to produce the first order coupled optomechanical Hamiltonian (J.1). Thus a large $\hat{b}^{\dagger}$ breaks our fundamental approximation and invalidates these equations. When driving blue detuned, we must therefore impose the restriction that

$$\gamma_{\mathrm{om}}(\omega) < |\gamma_{\mathrm{m}}| \quad : \quad \omega_{\mathrm{L}} = \omega_{\mathrm{om}} + \omega_{\mathrm{m}} \; ,$$

equivalently in the sideband resolved regime ($\omega_{\mathrm{m}} \gg |\gamma_{\mathrm{o}}|$), where

$$\gamma_{\mathrm{om}}(\omega = -\omega_{\mathrm{m}} = \Delta_{\mathrm{om}}) \approx \frac{4\,{g_{\mathrm{om}}}^{2}\,|\bar{a}|^{2}}{|\gamma_{\mathrm{o}}|} \; ,$$

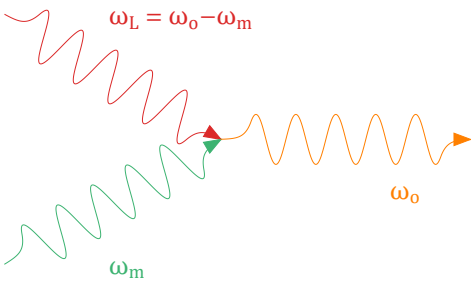

Figure J.1: Three wave mixing with a red detuned laser.

this is

$$\mathcal{C}_{\rm om} = \frac{4\,{g_{\rm om}}^2\,|\bar{a}|^2}{|\gamma_{\rm o}|\,|\gamma_{\rm m}|} < 1 \quad : \quad \omega_{\rm L} = \omega_{\rm om} + \omega_{\rm m} \wedge \omega_{\rm m} \gg |\gamma_{\rm o}|\,, \tag{J.8}$$

where $\mathcal{C}_{\rm om}$ is known as the cooperativity. Physically, this situation of a blue detuned laser drive and $\mathcal{C}_{\rm om} > 1$ corresponds to the laser pump exciting the mechanical oscillator faster than it can decay, putting it into a high energy state where the optomechanical coupling is highly non-linear.

J.4 Beam splitter

When the laser pump is red detuned from the optical cavity by the mechanical resonance frequency, the optomechanical interaction takes on a beam splitter form. For simplicity, consider our Hamiltonian without coupling to baths. With a laser drive, and rotated into the laser frame,

$$\hat{H}_{\rm rot} = \underbrace{\hbar\,\Delta_{\rm o}\left(\hat{a}^\dagger\,\hat{a} + \tfrac{1}{2}\right)}_{\hat{H}_{\rm optic}} + \underbrace{\hbar\,L\,\hat{a}^\dagger + \hbar\,L^*\,\hat{a}}_{\hat{H}_{\rm laser}} + \underbrace{\hbar\,\omega_{\rm m}\left(\hat{b}^\dagger\,\hat{b} + \tfrac{1}{2}\right)}_{\hat{H}_{\rm mech}} + \underbrace{\hbar\,g_{\rm om}\left(\hat{a}^\dagger\,\hat{a} + \tfrac{1}{2}\right)\left(\hat{b}^\dagger + \hat{b}\right)}_{\hat{H}_{\rm optomech}}\,.$$

As we found before there is a steady background occupancy, and we can transform to a background leveled frame

$$
\begin{aligned}
\hat{H}_{\substack{\text{rot}\\\text{lvl}}} &= \hat{D}_{\hat{a}}(\bar{a})^{\dagger}\,\hat{D}_{\hat{b}}(\bar{b})^{\dagger}\,\hat{H}_{\text{rot}}\,\hat{D}_{\hat{a}}(\bar{a})\,\hat{D}_{\hat{b}}(\bar{b}) \\
&= \hbar\,\Delta_{\text{o}}\left(\hat{a}^{\dagger}\,\hat{a}+\tfrac{1}{2}\right)+\hbar\,\Delta_{\text{o}}\,\bar{a}\,\hat{a}^{\dagger}+\hbar\,\Delta_{\text{o}}\,\bar{a}^{*}\,\hat{a}+\hbar\,\Delta_{\text{o}}\,|\bar{a}|^{2} \\
&\quad+\hbar\,L\,\hat{a}^{\dagger}+\hbar\,L^{*}\,\hat{a}+\hbar\,L\,\bar{a}^{*}+\hbar\,L^{*}\,\bar{a} \\
&\quad+\hbar\,\omega_{\text{m}}\left(\hat{b}^{\dagger}\,\hat{b}+\tfrac{1}{2}\right)+\hbar\,\omega_{\text{m}}\,\bar{b}\,\hat{b}^{\dagger}+\hbar\,\omega_{\text{m}}\,\bar{b}^{*}\,\hat{b}+\hbar\,\omega_{\text{m}}\,|\bar{b}|^{2} \\
&\quad+\hbar\,g_{\text{om}}\Big(\hat{a}^{\dagger}\,\hat{a}\,\hat{b}+\hat{a}^{\dagger}\,\hat{a}\,\hat{b}^{\dagger}+\bar{a}\,\hat{a}^{\dagger}\,\hat{b}+\bar{a}\,\hat{a}^{\dagger}\,\hat{b}^{\dagger}+\bar{a}^{*}\,\hat{a}\,\hat{b}+\bar{a}^{*}\,\hat{a}\,\hat{b}^{\dagger}+|\bar{a}|^{2}\,\hat{b}+|\bar{a}|^{2}\,\hat{b}^{\dagger} \\
&\qquad+\hat{a}^{\dagger}\,\hat{a}\,\bar{b}+\hat{a}^{\dagger}\,\hat{a}\,\bar{b}^{*}+\bar{a}\,\hat{a}^{\dagger}\,\bar{b}+\bar{a}\,\hat{a}^{\dagger}\,\bar{b}^{*}+\bar{a}^{*}\,\hat{a}\,\bar{b}+\bar{a}^{*}\,\hat{a}\,\bar{b}^{*}+|\bar{a}|^{2}\,\bar{b}+|\bar{a}|^{2}\,\bar{b}^{*} \\
&\qquad+\tfrac{\hat{b}^{\dagger}+\hat{b}}{2}+\tfrac{\bar{b}^{*}+\bar{b}}{2}\Big)\,.
\end{aligned}
$$

Using the background level values calculated previously, (J.4) and (J.5), (with $\gamma_{\text{o}}=\gamma_{\text{m}}=0$ as we have no baths present)

$$
\bar{a}=\frac{-L}{\Delta_{\text{om}}}\,,\qquad\qquad \bar{b}=\frac{-g_{\text{om}}\left(|\bar{a}|^{2}+\frac{1}{2}\right)}{\omega_{\text{m}}}\,,
$$

many of the terms cancel out. We are then left with

$$
\begin{aligned}
\hat{H}_{\substack{\text{rot}\\\text{lvl}}} &= \underbrace{\hbar\,\Delta_{\text{om}}\left(\hat{a}^{\dagger}\,\hat{a}+\tfrac{1}{2}\right)+\hbar\,\omega_{\text{m}}\left(\hat{b}^{\dagger}\,\hat{b}+\tfrac{1}{2}\right)}_{\hat{H}_{0}} \\
&\quad+\underbrace{\hbar\,g_{\text{om}}\left(\hat{a}^{\dagger}\,\hat{a}\,\hat{b}+\hat{a}^{\dagger}\,\hat{a}\,\hat{b}^{\dagger}+\bar{a}\,\hat{a}^{\dagger}\,\hat{b}+\bar{a}\,\hat{a}^{\dagger}\,\hat{b}^{\dagger}+\bar{a}^{*}\,\hat{a}\,\hat{b}+\bar{a}^{*}\,\hat{a}\,\hat{b}^{\dagger}\right)}_{\hat{H}_{\text{int}}} \\
&\quad+\underbrace{\hbar\,\Delta_{\text{om}}\,|\bar{a}|^{2}+\hbar\,L\,\bar{a}^{*}+\hbar\,L^{*}\,\bar{a}+\hbar\,\omega_{\text{m}}\,|\bar{b}|^{2}}_{\text{constants}}\,.
\end{aligned}
$$

Moving to the interaction picture with

$$\hat{U}(t) = \mathrm{e}^{-\frac{\mathrm{i}}{\hbar}\hat{H}_0\,t} = \mathrm{e}^{-\mathrm{i}\,\Delta_{\mathrm{om}}\,(\hat{a}^\dagger\,\hat{a}+\frac{1}{2})\,t}\,\mathrm{e}^{-\mathrm{i}\,\omega_{\mathrm{m}}\,(\hat{b}^\dagger\,\hat{b}+\frac{1}{2})\,t}\ ,$$

we find

$$\begin{aligned}\hat{H}^{\mathrm{I}}_{\mathrm{int}} &= \hat{U}(t)^\dagger\,\hat{H}_{\mathrm{int}}\,\hat{U}(t)\\ &= \hbar\,g_{\mathrm{om}}\Big(\hat{a}^\dagger\,\hat{a}\,\hat{b}\,\mathrm{e}^{-\mathrm{i}\,\omega_{\mathrm{m}}\,t} + \hat{a}^\dagger\,\hat{a}\,\hat{b}^\dagger\,\mathrm{e}^{\mathrm{i}\,\omega_{\mathrm{m}}\,t} + \bar{a}\,\hat{a}^\dagger\,\hat{b}\,\mathrm{e}^{\mathrm{i}\,(\Delta_{\mathrm{om}}-\omega_{\mathrm{m}})\,t} + \bar{a}\,\hat{a}^\dagger\,\hat{b}^\dagger\,\mathrm{e}^{\mathrm{i}\,(\Delta_{\mathrm{om}}+\omega_{\mathrm{m}})\,t}\\ &\qquad + \bar{a}^*\,\hat{a}\,\hat{b}\,\mathrm{e}^{-\mathrm{i}\,(\Delta_{\mathrm{om}}+\omega_{\mathrm{m}})\,t} + \bar{a}^*\,\hat{a}\,\hat{b}^\dagger\,\mathrm{e}^{-\mathrm{i}\,(\Delta_{\mathrm{om}}-\omega_{\mathrm{m}})\,t}\Big)\ . \end{aligned} \tag{J.9}$$

If we set $\Delta_{\mathrm{om}} = \omega_{\mathrm{m}}$ and use the rotating wave approximation to remove all the oscillating terms, we are left with

$$\hat{H}_{\mathrm{int}} = \hbar\,g_{\mathrm{om}}\,\left(\bar{a}\,\hat{a}^\dagger\,\hat{b} + \bar{a}^*\,\hat{a}\,\hat{b}^\dagger\right)\ .$$

Thus red detuning the laser to $\omega_{\mathrm{L}} = \omega_{\mathrm{om}} - \omega_{\mathrm{m}}$ provides a beam splitter Hamiltonian and allows photonic-phononic state conversion via the process depicted in Fig. J.1.

J.4.1 With heat bath

If we have $\Delta_{\mathrm{om}} = \omega_{\mathrm{m}}$ and use the beam splitter approximation with coupled heat baths,

$$\begin{aligned}
\hat{H}_{\substack{\mathrm{rot}\\\mathrm{lvl}}} &= \hbar\,\Delta_{\mathrm{om}}\left(\hat{a}^\dagger\,\hat{a} + \tfrac{1}{2}\right) + \hbar\,\omega_{\mathrm{m}}\left(\hat{b}^\dagger\,\hat{b} + \tfrac{1}{2}\right) + \hbar\,g_{\mathrm{om}}\left(\bar{a}\,\hat{a}^\dagger\,\hat{b} + \bar{a}^*\,\hat{a}\,\hat{b}^\dagger\right)\\
&\quad + \mathrm{i}\,\hbar\,\frac{|\gamma_{\mathrm{o}}|}{2}\,\bar{a}\,\hat{a}^\dagger - \mathrm{i}\,\hbar\,\frac{|\gamma_{\mathrm{o}}|}{2}\,\bar{a}^*\,\hat{a} + \mathrm{i}\,\hbar\,\frac{|\gamma_{\mathrm{m}}|}{2}\,\bar{b}\,\hat{b}^\dagger - \mathrm{i}\,\hbar\,\frac{|\gamma_{\mathrm{m}}|}{2}\,\bar{b}^*\,\hat{b}\\
&\quad + \sum_q \hbar\,\Delta_q\,\hat{d}_q^\dagger\,\hat{d}_q + \sum_q \hbar\left(\kappa_q\,\hat{a}^\dagger\,\hat{d}_q + \kappa_q^*\,\hat{a}\,\hat{d}_q^\dagger\right) + \sum_q \hbar\left(\kappa_q\,\bar{a}^*\,\hat{d}_q + \kappa_q^*\,\bar{a}\,\hat{d}_q^\dagger\right)\\
&\quad + \sum_q \hbar\,\omega_q\,\hat{e}_q^\dagger\,\hat{e}_q + \sum_q \hbar\left(\lambda_q\,\hat{b}^\dagger\,\hat{e}_q + \lambda_q^*\,\hat{b}\,\hat{e}_q^\dagger\right) + \sum_q \hbar\left(\lambda_q\,\bar{b}^*\,\hat{e}_q + \lambda_q^*\,\bar{b}\,\hat{e}_q^\dagger\right)\\
&\quad + \hbar\,\Delta_{\mathrm{om}}\,|\bar{a}|^2 + \hbar\,L\,\bar{a}^* + \hbar\,L^*\,\bar{a} + \hbar\,\omega_{\mathrm{m}}\,|\bar{b}|^2\,, \qquad \text{(J.10)}
\end{aligned}$$

where the terms in the second line are produced by the full definitions of $\bar{a}$ (J.4) and $\bar{b}$ (J.5). Note that,

$$\hbar\,L\,\bar{a}^* + \hbar\,L^*\,\bar{a} = -2\,\hbar\,\Delta_{\mathrm{om}}\,|\bar{a}|^2\,.$$

Deriving the Langevin equations

$$\begin{aligned}
\frac{\mathrm{d}}{\mathrm{d}t}\hat{a}(t) &= -\mathrm{i}\,\Delta_{\mathrm{om}}\,\hat{a}(t) - \mathrm{i}\,g_{\mathrm{om}}\,\bar{a}\,\hat{b}(t) + \frac{|\gamma_{\mathrm{o}}|}{2}\,\bar{a} - \frac{|\gamma_{\mathrm{o}}|}{2}\,\left(\hat{a}(t) + \bar{a}\right) - \sqrt{\gamma_{\mathrm{o}}}\,\hat{d}_{\mathrm{in}}(t)\\
&= -\mathrm{i}\,\Delta_{\mathrm{om}}\,\hat{a}(t) - \mathrm{i}\,g_{\mathrm{om}}\,\bar{a}\,\hat{b}(t) - \frac{|\gamma_{\mathrm{o}}|}{2}\,\hat{a}(t) - \sqrt{\gamma_{\mathrm{o}}}\,\hat{d}_{\mathrm{in}}(t)\,,
\end{aligned}$$

$$\begin{aligned}
\frac{\mathrm{d}}{\mathrm{d}t}\hat{b}(t) &= -\mathrm{i}\,\omega_{\mathrm{m}}\,\hat{b}(t) - \mathrm{i}\,g_{\mathrm{om}}\,\bar{a}^*\,\hat{a}(t) + \frac{|\gamma_{\mathrm{m}}|}{2}\,\bar{b} - \frac{|\gamma_{\mathrm{m}}|}{2}\,\left(\hat{b}(t) + \bar{b}\right) - \sqrt{\gamma_{\mathrm{m}}}\,\hat{e}_{\mathrm{in}}(t)\\
&= -\mathrm{i}\,\omega_{\mathrm{m}}\,\hat{b}(t) - \mathrm{i}\,g_{\mathrm{om}}\,\bar{a}^*\,\hat{a}(t) - \frac{|\gamma_{\mathrm{m}}|}{2}\,\hat{b}(t) - \sqrt{\gamma_{\mathrm{m}}}\,\hat{e}_{\mathrm{in}}(t)\,.
\end{aligned}$$

Taking Fourier transforms

$$\hat{a}(\omega) = \frac{-\mathrm{i}\, g_{\mathrm{om}}\, \bar{a}\, \hat{b}(\omega) - \sqrt{\gamma_{\mathrm{o}}}\, \hat{d}(\omega, t_0)}{\mathrm{i}\,(\Delta_{\mathrm{om}} - \omega) + \frac{|\gamma_{\mathrm{o}}|}{2}} \,,$$

$$\hat{b}(\omega) = \frac{-\mathrm{i}\, g_{\mathrm{om}}\, \bar{a}^*\, \hat{a}(\omega) - \sqrt{\gamma_{\mathrm{m}}}\, \hat{e}(\omega, t_0)}{\mathrm{i}\ (\omega_{\mathrm{m}} - \omega) + \frac{|\gamma_{\mathrm{m}}|}{2}} \,.$$

This approximation is equivalent to $|\gamma_{\mathrm{m}}| \ll \omega_m \wedge |\gamma_{\mathrm{o}}| \ll \Delta_{\mathrm{om}}$.

Combining these equations we deduce a strongly resolved optical spring effect,

$$\hat{b}(\omega) = \frac{\dfrac{\mathrm{i}\, g_{\mathrm{om}}\, \bar{a}^*\, \sqrt{\gamma_{\mathrm{o}}}\, \hat{d}(\omega, t_0)}{\mathrm{i}\,(\Delta_{\mathrm{om}} - \omega) + \frac{|\gamma_{\mathrm{o}}|}{2}} - \sqrt{\gamma_{\mathrm{m}}}\, \hat{e}(\omega, t_0)}{\mathrm{i}\,(\omega_{\mathrm{m}} + \delta\omega_{\mathrm{m}}(\omega) - \omega) + \frac{|\gamma_{\mathrm{m}}| + \gamma_{\mathrm{om}}(\omega)}{2}} \,,$$

with

$$\delta\omega_{\mathrm{m}}(\omega) = {g_{\mathrm{om}}}^2\, |\bar{a}|^2\, \Im\left[\frac{1}{\mathrm{i}\,(\Delta_{\mathrm{om}} - \omega) + \frac{|\gamma_{\mathrm{o}}|}{2}}\right] \,,$$

$$\gamma_{\mathrm{om}}(\omega) = 2\, {g_{\mathrm{om}}}^2\, |\bar{a}|^2\, \Re\left[\frac{1}{\mathrm{i}\,(\Delta_{\mathrm{om}} - \omega) + \frac{|\gamma_{\mathrm{o}}|}{2}}\right]$$

$$= -\frac{{g_{\mathrm{om}}}^2\, |\bar{a}|^2\, |\gamma_{\mathrm{o}}|}{(\Delta_{\mathrm{om}} - \omega)^2 + \left(\frac{|\gamma_{\mathrm{o}}|}{2}\right)^2} \,.$$

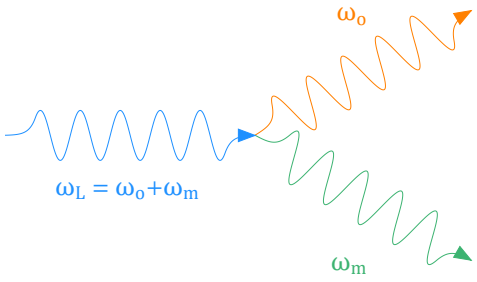

Figure J.2: Three wave mixing with a blue detuned laser.

At $\omega = \omega_{\mathrm{m}}$,

$$\hat{b}(\omega = \omega_{\mathrm{m}}) = \frac{\frac{\mathrm{i}\, g_{\mathrm{om}}\, \bar{a}^*}{\frac{|\gamma_{\mathrm{o}}|}{2}} \sqrt{\gamma_{\mathrm{o}}}\, \hat{d}(\omega_{\mathrm{m}}, t_0) - \sqrt{\gamma_{\mathrm{m}}}\, \hat{e}(\omega_{\mathrm{m}}, t_0)}{\frac{|\gamma_{\mathrm{m}}|}{2} + \frac{{g_{\mathrm{om}}}^2\, |\bar{a}|^2}{\frac{|\gamma_{\mathrm{o}}|}{2}}} \ .$$

J.5 Entangling

If in equation (J.9), we instead set $\Delta_{\mathrm{om}} = -\omega_{\mathrm{m}}$ and apply the rotating wave approximation, we end up with

$$\hat{H}_{\mathrm{int}} = \hbar\, g_{\mathrm{om}} \left(\bar{a}\, \hat{a}^\dagger\, \hat{b}^\dagger + \bar{a}^*\, \hat{a}\, \hat{b} \right) \ .$$

Thus blue detuning the laser to $\omega_{\mathrm{L}} = \omega_{\mathrm{om}} + \omega_{\mathrm{m}}$ provides an entangling Hamiltonian that deals with photon-phonon pairs as depicted in Fig. J.2.

J.6 Optomechanically induced transparency

Similar in idea to electromagnetically induced transparency, the coupling of an optical cavity to a mechanical mode, and pumped with a red detuned laser at $\omega_{\rm L} = \omega_{\rm om} - \omega_{\rm m}$, opens up a transparency in the transmission spectrum of the cavity probed by a second laser signal.

To study this effect we take the beam splitter Hamiltonian (J.10) derived from a red detuned pump ($\Delta_{\rm om} \sim \omega_{\rm m}$), and add additional heat baths, with loss parameter $\gamma_{\rm o}^{\rm wg}$, to model the waveguide ports. Following the input/output theory of a symmetric non-directional waveguide resonator (see App. Θ) we get the following system of equations,

$$\begin{aligned}\frac{\rm d}{{\rm d}t}\hat{a}(t) = & -{\rm i}\,\Delta_{\rm om}\,\hat{a}(t) - {\rm i}\,g_{\rm om}\,\bar{a}\,\hat{b}(t) - \frac{\gamma_{\rm o}}{2}\,\hat{a}(t) \\ & - \sqrt{\gamma_{\rm o}^{\rm int}}\,\hat{d}_{\rm in}^{\rm int}(t) - \sqrt{\gamma_{\rm o}^{\rm wg}}\,\hat{d}_{\rm in}^{1}(t) - \sqrt{\gamma_{\rm o}^{\rm wg}}\,\hat{d}_{\rm in}^{2}(t)\ ,\end{aligned}$$

$$\frac{\rm d}{{\rm d}t}\hat{b}(t) = -{\rm i}\,\omega_{\rm m}\,\hat{b}(t) - {\rm i}\,g_{\rm om}\,\bar{a}^{*}\,\hat{a}(t) - \frac{\gamma_{\rm m}}{2}\,\hat{b}(t) - \sqrt{\gamma_{\rm m}}\,\hat{e}_{\rm in}^{\rm int}(t)\ ,$$

$$\hat{d}_{\rm out}^{1}(t) = \sqrt{\gamma_{\rm o}^{\rm wg}}\,\hat{a}(t) + \hat{d}_{\rm in}^{2}(t)\ ,$$

$$\hat{d}_{\rm out}^{2}(t) = \sqrt{\gamma_{\rm o}^{\rm wg}}\,\hat{a}(t) + \hat{d}_{\rm in}^{1}(t)\ ,$$

with

$$\gamma_{\rm o} = \gamma_{\rm o}^{\rm int} + 2\,\gamma_{\rm o}^{\rm wg}\ ,$$

where we have made all the γ real (moving any complex components to the frequency) and chosen all the phases to be zero. For simplicity we will set the environmental inputs $\hat{d}_{\rm in}^{\rm int}$ and

$\hat{e}_{\rm in}^{\rm int}$, which are negligible compared to the waveguide input, to zero.

Taking the Fourier transform of our equations we get

$$\hat{a}(\omega) = \frac{-\mathrm{i}\, g_{\rm om}\, \bar{a}\, \hat{b}(\omega) - \sqrt{\gamma_{\rm o}^{\rm wg}}\, \hat{d}_{\rm in}^{1}(\omega) - \sqrt{\gamma_{\rm o}^{\rm wg}}\, \hat{d}_{\rm in}^{2}(\omega)}{\mathrm{i}\,(\Delta_{\rm om} - \omega) + \frac{\gamma_{\rm o}}{2}} \,,$$

$$\hat{b}(\omega) = \frac{-\mathrm{i}\, g_{\rm om}\, \bar{a}^{*}\, \hat{a}(\omega)}{\mathrm{i}\,(\omega_{\rm m} - \omega) + \frac{\gamma_{\rm m}}{2}} \,,$$

where $\hat{a}(\omega)$ is rotated into the laser frame. Solving for $\hat{a}$,

$$\hat{a}(\omega) = \frac{-\sqrt{\gamma_{\rm o}^{\rm wg}}\, \hat{d}_{\rm in}^{1}(\omega) - \sqrt{\gamma_{\rm o}^{\rm wg}}\, \hat{d}_{\rm in}^{2}(\omega)}{\mathrm{i}\,(\Delta_{\rm om} - \omega) + \frac{\gamma_{\rm o}}{2} + \frac{{g_{\rm om}}^{2}\,|\bar{a}|^{2}}{\mathrm{i}\,(\omega_{\rm m} - \omega) + \frac{\gamma_{\rm m}}{2}}} \,,$$

and using our waveguide in/out relations we find the transmission to be

$$S_{2\,1}(\omega) = \left.\frac{\hat{d}_{\rm out}^{2}(\omega)}{\hat{d}_{\rm in}^{1}(\omega)}\right|_{\hat{d}_{\rm in}^{2}(\omega)=0} = 1 - \frac{\gamma_{\rm o}^{\rm wg}}{\mathrm{i}\,(\Delta_{\rm om} - \omega) + \frac{\gamma_{\rm o}}{2} + \frac{{g_{\rm om}}^{2}\,|\bar{a}|^{2}}{\mathrm{i}\,(\omega_{\rm m} - \omega) + \frac{\gamma_{\rm m}}{2}}} \,.$$

In Fig. J.3 we plot $|S_{2\,1}(\omega)|^{2}$ at critical coupling showing the transparent peak that appears over an uncoupled optical cavity ($g_{\rm om} = 0$). Typically the probe frequency is taken from a sideband of the pump laser, in which case ω will be the modulation frequency.

When everything is aligned, $\Delta_{\rm om} = \omega_{\rm m}$, and we probe at exactly the optical cavity frequency, $\omega = \omega_{\rm m}$ (i.e. $\omega_{\rm L} + \omega_{\rm m} = \omega_{\rm om}$), the peak transparency is

$$S_{2\,1}\left(\omega = \omega_{\rm m} = \Delta_{\rm om}\right) = 1 - \frac{2\,\gamma_{\rm o}^{\rm wg}}{\gamma_{\rm o} + \frac{4\,{g_{\rm om}}^{2}\,|\bar{a}|^{2}}{\gamma_{\rm m}}}$$

$$= 1 - \frac{\frac{2\,\gamma_{\rm o}^{\rm wg}}{\gamma_{\rm o}}}{1 + \mathcal{C}_{\rm om}} \,.$$

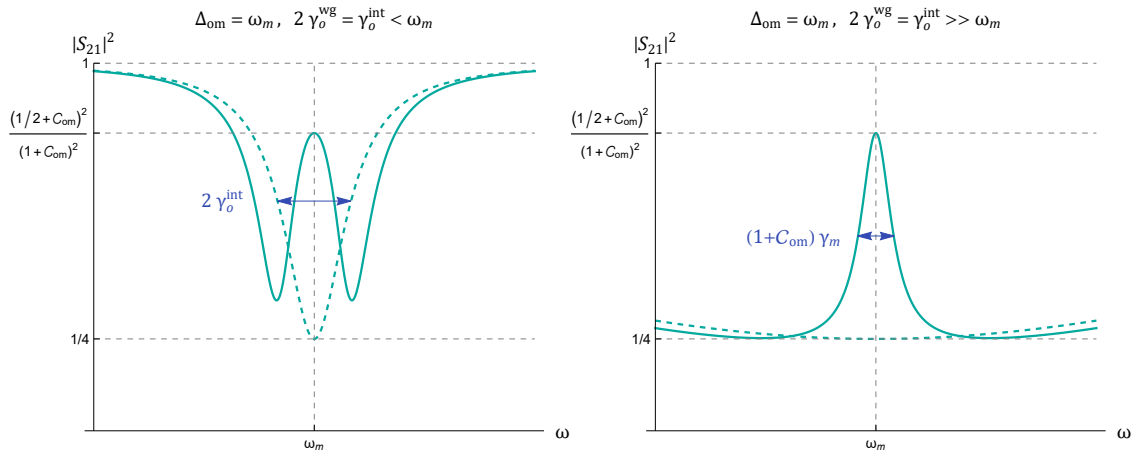

Figure J.3: Transmission plots showing optomechanical transparency (solid line) compared to a regular optical cavity (dashed line) in two different regimes of optical cavity linewidth.

At critical coupling, $2\gamma_{\mathrm{o}}^{\mathrm{wg}} = \gamma_{\mathrm{o}}^{\mathrm{int}} \Rightarrow \frac{2\gamma_{\mathrm{o}}^{\mathrm{wg}}}{\gamma_{\mathrm{o}}} = \frac{1}{2}$,

$$S_{21}\left(\omega = \omega_{\mathrm{m}} = \Delta_{\mathrm{om}}; \gamma_{\mathrm{o}}^{\mathrm{int}} = 2\gamma_{\mathrm{o}}^{\mathrm{wg}}\right) = \frac{\frac{1}{2} + \mathcal{C}_{\mathrm{om}}}{1 + \mathcal{C}_{\mathrm{om}}}\,.$$

J.7 Optomechanical induced absorption

If we instead pump with a blue detuned laser at $\omega_{\mathrm{L}} = \omega_{\mathrm{om}} + \omega_{\mathrm{m}}$, and keeping $\mathcal{C}_{\mathrm{om}} < 1$, we observe absorption when the cavity is probed at its optical resonant frequency. Doing the same as above except with the entangling Hamiltonian ($\Delta_{\mathrm{om}} \sim -\omega_{\mathrm{m}}$), the system of

equations is

$$\frac{\mathrm{d}}{\mathrm{d}t}\hat{a}(t) = -\mathrm{i}\,\Delta_{\mathrm{om}}\,\hat{a}(t) - \mathrm{i}\,g_{\mathrm{om}}\,\bar{a}\,\hat{b}^{\dagger}(t) - \frac{\gamma_{\mathrm{o}}}{2}\,\hat{a}(t) - \sqrt{\gamma_{\mathrm{o}}^{\mathrm{int}}}\,\hat{d}_{\mathrm{in}}^{\mathrm{int}}(t) - \sqrt{\gamma_{\mathrm{o}}^{\mathrm{wg}}}\,\hat{d}_{\mathrm{in}}^{1}(t) - \sqrt{\gamma_{\mathrm{o}}^{\mathrm{wg}}}\,\hat{d}_{\mathrm{in}}^{2}(t)\ ,$$

$$\frac{\mathrm{d}}{\mathrm{d}t}\hat{b}(t) = -\mathrm{i}\,\omega_{\mathrm{m}}\,\hat{b}(t) - \mathrm{i}\,g_{\mathrm{om}}\,\bar{a}\,\hat{a}^{\dagger}(t) - \frac{\gamma_{\mathrm{m}}}{2}\,\hat{b}(t) - \sqrt{\gamma_{\mathrm{m}}}\,\hat{e}_{\mathrm{in}}^{\mathrm{int}}(t)\ ,$$

$$\hat{d}_{\mathrm{out}}^{1}(t) = \sqrt{\gamma_{\mathrm{o}}^{\mathrm{wg}}}\,\hat{a}(t) + \hat{d}_{\mathrm{in}}^{2}(t)\ ,$$

$$\hat{d}_{\mathrm{out}}^{2}(t) = \sqrt{\gamma_{\mathrm{o}}^{\mathrm{wg}}}\,\hat{a}(t) + \hat{d}_{\mathrm{in}}^{1}(t)\ .$$

Again setting $\hat{d}_{\mathrm{in}}^{\mathrm{int}} = \hat{e}_{\mathrm{in}}^{\mathrm{int}} = 0$ and taking the Fourier transform we get

$$\hat{a}(\omega) = \frac{-\mathrm{i}\,g_{\mathrm{om}}\,\bar{a}\,\hat{b}^{\dagger}(\omega) - \sqrt{\gamma_{\mathrm{o}}^{\mathrm{wg}}}\,\hat{d}_{\mathrm{in}}^{1}(\omega) - \sqrt{\gamma_{\mathrm{o}}^{\mathrm{wg}}}\,\hat{d}_{\mathrm{in}}^{2}(\omega)}{\mathrm{i}\,(\Delta_{\mathrm{om}} - \omega) + \frac{\gamma_{\mathrm{o}}}{2}}\ ,$$

$$\hat{b}(\omega) = \frac{-\mathrm{i}\,g_{\mathrm{om}}\,\bar{a}\,\hat{a}^{\dagger}(\omega)}{\mathrm{i}\,(\omega_{\mathrm{m}} - \omega) + \frac{\gamma_{\mathrm{m}}}{2}}\ ,$$

$$\Rightarrow \quad \hat{b}^{\dagger}(\omega) = \frac{-\mathrm{i}\,g_{\mathrm{om}}\,\bar{a}^{*}\,\hat{a}(\omega)}{\mathrm{i}\,(\omega_{\mathrm{m}} + \omega) - \frac{\gamma_{\mathrm{m}}}{2}}\ ,$$

where $\hat{a}(\omega)$ is rotated into the laser frame Solving for $\hat{a}$,

$$\hat{a}(\omega) = \frac{-\sqrt{\gamma_{\mathrm{o}}^{\mathrm{wg}}}\,\hat{d}_{\mathrm{in}}^{1}(\omega) - \sqrt{\gamma_{\mathrm{o}}^{\mathrm{wg}}}\,\hat{d}_{\mathrm{in}}^{2}(\omega)}{\mathrm{i}\,(\Delta_{\mathrm{om}} - \omega) + \frac{\gamma_{\mathrm{o}}}{2} + \frac{{g_{\mathrm{om}}}^{2}\,|\bar{a}|^{2}}{\mathrm{i}\,(\omega_{\mathrm{m}} + \omega) - \frac{\gamma_{\mathrm{m}}}{2}}}\ ,$$

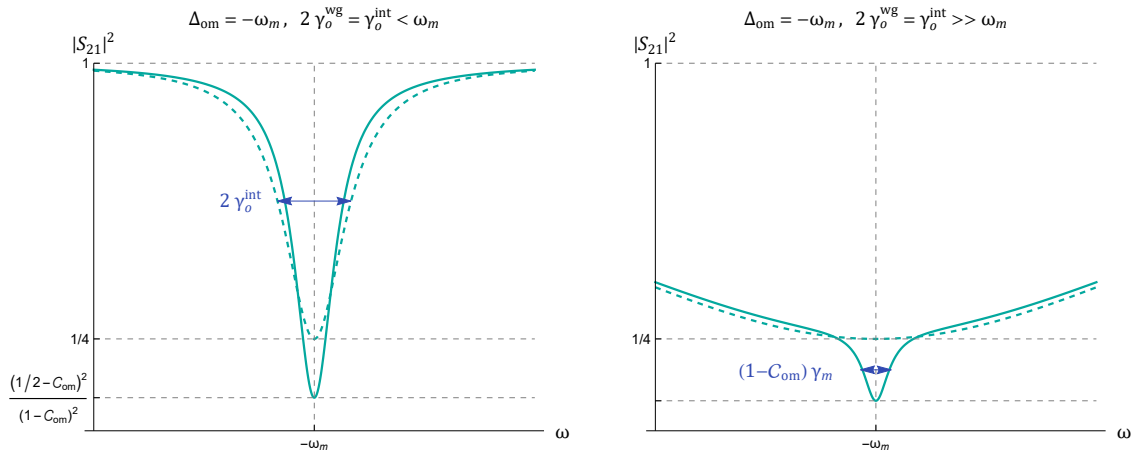

Figure J.4: Transmission plots showing optomechanical amplification (solid line) compared to a regular optical cavity (dashed line) in two different regimes of optical cavity linewidth.

and using our waveguide in/out relations we find the transmission to be

$$S_{21}(\omega) = \left.\frac{\hat{d}^2_{\text{out}}(\omega)}{\hat{d}^1_{\text{in}}(\omega)}\right|_{\hat{d}^2_{\text{in}}(\omega)=0} = 1 - \frac{\gamma_{\text{o}}^{\text{wg}}}{\text{i}\,(\Delta_{\text{om}} - \omega) + \frac{\gamma_{\text{o}}}{2} + \frac{{g_{\text{om}}}^2\,|\bar{a}|^2}{\text{i}\,(\omega_{\text{m}}+\omega) - \frac{\gamma_{\text{m}}}{2}}}\,.$$

In Fig. J.4 we plot $|S_{21}(\omega)|^2$ at critical coupling showing the amplification peak that appears over an uncoupled optical cavity ($g_{\text{om}} = 0$). Typically the probe frequency is taken from a sideband of the pump laser, in which case ω will be the modulation frequency.

When everything is aligned, $\Delta_{\text{om}} = -\omega_{\text{m}}$, and we probe at exactly the optical cavity frequency, $\omega = -\omega_{\text{m}}$ (i.e. $\omega_{\text{L}} - \omega_{\text{m}} = \omega_{\text{om}}$), the peak value is

$$S_{21}\left(\omega = -\omega_{\text{m}} = \Delta_{\text{om}}\right) = 1 - \frac{2\,\gamma_{\text{o}}^{\text{wg}}}{\gamma_{\text{o}} - \frac{4\,{g_{\text{om}}}^2\,|\bar{a}|^2}{\gamma_{\text{m}}}}$$

$$= 1 - \frac{\frac{2\,\gamma_{\text{o}}^{\text{wg}}}{\gamma_{\text{o}}}}{1 - \mathcal{C}_{\text{om}}}\,.$$

At critical coupling, $2\,\gamma_{\mathrm{o}}^{\mathrm{wg}} = \gamma_{\mathrm{o}}^{\mathrm{int}} \;\Rightarrow\; \frac{2\,\gamma_{\mathrm{o}}^{\mathrm{wg}}}{\gamma_{\mathrm{o}}} = \frac{1}{2}$,

$$S_{2\,1}\left(\omega = -\omega_{\mathrm{m}} = \Delta_{\mathrm{om}}; \gamma_{\mathrm{o}}^{\mathrm{int}} = 2\,\gamma_{\mathrm{o}}^{\mathrm{wg}}\right) = \frac{\frac{1}{2} - \mathcal{C}_{\mathrm{om}}}{1 - \mathcal{C}_{\mathrm{om}}}\,.$$

This result suggests that at $\mathcal{C}_{\mathrm{om}} > 3/4$ there is optomechanical induced amplification (divergent at $\mathcal{C}_{\mathrm{om}} = 1$) but the limitation imposed by (J.8), that is $\mathcal{C}_{\mathrm{om}} < 1$, applies here meaning such a regime is outside the scope of the linear optomechanical coupling Hamiltonian (J.1) used to deduce these results.

J.8 Non-rotating frame

In the non-rotating frame with multiple laser drives, the full Hamiltonian is

$$\begin{aligned}\hat{H} = {} & \underbrace{\hbar\,\omega_{\mathrm{o}}\left(\hat{a}^{\dagger}\,\hat{a} + \tfrac{1}{2}\right)}_{\hat{H}_{\mathrm{optic}}} + \underbrace{\hbar\,\omega_{\mathrm{m}}\left(\hat{b}^{\dagger}\,\hat{b} + \tfrac{1}{2}\right)}_{\hat{H}_{\mathrm{mech}}} + \underbrace{\hbar\,g_{\mathrm{om}}\left(\hat{a}^{\dagger}\,\hat{a} + \tfrac{1}{2}\right)\left(\hat{b}^{\dagger} + \hat{b}\right)}_{\hat{H}_{\mathrm{optomech}}} \\ & + \underbrace{\sum_{l} \hbar\left(L_l\,\hat{a}^{\dagger}\,\mathrm{e}^{-\mathrm{i}\,\omega_{\mathrm{l}}\,t} + L_l^{*}\,\hat{a}\,\mathrm{e}^{\mathrm{i}\,\omega_{\mathrm{l}}\,t}\right)}_{\hat{H}_{\mathrm{laser}}} \\ & + \underbrace{\sum_{q} \hbar\,\omega_q\,\hat{d}_q^{\dagger}\,\hat{d}_q}_{\substack{\hat{H}_{\mathrm{optic}} \\ \mathrm{bath}}} + \underbrace{\sum_{q} \hbar\left(\kappa_q\,\hat{a}^{\dagger}\,\hat{d}_q + \kappa_q^{*}\,\hat{a}\,\hat{d}_q^{\dagger}\right)}_{\substack{\hat{H}_{\mathrm{optic}} \\ \mathrm{bath} \\ \mathrm{int}}} + \underbrace{\sum_{q} \hbar\,\omega_q\,\hat{e}_q^{\dagger}\,\hat{e}_q}_{\substack{\hat{H}_{\mathrm{mech}} \\ \mathrm{bath}}} + \underbrace{\sum_{q} \hbar\left(\lambda_q\,\hat{b}^{\dagger}\,\hat{e}_q + \lambda_q^{*}\,\hat{b}\,\hat{e}_q^{\dagger}\right)}_{\substack{\hat{H}_{\mathrm{mech}} \\ \mathrm{bath} \\ \mathrm{int}}}\,,\end{aligned}$$

with equations of motion

$$\frac{\mathrm{d}}{\mathrm{d}t}\hat{a}(t) = -\mathrm{i}\,\omega_{\mathrm{o}}\,\hat{a}(t) - \mathrm{i}\,g_{\mathrm{om}}\,\hat{a}(t)\left(\hat{b}^{\dagger}(t) + \hat{b}(t)\right) - \frac{|\gamma_{\mathrm{o}}|}{2}\hat{a}(t) - \sum_{l}\mathrm{i}\,L_l\,\mathrm{e}^{-\mathrm{i}\,\omega_l\,t} - \sqrt{\gamma_{\mathrm{o}}}\,\hat{d}_{\mathrm{in}}(t)\;,$$

$$\frac{\mathrm{d}}{\mathrm{d}t}\hat{b}(t) = -\mathrm{i}\,\omega_{\mathrm{m}}\,\hat{b}(t) - \mathrm{i}\,g_{\mathrm{om}}\left(\hat{a}^{\,\dagger}(t)\,\hat{a}(t) + \frac{1}{2}\right) - \frac{|\gamma_{\mathrm{m}}|}{2}\hat{b}(t) - \sqrt{\gamma_{\mathrm{m}}}\,\hat{e}_{\mathrm{in}}(t)\;.$$

J.8.1 Multiple drive displacement

Following that of Sec. I.6, we can try displacements of the form

$$\hat{a}(t) \mapsto \hat{a}(t) + \sum_{j=1}^{n}\bar{a}_j(t)\,\mathrm{e}^{-\mathrm{i}\,\omega_j\,t}\;,$$
$$\hat{b}(t) \mapsto \hat{b}(t) + \bar{b}(t)\;,$$

and try to find functions $\bar{a}_j(t)$, $\bar{b}(t)$ that cancel the L_j terms. Substituting these displacements in to our equations of motion and ignoring all the operator terms, we get

$$\left(\mathrm{i}\,\left(\omega_{\mathrm{o}} - \omega_j + g_{\mathrm{om}}(\bar{b}(t)^{*} + \bar{b}(t))\right) + \frac{|\gamma_{\mathrm{o}}|}{2}\right)\bar{a}_j(t) + \frac{\mathrm{d}}{\mathrm{d}t}\bar{a}_j(t) + \mathrm{i}\,L_j = 0 \quad : \quad j \in \{1,\ldots,n\}\;,$$

$$\left(\mathrm{i}\,\omega_{\mathrm{m}} + \frac{|\gamma_{\mathrm{m}}|}{2}\right)\bar{b}(t) + \frac{\mathrm{d}}{\mathrm{d}t}\bar{b}(t) + \mathrm{i}\,g_{\mathrm{om}}\left(\sum_{j=1}^{n}\sum_{k=1}^{n}\bar{a}_j(t)^{*}\,\bar{a}_k(t)\,\mathrm{e}^{\mathrm{i}\,(\omega_j-\omega_k)\,t} + \frac{1}{2}\right) = 0\;.$$

For $n > 1$ these equations do not seem solvable by functions of the form $\sum_i c_i\,\mathrm{e}^{-\mathrm{i}\,\omega_i\,t}$ which would accommodate a Fourier transform.

J.8.2 Single drive displacement

If we displace by only a single laser drive ($n = 1$), denoted $\star$, perhaps because it is big enough to linearize the equation of motions by itself, then we get some significant simplifications. Due to the lack of cross terms in the sum for the $\bar{b}$ equation, we can have a solution where $\bar{a}(t)$ and $\bar{b}(t)$ have no time dependence, i.e.

$$\bar{a}_\star = \frac{-\mathrm{i}\, L_\star}{\mathrm{i}\,\left(\omega_\mathrm{o} - \omega_\star + g_\mathrm{om}\,(\bar{b}_\star^* + \bar{b}_\star)\right) + \frac{|\gamma_\mathrm{o}|}{2}} ,$$

$$\bar{b}_\star = \frac{-\mathrm{i}\, g_\mathrm{om}\,\left(|\bar{a}_\star|^2 + \frac{1}{2}\right)}{\mathrm{i}\,\omega_\mathrm{m} + \frac{|\gamma_\mathrm{m}|}{2}} .$$

Making this displacement,

$$\hat{a}(t) \mapsto \hat{a}(t) + \bar{a}_\star\,\mathrm{e}^{-\mathrm{i}\,\omega_\star\,t} ,$$
$$\hat{b}(t) \mapsto \hat{b}(t) + \bar{b}_\star ,$$

we obtain the single laser drive leveled equations of motion

$$\begin{aligned}\frac{\mathrm{d}}{\mathrm{d}t}\hat{a}(t) = &-\left(\mathrm{i}\,\left(\omega_\mathrm{o} + g_\mathrm{om}\,(\bar{b}_\star + \bar{b}_\star^*)\right) + \frac{|\gamma_\mathrm{o}|}{2}\right)\,\hat{a}(t)\;-\mathrm{i}\,g_\mathrm{om}\,\left(\hat{b}^\dagger(t) + \hat{b}(t)\right)\,\hat{a}(t)\\ &-\mathrm{i}\,g_\mathrm{om}\,\left(\hat{b}^\dagger(t) + \hat{b}(t)\right)\,\bar{a}_\star\,\mathrm{e}^{-\mathrm{i}\,\omega_\star\,t} - \sqrt{\gamma_\mathrm{o}}\,\hat{d}_\mathrm{in}(t) - \sum_{l\neq\star}\mathrm{i}\,L_l\,\mathrm{e}^{-\mathrm{i}\,\omega_l\,t} ,\end{aligned}$$

$$\begin{aligned}\frac{\mathrm{d}}{\mathrm{d}t}\,\hat{b}(t) = &-\left(\mathrm{i}\,\omega_\mathrm{m} + \frac{|\gamma_\mathrm{m}|}{2}\right)\,\hat{b}(t)\;-\mathrm{i}\,g_\mathrm{om}\,\hat{a}^\dagger(t)\,\hat{a}(t)\\ &-\mathrm{i}\,g_\mathrm{om}\left(\bar{a}_\star\,\mathrm{e}^{-\mathrm{i}\,\omega_\star\,t}\,\hat{a}^\dagger(t) + \bar{a}_\star^*\,\mathrm{e}^{\mathrm{i}\,\omega_\star\,t}\,\hat{a}(t)\right) - \sqrt{\gamma_\mathrm{m}}\,\hat{e}_\mathrm{in}(t) .\end{aligned}$$

For completeness, the Hamiltonian is

$$\hat{H}_{\mathrm{lvl}\,\star} = \hat{D}_{\hat{b}}(\bar{b}_\star)^\dagger\, \hat{D}_{\hat{a}}(\bar{a}_\star\, \mathrm{e}^{-\mathrm{i}\,\omega_\star\, t})^\dagger\, \left(\hat{H} - \mathrm{i}\,\hbar\,\frac{\partial}{\partial t}\right)\, \hat{D}_{\hat{a}}(\bar{a}_\star\, \mathrm{e}^{-\mathrm{i}\,\omega_\star\, t})\, \hat{D}_{\hat{b}}(\bar{b}_\star) \tag{J.11}$$

$$\begin{aligned}
&= \hbar\,\omega_{\mathrm{om}}\, \left(\hat{a}^\dagger\,\hat{a} + \frac{1}{2}\right) + \hbar\,\omega_{\mathrm{m}}\, \left(\hat{b}^\dagger\,\hat{b} + \frac{1}{2}\right) \\
&\quad + \hbar\, g_{\mathrm{om}}\, \hat{a}^\dagger\,\hat{a}\, \left(\hat{b}^\dagger + \hat{b}\right) + \hbar\, g_{\mathrm{om}}\, \left(\bar{a}_\star\, \hat{a}^\dagger\, \mathrm{e}^{-\mathrm{i}\,\omega_\star\, t} + \bar{a}_\star^*\, \hat{a}\, \mathrm{e}^{\mathrm{i}\,\omega_\star\, t}\right)\, \left(\hat{b}^\dagger + \hat{b}\right) \\
&\quad + \mathrm{i}\,\hbar\,\frac{|\gamma_{\mathrm{o}}|}{2}\, \left(\bar{a}_\star\, \hat{a}^\dagger\, \mathrm{e}^{-\mathrm{i}\,\omega_\star\, t} - \bar{a}_\star^*\, \hat{a}\, \mathrm{e}^{\mathrm{i}\,\omega_\star\, t}\right) + \mathrm{i}\,\hbar\,\frac{|\gamma_{\mathrm{m}}|}{2}\, \left(\bar{b}_\star\, \hat{b}^\dagger - \bar{b}_\star^*\, \hat{b}\right) \\
&\quad + \sum_{l\neq\star} \hbar\, \left(L_l\, \hat{a}^\dagger\, \mathrm{e}^{-\mathrm{i}\,\omega_{\mathrm{l}}\, t} + L_l^*\, \hat{a}\, \mathrm{e}^{\mathrm{i}\,\omega_{\mathrm{l}}\, t}\right) \\
&\quad + \sum_q \hbar\,\omega_q\, \hat{d}_q^\dagger\, \hat{d}_q + \sum_q \hbar\, \left(\kappa_q\, \hat{a}^\dagger\, \hat{d}_q + \kappa_q^*\, \hat{a}\, \hat{d}_q^\dagger\right) + \sum_q \hbar\, \left(\kappa_q\, \bar{a}_\star^*\, \hat{d}_q\, \mathrm{e}^{\mathrm{i}\,\omega_\star\, t} + \kappa_q^*\, \bar{a}\, \hat{d}_q^\dagger \mathrm{e}^{-\mathrm{i}\,\omega_\star\, t}\right) \\
&\quad + \sum_q \hbar\,\omega_q\, \hat{e}_q^\dagger\, \hat{e}_q + \sum_q \hbar\, \left(\lambda_q\, \hat{b}^\dagger\, \hat{e}_q + \lambda_q^*\, \hat{b}\, \hat{e}_q^\dagger\right) + \sum_q \hbar\, \left(\lambda_q\, \bar{b}_\star^*\, \hat{e}_q + \lambda_q^*\, \bar{b}_\star\, \hat{e}_q^\dagger\right) \\
&\quad + \mathrm{i}\,\hbar\,\frac{|\gamma_{\mathrm{o}}|}{2}\, |\bar{a}_\star|^2 + \hbar\,\omega_{\mathrm{m}}\, |\bar{b}_\star|^2 \\
&\quad + \sum_{l\neq\star} \hbar\, \left(L_l\, \bar{a}_\star^*\, \mathrm{e}^{-\mathrm{i}\,(\omega_{\mathrm{l}}-\omega_\star)\, t} + L_l^*\, \bar{a}_\star\, \mathrm{e}^{\mathrm{i}\,(\omega_{\mathrm{l}}-\omega_\star)\, t}\right)\ ,
\end{aligned} \tag{J.12}$$

where

$$\omega_{\mathrm{om}} = \omega_{\mathrm{o}} + g_{\mathrm{om}}\, \left(\bar{b}_\star^* + \bar{b}_\star\right)\ .$$

J.8.3 Linearized system

For $\bar{a}_\star^* \, \bar{a}_\star \gg \hat{a}^\dagger \, \hat{a}$ and $\bar{b}_\star^* + \bar{b}_\star \gg \hat{b}^\dagger + \hat{b}$ the equations of motion can be linearized, equivalently dropping the $\hbar \, g_{\rm om} \, \hat{a}^\dagger \, \hat{a} \, \left(\hat{b}^\dagger + \hat{b} \right)$ term in (J.12), to

$$\begin{aligned} \frac{\mathrm{d}}{\mathrm{d}t} \hat{a}(t) = & - \left(\mathrm{i} \, \left(\omega_{\rm o} + g_{\rm om} \, (\bar{b}_\star + \bar{b}_\star^*) \right) + \frac{|\gamma_{\rm o}|}{2} \right) \, \hat{a}(t) \\ & - \mathrm{i} \, g_{\rm om} \, \left(\hat{b}^\dagger(t) + \hat{b}(t) \right) \, \bar{a}_\star \, \mathrm{e}^{-\mathrm{i} \, \omega_\star \, t} - \sqrt{\gamma_{\rm o}} \, \hat{d}_{\rm in}(t) - \sum_{l \neq \star} \mathrm{i} \, L_l \, \mathrm{e}^{-\mathrm{i} \, \omega_l \, t} \, , \end{aligned} \tag{J.13}$$

$$\begin{aligned} \frac{\mathrm{d}}{\mathrm{d}t} \, \hat{b}(t) = & - \left(\mathrm{i} \, \omega_{\rm m} + \frac{|\gamma_{\rm m}|}{2} \right) \, \hat{b}(t) \\ & - \mathrm{i} \, g_{\rm om} \Big(\bar{a}_\star \, \mathrm{e}^{-\mathrm{i} \, \omega_\star \, t} \, \hat{a}^\dagger(t) + \bar{a}_\star^* \, \mathrm{e}^{\mathrm{i} \, \omega_\star \, t} \, \hat{a}(t) \Big) - \sqrt{\gamma_{\rm m}} \, \hat{e}_{\rm in}(t) \, , \end{aligned} \tag{J.14}$$

allowing us to take the Fourier transforms

$$\hat{a}(\omega) = \frac{-\mathrm{i} \, g_{\rm om} \, \bar{a}_\star \, \left(\hat{b}^\dagger(\omega - \omega_\star) + \hat{b}(\omega - \omega_\star) \right) - \sqrt{\gamma_{\rm o}} \, \hat{d}_{\rm in}(\omega) - \sum_{l \neq \star} \mathrm{i} \, L_l \, \sqrt{2 \, \pi} \, \delta(\omega - \omega_l)}{\mathrm{i} \, \left(\omega_{\rm o} + g_{\rm om} \, (\bar{b}_\star^* + \bar{b}_\star) - \omega \right) + \frac{|\gamma_{\rm o}|}{2}} \, ,$$

$$\hat{b}(\omega) = \frac{-\mathrm{i} \, g_{\rm om} \, \left(\bar{a}_\star \, \hat{a}^\dagger(\omega - \omega_\star) + \bar{a}_\star^* \, \hat{a}(\omega + \omega_\star) \right) - \sqrt{\gamma_{\rm m}} \, \hat{e}_{\rm in}(\omega)}{\mathrm{i} \, \left(\omega_{\rm m} - \omega \right) + \frac{|\gamma_{\rm m}|}{2}} \, ,$$

with Hermitian conjugates

$$\hat{a}^\dagger(\omega) = \frac{\mathrm{i} \, g_{\rm om} \, \bar{a}_\star^* \, \left(\hat{b}(\omega + \omega_\star) + \hat{b}^\dagger(\omega + \omega_\star) \right) - \sqrt{\gamma_{\rm o}^*} \, \hat{d}_{\rm in}^\dagger(\omega) + \sum_{l \neq \star} \mathrm{i} \, L_l^* \, \sqrt{2 \, \pi} \, \delta(\omega + \omega_l)}{-\mathrm{i} \, \left(\omega_{\rm o} + g_{\rm om} \, (\bar{b}_\star^* + \bar{b}_\star) + \omega \right) + \frac{|\gamma_{\rm o}|}{2}} \, ,$$

$$\hat{b}^\dagger(\omega) = \frac{\mathrm{i} \, g_{\rm om} \, \left(\bar{a}_\star^* \, \hat{a}(\omega + \omega_\star) + \bar{a}_\star \, \hat{a}^\dagger(\omega - \omega_\star) \right) - \sqrt{\gamma_{\rm m}^*} \, \hat{e}_{\rm in}^\dagger(\omega)}{-\mathrm{i} \, \left(\omega_{\rm m} + \omega \right) + \frac{|\gamma_{\rm m}|}{2}} \, .$$

From the above equations we note that

$$\begin{aligned} \hat{a}(\omega) &\text{ peaked around } \omega_{\mathrm{om}} \ , \\ \hat{a}^\dagger(\omega) &\text{ peaked around } -\omega_{\mathrm{om}} \ , \\ \hat{b}(\omega) &\text{ peaked around } \omega_{\mathrm{m}} \ , \\ \hat{b}^\dagger(\omega) &\text{ peaked around } -\omega_{\mathrm{m}} \ , \end{aligned} \tag{J.15}$$

allowing approximations to be made in various situations by dropping insignificant terms.

J.8.4 Optical spring

For a high quality mechanical resonator ($|\gamma_{\mathrm{m}}| \ll \omega_{\mathrm{m}}$) we can use (J.15) to make some simplifications when studying the mechanics on resonance. First we have

$$\hat{b}(\omega = \omega_{\mathrm{m}}) \propto \hat{a}^\dagger(\omega_{\mathrm{m}} - \omega_\star) + \hat{a}(\omega_{\mathrm{m}} + \omega_\star) \ ,$$

then

$$\hat{a}^\dagger(\omega = \omega_{\mathrm{m}} - \omega_\star) \propto \underbrace{\hat{b}(\omega_{\mathrm{m}})}_{\text{dominates}} + \hat{b}^\dagger(\omega_{\mathrm{m}}) \ ,$$

$$\hat{a}(\omega = \omega_{\mathrm{m}} + \omega_\star) \propto \hat{b}^\dagger(\omega_{\mathrm{m}}) + \underbrace{\hat{b}(\omega_{\mathrm{m}})}_{\text{dominates}} \ .$$

Substituting $\hat{a}$ and $\hat{a}^\dagger$ into $\hat{b}$ with just the dominating terms, and no additional laser drives ($L_{l \neq \star} = 0$), then produces the same results as Sec. J.3.

J.8.5 Beam splitter and entangling

If our main laser drive, $\star$, is $\left\{ \begin{smallmatrix} \text{red} \\ \text{blue} \end{smallmatrix} \right\}$ detuned from the optical resonance by the mechanical resonance ($\omega_\star = \omega_{\text{om}} \mp \omega_{\text{m}}$), and we are sideband resolved ($|\gamma_{\text{o}}| \ll \omega_{\text{m}}$), we get a $\left\{ \begin{smallmatrix} \text{beam splitter} \\ \text{entangling} \end{smallmatrix} \right\}$ interaction. Using (J.15) find

$$\hat{a}(\omega = \omega_{\text{om}}) \propto \underbrace{\hat{b}^\dagger(\pm\omega_{\text{m}})}_{\substack{\text{dominates} \\ \text{for blue}}} + \underbrace{\hat{b}(\pm\omega_{\text{m}})}_{\substack{\text{dominates} \\ \text{for red}}} ,$$

$$\hat{a}^\dagger(\omega = -\omega_{\text{om}}) \propto \underbrace{\hat{b}(\mp\omega_{\text{m}})}_{\substack{\text{dominates} \\ \text{for blue}}} + \underbrace{\hat{b}^\dagger(\mp\omega_{\text{m}})}_{\substack{\text{dominates} \\ \text{for red}}} ,$$

$$\hat{b}(\omega = \omega_{\text{m}}) \propto \underbrace{\hat{a}^\dagger(-\omega_{\text{om}} + \left\{ \begin{smallmatrix} 2\,\omega_{\text{m}} \\ 0 \end{smallmatrix} \right\})}_{\substack{\text{dominates} \\ \text{for blue}}} + \underbrace{\hat{a}(\omega_{\text{om}} + \left\{ \begin{smallmatrix} 0 \\ 2\,\omega_{\text{m}} \end{smallmatrix} \right\})}_{\substack{\text{dominates} \\ \text{for red}}} ,$$

$$\hat{b}^\dagger(\omega = -\omega_{\text{m}}) \propto \underbrace{\hat{a}(\omega_{\text{om}} - \left\{ \begin{smallmatrix} 2\,\omega_{\text{m}} \\ 0 \end{smallmatrix} \right\})}_{\substack{\text{dominates} \\ \text{for blue}}} + \underbrace{\hat{a}^\dagger(-\omega_{\text{om}} - \left\{ \begin{smallmatrix} 0 \\ 2\,\omega_{\text{m}} \end{smallmatrix} \right\})}_{\substack{\text{dominates} \\ \text{for red}}} ,$$

and obtain frequency-space expressions

$$\hat{a}(\omega) = \frac{-\mathrm{i}\, g_{\mathrm{om}}\, \bar{a}_\star \left\{ \begin{smallmatrix} \hat{b} \\ \hat{b}^\dagger \end{smallmatrix} \right\} (\omega - \omega_{\mathrm{om}} \pm \omega_{\mathrm{m}}) - \sqrt{\gamma_{\mathrm{o}}}\, \hat{d}_{\mathrm{in}}(\omega) - \sum_{l \neq \star} \mathrm{i}\, L_l \sqrt{2\,\pi}\, \delta(\omega - \omega_l)}{\mathrm{i}\, (\omega_{\mathrm{om}} - \omega) + \frac{|\gamma_{\mathrm{o}}|}{2}} ,$$

$$\hat{b}(\omega) = \frac{-\mathrm{i}\, g_{\mathrm{om}} \left\{ \begin{smallmatrix} \bar{a}_\star^* \\ \bar{a}_\star \end{smallmatrix} \right\} \left\{ \begin{smallmatrix} \hat{a} \\ \hat{a}^\dagger \end{smallmatrix} \right\} (\omega \pm \omega_{\mathrm{om}} - \omega_{\mathrm{m}}) - \sqrt{\gamma_{\mathrm{m}}}\, \hat{e}_{\mathrm{in}}(\omega)}{\mathrm{i}\, (\omega_{\mathrm{m}} - \omega) + \frac{|\gamma_{\mathrm{m}}|}{2}} ,$$

$$\hat{a}^\dagger(\omega) = \frac{\mathrm{i}\, g_{\mathrm{om}}\, \bar{a}_\star^* \left\{ \begin{smallmatrix} \hat{b}^\dagger \\ \hat{b} \end{smallmatrix} \right\} (\omega + \omega_{\mathrm{om}} \mp \omega_{\mathrm{m}}) - \sqrt{\gamma_{\mathrm{o}}^*}\, \hat{d}_{\mathrm{in}}^\dagger(\omega) + \sum_{l \neq \star} \mathrm{i}\, L_l^* \sqrt{2\,\pi}\, \delta(\omega + \omega_l)}{-\mathrm{i}\, (\omega_{\mathrm{om}} + \omega) + \frac{|\gamma_{\mathrm{o}}|}{2}} ,$$

$$\hat{b}^\dagger(\omega) = \frac{\mathrm{i}\, g_{\mathrm{om}} \left\{ \begin{smallmatrix} \bar{a}_\star \\ \bar{a}_\star^* \end{smallmatrix} \right\} \left\{ \begin{smallmatrix} \hat{a}^\dagger \\ \hat{a} \end{smallmatrix} \right\} (\omega \mp \omega_{\mathrm{om}} + \omega_{\mathrm{m}}) - \sqrt{\gamma_{\mathrm{m}}^*}\, \hat{e}_{\mathrm{in}}^\dagger(\omega)}{-\mathrm{i}\, (\omega_{\mathrm{m}} + \omega) + \frac{|\gamma_{\mathrm{m}}|}{2}} .$$

J.8.6 Optomechanical induced windows

A $\left\{ \begin{smallmatrix} \text{red} \\ \text{blue} \end{smallmatrix} \right\}$ detuned laser pump will produce optomechanical induced $\left\{ \begin{smallmatrix} \text{transparency} \\ \text{absorption} \end{smallmatrix} \right\}$. Adding additional heat baths, with loss parameter $\gamma_{\mathrm{o}}^{\mathrm{wg}}$, to model the waveguide ports and following the input-output theory of a symmetric non-directional waveguide resonator (see Sec. Θ.4.1)

we get the following system of equations,

$$\frac{\mathrm{d}}{\mathrm{d}t}\hat{a}(t) = -\left(\mathrm{i}\,\omega_{\mathrm{om}} + \frac{\gamma_{\mathrm{o}}}{2}\right)\,\hat{a}(t) - \mathrm{i}\,g_{\mathrm{om}}\,\bar{a}_{\star}\,\left\{\begin{array}{c}\hat{b}\\ \hat{b}^{\dagger}\end{array}\right\}(t)\,\mathrm{e}^{-\mathrm{i}\,(\omega_{\mathrm{om}}\mp\omega_{\mathrm{m}})\,t} - \sqrt{\gamma_{\mathrm{o}}^{\mathrm{int}}}\,\hat{d}_{\mathrm{in}}^{\mathrm{int}}(t) - \sqrt{\gamma_{\mathrm{o}}^{\mathrm{wg}}}\,\hat{d}_{\mathrm{in}}^{1}(t) - \sqrt{\gamma_{\mathrm{o}}^{\mathrm{wg}}}\,\hat{d}_{\mathrm{in}}^{2}(t)\;,$$

$$\frac{\mathrm{d}}{\mathrm{d}t}\hat{b}(t) = -\left(\mathrm{i}\,\omega_{\mathrm{m}} + \frac{\gamma_{\mathrm{m}}}{2}\right)\,\hat{b}(t) - \mathrm{i}\,g_{\mathrm{om}}\,\left\{\begin{array}{c}\bar{a}_{\star}^{*}\\ \bar{a}_{\star}\end{array}\right\}\,\left\{\begin{array}{c}\hat{a}\\ \hat{a}^{\dagger}\end{array}\right\}(t)\,\mathrm{e}^{\pm\mathrm{i}\,(\omega_{\mathrm{om}}\mp\omega_{\mathrm{m}})\,t} - \sqrt{\gamma_{\mathrm{m}}}\,\hat{e}_{\mathrm{in}}^{\mathrm{int}}(t)\;,$$

$$\hat{d}_{\mathrm{out}}^{1}(t) = \sqrt{\gamma_{\mathrm{o}}^{\mathrm{wg}}}\,\hat{a}(t) + \hat{d}_{\mathrm{in}}^{2}(t)\;,$$

$$\hat{d}_{\mathrm{out}}^{2}(t) = \sqrt{\gamma_{\mathrm{o}}^{\mathrm{wg}}}\,\hat{a}(t) + \hat{d}_{\mathrm{in}}^{1}(t)\;,$$

with

$$\gamma_{\mathrm{o}} = \gamma_{\mathrm{o}}^{\mathrm{int}} + 2\,\gamma_{\mathrm{o}}^{\mathrm{wg}}\;,$$

where we have made all the γ real (moving any complex components to the frequency) and chosen all the phases to be zero. For simplicity we will set the environmental inputs $\hat{d}_{\mathrm{in}}^{\mathrm{int}}$ and $\hat{e}_{\mathrm{in}}^{\mathrm{int}}$, which are negligible compared to the waveguide input, to zero.

Taking the Fourier transform of our equations we get

$$\hat{a}(\omega) = \frac{-\mathrm{i}\, g_{\mathrm{om}}\, \bar{a} \left\{ \begin{smallmatrix} \hat{b} \\ \hat{b}^\dagger \end{smallmatrix} \right\} (\omega - \omega_{\mathrm{om}} \pm \omega_{\mathrm{m}}) - \sqrt{\gamma_{\mathrm{o}}^{\mathrm{wg}}}\, \hat{d}^1_{\mathrm{in}}(\omega) - \sqrt{\gamma_{\mathrm{o}}^{\mathrm{wg}}}\, \hat{d}^2_{\mathrm{in}}(\omega)}{\mathrm{i}\,(\omega_{\mathrm{om}} - \omega) + \frac{\gamma_{\mathrm{o}}}{2}} ,$$

$$\hat{b}(\omega) = \frac{-\mathrm{i}\, g_{\mathrm{om}} \left\{ \begin{smallmatrix} \bar{a}^*_\star \\ \bar{a}_\star \end{smallmatrix} \right\} \left\{ \begin{smallmatrix} \hat{a} \\ \hat{a}^\dagger \end{smallmatrix} \right\} (\omega \pm \omega_{\mathrm{om}} - \omega_{\mathrm{m}})}{\mathrm{i}\ (\omega_{\mathrm{m}} - \omega) + \frac{\gamma_{\mathrm{m}}}{2}} ,$$

$$\hat{a}^\dagger(\omega) = \frac{\mathrm{i}\, g_{\mathrm{om}}\, \bar{a}^*_\star \left\{ \begin{smallmatrix} \hat{b}^\dagger \\ \hat{b} \end{smallmatrix} \right\} (\omega + \omega_{\mathrm{om}} \mp \omega_{\mathrm{m}}) - \sqrt{\gamma_{\mathrm{o}}^{\mathrm{wg}\,*}}\, \hat{d}^{1\,\dagger}_{\mathrm{in}}(\omega) - \sqrt{\gamma_{\mathrm{o}}^{\mathrm{wg}\,*}}\, \hat{d}^{2\,\dagger}_{\mathrm{in}}(\omega)}{-\mathrm{i}\ (\omega_{\mathrm{om}} + \omega) + \frac{|\gamma_{\mathrm{o}}|}{2}} ,$$

$$\hat{b}^\dagger(\omega) = \frac{\mathrm{i}\, g_{\mathrm{om}} \left\{ \begin{smallmatrix} \bar{a}_\star \\ \bar{a}^*_\star \end{smallmatrix} \right\} \left\{ \begin{smallmatrix} \hat{a}^\dagger \\ \hat{a} \end{smallmatrix} \right\} (\omega \mp \omega_{\mathrm{om}} + \omega_{\mathrm{m}})}{-\mathrm{i}\ (\omega_{\mathrm{m}} + \omega) + \frac{|\gamma_{\mathrm{m}}|}{2}} .$$

Solving for $\hat{a}$,

$$\hat{a}(\omega) = \frac{-\sqrt{\gamma_{\mathrm{o}}^{\mathrm{wg}}}\, \hat{d}^1_{\mathrm{in}}(\omega) - \sqrt{\gamma_{\mathrm{o}}^{\mathrm{wg}}}\, \hat{d}^2_{\mathrm{in}}(\omega)}{\mathrm{i}\,(\omega_{\mathrm{om}} - \omega) + \frac{\gamma_{\mathrm{o}}}{2} + \frac{{g_{\mathrm{om}}}^2\, |\bar{a}|^2}{\mathrm{i}\,(\omega_{\mathrm{om}} \mp \omega) \pm \frac{\gamma_{\mathrm{m}}}{2}}} ,$$

and using our waveguide in/out relations we find the transmission to be

$$S_{2\,1}(\omega) = \left. \frac{\hat{d}^2_{\mathrm{out}}(\omega)}{\hat{d}^1_{\mathrm{in}}(\omega)} \right|_{\hat{d}^2_{\mathrm{in}}(\omega)=0} = 1 - \frac{\gamma_{\mathrm{o}}^{\mathrm{wg}}}{\mathrm{i}\,(\omega_{\mathrm{om}} - \omega) + \frac{\gamma_{\mathrm{o}}}{2} + \frac{{g_{\mathrm{om}}}^2\, |\bar{a}|^2}{\mathrm{i}\,(\omega_{\mathrm{om}} \mp \omega) \pm \frac{\gamma_{\mathrm{m}}}{2}}} .$$

The peak transmission is

$$S_{2\,1}\left(\omega=\omega_{\rm om}\right)=1-\frac{2\,\gamma_{\rm o}^{\rm wg}}{\gamma_{\rm o}\pm\frac{4\,{g_{\rm om}}^2\,|\bar{a}|^2}{\gamma_{\rm m}}}$$

$$=1-\frac{\frac{2\,\gamma_{\rm o}^{\rm wg}}{\gamma_{\rm o}}}{1\pm\mathcal{C}_{\rm om}}\ .$$

At critical coupling, $2\,\gamma_{\rm o}^{\rm wg}=\gamma_{\rm o}^{\rm int}\ \Rightarrow\ \frac{2\,\gamma_{\rm o}^{\rm wg}}{\gamma_{\rm o}}=\frac{1}{2}$,

$$S_{2\,1}\left(\omega=\omega_{\rm om};\gamma_{\rm o}^{\rm int}=2\,\gamma_{\rm o}^{\rm wg}\right)=\frac{\frac{1}{2}\pm\mathcal{C}_{\rm om}}{1\pm\mathcal{C}_{\rm om}}\ .$$

Or with no internal loss, $\gamma_{\rm o}^{\rm int}=0\ \Rightarrow\ \frac{2\,\gamma_{\rm o}^{\rm wg}}{\gamma_{\rm o}}=1$,

$$S_{2\,1}\left(\omega=\omega_{\rm om};\gamma_{\rm o}^{\rm int}=0\right)=\frac{\pm\mathcal{C}_{\rm om}}{1\pm\mathcal{C}_{\rm om}}\ .$$

J.8.7 Post linearization sideband drive displacement

Once our system is linearized by the main drive $\star$, displacements to account for additional drives can be made, but only if they come in pairs about the main drive (i.e. sidebands) $\omega_\pm=\omega_\star\pm\omega_\Delta$. The displacement required takes the form

$$\hat{a}(t)\mapsto\hat{a}(t)+\bar{a}_+\,{\rm e}^{-{\rm i}\,(\omega_\star+\omega_\Delta)\,t}+\bar{a}_-\,{\rm e}^{-{\rm i}\,(\omega_\star-\omega_\Delta)\,t}\ ,$$
$$\hat{b}(t)\mapsto\hat{b}(t)+\bar{b}_+\,{\rm e}^{-{\rm i}\,\omega_\Delta\,t}+\bar{b}_-\,{\rm e}^{{\rm i}\,\omega_\Delta\,t}\ .$$

Applying this to the linearized equations of motion (J.13) and (J.14), and keeping non-operator terms we find

$$\begin{aligned}
&\left(\left(\mathrm{i}\,(\omega_{\mathrm{om}}-\omega_\star-\omega_\Delta)+\frac{|\gamma_{\mathrm{o}}|}{2}\right)\bar{a}_+ +\mathrm{i}\,L_+\right)\mathrm{e}^{-\mathrm{i}\,\omega_\Delta\,t}\\
&+\left(\left(\mathrm{i}\,(\omega_{\mathrm{om}}-\omega_\star+\omega_\Delta)+\frac{|\gamma_{\mathrm{o}}|}{2}\right)\bar{a}_- +\mathrm{i}\,L_-\right)\mathrm{e}^{\mathrm{i}\,\omega_\Delta\,t}\\
=\;&-\mathrm{i}\,g_{\mathrm{om}}\,\bar{a}_\star\,\left(\bar{b}_+^*\,\mathrm{e}^{\mathrm{i}\,\omega_\Delta\,t}+\bar{b}_-^*\,\mathrm{e}^{-\mathrm{i}\,\omega_\Delta\,t}+\bar{b}_+\,\mathrm{e}^{-\mathrm{i}\,\omega_\Delta\,t}+\bar{b}_-\,\mathrm{e}^{\mathrm{i}\,\omega_\Delta\,t}\right)
\end{aligned}$$

$$\begin{aligned}
&\left(\mathrm{i}\,(\omega_{\mathrm{m}}-\omega_\Delta)+\frac{|\gamma_{\mathrm{m}}|}{2}\right)\bar{b}_+\,\mathrm{e}^{-\mathrm{i}\,\omega_\Delta\,t}+\left(\mathrm{i}\,(\omega_{\mathrm{m}}+\omega_\Delta)+\frac{|\gamma_{\mathrm{m}}|}{2}\right)\bar{b}_-\,\mathrm{e}^{\mathrm{i}\,\omega_\Delta\,t}\\
=\;&-\mathrm{i}\,g_{\mathrm{om}}\,\left(\bar{a}_\star\,\bar{a}_+^*\,\mathrm{e}^{\mathrm{i}\,\omega_\Delta\,t}+\bar{a}_\star^*\,\bar{a}_+\,\mathrm{e}^{-\mathrm{i}\,\omega_\Delta\,t}+\bar{a}_\star\,\bar{a}_-^*\,\mathrm{e}^{-\mathrm{i}\,\omega_\Delta\,t}+\bar{a}_\star^*\,\bar{a}_-\,\mathrm{e}^{\mathrm{i}\,\omega_\Delta\,t}\right)
\end{aligned}$$

where the time dependence only occurring in factors of $\exp(\pm\mathrm{i}\,\omega_\Delta\,t)$ is attributed to the careful choice made for the displacement's time dependence. Collecting the two sets of terms in each equation, we determine

$$\bar{a}_+ = \frac{-\mathrm{i}\,L_+ - \mathrm{i}\,g_{\mathrm{om}}\,\bar{a}_\star\,\left(\bar{b}_-^*+\bar{b}_+\right)}{\mathrm{i}\,(\omega_{\mathrm{om}}-\omega_\star-\omega_\Delta)+\frac{|\gamma_{\mathrm{o}}|}{2}}\,,$$

$$\bar{a}_- = \frac{-\mathrm{i}\,L_- - \mathrm{i}\,g_{\mathrm{om}}\,\bar{a}_\star\,\left(\bar{b}_+^*+\bar{b}_-\right)}{\mathrm{i}\,(\omega_{\mathrm{om}}-\omega_\star+\omega_\Delta)+\frac{|\gamma_{\mathrm{o}}|}{2}}\,,$$

$$\bar{b}_+ = \frac{-\mathrm{i}\,g_{\mathrm{om}}\,\left(\bar{a}_\star^*\,\bar{a}_+ + \bar{a}_\star\,\bar{a}_-^*\right)}{\mathrm{i}\,(\omega_{\mathrm{m}}-\omega_\Delta)+\frac{|\gamma_{\mathrm{m}}|}{2}}\,,$$

$$\bar{b}_- = \frac{-\mathrm{i}\,g_{\mathrm{om}}\,\left(\bar{a}_\star^*\,\bar{a}_- + \bar{a}_\star\,\bar{a}_+^*\right)}{\mathrm{i}\,(\omega_{\mathrm{m}}+\omega_\Delta)+\frac{|\gamma_{\mathrm{m}}|}{2}}\,.$$

These parameters have varying significance however,

$$\begin{aligned} |\bar{a}_+| > |\bar{a}_-| \quad &: \quad \omega_\star = \omega_{\rm om} - \omega_\Delta \ , \\ |\bar{a}_-| > |\bar{a}_+| \quad &: \quad \omega_\star = \omega_{\rm om} + \omega_\Delta \ , \\ |\bar{b}_+| > |\bar{b}_-| \quad &: \quad \text{generally} \ . \end{aligned}$$

With these definitions the sideband displaced equations of motion are structurally unchanged from (J.13) and (J.14),

$$\begin{aligned} \frac{\mathrm{d}}{\mathrm{d}t}\hat{a}(t) = & -\left(\mathrm{i}\,\omega_{\rm om} + \frac{|\gamma_{\rm o}|}{2}\right)\hat{a}(t) \\ & -\mathrm{i}\,g_{\rm om}\left(\hat{b}^\dagger(t) + \hat{b}(t)\right)\bar{a}_\star\,\mathrm{e}^{-\mathrm{i}\,\omega_\star\,t} - \sqrt{\gamma_{\rm o}}\,\hat{d}_{\rm in}(t) - \sum_{l\neq\{\star,\pm\}} \mathrm{i}\,L_l\,\mathrm{e}^{-\mathrm{i}\,\omega_l\,t} \ , \end{aligned}$$

$$\begin{aligned} \frac{\mathrm{d}}{\mathrm{d}t}\,\hat{b}(t) = & -\left(\mathrm{i}\,\omega_{\rm m} + \frac{|\gamma_{\rm m}|}{2}\right)\hat{b}(t) \\ & -\mathrm{i}\,g_{\rm om}\left(\bar{a}_\star\,\mathrm{e}^{-\mathrm{i}\,\omega_\star\,t}\,\hat{a}^\dagger(t) + \bar{a}_\star^*\,\mathrm{e}^{\mathrm{i}\,\omega_\star\,t}\,\hat{a}(t)\right) - \sqrt{\gamma_{\rm m}}\,\hat{e}_{\rm in}(t) \ . \end{aligned}$$

APPENDIX K

Quantum electro-opto-mechanics

In this appendix we put together the full electro-opto-mechanical input-output.

K.1 Electromechanic hamiltonian

With the optomechanical part covered in App. J, the last step in modelling our system is to incorporate electromechanics, i.e. the coupling between mechanical waves and an electrical circuit. To do this we'll start with an ideal electronic resonator,

$$\hbar\,\omega_{\mathrm{e}}\left(\hat{c}^{\dagger}\,\hat{c}+\frac{1}{2}\right)=\frac{\hat{q}^{2}}{2\,C}+\frac{\hat{\phi}^{2}}{2\,L}\,,$$

with

$$\underset{\text{capacitance}}{C}\,,\qquad \underset{\text{inductance}}{L}\,,\qquad \underset{\substack{\text{resonance}\\ \text{frequency}}}{\omega_{\mathrm{e}}}=\sqrt{\frac{1}{L\,C}}\,,\qquad \underset{\substack{\text{characteristic}\\ \text{impedance}}}{Z_{\mathrm{C}}}=\sqrt{\frac{L}{C}}\,,$$

$$\underset{\text{charge}}{\hat{q}}=\sqrt{\frac{\hbar}{2\,Z_{\mathrm{C}}}}\left(\hat{c}^{\dagger}+\hat{c}\right)\,,\qquad \underset{\text{annihilation}}{\hat{c}}=\sqrt{\frac{Z_{\mathrm{C}}}{2\,\hbar}}\left(\hat{q}+\frac{\mathrm{i}}{Z_{\mathrm{C}}}\hat{\phi}\right)\,,$$

$$\underset{\text{flux}}{\hat{\phi}}=\mathrm{i}\sqrt{\frac{\hbar\,Z_{\mathrm{C}}}{2}}\left(\hat{c}^{\dagger}-\hat{c}\right)\,,\qquad \underset{\text{creation}}{\hat{c}^{\dagger}}=\sqrt{\frac{Z_{\mathrm{C}}}{2\,\hbar}}\left(\hat{q}-\frac{\mathrm{i}}{Z_{\mathrm{C}}}\hat{\phi}\right)\,,$$

$$\left[\hat{q},\hat{\phi}\right] = \mathrm{i}\,\hbar\,, \qquad\qquad \left[\hat{c},\hat{c}^\dagger\right] = 1\,.$$

In the case piezoelectricity[1] (see App. B), the strain ϵ produces an additional electric field E_{piezo} driving the capacitor and hence voltage across it. The charge then acquires an additional contribution $\hat{q} \mapsto \hat{q} + C\,V_{\mathrm{piezo}}$. With

$$V_{\mathrm{piezo}} \quad \propto \quad E_{\mathrm{piezo}} \quad \propto \quad \epsilon \quad \propto \quad \hat{x}\,,$$

let us write

$$V_{\mathrm{piezo}} = G_{\mathrm{em}}\,\hat{x}\,.$$

Putting this into the Hamiltonian,

$$\frac{\hat{q}^2}{2\,C} \mapsto \frac{\left(\hat{q} + C\,G_{\mathrm{em}}\,\hat{x}\right)^2}{2\,C} = \frac{\hat{q}^2}{2\,C} + G_{\mathrm{em}}\,\hat{q}\,\hat{x} + \frac{C\,{G_{\mathrm{em}}}^2\,\hat{x}^2}{2}$$

$$= \frac{\hat{q}^2}{2\,C} + \underbrace{\hbar\,g_{\mathrm{em}}\left(\hat{b}^\dagger + \hat{b}\right)\left(\hat{c}^\dagger + \hat{c}\right)}_{\text{electromechanical interaction}} + \underbrace{\frac{2\,m\,{g_{\mathrm{em}}}^2\,\omega_{\mathrm{m}}}{\omega_{\mathrm{e}}}\,\hat{x}^2}_{\text{non-linear } \omega_{\mathrm{m}} \text{ shift}}\,,$$

we obtain a simple electromechanical coupling term [236]. Under the rotating wave approximation with $\omega_{\mathrm{m}} \approx \omega_{\mathrm{e}}$ this interaction simplifies to

$$\hbar\,g_{\mathrm{em}}\left(\hat{b}^\dagger\,\hat{c} + \hat{b}\,\hat{c}^\dagger\right).$$

We'll consider both the red and blue detuned pump optomechanical interaction by using

1. Differing from the capacitor on a spring system which produces a $\hat{x}\,\hat{q}^2$ term.

coloured symbols that only appear in their respective case,

$$\hbar\, g_{\mathrm{om}} \left(\bar{a}\, \hat{a}^\dagger\, \hat{b}^\dagger + \bar{a}^*\, \hat{a}\, \hat{b}^\dagger \right) .$$

K.2 Single drive displacement

The single drive $\star$ displacement is now

$$\begin{aligned} \hat{a}(t) &\mapsto \hat{a}(t) + \bar{a}_\star\, \mathrm{e}^{-\mathrm{i}\,\omega_\star\, t} , \\ \hat{b}(t) &\mapsto \hat{b}(t) + \bar{b}_\star , \\ \hat{c}(t) &\mapsto \hat{c}(t) + \bar{c}_\star , \end{aligned}$$

with

$$\bar{a}_\star = \frac{-\mathrm{i}\, L_\star}{\mathrm{i}\, \left(\omega_{\mathrm{o}} - \omega_\star + g_{\mathrm{om}} \left(\bar{b}_\star^* + \bar{b}_\star \right) \right) + \frac{\gamma_{\mathrm{o}}}{2}} ,$$

$$\bar{b}_\star = \frac{-\mathrm{i}\, g_{\mathrm{om}} \left(|\bar{a}_\star|^2 + \frac{1}{2} \right) - \mathrm{i}\, g_{\mathrm{em}}\, \bar{c}_\star}{\mathrm{i}\, \omega_{\mathrm{m}} + \frac{\gamma_{\mathrm{m}}}{2}} ,$$

$$\bar{c}_\star = \frac{-\mathrm{i}\, g_{\mathrm{em}}\, \bar{b}_\star}{\mathrm{i}\, \omega_{\mathrm{e}} + \frac{\gamma_{\mathrm{e}}}{2}} .$$

K.3 Equations of motion

In the non-rotating frame, the equations of motion for the $\omega_\star = \omega_{\mathrm{om}} \pm \omega_{\mathrm{m}}$ pumped and displaced, linearized system, with bi-directional optic waveguide ports and single electrical

transmission line port are

$$\frac{\mathrm{d}}{\mathrm{d}t}\hat{a}(t) = -\left(\mathrm{i}\,\omega_{\mathrm{om}} + \frac{\gamma_{\mathrm{o}}}{2}\right)\,\hat{a}(t) - \mathrm{i}\,g_{\mathrm{om}}\,\bar{a}_{\star}\,\hat{b}^{\dagger}(t)\,\mathrm{e}^{-\mathrm{i}\,(\omega_{\mathrm{om}} \pm \omega_{\mathrm{m}})\,t} - \sqrt{\gamma_{\mathrm{o}}^{\mathrm{int}}}\,\hat{d}_{\mathrm{in}}^{\mathrm{int}}(t) - \sqrt{\gamma_{\mathrm{o}}^{\mathrm{wg}}}\,\hat{d}_{\mathrm{in}}^{1}(t) - \sqrt{\gamma_{\mathrm{o}}^{\mathrm{wg}}}\,\hat{d}_{\mathrm{in}}^{2}(t)\ ,$$

$$\frac{\mathrm{d}}{\mathrm{d}t}\hat{b}(t) = -\left(\mathrm{i}\,\omega_{\mathrm{m}} + \frac{\gamma_{\mathrm{m}}}{2}\right)\,\hat{b}(t) - \mathrm{i}\,g_{\mathrm{om}}\,\bar{a}_{\star}^{*}\,\hat{a}^{\dagger}(t)\,\mathrm{e}^{\pm\,\mathrm{i}\,(\omega_{\mathrm{om}} \pm \omega_{\mathrm{m}})\,t} - \mathrm{i}\,g_{\mathrm{em}}\,\hat{c}(t) - \sqrt{\gamma_{\mathrm{m}}}\,\hat{e}_{\mathrm{in}}^{\mathrm{int}}(t)\ ,$$

$$\frac{\mathrm{d}}{\mathrm{d}t}\hat{c}(t) = -\left(\mathrm{i}\,\omega_{\mathrm{e}} + \frac{\gamma_{\mathrm{e}}}{2}\right)\,\hat{c}(t) - \mathrm{i}\,g_{\mathrm{em}}\,\hat{b}(t) - \sqrt{\gamma_{\mathrm{e}}^{\mathrm{int}}}\,\hat{f}_{\mathrm{in}}^{\mathrm{int}}(t) - \sqrt{\gamma_{\mathrm{e}}^{\mathrm{tx}}}\,\hat{f}_{\mathrm{in}}^{\mathrm{tx}}(t)\ ,$$

$$\hat{d}_{\mathrm{out}}^{1}(t) = \sqrt{\gamma_{\mathrm{o}}^{\mathrm{wg}}}\,\hat{a}(t) + \hat{d}_{\mathrm{in}}^{2}(t)\ ,$$

$$\hat{d}_{\mathrm{out}}^{2}(t) = \sqrt{\gamma_{\mathrm{o}}^{\mathrm{wg}}}\,\hat{a}(t) + \hat{d}_{\mathrm{in}}^{1}(t)\ ,$$

$$\hat{f}_{\mathrm{out}}^{\mathrm{tx}}(t) = \sqrt{\gamma_{\mathrm{e}}^{\mathrm{tx}}}\,\hat{c}(t) + \hat{f}_{\mathrm{in}}^{\mathrm{tx}}(t)\ ,$$

with

$$\gamma_{\rm o}^{\rm wg} = \gamma_{\rm o}^{1} = \gamma_{\rm o}^{2} = \gamma_{\rm o}^{12}/2 \; ,$$

$$\gamma_{\rm o} = \gamma_{\rm o}^{\rm int} + 2\,\gamma_{\rm o}^{\rm wg} \; ,$$

$$\gamma_{\rm m} = \gamma_{\rm m}^{\rm int} \; ,$$

$$\gamma_{\rm e} = \gamma_{\rm e}^{\rm int} + \gamma_{\rm e}^{\rm tx} \; .$$

Taking the Fourier transforms, we get

$$\hat{a}(\omega) = \frac{-\mathrm{i}\, g_{\mathrm{om}}\, \bar{a}_\star\, \hat{b}^\dagger(\omega - \omega_{\mathrm{om}} \pm \omega_{\mathrm{m}}) - \sqrt{\gamma_{\mathrm{o}}^{\mathrm{int}}}\, \hat{d}_{\mathrm{in}}^{\mathrm{int}}(\omega) - \sqrt{\gamma_{\mathrm{o}}^{\mathrm{wg}}}\, \hat{d}_{\mathrm{in}}^{1}(\omega) - \sqrt{\gamma_{\mathrm{o}}^{\mathrm{wg}}}\, \hat{d}_{\mathrm{in}}^{2}(\omega)}{\mathrm{i}\,(\omega_{\mathrm{om}} - \omega) + \frac{\gamma_{\mathrm{o}}}{2}}\,,$$

$$\hat{a}^\dagger(\omega) = \frac{-\mathrm{i}\, g_{\mathrm{om}}\, \bar{a}_\star^*\, \hat{b}^\dagger(\omega + \omega_{\mathrm{om}} \pm \omega_{\mathrm{m}}) + \sqrt{\gamma_{\mathrm{o}}^{\mathrm{int}}}\, \hat{d}_{\mathrm{in}}^{\mathrm{int}\,\dagger}(\omega) + \sqrt{\gamma_{\mathrm{o}}^{\mathrm{wg}}}\, \hat{d}_{\mathrm{in}}^{1\,\dagger}(\omega) + \sqrt{\gamma_{\mathrm{o}}^{\mathrm{wg}}}\, \hat{d}_{\mathrm{in}}^{2\,\dagger}(\omega)}{\mathrm{i}\,(\omega_{\mathrm{om}} + \omega) - \frac{\gamma_{\mathrm{o}}}{2}}\,,$$

$$\hat{b}(\omega) = \frac{-\mathrm{i}\, g_{\mathrm{om}}\, \bar{a}_\star^*\, \hat{a}^\dagger(\omega \pm \omega_{\mathrm{om}} - \omega_{\mathrm{m}}) - \mathrm{i}\, g_{\mathrm{em}}\, \hat{c}(\omega) - \sqrt{\gamma_{\mathrm{m}}^{\mathrm{int}}}\, \hat{e}_{\mathrm{in}}^{\mathrm{int}}(\omega)}{\mathrm{i}\,(\omega_{\mathrm{m}} - \omega) + \frac{\gamma_{\mathrm{m}}}{2}}\,,$$

$$\hat{b}^\dagger(\omega) = \frac{-\mathrm{i}\, g_{\mathrm{om}}\, \bar{a}_\star^*\, \hat{a}^\dagger(\omega \pm \omega_{\mathrm{om}} + \omega_{\mathrm{m}}) - \mathrm{i}\, g_{\mathrm{em}}\, \hat{c}^\dagger(\omega) + \sqrt{\gamma_{\mathrm{m}}^{\mathrm{int}}}\, \hat{e}_{\mathrm{in}}^{\mathrm{int}\,\dagger}(\omega)}{\mathrm{i}\,(\omega_{\mathrm{m}} + \omega) - \frac{\gamma_{\mathrm{m}}}{2}}\,,$$

$$\hat{c}(\omega) = \frac{-\mathrm{i}\, g_{\mathrm{em}}\, \hat{b}(\omega) - \sqrt{\gamma_{\mathrm{e}}^{\mathrm{int}}}\, \hat{f}_{\mathrm{in}}^{\mathrm{int}}(\omega) - \sqrt{\gamma_{\mathrm{e}}^{\mathrm{tx}}}\, \hat{f}_{\mathrm{in}}^{\mathrm{tx}}(\omega)}{\mathrm{i}\,(\omega_{\mathrm{e}} - \omega) + \frac{\gamma_{\mathrm{e}}}{2}}\,,$$

$$\hat{c}^\dagger(\omega) = \frac{-\mathrm{i}\, g_{\mathrm{em}}\, \hat{b}^\dagger(\omega) + \sqrt{\gamma_{\mathrm{e}}^{\mathrm{int}}}\, \hat{f}_{\mathrm{in}}^{\mathrm{int}\,\dagger}(\omega) + \sqrt{\gamma_{\mathrm{e}}^{\mathrm{tx}}}\, \hat{f}_{\mathrm{in}}^{\mathrm{tx}\,\dagger}(\omega)}{\mathrm{i}\,(\omega_{\mathrm{e}} + \omega) - \frac{\gamma_{\mathrm{e}}}{2}}\,.$$

For convenience, denote

$$\upsilon_{\mathrm{x}}(\Omega;\omega) = \mathrm{i}\,(\Omega - \omega) + \frac{\gamma_{\mathrm{x}}}{2}\,.$$

Eliminating $\hat{b}^\dagger$ in $\hat{a}$,

$$\left(\upsilon_{\mathrm{o}}(\omega_{\mathrm{om}};\omega) \pm \frac{{g_{\mathrm{om}}}^2\,|\bar{a}_\star|^2}{\upsilon_{\mathrm{m}}(\omega_{\mathrm{om}};\omega)}\right)\,\hat{a}(\omega) = \pm\,\frac{-\mathrm{i}\,g_{\mathrm{om}}\,\bar{a}_\star}{\upsilon_{\mathrm{m}}(\omega_{\mathrm{om}};\omega)}\begin{pmatrix} -\mathrm{i}\,g_{\mathrm{em}}\,\hat{c}^\dagger(\omega-\omega_{\mathrm{om}}\pm\omega_{\mathrm{m}}) \\ \pm\sqrt{\gamma_{\mathrm{m}}^{\mathrm{int}}}\,\hat{e}_{\mathrm{in}}^{\mathrm{int}\,\dagger}(\omega-\omega_{\mathrm{om}}\pm\omega_{\mathrm{m}})\end{pmatrix}$$
$$-\sqrt{\gamma_{\mathrm{o}}^{\mathrm{int}}}\,\hat{d}_{\mathrm{in}}^{\mathrm{int}}(\omega)-\sqrt{\gamma_{\mathrm{o}}^{\mathrm{wg}}}\,\hat{d}_{\mathrm{in}}^{1}(\omega)-\sqrt{\gamma_{\mathrm{o}}^{\mathrm{wg}}}\,\hat{d}_{\mathrm{in}}^{2}(\omega)\;,$$

and eliminating $\hat{b}^\dagger$ in $\hat{c}^\dagger$,

$$\left(\upsilon_{\mathrm{e}}(\pm\omega_{\mathrm{e}};\omega)+\frac{{g_{\mathrm{em}}}^2}{\upsilon_{\mathrm{m}}(\pm\omega_{\mathrm{m}};\omega)}\right)\,\hat{c}^\dagger(\omega) = \frac{-\mathrm{i}\,g_{\mathrm{em}}}{\upsilon_{\mathrm{m}}(\pm\omega_{\mathrm{m}};\omega)}\begin{pmatrix} -\mathrm{i}\,g_{\mathrm{om}}\,\bar{a}_\star^*\,\hat{a}(\omega+\omega_{\mathrm{om}}\pm\omega_{\mathrm{m}}) \\ \pm\sqrt{\gamma_{\mathrm{m}}^{\mathrm{int}}}\,\hat{e}_{\mathrm{in}}^{\mathrm{int}\,\dagger}(\omega)\end{pmatrix}$$
$$-\sqrt{\gamma_{\mathrm{e}}^{\mathrm{int}}}\,\hat{f}_{\mathrm{in}}^{\mathrm{int}\,\dagger}(\omega)-\sqrt{\gamma_{\mathrm{e}}^{\mathrm{tx}}}\,\hat{f}_{\mathrm{in}}^{\mathrm{tx}\,\dagger}(\omega)\;,$$

and solving for $\hat{a}$,

$$\left(1 \pm \frac{{g_{\mathrm{om}}}^2\,|\bar{a}_\star|^2}{\upsilon_{\mathrm{o}}(\omega_{\mathrm{om}};\omega)\,\upsilon_{\mathrm{m}}(\omega_{\mathrm{om}};\omega)}+\frac{{g_{\mathrm{em}}}^2}{\upsilon_{\mathrm{e}}(\omega_{\mathrm{om}}\pm\omega_{\mathrm{e}}\pm\omega_{\mathrm{m}};\omega)\,\upsilon_{\mathrm{m}}(\omega_{\mathrm{om}};\omega)}\right)\,\hat{a}(\omega) =$$

$$-\frac{\upsilon_{\mathrm{e}}(\omega_{\mathrm{om}}\pm\omega_{\mathrm{e}}\pm\omega_{\mathrm{m}};\omega)\,\upsilon_{\mathrm{m}}(\omega_{\mathrm{om}};\omega)+{g_{\mathrm{em}}}^2}{\upsilon_{\mathrm{o}}(\omega_{\mathrm{om}};\omega)\,\upsilon_{\mathrm{m}}(\omega_{\mathrm{om}};\omega)\,\upsilon_{\mathrm{e}}(\omega_{\mathrm{om}}\pm\omega_{\mathrm{e}}\pm\omega_{\mathrm{m}};\omega)}\begin{pmatrix}\sqrt{\gamma_{\mathrm{o}}^{\mathrm{int}}}\,\hat{d}_{\mathrm{in}}^{\mathrm{int}}(\omega)+\sqrt{\gamma_{\mathrm{o}}^{\mathrm{wg}}}\,\hat{d}_{\mathrm{in}}^{1}(\omega) \\ +\sqrt{\gamma_{\mathrm{o}}^{\mathrm{wg}}}\,\hat{d}_{\mathrm{in}}^{2}(\omega)\end{pmatrix}$$

$$+\frac{\mathrm{i}\,g_{\mathrm{om}}\,\bar{a}_\star}{\upsilon_{\mathrm{o}}(\omega_{\mathrm{om}};\omega)\,\upsilon_{\mathrm{m}}(\omega_{\mathrm{om}};\omega)}\sqrt{\gamma_{\mathrm{m}}^{\mathrm{int}}}\,\hat{e}_{\mathrm{in}}^{\mathrm{int}\,\dagger}(\omega-\omega_{\mathrm{om}}\pm\omega_{\mathrm{m}})$$

$$\pm\frac{g_{\mathrm{om}}\,\bar{a}_\star\,g_{\mathrm{em}}}{\upsilon_{\mathrm{o}}(\omega_{\mathrm{om}};\omega)\,\upsilon_{\mathrm{m}}(\omega_{\mathrm{om}};\omega)\,\upsilon_{\mathrm{e}}(\omega_{\mathrm{om}}\pm\omega_{\mathrm{e}}\pm\omega_{\mathrm{m}};\omega)}\begin{pmatrix}\sqrt{\gamma_{\mathrm{e}}^{\mathrm{int}}}\,\hat{f}_{\mathrm{in}}^{\mathrm{int}\,\dagger}(\omega-\omega_{\mathrm{om}}\pm\omega_{\mathrm{m}}) \\ +\sqrt{\gamma_{\mathrm{e}}^{\mathrm{tx}}}\,\hat{f}_{\mathrm{in}}^{\mathrm{tx}\,\dagger}(\omega-\omega_{\mathrm{om}}\pm\omega_{\mathrm{m}})\end{pmatrix}\;,$$

or solving for $\hat{c}^\dagger$,

$$\left(1 \pm \frac{{g_{\rm om}}^2\,|\bar{a}_\star|^2}{\upsilon_{\rm o}(\pm\omega_{\rm m};\omega)\,\upsilon_{\rm m}(\pm\omega_{\rm m};\omega)} + \frac{{g_{\rm em}}^2}{\upsilon_{\rm e}(\pm\omega_{\rm e};\omega)\,\upsilon_{\rm m}(\pm\omega_{\rm m};\omega)}\right)\hat{c}^\dagger(\omega) =$$

$$-\frac{\upsilon_{\rm o}(\pm\omega_{\rm m};\omega)\,\upsilon_{\rm m}(\pm\omega_{\rm m};\omega) \pm {g_{\rm om}}^2|\bar{a}_\star|^2}{\upsilon_{\rm o}(\pm\omega_{\rm m};\omega)\,\upsilon_{\rm m}(\pm\omega_{\rm m};\omega)\,\upsilon_{\rm e}(\pm\omega_{\rm e};\omega)}\left(\sqrt{\gamma_{\rm e}^{\rm int}}\,\hat{f}_{\rm in}^{\rm int\,\dagger}(\omega) + \sqrt{\gamma_{\rm e}^{\rm tx}}\,\hat{f}_{\rm in}^{\rm tx\,\dagger}(\omega)\right)$$

$$\pm\frac{{\rm i}\,g_{\rm em}}{\upsilon_{\rm e}(\pm\omega_{\rm e};\omega)\,\upsilon_{\rm m}(\pm\omega_{\rm m};\omega)}\sqrt{\gamma_{\rm m}^{\rm int}}\,\hat{e}_{\rm in}^{\rm int\,\dagger}(\omega)$$

$$+\frac{g_{\rm om}\,\bar{a}_\star\,g_{\rm em}}{\upsilon_{\rm o}(\pm\omega_{\rm m};\omega)\,\upsilon_{\rm m}(\pm\omega_{\rm m};\omega)\,\upsilon_{\rm e}(\pm\omega_{\rm e};\omega)}\begin{pmatrix}\sqrt{\gamma_{\rm o}^{\rm int}}\,\hat{d}_{\rm in}^{\rm int}(\omega+\omega_{\rm om}\pm\omega_{\rm m})\\ +\sqrt{\gamma_{\rm o}^{\rm wg}}\,\hat{d}_{\rm in}^{1}(\omega+\omega_{\rm om}\pm\omega_{\rm m})\\ +\sqrt{\gamma_{\rm o}^{\rm wg}}\,\hat{d}_{\rm in}^{2}(\omega+\omega_{\rm om}\pm\omega_{\rm m})\end{pmatrix}.$$

At $\omega_{\rm e}=\omega_{\rm m}$, microwave to optic transmission is then given by

$$\left|\frac{\hat{d}_{\rm out}^{2}(\omega_{\rm om})}{\hat{f}_{\rm in}^{\rm tx}(\omega_{\rm e})}\right|^2_{\text{other in}\,=\,0} = \frac{4\,\frac{\gamma_{\rm o}^{\rm wg}}{\gamma_{\rm o}}\,\frac{\gamma_{\rm e}^{\rm tx}}{\gamma_{\rm e}}\,\mathcal{C}_{\rm om}\,\mathcal{C}_{\rm em}}{\left(1 \pm \mathcal{C}_{\rm om} + \mathcal{C}_{\rm em}\right)^2},$$

whilst optic to microwave transmission is

$$\left|\frac{\hat{f}_{\rm out}^{\rm tx\,\dagger}(\pm\omega_{\rm e})}{\hat{d}_{\rm in}^{1}(\omega_{\rm om})}\right|^2_{\text{other in}\,=\,0} = \frac{4\,\frac{\gamma_{\rm o}^{\rm wg}}{\gamma_{\rm o}}\,\frac{\gamma_{\rm e}^{\rm tx}}{\gamma_{\rm e}}\,\mathcal{C}_{\rm om}\,\mathcal{C}_{\rm em}}{\left(1 \pm \mathcal{C}_{\rm om} + \mathcal{C}_{\rm em}\right)^2},$$

identical. The cooperativities are defined as

$$\mathcal{C}_{\rm om} = \frac{4\,{g_{\rm om}}^2\,|\bar{a}|^2}{\gamma_{\rm o}\,\gamma_{\rm m}}, \qquad\qquad \mathcal{C}_{\rm em} = \frac{4\,{g_{\rm em}}^2}{\gamma_{\rm e}\,\gamma_{\rm m}}.$$

For investigating the mechanics, eliminating $\hat{a}^{\dagger}$ and $\hat{c}$ in $\hat{b}$,

$$\left(1 \pm \frac{{g_{\mathrm{om}}}^2\,|\bar{a}_\star|^2}{\upsilon_{\mathrm{o}}(\omega_{\mathrm{m}};\omega)\,\upsilon_{\mathrm{m}}(\omega_{\mathrm{m}};\omega)} + \frac{{g_{\mathrm{em}}}^2}{\upsilon_{\mathrm{e}}(\omega_{\mathrm{e}};\omega)\,\upsilon_{\mathrm{m}}(\omega_{\mathrm{m}};\omega)}\right)\hat{b}(\omega) =$$

$$-\frac{1}{\upsilon_{\mathrm{m}}(\omega_{\mathrm{m}};\omega)}\sqrt{\gamma_{\mathrm{m}}^{\mathrm{int}}}\,\hat{e}_{\mathrm{in}}^{\mathrm{int}}(\omega) + \frac{\mathrm{i}\,g_{\mathrm{em}}}{\upsilon_{\mathrm{e}}(\omega_{\mathrm{e}};\omega)\,\upsilon_{\mathrm{m}}(\omega_{\mathrm{m}};\omega)}\left(\sqrt{\gamma_{\mathrm{e}}^{\mathrm{int}}}\,\hat{f}_{\mathrm{in}}^{\mathrm{int}}(\omega) + \sqrt{\gamma_{\mathrm{e}}^{\mathrm{tx}}}\,\hat{f}_{\mathrm{in}}^{\mathrm{tx}}(\omega)\right)$$

$$+\frac{\mathrm{i}\,g_{\mathrm{om}}\,\bar{a}_\star^*}{\upsilon_{\mathrm{o}}(\omega_{\mathrm{m}};\omega)\,\upsilon_{\mathrm{m}}(\omega_{\mathrm{m}};\omega)}\left(\begin{array}{l}\sqrt{\gamma_{\mathrm{o}}^{\mathrm{int}}}\,\hat{d}_{\mathrm{in}}^{\mathrm{int}\,\dagger}(\omega \pm \omega_{\mathrm{om}} - \omega_{\mathrm{m}}) + \sqrt{\gamma_{\mathrm{o}}^{\mathrm{wg}}}\,\hat{d}_{\mathrm{in}}^{1\,\dagger}(\omega \pm \omega_{\mathrm{om}} - \omega_{\mathrm{m}}) \\ \quad + \sqrt{\gamma_{\mathrm{o}}^{\mathrm{wg}}}\,\hat{d}_{\mathrm{in}}^{2\,\dagger}(\omega \pm \omega_{\mathrm{om}} - \omega_{\mathrm{m}})\end{array}\right).$$

APPENDIX L

Thermal optomechanics

In this appendix we derive the output of a hot optomechanical resonator and the associated measurement of the optomechanical coupling.

L.1 Spectrum

Let us consider the case of a hot mechanical resonator, $k_{\mathrm{B}}\,\mathbb{T} \gg \hbar\,\omega_{\mathrm{m}}$, and optical cavity being probed by a laser at ω_{L}. The equations of motion, from App. J, are

$$\frac{\mathrm{d}}{\mathrm{d}t}\hat{a}(t) = -\,\mathrm{i}\,\omega_{\mathrm{o}}\,\hat{a}(t) - \frac{|\gamma_{\mathrm{o}}|}{2}\,\hat{a}(t) - \mathrm{i}\,g_{\mathrm{om}}\,\hat{a}(t)\left(\hat{b}^{\dagger}(t) + \hat{b}(t)\right) - \mathrm{i}\,L\,\mathrm{e}^{-\mathrm{i}\,\omega_{\mathrm{L}}\,t}\,,$$

$$\frac{\mathrm{d}}{\mathrm{d}t}\hat{b}(t) = -\,\mathrm{i}\,\omega_{\mathrm{m}}\,\hat{b}(t) - \frac{|\gamma_{\mathrm{m}}|}{2}\,\hat{b}(t) - \mathrm{i}\,g_{\mathrm{om}}\,\left(\hat{a}^{\dagger}(t)\,\hat{a}(t) + \frac{1}{2}\right) - \sqrt{\gamma_{\mathrm{m}}}\,\hat{e}_{\mathrm{in}}(t)\,.$$

We can displace out our laser drive, and static mechanic shift as

$$\hat{a}(t) = \hat{a}'(t) + \bar{a}\,\mathrm{e}^{-\mathrm{i}\,\omega_{\mathrm{L}}\,t}\,, \qquad \bar{a} = \frac{-\mathrm{i}\,L}{\mathrm{i}\,(\omega_{\mathrm{o}} - \omega_{\mathrm{L}}) - \mathrm{i}\,g_{\mathrm{om}}\,(\bar{b}^{*} + \bar{b}) + \frac{|\gamma_{\mathrm{o}}|}{2}} \gg \hat{a}'(t)\,,$$

$$\hat{b}(t) = \hat{b}'(t) + \bar{b}\,, \qquad \bar{b} = \frac{-\mathrm{i}\,g_{\mathrm{om}}\,\left(|\bar{a}|^2 + \frac{1}{2}\right)}{\mathrm{i}\,\omega_{\mathrm{m}} + \frac{|\gamma_{\mathrm{m}}|}{2}}\,.$$

Letting $\hat{y}(t) = \hat{b}'^{\,\dagger}(t) + \hat{b}'(t)$ and $\bar{y} = \bar{b}^* + \bar{b}$, we now have

$$\frac{\mathrm{d}}{\mathrm{d}t}\hat{a}'(t) = -\mathrm{i}\,\omega_\mathrm{o}\,\hat{a}'(t) - \frac{|\gamma_\mathrm{o}|}{2}\,\hat{a}'(t) - \mathrm{i}\,g_\mathrm{om}\,\bar{y}\,\hat{a}'(t) - \mathrm{i}\,g_\mathrm{om}\,\bar{a}\,\hat{y}(t)\,\mathrm{e}^{-\mathrm{i}\,\omega_\mathrm{L}\,t} - \mathrm{i}\,g_\mathrm{om}\,\hat{a}'(t)\,\hat{y}'(t)\;,$$

$$\frac{\mathrm{d}}{\mathrm{d}t}\hat{b}'(t) = -\mathrm{i}\,\omega_\mathrm{m}\,\hat{b}'(t) - \frac{|\gamma_\mathrm{m}|}{2}\,\hat{b}'(t) - \sqrt{\gamma_\mathrm{m}}\,\hat{e}_\mathrm{in}(t) - \mathrm{i}\,g_\mathrm{om}\left(\bar{a}^*\,\hat{a}'(t)\,\mathrm{e}^{\mathrm{i}\,\omega_\mathrm{L}\,t} + \bar{a}\,\hat{a}'^{\,\dagger}(t)\,\mathrm{e}^{-\mathrm{i}\,\omega_\mathrm{L}\,t}\right)\;,$$

in which the last term in $\frac{\mathrm{d}}{\mathrm{d}t}\hat{a}'(t)$ is small by $\bar{a} \gg \hat{a}'(t)$, and the last two terms in $\frac{\mathrm{d}}{\mathrm{d}t}\hat{b}'(t)$ are small compared to the large thermal drive $\hat{e}_\mathrm{in}(t)$ which dominates the dynamics. From Sec. I.4.2 we know the thermal spectrum for a harmonic oscillator $\hat{b}'$.

Denoting $\omega_\mathrm{om} = \omega_\mathrm{o} + g_\mathrm{om}\,\bar{y}$, the solution for $\hat{a}'(t)$ is

$$\hat{a}'(t) = -\mathrm{i}\,g_\mathrm{om}\,\bar{a}\int_{t_0}^{t}\mathrm{e}^{\left(-\mathrm{i}\,\omega_\mathrm{om}-\frac{|\gamma_\mathrm{o}|}{2}\right)(t-t')}\,\hat{y}(t')\,\mathrm{e}^{-\mathrm{i}\,\omega_\mathrm{L}\,t'}\,\mathrm{d}t' + \mathrm{e}^{\left(-\mathrm{i}\,\omega_\mathrm{om}-\frac{|\gamma_\mathrm{o}|}{2}\right)(t-t_0)}\,\hat{a}'(t_0)\;,$$

and we can take $t_0 \to -\infty$, sending the last term to zero. Thus we have

$$\hat{a}(t) = \bar{a}\,\mathrm{e}^{-\mathrm{i}\,\omega_\mathrm{L}\,t} - \mathrm{i}\,g_\mathrm{om}\,\bar{a}\int_{-\infty}^{t}\mathrm{e}^{\left(-\mathrm{i}\,\omega_\mathrm{om}-\frac{|\gamma_\mathrm{o}|}{2}\right)(t-t')}\,\hat{y}(t')\,\mathrm{e}^{-\mathrm{i}\,\omega_\mathrm{L}\,t'}\,\mathrm{d}t'\;.$$

The power output of our optical cavity is $\propto|\hat{a}(t)|^2$, which is

$$\begin{aligned}|\hat{a}(t)|^2 = |\bar{a}|^2 &- \mathrm{i}\,g_\mathrm{om}\,|\bar{a}|^2\int_{-\infty}^{t}\mathrm{e}^{\left(-\mathrm{i}\,(\omega_\mathrm{om}-\omega_\mathrm{L})-\frac{|\gamma_\mathrm{o}|}{2}\right)(t-t')}\,\hat{y}(t')\,\mathrm{d}t' \\ &+ \mathrm{i}\,g_\mathrm{om}\,|\bar{a}|^2\int_{-\infty}^{t}\mathrm{e}^{\left(\mathrm{i}\,(\omega_\mathrm{om}-\omega_\mathrm{L})-\frac{|\gamma_\mathrm{o}|}{2}\right)(t-t')}\,\hat{y}(t')\,\mathrm{d}t' + \mathcal{O}[g_\mathrm{om}]^2\;,\end{aligned}$$

using $\hat{y}^\dagger(t) = \hat{y}(t)$. Letting

$$h(t) = \Theta(t)\,\mathrm{e}^{\left(-\mathrm{i}\,(\omega_\mathrm{om}-\omega_\mathrm{L})-\frac{|\gamma_\mathrm{o}|}{2}\right)t}\;,$$

and dropping $\mathcal{O}[g_{\mathrm{om}}]^2$, we can rewrite this as

$$\begin{aligned}|\hat{a}(t)|^2 &= |\bar{a}|^2 - \mathrm{i}\, g_{\mathrm{om}}\, |\bar{a}|^2 \int_{-\infty}^{\infty} h(t-t')\, \hat{y}(t')\, \mathrm{d}t' + \mathrm{i}\, g_{\mathrm{om}}\, |\bar{a}|^2 \int_{-\infty}^{\infty} h^*(t-t')\, \hat{y}(t')\, \mathrm{d}t' \\ &= |\bar{a}|^2 - \mathrm{i}\, g_{\mathrm{om}}\, |\bar{a}|^2 \big(h * \hat{y}\big)(t) + \mathrm{i}\, g_{\mathrm{om}}\, |\bar{a}|^2 \big(h^* * \hat{y}\big)(t)\ .\end{aligned}$$

A photodetector measuring this power will output a proportional voltage amplitude, hence denote $\hat{A}(t) = |\hat{a}(t)|^2$. Then using App. H

$$h(\omega) = \frac{1}{\sqrt{2\,\pi}}\, \frac{1}{\mathrm{i}\,(\omega_{\mathrm{o}} - \omega_{\mathrm{L}} - \omega) + \frac{|\gamma_{\mathrm{o}}|}{2}}\ , \qquad\qquad h^*(\omega) = h(-\omega)^*\ ,$$

and

$$\begin{aligned}\hat{A}(\omega) &= |\bar{a}|^2\, \sqrt{2\,\pi}\, \delta(\omega) - \mathrm{i}\, g_{\mathrm{om}}\, |\bar{a}|^2\, \sqrt{2\,\pi}\, h(\omega)\, \hat{y}(\omega) + \mathrm{i}\, g_{\mathrm{om}}\, |\bar{a}|^2\, \sqrt{2\,\pi}\, h^*(\omega)\, \hat{y}(\omega) \\ &= |\bar{a}|^2\, \sqrt{2\,\pi}\, \delta(\omega) + \frac{\mathrm{i}\, g_{\mathrm{om}}\, |\bar{a}|^2\, \hat{y}(\omega)}{\mathrm{i}\,(\omega - \omega_{\mathrm{om}} + \omega_{\mathrm{L}}) - \frac{|\gamma_{\mathrm{o}}|}{2}} - \frac{\mathrm{i}\, g_{\mathrm{om}}\, |\bar{a}|^2\, \hat{y}(\omega)}{\mathrm{i}\,(\omega + \omega_{\mathrm{om}} - \omega_{\mathrm{L}}) - \frac{|\gamma_{\mathrm{o}}|}{2}} \\ &= |\bar{a}|^2\, \sqrt{2\,\pi}\, \delta(\omega) + g_{\mathrm{om}}\, |\bar{a}|^2\, \hat{y}(\omega)\, \mathfrak{V}(\omega)\ ,\end{aligned}$$

with

$$\mathfrak{V}(\omega) = \frac{\mathrm{i}}{\mathrm{i}\,(\omega - \omega_{\mathrm{om}} + \omega_{\mathrm{L}}) - \frac{|\gamma_{\mathrm{o}}|}{2}} - \frac{\mathrm{i}}{\mathrm{i}\,(\omega + \omega_{\mathrm{om}} - \omega_{\mathrm{L}}) - \frac{|\gamma_{\mathrm{o}}|}{2}} = \frac{2\,(\omega_{\mathrm{L}} - \omega_{\mathrm{om}})}{(\frac{|\gamma_{\mathrm{o}}|}{2} - \mathrm{i}\,\omega)^2 + (\omega_{\mathrm{L}} - \omega_{\mathrm{om}})^2}\ ,$$

$$\mathfrak{V}(t) = \mathrm{i}\,\sqrt{2\,\pi}\, \big(h^*(t) - h(t)\big)\ .$$

With $\langle \hat{y}(t) \rangle = 0$, the spectral density is easily obtained to be

$$S_{\hat{A}\hat{A}}(\omega) = |\bar{a}|^4 \, 2\,\pi\,\delta(\omega) + {g_{\mathrm{om}}}^2 \, |\bar{a}|^4 \, |\mathcal{U}(\omega)|^2 \, S_{\hat{y}\hat{y}}(\omega) \; .$$

Expanding this out near $\omega = \omega_{\mathrm{m}}$,

$$S_{\hat{A}\hat{A}}(\omega \approx \omega_{\mathrm{m}}) = {g_{\mathrm{om}}}^2 \, \frac{|L|^4}{\left((\omega_{\mathrm{L}} - \omega_{\mathrm{om}})^2 + \frac{|\gamma_{\mathrm{o}}|^2}{4}\right)^2} \, \frac{\bar{n}(\omega_{\mathrm{m}})}{(\omega - \omega_{\mathrm{m}})^2 + \frac{|\gamma_{\mathrm{m}}|^2}{4}}$$

$$\times \, \frac{4\,(\omega_{\mathrm{L}} - \omega_{\mathrm{om}})^2}{\left(\omega^2 - (\omega_{\mathrm{L}} - \omega_{\mathrm{om}})^2\right)^2 + \frac{|\gamma_{\mathrm{o}}|}{2}\left(\omega^2 + (\omega_{\mathrm{L}} - \omega_{\mathrm{om}})^2\right)^2 + \frac{|\gamma_{\mathrm{o}}|^4}{16}} \; ,$$

which is notably zero when $\omega_{\mathrm{L}} = \omega_{\mathrm{om}}$.

L.2 Hanger resonator experiment

For an optical cavity in a hanger configuration with the optical waveguide (see Sec. Θ.4.1),

$$\gamma_{\mathrm{o}} = \underbrace{\gamma_{\mathrm{o}}^{0}}_{\substack{\text{internal} \\ \text{loss}}} + \underbrace{\gamma_{\mathrm{o}}^{12}}_{\substack{\text{waveguide} \\ \text{coupling}}} \; , \qquad\qquad a_{\mathrm{out}}^{2}(t) = \mathrm{e}^{\mathrm{i}\,\theta} \sqrt{\frac{\gamma_{\mathrm{o}}^{12}}{2}}\, a(t) + \mathrm{e}^{\mathrm{i}\,\phi}\, a_{\mathrm{in}}^{1}(t) \; ,$$

with

$$a_{\mathrm{in}}^{1}(t) = \sqrt{\hbar\,\omega_{\mathrm{L}}}\, \hat{d}_{\mathrm{in}}^{L}(t) = \sqrt{P_{\mathrm{L}}}\, \mathrm{e}^{-\mathrm{i}\,\omega_{\mathrm{L}}\,t} \; , \qquad\qquad L = \sqrt{\frac{\gamma_{\mathrm{o}}^{12}}{2}}\, \frac{\sqrt{P_{\mathrm{L}}}}{\sqrt{\hbar\,\omega_{\mathrm{L}}}} \; ,$$

noting that a is a complex amplitude with $\sqrt{\text{power}}$ units, whilst $\hat{a}$ in the first section is an operator with $\sqrt{\text{number}}$ units. Thus

$$a^2_{\text{out}}(t) = \sqrt{P_{\text{L}}}\,\mathrm{e}^{-\mathrm{i}\,\omega_{\text{L}}\,t} + \frac{\frac{\gamma^{12}_{\text{o}}}{2}\,\sqrt{P_{\text{L}}}\,\mathrm{e}^{-\mathrm{i}\,\omega_{\text{L}}\,t}}{\mathrm{i}\,(\omega_{\text{L}} - \omega_{\text{om}}) - \frac{\gamma_{\text{o}}}{2}}\left(1 - \mathrm{i}\,g_{\text{om}}\,\big(h * \hat{y}\big)(t)\right)$$

$$= \sqrt{P_{\text{L}}}\,\mathrm{e}^{-\mathrm{i}\,\omega_{\text{L}}\,t}\left(S_{2\,1}(\omega_{\text{L}}) - \mathrm{i}\,g_{\text{om}}\,S_{1\,1}(\omega_{\text{L}})\,\big(h * \hat{y}\big)(t)\right),$$

with

$$S_{2\,1}(\omega_{\text{L}}) = 1 + \frac{\frac{\gamma^{12}_{\text{o}}}{2}}{\mathrm{i}\,(\omega_{\text{L}} - \omega_{\text{om}}) - \frac{\gamma_{\text{o}}}{2}}\,, \qquad S_{1\,1}(\omega_{\text{L}}) = \frac{\frac{\gamma^{12}_{\text{o}}}{2}}{\mathrm{i}\,(\omega_{\text{L}} - \omega_{\text{om}}) - \frac{\gamma_{\text{o}}}{2}}\,.$$

This gives the power out as

$$\begin{aligned} P_{\text{D}}(t) &= |a^2_{\text{out}}(t)|^2 \\ &= P_{\text{L}}\left(|S_{2\,1}(\omega_{\text{L}})|^2 - \mathrm{i}\,g_{\text{om}}\,S_{2\,1}(\omega_{\text{L}})^*\,S_{1\,1}(\omega_{\text{L}})\,\big(h * \hat{y}\big)(t)\right. \\ &\qquad\qquad \left. + \mathrm{i}\,g_{\text{om}}\,S_{2\,1}(\omega_{\text{L}})\,S_{1\,1}(\omega_{\text{L}})^*\,\big(h^* * \hat{y}\big)(t)\right) + \mathcal{O}[g_{\text{om}}]^2\,, \end{aligned}$$

with Fourier transform

$$P_{\text{D}}(\omega) = P_{\text{L}}\left(|S_{2\,1}(\omega_{\text{L}})|^2\,\sqrt{2\,\pi}\,\delta(\omega) + g_{\text{om}}\,W^{-1}(\omega_{\text{L}};\omega)\,\hat{y}(\omega)\right),$$

denoting

$$W^{-1}(\omega_{\mathrm{L}};\omega) = -\,\mathrm{i}\,S_{2\,1}(\omega_{\mathrm{L}})^{*}\,S_{1\,1}(\omega_{\mathrm{L}})\,\sqrt{2\,\pi}\,h(\omega) + \mathrm{i}\,S_{2\,1}(\omega_{\mathrm{L}})\,S_{1\,1}(\omega_{\mathrm{L}})^{*}\,\sqrt{2\,\pi}\,h^{*}(\omega)$$

$$= \mathrm{i}\,\frac{2}{\gamma_{\mathrm{o}}^{12}}\,S_{2\,1}(\omega_{\mathrm{L}})^{*}\,S_{1\,1}(\omega_{\mathrm{L}})\,S_{1\,1}(\omega_{\mathrm{L}}+\omega) - \mathrm{i}\,\frac{2}{\gamma_{\mathrm{o}}^{12}}\,S_{2\,1}(\omega_{\mathrm{L}})\,S_{1\,1}(\omega_{\mathrm{L}})^{*}\,S_{1\,1}(\omega_{\mathrm{L}}-\omega)^{*}$$

$$= \left(\frac{\mathrm{i}}{(\Delta_{\mathrm{om}})^{2} + \frac{(\gamma_{\mathrm{o}})^{2}}{4}}\right) \times \left(\frac{\frac{(\gamma_{\mathrm{o}}^{12})^{2}}{4} - \frac{\gamma_{\mathrm{o}}\,\gamma_{\mathrm{o}}^{12}}{4} + \mathrm{i}\,\frac{\gamma_{\mathrm{o}}^{12}}{2}\,\Delta_{\mathrm{om}}}{\mathrm{i}\,(\omega-\Delta_{\mathrm{om}}) - \frac{\gamma_{\mathrm{o}}}{2}} - \frac{\frac{(\gamma_{\mathrm{o}}^{12})^{2}}{4} - \frac{\gamma_{\mathrm{o}}\,\gamma_{\mathrm{o}}^{12}}{4} - \mathrm{i}\,\frac{\gamma_{\mathrm{o}}^{12}}{2}\,\Delta_{\mathrm{om}}}{\mathrm{i}\,(\omega+\Delta_{\mathrm{om}}) - \frac{\gamma_{\mathrm{o}}}{2}}\right),$$

with $\Delta_{\mathrm{om}} = \omega_{\mathrm{om}} - \omega_{\mathrm{L}}$.

In our experiment,

$$P_{\mathrm{L}} = P_{\mathrm{delivered}} \quad \underset{\text{coupler}}{\eta_{\mathrm{grating}}}\,,$$

and the signal measured by the spectrum analyzer is

$$\underset{\text{analyzer}}{X_{\mathrm{spectrum}}} = I_{\mathrm{PD}}\,\sqrt{Z_{\mathrm{C}}} = P_{\mathrm{D}} \quad \underset{\text{coupler}}{\eta_{\mathrm{grating}}} \quad f_{\mathrm{split}} \quad \underset{\text{amp}}{G_{\mathrm{fiber}}} \quad T_{\mathrm{filter}} \quad \underset{\text{responsivity}}{R_{\mathrm{PD}}} \quad \sqrt{Z_{\mathrm{C}}}\,,$$

where $Z_{\mathrm{C}} = 50\,\Omega$ is the spectrum analyzer input impedance. Capturing all of these into some factor

$$\mathfrak{X} = P_{\mathrm{delivered}} \quad \left(\underset{\text{coupler}}{\eta_{\mathrm{grating}}}\right)^{2} \quad f_{\mathrm{split}} \quad \underset{\text{amp}}{G_{\mathrm{fiber}}} \quad T_{\mathrm{filter}} \quad \underset{\text{responsivity}}{R_{\mathrm{PD}}} \quad \sqrt{Z_{\mathrm{C}}}\,,$$

such that $\mathfrak{X}^2$ is a power, we get

$$S_{XX}(\omega) = \mathfrak{X}(\omega_{\mathrm{L}})^2 \left(|S_{2\,1}(\omega_{\mathrm{L}})|^4 \, 2\,\pi\,\delta(\omega) + {g_{\mathrm{om}}}^2 \, |W(\omega_{\mathrm{L}};\omega)|^{-2} \, \bar{S}_{\hat{y}\hat{y}}(\omega) \right) ,$$

with

$$|S_{2\,1}(\omega_{\mathrm{L}})|^2 = 1 - \frac{\frac{\gamma_{\mathrm{o}}^{12}}{2} \left(\gamma_{\mathrm{o}} - \frac{\gamma_{\mathrm{o}}^{12}}{2} \right)}{(\Delta_{\mathrm{om}})^2 + \frac{(\gamma_{\mathrm{o}})^2}{4}} ,$$

$$|W(\omega_{\mathrm{L}};\omega)|^{-2} = \left(\frac{1}{(\Delta_{\mathrm{om}})^2 + \frac{(\gamma_{\mathrm{o}})^2}{4}} \right)^2 \frac{(\gamma_{\mathrm{o}}^{12})^2 \, (\Delta_{\mathrm{om}})^2 \, \left(\omega^2 + \left(\gamma_{\mathrm{o}} - \frac{\gamma_{\mathrm{o}}^{12}}{2} \right)^2 \right)}{\left((\omega + \Delta_{\mathrm{om}})^2 + \frac{(\gamma_{\mathrm{o}})^2}{4} \right) \left((\omega - \Delta_{\mathrm{om}})^2 + \frac{(\gamma_{\mathrm{o}})^2}{4} \right)} ,$$

$$\bar{S}_{\hat{y}\hat{y}}(\omega) = \frac{1}{2} \, \coth\!\left[\frac{k_{\mathrm{B}}\,\mathbb{T}}{2\,\hbar\,\omega_{\mathrm{m}}} \right] \left(\frac{\gamma_{\mathrm{m}}}{(\omega + \omega_{\mathrm{m}})^2 + \frac{(\gamma_{\mathrm{m}})^2}{4}} + \frac{\gamma_{\mathrm{m}}}{(\omega - \omega_{\mathrm{m}})^2 + \frac{(\gamma_{\mathrm{m}})^2}{4}} \right)$$

$$\bar{n}(\omega_{\mathrm{m}}) = \frac{1}{2} \, \coth\!\left[\frac{k_{\mathrm{B}}\,\mathbb{T}}{2\,\hbar\,\omega_{\mathrm{m}}} \right] \overset{k_{\mathrm{B}}\,\mathbb{T} \gg \hbar\,\omega_{\mathrm{m}}}{\approx} \frac{k_{\mathrm{B}}\,\mathbb{T}}{\hbar\,\omega_{\mathrm{m}}} .$$

For a sufficiently narrow γ_{m}, the factor $W(\omega_{\mathrm{L}};\omega)$ is approximately constant and can be determined from a measurement of the optical transmission. When not sideband resolved, $|W(\omega_{\mathrm{L}};\omega)|^{-2}$ is maximized when

$$\Delta_{\mathrm{om}} = \pm \sqrt{\frac{\omega^2 + \frac{(\gamma_{\mathrm{o}})^2}{4}}{3}} .$$

The total power in the thermal mechanical spectrum is

$$P_{\mathrm{m}} \approx \frac{1}{2\,\pi} \int_{-\infty}^{\infty} \mathfrak{X}(\omega_{\mathrm{L}})^2 \, {g_{\mathrm{om}}}^2 \, |W(\omega_{\mathrm{L}};\omega_{\mathrm{m}})|^{-2} \, \bar{S}_{\hat{y}\hat{y}}(\omega) \, \mathrm{d}\omega = 2\,\mathfrak{X}(\omega_{\mathrm{L}})^2 \, {g_{\mathrm{om}}}^2 \, \bar{n}(\omega_{\mathrm{m}}) \, |W(\omega_{\mathrm{L}};\omega_{\mathrm{m}})|^{-2} .$$

L.2.1 DC monitor calibration

The fast photodetector has a DC monitor that effectively measures the zero frequency component of our spectrum, allowing us to determine $\mathfrak{X}$. This measured voltage (for our particular photodetector) is

$$V_{\substack{\mathrm{DC}\\ \mathrm{monitor}}} = \bar{I}_{\mathrm{PD}}\,\left(\mathrm{mV}/\mu\mathrm{A}\right) = |S_{2\,1}(\omega_{\mathrm{L}})|^2\,\frac{\mathfrak{X}(\omega_{\mathrm{L}})}{\sqrt{Z_{\mathrm{C}}}}\,\left(\mathrm{mV}/\mu\mathrm{A}\right)\,,$$

$$\Rightarrow \quad \mathfrak{X}(\omega_{\mathrm{L}}) = \frac{V_{\substack{\mathrm{DC}\\ \mathrm{monitor}}}}{|S_{2\,1}(\omega_{\mathrm{L}})|^2}\,\sqrt{Z_{\mathrm{C}}}\,\left(\mu\mathrm{A}/\mathrm{mV}\right)\,.$$

L.2.2 Phase modulated sideband drive

We can also calibrate out $\mathfrak{X}$ by phase modulating our laser and generating sidebands near but not within the mechanical resonance [230, 237]. Applying a phase modulation, we can use the Jacobi-Anger expansion,

$$L\,\mathrm{e}^{-\mathrm{i}\left(\omega_{\mathrm{L}}\,t - A_{\Phi}\,\sin[\omega_{\Phi}\,t]\right)} = L\,\mathrm{e}^{-\mathrm{i}\,\omega_{\mathrm{L}}\,t}\sum_{j=-\infty}^{\infty} J_j[A_{\Phi}]\,\mathrm{e}^{-\mathrm{i}\,j\,\omega_{\Phi}\,t}\,,$$

where J_j are Bessel functions of the first kind. Matching this to laser drives of the form

$$\sum_{j=-\infty}^{\infty} L_j\,\mathrm{e}^{-\mathrm{i}\,(\omega_{\mathrm{L}}+j\,\omega_{\Phi})\,t} \qquad\qquad \Rightarrow \quad L_j = L\,J_j[A_{\Phi}]\,.$$

Following Sec. J.8.7 for weak symmetric sidebands, we can apply serial linearization

$$\hat{a}(t) = \hat{a}'(t) + \sum_{j=-n}^{n} \bar{a}_j \, \mathrm{e}^{-\mathrm{i}\,(\omega_\mathrm{L} + j\,\omega_\Phi)\,t} \,, \qquad \hat{b}(t) = \hat{b}'(t) + \sum_{j=-n}^{n} \bar{b}_j \, \mathrm{e}^{-\mathrm{i}\,j\,\omega_\Phi\,t} \,,$$

with

$$\bar{a}_{j\neq 0} = \frac{-\mathrm{i}\,L_j - \mathrm{i}\,g_\mathrm{om}\,\bar{a}\,\left(\bar{b}^*_{-j} + \bar{b}_j\right)}{\mathrm{i}\,(\omega_\mathrm{om} - \omega_\mathrm{L} - j\,\omega_\Phi) + \frac{|\gamma_\mathrm{o}|}{2}} \,, \qquad \bar{a}_0 = \bar{a} = \frac{-\mathrm{i}\,L_0}{\mathrm{i}\,(\omega_\mathrm{om} - \omega_\mathrm{L}) + \frac{|\gamma_\mathrm{o}|}{2}}$$

$$\bar{b}_{j\neq 0} = \frac{-\mathrm{i}\,g_\mathrm{om}\,\left(\bar{a}^*\,\bar{a}_j + \bar{a}\,\bar{a}^*_{-j}\right)}{\mathrm{i}\,(\omega_\mathrm{m} - j\,\omega_\Phi) + \frac{|\gamma_\mathrm{m}|}{2}} \,, \qquad \bar{b}_0 = \bar{b} = \frac{-\mathrm{i}\,g_\mathrm{om}\,\left(|\bar{a}|^2 + \frac{1}{2}\right)}{\mathrm{i}\,\omega_\mathrm{m} + \frac{|\gamma_\mathrm{m}|}{2}} \,,$$

keeping the same solution to $\hat{a}'(t)$ as before. If ω_Φ is outside the mechanical resonance then $\bar{b}_{j\neq 0} \approx 0$.

We now have

$$\begin{aligned}
\hat{a}(t) &= \mathrm{e}^{-\mathrm{i}\,\omega_\mathrm{L}\,t} \left(\sum_{j=-\infty}^{\infty} \bar{a}_j \, \mathrm{e}^{-\mathrm{i}\,j\,\omega_\Phi\,t} - \mathrm{i}\,g_\mathrm{om}\,\bar{a}\,\big(h * \hat{y}\big)(t) \right) , \\
a^1_\mathrm{in}(t) &= \sqrt{P_\mathrm{L}}\,\mathrm{e}^{-\mathrm{i}\,\omega_\mathrm{L}\,t} \sum_{j=-\infty}^{\infty} J_j[A_\Phi]\,\mathrm{e}^{-\mathrm{i}\,j\,\omega_\Phi\,t} \,, \\
a^2_\mathrm{out}(t) &= \sqrt{P_\mathrm{L}}\,\mathrm{e}^{-\mathrm{i}\,\omega_\mathrm{L}\,t} \left(\sum_{j=-\infty}^{\infty} J_j[A_\Phi]\,S_{2\,1}(\omega_\mathrm{L} + j\,\omega_\Phi)\,\mathrm{e}^{-\mathrm{i}\,j\,\omega_\Phi\,t} \right. \\
&\qquad \left. - \mathrm{i}\,g_\mathrm{om}\,J_0[A_\Phi]\,S_{1\,1}(\omega_\mathrm{L})\,\big(h * \hat{y}\big)(t) \right) ,
\end{aligned}$$

with

$$S_{2\,1}(\omega_\mathrm{L}) = 1 + \frac{\frac{\gamma^{12}_\mathrm{o}}{2}}{\mathrm{i}\,(\omega_\mathrm{L} - \omega_\mathrm{om}) - \frac{\gamma_\mathrm{o}}{2}} \,, \qquad S_{1\,1}(\omega_\mathrm{L}) = \frac{\frac{\gamma^{12}_\mathrm{o}}{2}}{\mathrm{i}\,(\omega_\mathrm{L} - \omega_\mathrm{om}) - \frac{\gamma_\mathrm{o}}{2}} \,.$$

This form assumes the sidebands are much lower in power than the main carrier.

The output power is

$$
\begin{aligned}
P_{\mathrm{D}}(t) &= |a^2_{\mathrm{out}}(t)|^2 \\
&= P_{\mathrm{L}} \left(\sum_{k=-\infty}^{\infty} \sum_{j=-\infty}^{\infty} J_j[A_\Phi]\, J_{j+k}[A_\Phi]\, S_{2\,1}\big(\omega_{\mathrm{L}} + j\,\omega_\Phi\big)\, S_{2\,1}\big(\omega_{\mathrm{L}} + (j+k)\,\omega_\Phi\big)^*\, \mathrm{e}^{-\mathrm{i}\,k\,\omega_\Phi\,t} \right. \\
&\qquad - \mathrm{i}\, g_{\mathrm{om}} \sum_{j=-\infty}^{\infty} J_j[A_\Phi]\, J_0[A_\Phi]\, S_{2\,1}(\omega_{\mathrm{L}} + j\,\omega_\Phi)^*\, S_{1\,1}(\omega_{\mathrm{L}})\, \big(h * \hat{y}\big)(t)\, \mathrm{e}^{\mathrm{i}\,j\,\omega_\Phi\,t} \\
&\qquad \left. + \mathrm{i}\, g_{\mathrm{om}} \sum_{j=-\infty}^{\infty} J_j[A_\Phi]\, J_0[A_\Phi]\, S_{2\,1}(\omega_{\mathrm{L}} + j\,\omega_\Phi)\, S_{1\,1}(\omega_{\mathrm{L}})^*\, \big(h^* * \hat{y}\big)(t)\, \mathrm{e}^{-\mathrm{i}\,j\,\omega_\Phi\,t} \right) \\
&\quad + \mathcal{O}[g_{\mathrm{om}}]^2 \,,
\end{aligned}
$$

with Fourier transform $P_{\mathrm{D}}(\omega) =$

$$
\begin{aligned}
&P_{\mathrm{L}} \left(\sum_{k=-\infty}^{\infty} \sum_{j=-\infty}^{\infty} J_j[A_\Phi]\, J_{j+k}[A_\Phi]\, S_{2\,1}\big(\omega_{\mathrm{L}} + j\,\omega_\Phi\big)\, S_{2\,1}\big(\omega_{\mathrm{L}} + (j+k)\,\omega_\Phi\big)^*\, \sqrt{2\,\pi}\,\delta(\omega - k\,\omega_\Phi) \right. \\
&\qquad - \mathrm{i}\, g_{\mathrm{om}} \sum_{j=-\infty}^{\infty} J_j[A_\Phi]\, J_0[A_\Phi]\, S_{2\,1}(\omega_{\mathrm{L}} + j\,\omega_\Phi)^*\, S_{1\,1}(\omega_{\mathrm{L}})\, \sqrt{2\,\pi}\, h(\omega + j\,\omega_\Phi)\, \hat{y}(\omega + j\,\omega_\Phi) \\
&\qquad \left. + \mathrm{i}\, g_{\mathrm{om}} \sum_{j=-\infty}^{\infty} J_j[A_\Phi]\, J_0[A_\Phi]\, S_{2\,1}(\omega_{\mathrm{L}} + j\,\omega_\Phi)\, S_{1\,1}(\omega_{\mathrm{L}})^*\, \sqrt{2\,\pi}\, h^*(\omega - j\,\omega_\Phi)\, \hat{y}(\omega - j\,\omega_\Phi) \right) .
\end{aligned}
$$

Note that if $S_{2\,1}$ is constant, then

$$
\sum_{j=-\infty}^{\infty} J_j[A_\Phi]\, J_{j+k}[A_\Phi] = \delta_{k\,0} \,,
$$

i.e. phase modulation does not cause any power fluctuations and only performs spectroscopy. To use this we need to know $S_{2\,1}$ accurately, which likely means dither locking to a known part of the resonance and time averaging the dither sweep.

Assuming $\langle \hat{e}_{\rm in}(\omega)^\dagger \, \hat{e}_{\rm in}(\omega' \neq \omega) \rangle = 0$, the power spectral density is $S_{XX}(\omega) =$

$$\mathfrak{X}(\omega_{\rm L})^2 \Bigg(\sum_{k=-\infty}^{\infty} \Bigg| \sum_{j=-\infty}^{\infty} J_j[A_\Phi] \, J_{j+k}[A_\Phi] \, S_{2\,1}\big(\omega_{\rm L} + j\,\omega_\Phi\big) \, S_{2\,1}\big(\omega_{\rm L} + (j+k)\,\omega_\Phi\big)^* \Bigg|^2 2\,\pi\,\delta(\omega - k\,\omega_\Phi) + {g_{\rm om}}^2 \sum_{j=-\infty}^{\infty} J_j[A_\Phi]^2 \, J_0[A_\Phi]^2 \, |W_j(\omega_{\rm L};\omega)|^{-2} \, \bar{S}_{\hat{y}\hat{y}}(\omega + j\,\omega_\Phi) \Bigg) ,$$

with

$$\begin{aligned} W_j^{-1}(\omega_{\rm L};\omega) = & -\mathrm{i}\, S_{2\,1}(\omega_{\rm L} + j\,\omega_\Phi)^* \, S_{1\,1}(\omega_{\rm L}) \, \sqrt{2\,\pi}\, h(\omega + j\,\omega_\Phi) \\ & + \mathrm{i}\, S_{2\,1}(\omega_{\rm L} - j\,\omega_\Phi) \, S_{1\,1}(\omega_{\rm L})^* \, \sqrt{2\,\pi}\, h^*(\omega + j\,\omega_\Phi) \end{aligned}$$

$$\begin{aligned} = & \, \mathrm{i}\, \frac{2}{\gamma_{\rm o}^{12}} \, S_{2\,1}(\omega_{\rm L} + j\,\omega_\Phi)^* \, S_{1\,1}(\omega_{\rm L}) \, S_{1\,1}(\omega_{\rm L} + j\,\omega_\Phi + \omega) \\ & - \mathrm{i}\, \frac{2}{\gamma_{\rm o}^{12}} \, S_{2\,1}(\omega_{\rm L} - j\,\omega_\Phi) \, S_{1\,1}(\omega_{\rm L})^* \, S_{1\,1}(\omega_{\rm L} - j\,\omega_\Phi - \omega)^* \, . \end{aligned}$$

We can now use power measurements at $k\,\omega_\Phi$ to determine $\mathfrak{X}$. Selecting out the appropriate coefficients from $S_{XX}(\omega)$, we have for each measured sideband peak $k > 0$,

$$\begin{aligned} P_{k\,\omega_\Phi} &= 2\,\mathfrak{X}(\omega_{\rm L})^2 \Bigg| \sum_{j=-\infty}^{\infty} J_j[A_\Phi] \, J_{j+k}[A_\Phi] \, S_{2\,1}\big(\omega_{\rm L} + j\,\omega_\Phi\big) \, S_{2\,1}\big(\omega_{\rm L} + (j+k)\,\omega_\Phi\big)^* \Bigg|^2 \\ &= \mathfrak{X}(\omega_{\rm L})^2 \sum_{m=0}^{\infty} C_{k\,m} \, {A_\Phi}^m \, , \end{aligned}$$

including both positive and negative frequency (identical) contributions. If $A_\Phi \ll 1$ then this summation can be terminated. For $k = 1$ and to the lowest order in A_Φ,

$$P_{\omega_\Phi} = \mathfrak{X}(\omega_{\rm L})^2 \Big| S_{2\,1}(\omega_{\rm L}) \, S_{2\,1}(\omega_{\rm L} + \omega_\Phi)^* - S_{2\,1}(\omega_{\rm L})^* \, S_{2\,1}(\omega_{\rm L} - \omega_\Phi) \Big|^2 \frac{{A_\Phi}^2}{2} + \mathcal{O}[A_\Phi]^4 \, .$$

Interestingly, this has an equivalence to the thermal response at leading order in A_Φ [237],

$$\left| S_{21}(\omega_\mathrm{L})\, S_{21}(\omega_\mathrm{L}+\omega_\Phi)^* - S_{21}(\omega_\mathrm{L})^*\, S_{21}(\omega_\mathrm{L}-\omega_\Phi) \right|^2 = |W_0(\omega_\mathrm{L};\omega_\Phi)|^{-2}\, {\omega_\Phi}^2 \,,$$

giving at weak phase modulation

$$P_{\omega_\Phi} \approx \mathfrak{X}(\omega_\mathrm{L})^2\, |W_0(\omega_\mathrm{L};\omega_\Phi)|^{-2}\, {\omega_\Phi}^2\, \frac{{A_\Phi}^2}{2} \,.$$

If $\mathfrak{X}$ is constant, and S_{21} is known, measuring at least two sideband peaks will allow us to solve or fit for A_Φ and $\mathfrak{X}$. In reality however, $\mathfrak{X}$ will have some unknown frequency dependence $\mathfrak{X}(\omega)$ and S_{21} will be complicated. In particular the optical fiber filter and grating coupler can not be modelled. If A_Φ is known from a previous calibration, then a single spike at $\omega_\Phi \sim \omega_\mathrm{m}$ can be used to determine $\mathfrak{X}(\omega_\mathrm{m})$ in the immediate vicinity of ω_m.

L.2.3 Frequency representation

Denoting $f = \frac{\omega}{2\pi}$, $\cancel{\alpha} = \frac{\alpha}{2\pi} = \frac{1}{2\pi}\,\frac{\gamma}{2}$, $\cancel{g} = \frac{g}{2\pi}$, and $\cancel{W} = \frac{W}{2\pi}$,

$$S_{XX}(f) = \mathfrak{X}(f_\mathrm{L})^2 \left(|S_{21}(f_\mathrm{L})|^4\, \delta(f) + {\cancel{g}_\mathrm{om}}^2\, |\cancel{W}(f_\mathrm{L};f)|^{-2}\, \bar{S}_{\hat{y}\hat{y}}(f) \right) ,$$

with

$$S_{2\,1}(f_{\mathrm{L}}) = 1 + \frac{\text{Ø}_{\mathrm{o}}^{12}}{\mathrm{i}\,(f_{\mathrm{L}} - f_{\mathrm{om}}) - \text{Ø}_{\mathrm{o}}} \,, \qquad |S_{2\,1}(f_{\mathrm{L}})|^2 = \; 1 - \frac{\text{Ø}_{\mathrm{o}}^{12}\;\left(2\,\text{Ø}_{\mathrm{o}} - \text{Ø}_{\mathrm{o}}^{12}\right)}{(f_{\mathrm{om}} - f_{\mathrm{L}})^2 + (\text{Ø}_{\mathrm{o}})^2} \,,$$

$$\begin{aligned} |\text{Ø}\!\!\!\text{W}_0(f_{\mathrm{L}}; f)|^{-2} = \; & \left(\frac{1}{(f_{\mathrm{om}} - f_{\mathrm{L}})^2 + (\text{Ø}_{\mathrm{o}})^2}\right)^2 \\ & \times \frac{(2\,\text{Ø}_{\mathrm{o}}^{12})^2\,(f_{\mathrm{om}} - f_{\mathrm{L}})^2\;\left(f^2 + \left(2\,\text{Ø}_{\mathrm{o}} - \text{Ø}_{\mathrm{o}}^{12}\right)^2\right)}{\left((f + f_{\mathrm{om}} - f_{\mathrm{L}})^2 + (\text{Ø}_{\mathrm{o}})^2\right)\left((f - f_{\mathrm{om}} + f_{\mathrm{L}})^2 + (\text{Ø}_{\mathrm{o}})^2\right)} \,, \end{aligned}$$

$$\bar{S}_{\hat{y}\hat{y}}(f) = \frac{1}{2}\,\coth\Big[\frac{k_{\mathrm{B}}\,\mathbb{T}}{2\,h\,f_{\mathrm{m}}}\Big]\,\frac{1}{2\,\pi}\,\left(\frac{2\,\text{Ø}_{\mathrm{m}}}{(f + f_{\mathrm{m}})^2 + (\text{Ø}_{\mathrm{m}})^2} + \frac{2\,\text{Ø}_{\mathrm{m}}}{(f - f_{\mathrm{m}})^2 + (\text{Ø}_{\mathrm{m}})^2}\right) \,.$$

L.2.4 Coherent drive approximation

Some authors [120] approximate the mechanics by a coherent drive

$$\hat{b}(t) = \bar{b}_{\mathbb{T}}\,\mathrm{e}^{-\mathrm{i}\,\omega_{\mathrm{m}}\,t} \,, \qquad\qquad \bar{b}_{\mathbb{T}} = \sqrt{\bar{n}(\omega_{\mathrm{m}})} \overset{k_{\mathrm{B}}\,\mathbb{T} \gg \hbar\,\omega_{\mathrm{m}}}{\approx} \sqrt{\frac{k_{\mathrm{B}}\,\mathbb{T}}{\hbar\,\omega_{\mathrm{m}}}} \,.$$

This gives

$$\big(h * \hat{y}\big)(t) = \frac{\bar{b}_{\mathbb{T}}\,\mathrm{e}^{-\mathrm{i}\,\omega_{\mathrm{m}}\,t}}{\mathrm{i}\,(\Delta_{\mathrm{om}} - \omega_{\mathrm{m}}) + \frac{\gamma_{\mathrm{o}}}{2}} + \frac{\bar{b}_{\mathbb{T}}\,\mathrm{e}^{\mathrm{i}\,\omega_{\mathrm{m}}\,t}}{\mathrm{i}\,(\Delta_{\mathrm{om}} + \omega_{\mathrm{m}}) + \frac{\gamma_{\mathrm{o}}}{2}} \,,$$

$$\big(h^* * \hat{y}\big)(t) = \frac{\bar{b}_{\mathbb{T}}\,\mathrm{e}^{-\mathrm{i}\,\omega_{\mathrm{m}}\,t}}{-\mathrm{i}\,(\Delta_{\mathrm{om}} + \omega_{\mathrm{m}}) + \frac{\gamma_{\mathrm{o}}}{2}} + \frac{\bar{b}_{\mathbb{T}}\,\mathrm{e}^{\mathrm{i}\,\omega_{\mathrm{m}}\,t}}{-\mathrm{i}\,(\Delta_{\mathrm{om}} - \omega_{\mathrm{m}}) + \frac{\gamma_{\mathrm{o}}}{2}} \,,$$

and

$$S_{XX}(\omega) = \mathfrak{X}(\omega_{\mathrm{L}})^2 \Big(|S_{2\,1}|^2\, 2\,\pi\,\delta(\omega) + {g_{\mathrm{om}}}^2\, |W(\omega_{\mathrm{L}};\omega_{\mathrm{m}})|^{-2}\, \bar{n}(\omega_{\mathrm{m}})\, 2\,\pi \left(\delta(\omega-\omega_{\mathrm{m}}) + \delta(\omega+\omega_{\mathrm{m}})\right) \Big) .$$

If $W(\omega_{\mathrm{L}};\omega \approx \omega_{\mathrm{m}}) \approx W(\omega_{\mathrm{L}};\omega_{\mathrm{m}})$ is constant then this is the same as above under integration of $S_{XX}(\omega)$.

In Ref. [120] the factors $S^*_{2\,1}\, S_{1\,1} = S_{1\,1} + |S_{1\,1}|^2$ are approximated to $S_{1\,1}$ under the assumption that $S_{1\,1}$ is small but this is only true (at $\omega \approx \omega_{\mathrm{m}}$) when sideband resolved.

L.2.5 Phase modulation spectroscopy

Using a vector network analyzer to drive the phase modulator and detect the first sideband at f_Φ, we can perform spectroscopy. The output of the vector network analyzer, is input to our phase modulator, and drives (assumed linearly)

$$A_\Phi = \mathfrak{A}\, X_{\mathrm{in}} .$$

The output of the system is the signal $P_{\mathrm{D}}(\omega = \omega_\Phi) + P_{\mathrm{D}}(\omega = -\omega_\Phi)$,

$$X_{\mathrm{out}} = 2\,\mathfrak{X}(\omega_{\mathrm{L}}) \sum_{j=-\infty}^{\infty} J_j[A_\Phi]\, J_{j+1}[A_\Phi]\, S_{2\,1}\big(\omega_{\mathrm{L}} + j\,\omega_\Phi\big)\, S_{2\,1}\big(\omega_{\mathrm{L}} + (j+1)\,\omega_\Phi\big)^* ,$$

such that

$$S_{\Phi 2\,1}(\omega_\Phi) = 2\,\frac{\mathfrak{X}(\omega_\mathrm{L})}{\mathfrak{A}}\sum_{j=-\infty}^{\infty}\frac{J_j[A_\Phi]\,J_{j+1}[A_\Phi]}{A_\Phi}\,S_{2\,1}\big(\omega_\mathrm{L}+j\,\omega_\Phi\big)\,S_{2\,1}\big(\omega_\mathrm{L}+(j+1)\,\omega_\Phi\big)^*$$

$$\begin{aligned}
&= 2\,\frac{\mathfrak{X}}{\mathfrak{A}}\Bigg(\frac{1}{2}\Big(S_{2\,1}(\omega_\mathrm{L})\,S_{2\,1}(\omega_\mathrm{L}+\omega_\Phi)^* - S_{2\,1}(\omega_\mathrm{L})^*\,S_{2\,1}(\omega_\mathrm{L}-\omega_\Phi)\Big)\\
&\qquad + \frac{{A_\Phi}^2}{16}\Big(S_{2\,1}(\omega_\mathrm{L}+\omega_\Phi)\,S_{2\,1}(\omega_\mathrm{L}+2\,\omega_\Phi)^* - 3\,S_{2\,1}(\omega_\mathrm{L}+\omega_\Phi)^*\,S_{2\,1}(\omega_\mathrm{L})\\
&\qquad\qquad + 3\,S_{2\,1}(\omega_\mathrm{L}-\omega_\Phi)\,S_{2\,1}(\omega_\mathrm{L})^* - S_{2\,1}(\omega_\mathrm{L}-\omega_\Phi)^*\,S_{2\,1}(\omega_\mathrm{L}-2\,\omega_\Phi)\Big)\\
&\qquad\Bigg) + \mathcal{O}[A_\Phi]^4\,.
\end{aligned}$$

L.3 Interposed resonator experiment

For an optical cavity interposing the optical waveguide (see Sec. Θ.3),

$$\gamma_{\mathrm{o}} = \underbrace{\gamma_{\mathrm{o}}^{0}}_{\substack{\text{internal}\\ \text{loss}}} + \underbrace{\gamma_{\mathrm{o}}^{1}}_{\substack{\text{port 1}\\ \text{coupling}}} + \underbrace{\gamma_{\mathrm{o}}^{2}}_{\substack{\text{port 2}\\ \text{coupling}}} , \qquad a_{\mathrm{out}}^{2}(t) = \mathrm{e}^{\mathrm{i}\,\theta}\,\sqrt{\gamma_{\mathrm{o}}^{2}}\,a(t) ,$$

with

$$a_{\mathrm{in}}^{1}(t) = \sqrt{\hbar\,\omega_{\mathrm{L}}}\,\hat{d}_{\mathrm{in}}^{L}(t) = \sqrt{P_{\mathrm{L}}}\,\mathrm{e}^{-\mathrm{i}\,\omega_{\mathrm{L}}\,t} , \qquad L = \sqrt{\gamma_{\mathrm{o}}^{1}}\,\frac{\sqrt{P_{\mathrm{L}}}}{\sqrt{\hbar\,\omega_{\mathrm{L}}}} .$$

Thus

$$a_{\mathrm{out}}^{2}(t) = \frac{\sqrt{\gamma_{\mathrm{o}}^{1}\,\gamma_{\mathrm{o}}^{2}}\,\sqrt{P_{\mathrm{L}}}\,\mathrm{e}^{-\mathrm{i}\,\omega_{\mathrm{L}}\,t}}{\mathrm{i}\,(\omega_{\mathrm{L}} - \omega_{\mathrm{om}}) - \frac{\gamma_{\mathrm{o}}}{2}}\,\Big(1 - \mathrm{i}\,g_{\mathrm{om}}\,\big(h * \hat{y}\big)(t)\Big)$$

$$= \sqrt{P_{\mathrm{L}}}\,\mathrm{e}^{-\mathrm{i}\,\omega_{\mathrm{L}}\,t}\,S_{2\,1}(\omega_{\mathrm{L}})\,\Big(1 - \mathrm{i}\,g_{\mathrm{om}}\,\big(h * \hat{y}\big)(t)\Big) ,$$

with

$$S_{2\,1}(\omega_{\mathrm{L}}) = \frac{\sqrt{\gamma_{\mathrm{o}}^{1}\,\gamma_{\mathrm{o}}^{2}}}{\mathrm{i}\,(\omega_{\mathrm{L}} - \omega_{\mathrm{om}}) - \frac{\gamma_{\mathrm{o}}}{2}} .$$

This gives the power out as

$$\begin{aligned} P_{\mathrm{D}}(t) &= |a_{\mathrm{out}}^{2}(t)|^{2} \\ &= P_{\mathrm{L}}\,\Big(|S_{2\,1}(\omega_{\mathrm{L}})|^{2} - \mathrm{i}\,g_{\mathrm{om}}\,|S_{2\,1}(\omega_{\mathrm{L}})|^{2}\,\big(h * \hat{y}\big)(t) \\ &\qquad + \mathrm{i}\,g_{\mathrm{om}}\,|S_{2\,1}(\omega_{\mathrm{L}})|^{2}\,\big(h^{*} * \hat{y}\big)(t)\Big) + \mathcal{O}[g_{\mathrm{om}}]^{2} , \end{aligned}$$

with Fourier transform

$$P_{\mathrm{D}}(\omega) = P_{\mathrm{L}} \left(|S_{2\,1}(\omega_{\mathrm{L}})|^2 \sqrt{2\,\pi}\, \delta(\omega) + g_{\mathrm{om}}\, W^{-1}(\omega_{\mathrm{L}};\omega)\, \hat{y}(\omega) \right) ,$$

and

$$\begin{aligned} W^{-1}(\omega_{\mathrm{L}};\omega) &= |S_{2\,1}(\omega_{\mathrm{L}})|^2 \left(-\mathrm{i}\sqrt{2\,\pi}\, h(\omega) + \mathrm{i}\sqrt{2\,\pi}\, h^*(\omega) \right) \\ &= \frac{\mathrm{i}}{\sqrt{\gamma_{\mathrm{o}}^1\, \gamma_{\mathrm{o}}^2}} |S_{2\,1}(\omega_{\mathrm{L}})|^2 \left(S_{2\,1}(\omega_{\mathrm{L}} + \omega) - S_{2\,1}(\omega_{\mathrm{L}} - \omega)^* \right) \\ &= \left(\frac{\mathrm{i}}{(\Delta_{\mathrm{om}})^2 + \frac{(\gamma_{\mathrm{o}})^2}{4}} \right) \left(\frac{\gamma_{\mathrm{o}}^1\, \gamma_{\mathrm{o}}^2}{\mathrm{i}\,(\omega - \Delta_{\mathrm{om}}) - \frac{\gamma_{\mathrm{o}}}{2}} - \frac{\gamma_{\mathrm{o}}^1\, \gamma_{\mathrm{o}}^2}{\mathrm{i}\,(\omega + \Delta_{\mathrm{om}}) - \frac{\gamma_{\mathrm{o}}}{2}} \right) , \end{aligned}$$

with $\Delta_{\mathrm{om}} = \omega_{\mathrm{om}} - \omega_{\mathrm{L}}$.

Again we have,

$$P_{\mathrm{L}} = P_{\mathrm{delivered}} \quad \underset{\text{coupler}}{\eta_{\mathrm{grating}}} ,$$

and the signal measured by the spectrum analyzer is

$$\underset{\text{analyzer}}{X_{\mathrm{spectrum}}} = I_{\mathrm{PD}} \sqrt{Z_{\mathrm{C}}} = P_{\mathrm{D}} \quad \underset{\text{coupler}}{\eta_{\mathrm{grating}}} \quad f_{\mathrm{split}} \quad \underset{\text{amp}}{G_{\mathrm{fiber}}} \quad T_{\mathrm{filter}} \quad \underset{\text{responsivity}}{R_{\mathrm{PD}}} \quad \sqrt{Z_{\mathrm{C}}} ,$$

where $Z_{\mathrm{C}} = 50\,\Omega$ is the spectrum analyzer input impedance. Capturing all of these into some factor

$$\mathfrak{X} = P_{\mathrm{delivered}} \quad \left(\underset{\text{coupler}}{\eta_{\mathrm{grating}}} \right)^2 \quad f_{\mathrm{split}} \quad \underset{\text{amp}}{G_{\mathrm{fiber}}} \quad T_{\mathrm{filter}} \quad \underset{\text{responsivity}}{R_{\mathrm{PD}}} \quad \sqrt{Z_{\mathrm{C}}} ,$$

such that $\mathfrak{X}^2$ is a power, we get

$$S_{XX}(\omega) = \mathfrak{X}(\omega_{\mathrm{L}})^2 \left(|S_{2\,1}(\omega_{\mathrm{L}})|^4 \, 2\,\pi\,\delta(\omega) + {g_{\mathrm{om}}}^2 \, |W(\omega_{\mathrm{L}};\omega)|^{-2} \, \bar{S}_{\hat{y}\hat{y}}(\omega) \right) ,$$

with

$$|S_{2\,1}(\omega_{\mathrm{L}})|^2 = \frac{\gamma_{\mathrm{o}}^1 \, \gamma_{\mathrm{o}}^2}{(\Delta_{\mathrm{om}})^2 + \frac{(\gamma_{\mathrm{o}})^2}{4}} ,$$

$$|W(\omega_{\mathrm{L}};\omega)|^{-2} = \left(\frac{\gamma_{\mathrm{o}}^1 \, \gamma_{\mathrm{o}}^2}{(\Delta_{\mathrm{om}})^2 + \frac{(\gamma_{\mathrm{o}})^2}{4}} \right)^2 \frac{4\,(\Delta_{\mathrm{om}})^2}{\left((\omega + \Delta_{\mathrm{om}})^2 + \frac{(\gamma_{\mathrm{o}})^2}{4}\right) \left((\omega - \Delta_{\mathrm{om}})^2 + \frac{(\gamma_{\mathrm{o}})^2}{4}\right)} ,$$

$$\bar{S}_{\hat{y}\hat{y}}(\omega) = \frac{1}{2} \, \coth\!\left[\frac{k_{\mathrm{B}}\,\mathbb{T}}{2\,\hbar\,\omega_{\mathrm{m}}} \right] \left(\frac{\gamma_{\mathrm{m}}}{(\omega + \omega_{\mathrm{m}})^2 + \frac{(\gamma_{\mathrm{m}})^2}{4}} + \frac{\gamma_{\mathrm{m}}}{(\omega - \omega_{\mathrm{m}})^2 + \frac{(\gamma_{\mathrm{m}})^2}{4}} \right)$$

$$\bar{n}(\omega_{\mathrm{m}}) = \frac{1}{2} \, \coth\!\left[\frac{k_{\mathrm{B}}\,\mathbb{T}}{2\,\hbar\,\omega_{\mathrm{m}}} \right] \overset{k_{\mathrm{B}}\,\mathbb{T} \gg \hbar\,\omega_{\mathrm{m}}}{\approx} \frac{k_{\mathrm{B}}\,\mathbb{T}}{\hbar\,\omega_{\mathrm{m}}} .$$

For a sufficiently narrow γ_{m}, the factor $W(\omega_{\mathrm{L}};\omega)$ is approximately constant and can be determined from a measurement of the optical transmission. When not sideband resolved, $|W(\omega_{\mathrm{L}};\omega)|^{-2}$ is maximized when

$$\Delta_{\mathrm{om}} = \pm\sqrt{\frac{\omega^2 + \frac{(\gamma_{\mathrm{o}})^2}{4}}{3}} .$$

The total power in the thermal mechanical spectrum is

$$\begin{aligned} P_{\mathrm{m}} &\approx \frac{1}{2\,\pi} \int_{-\infty}^{\infty} \mathfrak{X}(\omega_{\mathrm{L}})^2 \, {g_{\mathrm{om}}}^2 \, |W(\omega_{\mathrm{L}};\omega_{\mathrm{m}})|^{-2} \, \bar{S}_{\hat{y}\hat{y}}(\omega) \, \mathrm{d}\omega \\ &= 2\,\mathfrak{X}(\omega_{\mathrm{L}})^2 \, {g_{\mathrm{om}}}^2 \, \bar{n}(\omega_{\mathrm{m}}) \, |W(\omega_{\mathrm{L}};\omega_{\mathrm{m}})|^{-2} \, . \end{aligned}$$

L.3.1 Phase modulated sideband drive

Applying phase modulation, again using the Jacobi-Anger expansion,

$$L\,\mathrm{e}^{-\mathrm{i}\left(\omega_{\mathrm{L}}\,t - A_{\Phi}\,\sin[\omega_{\Phi}\,t]\right)} = L\,\mathrm{e}^{-\mathrm{i}\,\omega_{\mathrm{L}}\,t} \sum_{j=-\infty}^{\infty} J_j[A_{\Phi}]\,\mathrm{e}^{-\mathrm{i}\,j\,\omega_{\Phi}\,t} \, ,$$

where J_j are Bessel functions of the first kind, and matching to laser drives

$$\sum_{j=-\infty}^{\infty} L_j\,\mathrm{e}^{-\mathrm{i}\,(\omega_{\mathrm{L}}+j\,\omega_{\Phi})\,t} \qquad \Rightarrow \quad L_j = L\,J_j[A_{\Phi}] \, .$$

Following Sec. J.8.7 for weak symmetric sidebands, we apply serial linearization

$$\hat{a}(t) = \hat{a}'(t) + \sum_{j=-n}^{n} \bar{a}_j\,\mathrm{e}^{-\mathrm{i}\,(\omega_{\mathrm{L}}+j\,\omega_{\Phi})\,t} \, , \qquad \hat{b}(t) = \hat{b}'(t) + \sum_{j=-n}^{n} \bar{b}_j\,\mathrm{e}^{-\mathrm{i}\,j\,\omega_{\Phi}\,t} \, ,$$

with

$$\bar{a}_{j\neq 0} = \frac{-\mathrm{i}\,L_j - \mathrm{i}\,g_{\mathrm{om}}\,\bar{a}\,\left(\bar{b}^*_{-j} + \bar{b}_j\right)}{\mathrm{i}\,(\omega_{\mathrm{om}} - \omega_{\mathrm{L}} - j\,\omega_{\Phi}) + \frac{|\gamma_{\mathrm{o}}|}{2}} \, , \qquad \bar{a}_0 = \bar{a} = \frac{-\mathrm{i}\,L_0}{\mathrm{i}\,(\omega_{\mathrm{om}} - \omega_{\mathrm{L}}) + \frac{|\gamma_{\mathrm{o}}|}{2}}$$

$$\bar{b}_{j\neq 0} = \frac{-\mathrm{i}\,g_{\mathrm{om}}\,\left(\bar{a}^*\,\bar{a}_j + \bar{a}\,\bar{a}^*_{-j}\right)}{\mathrm{i}\,(\omega_{\mathrm{m}} - j\,\omega_{\Phi}) + \frac{|\gamma_{\mathrm{m}}|}{2}} \, , \qquad \bar{b}_0 = \bar{b} = \frac{-\mathrm{i}\,g_{\mathrm{om}}\,\left(|\bar{a}|^2 + \frac{1}{2}\right)}{\mathrm{i}\,\omega_{\mathrm{m}} + \frac{|\gamma_{\mathrm{m}}|}{2}} \, ,$$

keeping the same solution to $\hat{a}'(t)$ as originally. If ω_Φ is outside the mechanical resonance then $\bar{b}_{j\neq 0} \approx 0$.

We now have

$$\begin{aligned}
\hat{a}(t) &= \mathrm{e}^{-\mathrm{i}\,\omega_\mathrm{L}\,t}\left(\sum_{j=-\infty}^{\infty}\bar{a}_j\,\mathrm{e}^{-\mathrm{i}\,j\,\omega_\Phi\,t} - \mathrm{i}\,g_\mathrm{om}\,\bar{a}\,\big(h * \hat{y}\big)(t)\right)\,,\\
a^1_\mathrm{in}(t) &= \sqrt{P_\mathrm{L}}\,\mathrm{e}^{-\mathrm{i}\,\omega_\mathrm{L}\,t}\sum_{j=-\infty}^{\infty}J_j[A_\Phi]\,\mathrm{e}^{-\mathrm{i}\,j\,\omega_\Phi\,t}\,,\\
a^2_\mathrm{out}(t) &= \sqrt{P_\mathrm{L}}\,\mathrm{e}^{-\mathrm{i}\,\omega_\mathrm{L}\,t}\left(\sum_{j=-\infty}^{\infty}J_j[A_\Phi]\,S_{2\,1}(\omega_\mathrm{L}+j\,\omega_\Phi)\,\mathrm{e}^{-\mathrm{i}\,j\,\omega_\Phi\,t}\right.\\
&\qquad\left. - \mathrm{i}\,g_\mathrm{om}\,J_0[A_\Phi]\,S_{2\,1}(\omega_\mathrm{L})\,\big(h * \hat{y}\big)(t)\right)\,,
\end{aligned}$$

with

$$S_{2\,1}(\omega_\mathrm{L}) = \frac{\sqrt{\gamma^1_\mathrm{o}\,\gamma^2_\mathrm{o}}}{\mathrm{i}\,(\omega_\mathrm{L}-\omega_\mathrm{om}) - \frac{\gamma_\mathrm{o}}{2}}\,.$$

This form assumes the sidebands are much lower in power than the main carrier.

The output power is

$$\begin{aligned}
P_\mathrm{D}(t) &= |a^2_\mathrm{out}(t)|^2\\
&= P_\mathrm{L}\left(\sum_{k=-\infty}^{\infty}\sum_{j=-\infty}^{\infty}J_j[A_\Phi]\,J_{j+k}[A_\Phi]\,S_{2\,1}\big(\omega_\mathrm{L}+j\,\omega_\Phi\big)\,S_{2\,1}\big(\omega_\mathrm{L}+(j+k)\,\omega_\Phi\big)^*\,\mathrm{e}^{-\mathrm{i}\,k\,\omega_\Phi\,t}\right.\\
&\qquad - \mathrm{i}\,g_\mathrm{om}\sum_{j=-\infty}^{\infty}J_j[A_\Phi]\,J_0[A_\Phi]\,S_{2\,1}(\omega_\mathrm{L}+j\,\omega_\Phi)^*\,S_{2\,1}(\omega_\mathrm{L})\,\big(h * \hat{y}\big)(t)\,\mathrm{e}^{\mathrm{i}\,j\,\omega_\Phi\,t}\\
&\qquad \left. + \mathrm{i}\,g_\mathrm{om}\sum_{j=-\infty}^{\infty}J_j[A_\Phi]\,J_0[A_\Phi]\,S_{2\,1}(\omega_\mathrm{L}+j\,\omega_\Phi)\,S_{2\,1}(\omega_\mathrm{L})^*\,\big(h^* * \hat{y}\big)(t)\,\mathrm{e}^{-\mathrm{i}\,j\,\omega_\Phi\,t}\right)\\
&\quad + \mathcal{O}[g_\mathrm{om}]^2\,,
\end{aligned}$$

with Fourier transform $P_{\mathrm{D}}(\omega) =$

$$P_{\mathrm{L}} \Bigg(\sum_{k=-\infty}^{\infty} \sum_{j=-\infty}^{\infty} J_j[A_\Phi]\, J_{j+k}[A_\Phi]\, S_{2\,1}\big(\omega_{\mathrm{L}} + j\,\omega_\Phi\big)\, S_{2\,1}\big(\omega_{\mathrm{L}} + (j+k)\,\omega_\Phi\big)^*\, \sqrt{2\,\pi}\, \delta(\omega - k\,\omega_\Phi)$$
$$- \mathrm{i}\, g_{\mathrm{om}} \sum_{j=-\infty}^{\infty} J_j[A_\Phi]\, J_0[A_\Phi]\, S_{2\,1}(\omega_{\mathrm{L}} + j\,\omega_\Phi)^*\, S_{2\,1}(\omega_{\mathrm{L}})\, \sqrt{2\,\pi}\, h(\omega + j\,\omega_\Phi)\, \hat{y}(\omega + j\,\omega_\Phi)$$
$$+ \mathrm{i}\, g_{\mathrm{om}} \sum_{j=-\infty}^{\infty} J_j[A_\Phi]\, J_0[A_\Phi]\, S_{2\,1}(\omega_{\mathrm{L}} + j\,\omega_\Phi)\, S_{2\,1}(\omega_{\mathrm{L}})^*\, \sqrt{2\,\pi}\, h^*(\omega - j\,\omega_\Phi)\, \hat{y}(\omega - j\,\omega_\Phi) \Bigg) .$$

Assuming $\langle \hat{e}_{\mathrm{in}}(\omega)^\dagger\, \hat{e}_{\mathrm{in}}(\omega' \neq \omega) \rangle = 0$, the power spectral density is $S_{XX}(\omega) =$

$$\mathfrak{X}(\omega_{\mathrm{L}})^2 \Bigg(\sum_{k=-\infty}^{\infty} \Bigg| \sum_{j=-\infty}^{\infty} J_j[A_\Phi]\, J_{j+k}[A_\Phi]\, S_{2\,1}\big(\omega_{\mathrm{L}} + j\,\omega_\Phi\big)\, S_{2\,1}\big(\omega_{\mathrm{L}} + (j+k)\,\omega_\Phi\big)^* \Bigg|^2 2\,\pi\,\delta(\omega - k\,\omega_\Phi)$$
$$+ {g_{\mathrm{om}}}^2 \sum_{j=-\infty}^{\infty} J_j[A_\Phi]^2\, J_0[A_\Phi]^2\, |W_j(\omega_{\mathrm{L}};\omega)|^{-2}\, \bar{S}_{\hat{y}\hat{y}}(\omega + j\,\omega_\Phi) \Bigg) ,$$

with

$$W_j^{-1}(\omega_{\mathrm{L}};\omega) = -\mathrm{i}\, S_{2\,1}(\omega_{\mathrm{L}} + j\,\omega_\Phi)^*\, S_{2\,1}(\omega_{\mathrm{L}})\, \sqrt{2\,\pi}\, h(\omega + j\,\omega_\Phi)$$
$$+ \mathrm{i}\, S_{2\,1}(\omega_{\mathrm{L}} - j\,\omega_\Phi)\, S_{2\,1}(\omega_{\mathrm{L}})^*\, \sqrt{2\,\pi}\, h^*(\omega + j\,\omega_\Phi)$$

$$= \frac{\mathrm{i}}{\sqrt{\gamma_{\mathrm{o}}^1\, \gamma_{\mathrm{o}}^2}}\, S_{2\,1}(\omega_{\mathrm{L}} + j\,\omega_\Phi)^*\, S_{2\,1}(\omega_{\mathrm{L}})\, S_{2\,1}(\omega_{\mathrm{L}} + j\,\omega_\Phi + \omega)$$
$$- \frac{\mathrm{i}}{\sqrt{\gamma_{\mathrm{o}}^1\, \gamma_{\mathrm{o}}^2}}\, S_{2\,1}(\omega_{\mathrm{L}} - j\,\omega_\Phi)\, S_{2\,1}(\omega_{\mathrm{L}})^*\, S_{2\,1}(\omega_{\mathrm{L}} - j\,\omega_\Phi - \omega)^* .$$

We can now use power measurements at $k\,\omega_\Phi$ to determine $\mathfrak{X}$. Selecting out the appropriate

coefficients from $S_{XX}(\omega)$, we have for each measured sideband peak $k > 0$,

$$\begin{aligned} P_{k\,\omega_\Phi} &= 2\,\mathfrak{X}(\omega_\mathrm{L})^2 \left| \sum_{j=-\infty}^{\infty} J_j[A_\Phi]\, J_{j+k}[A_\Phi]\, S_{2\,1}\big(\omega_\mathrm{L} + j\,\omega_\Phi\big)\, S_{2\,1}\big(\omega_\mathrm{L} + (j+k)\,\omega_\Phi\big)^* \right|^2 \\ &= \mathfrak{X}(\omega_\mathrm{L})^2 \sum_{m=0}^{\infty} C_{k\,m}\, {A_\Phi}^m \,, \end{aligned}$$

including both positive and negative frequency (identical) contributions. If $A_\Phi \ll 1$ then this summation can be terminated. For $k = 1$ and to the lowest order in A_Φ,

$$P_{\omega_\Phi} = \mathfrak{X}(\omega_\mathrm{L})^2 \left| S_{2\,1}(\omega_\mathrm{L})\, S_{2\,1}(\omega_\mathrm{L} + \omega_\Phi)^* - S_{2\,1}(\omega_\mathrm{L})^*\, S_{2\,1}(\omega_\mathrm{L} - \omega_\Phi) \right|^2 \frac{{A_\Phi}^2}{2} + \mathcal{O}[A_\Phi]^4 \,.$$

Again, this has an equivalence to the thermal response at leading order in A_Φ,

$$\left| S_{2\,1}(\omega_\mathrm{L})\, S_{2\,1}(\omega_\mathrm{L} + \omega_\Phi)^* - S_{2\,1}(\omega_\mathrm{L})^*\, S_{2\,1}(\omega_\mathrm{L} - \omega_\Phi) \right|^2 = |W_0(\omega_\mathrm{L}; \omega_\Phi)|^{-2}\, {\omega_\Phi}^2 \,,$$

giving at weak phase modulation

$$P_{\omega_\Phi} \approx \mathfrak{X}(\omega_\mathrm{L})^2\, |W_0(\omega_\mathrm{L}; \omega_\Phi)|^{-2}\, {\omega_\Phi}^2\, \frac{{A_\Phi}^2}{2} \,.$$

L.3.2 Frequency representation

Denoting $f = \frac{\omega}{2\,\pi}$, ~~$\alpha$~~ $= \frac{\alpha}{2\,\pi} = \frac{1}{2\,\pi}\,\frac{\gamma}{2}$, ~~$g$~~ $= \frac{g}{2\,\pi}$, and ~~W~~ $= \frac{W}{2\,\pi}$,

$$S_{XX}(f) = \mathfrak{X}(f_\mathrm{L})^2 \left(|S_{2\,1}(f_\mathrm{L})|^4\, \delta(f) + {\mathfrak{g}_\mathrm{om}}^2\, |\mathfrak{W}(f_\mathrm{L}; f)|^{-2}\, \bar{S}_{\hat{y}\hat{y}}(f) \right) ,$$

with

$$S_{21}(f_{\mathrm{L}}) = \frac{2\sqrt{\text{ϰ}_{\mathrm{o}}^{1}\,\text{ϰ}_{\mathrm{o}}^{2}}}{\mathrm{i}\,(f_{\mathrm{L}} - f_{\mathrm{om}}) - \text{ϰ}_{\mathrm{o}}}\,, \qquad |S_{21}(f_{\mathrm{L}})|^2 = \frac{4\,\text{ϰ}_{\mathrm{o}}^{1}\,\text{ϰ}_{\mathrm{o}}^{2}}{(f_{\mathrm{om}} - f_{\mathrm{L}})^2 + (\text{ϰ}_{\mathrm{o}})^2}\,,$$

$$|\text{Ψ}_0(f_{\mathrm{L}}; f)|^{-2} = \left(\frac{4\,\text{ϰ}_{\mathrm{o}}^{1}\,\text{ϰ}_{\mathrm{o}}^{2}}{(f_{\mathrm{om}} - f_{\mathrm{L}})^2 + (\text{ϰ}_{\mathrm{o}})^2}\right)^2 \times \frac{4\,(f_{\mathrm{om}} - f_{\mathrm{L}})^2}{\left((f + f_{\mathrm{om}} - f_{\mathrm{L}})^2 + (\text{ϰ}_{\mathrm{o}})^2\right)\left((f - f_{\mathrm{om}} + f_{\mathrm{L}})^2 + (\text{ϰ}_{\mathrm{o}})^2\right)}\,,$$

$$\bar{S}_{\hat{y}\hat{y}}(f) = \frac{1}{2}\,\coth\!\left[\frac{k_{\mathrm{B}}\,\mathbb{T}}{2\,h\,f_{\mathrm{m}}}\right]\frac{1}{2\,\pi}\left(\frac{2\,\text{ϰ}_{\mathrm{m}}}{(f + f_{\mathrm{m}})^2 + (\text{ϰ}_{\mathrm{m}})^2} + \frac{2\,\text{ϰ}_{\mathrm{m}}}{(f - f_{\mathrm{m}})^2 + (\text{ϰ}_{\mathrm{m}})^2}\right)\,.$$

L.4 Time averaged measurement

If our measurement is occurring whilst dither locking, we'll want to time average our optic scattering coefficients over the dither cycle,

$$\left\langle S_{XX}(\omega_{\mathrm{L}})\right\rangle_{\mathrm{dither}} = \frac{1}{2\,\pi}\int_0^{2\,\pi} S_{XX}\left(\omega_{\mathrm{L}} + \underset{\mathrm{ampl}}{\omega_{\mathrm{dither}}}\,\sin[\theta]\right)\mathrm{d}\theta\,,$$

and ensure our spectrum analyzer video bandwidth VBW $\ll f_{\mathrm{dither}}$. This can be performed numerically with parameters extracted from the optic resonance fit.

L.5 Optomechanical coupling measurement

Regardless of the optical resonator configuration and transmission profile, the optomechanical coupling can be measured from the thermal spectrum and calibrated phase modulated signal with a spectrum analyzer (see App. Λ.12). The measured power spectral density in

the vicinity of the optomechanical response is

$$\mathrm{PSD}_1(f \sim f_\mathrm{m}) = \mathfrak{X}(f_\mathrm{L})^2 \left(\mathscr{g}_\mathrm{om}{}^2 \, |\mathscr{W}_0(f_\mathrm{L}; f)|^{-2} \, \frac{\bar{n}(f_\mathrm{m})}{\pi} \, \frac{2\,\mathscr{a}_\mathrm{m}}{(f - f_\mathrm{m})^2 + (\mathscr{a}_\mathrm{m})^2} + \mathrm{bg}(f) \right) ,$$

and the measured power at that phase modulation frequency (to leading order in A_Φ) is

$$P_1(f_\Phi) = \mathfrak{X}(f_\mathrm{L})^2 \left(|\mathscr{W}_0(f_\mathrm{L}; f_\Phi)|^{-2} \, f_\Phi{}^2 \, \frac{A_\Phi{}^2}{2} + \int_\mathrm{RBW} \mathrm{bg}(f) \, \mathrm{d}f \right) .$$

The power spectral density can be fit to a Lorentzian and quadratic background,

$$\mathrm{PSD}_1(f \sim f_\mathrm{m}) = \frac{\mathcal{A}}{(f - f_\mathrm{m})^2 + (\mathscr{a}_\mathrm{m})^2} + \mathcal{C}_0 + \mathcal{C}_1 \, (f - f_\mathrm{m}) + \mathcal{C}_2 \, (f - f_\mathrm{m})^2 .$$

An accurate measurement of P_{f_Φ} can be made in the regime of over-coverage ($\mathrm{RBW} \gg f_\mathrm{step}$) by fitting the window function,

$$P_{1\,\mathrm{meas}}(f \sim f_\Phi) = P_{f_\Phi} \, w(f; f_\Phi) + \mathcal{C}_0' .$$

The optomechanical coupling is then

$$\mathscr{g}_\mathrm{om}{}^2 = \frac{\mathcal{A} \, \pi \, f_\Phi{}^2 \, A_\Phi{}^2}{4 \, \bar{n}(f_\mathrm{m}) \, \mathscr{a}_\mathrm{m} \, P_{f_\Phi}} .$$

APPENDIX M

Material properties

M.1 Gallium arsenide (GaAs)

GaAs is semiconductor compound with a zincblende structure ($F\bar{4}3m$ space group) [238–241] as depcicted in Fig. M.1. Its density is given below.

	Low temp.	Room temp.
ρ	$(5332 \pm 4)\,\mathrm{kg\,m^{-3}}$	$5317\,\mathrm{kg\,m^{-3}}$

M.1.1 Mechanical properties

Owing to its cubic structure, GaAs has only 3 independent stiffness tensor elements, the (stress-like) Voigt transformed stiffness tensor is [241]

$$\underline{\underline{\tilde{c}}} = \begin{pmatrix} \tilde{c}^{11} & \tilde{c}^{12} & \tilde{c}^{12} & 0 & 0 & 0 \\ \tilde{c}^{12} & \tilde{c}^{11} & \tilde{c}^{12} & 0 & 0 & 0 \\ \tilde{c}^{12} & \tilde{c}^{12} & \tilde{c}^{11} & 0 & 0 & 0 \\ 0 & 0 & 0 & \tilde{c}^{44} & 0 & 0 \\ 0 & 0 & 0 & 0 & \tilde{c}^{44} & 0 \\ 0 & 0 & 0 & 0 & 0 & \tilde{c}^{44} \end{pmatrix}.$$

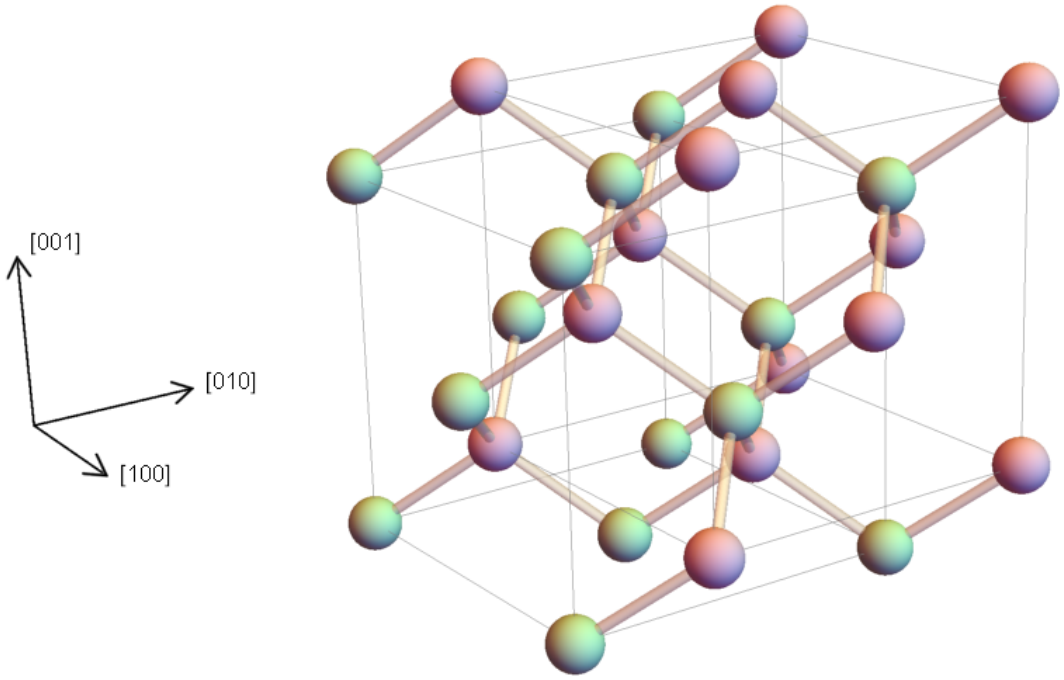

Figure M.1: Gallium arsendie has a tetrahedral coordination, where each atom is surrounded by four of the opposing type in a tetrahedron shape, that looks like two interposing face centered cubic lattices offset by $(1/4, 1/4, 1/4)$ $\times$ lattice constant.

The compliance tensor can be calculated from $\tilde{c}^{\,i\,j}\ \tilde{s}_{\,j\,k} = \delta^{i}_{\ k}$, and in (strain-like) Voigt form is

$$\tilde{\tilde{s}} = \begin{pmatrix} \tilde{s}_{1\,1} & \tilde{s}_{1\,2} & \tilde{s}_{1\,2} & 0 & 0 & 0 \\ \tilde{s}_{1\,2} & \tilde{s}_{1\,1} & \tilde{s}_{1\,2} & 0 & 0 & 0 \\ \tilde{s}_{1\,2} & \tilde{s}_{1\,2} & \tilde{s}_{1\,1} & 0 & 0 & 0 \\ 0 & 0 & 0 & \tilde{s}_{4\,4} & 0 & 0 \\ 0 & 0 & 0 & 0 & \tilde{s}_{4\,4} & 0 \\ 0 & 0 & 0 & 0 & 0 & \tilde{s}_{4\,4} \end{pmatrix}.$$

Values for the adiabatic elastic parameters, with crystal axis [100], are taken from Cottam and Saunders [242].

	Low temp.	Room temp.
$\tilde{c}^{1\,1}$	$(121.07 \pm 0.39) \times 10^9\,\mathrm{Pa}$	$(118.41 \pm 0.37) \times 10^9\,\mathrm{Pa}$
$\tilde{c}^{1\,2}$	$(54.77 \pm 1.65) \times 10^9\,\mathrm{Pa}$	$(53.78 \pm 1.57) \times 10^9\,\mathrm{Pa}$
$\tilde{c}^{4\,4}$	$(60.36 \pm 0.19) \times 10^9\,\mathrm{Pa}$	$(59.12 \pm 0.18) \times 10^9\,\mathrm{Pa}$
$\tilde{s}_{1\,1}$	$(11.150 \pm 0.905) \times 10^{-12}\,\mathrm{Pa}^{-1}$	$(11.790 \pm 0.910) \times 10^{-12}\,\mathrm{Pa}^{-1}$
$\tilde{s}_{1\,2}$	$(-3.582 \pm 0.386) \times 10^{-12}\,\mathrm{Pa}^{-1}$	$(-3.682 \pm 0.388) \times 10^{-12}\,\mathrm{Pa}^{-1}$
$\tilde{s}_{4\,4}$	$(16.567 \pm 1.758) \times 10^{-12}\,\mathrm{Pa}^{-1}$	$(16.915 \pm 1.761) \times 10^{-12}\,\mathrm{Pa}^{-1}$

M.1.2 Piezoelectric properties

The (stress-like) Voigt transformed piezoelectric stress tensor for GaAs has the form [241]

$$\underline{\underline{\tilde{e}}} = \begin{pmatrix} 0 & 0 & 0 & \tilde{e}^{1\,4} & 0 & 0 \\ 0 & 0 & 0 & 0 & \tilde{e}^{1\,4} & 0 \\ 0 & 0 & 0 & 0 & 0 & \tilde{e}^{1\,4} \end{pmatrix}.$$

Whilst the (strain-like) Voigt transformed piezoelectric strain tensor for GaAs has the form

$$\underline{\underline{\tilde{d}}} = \begin{pmatrix} 0 & 0 & 0 & \tilde{d}_{1\,4} & 0 & 0 \\ 0 & 0 & 0 & 0 & \tilde{d}_{1\,4} & 0 \\ 0 & 0 & 0 & 0 & 0 & \tilde{d}_{1\,4} \end{pmatrix}.$$

Values for the piezoelectric parameters are taken from Arlt and Quadflieg [243].

$\tilde{e}^{1\,4}$	$-0.16\,\mathrm{C\,m^{-2}}$
$\tilde{d}_{1\,4}$	$-2.7\times10^{-12}\,\mathrm{m\,V^{-1}}$

M.1.3 Elasto-optic properties

The (stress-like) Voigt transformed photoelasticity tensor for cubic materials has the form [224, 241, 244]

$$\underline{\underline{\tilde{p}}} = \begin{pmatrix} \tilde{p}^{1\,1} & \tilde{p}^{1\,2} & \tilde{p}^{1\,2} & 0 & 0 & 0 \\ \tilde{p}^{1\,2} & \tilde{p}^{1\,1} & \tilde{p}^{1\,2} & 0 & 0 & 0 \\ \tilde{p}^{1\,2} & \tilde{p}^{1\,2} & \tilde{p}^{1\,1} & 0 & 0 & 0 \\ 0 & 0 & 0 & \tilde{p}^{4\,4} & 0 & 0 \\ 0 & 0 & 0 & 0 & \tilde{p}^{4\,4} & 0 \\ 0 & 0 & 0 & 0 & 0 & \tilde{p}^{4\,4} \end{pmatrix}.$$

Values for the photoelastic parameters are taken from Dixon [245], however there is substantial uncertainty in these quantities.

	261 THz
$\tilde{p}^{1\,1}$	-0.165
$\tilde{p}^{1\,2}$	-0.140
$\tilde{p}^{4\,4}$	-0.072

M.1.4 Electro-optic properties

The (stress-like) Voigt transformed linear (Pockel's) electro-optic tensor for GaAs is [224, 241]

$$\underline{\underline{\tilde{r}}} = \begin{pmatrix} 0 & 0 & 0 \\ 0 & 0 & 0 \\ 0 & 0 & 0 \\ \tilde{r}^{41} & 0 & 0 \\ 0 & \tilde{r}^{41} & 0 \\ 0 & 0 & \tilde{r}^{41} \end{pmatrix} .$$

The linear electro-optic property can be measured at constant stress, $r|_T$, or constant strain, $r|_S$, and are related by

$$r|_T = r|_S + r|_P ,$$

where $r|_P$ is induced from piezoelectricity, and for a zincblende material like GaAs is given by

$$\tilde{r}^{41}|_P = \tilde{p}^{44}\, \tilde{s}_{44}\, \tilde{e}^{14} .$$

Values for the linear electro-optic parameter are taken from Suzuki and Tada [246].

	200 THz	229 THz	248 THz	282 THz
$\tilde{r}^{41}\|_T$	$-1.36\,\mathrm{pm\,V^{-1}}$	$-1.28\,\mathrm{pm\,V^{-1}}$	$-1.25\,\mathrm{pm\,V^{-1}}$	$-1.17\,\mathrm{pm\,V^{-1}}$
$\tilde{r}^{41}\|_S$	$-1.53\,\mathrm{pm\,V^{-1}}$	$-1.46\,\mathrm{pm\,V^{-1}}$	$-1.41\,\mathrm{pm\,V^{-1}}$	$-1.33\,\mathrm{pm\,V^{-1}}$

M.1.5 Optical properties

Various models exist to describe semiconductor dispersion relations [241] and experimental measurements have not always been consistent. Here we will simply provide some results on GaAs index of refraction in the transparent region as a function of frequency and temperature. In this region GaAs is a dielectric with minimal loss and optically isotropic, thus we have

$$\varepsilon \in \mathbb{R} \quad \Rightarrow \quad n = \sqrt{\varepsilon_{\mathrm{r}}}\,, \qquad\qquad \mu = \mu_0\,.$$

Blakemore (1987) [247] provides some interpolations of single oscillator models to give what is essentially a 2nd order Sellmeier equation form [248],

$$n(E)^2 = a + \frac{b_1}{1 - {c_1}^2\,E^2} + \frac{b_2}{1 - {c_2}^2\,E^2}\,,$$

with

	Low temp.	Room temp.
a	7.13	7.10
b_1	3.45	3.78
c_1	$0.418\,\mathrm{eV}^{-1}$	$0.424\,\mathrm{eV}^{-1}$
b_2	1.88	1.97
c_2	$29.6\,\mathrm{eV}^{-1}$	$30.08\,\mathrm{eV}^{-1}$

where $E = h\,f$ is the photon energy, valid for $0.04\,\mathrm{eV} < E < 1.4\,\mathrm{eV}$, and room temperature is $\sim 300\,\mathrm{K}$ and low temperature is $< 30\,\mathrm{K}$.

Skauli et. al. (2005) [249] offer two models, the first, a Pikhtin-Yas'kov form [250],

$$n(E)^2 = 1 + \frac{A}{\pi}\,\log\left[\frac{{E_1}^2 - E^2}{{E_0}^2 - E^2}\right] + \frac{\langle\varepsilon_2\rangle}{\pi}\,\log\left[\frac{{E_2}^2 - E^2}{{E_1}^2 - E^2}\right] + \frac{G_3}{{E_3}^2 - E^2}\ ,$$

with

E_0	$\left(1.425000 - 0.00037164\,(T - 295\,\mathrm{K}) - 7.497 \times 10^{-7}\,(T - 295\,\mathrm{K})^2\right)\mathrm{eV}$
E_1	$\left(2.400356 - 0.00051458\,(T - 295\,\mathrm{K})\right)\mathrm{eV}$
E_2	$\left(7.691979 - 0.00046545\,(T - 295\,\mathrm{K})\right)\mathrm{eV}$
E_3	$\left(0.034303 + 0.00001136\,(T - 295\,\mathrm{K})\right)\mathrm{eV}$
$\langle\varepsilon_2\rangle$	12.99386
G_3	$0.00218176\,\mathrm{eV}^2$
A	0.689578

where $E = h\,f$ is the photon energy, valid for $0.07\,\mathrm{eV} < E < 1.28\,\mathrm{eV}$, and T is temperature.

The second, a 3rd order Sellmeier form [248],

$$n(\lambda)^2 = g_0 + \frac{g_1}{{\lambda_1}^{-2} - \lambda^{-2}} + \frac{g_2}{{\lambda_2}^{-2} - \lambda^{-2}} + \frac{g_3}{{\lambda_3}^{-2} - \lambda^{-2}}\ ,$$

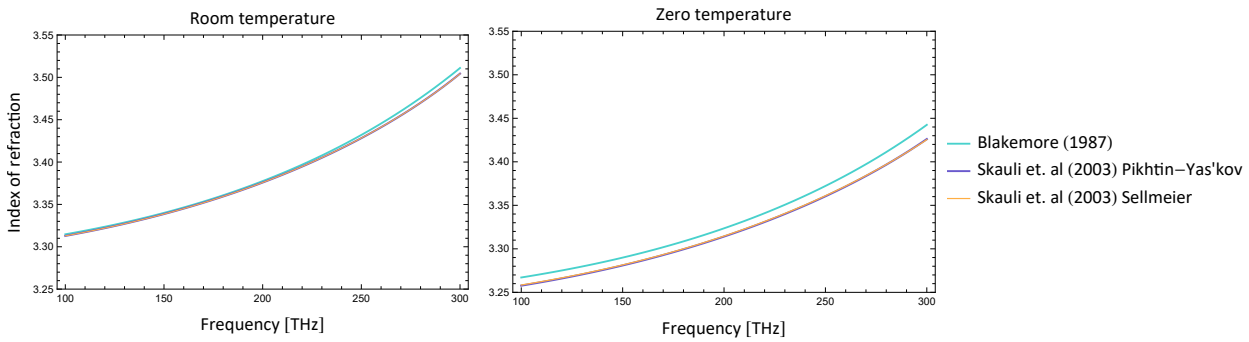

Figure M.2: Comparison of gallium arsenide index of refraction models from Blakemore [247] and Skauli et. al. [249].

with

λ_1	$\left(0.4431307 + 0.000050564\,(T - 295\,\mathrm{K})\right)\,\mu\mathrm{m}$
λ_2	$\left(0.8746453 + 0.0001913\,(T - 295\,\mathrm{K}) - 4.882 \times 10^{-7}\,(T - 295\,\mathrm{K})^2\right)\,\mu\mathrm{m}$
λ_3	$\left(36.9166 - 0.011622\,(T - 295\,\mathrm{K})\right)\,\mu\mathrm{m}$
g_0	5.372514
g_1	$27.83972\,\mu\mathrm{m}^{-2}$
g_2	$\left(0.031764 + 4.350 \times 10^{-7}\,(T - 295\,\mathrm{K}) + 4.664 \times 10^{-7}\,(T - 295\,\mathrm{K})^2\right)\,\mu\mathrm{m}^{-2}$
g_3	$0.00143636\,\mu\mathrm{m}^{-2}$

where $\lambda = c/f$ is the vaccum wavelength, valid for $0.97\,\mu\mathrm{m} < \lambda < 17\,\mu\mathrm{m}$, and T is temperature.

Comparisons of these different fits are given in Fig. M.2. Using the Skauili et. al. Pikhtin-

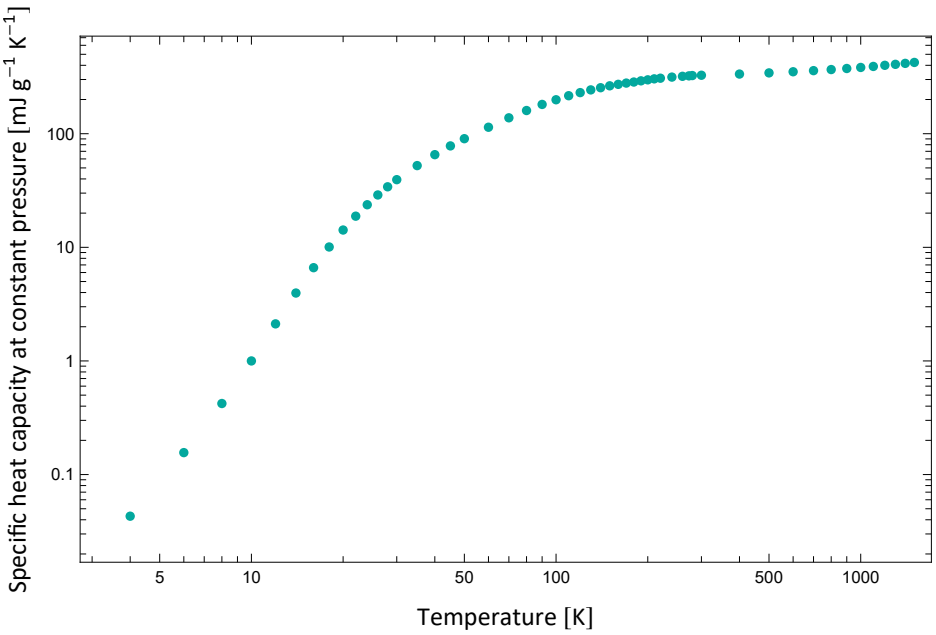

Figure M.3: Specific heat capacity at constant pressure of gallium arsenide. Compiled [238–240] from seprate low temperature data [252], mid temperature data [253], and high temperature data [251].

Yas'kov model we obtain the values below.

194 THz	Low temp.	Room temp.
n	3.310	3.371
ε_r	10.953	11.361

M.1.6 Thermal properties

Gallium arsenide melts at $\approx 1513\,\mathrm{K}$ [251].

The specific heat capacity is function of temperature; data from various experiments [251–

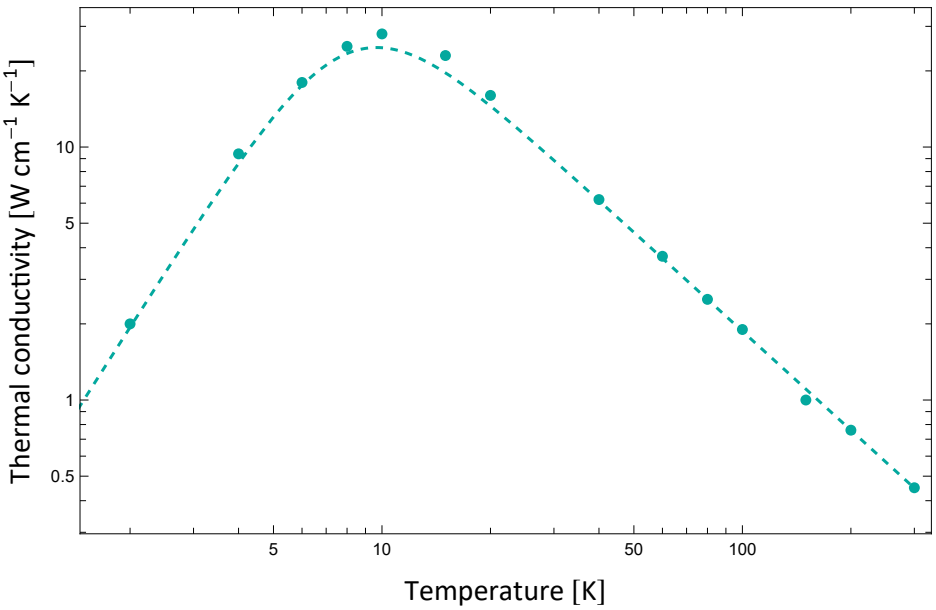

Figure M.4: Thermal conductance of gallium arsenide [254]. The dashed line is $\left(\left(0.41\,T^{2.25}\,\mathrm{W\,cm^{-1}\,K^{-3.25}}\right)^{-1} + \left(745\,T^{-1.3}\,\mathrm{W\,cm^{-1}\,K^{-0.3}}\right)^{-1}\right)^{-1}$.

253] has been compiled [238–240] and is given in Fig. M.3.

	Low temp.	Room temp.
c_P	0	$327\,\mathrm{J\,K^{-1}\,kg^{-1}}$

Thermal conductance is also strongly dependent on temperature. Some sample measurements taken up to room temperature by Holland [254] are shown in Fig. M.4 with the qualitative fit [240] below.

	Low temp.	Room temp.
κ	$41\,T^{2.25}\,\mathrm{W\,m^{-1}\,K^{-3.25}}$	$7.45\times10^{4}\;T^{-1.3}\,\mathrm{W\,m^{-1}\,K^{0.3}}$

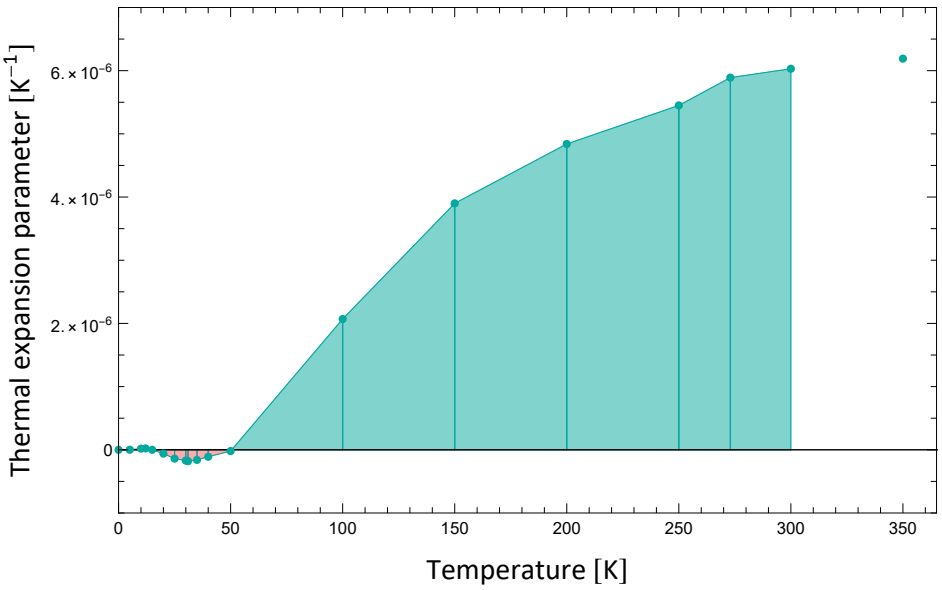

Figure M.5: Thermal expansion parameter of gallium arsenide [240, 255–258]. The shaded region depicts a trapezoidal integral used to estimate $\int_0^{300} \alpha \, \mathrm{d}T$.

The thermal expansion tensor for gallium arsenide has only one parameter,

$$\underline{\underline{\alpha}} = \begin{pmatrix} \alpha_{1\,1} & 0 & 0 \\ 0 & \alpha_{1\,1} & 0 \\ 0 & 0 & \alpha_{1\,1} \end{pmatrix} ,$$

which means for any length,

$$\frac{\mathrm{d}L}{\mathrm{d}T} = \alpha_{1\,1}\, L \quad \Rightarrow \quad \frac{L(T_2)}{L(T_1)} = \exp\left[\int_{T_1}^{T_2} \alpha_{1\,1}(T)\, \mathrm{d}T \right] .$$

Data summarized [240] from a number of experiments [255–258] is given in Fig. M.5. We can estimate the length ratios between room and low temperatures by employing a trapezoidal integral approximate, also depicted in Fig. M.5,

$$\frac{L_{\text{Room temp.}}}{L_{\text{Low temp.}}} \approx 1 + 9.65 \times 10^{-4} .$$

M.1.7 Symmetries

The stiffness, compliance, and photoelastic cubic tensors have $\pi/2$ rotation symmetry about each of the cardinal crystal axes [100], [010], [001], and mirror symmetry through each of the cardinal planes (100), (010), (001), and face diagonal planes (110), (101), (011). That is[1]

$$S^i_{\ a}\, S^j_{\ b}\, S^k_{\ c}\, S^l_{\ d}\, x^{a\,b\,c\,d} = x^{i\,j\,k\,l} \quad : \quad \left\{ \begin{array}{ll} x \in & \{c, s, p\} \\ S \in & \left\{ \begin{array}{lll} R_{[100]}[\pi/2], & R_{[010]}[\pi/2], & R_{[001]}[\pi/2], \\ P\big[[100]\big], & P\big[[010]\big], & P\big[[001]\big], \\ P\big[[110]\big], & P\big[[101]\big], & P\big[[011]\big] \end{array} \right\} \end{array} \right. .$$

Contrarily, the piezoelectric and electro-optic tensors have $\pi/2$ rotation antisymmetry about each of the cardinal crystal axes, and mirror antisymmetry through each of the cardinal

1. R is a rotation matrix and P is a Householder reflection matrix.

planes, but mirror symmetry through the cubic face diagonal planes,

$$S^i_{\ a}\, S^j_{\ b}\, S^k_{\ c}\, x^{a\,b\,c} = -\, x^{i\,j\,k} \quad : \quad \begin{cases} x \in \{e, d, r\} \\ \\ S \in \left\{ \begin{matrix} R_{[100]}[\pi/2], & R_{[010]}[\pi/2], & R_{[001]}[\pi/2], \\ P\Big[[100]\Big], & P\Big[[010]\Big], & P\Big[[001]\Big] \end{matrix} \right\} \end{cases} ,$$

$$S^i_{\ a}\, S^j_{\ b}\, S^k_{\ c}\, x^{a\,b\,c} = x^{i\,j\,k} \quad : \quad \begin{cases} x \in \{e, d, r\} \\ \\ S \in \Big\{ P\big[[011]\big], P\big[[101]\big], P\big[[110]\big] \Big\} \end{cases} .$$

M.2 Silicon (Si)

Isotropic silicon was used for some simulations, material properties (using Young's modulus and Poisson ratio) are given here.

ρ	$2329\,\mathrm{kg\,m^{-3}}$
E	$170\,\mathrm{GPa}$
ν	0.28
μ_r	1
ε_r	11.7

A better estimate of the silicon index of refraction at infra-red frequencies can be obtained from Edwards and Ochoa [259].

APPENDIX N

Proximity effect correction

Electron beam lithography is a fantastic modern tool for creating nanometer scale masks for device fabrication. The basic principle is to layer a charge sensitive resist over the sample, then shoot it with electrons (with a much smaller spot size than light) at resolutions and control (thanks to magnet steering) down to one nanometer. A chemical developer is then applied that removes (or retains) portions of the resist that have been hit by electrons, leaving behind a mask that can be used as a stencil for further fabrication. Ideally only the intended targets are hit by electrons, but scattering within the resist and back-scatter from the substrate lead to broader regions getting exposed. To counteract this, the pattern and dosages can be modified using proximity effect correction (PEC).

N.1 Point spread function

Applying a proximity effect correction is done through knowledge of the point spread function which describes the area spread in energy from an incident electron. For a single incident electron this is

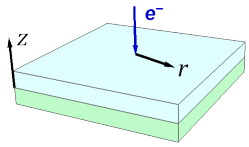

$$\underset{\substack{\text{energy density}\\ \text{per electron}\\ [\mathrm{J\,m^{-3}}]}}{\mathfrak{e}(r,z)} = \underset{\substack{\text{vertical absorption}\\ \text{per electron}\\ [\mathrm{J\,m^{-1}}]}}{\mathfrak{A}(z)} \times \underset{\substack{\text{point spread function}\\ [\mathrm{m^{-2}}]}}{\mathrm{PSF}(r,z)} \quad ,$$

where the point spread function is normalized across any horizontal plane

$$\iint\limits_{\vec{r}\,\in\,\mathbb{R}^2} \mathrm{PSF}(|\vec{r}|, z)\,\mathrm{d}\vec{r}^{\,2} = 1\ ,$$

but can vary for different heights in the resist. For many electrons incident at different locations $\vec{r}\,'$, we have

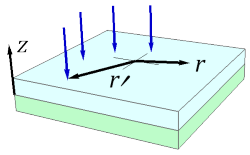

$$\underset{\substack{\text{total energy density}\\ [\mathrm{J\,m^{-3}}]}}{\mathfrak{E}(r,z)} = \iint\limits_{\vec{r}\,'\,\in\,\mathbb{R}^2} \underset{\substack{\text{energy density}\\ \text{per electron}\\ [\mathrm{J\,m^{-3}}]}}{\mathfrak{e}(|\vec{r}-\vec{r}\,'|,z)} \times \underset{\substack{\text{electron density}\\ [\mathrm{m^{-2}}]}}{\mathfrak{n}_{\mathrm{e}^-}(\vec{r}\,')}\ \mathrm{d}\vec{r}\,'^{\,2}\ ,$$

which is related to the injected dose by

$$\underset{\substack{\text{electron density}\\ [\mathrm{m^{-2}}]}}{\mathfrak{n}_{\mathrm{e}^-}(\vec{r}\,')} = \underset{\substack{\text{injected dose}\\ [\mathrm{C\,m^{-2}}]}}{\mathfrak{d}(\vec{r}\,')} \Big/ \underset{\substack{\text{electron charge}\\ [\mathrm{C}]}}{\mathrm{e}}\ .$$

The injected dose $\mathfrak{d}(\vec{r})$, which includes all pattern information, is the instructions given to an electron beam writer.

If the injected dose happens to be uniform everywhere, we get

$$\mathfrak{d}(\vec{r}) = \mathfrak{d} \quad \Rightarrow \quad \mathfrak{E}(\vec{r},z) = \mathfrak{A}(z)\,\frac{\mathfrak{d}}{\mathrm{e}}\ ,$$

i.e. the total energy density is uniform in the horizontal plane and only depends on some vertical absorption, or if electron beam was perfectly point like[1],

$$\mathrm{PSF}(\vec{r},z) = \frac{\delta(r)}{\pi\,r} \quad \Rightarrow \quad \mathfrak{E}(\vec{r},z) = \mathfrak{A}(z)\,\frac{\mathfrak{d}(\vec{r}\,')}{\mathrm{e}}\ .$$

1. $\delta(x)\,\delta(y) = \delta(r)/(\pi\,r)$

In order to do proximity effect correction, we need to assume a vertically constant (or averaged) point spread function $\mathrm{PSF}(\vec{r})$, then

$$\mathfrak{d}_{\mathrm{goal}}(\vec{r}) = \iint\limits_{\vec{r}\,' \in \mathbb{R}^2} \mathrm{PSF}(\vec{r} - \vec{r}\,')\, \mathfrak{d}(\vec{r}\,')\, \mathrm{d}\vec{r}\,'^{\,2} \ .$$

Thus given the goal pattern and dose $\mathfrak{d}_{\mathrm{goal}}$, and point spread function PSF, the above equation can be numerically deconvolved to find the required injection dose $\mathfrak{d}$. Specialized electron beam lithography software [201] can carry out this computation.

N.2 Modelling

The point spread function depends heavily on the incident electron energy and substrate-resist stack - different materials and heights will scatter the electrons differently. Determining the point spread function can be done computationally by particle tracing simulations [197, 198, 200], or using functional models with parameters specific to the situation.

Models of the point spread function are generally constructed from a sum of individually normalized distributions,

$$\mathrm{PSF}(r) = \frac{\sum_i \eta_i\, f_i(r)}{\sum_i \eta_i} \quad : \quad \forall i \quad \iint\limits_{\vec{r} \in \mathbb{R}^2} f_i\big(|\vec{r}|\big)\, \mathrm{d}\vec{r}^{\,2} = 1 \ ,$$

noting that there is one redundant parameter within the set of $\{\eta_i\}_{i=1}^{n}$. Each term corresponds to a different physical process happening within the substrate-resist stack.

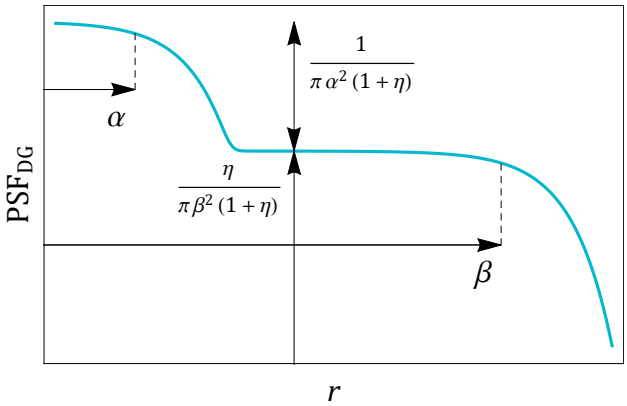

Figure N.1: Log-log plot of the double Gaussian point spread function model. The first, large peak is from primary electrons, the second, lower, wider peak is from back-scattered secondary electrons.

N.2.1 Gaussian

The most basic, and common, model is the double Gaussian shown in Fig. N.1,

$$\mathrm{PSF_{DG}}[\alpha,\beta,\eta;r] = \frac{f_{\mathrm{G}}[\alpha;r] + \eta\, f_{\mathrm{G}}[\beta;r]}{1+\eta}\ ,$$

constructed from two Gaussian terms,

$$f_{\mathrm{G}}[\sigma;r] = \frac{1}{\pi\,\sigma^2}\,\exp\!\big[-r^2/\sigma^2\big]\ .$$

Here α is the forward (primary) beam radius, β is the backward scattered (secondary) beam radius, and η is the scattering fraction.

N.2.2 Gamma

Some resist stacks can be modeled using a Gamma distribution term [260],

$$f_{\Gamma}[\theta,\kappa;r] = \frac{1}{2\,\pi\,\theta^{\kappa+1}\,\Gamma[\kappa+1]}\,\exp\!\big[-r/\theta\big]\,r^{\kappa-1} \quad : \quad \theta > 0\ .$$

N.2.3 Cauchy-Lorentz

For a distribution with slower decay we could turn to the Cauchy-Lorentz distribution, but as a function of radius it is not integrable over $\mathbb{R}^2$ and needs to be modified.

N.2.4 Pearson VII / Student's t

Modifying the power law in the Cauchy-Lorentz distribution we end up with a type of Pearson VII or student's t distribution, in particular,

$$\text{PearsonVII}\left[\mu, \gamma, \nu\right] \sim \text{StudentT}\left[\mu, \frac{\gamma}{\sqrt{2\,\nu - 1}}, 2\,\nu - 1\right] \overset{\nu=1}{\sim} \text{Cauchy}\left[\mu, \gamma\right] \ .$$

For $\mu = 0$, $\nu > 1$, and normalizing over $\mathbb{R}^2$, the Pearson VII point spread term is

$$f_{\text{P}_{\text{VII}}}[\gamma, \nu; r] = \frac{\nu - 1}{\pi\,\gamma^2}\left(\frac{r^2}{\gamma^2} + 1\right)^{-\nu} \quad : \quad \nu > 1 \ .$$

The parameterization $\gamma = \sigma\sqrt{2\,\nu - 3}$ for $\nu > 3/2$ is sometimes used with the Pearson VII distribution.

N.2.5 Voigt

Convolving the Cauchy-Lorentz distribution with the Gaussian distribution yields the Voigt distribution, however the distribution function is complicated and computationally difficult making it not practical for modeling purposes.

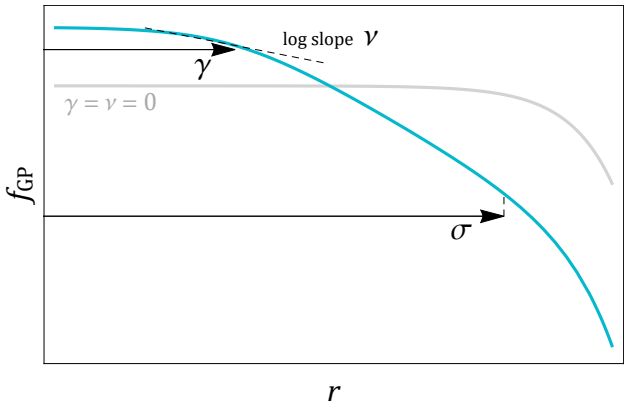

Figure N.2: Log-log plot of the Gaussian Pearson VII product point spread term.

N.2.6 Gaussian Pearson VII product

With convolution impractical, we can implement a Gaussian end to the Pearson VII term by using a product [261],

$$f_{\mathrm{GP}}[\sigma,\gamma,\nu;r] = \frac{\exp\left[-\gamma^2/\sigma^2\right]}{\pi\,\gamma^2\,\mathrm{E}_\nu\left[\gamma^2/\sigma^2\right]}\,\exp\left[-r^2/\sigma^2\right]\left(\frac{r^2}{\gamma^2}+1\right)^{-\nu}\,,$$

where E is the exponential integral function. Here $\gamma > 0$ is the onset radius for a power law (Pearson) drop off with slope determined by ν, and $\sigma > \gamma$ is the onset radius for exponential (Gaussian) drop off, as plotted in Fig N.2 . In the special case of $\gamma = \nu = 0$ it reduces to a Gaussian term, $f_{\mathrm{GP}}[\sigma,0,0;r] = f_{\mathrm{G}}[\sigma;r]$.

N.3 Fits to simulation

The effectiveness of the Gaussian Pearson VII product model is demonstrated in fits to simulated point spread functions for HSQ on GaAs stack shown in Fig N.3. For GaAs substrates, there is little dependence on the resist material or total resist thickness.

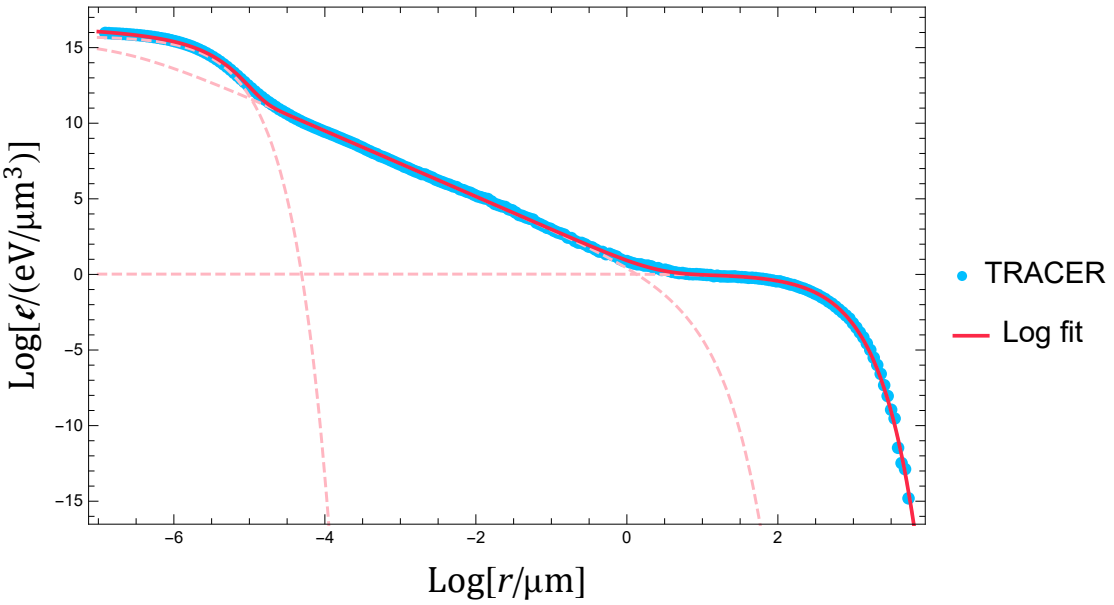

Figure N.3: TRACER [197] simulation of 100 kV electrons incident on 300 nm HSQ on GaAs, taken at a height of $z = 135$ nm. The fit, made using logarithmic data, uses a model with two purely Gaussian terms and one Gaussian Pearson VII product term, shown individually in dashed lighter colour.

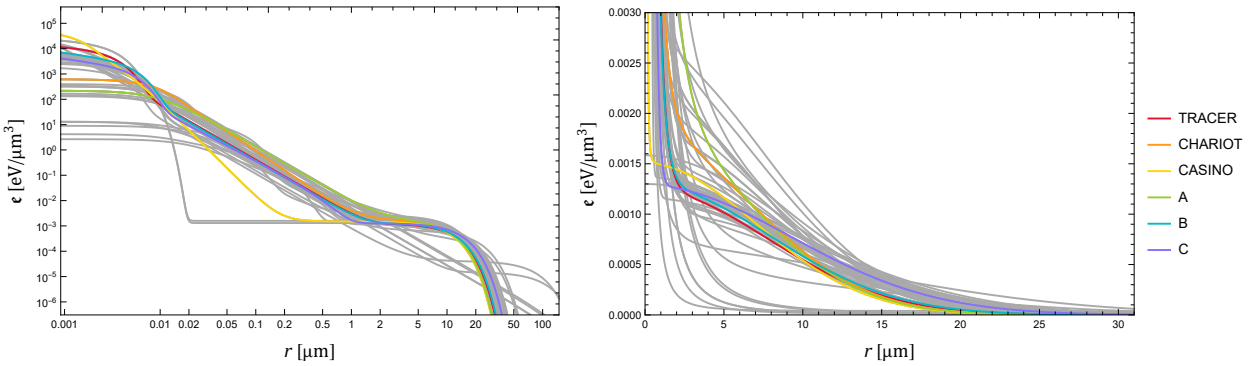

Figure N.4: Over fifty different point spread functions that were trialled with notable ones in colour, plotted (left) log-log and (right) linearly.

N.4 Utilized point spread functions

Many different point spread functions were tested and used during fabrication. Fig. N.4 highlights some point spread functions from simulations and custom built that were used for measured devices. Analysis of the various PECs were carried out according to the methods described in App. P.

The parameters for the highlighted PSFs are

■ TRACER [197] (fit):
$$0.221572\, f_{\mathrm{GP}}[1.588\,\mu\mathrm{m}, 0.001211\,\mu\mathrm{m}, 1.08659; r] + 0.304839\, f_{\mathrm{G}}[0.0033946\,\mu\mathrm{m}; r] + 0.473589\, f_{\mathrm{G}}[10.987\,\mu\mathrm{m}; r]\ ,$$

■ CHARIOT [200] (fit):
$$0.384615\, f_{\mathrm{GP}}[10\,\mu\mathrm{m}, 0.01\,\mu\mathrm{m}, 1.3; r] + 0.076923\, f_{\mathrm{G}}[0.01\,\mu\mathrm{m}; r] + 0.538462\, f_{\mathrm{G}}[10\,\mu\mathrm{m}; r]\ ,$$

■ CASINO [198] (fit):
$$0.331697\, f_{\mathrm{GP}}[9.8935\,\mu\mathrm{m}, 0.0025934\,\mu\mathrm{m}, 1.8917; r] + 0.205752\, f_{\mathrm{G}}[0.0013233\,\mu\mathrm{m}; r] + 0.462551\, f_{\mathrm{G}}[9.8935\,\mu\mathrm{m}; r]\ ,$$

■ A:
$$0.5\, f_{\mathrm{GP}}[10\,\mu\mathrm{m}, 0.01\,\mu\mathrm{m}, 1.1; r] + 0.5\, f_{\mathrm{G}}[10\,\mu\mathrm{m}; r]\ , \tag{N.1}$$

■ B:
$$0.204082\, f_{\mathrm{GP}}[1.6\,\mu\mathrm{m}, 0.0012\,\mu\mathrm{m}, 1.09; r] + 0.285714\, f_{\mathrm{G}}[0.005\,\mu\mathrm{m}; r] + 0.510204\, f_{\mathrm{G}}[11.2\,\mu\mathrm{m}; r]\ , \tag{N.2}$$

■ C:
$$0.143885\, f_{\mathrm{GP}}[0.685\,\mu\mathrm{m}, 0.001\,\mu\mathrm{m}, 1; r] + 0.172662\, f_{\mathrm{G}}[0.005\,\mu\mathrm{m}; r] + 0.683453\, f_{\mathrm{G}}[13\,\mu\mathrm{m}; r]\ . \tag{N.3}$$

The short range cut off is an important parameter in the PSF implementation, effectively setting shortest scales and domain of the PSF to use. The cut off should be sufficiently small to capture to variation in proximity effects, but not so small that applying the PEC becomes computationally expensive or excessive fracturing of the pattern occurs. Typical values that produced decent results were 0.05 µm to 0.1 µm. The interplay between base dose, point spread function, and short range cut off is complicated and required extensive iterations of each.

APPENDIX O

Patterning

A large library of python scripts were written to create device design files for use with the in-house package 'Playout' that generates DXF files from given polygon coordinates.

O.1 Manual dose scaling

In addition to the proximity effect correction for large scale patterns (see App. N), for the snowflake crystal pattern, manual dose scalings were made to provide sharper snowflake corners. Fig. O.1 depicts the snowflake polygon used for electron beam lithography with regions of varying dose.

The sizes and dose scales for the corners were varied haphazardly through fabrication runs. A sample set of measurements for the inner corner are shown in Fig. O.2. Final parameters used were $c_i = 18\,\text{nm}$ with dose scaling = 4, and $c_o = 15\,\text{nm}$ with dose scaling = 0.6.

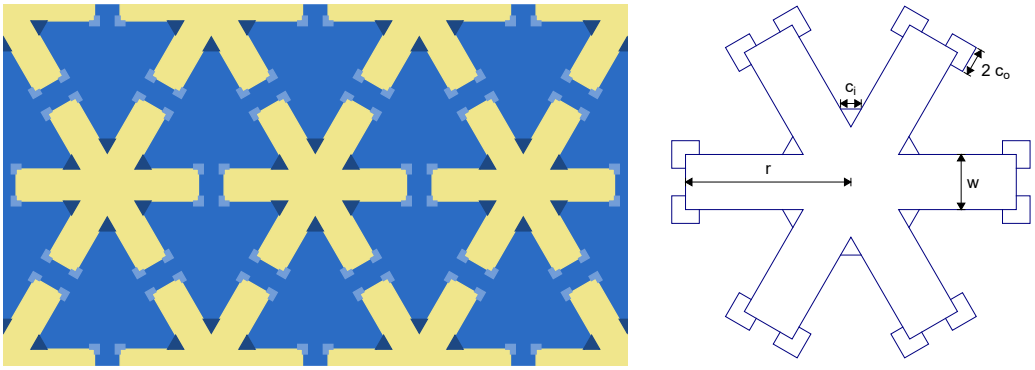

Figure O.1: Snowflake geometry used for patterning with inner corner regions dosed heavier, and outer corner regions dosed lighter.

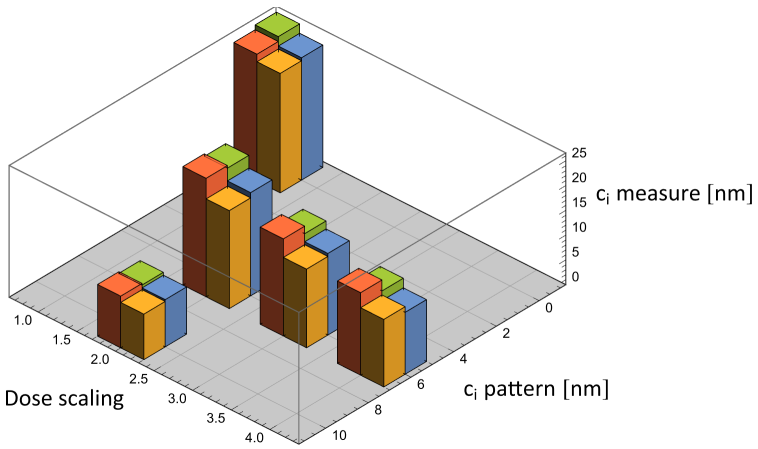

Figure O.2: Some measurements of the snowflake inner corner radius with different overdosings for various etch recipe sets (coloured).

O.2 Pattern building blocks

Because HSQ is a negative resist, we want to write the non-snowflake areas. Thus the basic building blocks are triangle 'drumheads' and rectangular bridges. For the corner dose scaling, additional (overlapping) triangle and square polygons are created to define the corner regions.

Snowflake crystal areas are created by tiling over rhomboids or with a set of snowflake crystal coordinates. In the case of coordinates, a large logic matrix is used with neighbouring element lookups to determine how to build at each crystal lattice site. Dimensional parameters can be varied by specifying functions over the space, and bridges automatically sized based on the connecting triangles.

O.3 BEAMER

The program BEAMER [201] is used with DXF layouts to produce GPF files for the electron beam, a typical procedure flowchart is shown in Fig. O.3. Corner regions are separated from

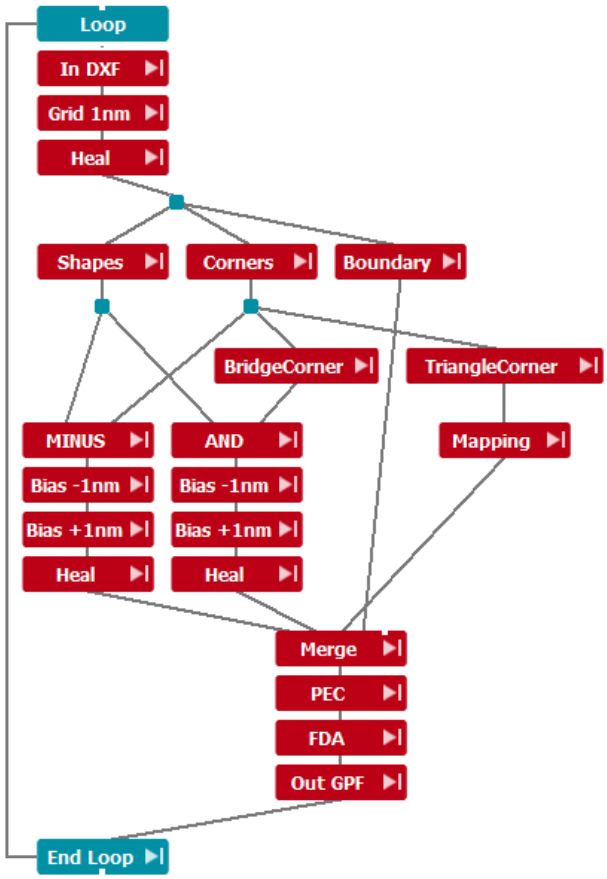

Figure O.3: Screenshot of BEAMER procedure.

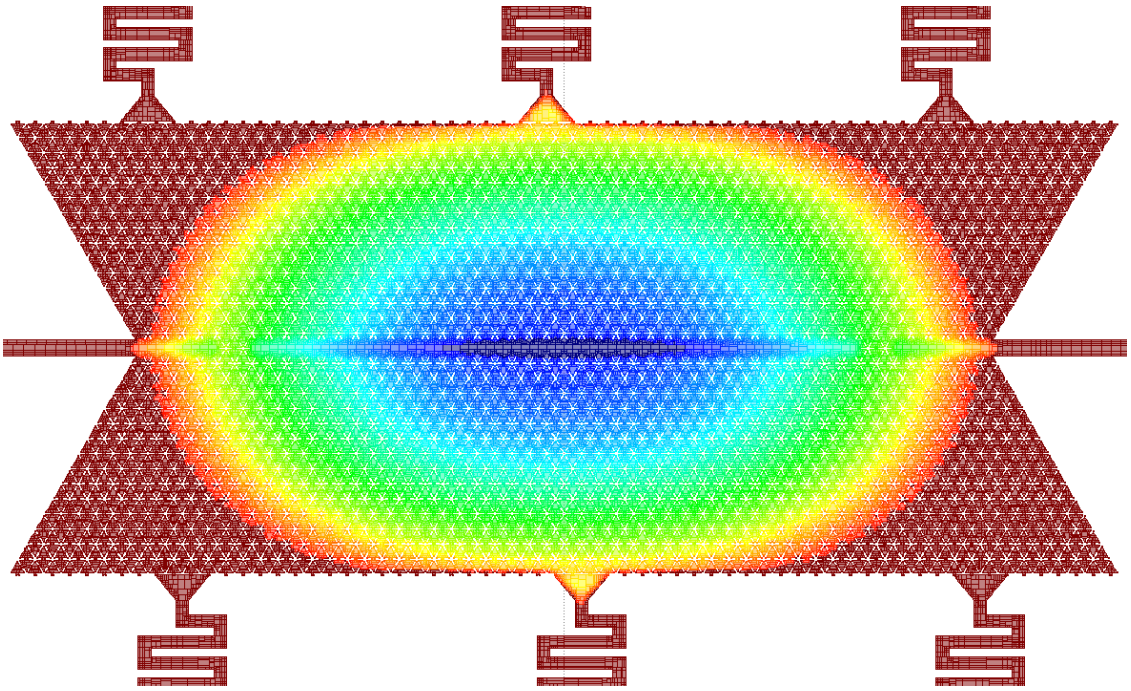

Figure O.4: Example screenshot of BEAMER fracturing and proximity effect correction for point spread function (N.3) with 0.1 µm short range cut-off. Scaling of 1 or below in blue and 1.5 or above in red.

the main shape regions to allow for appropriate scaling in the feature dose assignment (FDA) step. To avoid aliasing issues after polygon subtractions, shapes are biased down and then back up by a grid step (1 nm). Proximity effect correction (PEC) is carried out using a custom function (see App. N) that has been numericized into a table.

APPENDIX P

Snowflake shape analysis

An important part of fabrication development is the physical characterization of produced features. In particular we are concerned with the snowflake shaped holes that need to be precisely engineered to create a desired optomechanical crystal.

P.1 Snowflake parameters

The snowflake holes can be described with four parameters,

- r snowflake arm radius,
- w snowflake arm width,
- c_i inner radius of curvature,
- c_o outer radius of curvature,

which are depicted in Fig. P.1.

P.2 Boundary acquisition

Once fabricated, a scanning electron microscope (SEM) can be used to take a picture of the snowflake holes at high resolution. Edge detection image processing is used to provide points marking a boundary in the image, and then sets which form closed loops are taken to be the individual shape objects. The result is a set of points in $\mathbb{R}^2$ with a metric taken from the

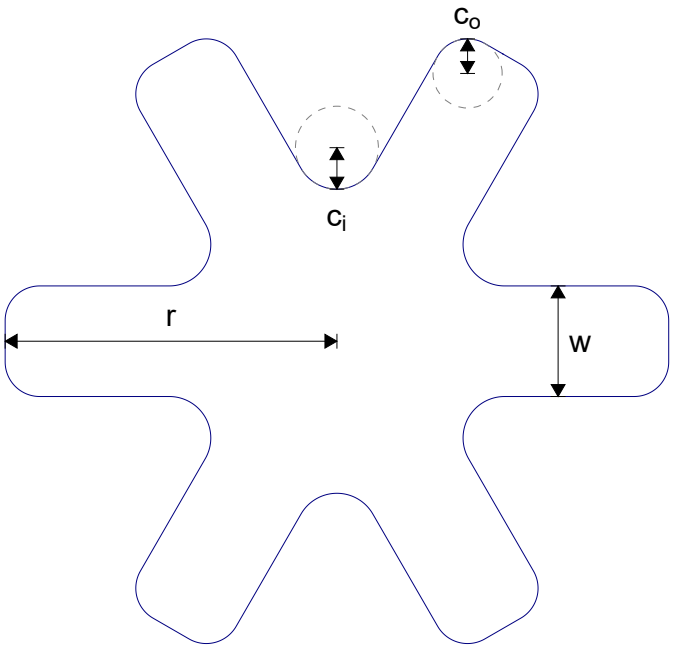

Figure P.1: Snowflake hole parameterization.

SEM picture scale.

$$\underset{\substack{\text{snowflake}\\ \text{boundary}}}{B} \quad \subset \quad \mathbb{R}^2$$

An example of such edge detection is given in Fig. P.2.

P.3 Alignment and functional fit method

To extract meaningful parameters, we need to fit the boundary of the snowflake to some function. To do this we use the snowflake's symmetry to fold the boundary into a domain such that the vertical coordinate (henceforth y) is a single-valued function of the horizontal coordinate (henceforth x). We define a canonical orientation with the origin at the center at the arms at polar angles $\{0, \pi/3, 2\,\pi/3, \pi, 4\,\pi/3, 5\,\pi/3\}$.

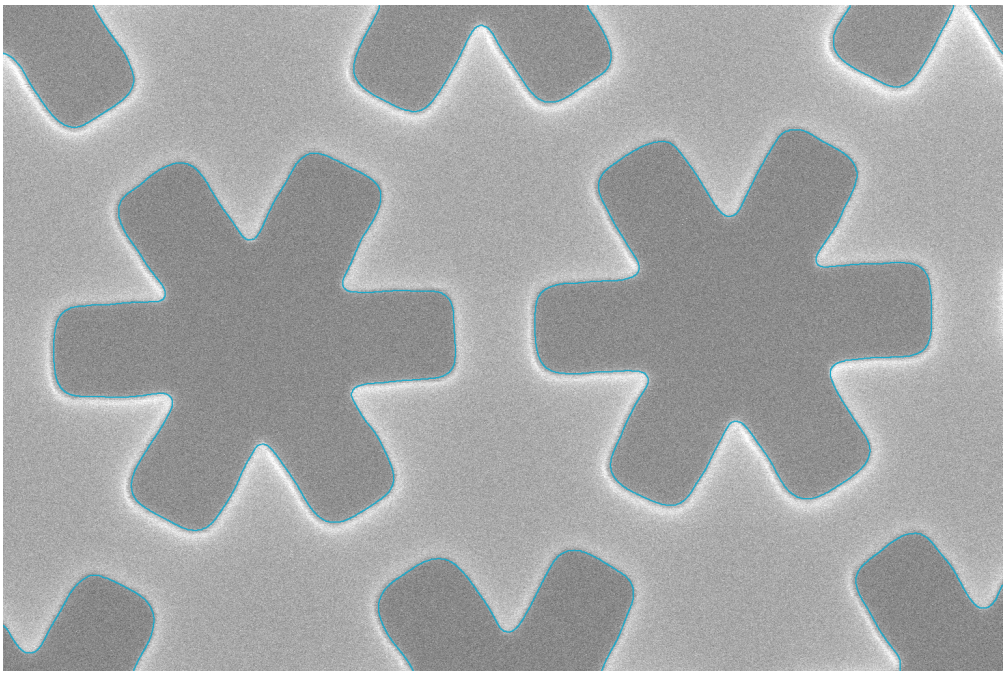

Figure P.2: SEM image of snowflakes and edge detection output.

P.3.1 Translation

Assuming our fabricated snowflake is sufficiently symmetric, the center can be found by taking the average of all the boundary points. The snowflake can then be shifted to an origin centric frame,

$$B \rightarrow B_{\text{shifted}}$$

$$\vec{p} \mapsto \vec{p} - \frac{1}{|B|} \sum_{\vec{q} \in B} \vec{q}\,.$$

P.3.2 Rotation

To properly rotate our snowflake boundary into the canonical orientation we first need to identify the locations of the snowflake arms. The snowflake shape has $\pi/3$ rotational sym-

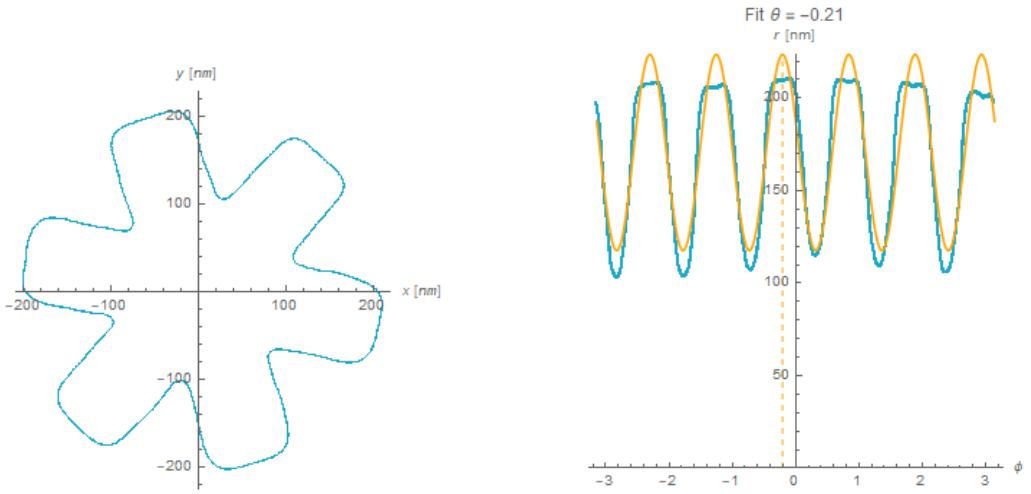

Figure P.3: (Left) shifted snowflake boundary. (Right) cosine fit to the polar snowflake boundary.

metry, which transformed into polar coordinates has a periodicity of 6, and can be crudely fit with a 6th order Fourier mode. Because our canonical orientation has an arm at $\phi = 0$, we'll use a cosine term with phase θ that tells us how much we need to rotate,

$$r(\phi) = a\,\cos\big[6\,(\phi - \theta)\big] + b\,. \tag{P.1}$$

We can estimate a and b with standard Fourier decomposition techniques (using simple discrete integration), and θ (the angle of one of the arms) by the global maximum,

$$a \approx \frac{1}{\pi}\sum_{i=1}^{|B|} r_i\,\cos\left[6\,\phi_i\right]\,(\phi_i - \phi_{i-1})\;,$$

$$b \approx \frac{1}{2\,\pi}\sum_{i=1}^{|B|} r_i\,(\phi_i - \phi_{i-1})\;,$$

$$\theta \approx \phi_j\;:\; r_j = \max\left[\{r_i\}_{i=1}^{|B|}\right]\;.$$

Completing the fit (P.1) with these starting estimates, as shown in Fig. P.3, we obtain the rotation away from canonical θ. Reversing this rotation to orient our snowflake,

$$B_{\text{shifted}} \;\rightarrow\; B_{\text{rotated}}$$

$$\vec{p} \;\mapsto\; \begin{pmatrix} \cos[-\theta] & -\sin[-\theta] \\ \sin[-\theta] & \cos[-\theta] \end{pmatrix} \cdot \vec{p}$$

P.3.3 Sector fit

Using the snowflake's $\pi/3$ rotational symmetry and mirror symmetry, there are 12 identical sectors which can each be mapped into $\phi \in [\pi/3, \pi/2]$ for a single-valued function $y = f(x)$. The function giving the snowflake boundary in this region is

$$f[x] = \begin{cases} -\sqrt{\mathsf{c_i}^2 - x^2} + \mathsf{w} + 2\,\mathsf{c_i} & : \quad 0 < x < \frac{\sqrt{3}\,\mathsf{c_i}}{2} \\ \sqrt{3}\,x + \mathsf{w} & : \quad \frac{\sqrt{3}\,\mathsf{c_i}}{2} < x < \frac{\mathsf{r}}{2} - \frac{\sqrt{3}\,\mathsf{w}}{4} - \frac{\mathsf{c_o}}{2} \\ \sqrt{\mathsf{c_o}^2 - \left(x - \frac{\mathsf{r}}{2} + \frac{\sqrt{3}\,\mathsf{w}}{4} - \frac{\sqrt{3}-1}{2}\,\mathsf{c_o}\right)^2} + & \\ \quad + \frac{\sqrt{3}\,\mathsf{r}}{2} + \frac{\mathsf{w}}{4} - \frac{\sqrt{3}-1}{2}\,\mathsf{c_o} & : \quad \frac{\mathsf{r}}{2} - \frac{\sqrt{3}\,\mathsf{w}}{4} - \frac{\mathsf{c_o}}{2} < x < \frac{\mathsf{r}}{2} - \frac{\sqrt{3}\,\mathsf{w}}{4} + \frac{\sqrt{3}\,\mathsf{c_o}}{2} \\ -\frac{x}{\sqrt{3}} + \frac{2\,\mathsf{r}}{\sqrt{3}} & : \quad \frac{\mathsf{r}}{2} - \frac{\sqrt{3}\,\mathsf{w}}{4} + \frac{\sqrt{3}\,\mathsf{c_o}}{2} < x < \frac{r}{2}\ . \end{cases}$$

The 12 sectors can be fit together as in Fig. P.4, or separately if investigating the distribution of snowflake parameters (even within a single snowflake).

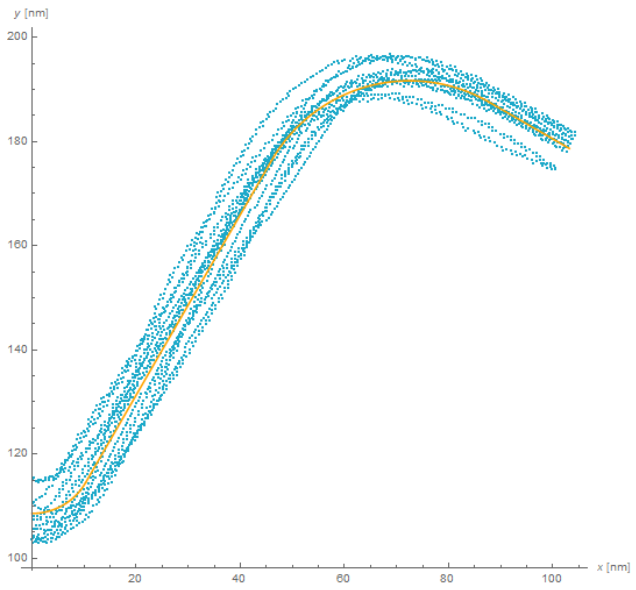

Figure P.4: Folded snowflake boundary and fit result $\mathsf{r} = 206.33$, $\mathsf{w} = 96.72$, $\mathsf{c_i} = 11.88$, $\mathsf{c_o} = 30.56$.

P.4 Polar fit method

Instead of performing a rotation and folding the snowflake boundary into a functional domain, it is possible to directly fit the snowflake boundary in polar coordinates. From the Cartesian boundary function $y(x)$ we can obtain the polar function $r(\phi)$ as follows. Firstly

$$\tan[\phi] = \frac{y(x)}{x} = g(x) \quad \Rightarrow \quad x = g^{-1}\big(\tan[\phi]\big) \ ,$$

then

$$x = r\,\cos[\phi] \quad \Rightarrow \quad r = \frac{x}{\cos[\phi]} \ ,$$

giving us

$$r(\phi) = \frac{g^{-1}\big(\tan[\phi]\big)}{\cos[\phi]} \ .$$

Applying this to the Cartesian function from before, for $\phi \in [\pi/3, \pi/2]$,

$$f_0[\phi] = \begin{cases} \sin[\phi]\,(2\,\mathsf{c_i} + \mathsf{w}) - \cos[\phi]\sqrt{\mathsf{c_i}^2\,\tan[\phi]^2 - 3\,\mathsf{c_i}^2 - 4\,\mathsf{c_i}\,\mathsf{w} - \mathsf{w}^2} \\ \qquad : \quad \arctan\left[\frac{3\,\mathsf{c_i}+2\,\mathsf{w}}{\sqrt{3}\,\mathsf{c_i}}\right] < \phi < \pi/2 \\ \\ \frac{-\mathsf{w}}{\sqrt{3}}\,\csc[\phi] \quad : \quad \arctan\left[\frac{2\sqrt{3}\,\mathsf{c_o}-2\sqrt{3}\,\mathsf{r}-\mathsf{w}}{2\,\mathsf{c_o}-2\,\mathsf{r}+\sqrt{3}\,\mathsf{w}}\right] < \phi < \arctan\left[\frac{3\,\mathsf{c_i}+2\,\mathsf{w}}{\sqrt{3}\,\mathsf{c_i}}\right] \\ \\ \frac{\cos[\phi]}{4}\Bigg(2\,\mathsf{r} - \sqrt{3}\,\mathsf{w} - 2(1-\sqrt{3})\,\mathsf{c_o} + (2\sqrt{3}\,\mathsf{r} + \mathsf{w} - 2(1+\sqrt{3})\,\mathsf{c_o})\,\tan[\phi] \\ \quad + \frac{1}{2}\Big(-16\left(4\,\mathsf{r}^2 + (\mathsf{w} - 2\,\mathsf{c_o})^2 - 8\,\mathsf{r}\,\mathsf{c_o}\right)\sec[\phi]^2 \\ \quad + \big(-4\,\mathsf{r} + 2\sqrt{3}\,\mathsf{w} + 4\,(1-\sqrt{3})\,\mathsf{c_o} - (4\sqrt{3}\,\mathsf{r} + 2\,\mathsf{w} - 4\,(1+\sqrt{3})\,\mathsf{c_o})\,\tan[\phi]\big)^2\Big)^{1/2}\Bigg) \\ \qquad : \quad \arctan\left[\frac{-2\,\mathsf{c_o}+2\sqrt{3}\,r+\mathsf{w}}{2\sqrt{3}\,\mathsf{c_o}+2\,\mathsf{r}-\sqrt{3}\,\mathsf{w}}\right] < \phi < \arctan\left[\frac{2\sqrt{3}\,\mathsf{c_o}-2\sqrt{3}\,\mathsf{r}-\mathsf{w}}{2\,\mathsf{c_o}-2\,\mathsf{r}+\sqrt{3}\,\mathsf{w}}\right] \\ \\ \frac{2\sqrt{3}\,\mathsf{r}\,\sec[\phi]}{\sqrt{3}+3\,\tan[\phi]} \quad : \quad \pi/3 < \phi < \arctan\left[\frac{-2\,\mathsf{c_o}+2\sqrt{3}\,\mathsf{r}+\mathsf{w}}{2\sqrt{3}\,\mathsf{c_o}+2\,\mathsf{r}-\sqrt{3}\,\mathsf{w}}\right]. \end{cases}$$

The fit function, is then

$$f[\phi] = f_0[\phi - \theta]\,,$$

however the complicated form of this function means this method takes longer than the rotation and Cartesian fit of the previous section.

P.5 Statistics

Each fit produces a set of parameter values and covariance matrix constituting a single measurement. Taking these to be multinormal distributions, the underlying multinormal distribution of snowflake parameters can be estimated using the methods described in Sec. Φ.4.

P.6 Snowflake fields

In order to analyze electron beam proximity effects we can measure large regions of snowflakes and map out fit results as a function of position. To do this, high resolution SEM images are taken and each edge detected closed curve forming a snowflake is fit independently. Polygon masks are made for each image to filter out not snowflake shapes that appear. An example snowflake field is shown in Fig. P.5 along with fit results as a function of position.

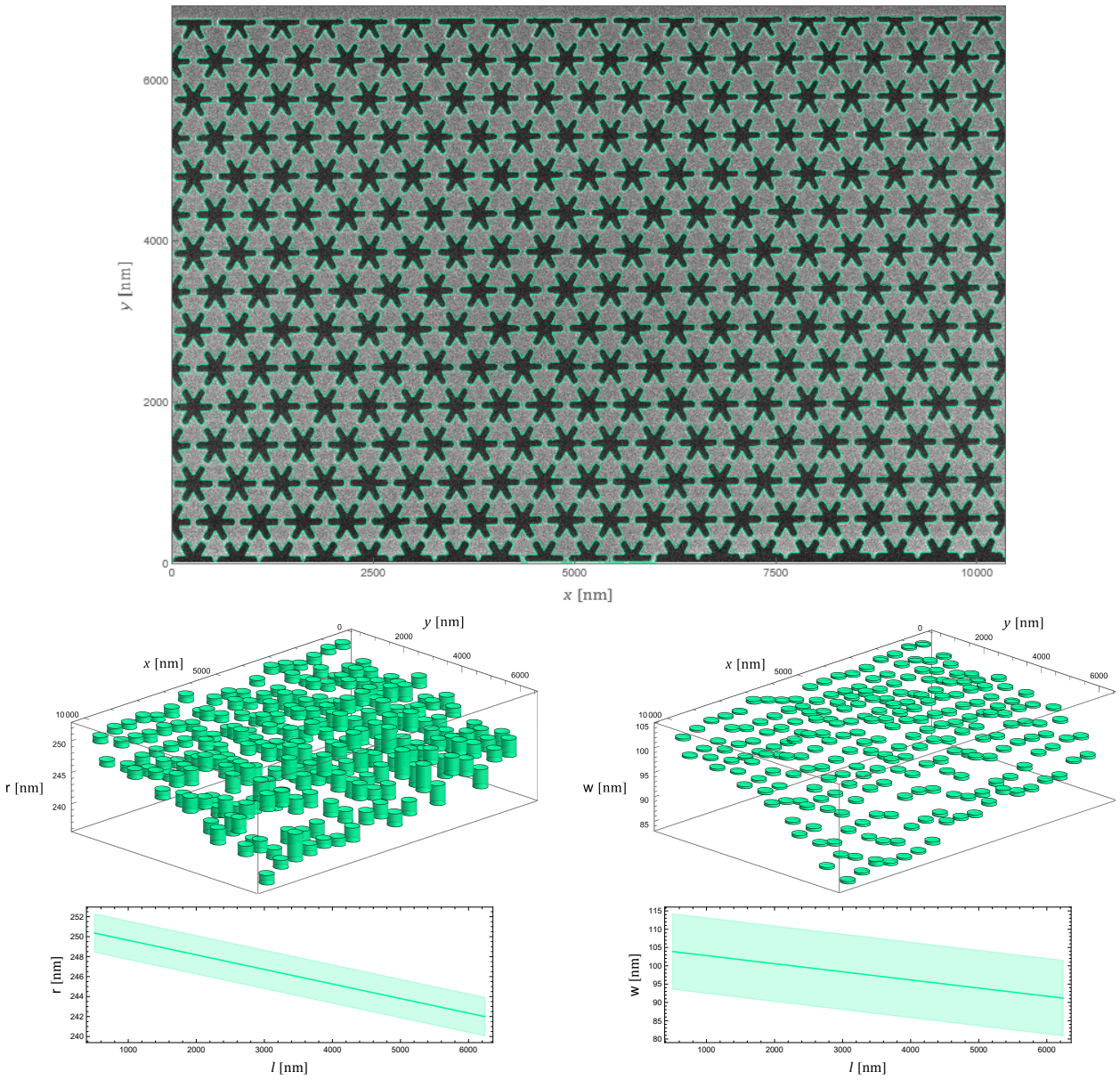

Figure P.5: (Top) SEM image of snowflake holes with edge detected pixels highlighted. (Middle) fit results for each of the snowflakes mapped to position in the image. Cylinder heights represent ± 1 standard deviation of the fit parameter. (Bottom) projecting fit results to a line running from the outer ($y = 0$) to interior region of snowflakes and fit to a linear model. The translucent region is ± 1 standard deviation of this fit and depicts the scatter of snowflake parameters.

APPENDIX Q

Sidewall angle measurement

The sidewall angle from an etch process can be measured from an image of a rectangular block array. This approach avoids the destructive nature of cleaving etched lines for a more direct sidewall angle measurement.

Q.1 Pattern

A rectangular array of blocks is needed, minimally 2×2, and most simply square. The periodic structure of the array provides known distances in resultant sample, and the rectangular blocks provide faces and edges to measure angles. The lattice vectors are $\vec{a_1}$ and $\vec{a_2}$, with known lengths a_1 and a_2, and orthogonal $\vec{a_1} \cdot \vec{a_2} = 0$. Fig. Q.1 demonstrates a suitable and simple pattern.

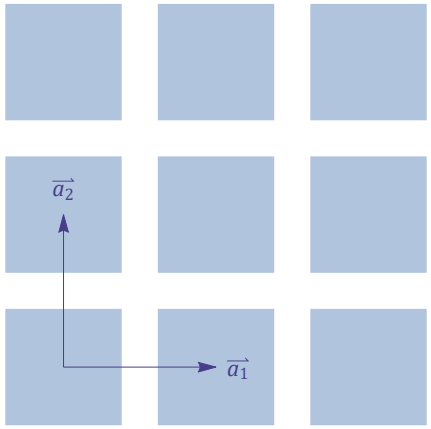

Figure Q.1: Periodic square lithography pattern.

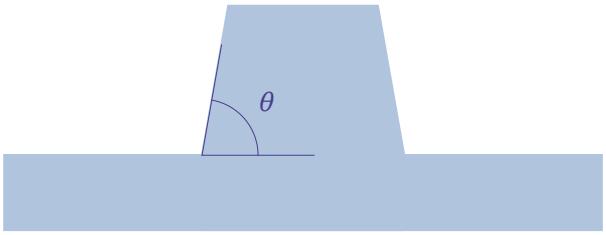

Figure Q.2: Definition of sidewall angle θ.

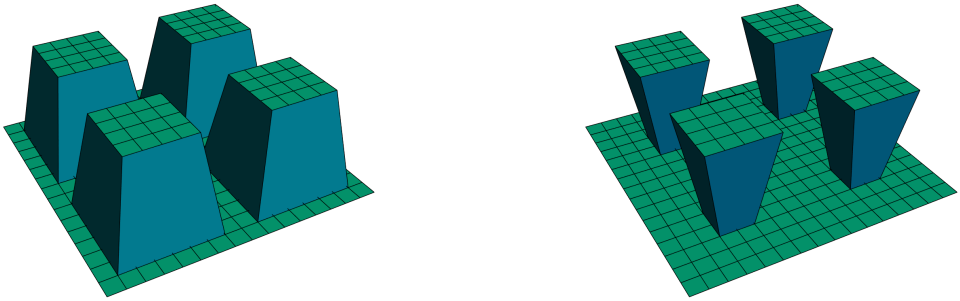

Figure Q.3: Models of the etched square array, with (left) $\theta \approx 70^{\circ}$ and (right) $\approx= 110^{\circ}$.

Q.2 Etch

A critical element of this technique is the assumption that the etch is isotropic in the plane of the sample, such that all sidewalls receive the same angled profile. The sidewall angle θ is defined in Fig. Q.2 as π subtract the angle between the sidewall and the top or bottom flat surface. After etching the rectangular block array will look something like Fig. Q.3.

Q.3 Projection plane

Imaging the sample, for example with a scanning electron microscope, projects the three-dimensional geometry onto a two-dimensional plane. This plane projection operation is

$$\Pi_{\perp\vec{p}}[\vec{r}] = \vec{r} - \left(\frac{\vec{r}\cdot\vec{p}}{\vec{p}\cdot\vec{p}}\right)\vec{p}\,, \tag{Q.1}$$

where $\vec{p} = (p_1, p_2, p_3) \in \mathbb{R}^3$ is a vector normal to the projection plane. Noting that the magnitude of $\vec{p}$ and the overall sign do not affect the projection, let us enforce $p_3 > 0$ and $|\vec{p}| = 1$, such that $p_3 = +\sqrt{1 - {p_1}^2 - {p_2}^2}$. In this regime p_1, p_2, p_3 are unitless, representing portions of $|\vec{p}|$.

For simplicity, we align our $\mathbb{R}^3$ coordinate system such that $\vec{a_1} = (a_1, 0, 0)$ and $\vec{a_2} = (0, a_2, 0)$, and for a square array $a_1 = a_2 = a$. Projecting these lattice vectors with (Q.1), we get the projected vectors (as seen in the image)

$$\vec{a_1'} = \left(a_1 - a_1\,{p_1}^2, -a_1\,p_1\,p_2, -a_1\,p_1\,p_3\right)\,,$$

$$\vec{a_2'} = \left(-a_2\,p_1\,p_2, a_2 - a_2\,{p_2}^2, -a_2\,p_2\,p_3\right)\,.$$

As $\Pi_{\perp\vec{p}}[\vec{0}] = \vec{0}$, we can determine the lattice distances in the image

$$|\vec{a_1'}| = a_1' = a_1\sqrt{{p_2}^2 + {p_3}^2} = a_1\sqrt{1 - {p_1}^2}\,,$$

$$|\vec{a_2'}| = a_2' = a_2\sqrt{{p_1}^2 + {p_3}^2} = a_2\sqrt{1 - {p_2}^2}\,,$$

and the angle between them

$$\vec{a_1'} \cdot \vec{a_2'} = a_1' \, a_2' \, \cos[\alpha'] = -a_1 \, a_2 \, p_1 \, p_2 \; .$$

Thus

$$p_1 = \pm \sqrt{1 - \frac{{a_1'}^2}{{a_1}^2}} \; ,$$

$$p_2 = \pm \sqrt{1 - \frac{{a_2'}^2}{{a_2}^2}} \; ,$$

$$p_3 = + \sqrt{\frac{{a_1'}^2}{{a_1}^2} + \frac{{a_2'}^2}{{a_2}^2} - 1} \; ,$$

with the relative sign between p_1 and p_2 determined by

$$\alpha' < 90^\circ \Rightarrow p_1 \, p_2 < 0 \; ,$$
$$\alpha' > 90^\circ \Rightarrow p_1 \, p_2 > 0 \; .$$

The overall sign of p_1, p_2 can be determined by looking at the projection of a vertical vector, or equivalently in which direction are the sidewall faces projected. If we consider a vertical

vector going down from the top of the blocks,

$$\vec{a_1'} \cdot \Pi_{\perp \vec{p}} \left[\begin{pmatrix} 0 \\ 0 \\ -h \end{pmatrix} \right] = a_1 \, h \, p_1 \, p_3 \ ,$$

$$\vec{a_2'} \cdot \Pi_{\perp \vec{p}} \left[\begin{pmatrix} 0 \\ 0 \\ -h \end{pmatrix} \right] = a_2 \, h \, p_2 \, p_3 \ ,$$

with $p_3 > 0$ the signs of p_1 and p_2 can be determined by these angles. Basically,

- if the sidewall face with edge $\vec{a_2'}$ extends in the positive $\vec{a_1'}$ direction : $p_1 > 0$,
- if the sidewall face with edge $\vec{a_2'}$ extends in the negative $\vec{a_1'}$ direction : $p_1 < 0$,
- if the sidewall face with edge $\vec{a_1'}$ extends in the positive $\vec{a_2'}$ direction : $p_2 > 0$,
- if the sidewall face with edge $\vec{a_1'}$ extends in the negative $\vec{a_2'}$ direction : $p_2 < 0$.

If $\vec{a_1'}$ is chosen to be 'horizontal, to the right' and you're looking at the sample from above, then $p_2 < 0$.

Sample projections for various $\vec{p}$ vectors are given in Fig. Q.4.

Q.4 Angle measurement

Knowing the plane projection vector $\vec{p}$ we can infer the sidewall angle θ from measurements of the angles in the projected sidewall face. Denote the block width w, and height h, following

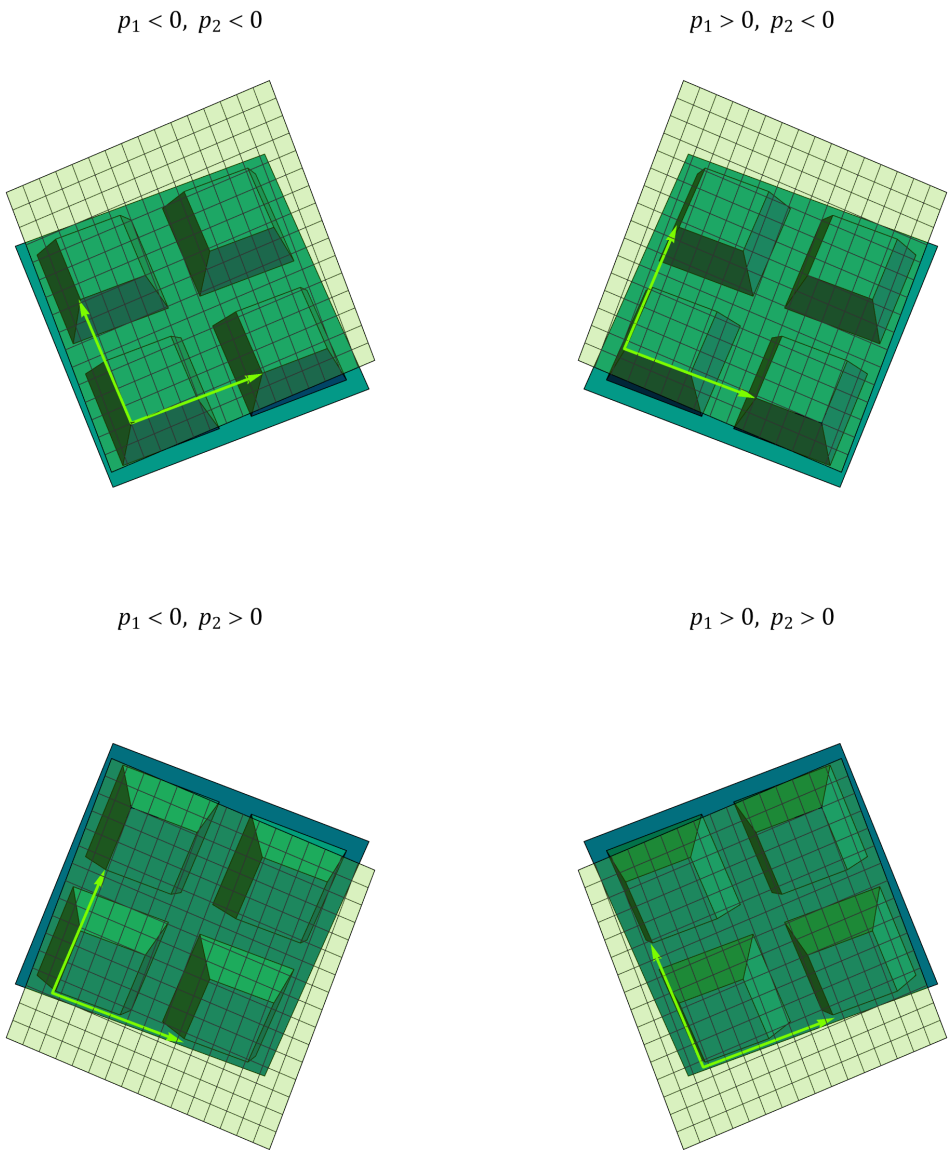

Figure Q.4: The four different perspective projections of the lattice vectors.

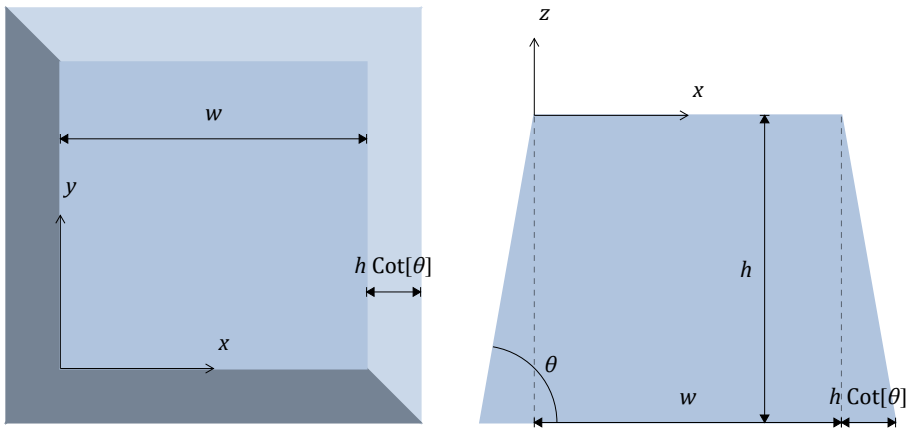

Figure Q.5: Coordinate system for the block.

the coordinate system defined in Fig. Q.5. Consider a visible sidewall face with top edge along $\vec{a_1}$, i.e. the line segment

$$T = \left\{ \begin{pmatrix} x \\ 0 \\ 0 \end{pmatrix} : 0 < x < w \right\} .$$

The two line segment edges of this angled trapezoid face are

$$L = \left\{ \begin{pmatrix} z \cot[\theta] \\ z \cot[\theta] \\ z \end{pmatrix} : -h < z < 0 \right\} ,$$

$$R = \left\{ \begin{pmatrix} w - z \cot[\theta] \\ z \cot[\theta] \\ z \end{pmatrix} : -h < z < 0 \right\} .$$

The projected image of these lines are

$$\Pi_{\perp\vec{p}}[T] = \left\{ \begin{pmatrix} x - x\,{p_1}^2 \\ -x\,p_1\,p_2 \\ -x\,p_1\,p_3 \end{pmatrix} : 0 < x < w \right\} ,$$

$$\Pi_{\perp\vec{p}}[L] = \left\{ \begin{pmatrix} -z\,p_1\,p_3 + \left(z - z\,{p_1}^2 - z\,p_1\,p_2\right)\cot[\theta] \\ -z\,p_2\,p_3 + \left(z - z\,{p_2}^2 - z\,p_1\,p_2\right)\cot[\theta] \\ z - z\,{p_3}^2 + \left(-z\,p_1\,p_3 - z\,p_2\,p_3\right)\cot[\theta] \end{pmatrix} : -h < z < 0 \right\} ,$$

$$\Pi_{\perp\vec{p}}[R] = \left\{ \begin{pmatrix} w - w\,{p_1}^2 - z\,p_1\,p_3 + \left(-z + z\,{p_1}^2 - z\,p_1\,p_2\right)\cot[\theta] \\ -w\,p_1\,p_2 - z\,p_2\,p_3 + \left(z - z\,{p_2}^2 + z\,p_1\,p_2\right)\cot[\theta] \\ -w\,p_1\,p_3 + z - z\,{p_3}^2 + \left(z\,p_1\,p_3 - z\,p_2\,p_3\right)\cot[\theta] \end{pmatrix} : -h < z < 0 \right\} .$$

To get the angles between the edges we need the tangent vectors, which can be found by taking derivatives with respect to x and z. Care needs to be taken with the direction of these vectors to ensure we get the interior angles of the sidewall face when we take dot products.

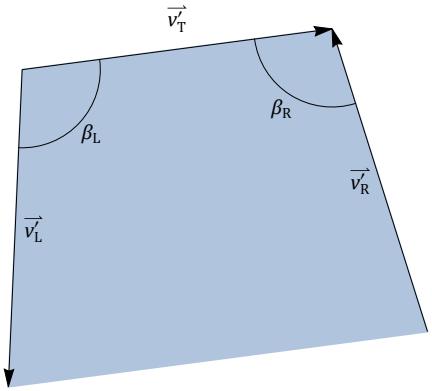

Figure Q.6: Sidewall face with edge vectors and interior angles.

Fig. Q.6 depicts the orientations used here,

$$\vec{v'_T} = \partial_x \, \Pi_{\perp \vec{p}}[T] = \begin{pmatrix} 1 - {p_1}^2 \\ -p_1 \, p_2 \\ -p_1 \, p_3 \end{pmatrix} ,$$

$$\vec{v'_L} = -\partial_z \, \Pi_{\perp \vec{p}}[L] = \begin{pmatrix} p_1 \, p_3 - \left(1 - {p_1}^2 - p_1 \, p_2\right) \cot[\theta] \\ p_2 \, p_3 - \left(1 - {p_2}^2 - p_1 \, p_2\right) \, \cot[\theta] \\ -1 + {p_3}^2 + (p_1 \, p_3 + p_2 \, p_3) \cot[\theta] \end{pmatrix} ,$$

$$\vec{v'_R} = \partial_z \, \Pi_{\perp \vec{p}}[R] = \begin{pmatrix} -p_1 \, p_3 - \left(1 - {p_1}^2 + p_1 \, p_2\right) \cot[\theta] \\ -p_2 \, p_3 + \left(1 - {p_2}^2 + p_1 \, p_2\right) \, \cot[\theta] \\ 1 - {p_3}^2 + (p_1 \, p_3 - p_2 \, p_3) \cot[\theta] \end{pmatrix} .$$

Carrying out some intermediate calculations with these vectors,

$$\begin{aligned}
|\vec{v_T'}| &= \sqrt{1-{p_1}^2}\ , \\
|\vec{v_L'}| &= \sqrt{1+2\ \cot[\theta]^2-((p_1+p_2)\cot[\theta]+p_3)^2}\ , \\
|\vec{v_R'}| &= \sqrt{1+2\ \cot[\theta]^2-((p_2-p_1)\cot[\theta]+p_3)^2}\ , \\
\vec{v_T'}\cdot\vec{v_L'} &= p_1\,p_3-\left(1-{p_1}^2-p_1\,p_2\right)\cot[\theta]\ , \\
\vec{v_T'}\cdot\vec{v_R'} &= \ -p_1\,p_3-\left(1-{p_1}^2+p_1\,p_2\right)\cot[\theta]\ .
\end{aligned}$$

The sidewall face interior angles β_L and β_R are then related to θ by

$$\cos[\beta_L]=\frac{p_1\,p_3-\left(1-{p_1}^2-p_1\,p_2\right)\cot[\theta]}{\sqrt{1-{p_1}^2}\sqrt{1+2\ \cot[\theta]^2-((p_1+p_2)\cot[\theta]+p_3)^2}}\ ,$$

$$\cos[\beta_R]=\frac{-p_1\,p_3-\left(1-{p_1}^2+p_1\,p_2\right)\cot[\theta]}{\sqrt{1-{p_1}^2}\sqrt{1+2\ \cot[\theta]^2-((p_2-p_1)\cot[\theta]+p_3)^2}}\ .$$

These provide quadratic equations for $\cot[\theta]$ with solutions

$$\cot[\theta]=\frac{p_2\,p_3+p_3({p_1}^2-1)(p_1+p_2)\sin[\beta_L]^2\pm({p_1}^2-1)(p_2-p_1)\sin[\beta_L]\ \cos[\beta_L]}{-(1-{p_1}^2-p_1\,p_2)^2+({p_1}^2-1)((p_1+p_2)^2-2)\cos[\beta_L]^2}\ ,$$

$$\cot[\theta]=\frac{p_2\,p_3+p_3({p_1}^2-1)(p_2-p_1)\sin[\beta_R]^2\pm({p_1}^2-1)(p_1+p_2)\sin[\beta_R]\ \cos[\beta_R]}{-(1-{p_1}^2+p_1\,p_2)^2+({p_1}^2-1)((p_2-p_1)^2-2)\cos[\beta_R]^2}\ .$$

Note that if $p_1=0$, $\beta_L=\beta_R=\beta$, and

$$\cot[\theta]=\frac{p_2\,p_3\ \cos[\beta]^2\pm p_2\ \sin[\beta]\ \cos[\beta]}{(2-{p_2}^2)\cos[\beta]^2-1}\ .$$

If $p_1 = p_3 = 0$, and $p_2 = -1$, then

$$\cot[\theta] = \ - \pm \cot[\beta] \ ,$$

and in this situation $\theta + \beta = \pi$ so

$$\cot[\theta] = \cot[\pi - \beta] = \cot[-\beta] = -\cot[\beta] \ ,$$

meaning + should be used in $\pm$. Thus we have the following rules

- if $p_2 > 0$, then $\pm \mapsto -$,
- if $p_2 < 0$, then $\pm \mapsto +$ (most common scenario).

Q.5 Limitations

This approach assumes the features are essentially flat and the observation point is an infinite distance from the focal plane such that everything is in focus and there are no depth perspective effects. In reality this is not the case and the location of the observation point needs to be included. Due to the compounding of often difficult and imprecise measurements, this quickly leads to large margins of error.

APPENDIX R

Optical plate

The absolute zeroth order geometry for our device is an infinite two-dimensional slab of gallium arsenide, and thus it is useful to understand the properties of such an object. Solving Maxwell's equations for the infinite dielectric plate is a fairly straight forward exercise and appears in many text books [220, 262], here we will only be detailing results.

R.1 Optical dispersion

The dispersion relation in an infinite dielectric plate is a transcendental equation that can be expressed in multiple ways. For a dielectric plate of refractive index n and thickness $\mathtt{t}$ in air (unity refractive index), one such expression is

$$\tan\left[\frac{\mathtt{t}}{2}\sqrt{\left(\frac{\omega\, n}{c}\right)^2 - k^2} + \left\{\begin{array}{c} 0 : \overset{+}{z} \\ \frac{\pi}{2} : \overset{-}{z} \end{array}\right\}\right] = \left\{\begin{array}{c} n^2 : \mathrm{TM} \\ 1 : \mathrm{TE} \end{array}\right\} \frac{\sqrt{k^2 - \left(\frac{\omega}{c}\right)^2}}{\sqrt{\left(\frac{\omega\, n}{c}\right)^2 - k^2}} \,,$$

where ω is angular frequency, k is wave number for the direction of propagation (parallel to the plate), c is the speed of light, $\overset{\pm}{z}$ is mirror symmetry (orthogonal to the plate), TM is transverse magnetic (zero magnetic field in propagation direction), and TE is transverse electric (zero electric field in the propagation direction). Solutions via numeric root-finding are depicted in Fig. R.1. The effective index of refraction is defined as

$$n_{\mathrm{eff}} = \frac{k\, c}{\omega} \,.$$

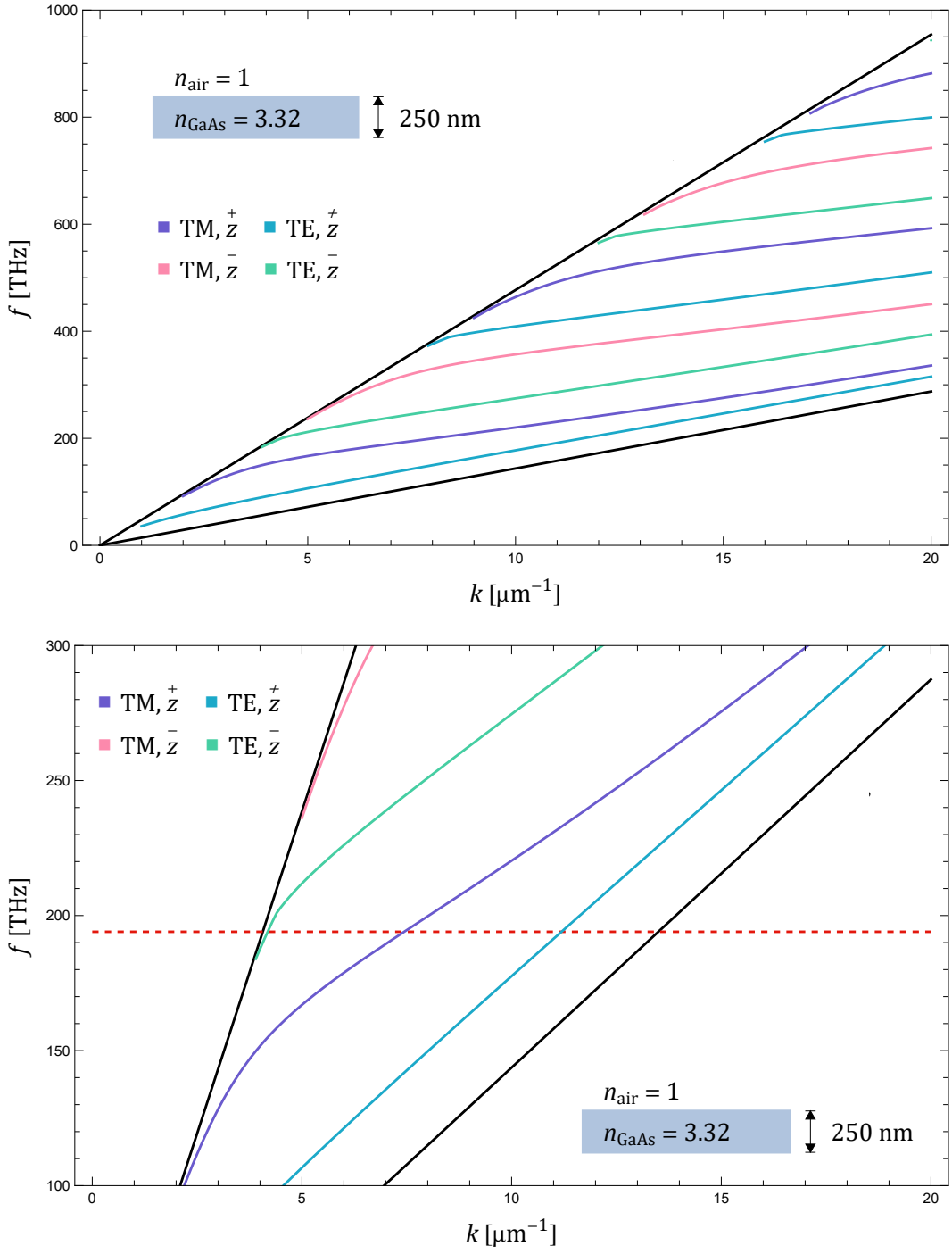

Figure R.1: Electromagnetic dispersion plot for an infinite plate of gallium arsenide, 250 nm thick. The bottom plot is zoomed-in around 194 THz.

APPENDIX S

Optical beam

A basic ingredient for manipulating light on the nanometer scale is that of a suspended dielectric beam waveguide. If there is a sufficient refractive index contrast between a rectangular prism and its surrounding, electromagnetic waves in supported frequency ranges will be guided through the beam. Unfortunately, unlike the infinite dielectric of App. R, it is not possible analytically solve Maxwell's equations for this geometry and numerical methods are required. For an infinite dielectric beam this is a two-dimensional problem and COMSOL's [181] (finite element modeling) boundary mode analysis is used to find modes. Using the geometry defined in Fig. T.1, optical modes travelling down the beam (x direction) can be characterized by their symmetry eigenvalues (see App. D) of the two mirror symmetries (vertical z and horizontal y) of the beam cross-section. The effective index of refraction is $k_x\, c\,/\,\omega$.

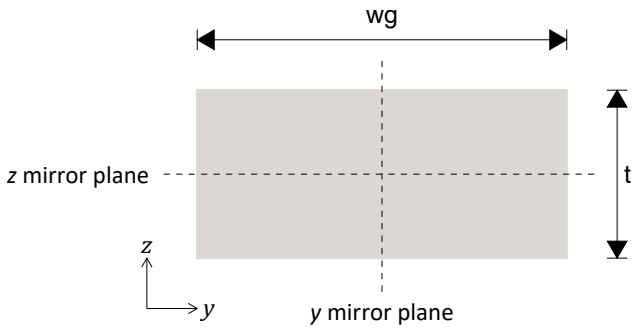

Figure S.1: Dielectric beam geometry, optical waves are guided through the page in the x direction.

S.1 Optical dispersion

Optical dispersion plots from simulation for a beam 250 nm high, and 400 nm and 550 nm wide are given in Fig. S.2.

S.2 Supported modes

An important feature of the beam waveguide is that for any particular set of dimensions, only certain modes are allowed, and restricted to $n_{\text{air}} < n_{\text{eff}} < n_{\text{solid}}$. If we are only interested in propagation at 194 THz, we can vary the beam dimensions and ask what modes are supported. In Fig. S.3 supported modes in terms of n_{eff} are plotted for varying height and width, and in Fig. S.4 a cross section is taken through a beam height of 250 nm. With this knowledge, a suitably small dielectric beam waveguide can help filter out unwanted modes in our system. To interface with a grating coupler and optomechanical resonance, the mode we are interested in is $\overset{-}{y}\overset{+}{z}$.

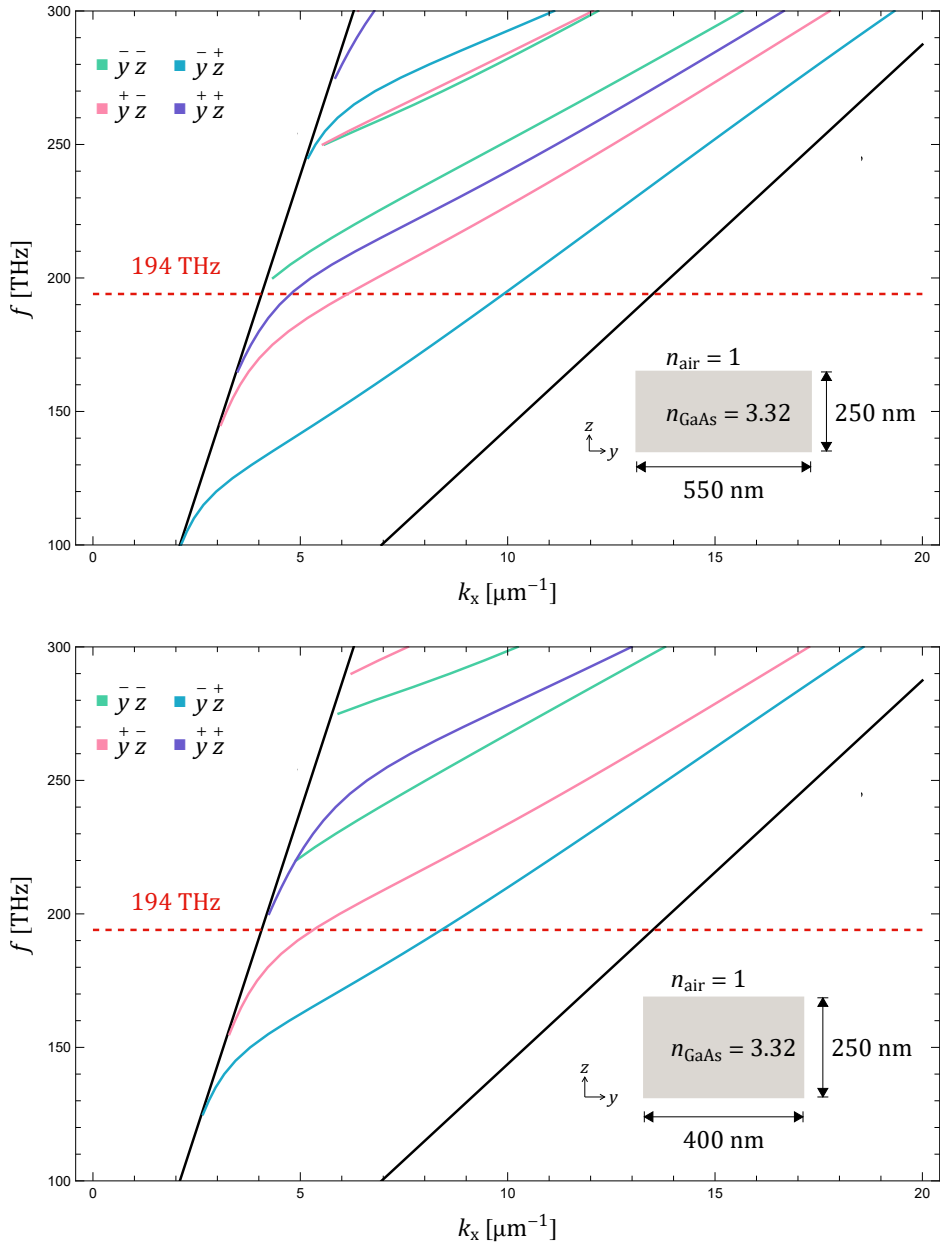

Figure S.2: Sample gallium arsenide beam electromagnetic dispersion plots.

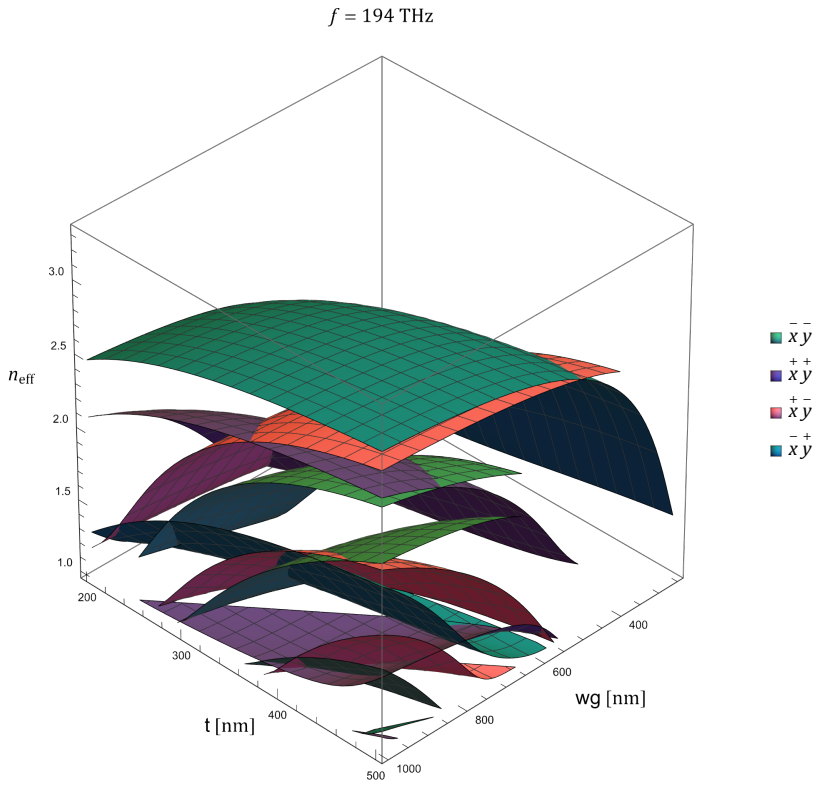

Figure S.3: Supported modes at 194 THz in a gallium arsenide beam waveguide of varying dimensions.

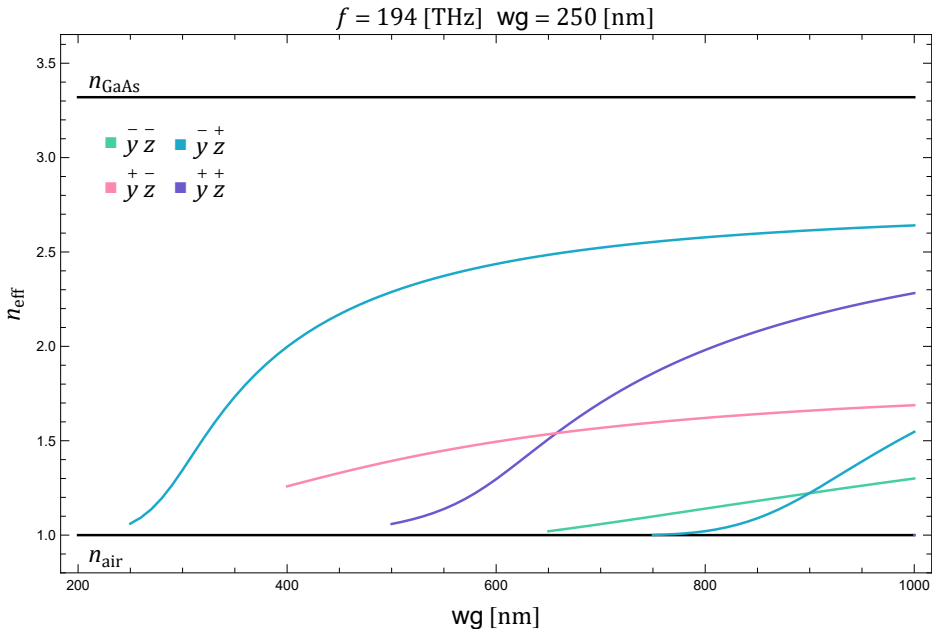

Figure S.4: Supported modes at 194 THz in a gallium arsenide beam waveguide 250 nm high with varying width.

APPENDIX T

Mechanical beam

In understanding the propagation of acoustic waves, one simple scenario is that of a suspended beam. Mechanical modes supported in the beam can be found by performing three dimensional simulations [181] on a periodic model. Using the geometry defined in Fig. T.1, acoustic modes traveling down the beam (x direction) can be characterized by their symmetry eigenvalues (see App. D) of the two mirror symmetries (vertical z and horizontal y) of the beam cross-section. As gallium arsenide is not isotropic, the alignment of the beam relative to the crystal structure is important.

Although the mechanical beam has continuous symmetry along x, we simulate using a periodic distance a. Doing so, however, causes modes to wrap around in wavenumber space in intervals of $2\,\pi/a$. To clean up the dispersion plot, modes are isolated by connecting points based on closest to linear extrapolation, then wrapped frequencies deleted, in a mode step-wise fashion.

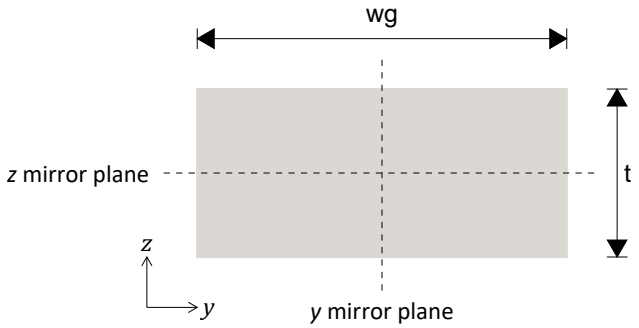

Figure T.1: Mechanical beam geometry, acoustic waves are guided through the page in the x direction.

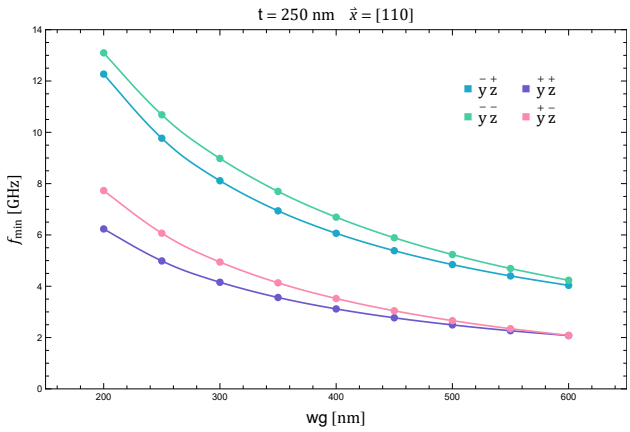

Figure T.2: Acoustic frequecy cutoffs for a fixed sides beam.

T.1 Free beam

Mechanical dispersion plots from simulation for a beam 250 nm high and 400 nm wide for two crystal orientations are given in Fig. T.3.

T.2 Fixed beam

We can also look at a beam which has fixed boundaries on two opposite sides, this loosely approximates a phononic crystal waveguide where the band gaped patterning on the sides restricts vibration. Mechanical dispersion plots from simulation for a beam 250 nm high and 400 nm wide with fixed sides for two crystal orientations are given in Fig. T.4. The presence of fixed sides induces a lower frequency bound, below which propagating acoustic modes are not supported. In Fig. T.2 we plot the frequency cutoffs when $\mathtt{t} = 250\,\mathrm{nm}$.

T.3 Infinite plate

Lastly we can consider an infinite suspended plate with no displacement in the transverse infinite direction (y). Mechanical dispersion plots from simulation for an infinite plate 250 nm thick for two crystal orientations are given in Fig. T.5.

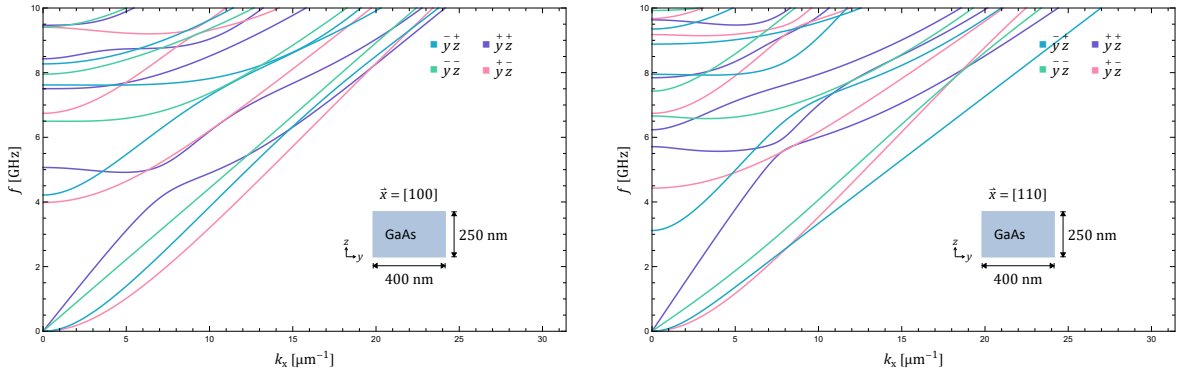

Figure T.3: Sample gallium arsenide free beam dispersion plots.

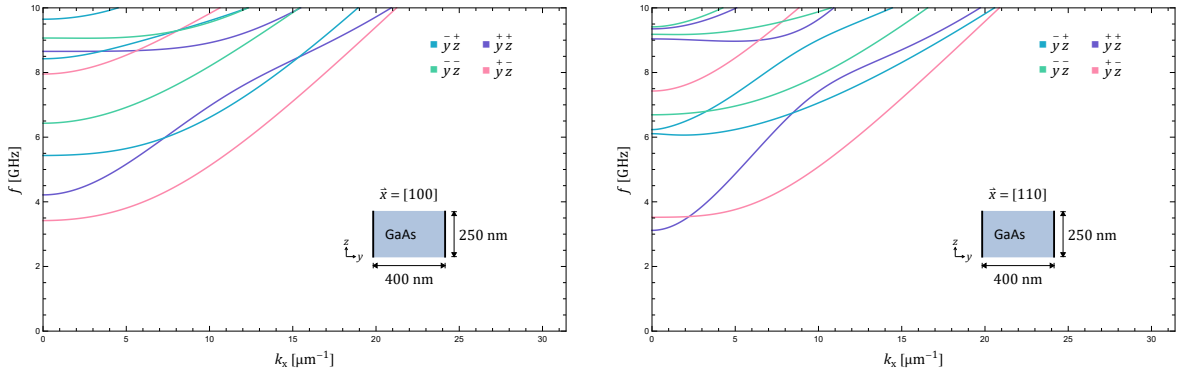

Figure T.4: Sample gallium arsenide fixed sides beam dispersion plots.

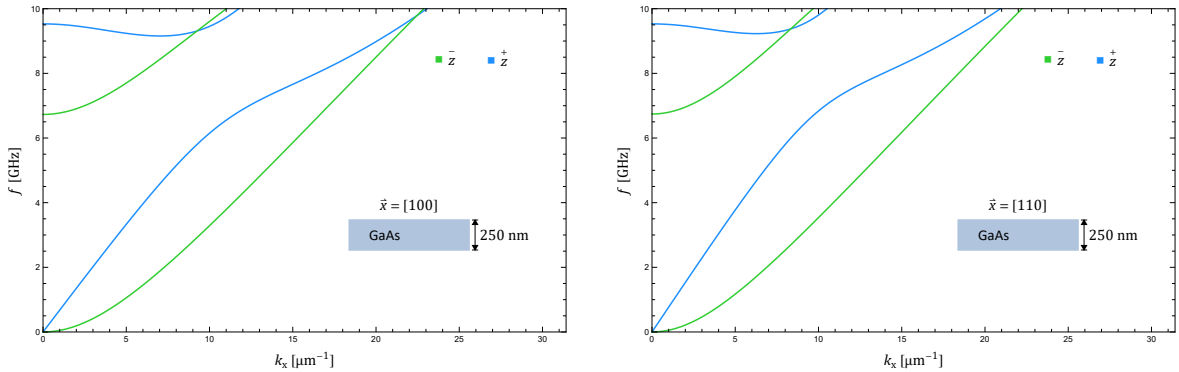

Figure T.5: Sample gallium arsenide infinite plate dispersion plots.

APPENDIX U

Optomechanical crystal dispersion

In this appendix we provide additional details and results of dispersion plots for optomechanical crystals. Following the arguments in Sec. 2.2, we primarily consider the p6m wallpaper group in suspended gallium arsenide.

U.1 Simulation

Dispersion relations were simulated using finite element modelling software [181]. The hexagonal unit cell was constructed in three dimensions with the suspended substrate and pattern parallel to the x-y plane. Perpendicular, in z, mirror symmetry or antisymmetry was enforced at a plane through the middle of the slab. Away from structure an air box terminating in a perfectly matched layer constituted the $z \to \infty$ boundary. Each of the three pairs of parallel boundaries to the hexagonal unit cell utilized periodic (Floquet) boundary conditions with a fixed given wavevector. For each set wavevector then, an eigenfrequency simulation is able to find a set of supported modes. Performing this for a sweep of wavevectors allows the dispersion plots to be built up. An example model is shown in Fig. U.1.

U.2 Shape

Typical two-dimensional optomechanical crystals appearing in literature are the snowflake [152, 177, 178, 263] and disc [170, 171, 174], but one can imagine many other possibilities. To this end a wide variety of shapes were simulated in isotropic silicon to see which would produce phononic and photonic bandgaps. A survey of many geometries is given in Fig. U.2 with

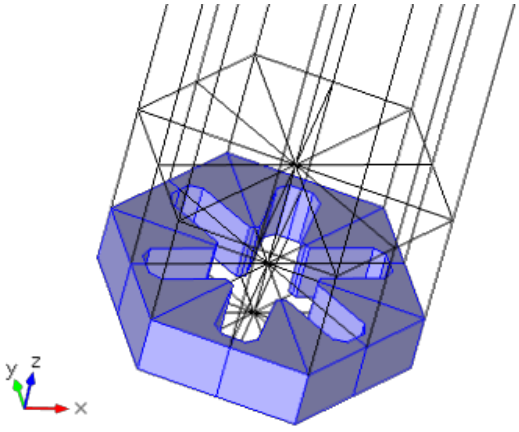

Figure U.1: Snowflake hexagon unit cell model with air box continuing upward.

the full dispersion plots for a selection of more interesting patterns shown in Figs. U.3, U.4.

Additional geometries, including ones with an additional circular hole through the unit cell center, and some without mirror symmetry were briefly tested but were not fruitful. Conventional wisdomSafaviNaeiniOMCdesign,CavityOptomechBook dictates that lattices with 'drumheads' and bridges connecting them help separate low frequency acoustics (with wavelengths larger than the drumhead and unit cell) from higher frequency acoustics that interact with the drumheads. Evidence of that was seen here with patterns offering no drumhead-like platforms tending not to produce acoustic bandgaps.

Whilst some of the patterns in Figs. U.3, U.4 show potential with optic bandgaps that can be moved down by scaling dimensions up, the associated mechanical dispersion is not as ideal. A handful of simulations were carried out with larger dimensions ($a \sim 750\,\mathrm{nm}$) but did not yield anything superior to the snowflake geometry. Given that larger shapes are significantly easier to fabricate, however, some of these pattern types could warrant further investigation.

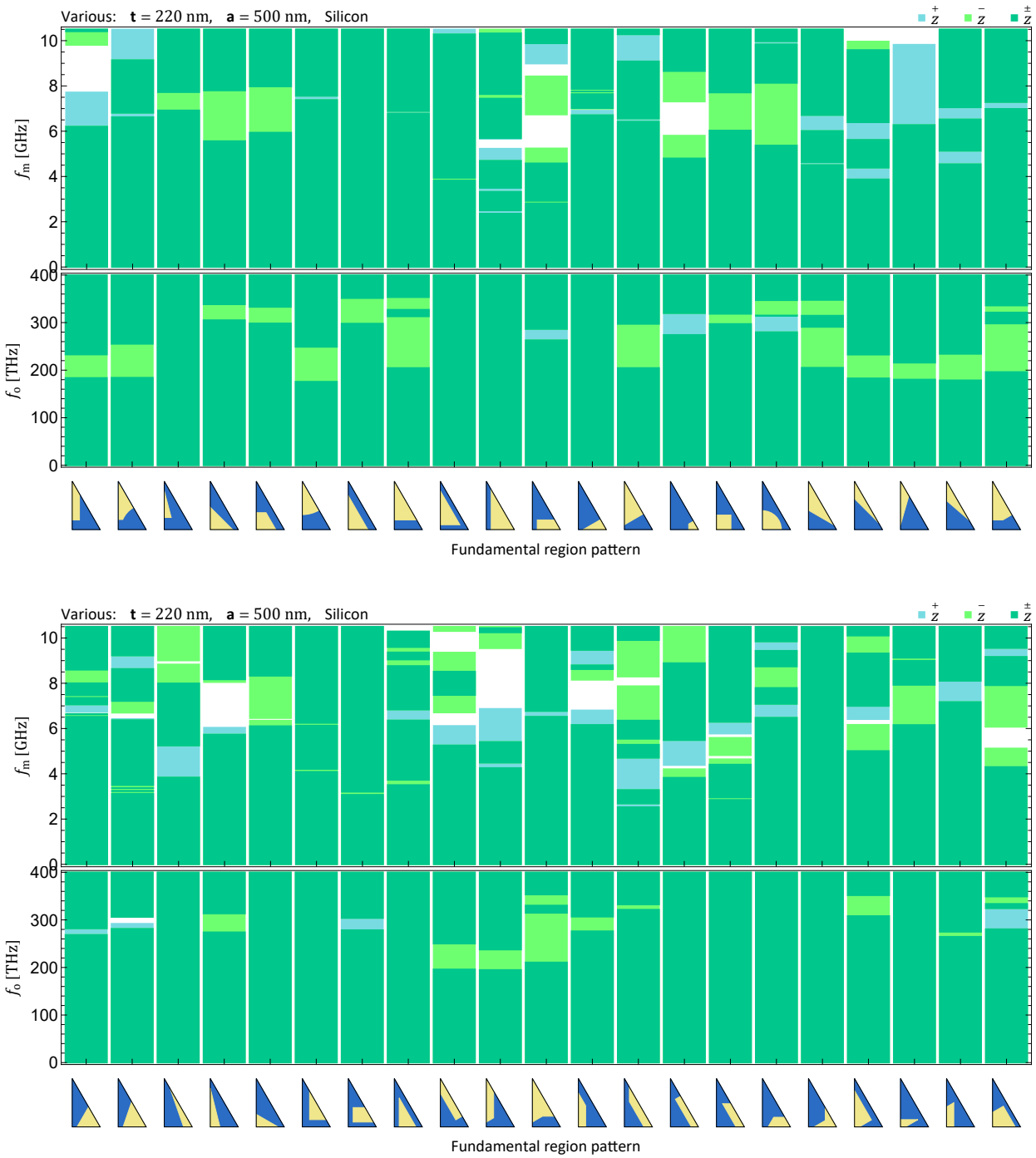

Figure U.2: Simulated acoustic and electromagnetic bands for a variety of geometries in 220 nm suspended silicon. In each case the unit cell has a size of 500 nm and is constructed by reflecting and rotating the depicted p6m fundamental regions (blue for solid, yellow for air holes).

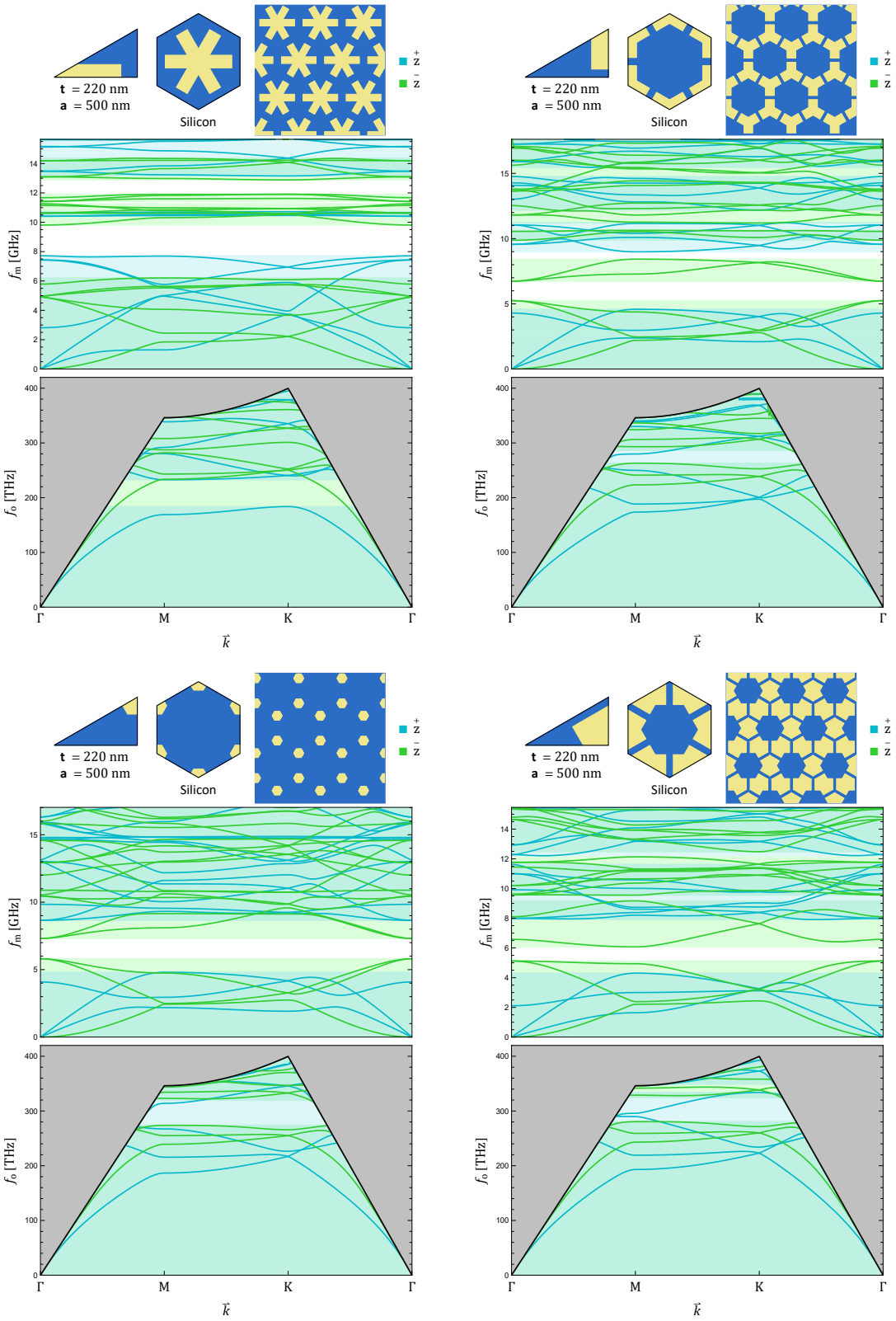

Figure U.3: Full dispersion plots for four patterns in suspended silicon. Simulations were carried out at 3×25 wavevector points along $\Gamma \to \mathrm{M} \to \mathrm{K} \to \Gamma$ and joined in curves.

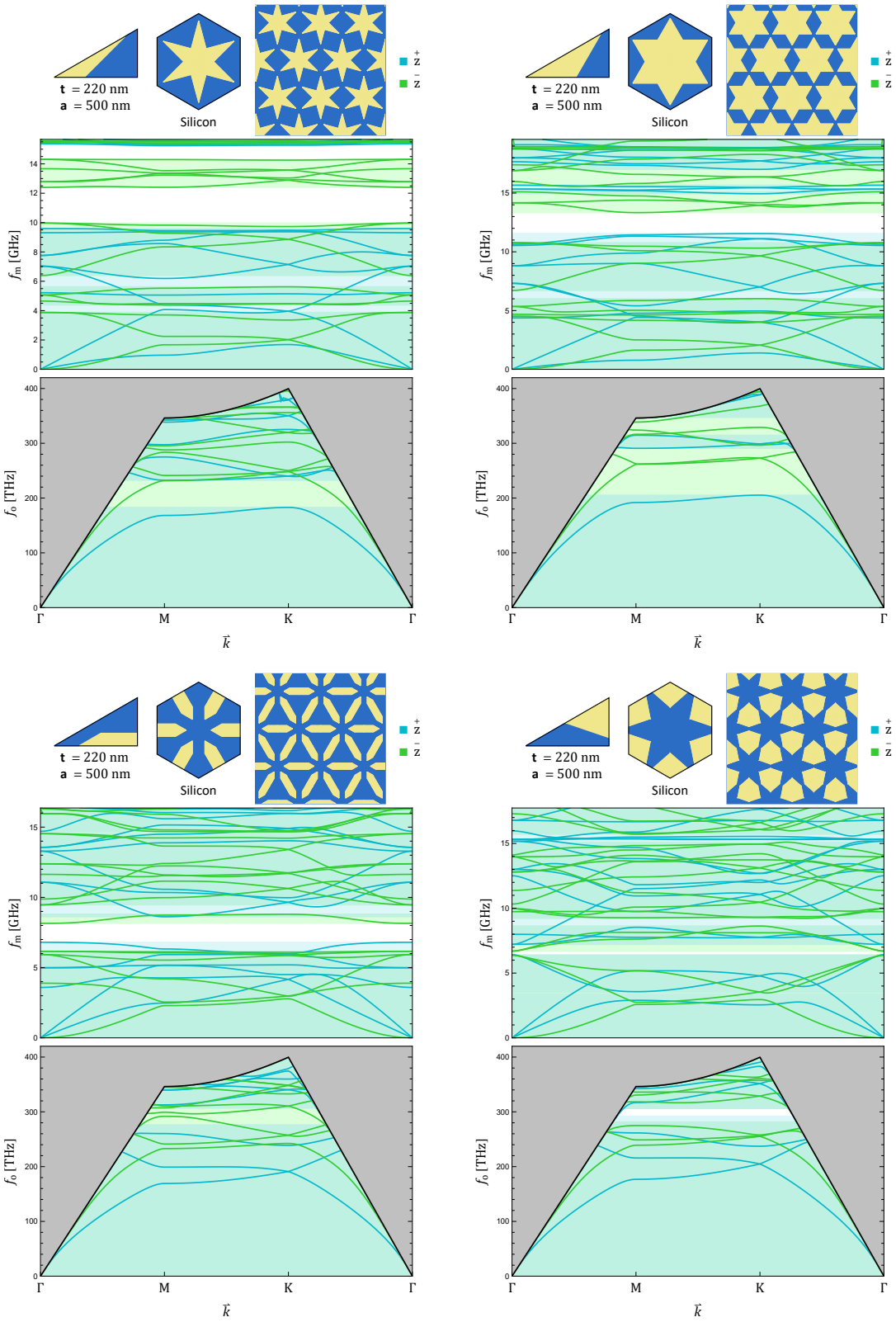

Figure U.4: Full dispersion plots for four patterns in suspended silicon. Simulations were carried out at 3×25 wavevector points along $\Gamma \to \mathrm{M} \to \mathrm{K} \to \Gamma$ and joined in curves.

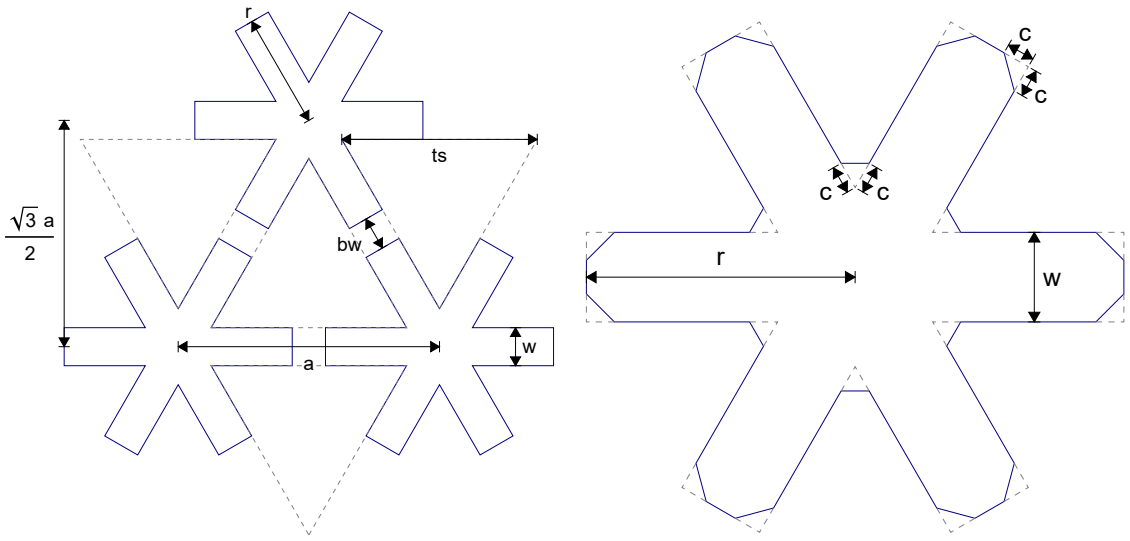

Figure U.5: (Right) Snowflake crystal lattice parameters. (Right) chamfer snowflake hole parameterization.

U.2.1 Chamfer snowflake

Further simulations featuring snowflakes, chosen for the best band gaps, use chamfered corners to account for some inevitable rounding during fabrication. The chamfer snowflake can be described with four parameters,

- a lattice spacing,
- r snowflake arm radius,
- w snowflake arm width,
- c corner chamfer,

which are depicted in Fig. U.5. Additional parameters, more apt for describing the solid parts of the pattern are

- ts triangle side,
- bw bridge width,

with

$$\mathsf{ts} = \mathsf{a} - \sqrt{3}\,\mathsf{w}\ , \qquad \mathsf{bw} = \mathsf{a} - 2\,\mathsf{r}\ ,$$

$$\mathsf{w} = \frac{\mathsf{a} - \mathsf{ts}}{\sqrt{3}}\ , \qquad \mathsf{r} = \frac{\mathsf{a} - \mathsf{bw}}{2}\ .$$

U.3 Rotation

Whilst the snowflake pattern has $\pi/3$ rotation symmetry, GaAs has $\pi/2$ rotation symmetry. As such, the mechanical modes propagating through the phononic crystal have some dependence on relative orientation between the material and pattern. Optically, GaAs is isotropic and there is no orientation dependence for the photonic crystal.

Following the symmetries in GaAs in Sec. M.1.7, if considering acoustics without any piezoelectric interaction then we expect $[0, \pi/6]$ rotations to be unique, mirrored over $[\pi/6, \pi/3]$ and then repeated. Including piezoelectric effects in acoustic wave propagation changes this to $[0, \pi/2]$ unique due to the different rotational symmetry of the piezoelectric coupling tensors.

In Fig. U.6 acoustic bands are plotted for the snowflake pattern with rotations from 0° to 30°, and every 15° to 180°. Where the x axis is perpendicular to a hexagonal unit cell boundary, a rotation of 0° corresponds to $\vec{x} = [100]$, and 45° corresponds to $\vec{x} = [1\bar{1}0]$.

Whilst there are some features following a 15° reflection, the piezoelectric influence is noticeable. The mechanical dispersion relations can be seen to repeat after a $\pi/2$ rotation. Fortunately, the large total bandgap covering 4 GHz remains for all orientations.

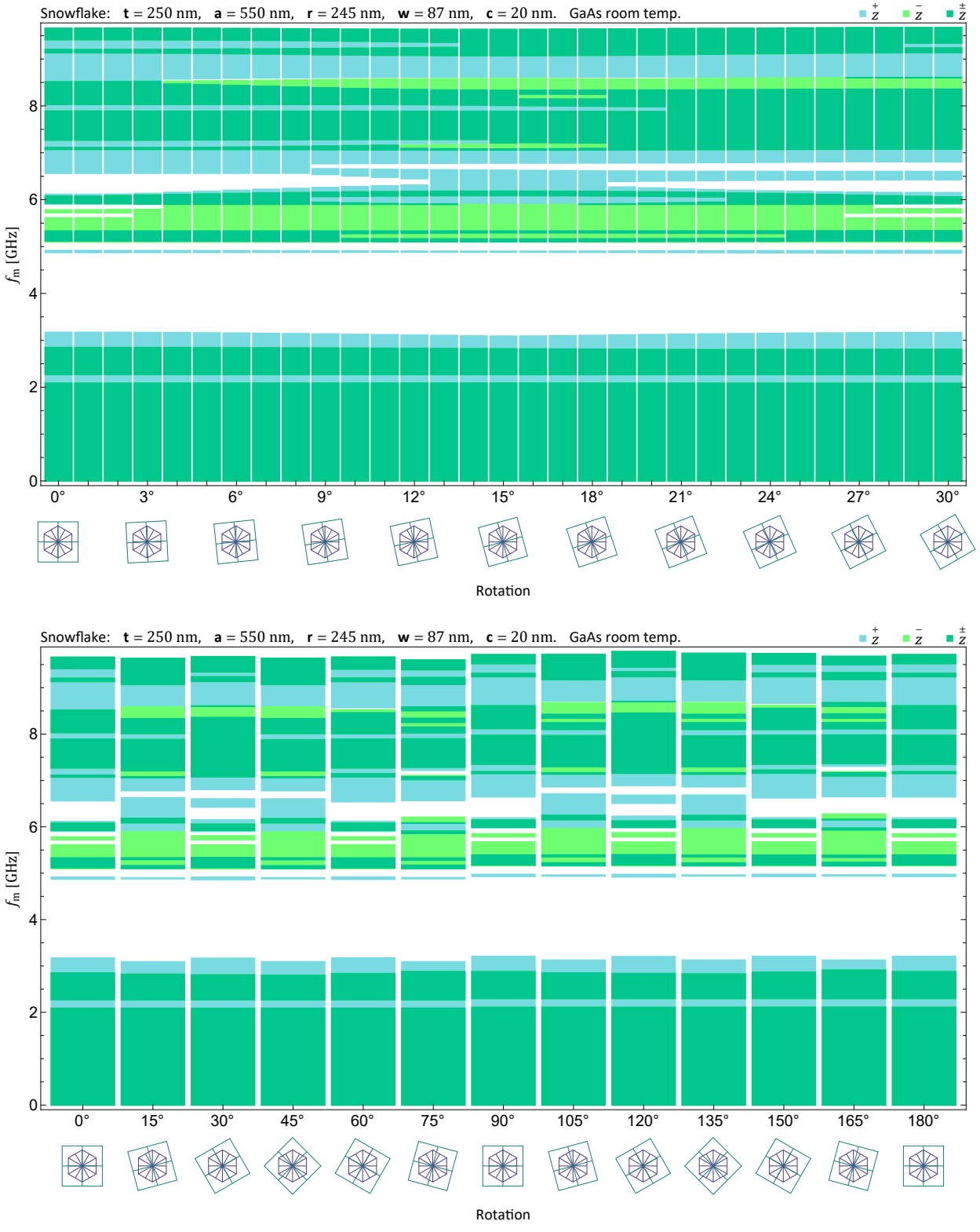

Figure U.6: Simulated acoustic bands, separated by out-of-plane z symmetry, for snowflakes in suspended GaAs membrane. Diagrams along rotation axis depict relative orientation of phononic crystal hexagonal unit cell against material square atomic lattice.

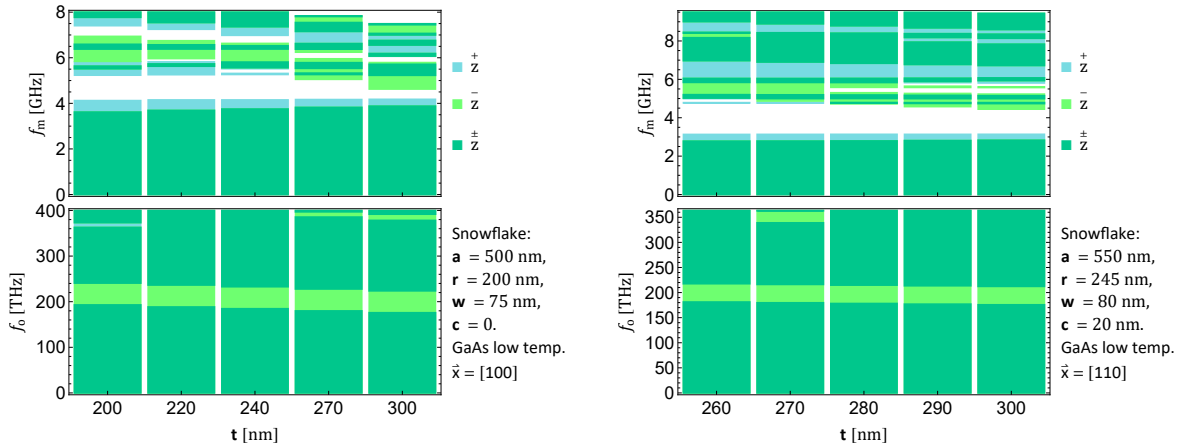

Figure U.7: Simulated acoustic and electromagnetic bands for snowflakes in GaAs, varying slab thickness.

U.4 Thickness

Whilst the suspended slab thickness is set during the wafer manufacturing and can't be easily modified during fabrication, its nonetheless useful to see its effect on the supported modes. In Fig. U.7 two sets of thickness sweeps are shown. As expected, the frequencies decrease with greater thickness, but otherwise the major bandgaps are stable.

U.5 Rounding

Ideally we want sharp corners but in practice some rounding will take place. In Fig. U.8 we show bands from simulating snowflakes with varying amounts of corner chamfer. Whilst the electromagnetic bands are relatively undisturbed, the acoustic band gap is shifted higher in frequency at greater chamfers. If our mechanical resonance mode is not sufficiently high in frequency, excessive rounding of corners during fabrication can present a problem.

U.6 Snowflake surveys

Using the snowflake shape, the heavy simulation workload is sweeping over dimension parameter combinations. For this, a fewer number of wavevectors are used, 3×10, and for analysis we only show the major bandgap. In Figs. U.9, U.10, U.11, U.12, U.13, snowflake bandgap surveys are given for $\mathsf{a} = 530\,\mathrm{nm}$ to $\mathsf{a} = 570\,\mathrm{nm}$.

A large set of known bandgaps is important for simulating the defect cavity resonator as we only want to probe frequencies that we know will be trapped by the optomechanical crystal, and, because the cavity size is defined by the crystal it's sitting in, variations to the cavity involve variations of the crystal pattern dimensions. Furthermore, an extensive sweep of snowflake dimensions for a particular lattice constant allows partial waveguides to be designed. By tuning the snowflake size, and hence shifting the bandgaps, one can create regions where, for a particular mechanical and optical frequency, only one is in a bandgap and blocked. This allows local variations in the optomechanical crystal to be made into partial waveguides that propagate optics whilst still acting as a phononic crystal, or propagate mechanics whilst still acting as a photonic crystal. Additionally if a partial waveguide configuration has a pathway through r, w to $\mathsf{r} \to 0$ and $\mathsf{w} \to 0$ without encountering bandgaps for the propagating wave, the optomechanical crystal partial waveguide can be smoothly transformed to a regular 'blank' waveguide for connecting to non-optomechanical crystal device elements.

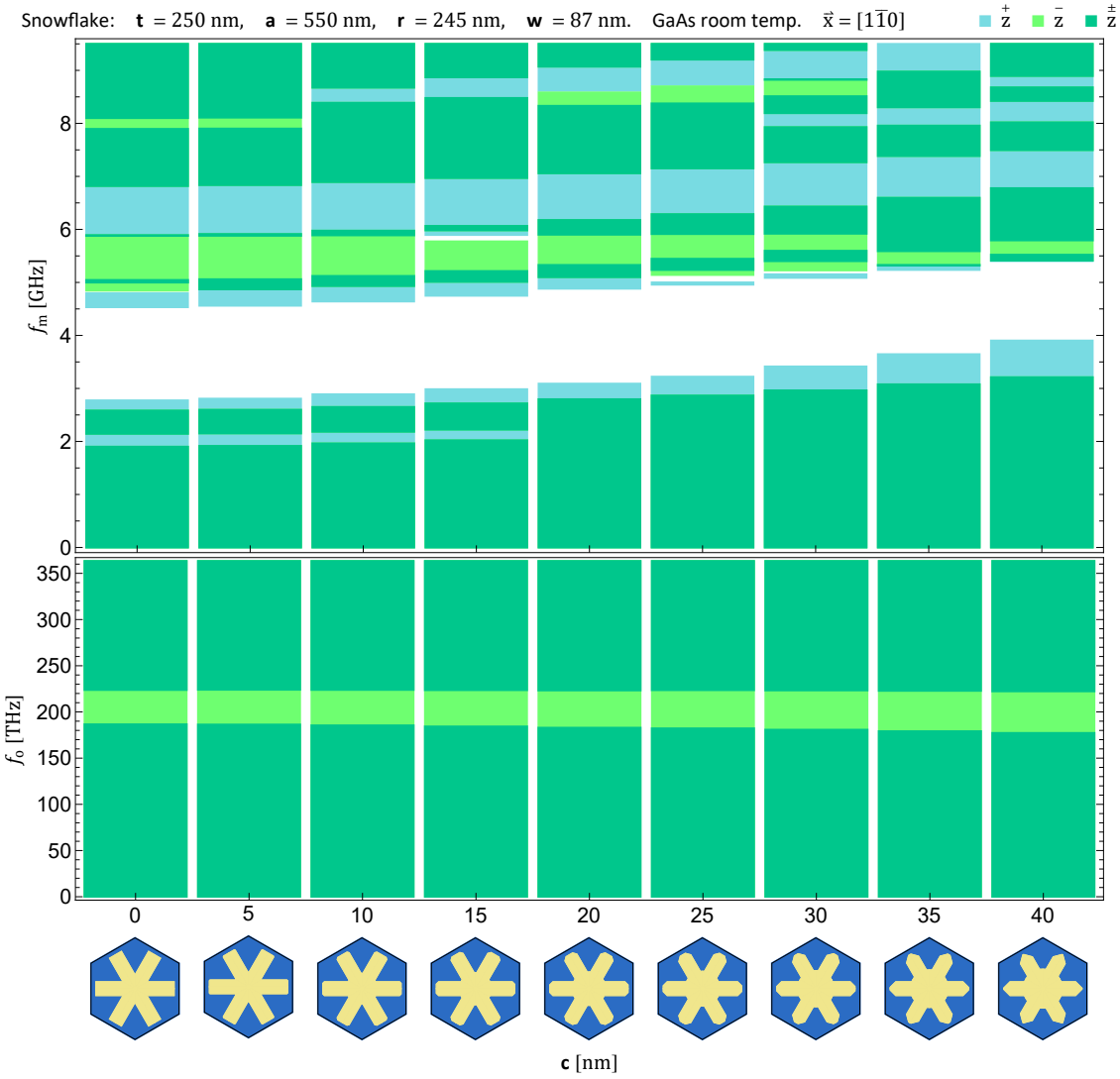

Figure U.8: Simulated acoustic and electromagnetic bands for varying snowflake chamfer in GaAs.

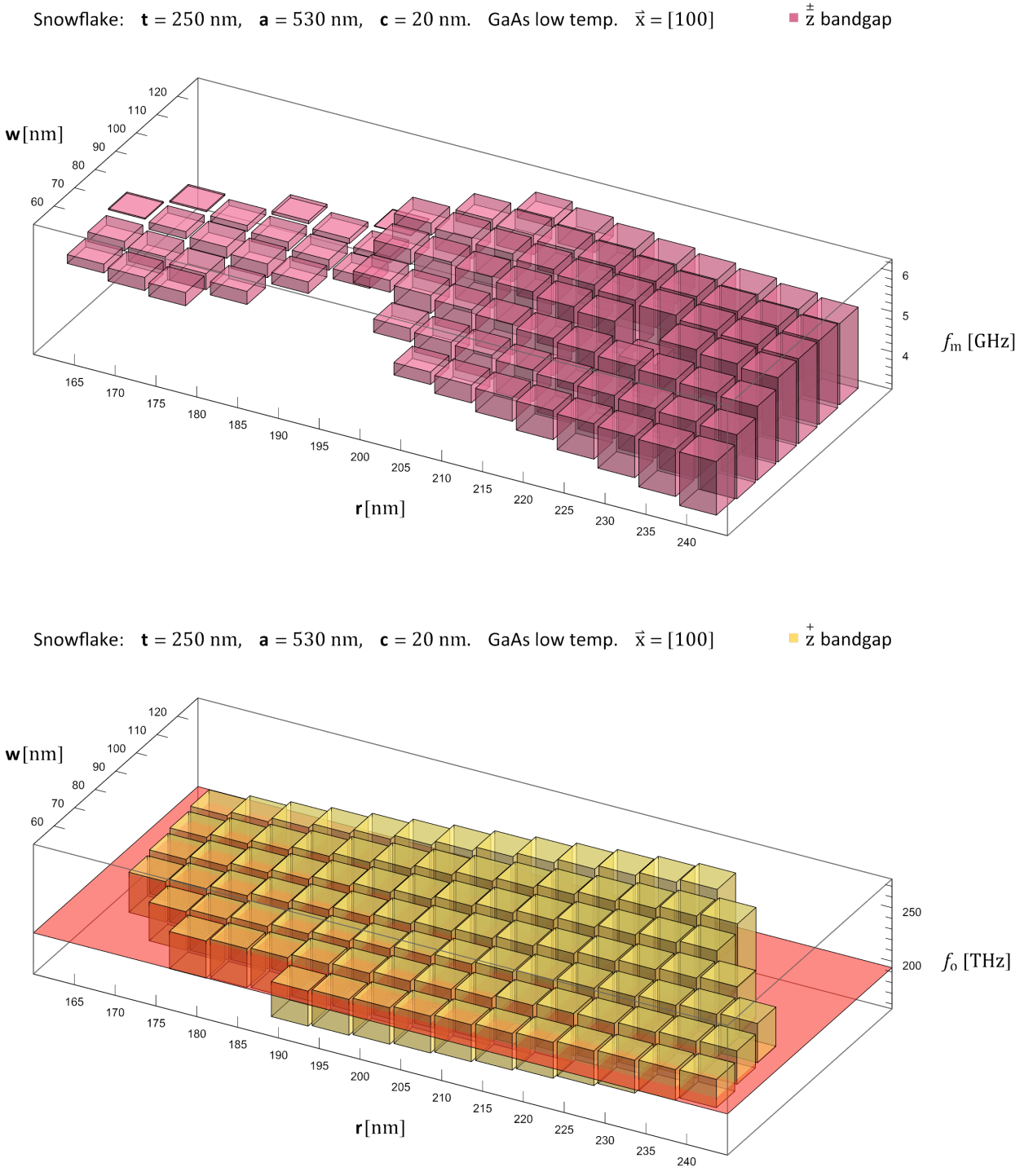

Figure U.9: Snowflake bandgap simulation survey with a = 530 nm. (Top) complete acoustic bandgaps, and (bottom) z mirror symmetric electromagnetic bandgaps that intersect with the laser frequency, 194 THz, shown in red.

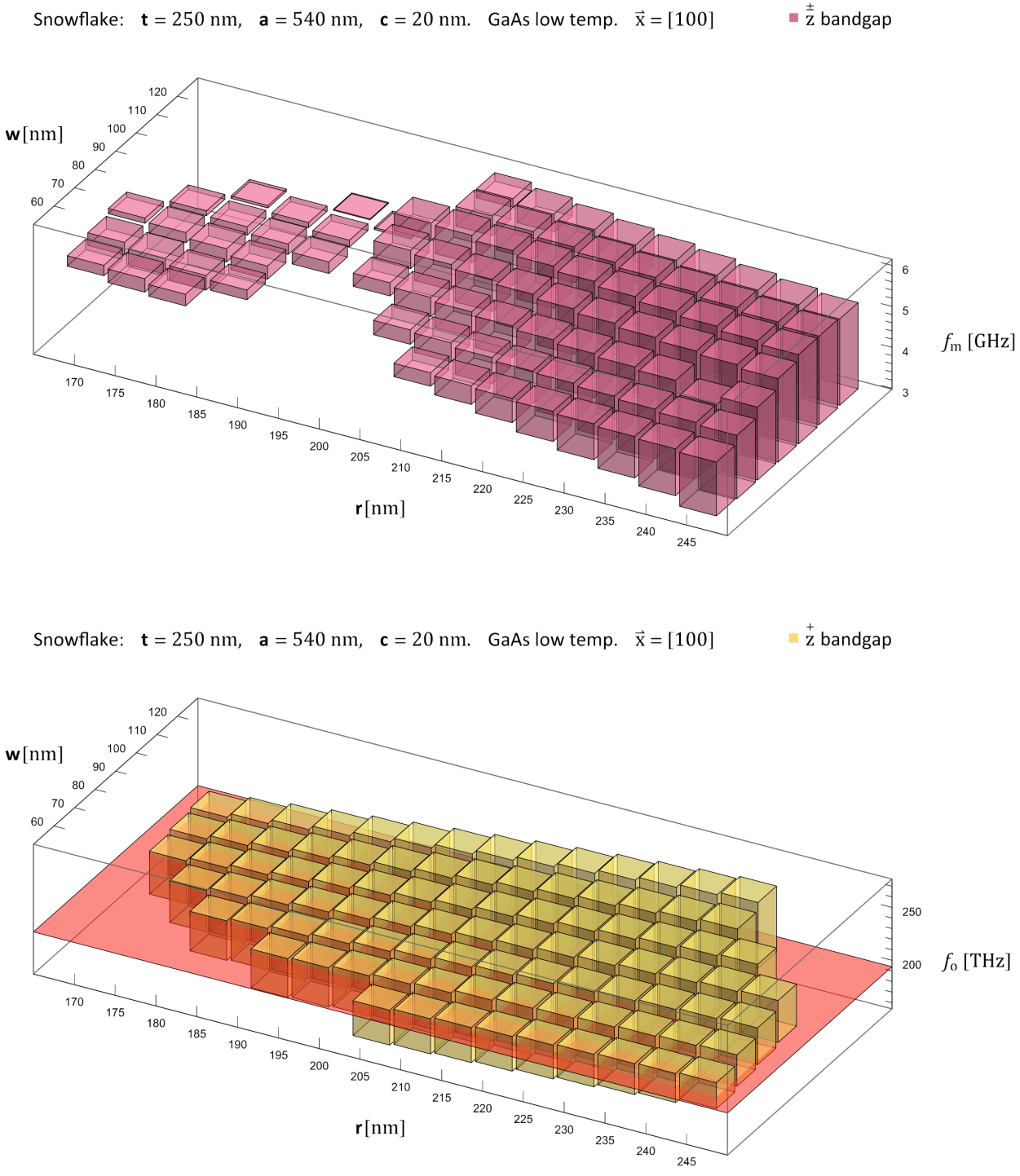

Figure U.10: Snowflake bandgap simulation survey with $\mathsf{a} = 540\,\text{nm}$. (Top) complete acoustic bandgaps, and (bottom) z mirror symmetric electromagnetic bandgaps that intersect with the laser frequency, 194 THz, shown in red.

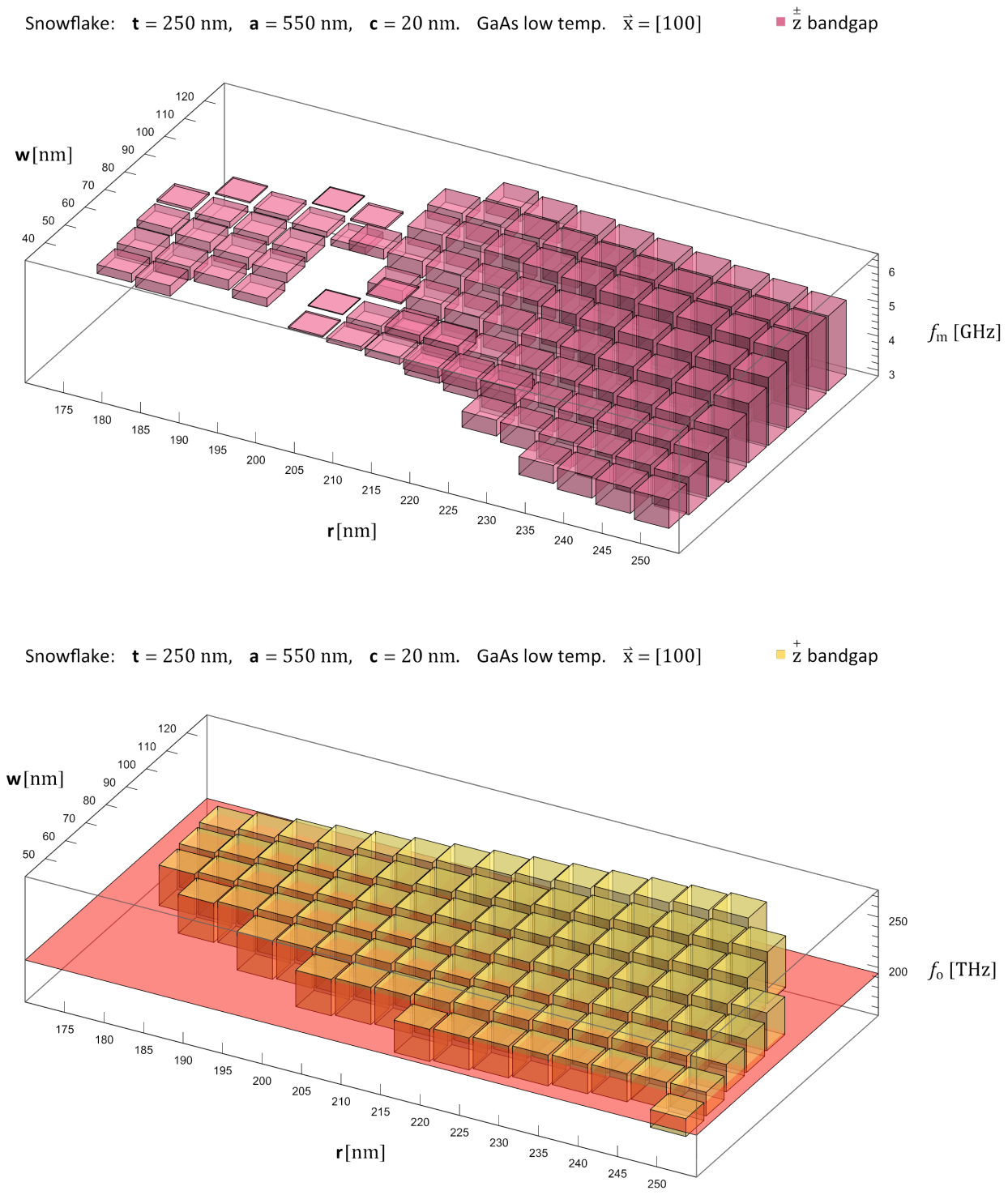

Figure U.11: Snowflake bandgap simulation survey with a = 550 nm. (Top) complete acoustic bandgaps, and (bottom) z mirror symmetric electromagnetic bandgaps that intersect with the laser frequency, 194 THz, shown in red.

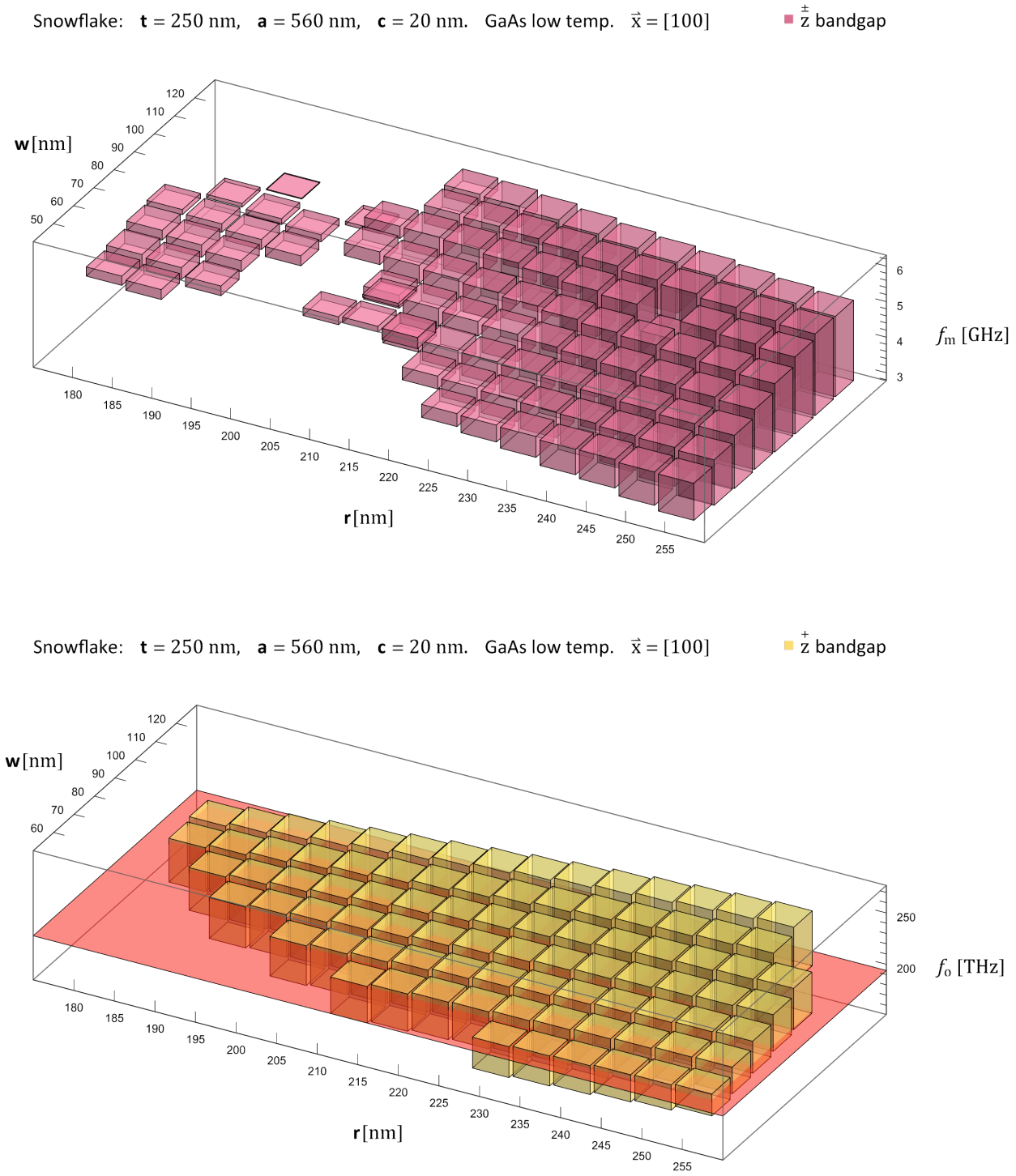

Figure U.12: Snowflake bandgap simulation survey with a = 560 nm. (Top) complete acoustic bandgaps, and (bottom) z mirror symmetric electromagnetic bandgaps that intersect with the laser frequency, 194 THz, shown in red.

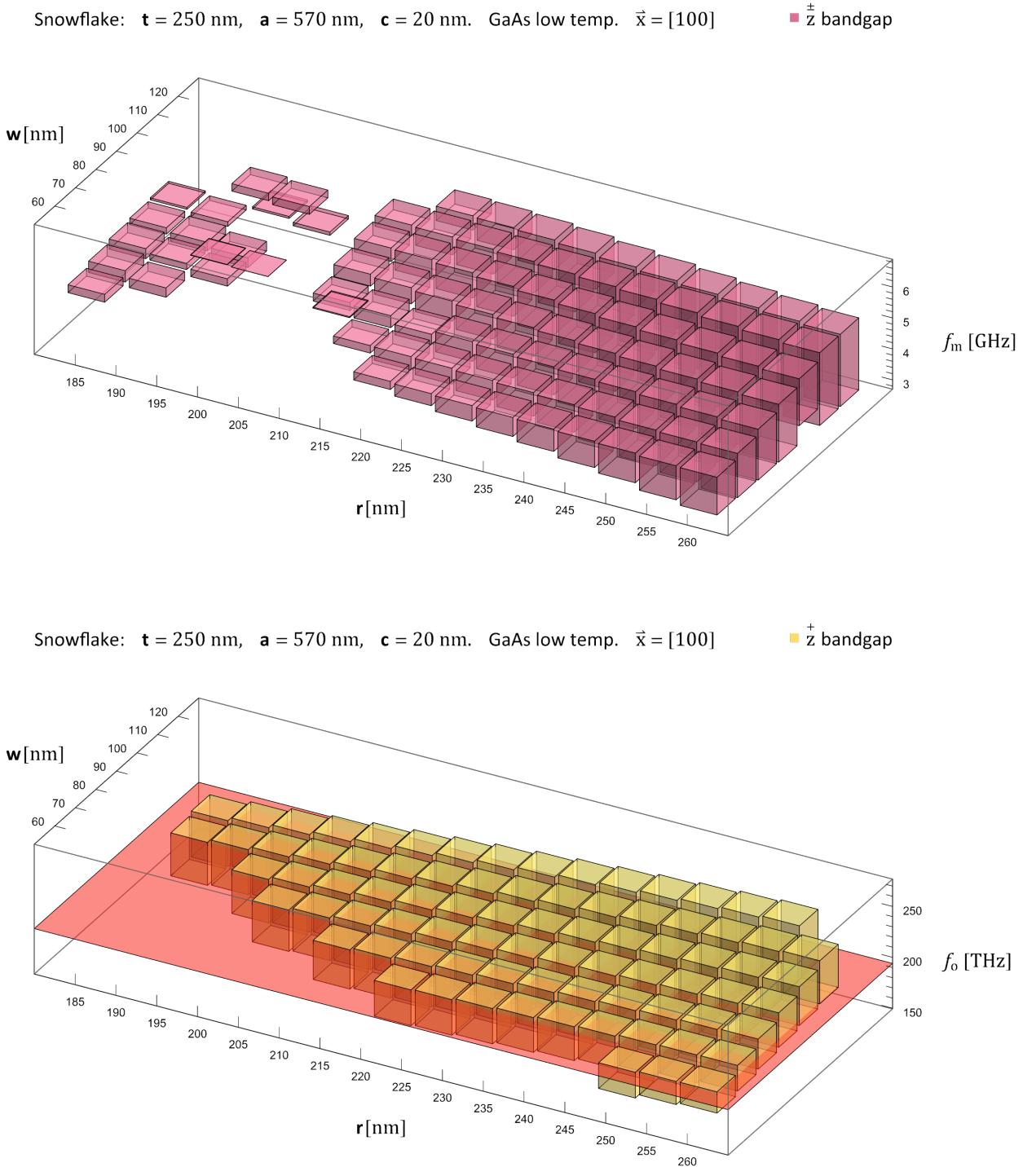

Figure U.13: Snowflake bandgap simulation survey with $\mathsf{a} = 570\,\text{nm}$. (Top) complete acoustic bandgaps, and (bottom) z mirror symmetric electromagnetic bandgaps that intersect with the laser frequency, 194 THz, shown in red.

APPENDIX V

Optical connection

In order to interface with the on chip photonics, we need a method of coupling light from the chip to a fiber optic. This connection is inherently difficult due to the vastly different spatial profiles of chip photonics and fiber optics. Photonic waveguides on our chip are less than a micron wide, whilst a standard fiber optic cable has a beam waist of 10 μm, although the emitted beam can be focused down with optical fiber tapering and polishing techniques.

V.1 Coupler types

To couple a fiber optic to on chip photonics, three main schemes, depicted in Fig. V.1, exist.

V.1.1 Direct coupler

Here an open fiber optic, in the plane of the chip, is shone directly down a photonic waveguide that comes to the edge of the chip. Whilst this method provides good coupling, it can only

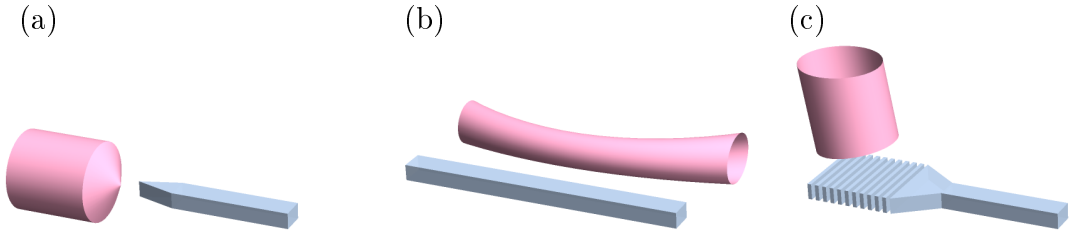

Figure V.1: Fiber optic to photonic waveguide coupling methods, (a) direct, (b) evanescent, and (c) grating.

access photonics that come to the edge of the chip and thus often requires long waveguides and cleaved edges. This method also suffers from cross coupling, light from the fiber optic which does not enter the waveguide can interact with other on chip photonics or scatter into other fiber optic ports. To improve coupling the on chip waveguide can be shaped into a spike [264] or disc [265]. For a ridge waveguide, improvements can also be made with the use of a large polymer cladding [266, 267].

V.1.2 Evanescent coupler

In this approach, a minor defect in a section of fiber optic cable is created and simply placed near an on chip waveguide for evanescent coupling [268–270]. Typically this involves tapering a region of the fiber to be very thin. This method has some useful advantages in that it can exploit the vertical dimension above the chip and can couple directly into a photonic waveguide or resonator. From an engineering side, however, tapering the optical fiber out [271] and securely positioning it in the right location can be a challenge.

V.1.3 Grating coupler

In a grating a coupler, a diffraction grating is used to scatter light out of the plane of the chip and into a fiber position above and aimed down [272]. This approach is the most convenient as it can exist anywhere on the surface of the chip and is easily swapped into an optical fiber setup. It suffers, however, from poor efficiency as much of the light scatters in unwanted directions. Many different designs of the grating exist, including curvature [273], grate variation [274], sub-wavelength transverse gratings [275, 276], and photonic crystal grates [277]. Due to it's ease with experimental probing, this is the method we use for developing a first generation device.

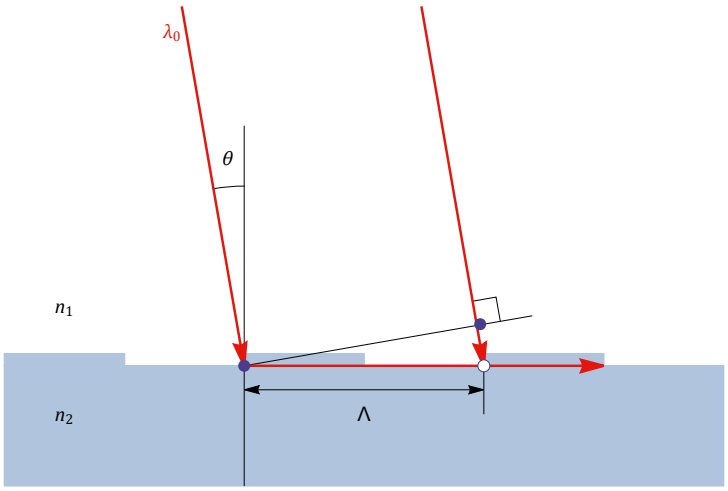

Figure V.2: Rays of vacuum wavelength λ_0 in a material of refractive index n_1 incident at angle θ onto a Bragg grating surface with pitch Λ and (effective) refractive index n_2. The two filled points are on the same incoming light wave front and have the same phase, whilst the empty point is where the phase needs to be matched.

V.2 Grating coupler theory

Numerous theses [278–280] have been written solely about grating couplers, and whilst certain guidelines exist, numerical simulation is required to analyze any particular grating design and set up. Here we will introduce the basic underlying theory to grating couplers.

V.2.1 Bragg grating

If we consider a plane wave incident, at angle θ, onto a bragg grating, of pitch Λ, we can expect maximal transmission when there is constructive interference between the incident light and scattered light propagating through the grating. Analyzing this using ray optics we can draw the picture in Fig. V.2. If we compare the paths of the two incoming rays, a multiple of pitches apart, and enforce phase matching at the point that they meet up, we

get

$$\Lambda \frac{n_2}{\lambda_0} - \Lambda \sin[\theta] \frac{n_1}{\lambda_0} = m \in \mathbb{Z} \, ,$$

$$\Rightarrow \quad m = \left(n_2 - n_1 \sin[\theta] \right) \frac{\Lambda}{\lambda_0} \in \mathbb{Z} \, , \tag{V.1}$$

which is the Bragg matching condition. The index of refraction n_2 here is an effective index for propagation through the grating coupler. Determining this typically requires some numerical computation and to complicates things more will depend on the pitch. As an approximation we can start with the effective index of refraction for an infinite dielectric plate and use the derived pitch as a starting point.

V.2.2 Curvature

To save space and focus the light to single point in the grating, we will want to use curved grating couplers. Following the diagram in Fig. V.3, if we have a plane wave incident at angle θ in the x-z plane, we want to find the set of points (x, y) in the device plane that will give the same phase at a focus placed at the origin. Enforcing this gives us the following equation for the grating shape,

$$\sqrt{x^2 + y^2} \frac{n_2}{\lambda_0} - x \sin[\theta] \frac{n_1}{\lambda_0} = \text{constant} \, ,$$

or

$$a = b\, x + \sqrt{x^2 + y^2} \, , \tag{V.2}$$

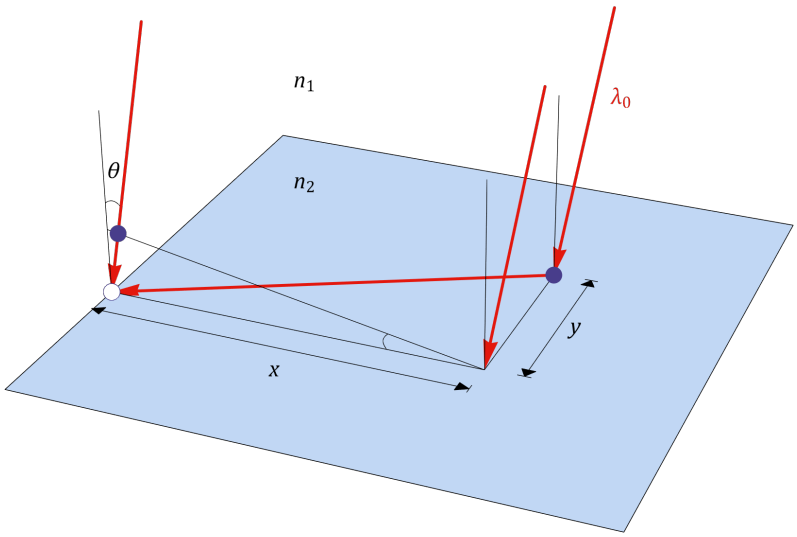

Figure V.3: Rays of vacuum wavelength λ_0 in a material of refractive index n_1 incident at angle θ onto a plane with (effective) refractive index n_2. The two filled points are on the same incoming light wave front and have the same phase, whilst the empty point, at the focus, is where the phase needs to be matched.

where a is the radius along the y axis ($x = 0$), and

$$b = -\frac{n_1}{n_2} \sin[\theta] \in (-1, 1) \tag{V.3}$$

is the curvature extension parameter. A plot of the curvature function (V.2) is given in Fig. V.4; when $b = 0$ the function produces a circle, but in general it is not elliptical. For this geometry we define pitch and filling factor along the x axis.

V.2.3 Polarization

Grating couplers tend to work with the electric field polarized along the grates (transverse to the propagation direction). This orientation puts the electric field in the direction of con-

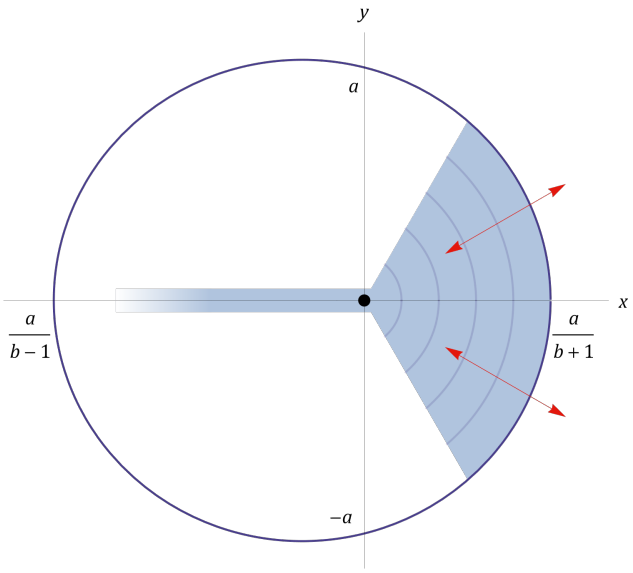

Figure V.4: Plot of the curvature function (V.2), with $b = 0.25$, highlighting the $x > 0$ region used for the grating coupler.

tinuous symmetry, y-direction using the coordinates here, as determined by the geometry's electric permittivity. Thus for light travelling in the x-direction of an attached waveguide, the mode will neccessarily have y anti-mirror symmetry.

Considerations from the opticmechanical cavity and photonic crystal band structure (see App. U) dictate that we want an electric field that is z (normal to the device plane) mirror symmetric. Hence the input/output mode to the device waveguide beam (see App. S) must be $\overset{-}{y}\overset{+}{z}$ (see App. D).

In a single mode optical fiber the carried electromagnetic mode is HE_{11} or approximately linearly polarized LP_{01}. To work with the grating coupler, the fiber optic cable needs to be orientated such that its $\vec{E}$ polarization axis aligns parallel to the grates, i.e. y-direction.

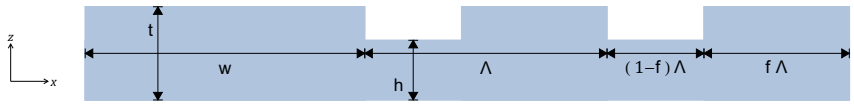

Figure V.5: Diagram of grating coupler dimensions, t is the suspended layer thickness, Λ is the grating pitch, f is the filling factor, and h is the grate gap height.

V.3 Grating coupler design

The heterostructure wafers being used are 250 nm GaAs on AlGaAs, however due to the low permittivity contrast this a poor material stack for making a grating coupler [278]. Instead we will want to have a suspended grating coupler, as is the case for the optomechanic crystal part of the device. Furthermore as this device will be using an existing experimental set up, the fiber optic cables are fixed to be incident at $\theta = 8^\circ$ from normal[1].

The remaining parameters to design for are pitch Λ, filling factor (a.k.a. duty cycle) f, curvature b, and grate gap height h, as depicted in Fig. V.5. The number of total grates needs to be sufficiently large such that the 10 μm diameter fiber optic beam is covered, but not too great that the grating coupler can not be suspended. Optimization of these parameters can be carried out by running numerical simulations but it helps to start with some estimates.

The grating coupler pitch can be derived from the Bragg matching condition (V.1). Above the grating coupler we have air/vacuum with $n_1 = 1$ and in the grating coupler we can use an infinite plate model, App. R; for a TE $\overset{+}{z}$ mode at 194 THz in 250 nm thick $n_{\text{GaAs}} = 3.32$, the effective index of refraction is $n_2 = 2.78$. Putting these numbers into (V.1) with $\lambda_0 = c/(194\,\text{THz}) = 1545\,\text{nm}$ and $\theta = 8^\circ$, we get $\Lambda = 585\,\text{nm}$ for $m = 1$. Similarly we can estimate the curvature extension parameter b from (V.3) to be $b = -0.050$.

1. This is an optimal angle for 220 nm silicon on insulator grating couplers.

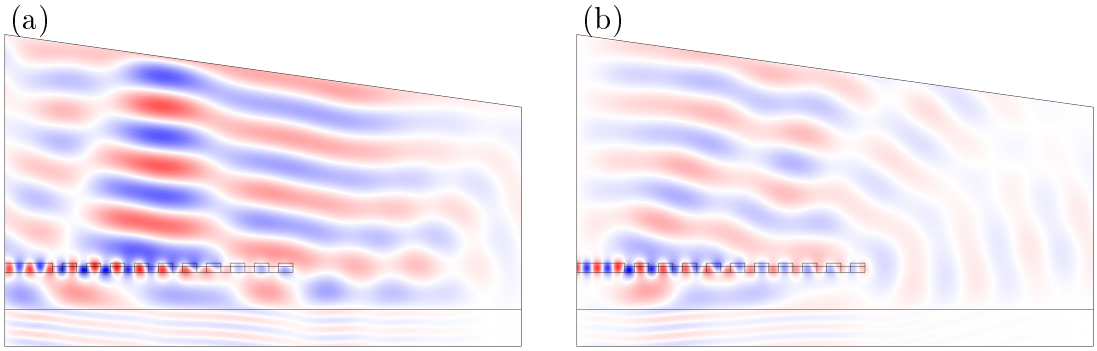

Figure V.6: Two-dimensional models of a suspended 10 period grating coupler with $\Lambda = 650\,\text{nm}$, $\mathsf{f} = 0.6$, $\mathsf{h} = 150\,\text{nm}$, $\theta = 8^\circ$, showing E_y (into the page) at 194 THz. Model (a) has an aerial input port, whilst (b) has a slab input port.

V.3.1 Two-dimensional simulations

Two-dimensional simulations are significantly faster than full three-dimensional simulations and allow us to quickly narrow down some of the design parameters. In the two-dimensional model the grating is assumed to extend infinitely in the y-direction, and our parameters of concern are pitch, filling factor, and the grate gap height. Finite element modeling is carried out using Comsol [181] with typical models depicted in Fig. V.6. For each set of geometry parameters a two models are made, one with an input port connected to the slab, and one with an input port above the coupler in a Gaussian shape and titled at 8°, both with an E_y incoming field. For each model the proportional power flowing through the opposing port is measured and then combined for an overall rating of effectiveness. The simulations also included bulk GaAs 1 µm below the suspended slab.

Simulations were carried out with pitches ranging from 500 nm to 1200 nm, filling factors from 0.2 to 0.8, and grate gap heights from 0 to 200 nm; significantly higher sampling was carried out in the 600 nm to 700 nm pitch range. A 3D plot summarizing the combined transfer efficiencies is given in Fig. V.7 along with sample 2D slices. From these results it is immediately obvious that a grate gap height of more than half the total thickness is needed

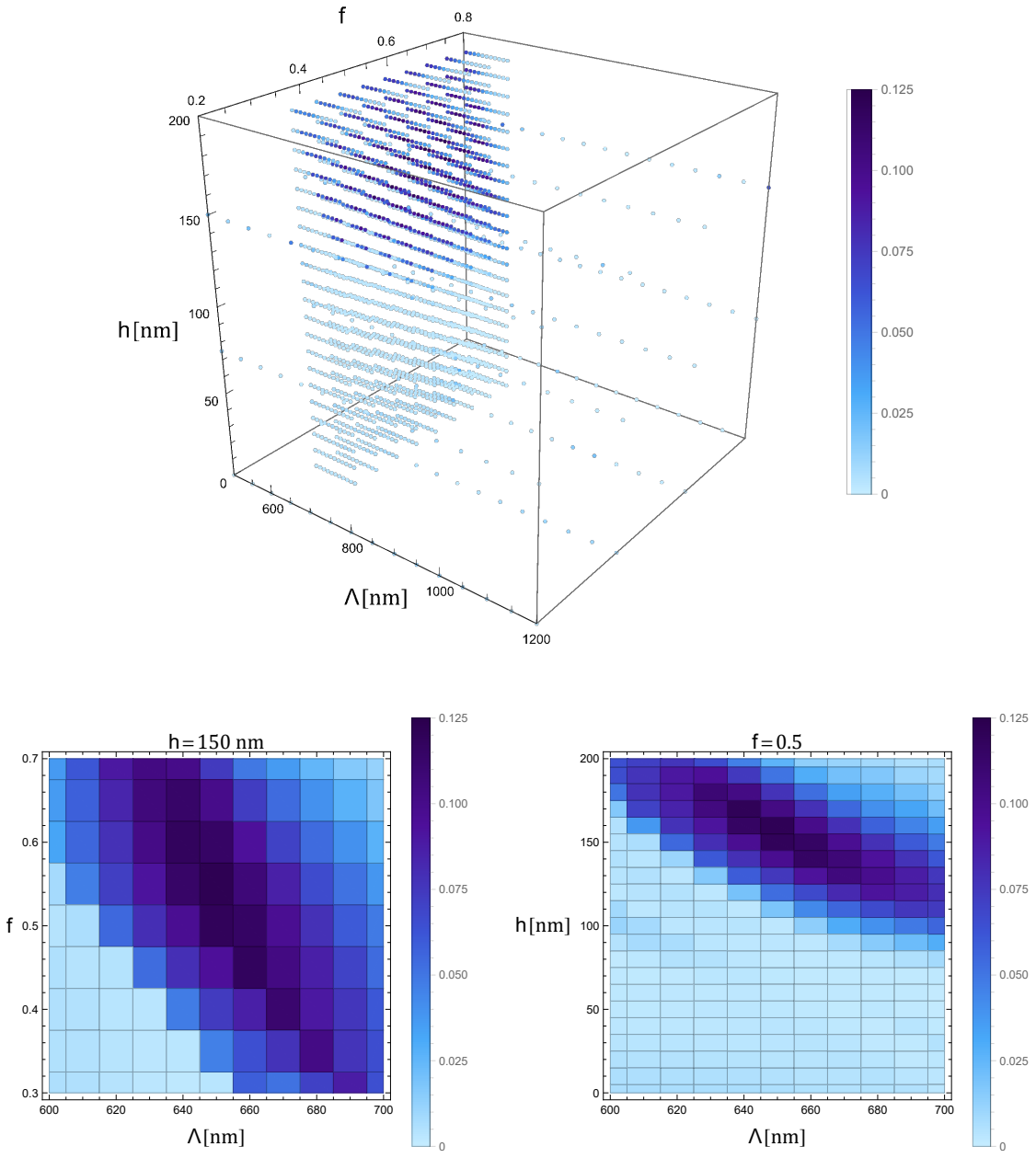

Figure V.7: Plots of the simulated combined transfer efficiency of two-dimensional 10 period grating coupler models with $\mathtt{t} = 250\,\mathrm{nm}$, and $\theta = 8^{\circ}$. Combined refers to multiplication between the slab input and the air input transfers.

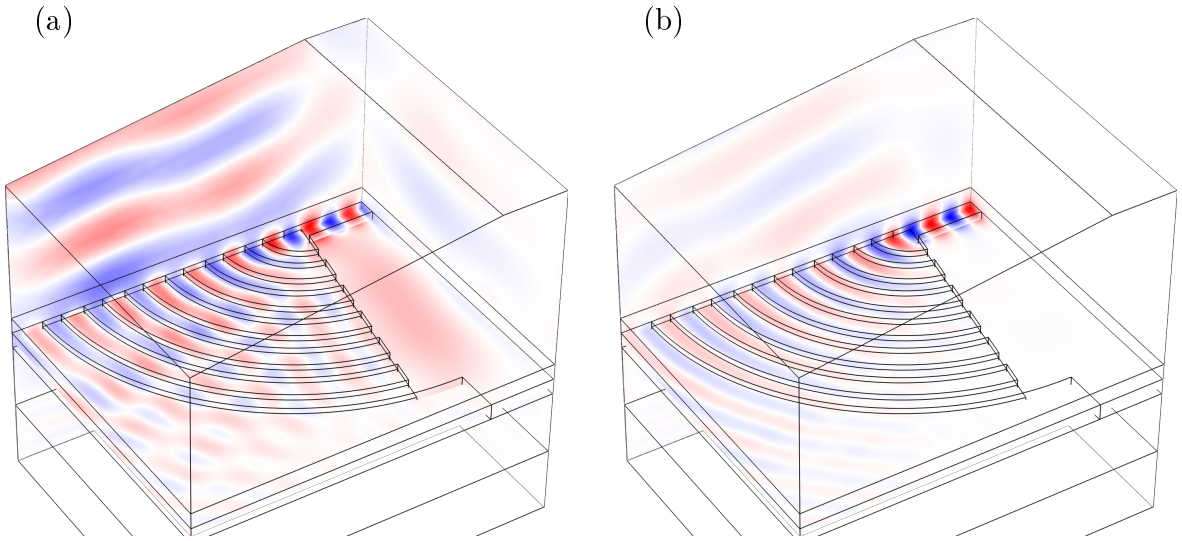

Figure V.8: Three-dimensional models of a suspended 6 period grating coupler with $\Lambda = 640\,\text{nm}$, $\mathsf{f} = 0.55$, $\mathsf{h} = 160\,\text{nm}$, $b = -0.05$, $\theta = 8^\circ$, showing E_y at 194 THz. Model (a) has an aerial input port, whilst (b) has a beam input port.

to have any appreciable transfer through the grating coupler. Looking at Fig. V.7 (c), we also note that as the grate gap height approaches the full thickness of the slab, the optimal pitch tends toward the value estimated by the Bragg matching condition under the assumption of an infinite dielectric plate. The introduction of partial air gaps in the slab lowers the effective index of refraction, leading to larger optimal pitch than first estimated. The best combined transfer efficiency found was 0.124 at $\Lambda = 640\,\text{nm}$, $\mathsf{f} = 0.55$, $\mathsf{h} = 160\,\text{nm}$.

If we use (V.1) with $\Lambda = 640\,\text{nm}$ to recalculate an effective index of refraction, we get $n_2 = 2.55$. Putting this into V.3 gives an updated curvature extension parameter of $b = -0.054$, only marginally different.

V.3.2 Three-dimensional simulations

Three-dimensional simulations are far more computationally intensive but, importantly, closer to reality. Typical models created using Comsol [181] are shown in Fig. V.8. Due to limitations in computing power however, non-vertically symmetric models were limited

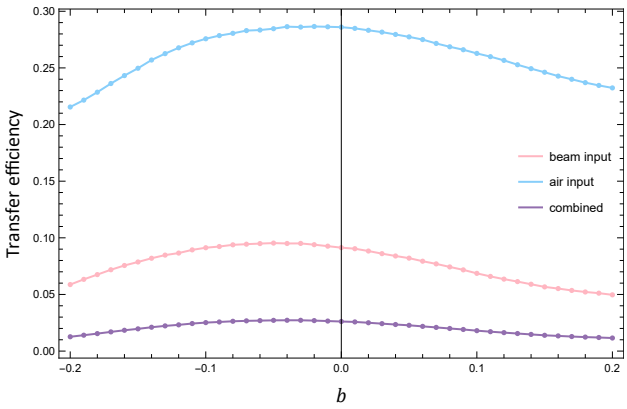

Figure V.9: Plot of transfer efficiency at 194 THz against varying curvature extension parameter b for three-dimensional supsended 6 period grating couplers models with $\mathsf{t} = 250\,\text{nm}$, $\Lambda = 640\,\text{nm}$, $\mathsf{f} = 0.55$, $\mathsf{h} = 160\,\text{nm}$, $\theta = 8^\circ$.

to 6 grates, which leads to some difficulties when simulating power coming in from an aerial port that is 10 µm wide and hence larger than the model and grate collecting region.

The three-dimensional model allows us to optimize the curvature parameter b, plotted in Fig. V.9, and agrees with the predicted values. Sweeping the remaining parameters in the vicinity of the two-dimensional model optimal point we can build a new set of combined transfer efficiency plots in Fig. V.10 and Fig. V.11. The best combined transfer efficiency found was 0.030 at $\Lambda = 640\,\text{nm}$, $\mathsf{f} = 0.65$, $\mathsf{h} = 150\,\text{nm}$.

V.3.3 Suspended beam to photonic crystal

Early designs of the grating coupler had it directly attached to the photonic crystal but difficulties in aligning the partial etch step to within 100 nm as would be needed necessitated separating the grating coupler with a suspended beam waveguide. This separation introduces two new design variables, the photonic crystal edge shape, and the suspended beam width.

Four styles of photonic crystal edges, depicted in Fig. V.12 were investigated. Three-dimensional simulations were carried out with a suspended beam waveguide input and output

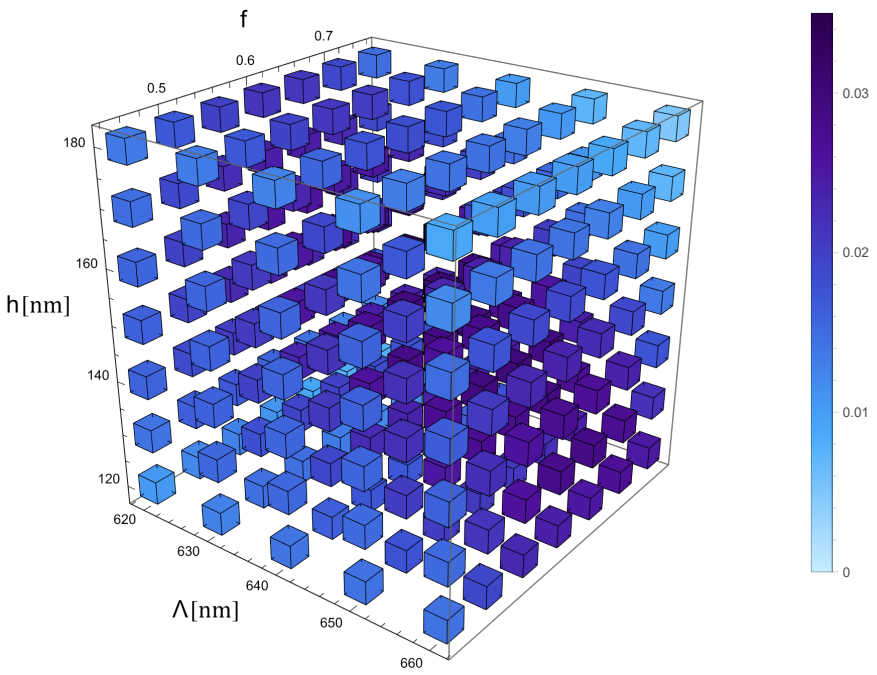

Figure V.10: Three-parameter plot of the simulated combined transfer efficiency of three-dimensional 6 period grating coupler models with $\mathsf{t} = 250\,\text{nm}$, and $\theta = 8^{\circ}$. Combined refers to multiplication between the slab input and the air input transfers.

($\bar{y}\,\overset{+}{z}$ mode), the photonic crystal with a blank row waveguide in the middle, and different combinations of photonic crystal edge interfaces on each side. Results for varying sizes of the photonic crystal center are given in Fig. V.13. The best photonic crystal to suspended waveguide interface is consistently that of an 'angled out' shape.

The final variable we have control over is the suspended beam waveguide width, and we can simulate it's effect when interfacing with both the photonic crystal and grating coupling. For the photonic crystal side, simulations of the type used for the edge shape were carried out, with results given in Fig.V.14. For the grating coupler side, simulations of the type used for the three-dimensional grating coupler were carried out, with results given in Fig.V.15. Above 400 nm the response to the suspended beam waveguide width is flat. Following the dispersion information for a dielectric beam, App. S, we want the beam to be as narrow as

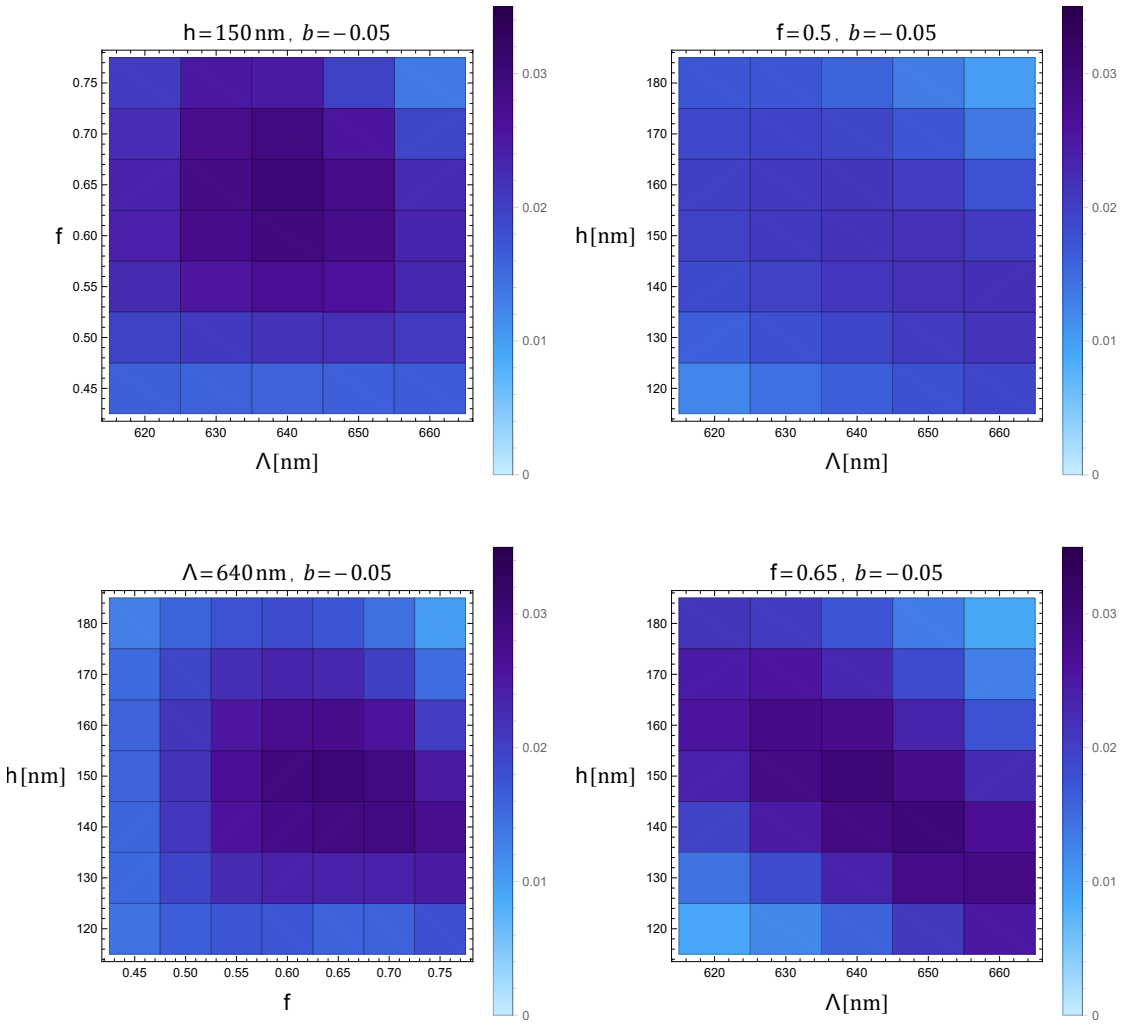

Figure V.11: Two-parameter slices of the simulated combined transfer efficiency of three-dimensional 6 period grating coupler models with $\mathsf{t} = 250\,\text{nm}$, and $\theta = 8^{\circ}$.

possible to help filter out unwanted modes, and thus use a width of $\mathsf{wg} = 400\,\text{nm}$.

V.4 Grating coupler fabrication

The grates are marked out using electron beam lithography concurrent with the optomechanical crystal, the non-zero grating gap height h, however, requires a partial etch step to be carried out separate to the full etch that goes all the way through the top GaAs layer.

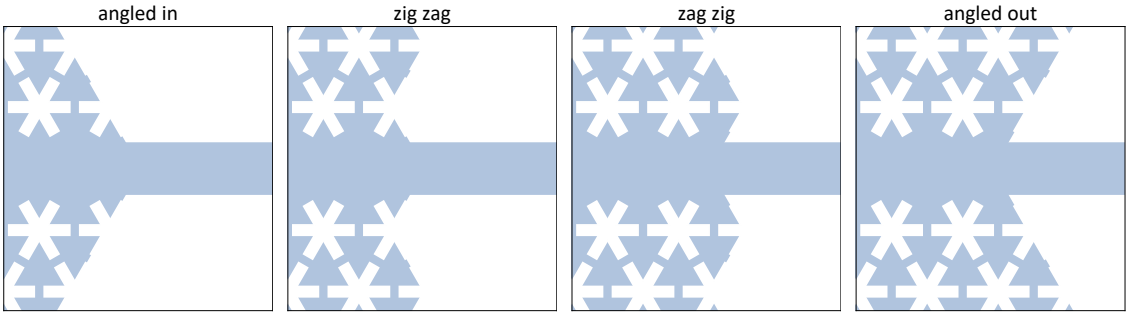

Figure V.12: Diagrams of photonic crystal to suspended beam waveguide interfaces.

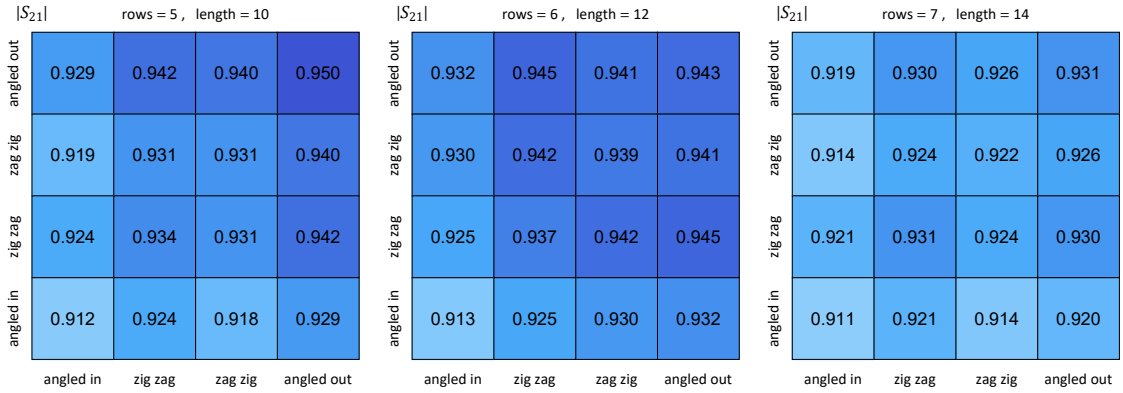

Figure V.13: Transmissions $|S_{21}|$ at 194 THz through a photonic crystal of various sizes with a blank row waveguide and various combinations of photonic crystal edges to a suspended beam input and output. The model enforces $\overset{-}{y}\,\overset{+}{z}$ mirror symmetries with wave propagation in the x-direction. The snowflake photonic crystal has dimensions $\mathsf{t} = 250\,\text{nm}$, $\mathsf{a} = 560\,\text{nm}$, $\mathsf{r} = 240\,\text{nm}$, $\mathsf{w} = 80\,\text{nm}$, $\mathsf{c} = 20\,\text{nm}$.

For nominally 250 nm thick GaAs and $\mathsf{h} = 150\,\text{nm}$, a 100 nm deep etch was achieved with 30 s of the chlorine argon etch described in Sec. 4.2. To accommodate the release, windows are etched through behind the grating. A scanning electron microscope (SEM) image of a grating coupler is shown in Fig. V.16.

V.5 Grating coupler performance

The chip optical coupling was tested by simply connecting two grating couplers together with a suspended waveguide, sometimes with side coupled ring resonator. Optical measurements

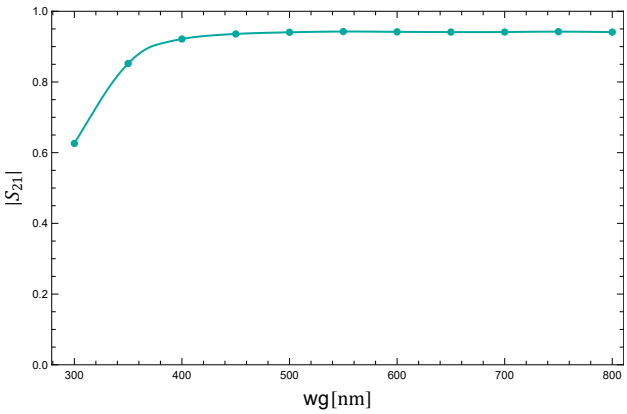

Figure V.14: Transmission $|S_{21}|$ at 194 THz through a photonic crystal (6 rows and 12 length in snowflakes) with a blank row waveguide, and angled out edges, to suspended beam waveguides (width wg) at the input and output. The model enforces $\overset{-}{y}\,\overset{+}{z}$ mirror symmetries with wave propagation in the x-direction. The snowflake photonic crystal has dimensions t = 250 nm, a = 560 nm, r = 240 nm, w = 80 nm, c = 20 nm.

were performed with the setup described in App. Σ. Geometry measurements were carried out by analyzing SEM pictures as described in App. W. Peak individual grating coupler transmissions of $> 35\%$ were found with patterns of $\Lambda_{\text{pattern}} = 638\,\text{nm}$ and measured $\Lambda_{\text{SEM}} = 633\,\text{nm}$[2], $\mathsf{f}_{\text{SEM}} = 0.51$. A sample transmission of a test device is given in Fig. V.17.

2. A scale error of $\lesssim 1\%$ is typical.

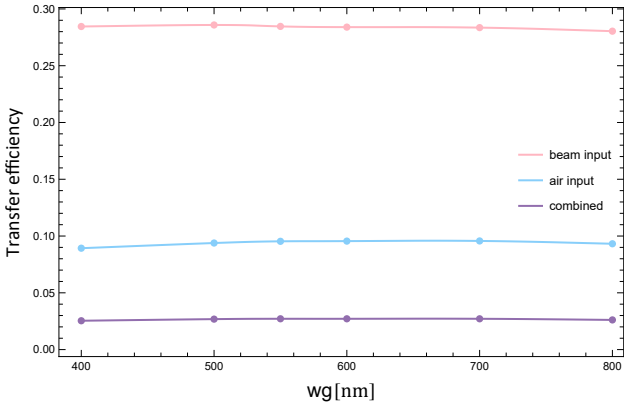

Figure V.15: Transfer efficiencies at 194 THz of a suspended beam waveguide (width wg) connected to a grating coupler with aerial port. The model enforces $\bar{y}\,\dot{z}$ mirror symmetries with wave propagation in the x-direction. The grating coupler has 6 grate periods and parameters $\Lambda = 640\,\text{nm}$, $\mathsf{f} = 0.55$, $\mathsf{h} = 160\,\text{nm}$, $b = -0.05$, $\theta = 8^\circ$.

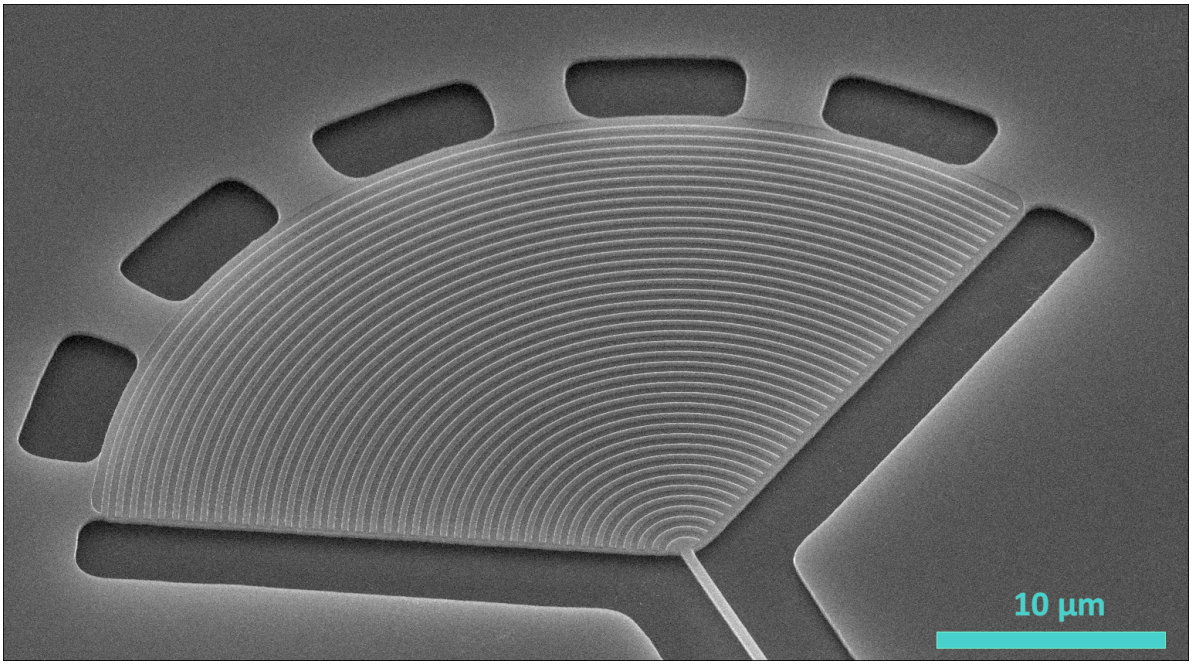

Figure V.16: SEM image of a suspended grating coupler.

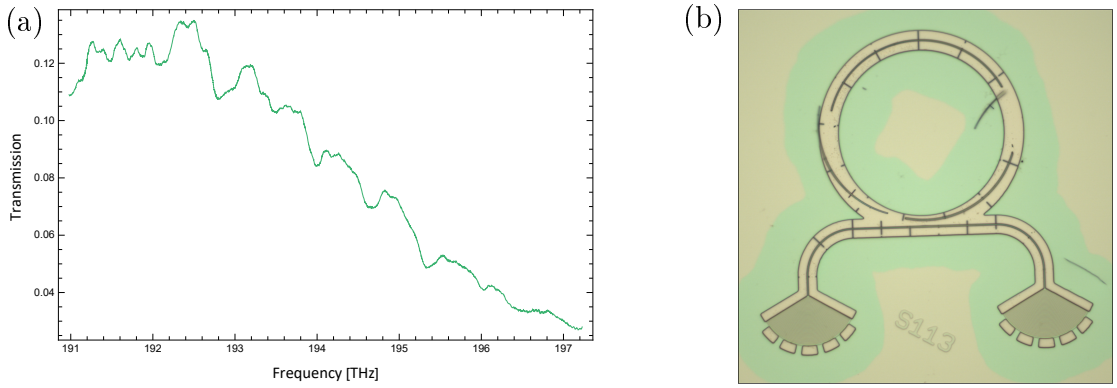

Figure V.17: Example test device with particularly good optical transmission. (a) Device transmission spectrum, as there are two grating couplers their individual performance is at worst the square root. (b) Microscope image of the measured test device, with unfortunately a broken ring resonator. The two coupler focii are 127 µm apart.

APPENDIX W

Grating analysis

Fabrication outcomes of the grate structures in the grating couplers can be carried out through image analysis and curve fitting.

W.1 Grate parameters

Following App. V, grates are designed according to

$$r = \frac{a}{b\,\cos[\phi] + 1}\,,$$

where a is a constant for each individual grate curve. The grating pitch is defined along the x axis ($\phi = 0$) such that,

$$\frac{a[k]}{b+1} = \mathsf{w} + \Lambda\, k \quad : \quad k \in \{0, 1-\mathsf{f}, 1, 2-\mathsf{f}, 2, 3-\mathsf{f}, \dots\}\,,$$

according to Fig.W.1.

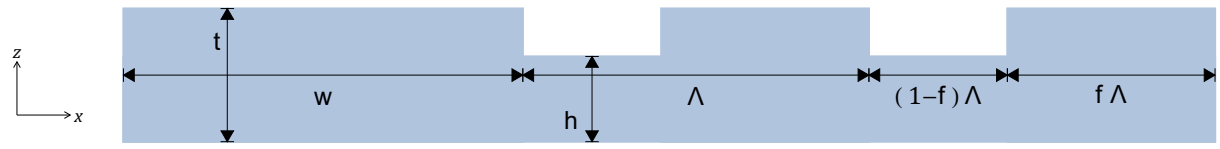

Figure W.1: Diagram of grating coupler dimensions.

For an arbitrary grating focus, (x_0, y_0) and orientation, ϕ_0, we have

$$\sqrt{\left(x - x_0\right)^2 + \left(y - y_0\right)^2} = \frac{a[k]}{b\,\cos\left[\arctan\left[\frac{y-y_0}{x-x_0}\right] - \phi_0\right] + 1}\,,$$

for points $\{(x, y)\}_k$ in a particular curve k. The full set of parameters are

Λ	grating pitch,
f	grating fill factor,
w	distance from grating focus to first grate,
b	curvature extension parameter,
(x_0, y_0)	grating focus,
ϕ_0	grating orientation,
t	suspended slab thickness,
h	lower grating height.

W.2 Image analysis

From a scanning electron microscope (SEM) image, pixels associated to the grate curves can be found by performing edge detection. Separating the points into sets for separate curves is done by collecting points into connected sets, and stitching together as needed, The sets can then be ordered based on their mean distance to an estimated grating focus. An example image with fits described below is depicted in Fig. W.2.

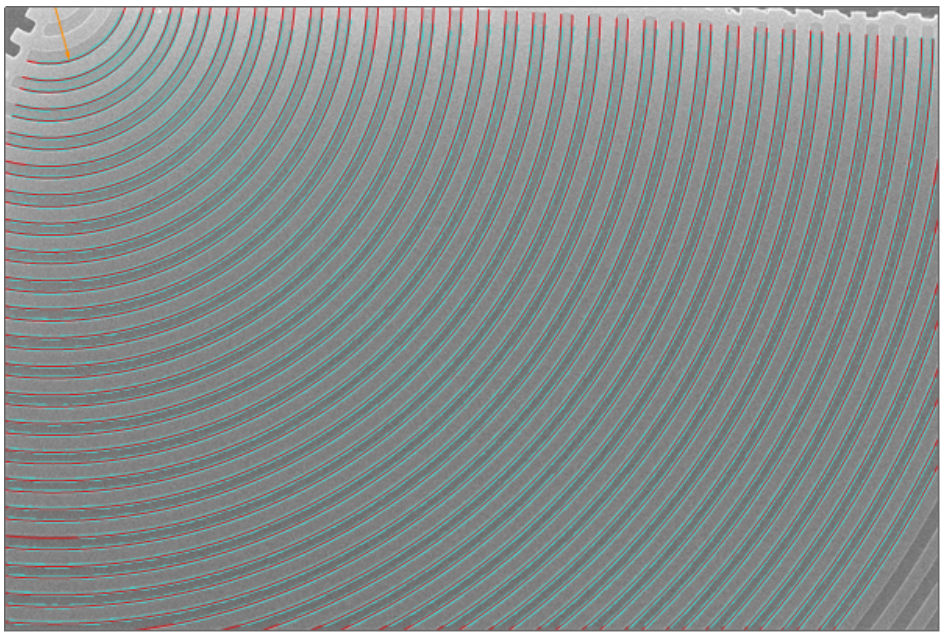

Figure W.2: SEM image of a grating coupler. Edge detected points in cyan, and grating fit in red with orange arrow indicating (x_0, y_0), ϕ_0 and w'.

W.3 Fitting

For an ordered list of sets of points, $\{(x, y) \in A_i\}_{i=1}^{m}$, corresponding to successive curves $i = 1, 2, 3, \ldots, m$ we can write

$$\frac{a_i}{b+1} = \mathsf{w}' + \Lambda\left(\lfloor (i-1)/2 \rfloor + \big((i-1) \bmod 2\big)\,\mathsf{f}'\right)$$

where w' and f' are parameters specific to the subregion of the grating we are fitting. Thus for each point from our image analysis (x, y), associated with curve i, the residual distance is

$$\sqrt{(x-x_0)^2 + (y-y_0)^2} - \frac{(b+1)\left(\mathsf{w}' + \Lambda\left(\lfloor (i-1)/2 \rfloor + \big((i-1) \bmod 2\big)\,\mathsf{f}'\right)\right)}{b\,\cos\left[\arctan\left[\frac{y-y_0}{x-x_0}\right] - \phi_0\right] + 1}\,.$$

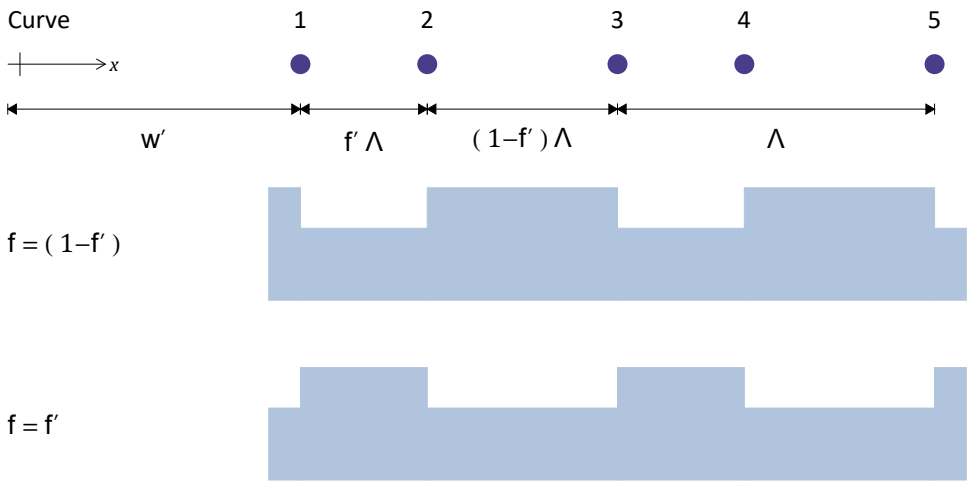

Figure W.3: Diagram of grating curve fit situations.

Thus we can fit our full set of points by minimizing the objective function

$$S = \sum_{i=1}^{m} \sum_{(x,y)\in A_i} \left(\sqrt{(x-x_0)^2 + (y-y_0)^2} - \frac{(b+1)\left(\mathsf{w}' + \Lambda\left(\lfloor (i-1)/2 \rfloor + ((i-1) \bmod 2)\,\mathsf{f}'\right)\right)}{b\cos\left[\arctan\left[\frac{y-y_0}{x-x_0}\right] - \phi_0\right] + 1} \right)^2 .$$

This is equivalent to a self-dependent multivariate fit of the form

$$\begin{pmatrix} x \\ y \end{pmatrix} \sim \vec{f}(x,y,i) = \begin{pmatrix} x_0 \\ y_0 \end{pmatrix} + \frac{(b+1)\left(\mathsf{w}' + \Lambda\left(\lfloor (i-1)/2 \rfloor + ((i-1) \bmod 2)\,\mathsf{f}'\right)\right)}{b\cos\left[\arctan\left[\frac{y-y_0}{x-x_0}\right] - \phi_0\right] + 1} \begin{pmatrix} \cos\left[\arctan\left[\frac{y-y_0}{x-x_0}\right]\right] \\ \sin\left[\arctan\left[\frac{y-y_0}{x-x_0}\right]\right] \end{pmatrix} .$$

Our full set of fit parameters are $\underline{p} = \{x_0, y_0, \phi_0, \Lambda, \mathsf{f}', \mathsf{w}', b\}$, which can be given starting estimates from the design or manually based on the original image.

Unless our image and fit includes the first grate, w' will be some arbitrary value we're not

interested in, and f will be $(1-\mathsf{f}')$ or f' based on the 'polarity' of our fitting region. We can determine the polarity for our image's fit by doing a brightness comparison of the region between curves 1 and 2, and between 2 and 3,

$$\mathsf{f} = \begin{cases} \mathsf{f}' & : \quad \text{height}[1,2] > \text{height}[2,3] \\ (1-\mathsf{f}') & : \quad \text{height}[2,3] > \text{height}[1,2] \end{cases} .$$

A diagram of the two situations is given in Fig. W.3.

If $\underline{\hat{p}}$ are the found parameters, the covariance matrix is

$$\underline{\underline{\Sigma_p}} = \frac{2\,S(\underline{p})}{n_{\text{pts}} - n_{\underline{p}}} \left(\frac{\partial}{\partial \underline{p}} \otimes \frac{\partial}{\partial \underline{p}} S(\underline{p}) \right)^{-1} \Bigg|_{\underline{p}=\underline{\hat{p}}} ,$$

where $n_{\text{pts}} = \sum_{i=1}^{m} |A_i|$ is the number of points fit to, and $n_{\underline{p}} = 7$ is the number of parameters. Computing the covariance matrix can be time consuming.

W.4 Edge adjustment

The edge detection algorithm tends to return the shorter side of an edge. To fix this, we can adjust

$$\mathsf{w}' \mapsto \begin{cases} \mathsf{w}' + \Delta & : \quad \text{height}[1,2] > \text{height}[2,3] \\ \mathsf{w}' - \Delta & : \quad \text{height}[2,3] > \text{height}[1,2] \end{cases} ,$$

$$\mathsf{f} \mapsto \mathsf{f} - \frac{2\,\Delta}{\Lambda} ,$$

where $\Delta \sim 1\,\text{px}$ is the adjustment.

APPENDIX X

Disc resonators

The first optomechanical resonator designs explored were disc resonators suspended within a snowflake optomechanical crystal slab of gallium arsenide, as depicted in Fig. X.1. To first order, acoustic modes in the resonator can be notated by drum modes [281] (that of a two-dimensional disc membrane) along with out-of-plane mirror symmetry, and electromagnetic modes notated by cylindrical cavity modes [220, 282]. For small discs, with sizes on the order of one wavelength, we're primarily interested in the fundamental mirror symmetric acoustic mode (breathing mode) $(0,1)+$, and electromagnetic modes $\mathrm{TE}_{0\,1\,1}$, $\mathrm{TE}_{0\,2\,1}$. Mirror symmetry of the acoustic mode is vital for optomechanical coupling (see App. E).

Simulations were carried out as described in Ch. 3, but ultimately disc resonators never made it to fabrication as their optical quality factors were found to be inadequate.

X.1 Proximity variations

In addition to the basic structures suspending the disc shown in Fig. X.1, a host of other styles were also toyed with. Fig. X.2 depicts a wide range of geometries connecting the disc to the surrounding crystal pattern. Whilst the different styles shift the resonance frequencies around, they didn't offer any improvements to the optomechanical coupling or quality factors.

X.2 Tuning algorithm

For particular snowflake crystal pattern dimensions and cut-out geometry, the disc's optical resonance was tuned to 194 THz by adjusting the disc radius. This was carried out by

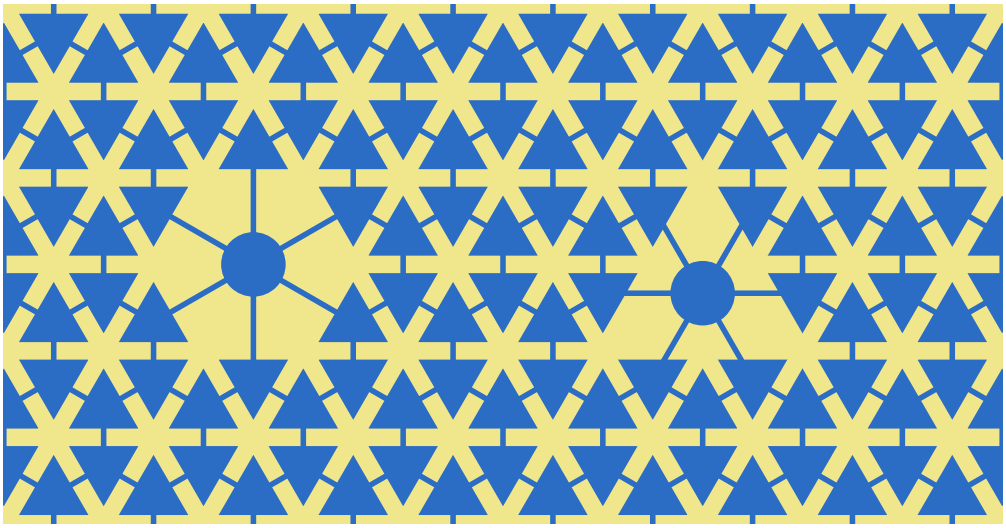

Figure X.1: Basic disc resonator designs.

iterative simulations guided by a simple algorithm to estimate the appropriate disc radius from obtained simulation results. The flowchart for the full algorithm flow is given in Fig. X.3.

The first step in the algorithm was create the snowflake primitive cell model to determine the dispersion relations (see App. U) and extract the band gaps (if they exist) for the given set of snowflake dimensions. If 194 THz is not covered by a $\overset{+}{z}$ band gap the algorithm simply ends as those snowflake dimensions do not support trapping of the desired optical frequency. If 194 THz is covered, the algorithm proceeds by creating a model of a disc resonator with a rough guess for the disc radius. This model was built enforcing $\overset{+}{x}$, $\overset{+}{y}$, $\overset{+}{z}$ mirror symmetries for the mechanics, and $\overset{-}{x}$, $\overset{-}{y}$, $\overset{+}{z}$ mirror symmetries for the electromagnetics corresponding to $\mathrm{TE}_{0\,n\,1}$ like modes.

With one disc radius to optical resonance frequency data point acquired, the first estimate is made crudely according $f_\mathrm{o} = a/(\text{disc radius})$ where a is fit from the first result. Once there are two or more data points the resonance estimate is made, following the from for cylindrical modes, by ${f_\mathrm{o}}^2 = a^2/(\text{disc radius})^2 + b^2$, where a and b are fit from previous results. This is usually enough to get the required disc radius, with 3 disc simulations being the average

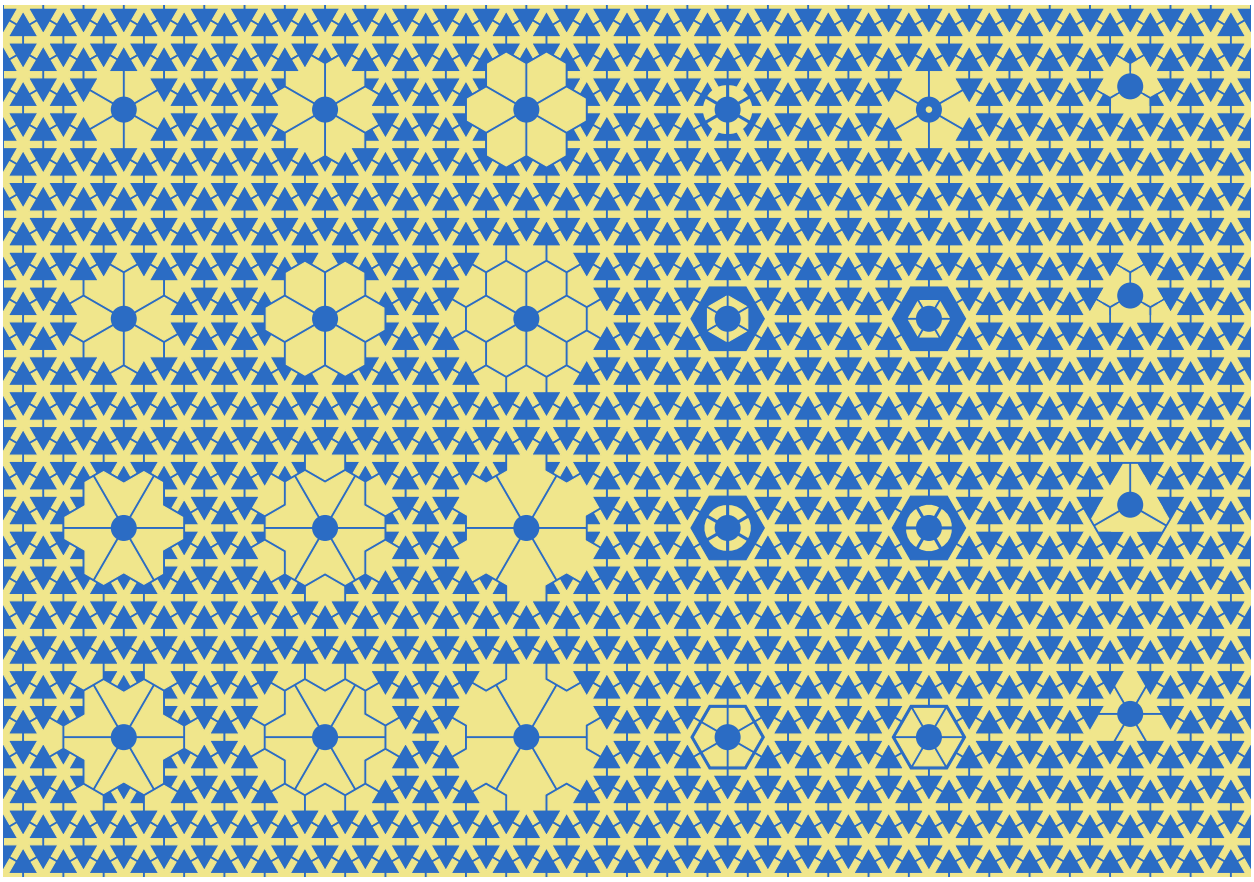

Figure X.2: Various extravagant geometries suspending the disc within a snowflake crystal pattern.

number performed by the algorithm. With the final disc model, the mechanical modes are also simulated and optomechanical couplings calculated.

X.3 Simulations results

An example disc resonator model showing typical mode profiles is shown in Fig. X.4. A compilation of f_{o}, f_{m}, g_{om} outcomes for a set of snowflake crystal dimensions (all with $\mathsf{t} = 250\,\mathrm{nm}$) is given in Fig. X.5. Unfortunately optomechanical couplings of $\sim 300\,\mathrm{kHz}$ are mediocre at best, but of even more concern the optical resonances had very low simulated quality factors of ~ 300. Whilst this may be in part to the small model size with only 3

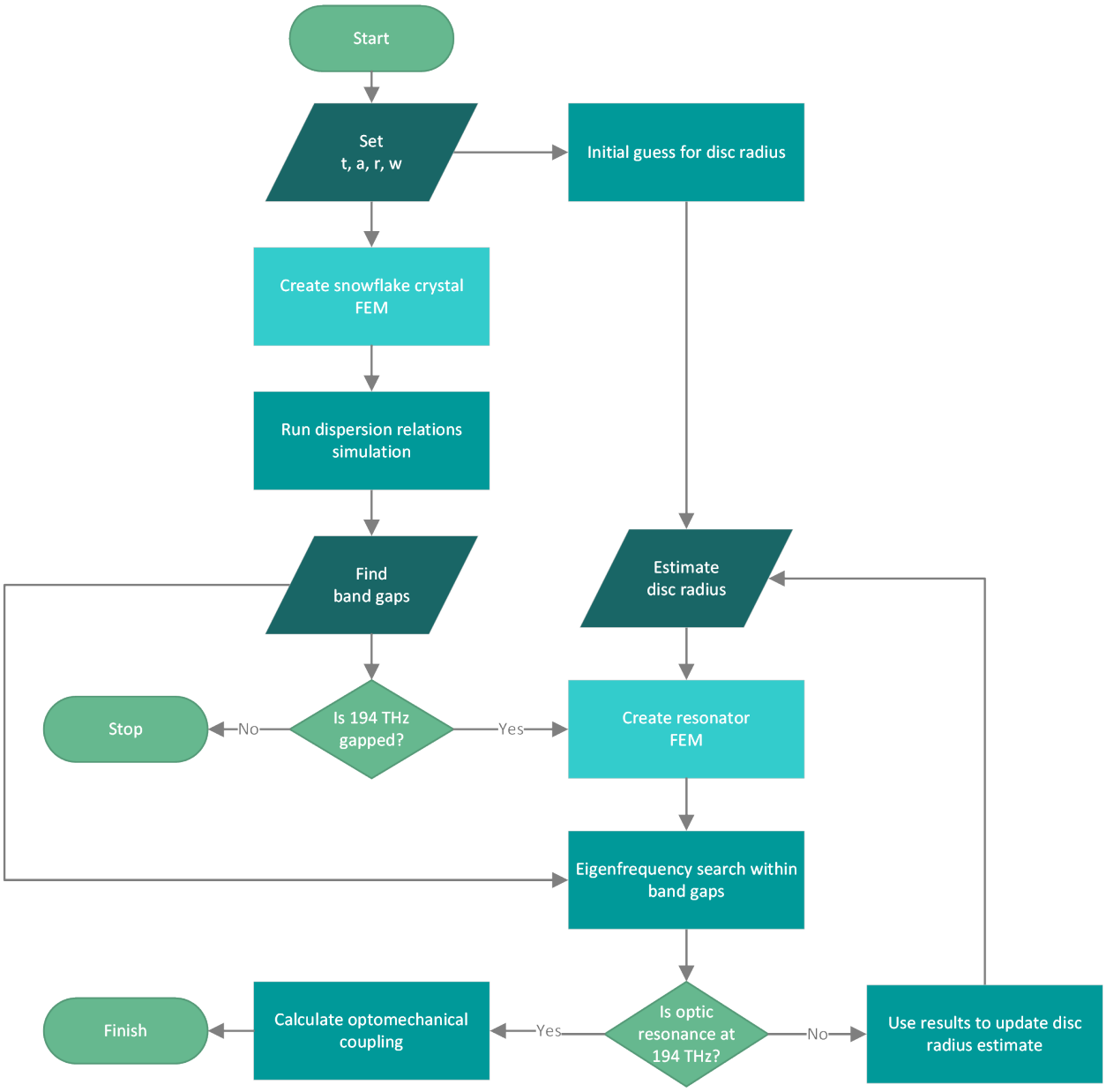

Figure X.3: Disc resonator simulation and tuning algorithm flow chart.

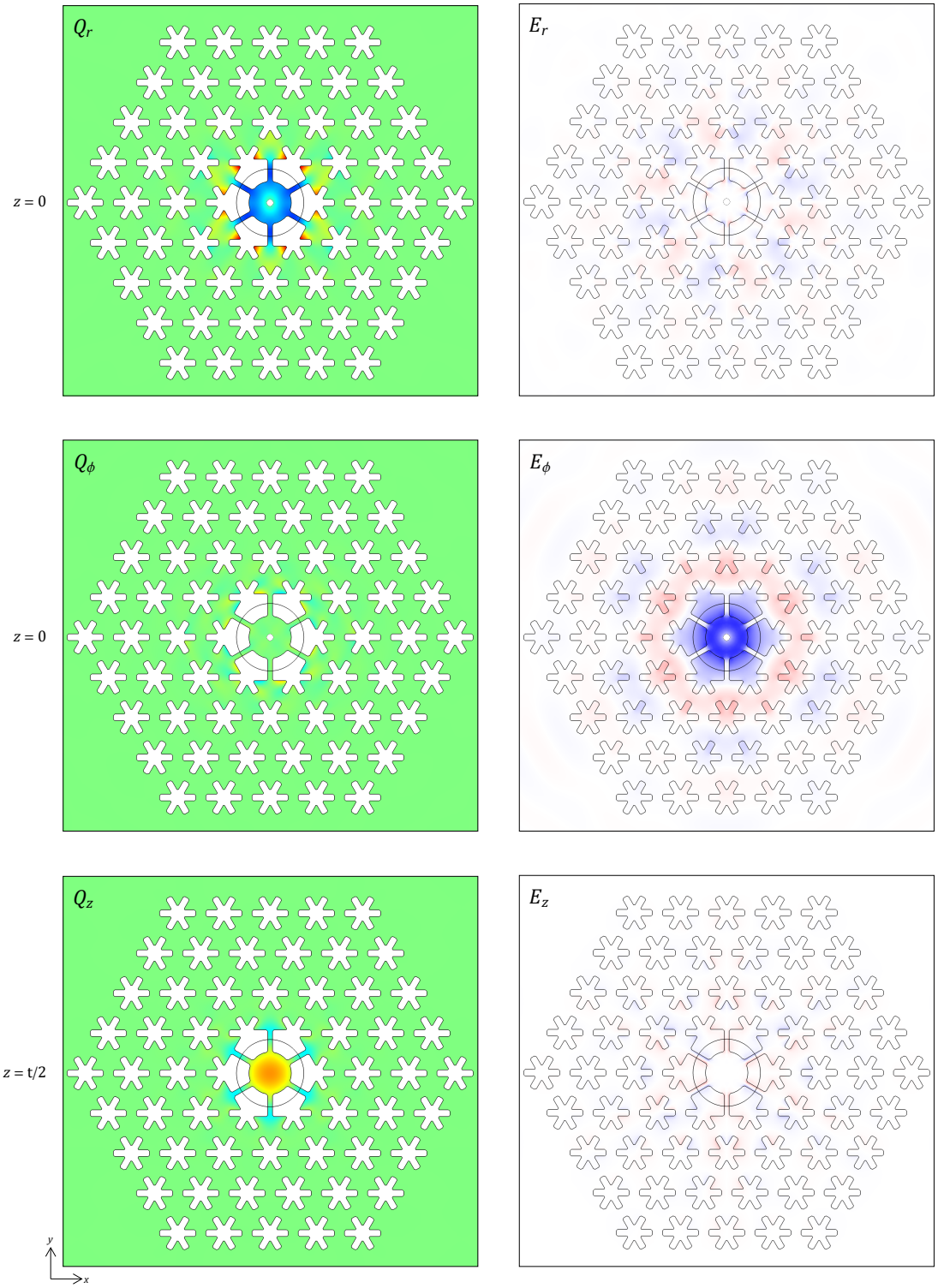

Figure X.4: Simulated mechanical displacement ($\vec{Q}$) at 5.24 GHz and electric field ($\vec{E}$) at 193.9 THz mode profiles for a disc resonator of radius 222 nm embedded in snowflake crystals with t = 250 nm, a = 485 nm, r = 190 nm, w = 70 nm, c = 15 nm and GaAs oriented $\vec{x} = [100]$.

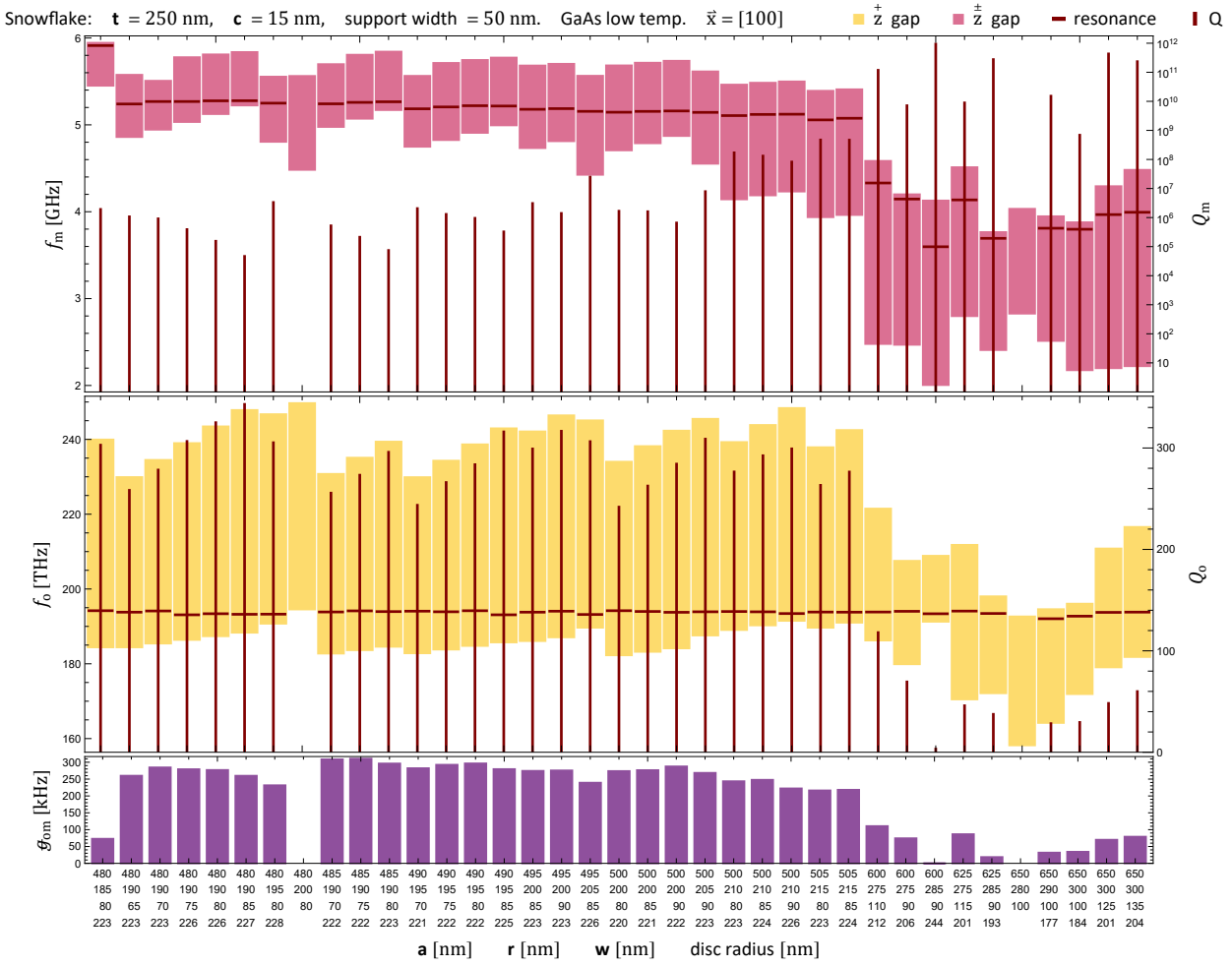

Figure X.5: Results from the disc tuning algorithm with different starting snowflake parameters.

layers of snowflake crystal, larger model trials did not offer significant improvements. High Q dielectric disc resonators are typically associated with whispering gallery modes [283] which is far from this regime.

APPENDIX Y

Trapezium resonators

Within the framework of the snowflake shape crystal pattern, a simple category of defects is those constructed by connecting triangular 'drum heads' together. Whilst many shapes are possible with an increasing number of triangles, optomechanical coupling considerations suggest small shapes (focused modes) with mirror symmetries are preferred. Conforming to this, one of the simplest triangle-constructed resonators is three in a line forming a trapezium, as depicted in Fig. Y.1.

A major drawback of this style is the strong dependency of the resonator parameters on the surrounding snowflake pattern parameters, the base resonator design can not be tuned independently of the crystal. In practice, however, minor size adjustments $\sim 1\%$ are made to the resonator dimensions independent of the crystal to create sets of resonators slightly detuned from each other.

Y.1 Simulations

Simulations were carried out using finite element modelling software [181] with mirror symmetries in x (aligning with trapezium mirror symmetry) and z (vertical slab thickness). Mechanical modes obeyed $\overset{+}{x}\overset{+}{z}$ mirror symmetries, whilst the best electromagnetic modes were found to have $\overset{-}{x}\overset{+}{z}$ mirror symmetries. Example mode profile pictures are shown in Fig. Y.2.

Results for different snowflake crystal lattice dimensions are given in Fig. Y.3. The best optomechanical couplings (calculated using App. C) were found to be $g_{\mathrm{om}}/(2\,\pi) \sim 500\,\mathrm{kHz}$.

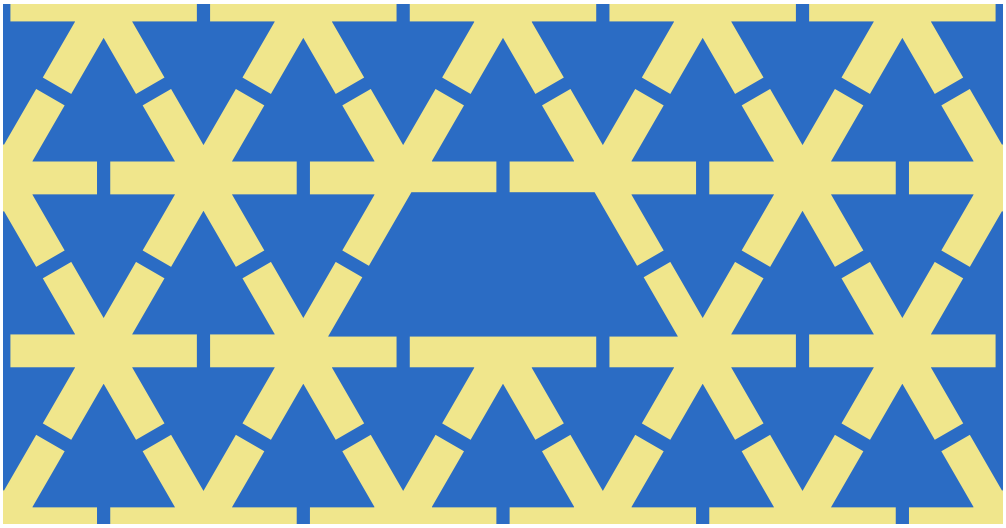

Figure Y.1: Three triangles in a line trapezium resonator.

Y.2 Coupling orientation

One of the drawbacks of two-dimensional optomechanicals crystal is that coupling distances between the resonator and waveguide have to take discrete values. This can be problematic because, as seen in nanobeams and ring resonators, the coupling is sensitive to variations on the order of $\sim 10\,\mathrm{nm}$. For trapezium resonators in snowflakes, we have three ways to adjust the coupling: number of unit cells separating, resonator orientation, and waveguide width if we allow it to break the crystal. With lattice constants of $\mathsf{a} \sim 500\,\mathrm{nm}$ the gap can only be one unit cell, any more is too weak, and any less (zero) has the trapezium ceasing to be a resonator. If our device design has a waveguide that is not part of the crystal lattice, we can vary its width down to some minimum value that permits modes (see App. S). Narrower waveguides tend to push the field out further beyond the waveguide, whilst wider waveguides keep more of the field contained within.

The orientation of the trapezium resonator has four possible options, depicted in Fig. Y.4. Optical measurements found the 'corner' orientation to be the most suitable. With this rotated resonator it's important to keep in mind the crystal structure of the underlying GaAs

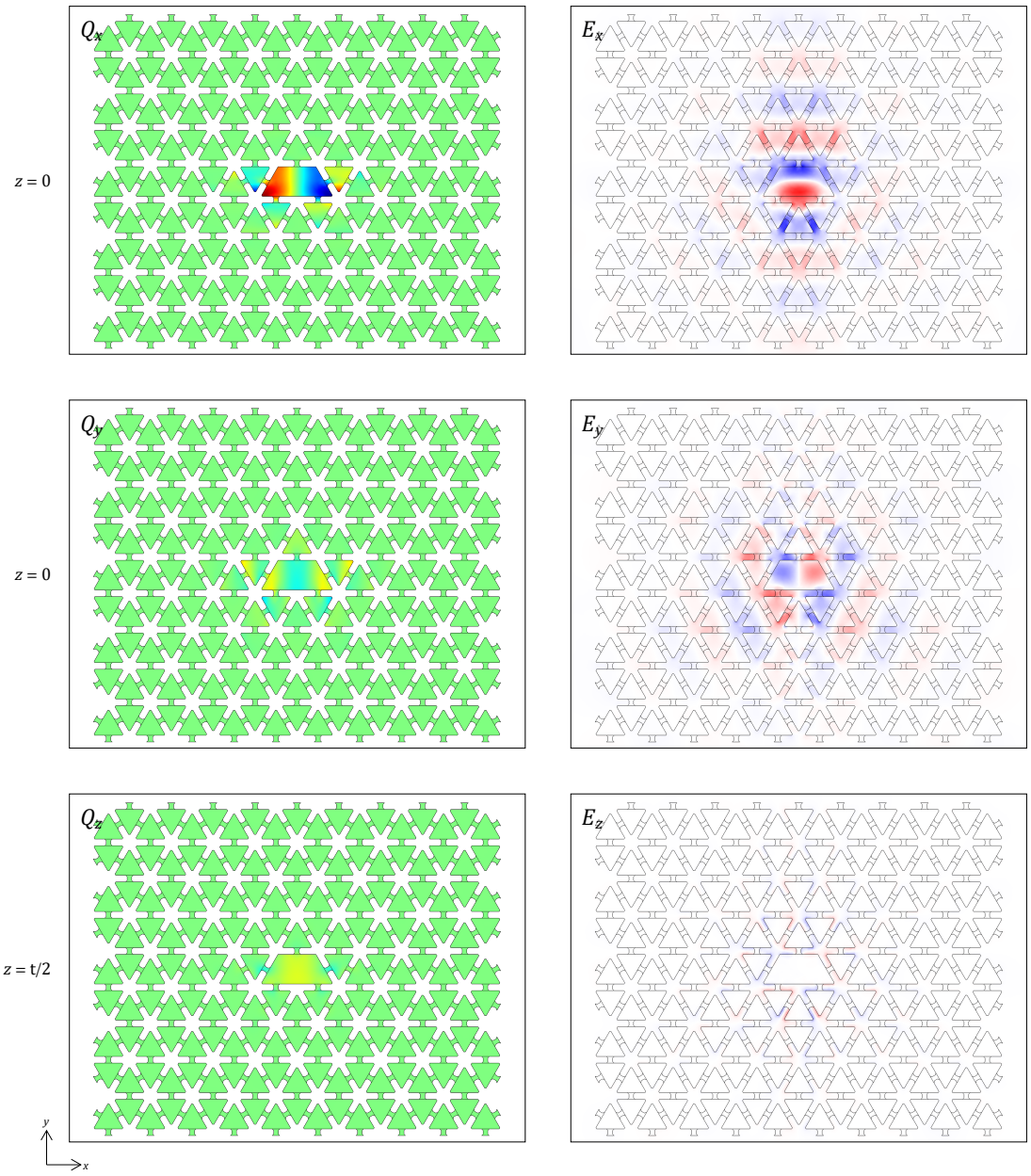

Figure Y.2: Simulated mechanical displacement ($\vec{Q}$) at 3.527 GHz and electric field ($\vec{E}$) at 191.72 THz mode profiles for a trapezium resonatorin snowflake crystals with $\mathsf{t} = 250\,\mathrm{nm}$, $\mathsf{a} = 550\,\mathrm{nm}$, $\mathsf{r} = 245\,\mathrm{nm}$, $\mathsf{w} = 87\,\mathrm{nm}$, $\mathsf{c} = 20\,\mathrm{nm}$ and GaAs oriented $\vec{x} = [1\bar{1}0]$. This simulation had a calculated optomechanical coupling of $g_{\mathrm{om}}/(2\,\pi) = 619\,\mathrm{kHz}$.

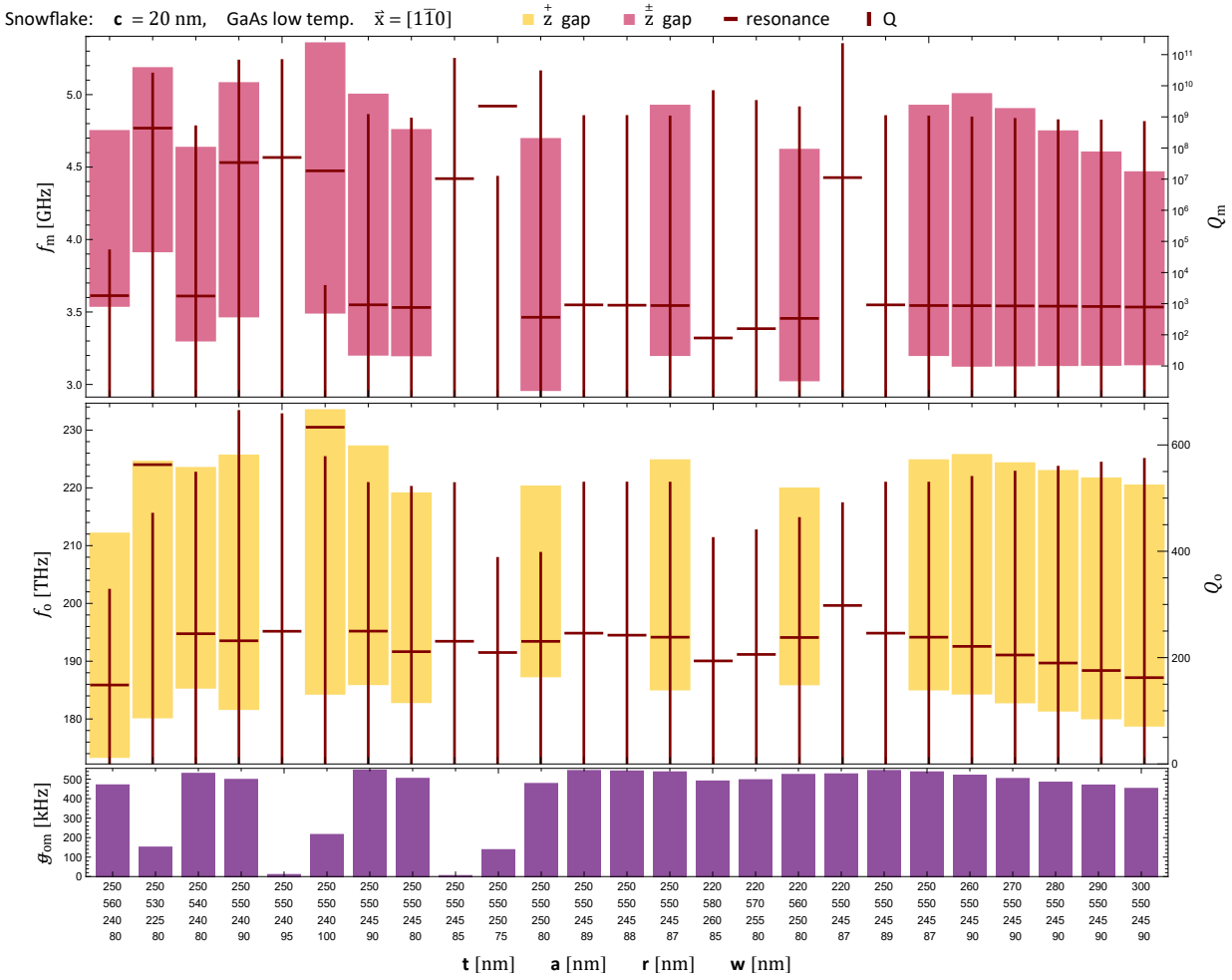

Figure Y.3: Simulations of trapezium resonators in various snowflake crystal patterns. The parallel edges of the trapezium are aligned with GaAs [1$\bar{1}$0]. Band gaps from simulations in Sec. U.6 are displayed when available.

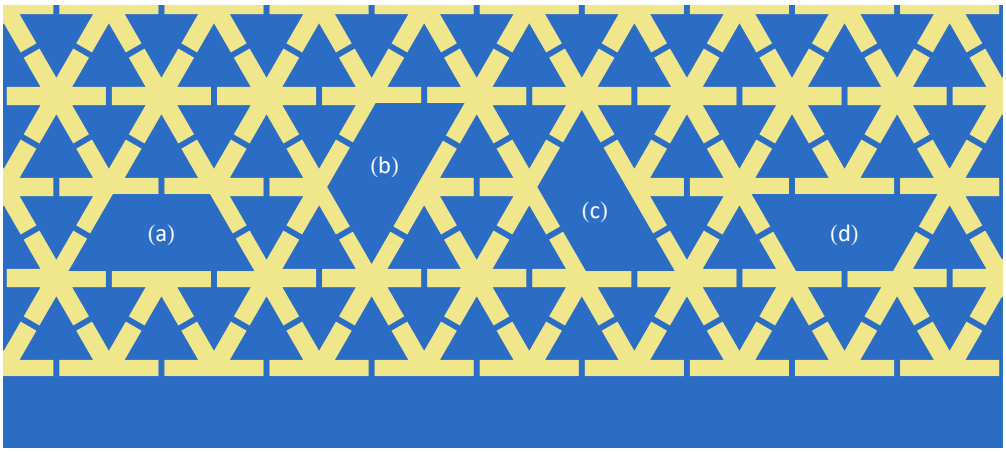

Figure Y.4: Trapezium resonator orientations with respect to a waveguide: (a) 'upward', (b) 'corner', (c) 'side', (d) 'downward'. All with a single unit cell of separation from the waveguide.

material. Mirror symmetries in the resonator design need to align with mirror symmetries in the material, in particular for the best performance, the parallel edges of the trapezium (long axis) need to be aligned with [110]. Thus the waveguide and device orientation with respect to the substrate must be carefully chosen.

Y.3 Bridge connections

Fabrication of a partial waveguide that only admitted optics was beyond the reach of our electron beam lithography process - the required shape dimensions were too small and unable to be successfully created. Thus the closeness of the resonator to the waveguide raised concerns that acoustic modes would undesirably also couple into the waveguide. To mitigate this, one strategy was to remove some of the bridges connecting the trapezium resonator to the surrounding snowflake crystal. Unfortunately this negatively impacted the mechanical resonance modes by lowering the frequency to be perilously close to the band gap edge and reducing the intrinsic quality factor. Plots of simulation results are given in Fig. Y.5.

An alternative approach was to remove bridges along the waveguide connecting it to the

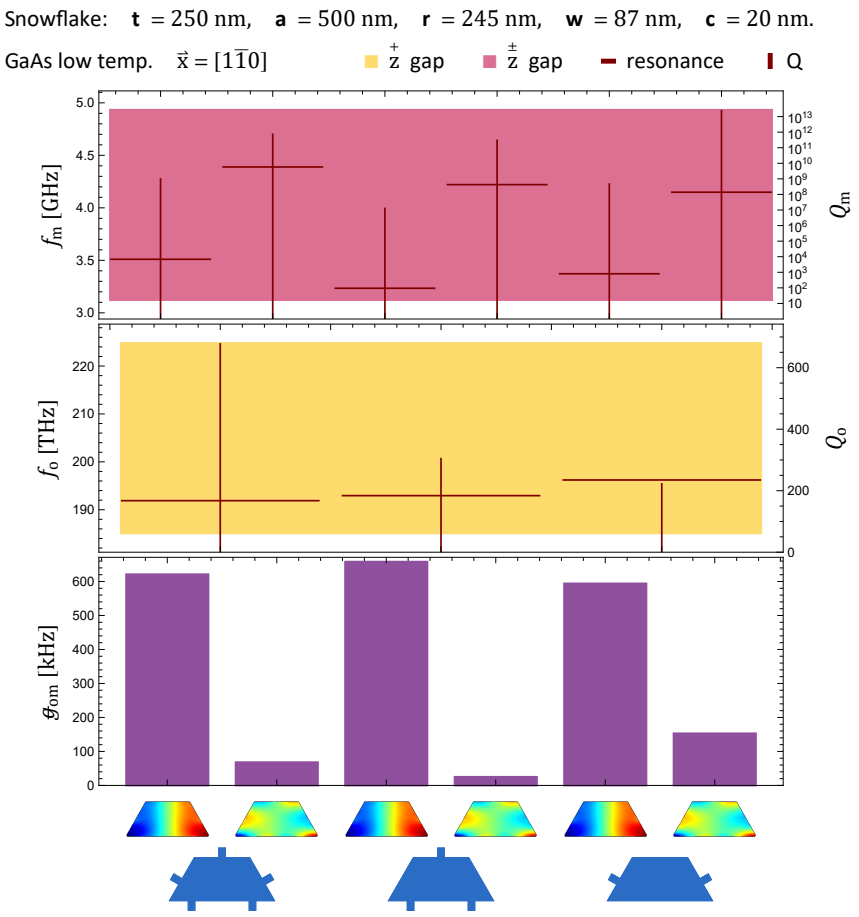

Figure Y.5: Simulations of trapezium resonators with connecting bridges removed. Two different mechanical modes are looked at, and depicted by Q_x.

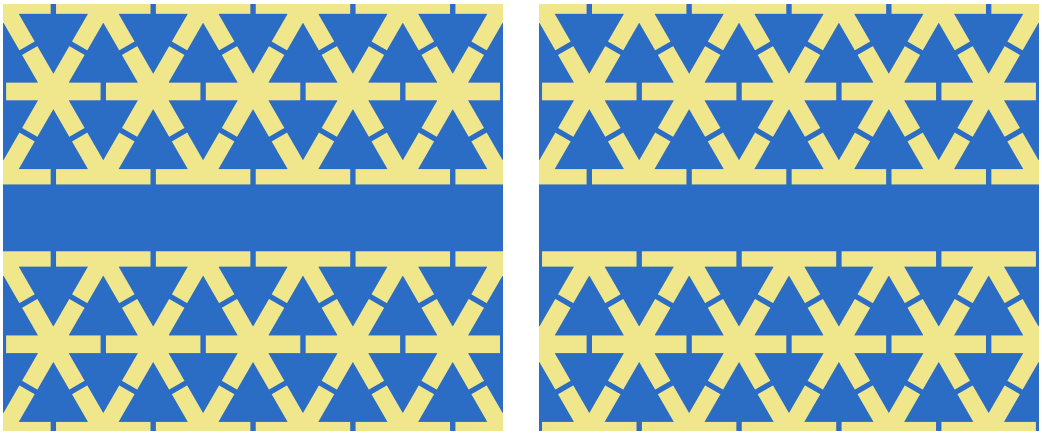

Figure Y.6: Snowflake crystal patterns about a central waveguide: (left) mirror symmetric opposed, (right) off-set by a/2.

snowflake crystal in the vicinity of the trapezium. Whilst there's potentially some edge mode participation in the resonance, simulations suggest this is at least a minor improvement.

Y.4 Crystal offsets

With separate crystals on either side of the waveguide, their relative positions can be adjusted. In particular, there are two major configurations as depicted in Fig. Y.6. Optical transmission measurements strongly favoured devices with the off-set by a/2 configuration.

Y.5 Fabrication

Trapezium resonator devices were fabricated with varying snowflake dimensions, each having $\sim$ 10 resonators with slightly different sizes along a central waveguide that broke the snowflake crystal lattice (allowing waveguide width adjustments). The free suspended waveguide was typically 500 nm wide, and narrowed to 475 nm within the optomechanical crystal for improved optical coupling. The main plate was typically 50 snowflake cells long and 15 rows on each side of the waveguide. Tethers for the main plate and waveguide are styled ser-

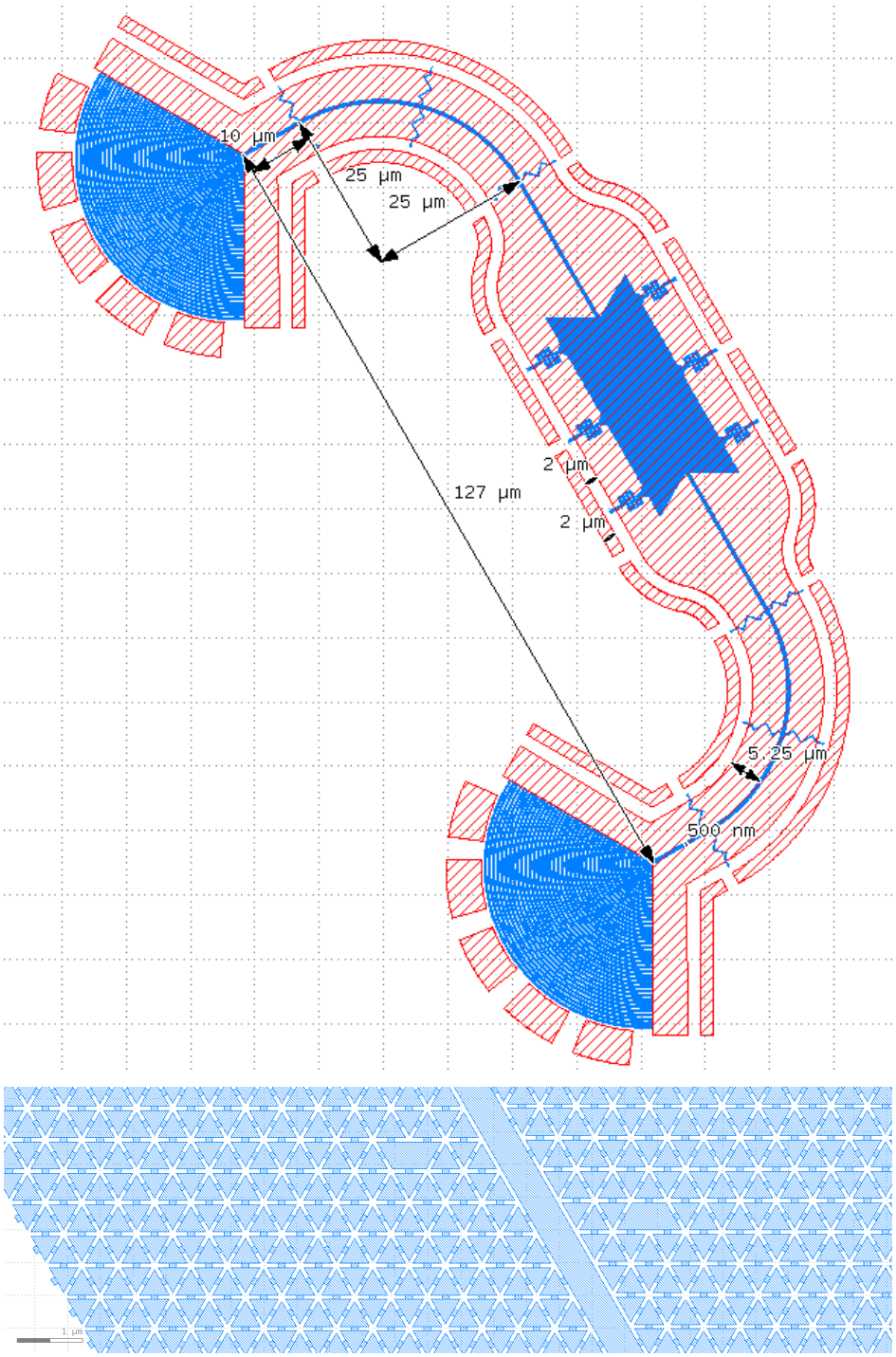

Figure Y.7: (Top) pattern dxf image of the device design with large scale dimensions labelled. (Bottom) zoom in of trapezium resonators along the waveguide. Blue is the HSQ layer making up the suspended structure, and red is the complete etch released regions. Horizontal and vertical directions line up with GaAs [110] crystal axes.

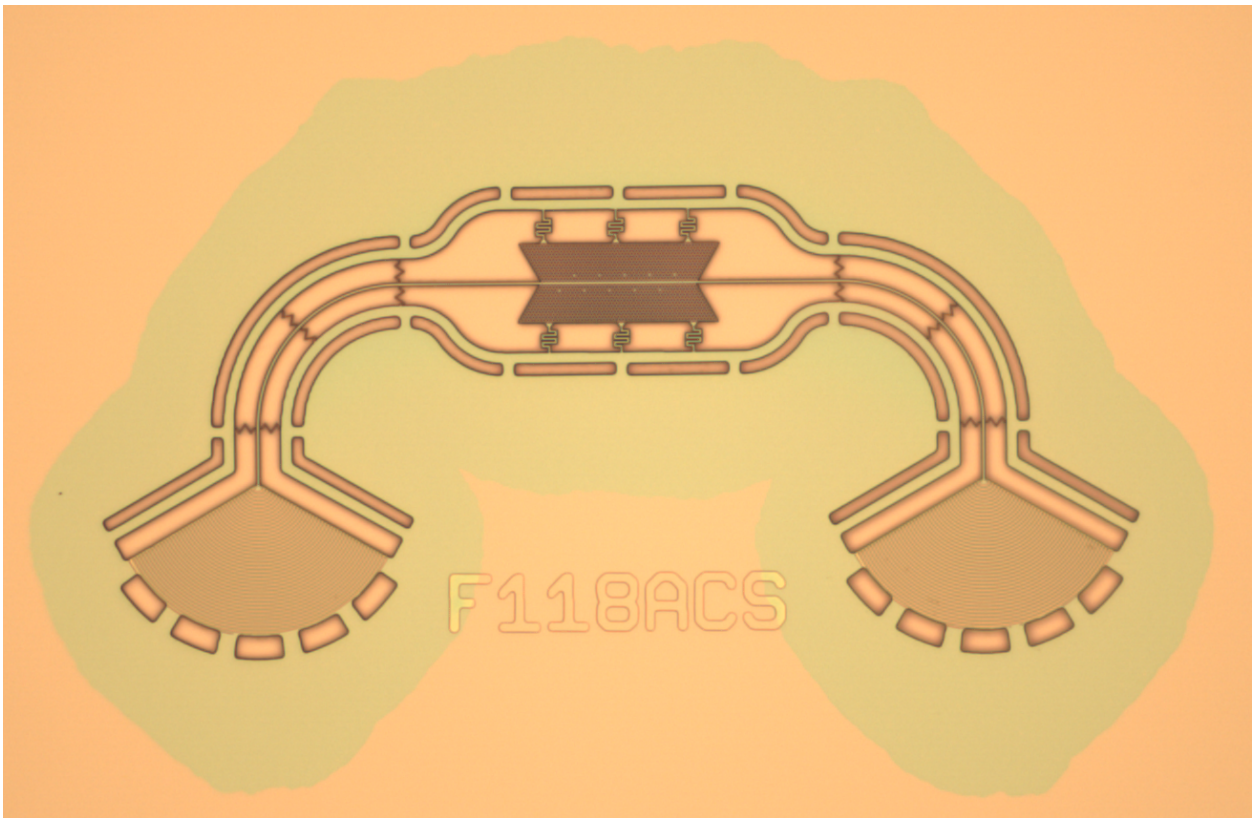

Figure Y.8: Optical microscope image of a trapezium resonator device.

pentine and zigzag to provide flexibility during the release process. Secondary release holes around the entire device protect against any large cracks that form. An example pattern design is shown in Fig. Y.7.

Fabrication was carried out according to Ch. 4, fine tuning the proximity effect correction was vital for creating uniform snowflakes across the plate. Electron beam writing was carried out with two passes at $390\,\mu C/cm^2$ with proximity effect correction (N.3). Images of fabricated devices are shown in Figs. Y.8, Y.9.

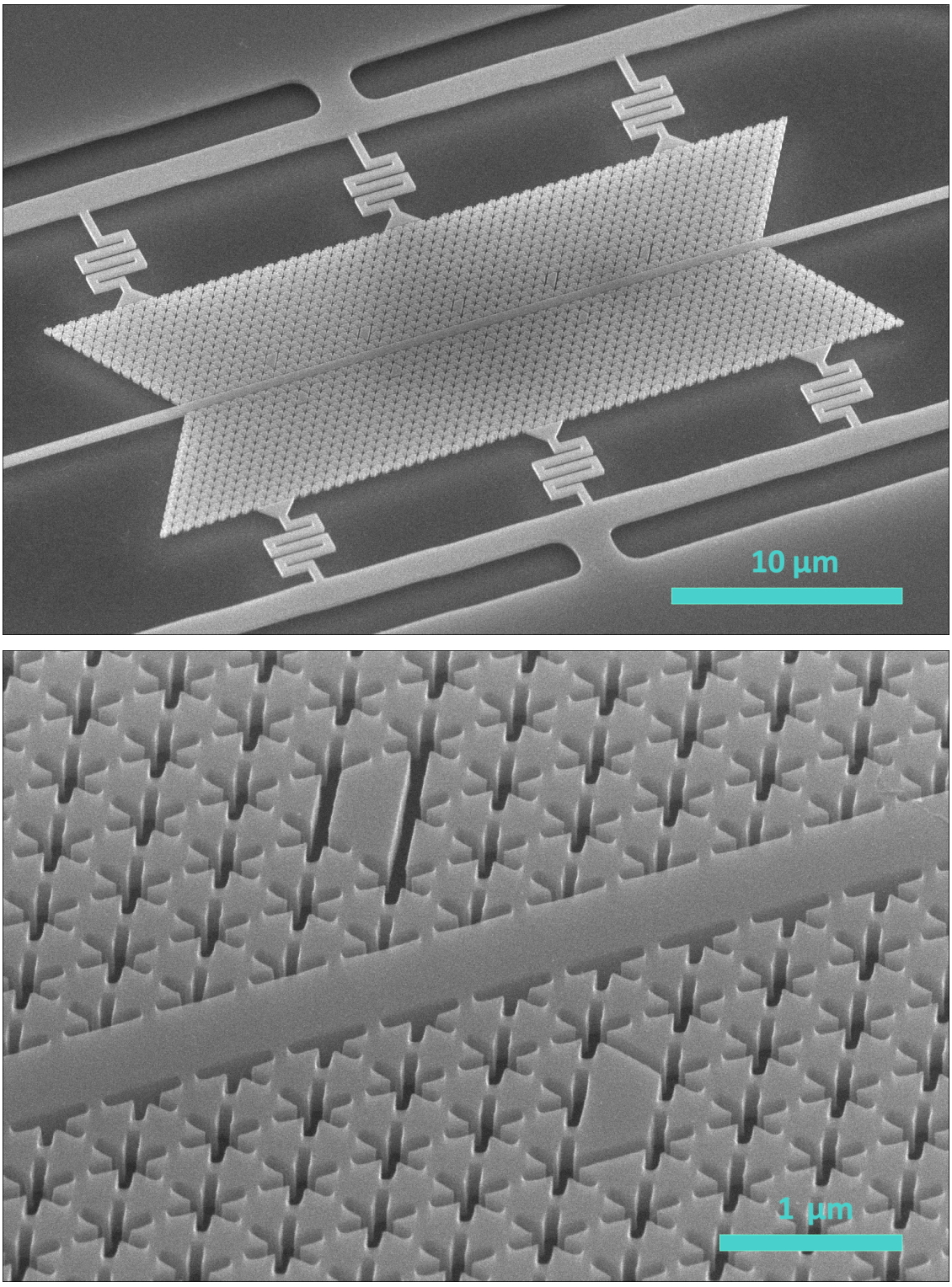

Figure Y.9: 45° angle scanning electron microscope images of a trapezium resonator device. This particular device featured trapezium resonators with partial bridge connections.

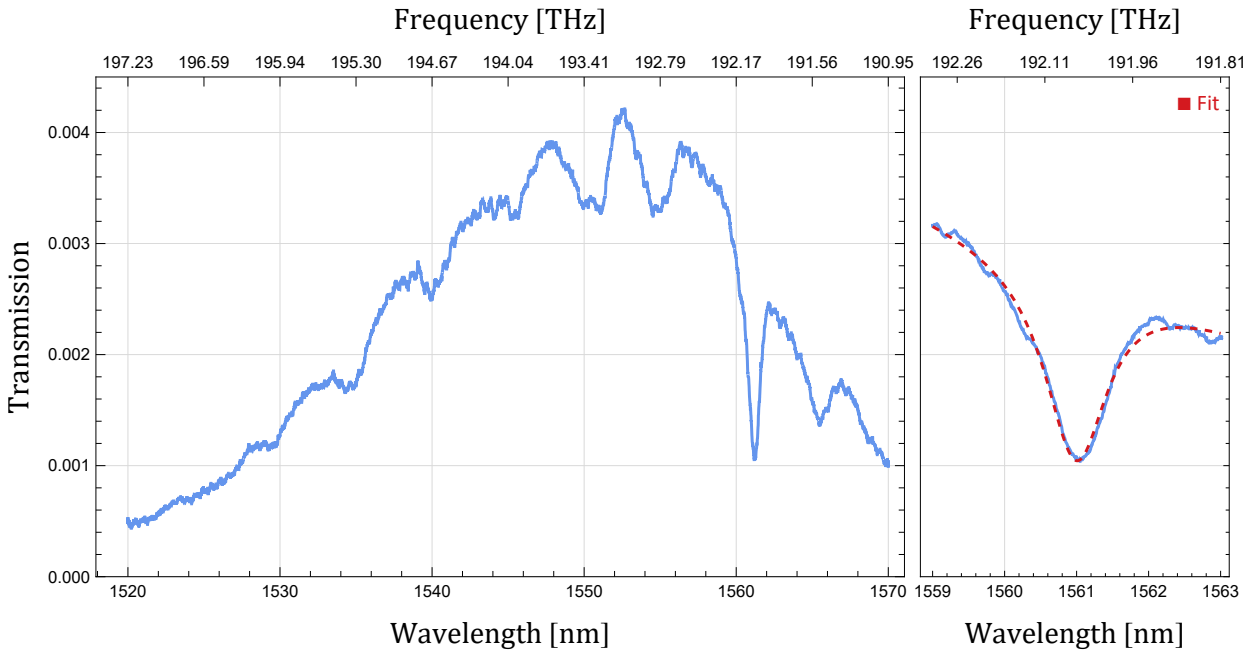

Figure Y.10: Optical transmission scan of a device with trapezium resonators. The fit to this resonance yielded $f = 192.05\,\mathrm{THz}$, $\beta^{12} = 0.63$, $Q^{\mathrm{L}} = (1467 \pm 10)$, $Q^{0} = (2397 \pm 20)$, $Q^{12} = (3785 \pm 22)$, $\gamma/(2\,\pi) = (130.9 \pm 0.9)\,\mathrm{GHz}$.

Y.6 Measurements

Many hundreds of trapezium resonator devices were fabricated and measured with the optical set up described in App. Σ. Unfortunately, typical quality factors were $Q^{\mathrm{L}} \sim 1000$ and $\beta^{12} \sim 0.5$, much too low to observe optomechanical behaviour which scales with Q^2 (See App. L). One of the better devices is plotted in Fig. Y.10.

APPENDIX Z

Vertebrae resonators

The 'vertebrae' resonator is a recently demonstrated [152] quasi-two-dimensional optomechanical crystal cavity that has so far only been realized in silicon [152, 178]. Depicted in Fig. Z.1, it is constructed from C-shape holes to create a one-dimensional optomechanical crystal and Fabry-Pérot defect cavity within the waveguide of a two-dimensional snowflake optomechanical crystal.

Z.1 Dispersion plots

The C-shape hole dimensions are defined in Fig. Z.2, and together with the snowflake dimensions of Sec. U.2.1, lattice spacing, waveguide width, and slab thickness make up the dimensional parameters for a vertebrae unit cell. With periodicity in the x direction, the unit cell exhibits y and z mirror symmetry that allows modes to classified under those symmetries (see App. D).

Figure Z.1: Vertebrae resonator concept.

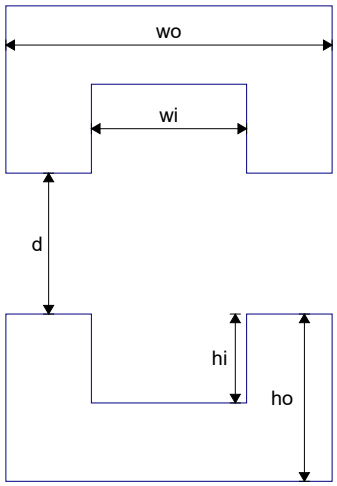

Figure Z.2: Definition of C-shape hole dimensions.

Our target mechanical cavity mode is the $\overset{+}{y}\,\overset{+}{z}$ 'paddle' breathing mode, where the inner rectangular region of the C-shape holes has a strong Q_y component and stretches into the air hole. The frequency of this mode is dominated by an inverse proportionality to hi. There is a slight inverse proportionality to wi, and minimal dependence on other parameters. Our target optical cavity mode has $\overset{-}{y}\,\overset{+}{z}$ symmetry, matching the waveguide propagation mode, and is localized to the air holes. It has a frequency that scales with the size of the air hole, $\mathsf{wo} \times (\mathsf{ho} - \mathsf{hi})$.

Design of the vertebrae resonator requires an appropriate mirror geometry that can be gradient deformed to put the target modes into the mirror's band gaps. For this, we study dispersion relations for the vertebrae unit cell, and following a manually guided parameter search arrive at the mirror unit cell given in Fig. Z.3. From this, the $\overset{+}{y}\,\overset{+}{z}$ paddle breathing mode and $\overset{-}{y}\,\overset{+}{z}$ optical mode can be brought into the band gap by increasing hi, as seen in Fig. Z.4.

Here we only considered cases with the C-shape lattice distance equal to the snowflake lattice distance, a, but it is possible to relax this constraint [178]. There are two reasonable relative lattice positions: the C-shape sitting between the snowflakes as in Fig. Z.1, or shifted such

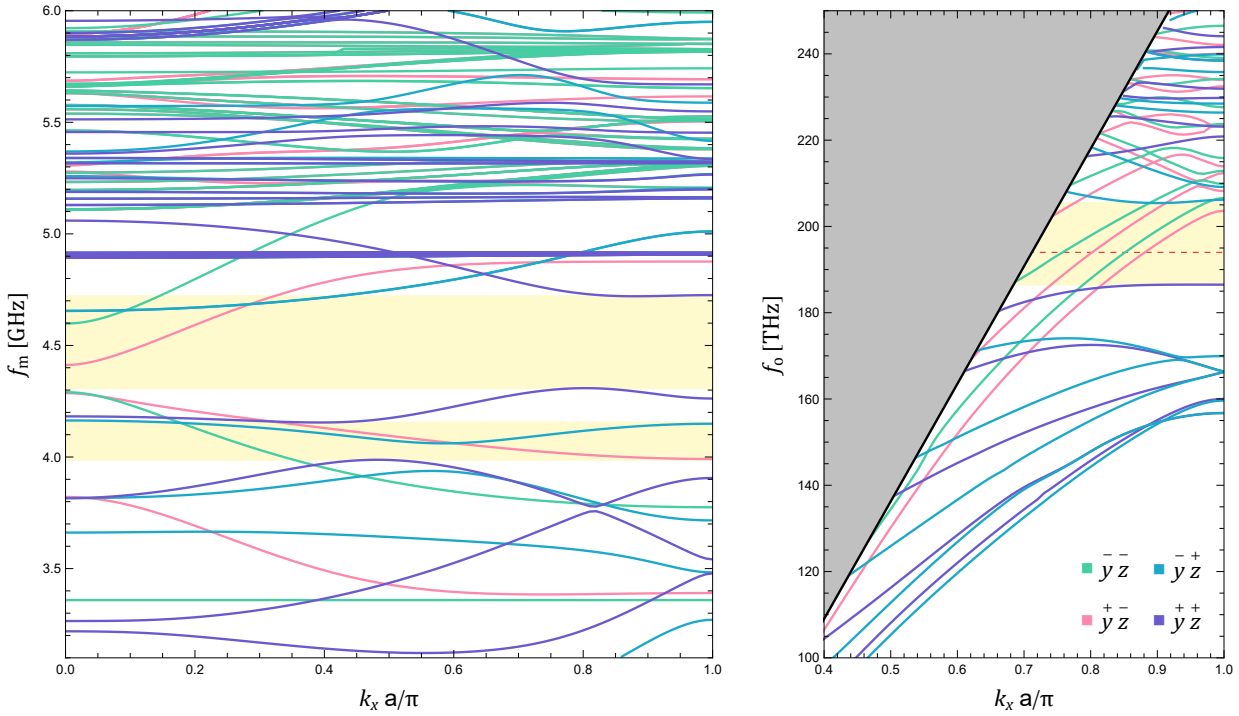

Figure Z.3: Dispersion plots for vertebrae unit cell with t = 250 nm, a = 550 nm, r = 245 nm, w = 87 nm, c = 20 nm, ho = 320 nm, wo = 480 nm, hi = 175 nm, wi = 210 nm, d = 80 nm, wg = 868 nm, and GaAs at room temperature aligned with $\vec{x} = [1\bar{1}0]$. (Left) mechanics with highlighted $\overset{+}{y}\,\overset{+}{z}$ bands gaps, and (right) topics with highlighted $\overset{\pm}{y}\,\overset{+}{z}$ bands gaps.

that the C-shape holes are vertically below the edge snowflakes. Examples of both are given in Fig. Z.5. A cursory exploration of the shifted case was undertaken but it did not provide any immediate benefits.

The waveguide in the snowflake crystal is formed by a missing row with additional widening. This widening breaks the crystal lattice, removing the possibility of waveguide cornering through the crystal. Another option involves truncating the snowflakes along the waveguide as shown in Fig. Z.5 (bottom). Only a brief investigation of this style was carried out with unfavourable dispersion plot results.

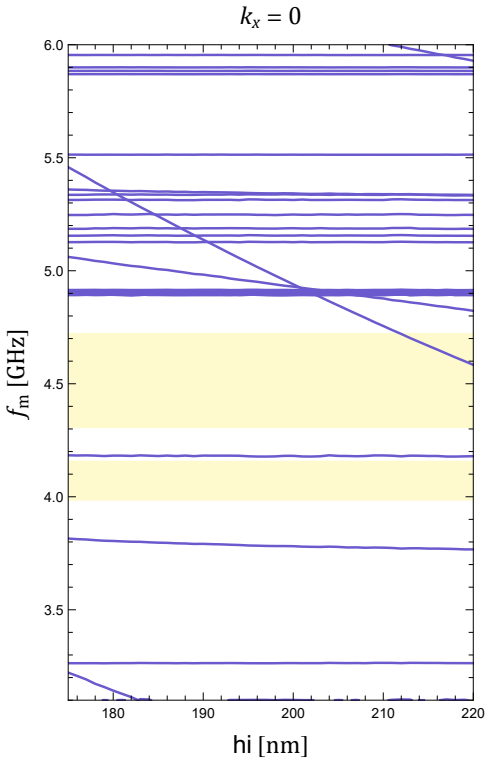

Figure Z.4: Dispersion for $\overset{+}{y}\,\overset{+}{z}$ acoustic modes at $k_x = 0$, varying the paddle height hi. Bands gaps for the mirror unit cell are highlighted.

Z.2 Designs

Various design options were considered for the vertebrae resonator. These included defect cell parity, missing or truncated snowflake waveguides, snowflake to C-shape lattice shift, gradient function, waveguide widths, and tapering to the waveguide. Diagrams of these options and parameterizations are given in Fig. Z.5.

The defect can have an even number of defect cells with $\bar{x}$ electromagnetic symmetry, or odd number of defect cells with $\overset{+}{x}$ electromagnetic symmetry. In both cases the mechanics are $\overset{+}{x}$ symmetric, as required by App. E, and are paddle breathing modes. Previous designs have all used even $n_{defect} = 2$ [152, 178] which provides good optomechanical coupling, but fabricating two identical paddles in gallium arsenide proved challenging and later designs

restricted to $\mathsf{n}_{\text{defect}} = 1$.

As discussed in the previous section, the base waveguide can made from a missing row or additionally truncating the snowflakes, and the snowflake to C-shape lattice can be in one of two shifted positions. Early simulations of 'shifted' lattices, and truncated snowflake waveguides, despite their use in App. Y, were unfavourable and these styles were not further investigated.

Two classes of gradient functions are considered, polynomials and a smooth step, defined over $[0,1] \to [0,1]$ as[1]

$$\text{PolyStep}_n[x] = x^n \ ,$$

$$\text{SmoothStep}_n[x] = x^{n+1} \sum_{k=0}^{n} \binom{n+k}{k} \binom{2\,n+1}{n-k} (-x)^k \ ,$$

to be combined with $0 : x < 0, 1 : x > 1$. Polynomial step functions are differentiable at $x = 0$ for $n > 1$ and never at $x = 1$, whilst the smooth step is n-differentiable at both. Given the few discretized points in our gradient region, we consider only PolyStep_1, PolyStep_2, and SmoothStep_1, plotted in Fig. Z.6.

Tapering styles were mostly explored in fabrication as simulating external couplings is burdensome and unreliable. These involved designs that tapered to narrow slots (wider slots blocked transmission) or tapered to open blank waveguides, and different lengths. Results as to which implementation was best were inconclusive although some of the better optical devices measured had very short $\mathsf{n}_{\text{taper}} = 1$ interfaces. Shorter snowflake plates that transitioned from waveguide to suspended beams sooner improved overall transmission.

1. Where $\binom{a}{b}$ = Binomial$[a, b]$ is 'a choose b'.

Z.2.1 Simulations

Simulations were carried out with finite element modelling software with x, y, and z symmetries imposed. Layouts are built using Python to create DXF files and then MATLAB [182] scripts to assemble COMSOL [181] models. Fig. Z.7 depicts a $\mathsf{n}_{\mathrm{defect}} = 2$ cavity and Fig. Z.8 depicts a $\mathsf{n}_{\mathrm{defect}} = 3$ cavity. Optomechanical couplings were calculated according App. C and a compilation of results given in Fig. Z.9.

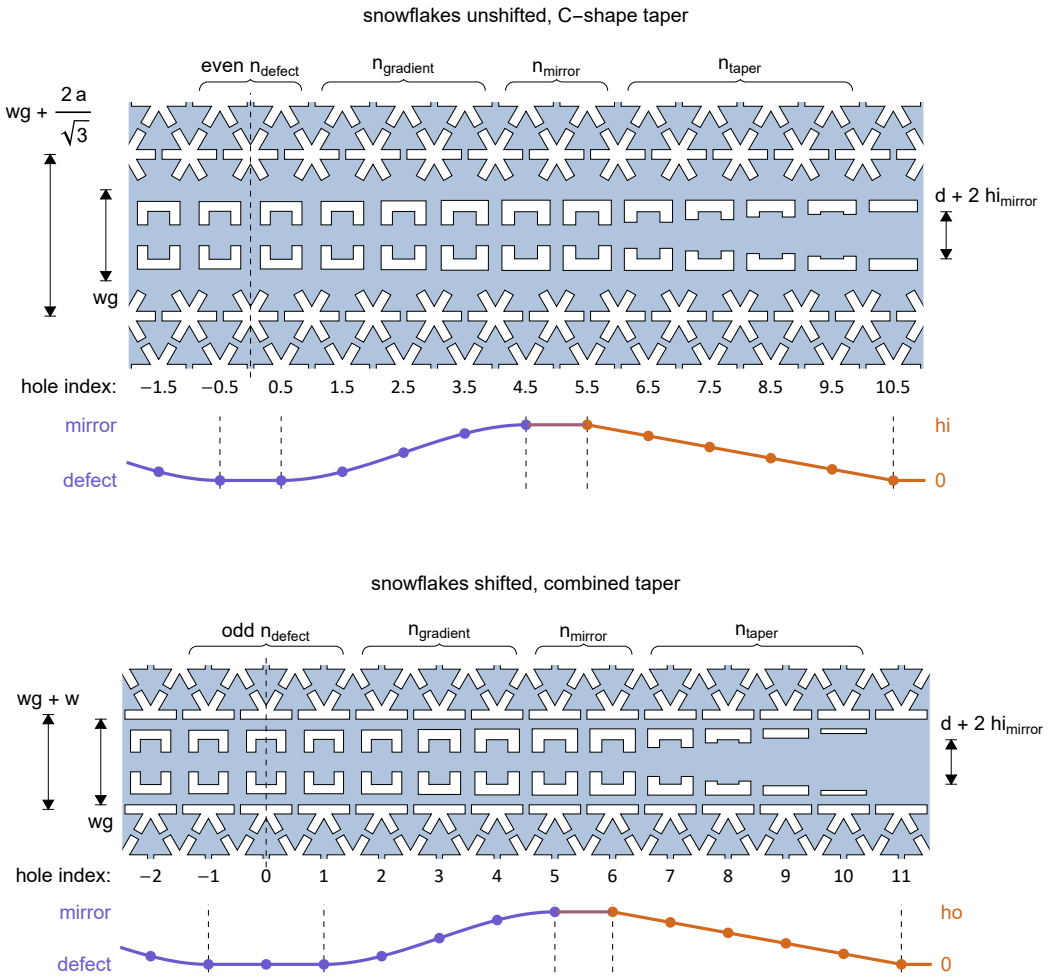

Figure Z.5: Vertebrae resonator defect cavity resonator designs. (Top) even $\mathsf{n}_{\text{defect}}$ in a widened missing-row waveguide with C-shape hole tapering, and (bottom) odd $\mathsf{n}_{\text{defect}}$ in a truncated-snowflake missing-row waveguide with shifted snowflakes and combined taper. The plots depict a SmoothStep_1 gradient transition of parameters between the defect and mirror, and linear taper of $\mathsf{hi}, \mathsf{ho}, \mathsf{d}$ to the waveguide region.

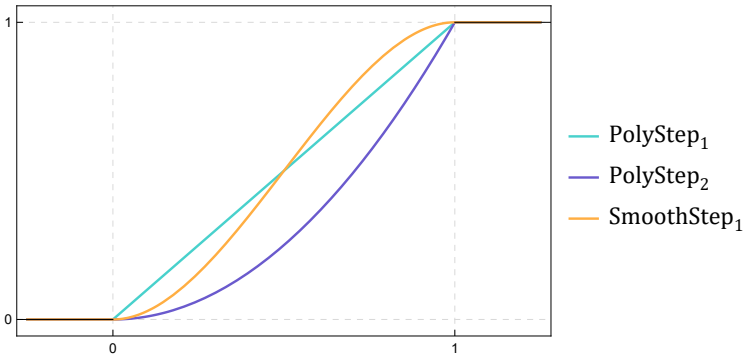

Figure Z.6: Plots of gradient functions considered.

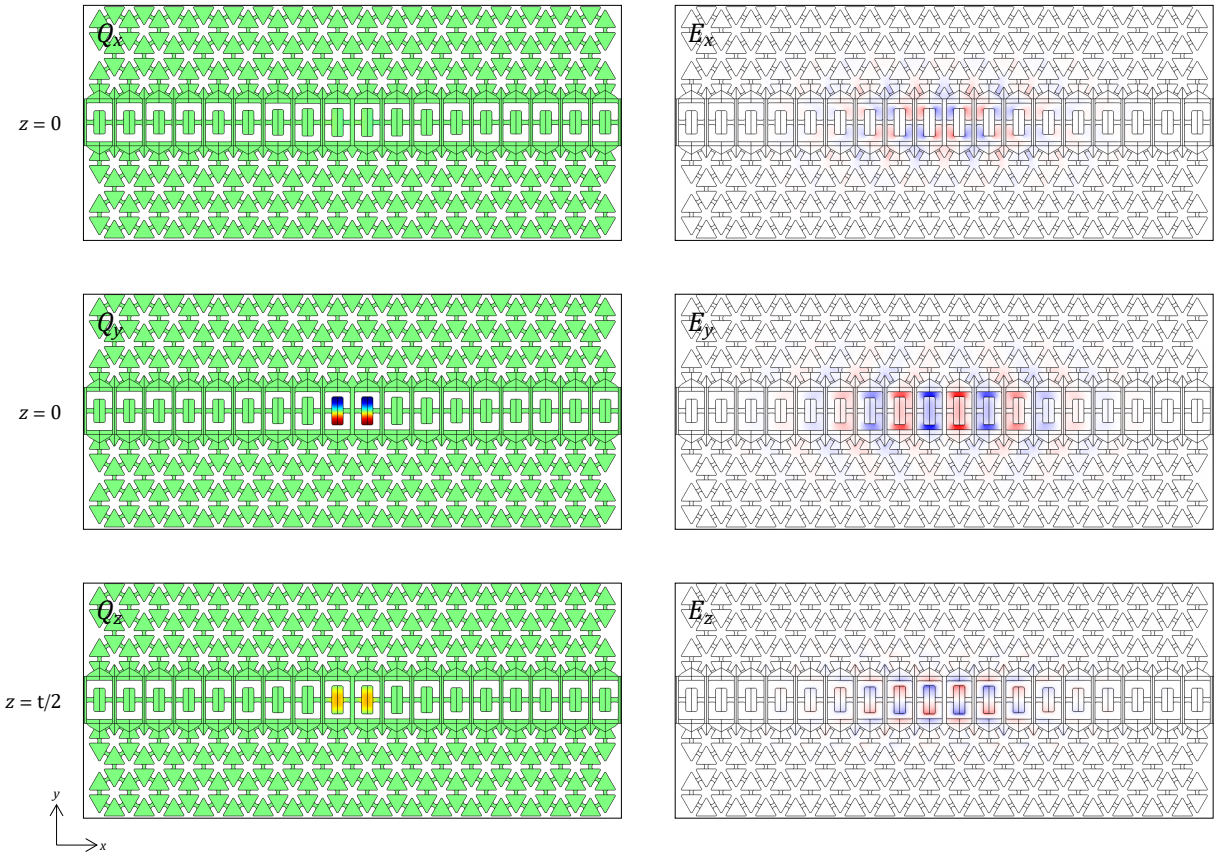

Figure Z.7: Simulations of an even $\mathsf{n}_{\text{defect}} = 2$ mode, with $\mathsf{t} = 250\,\text{nm}$, $\mathsf{a} = 550\,\text{nm}$, $\mathsf{r} = 245\,\text{nm}$, $\mathsf{w} = 87\,\text{nm}$, $\mathsf{c} = 20\,\text{nm}$, $\mathsf{ho}_{\text{mirror}} = 320\,\text{nm}$, $\mathsf{wo}_{\text{mirror}} = 480\,\text{nm}$, $\mathsf{hi}_{\text{mirror}} = 175\,\text{nm}$, $\mathsf{wi}_{\text{mirror}} = 210\,\text{nm}$, $\mathsf{ho}_{\text{defect}} = 310\,\text{nm}$, $\mathsf{wo}_{\text{defect}} = 470\,\text{nm}$, $\mathsf{hi}_{\text{defect}} = 320\,\text{nm}$, $\mathsf{wi}_{\text{defect}} = 210\,\text{nm}$, $\mathsf{d} = 80\,\text{nm}$, $\mathsf{wg} = 868\,\text{nm}$, $\mathsf{n}_{\text{gradient}} = 3$ with SmoothStep$_1$, $\mathsf{n}_{\text{mirror}} = 3$, and GaAs at room temperature aligned with $\vec{x} = [1\bar{1}0]$. The mechanical mode at $f_{\text{m}} = 4.5843\,\text{GHz}$ has $\overset{+}{x}\,\overset{+}{y}\,\overset{+}{z}$ mirror symmetry, whilst the optical mode at $f_{\text{o}} = 194.25\,\text{THz}$ has $\overset{-}{x}\,\overset{-}{y}\,\overset{+}{z}$ mirror symmetry.

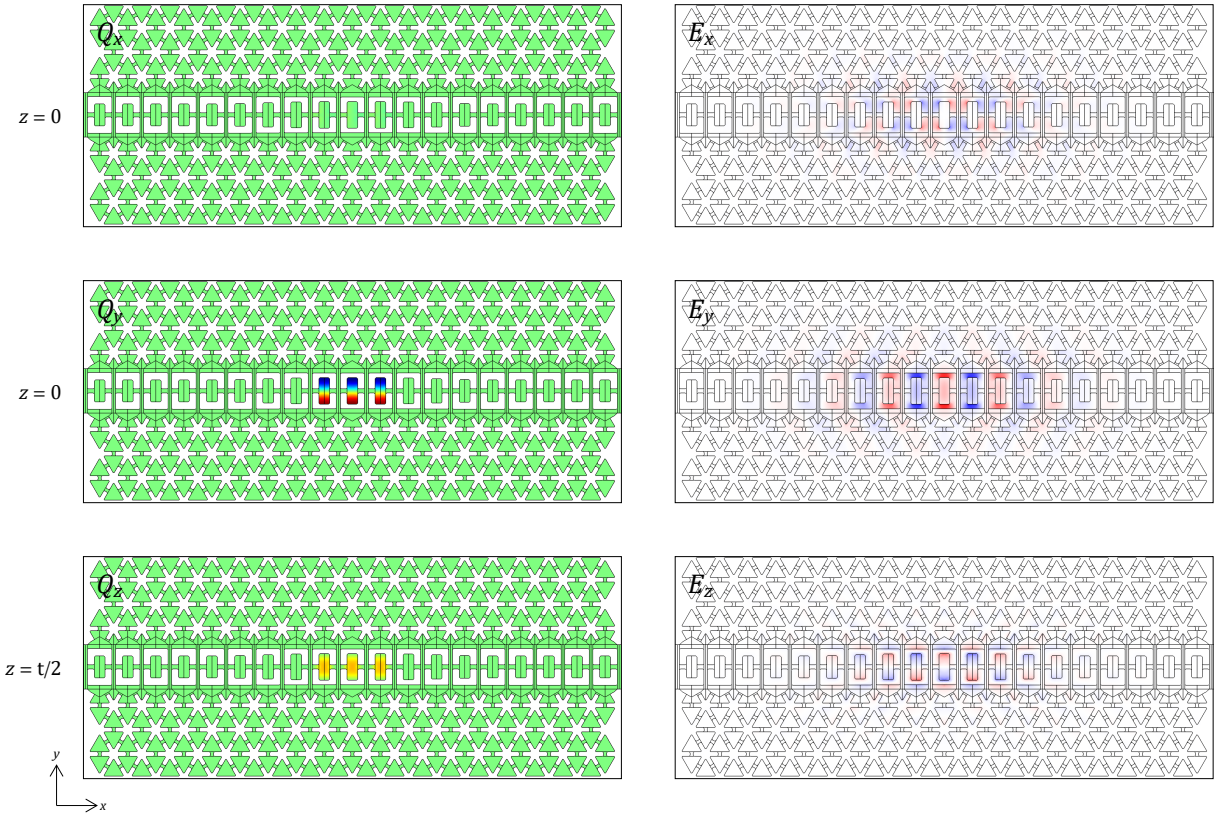

Figure Z.8: Simulations of an odd $\mathsf{n}_{\text{defect}} = 3$ mode, with $\mathsf{t} = 250\,\text{nm}$, $\mathsf{a} = 550\,\text{nm}$, $\mathsf{r} = 245\,\text{nm}$, $\mathsf{w} = 87\,\text{nm}$, $\mathsf{c} = 20\,\text{nm}$, $\mathsf{ho}_{\text{mirror}} = 320\,\text{nm}$, $\mathsf{wo}_{\text{mirror}} = 480\,\text{nm}$, $\mathsf{hi}_{\text{mirror}} = 175\,\text{nm}$, $\mathsf{wi}_{\text{mirror}} = 210\,\text{nm}$, $\mathsf{ho}_{\text{defect}} = 310\,\text{nm}$, $\mathsf{wo}_{\text{defect}} = 470\,\text{nm}$, $\mathsf{hi}_{\text{defect}} = 320\,\text{nm}$, $\mathsf{wi}_{\text{defect}} = 210\,\text{nm}$, $\mathsf{d} = 80\,\text{nm}$, $\mathsf{wg} = 868\,\text{nm}$, $\mathsf{n}_{\text{gradient}} = 3$ with SmoothStep_1, $\mathsf{n}_{\text{mirror}} = 3$, and GaAs at room temperature aligned with $\vec{x} = [1\bar{1}0]$. The mechanical mode at $f_{\text{m}} = 4.5846\,\text{GHz}$ has $\overset{+}{x}\,\overset{+}{y}\,\overset{+}{z}$ mirror symmetry, whilst the optical mode at $f_{\text{o}} = 193.09\,\text{THz}$ has $\overset{+}{x}\,\overset{-}{y}\,\overset{+}{z}$ mirror symmetry.

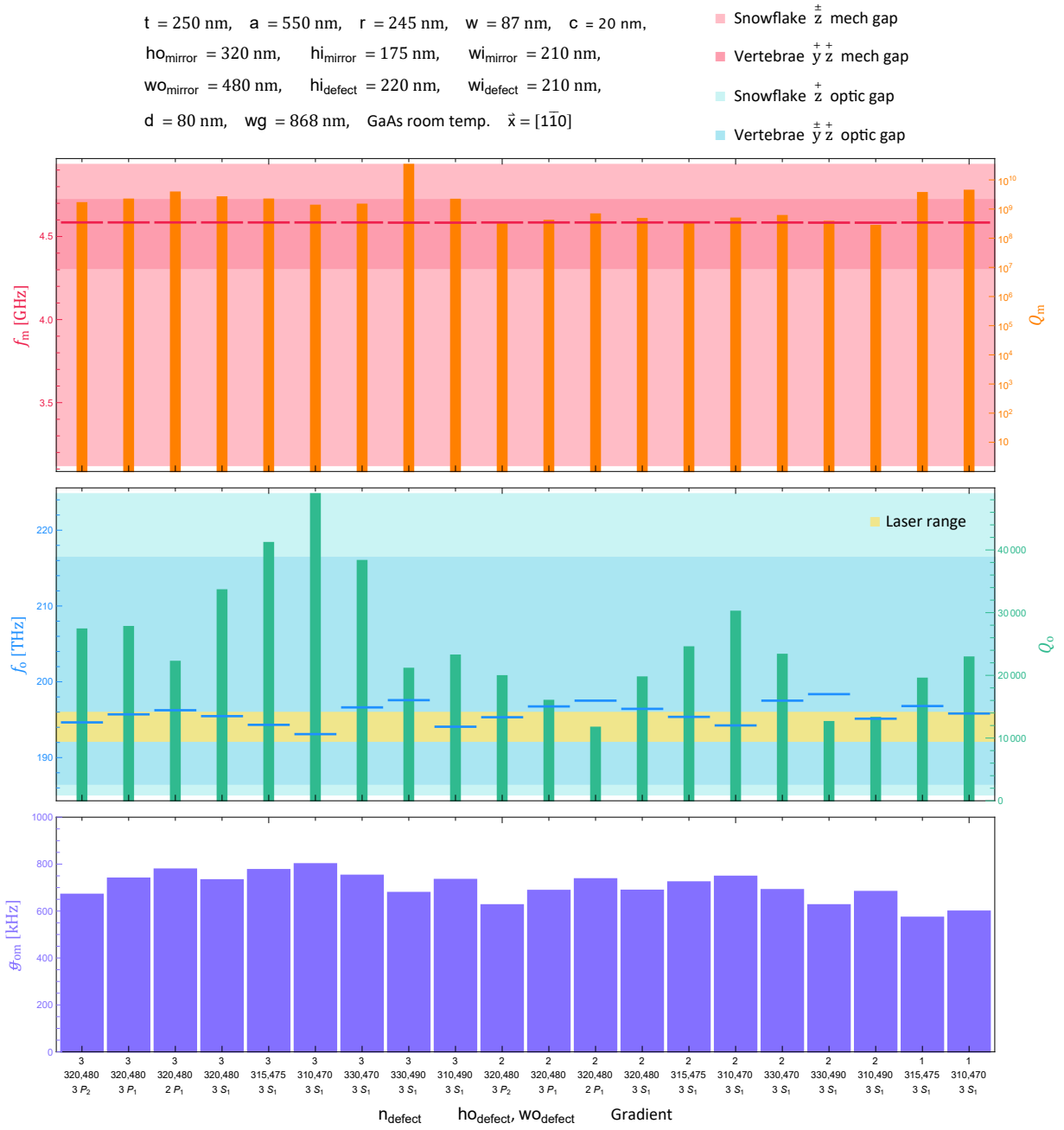

Figure Z.9: Simulation results varying the gradient function and $\mathrm{wo}_{\mathrm{defect}}$, $\mathrm{ho}_{\mathrm{defect}}$ exhibiting fine tuning of the optical resonance frequency. Quality factors are limited by the simulation size, here with 3 rows of snowflakes.

Z.3 Fabrication

Fabrication was carried out following Ch. 4 using proximity effect correction (N.3) with 0.1 μm short range cut-off and 395 $\mu C\,\mathrm{cm}^{-2}$ dose with two passes for electron beam lithography. During the development process, devices were imaged with a scanning electron microscope (SEM) and analyzed using edge detection. Pattern dimensions were adjusted and iterated to realize the simulation targets, an example step in this process is shown in Fig. Z.10.

The C-shape hole, lacking rotational symmetry, does not lend itself to the tricks used for snowflake shape fitting of App. P, and instead was estimated from edge detection pixel distances assuming a canonical orientation. Details of this method are outlined in Fig. Z.11. If the image is not perfectly oriented, lattice periodicity analysis (see App. Ξ) can be carried out on the surrounding snowflakes to provide a rotation correction angle.

Our laser for measuring (see Sec. Σ.1.1), and the optical grating couplers (see App. V), have a narrow wavelength operating band so devices were made in series of varying global scaling parameters. Furthermore, due to the temperamental nature of HSQ resist variations on the order of $\sim 1\%$ were common between fabrication runs. A fabricated device is pictured in Fig. Z.12.

Pattern dimensions that produced measurable devices were in the vicinity of

$$
\begin{aligned}
\mathsf{a} &= 578\,\mathrm{nm}\,, & \mathsf{ho}_{\mathrm{mirror}} &= 302\,\mathrm{nm}\,, & \mathsf{ho}_{\mathrm{defect}} &= 288\,\mathrm{nm}\,,\\
\mathsf{r} &= 247\,\mathrm{nm}\,, & \mathsf{wo}_{\mathrm{mirror}} &= 477\,\mathrm{nm}\,, & \mathsf{wo}_{\mathrm{defect}} &= 462\,\mathrm{nm}\,,\\
\mathsf{w} &= 63\,\mathrm{nm}\,, & \mathsf{hi}_{\mathrm{mirror}} &= 184\,\mathrm{nm}\,, & \mathsf{hi}_{\mathrm{defect}} &= 230\,\mathrm{nm}\,,\\
\mathsf{c_i} &= 18\,\mathrm{nm}\,, & \mathsf{wi}_{\mathrm{mirror}} &= 255\,\mathrm{nm}\,, & \mathsf{wi}_{\mathrm{defect}} &= 252\,\mathrm{nm}\,,\\
\mathsf{c_o} &= 15\,\mathrm{nm}\,, & \mathsf{d} &= 116\,\mathrm{nm}\,, & \mathsf{wg} &= 912\,\mathrm{nm}\,.
\end{aligned}
$$

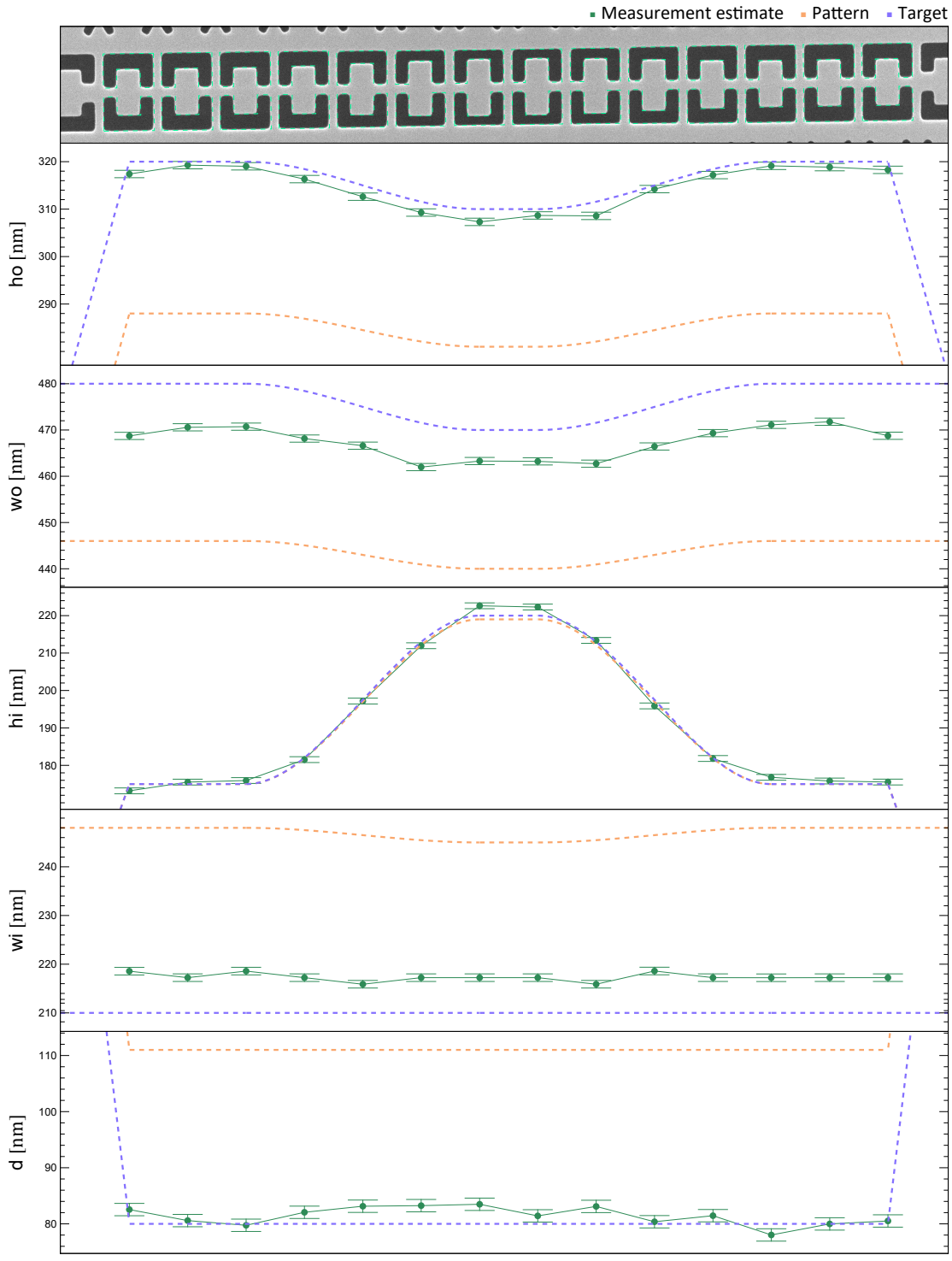

Figure Z.10: SEM image of a vertebrae cavity with edge detection and measured C-shape hole dimensions. Pattern and target dimensions are also plotted.

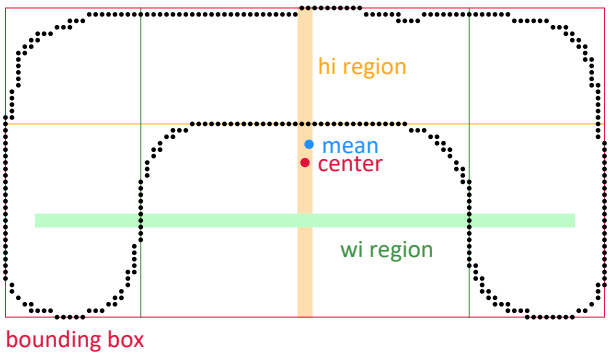

Figure Z.11: Estimating C-shape hole dimensions from edge detected pixels (black) assuming canonical orientation. Step 1: determine the bounding box (red) from maximum extents, this gives wo and ho. Step 2: compare the bounding box center (red) with the pixel mean (blue) to device if this is a top C-shape with mean above center, or bottom C-shape with mean below center. Step 3: use pixels in a vertical region (orange) around the center to determine hi. Here, for a top C-shape, taking the lowest. Step 4: use pixels in a horizontal region (green) half way between hi and the bounding box, 90% wo wide, to determine wi.

Snowflake pattern dimensions are defined in App. O. The majority of devices fabricated used SmoothStep$_1$ with $\mathsf{n}_{\text{gradient}} = 3$. Grating couplers had pattern values (see App. V and App. W)

$$\mathsf{n}_{\text{grates}} = 40\,, \qquad \Lambda = 632\,\text{nm}\,, \qquad \mathsf{f} = 0.58\,, \qquad b = -0.05\,, \qquad \mathsf{w} = 1\,\mu\text{m}\,.$$

Tethers in a zigzag pattern are kept thin (125 nm) such as not to support optical modes (see App. S).

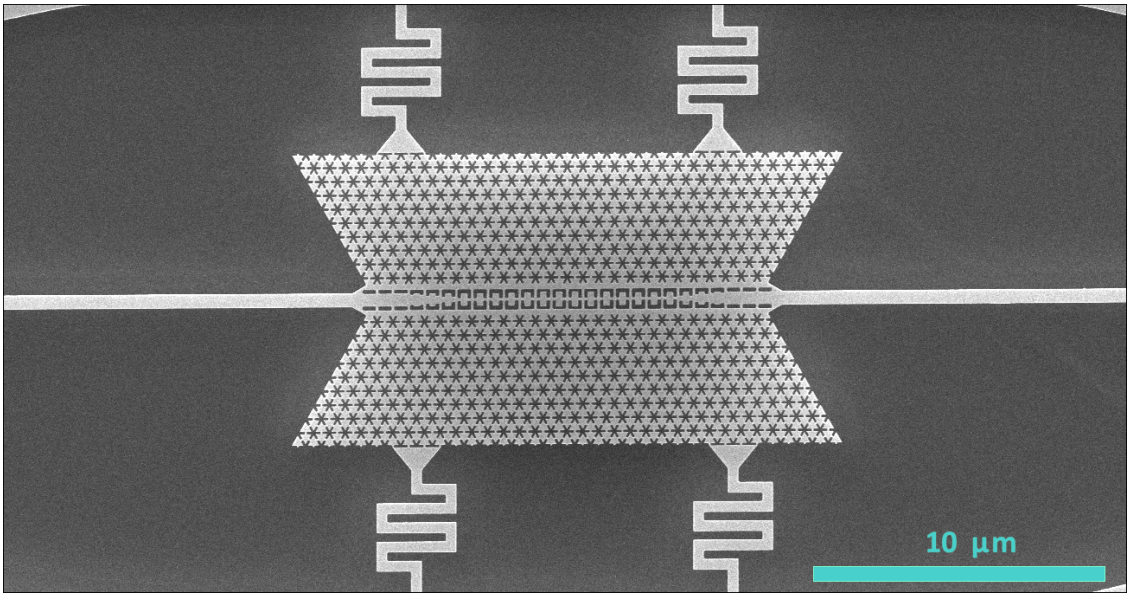

Figure Z.12: SEM image of a vertebrae resonator device.

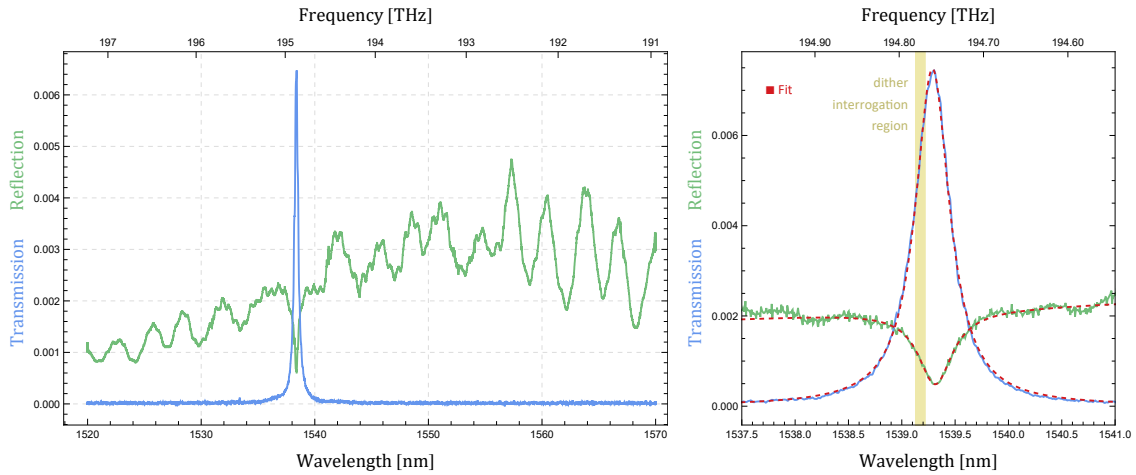

Figure Z.13: Optical transmission and reflection through a vertebrae resonator device. Fits, shown in red, produced $f_{\mathrm{o}} = 194.759\,\mathrm{THz}$, $Q_{\mathrm{o}}^{\mathrm{L}} = 3954 \pm 5$, $\beta_{\mathrm{o}}^{1} = 0.54 \pm 0.01$, and $Q_{\mathrm{o}}^{0} = 8221 \pm 79$.

Z.4 Measurement

Measurements were made using the setup described in App. Σ. Good devices typically had $\mathsf{n}_{\mathrm{mirror}} = 3$ and $\mathsf{n}_{\mathrm{taper}} = 3$, or $\mathsf{n}_{\mathrm{mirror}} = 4$ and a short abrupt $\mathsf{n}_{\mathrm{taper}} = 1$, and measured quality factors $Q_{\mathrm{o}}^{\mathrm{L}} \sim [3000, 4000]$.

Z.4.1 Optical properties

The optical resonator was modelled as an interposed two port cavity (see Sec. Θ.3) assuming the ports are symmetric, i.e. $\beta_1 = \beta_2$. Over a limited range, transmission was fit to

$$T(f) = \mathcal{C}_{\mathrm{o}}\, T + \frac{\mathcal{A}_{\mathrm{o}}}{1 + 4\,(Q_{\mathrm{o}}^{\mathrm{L}})^2\,\left(\frac{f}{f_{\mathrm{o}}} - 1\right)}\,,$$

and reflection to

$$R(f) = \left(\mathcal{C}^0_{\mathrm{o}\,R} + \mathcal{C}^1_{\mathrm{o}\,R}\,(f - f_{\mathrm{m}})\right)\,\left(1 - \frac{1 - \frac{1}{(1+2\,\beta^1_{\mathrm{o}})^2}}{1 + 4\,(Q^{\mathrm{L}}_{\mathrm{o}})^2\,\left(\frac{f}{f_{\mathrm{o}}} - 1\right)}\right)\,,$$

independently of each other. Reflection signals contained substantial systematic uncertainty from the measurement setup and was only used to extract β_1. An example optical scan and fit is given in Fig. Z.13.

Interestingly, higher quality factor measurements were often associated with devices that suffered some contortion during the suspended layer release process, but were still able to successfully guide optics. These devices were pulled higher and further away from the bulk substrate, possibly suggesting that the shallow 1 µm gap for most devices is a considerable source of loss.

Z.4.2 Mechanical properties

The thermal spectrum is fit according to Sec. L.5 with quadratic background[2]

$$S_{XX} = \mathcal{C}^0_{\mathrm{m}} + \mathcal{C}^1_{\mathrm{m}}\,(f - f_{\mathrm{m}}) + \mathcal{C}^2_{\mathrm{m}}\,(f - f_{\mathrm{m}})^2 + \frac{\mathcal{A}}{(f - f_{\mathrm{m}})^2 + \text{ϵ}_{\mathrm{m}}{}^2}\,.$$

Mechanical resonances typically showed up near 4.5 GHz with quality factors $Q^{\mathrm{L}}_{\mathrm{m}} \sim 1000$ at room temperature.

2. Defining $\text{ϵ} = \alpha/(2\,\pi)$.

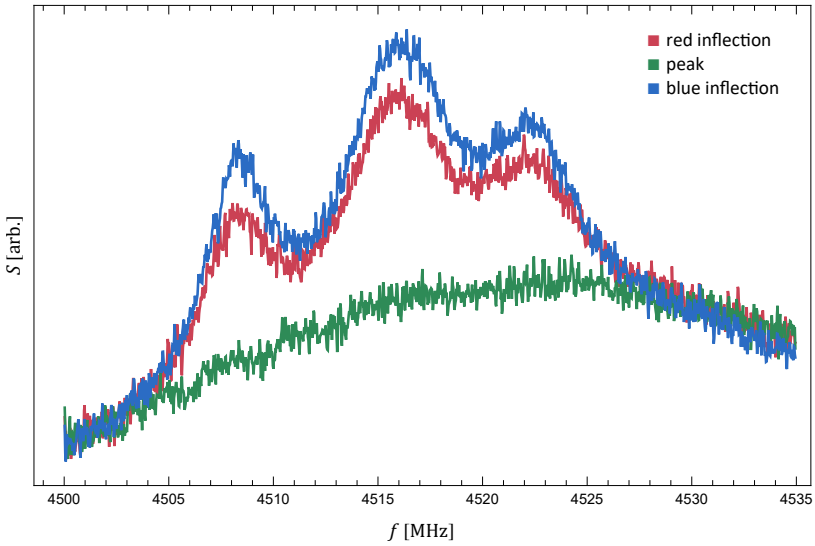

Figure Z.14: Measured power spectral density for a device with $n_{\text{defect}} = 3$ showing a splitting into three distinct mechanical modes due to variation in paddle size. Measurements were taken with the laser at different locations in the optical resonance. As expected there is no optomechanical signal when probing the peak of the optical resonance.

Z.4.3 Optomechanical coupling

Optomechanical couplings were measured from the thermal mechanical spectrum and a phase modulated signal following App. L with calibration in Sec. Σ.1.2. Due to ubiquitous thermal drifts affecting both the resonator device and measurement setup, significant systematic uncertainties affected measurement. Fast spectrum analyzer scans that were able to capture both the thermal spectrum and calibration signal together over a short period of time (typically 30 s) were favoured, with repetition counts ~ 100 used to build up statistics.

Single paddle devices, $\mathsf{n}_{\text{defect}} = 1$, exhibited optomechanical couplings $\sim [400, 500]$ kHz. One double paddle device, $\mathsf{n}_{\text{defect}} = 2$, with a single (overlapping) resonance may have had $\mathscr{g}_{\text{om}} \sim 800$ kHz but suffered from weak optical transmission making it difficult to measure.

Z.5 Mechanical splitting

One problem with multiple paddles in the resonator, i.e. $\mathsf{n}_{\mathrm{defect}} > 1$, is the vulnerability to minor variations in $\mathsf{hi}_{\mathrm{defect}}$ due to fabrication. Simulations with adjacent defect sites exhibiting $\pm 1\,\mathrm{nm}$ in $\mathsf{hi}_{\mathrm{defect}}$ generated mode splittings of $\mp 17\,\mathrm{MHz}$. Fig. Z.14 demonstrates such a situation in the measurement of the power spectral density.

APPENDIX Γ

Ring resonators

Ring resonators are simple resonance structures made from a loop of waveguide.

Γ.1 Resonance condition

The resonance condition for a ring is simply

$$\underset{\substack{\text{track}\\\text{length}}}{L} = \left(\begin{array}{c} \lambda \\ \text{propagating} \\ \text{wavelength} \end{array} \right) \times \left(m \in \mathbb{Z}^+ \right) ,$$

where for a circular track $L = 2\,\pi\,R$. Due to the waveguide nature of the resonator, the appropriate wave speed is the group velocity,

$$f\,\lambda = v_g = \frac{\partial \omega}{\partial k} = \frac{c}{n_g} ,$$

where n_g is the 'group index of refraction'. The resonant frequencies are thus

$$f_m = \frac{c\,m}{n_g\,L} \quad : \quad m \in \mathbb{Z}^+ ,$$

and the free spectral range is

$$\text{FSR} = \frac{c}{n_g\,L} .$$

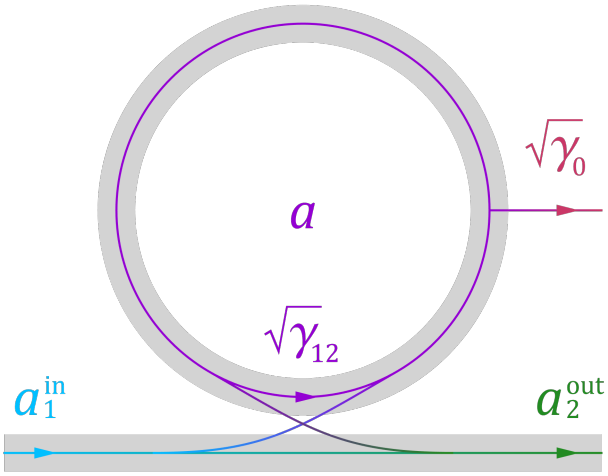

Figure Γ.1: Diagram of a ring resonator connected to a waveguide.

Γ.2 Input-output relations

From Sec. Θ.4.2 and Fig. Γ.1, the equations of motion for a single resonance f_0 are

$$\frac{\mathrm{d}}{\mathrm{d}t}a(t) = -\mathrm{i}\,\omega_0\,a(t) - \frac{\gamma_0 + \gamma_{1\,2}}{2}\,a(t) - \sqrt{\gamma_{1\,2}}\,\mathrm{e}^{\mathrm{i}\,(\phi-\theta)}\ ,$$

$$a_2^{\text{out}}(t) = \sqrt{\gamma_{1\,2}}\,\mathrm{e}^{\mathrm{i}\,\theta}\,a(t) + \mathrm{e}^{\mathrm{i}\,\phi}\,a_1^{\text{in}}(t)\ .$$

Taking the Fourier transform, the scattering element is

$$\frac{a_2^{\mathrm{out}}(t)}{a_1^{\mathrm{in}}(t)} = S_{2\,1} = \mathrm{e}^{\mathrm{i}\,\phi}\left(1 - \frac{\gamma_{1\,2}}{\frac{\gamma_0+\gamma_{1\,2}}{2} - \mathrm{i}\,(\omega-\omega_0)}\right),$$

$$|S_{2\,1}|^2 = 1 - \frac{\gamma_0\,\gamma_{1\,2}}{\left(\frac{\gamma_0+\gamma_{1\,2}}{2}\right)^2 + (\omega-\omega_0)^2}$$

$$= 1 - \frac{\frac{4\,\beta_{1\,2}}{(1+\beta_{1\,2})^2}}{1 + 4\,{Q_{\mathrm{L}}}^2\,\left(\frac{\omega-\omega_0}{\omega_0}\right)^2}\,.$$

Critical coupling occurs at $\beta_{1\,2} = 1$.

Γ.3 Suspended GaAs rings

From simulations of suspended GaAs beams in App. S, for dimensions of ($l_z = 250\,\mathrm{nm}$) × ($l_y = 450\,\mathrm{nm}$) and $n_{\mathrm{GaAs}} = 3.32$, the $\overset{-}{y}\overset{+}{z}$ mode near 194 THz has a group velocity $v_g = 6.72 \times 10^7\,\mathrm{m\,s^{-1}}$ ($n_g = 4.46$). For a track radius of 52 μm the predicted FSR = 206 GHz.

Γ.4 Measurements

To test our optical setup, App. Σ, and grating coupler fabrication, App. V, optical ring resonators were produced. Fig. Γ.2 shows the transmission through an example suspended GaAs ring resonator. Comparing the measured free spectral range to theory suggests the group velocity is slower than predicted, likely from inaccurate beam dimensions.

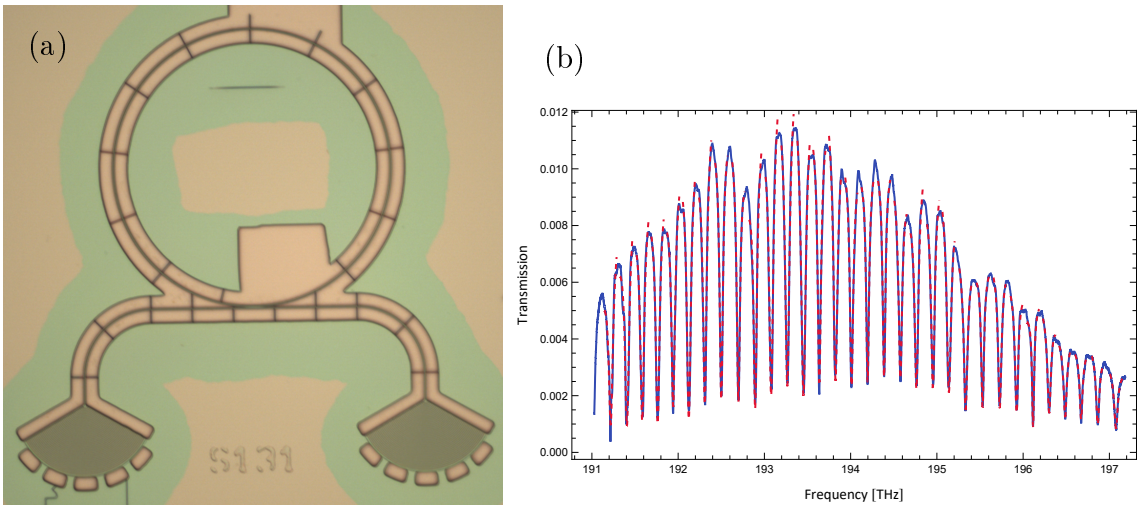

Figure Γ.2: (a) Microscope image of a suspended GaAs ring resonator. The ring outer radius is 52 μm with design width 450 nm and thickness 250 nm. (b) Transmission through the ring resonator (blue) with fits to each resonance (dashed red). The loaded Q factors are approximately distributed $Q_L \sim \text{Normal}[3826, 679]$ and free spectral range is measured to be $\text{FSR} = (192.370 \pm 0.033)\,\text{GHz}$.

APPENDIX Δ

Nanobeam

The nanobeam is one of the most widely used optomechanic devices. Typically it refers to a suspended dielectric beam with holes punctuated to produce a one-dimensional optomechanical crystal, and gradient defect to create a 'cavity' optical and mechanical resonance. Early one-dimensional optomechanical crystals involved different designs, such as ladders [115, 165, 284] and blocks [176], but holes proved to be best performer. Since 2010 nanobeams have become a popular optomechanical system and have been made from silicon [116, 117, 122, 126, 127, 133, 134, 136, 137, 143, 179, 213, 226, 285–296], diamond[162], aluminium nitrite [120, 121], gallium arsenide [123, 128, 157, 158], silicon nitride [297–302], gallium nitride [227], lithium niobate[124, 130–132, 192, 303], and gallium phosphide [135].

Δ.1 Design

Gallium arsenide ($n = 3.37$) (see Sec. M.1.5) has similar optical properties to silicon ($n = 3.47$) [259], such that design dimensional parameters originally optimized for a silicon nanobeam [122, 304] can be used to target 194 THz.

Using the parameters specified by Fig. Δ.1, along with thickness `t`, the nanobeam design

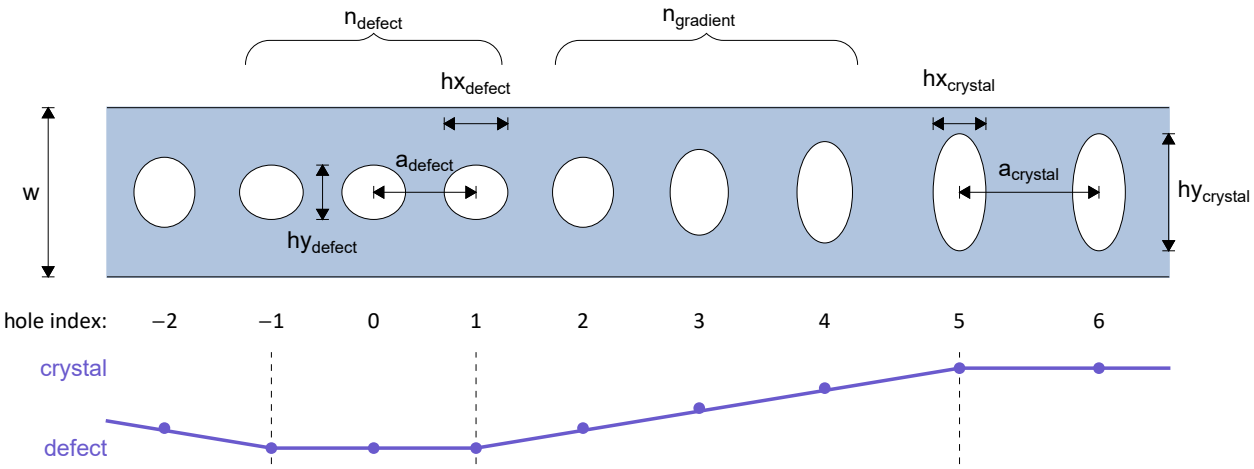

Figure Δ.1: Nanobeam dimensions specifications, the linear gradient is a function of hole index.

parameters were

$$\mathsf{t} = 250\,\text{nm}\,, \qquad \mathsf{w} = 529\,\text{nm}\,,$$
$$\mathsf{a}_{\text{crystal}} = 436\,\text{nm}\,, \qquad \mathsf{a}_{\text{defect}} = 320\,\text{nm}\,,$$
$$\mathsf{hx}_{\text{crystal}} = 165\,\text{nm}\,, \qquad \mathsf{hx}_{\text{defect}} = 199\,\text{nm}\,,$$
$$\mathsf{hy}_{\text{crystal}} = 375\,\text{nm}\,, \qquad \mathsf{hy}_{\text{defect}} = 174\,\text{nm}\,,$$
$$\mathsf{n}_{\text{gradient}} = 3\,, \qquad \mathsf{n}_{\text{defect}} = 3\,.$$

The nanobeam is effervescently coupled to nearby waveguide that is completely suspended and connected to suspended grating couplers. Suspension is provided by zig-zag tethers that offer some spring-like give during the release process. The waveguide has a width of 500 nm and features a weave that brings it closer to the nanobeam and simultaneously reduces the width to 450 nm in the coupling region. Spacing between the nanobeam and waveguide affects the resonance coupling and was varied between devices, the measurements presented here belong to a device with a 100 nm gap. Additional tethers between the nanobeam and

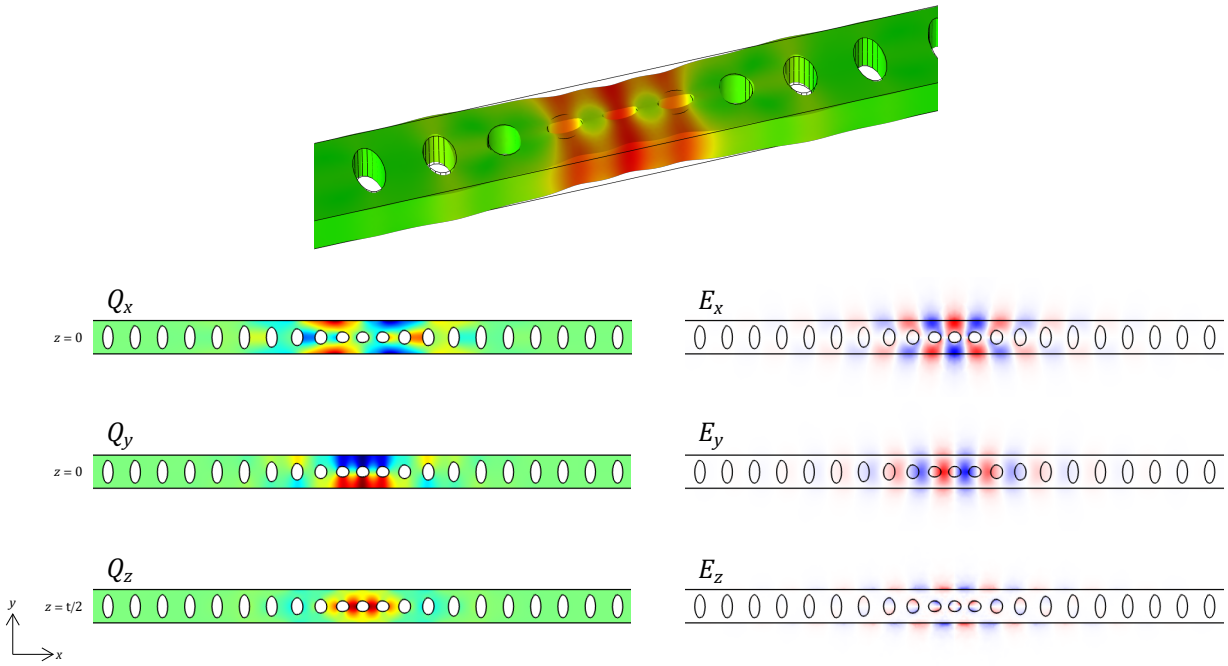

Figure Δ.2: (Top) 3D model showing the mechanical breathing mode of interest with exagerated deformation. (Bottom) 2D plane cuts showing the displacement field at 2.96 GHz and electric field at 195 THz.

waveguide away from the coupling region were also included. A secondary release trench surrounds the main release area to help reduce cracking and flaking during the release (see Sec. 4.5).

Δ.1.1 Simulation

The nanobeam described in Sec. Δ.1 was simulated in the finite element modelling software COMSOL [181], using MATLAB [182] scripts to build the model. Material properties follow that given in Sec. M.1.1 with the crystal [110] direction aligned parallel to the nanobeam. Symmetries in all three planes were used to speed up the simulation. Depicted in Fig. Δ.2 the mechanical mode of interest exhibits mirror symmetry (see App. E) in each Cartesian plane through the center $(\overset{+}{x}\,\overset{+}{y}\,\overset{+}{z})$, and the optical mode of interest has mirror symmetry in

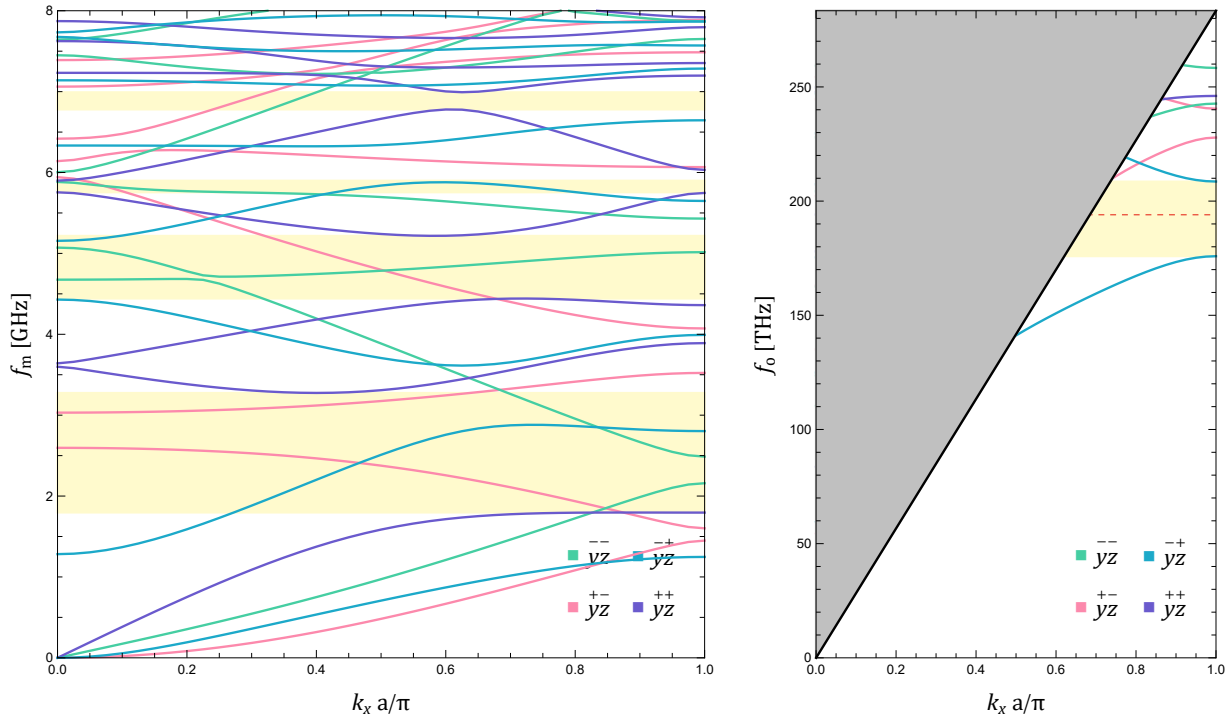

Figure Δ.3: Dispersion plots of periodic elliptical holes in GaAs with t = 250 nm, a = 436 nm, hx = 165 nm, hy = 375 nm. (Left) mechanical modes with band gaps for $\overset{+}{y}\,\overset{+}{z}$ in yellow. (Right) optical modes with band gaps for $\overset{-}{y}\,\overset{+}{z}$ in yellow and target frequency (194 THz) in dashed red.

z and mirror antisymmetry in x and y ($\overset{-}{x}\,\overset{-}{y}\,\overset{+}{z}$). The optomechanical coupling was calculated according to App. C with the major contribution coming from the photoelastic effect. Simulated frequencies[1] are

$$\begin{aligned} f_{\mathrm{m}}^{(\mathrm{sim})} &= 2.955\,\mathrm{GHz}\,, \\ f_{\mathrm{o}}^{(\mathrm{sim})} &= 194.7\,\mathrm{THz}\,, \\ \text{g}\!\!\!^{-}_{\mathrm{om}}^{(\mathrm{sim})} &= 1.140\,\mathrm{MHz}\,. \end{aligned}$$

In Fig. Δ.3 simulations of the elliptical hole optomechanical crystal using Floquet periodic

1. Defining $\text{g}\!\!\!^{-} = g/(2\,\pi)$.

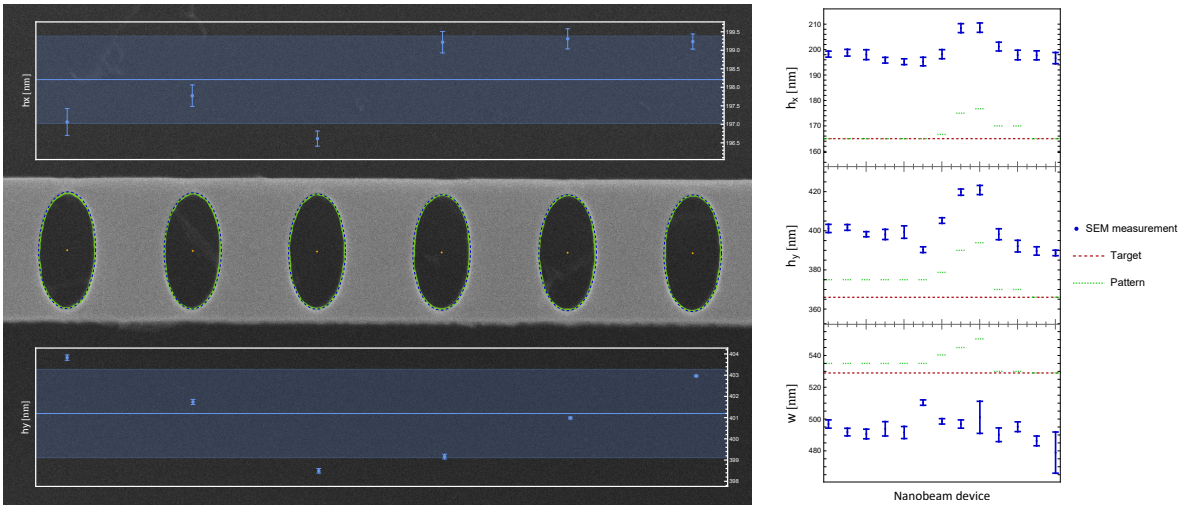

Figure Δ.4: (Left) SEM image of a nanobeam optomechanical crystal, with edge detected points making up the holes in green, centers in orange, and elliptical shape fits in dashed blue. Inset are the corresponding fit parameter results, with mean and standard deviation given by the translucent background. (Right) Comparison of SEM optomechanical crystal analysis between different nanobeam devices that had varying pattern dimensions and electron beam dosages.

boundary conditions were made to produce dispersion plots exhibiting the desired band gaps.

Δ.2 Fabrication

Using the target dimensions of Sec. Δ.1 as a guide, various pattern design dimensions (within a few percent), electron beam dosages, and proximity effect correction schemes were trialled. Variations on the waveguide thickness (affects propagation and evanescence) and curvature, waveguide to nanobeam proximity (affects coupling), nanobeam tethering (to reduce vertical misalignment) were also carried out. Nanobeam optomechanical crystal dimensions measurements were carried out from SEM images following similar techniques to App. P. Measurements and comparisons of the sort in Fig. Δ.4 were made to evaluate fabrication results and direct new trials.

The device measured here had nanobeam pattern parameters matching that of the design

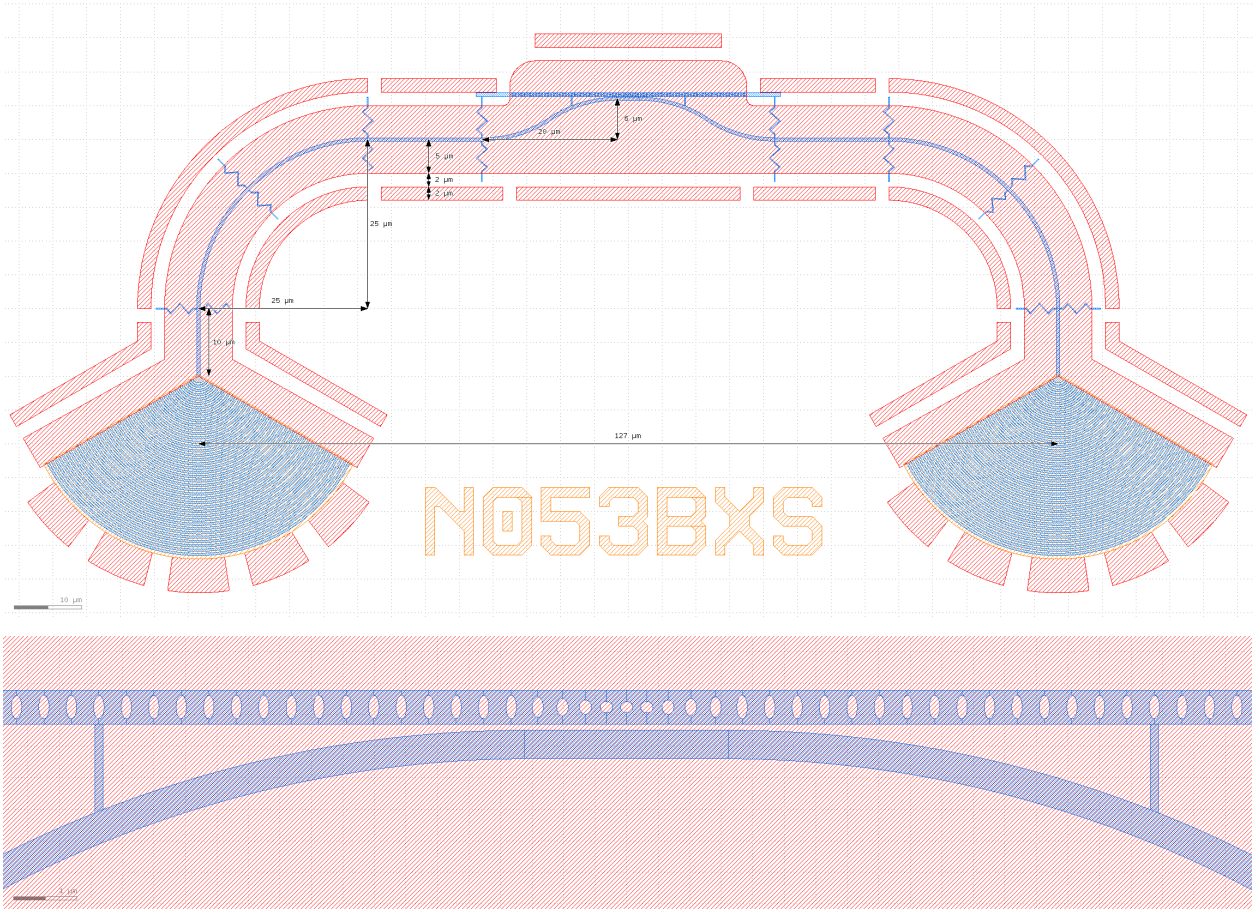

Figure Δ.5: (Top) pattern DXF image of the device design with large scale dimensions labelled. (Bottom) zoom in of the nanobeam resonator region. Blue is the HSQ layer making up the suspended structure, red is the complete etch and released regions, and orange is the partial etch into the top layer.

except with $\mathsf{w} = 535\,\text{nm}$, and t at the mercy of the wafer. An image of the DXF pattern for this device is given in Fig. Δ.5. The waveguide had pattern measurements

$$\text{waveguide width} = 500\,\text{nm}\,,$$

$$\text{waveguide width near nanobeam} = 450\,\text{nm}\,,$$

$$\text{waveguide to nanobeam gap} = 100\,\text{nm}\,,$$

with the close region spanning the defect and gradient portion of the nanobeam holes. Connecting the close waveguide section to the main track is a curve made from two circular arcs,

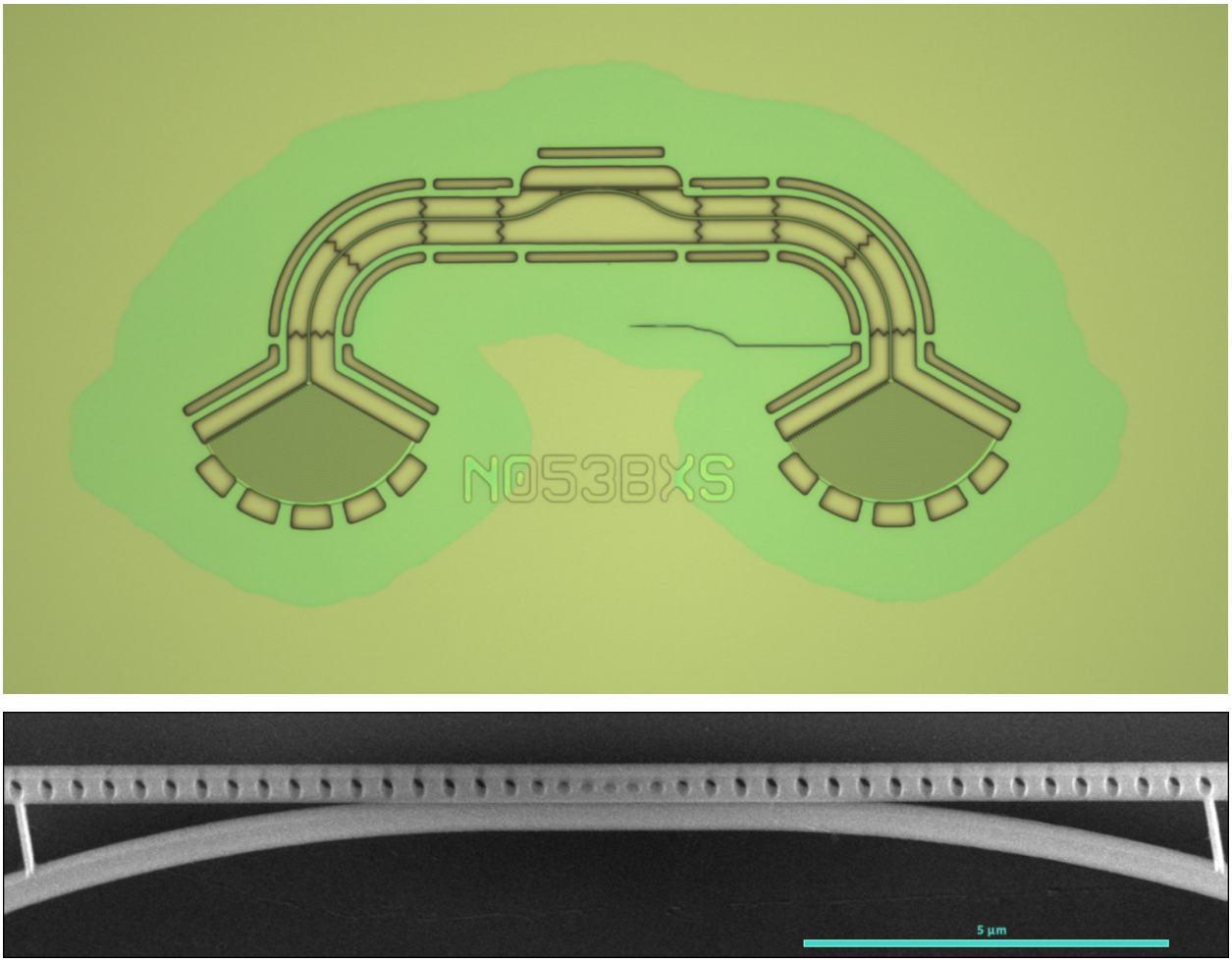

Figure Δ.6: (Top) optical microscope image of the measured device. (Bottom) 45° angle scanning electron microscope image of an identical device's nanobeam and accompanying waveguide.

of the same radius of curvature and angle, that form a smooth curve, along which the width is linearly gradated. The grating coupler had pattern values (see App. V and App. W)

$$\mathsf{n}_{\text{grates}} = 40\,, \qquad \Lambda = 638\,\text{nm}\,, \qquad \mathsf{f} = 0.54\,, \qquad b = -0.05\,, \qquad \mathsf{w} = 1\,\mu\text{m}\,.$$

Tethers in a zigzag pattern are kept thin (125 nm) such as not to support optical modes (see App. S).

Electron beam exposure was made using proximity effect correction (N.2), with two passes,

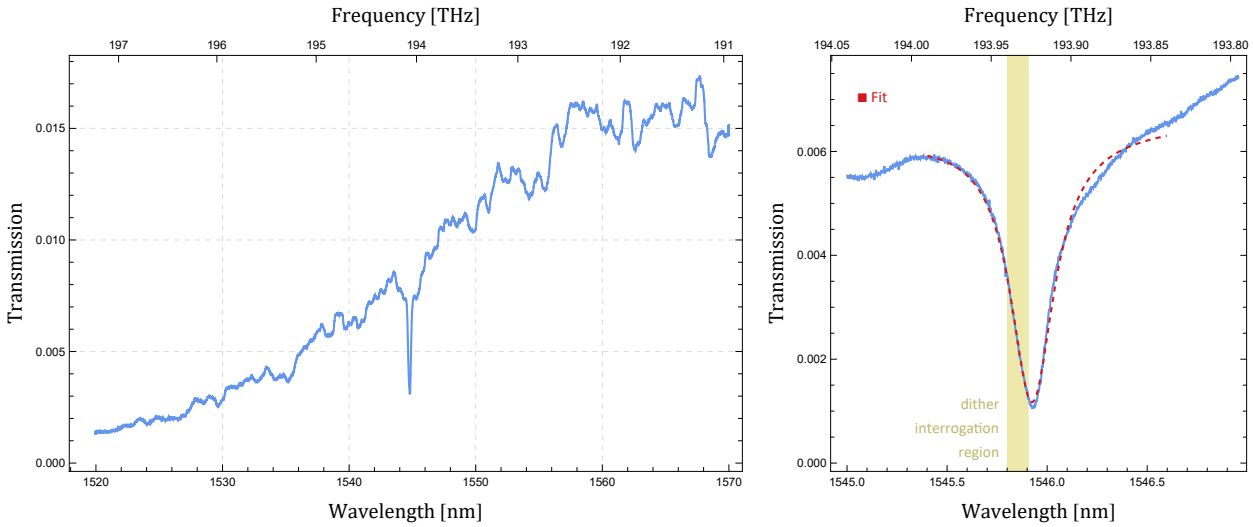

Figure Δ.7: Optical transmission scans through the device made by forward sweeping the laser wavelength. The optical resonance fit is shown in dashed red, and the region used for second harmonic dither locking and thermal mechanics spectrum interrogation is highlighted.

at 450 μC/cm^2. Other fabrication recipes followed that of Ch. 4. Pictures are provided in Fig. Δ.6[2].

Δ.3 Measurements

Using the measurement setup described in App. Σ, devices were probed optically to measure their optical and mechanical resonance properties. Here we detail measurements for a particular device that exhibited the best optical resonance.

$\triangle$.3.1 Optical properties

Fig. Δ.7 shows the optical transmission spectrum through the device, and the optical resonance fit (over a limited region) to (see Sec. Θ.4.1)

$$T(f) = \left(\mathcal{C}_{\rm o}^0 + \mathcal{C}_{\rm o}^1\,(f - f_{\rm o})\right)\,\left(1 - \frac{1 - \frac{1}{(1+\beta_{\rm o}^{12})^2}}{1 + 4\,(Q_{\rm o}^{\rm L})^2\,\left(\frac{f}{f_{\rm o}} - 1\right)}\right)\,,$$

with results averaged between the forward and backward scans,

$$f_{\rm o}^{\rm (meas)} = (193.92338 \pm 0.00003)\,{\rm THz}\,, \qquad \lambda_{\rm o}^{\rm (meas)} = (1545.9325 \pm 0.0002)\,{\rm nm}\,,$$

$$\beta_{\rm o}^{12} = 1.334 \pm 0.008\,,$$

$$Q_{\rm o}^{\rm L} = 5856 \pm 20\,, \qquad \frac{\gamma_{\rm o}}{2\,\pi} = (33.17 \pm 0.11)\,{\rm GHz}\,, \qquad \frac{\alpha_{\rm o}}{2\,\pi} = (16.59 \pm 0.06)\,{\rm GHz}\,,$$

$$Q_{\rm o}^{0} = 13645 \pm 85\,, \qquad \frac{\gamma_{\rm o}^{0}}{2\,\pi} = (14.21 \pm 0.09)\,{\rm GHz}\,, \qquad \frac{\alpha_{\rm o}^{0}}{2\,\pi} = (7.11 \pm 0.04)\,{\rm GHz}\,,$$

$$Q_{\rm o}^{12} = 10228 \pm 28\,, \qquad \frac{\gamma_{\rm o}^{12}}{2\,\pi} = (18.96 \pm 0.05)\,{\rm GHz}\,, \qquad \frac{\alpha_{\rm o}^{12}}{2\,\pi} = (9.48 \pm 0.03)\,{\rm GHz}\,.$$

The blue-side inflection point is thus located at (see App. Υ)

$$f_{\substack{\rm o\ blue\\ \rm infl}} = f_{\rm o\ res} + (9.577 \pm 0.032)\,{\rm GHz}\,, \qquad \lambda_{\substack{\rm o\ blue\\ \rm infl}} = \lambda_{\rm o\ res} - (0.2644 \pm 0.0007)\,{\rm nm}\,.$$

2. SEM exposure can degrade devices.

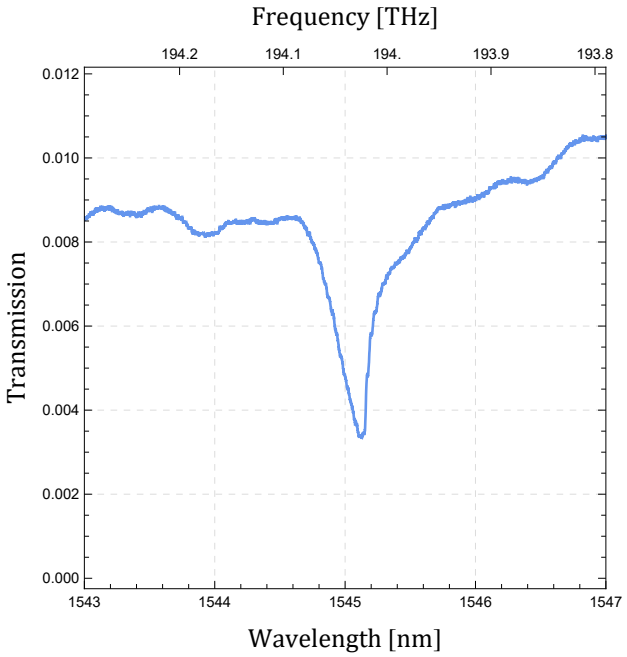

Figure Δ.8: Optical transmission scan through the resonance at high power, $P_{\text{delivered}} \approx 1.45\,\text{mW}$, showing the non-linear snapping effect.

At high powers the nanobeam optical resonance exhibits a non-linear snapping effect that strongly skews the optical resonance, as shown in Fig. Δ.8. To avoid this, measurements were made at $P_{\text{delivered}} \approx 300\,\mu\text{W}$.

If the power output in the absence of the cavity is $\mathcal{C}_0\,P_{\text{delivered}}$ and our device is symmetric, we can assign $\sqrt{\mathcal{C}_0}$ transmission to each grating coupler and waveguide, such that $P_{\text{L}} = \sqrt{\mathcal{C}_0}\,P_{\text{delivered}}$. An estimation of the cavity occupation is then (see App. I and App. Θ)

$$\bar{n}_{\text{o}}(\omega_{\text{L}}) = |\bar{a}|^2 = \frac{\alpha_{\text{o}}^{12}}{(\omega_{\text{o}} - \omega_{\text{L}})^2 + {\alpha_{\text{o}}}^2} \frac{\sqrt{\mathcal{C}_0}\,P_{\text{delivered}}}{\hbar\,\omega_{\text{L}}} \ ,$$

and for $\omega_{\text{L}} = f_{\text{o}\,\underset{\text{infl}}{\text{blue}}}$,

$$\bar{n}_{\text{o}}\left(f_{\text{o}\,\underset{\text{infl}}{\text{blue}}}\right) = (3.03 \pm 0.11) \times 10^4 \ .$$

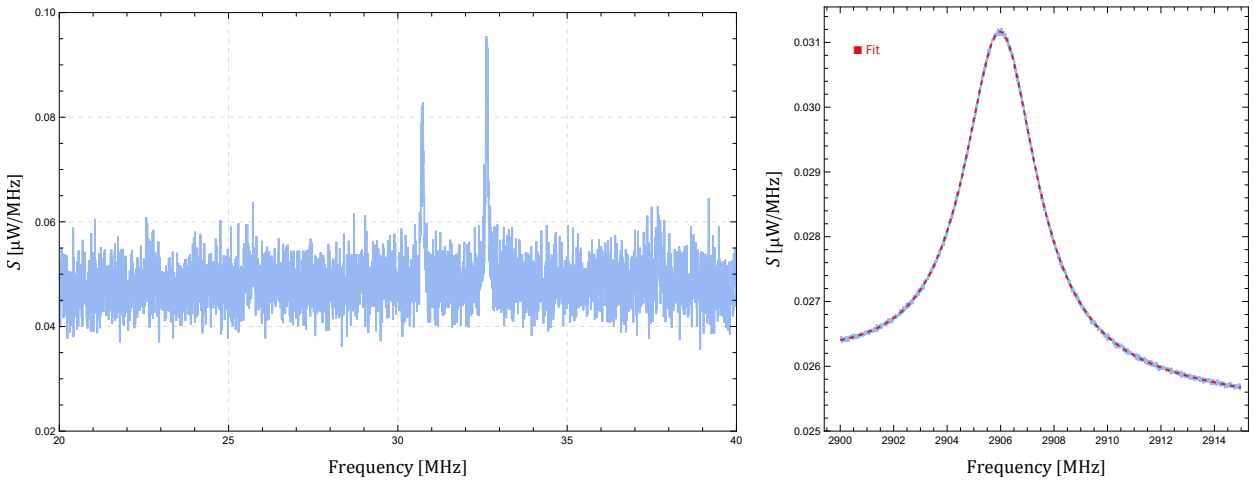

Figure Δ.9: Optical detected power spectrums showing features from mechanical vibration. (Left) low frequency spectrum and features from large scale modes (i.e. the whole device or waveguide oscillating). (Right) microwave frequency mechanical thermal spectrum from the optomechanical cavity, taken over half a day with averaging. Spectrum analyzer instrument noise (400 kHz sawtooth) has been subtracted in this plot.

Δ.3.2 Mechanical properties

Targeting the laser to the side of the resonance will let the thermal mechanical spectrum be imprinted on the transmission signal and be measurable (see App. L) by a sufficiently fast photodetector. Over medium to long time scales the optical resonance drifts in both frequency and power. To track the resonance from the side (blue inflection point) a second harmonic dither lock is used (see App. ϒ), with $f_{\text{dither}} = 100\,\text{Hz}$ and $V_{\underset{\text{amp}}{\text{dither}}} = 1\,\text{V}$, covering a region of $\sim 0.1\,\text{nm}$. Spectrum analyzer measurements in this operating regime need VBW $\ll$ $f_{\text{dither}} = 100$ to appropriately average the dithering.

Fig. Δ.9 shows some low frequency mechanical features from large scale elements in the device, and the microwave frequency mechanical mode in the nanobeam. The thermal spectrum

is fit according to Sec. L.5[3]

$$S_{XX} = \mathcal{C}_{\rm m}^0 + \mathcal{C}_{\rm m}^1\,(f - f_{\rm m}) + \frac{\mathcal{A}}{(f - f_{\rm m})^2 + \text{ϵ}_{\rm m}{}^2} \ ,$$

with results

$$f_{\rm m}^{(\rm meas)} = (2905.9585 \pm 0.0008)\,\text{MHz} \ ,$$

$$Q_{\rm m}^{\rm L} = 873.8 \pm 0.9 \ , \qquad \frac{\gamma_{\rm m}}{2\,\pi} = (3.326 \pm 0.004)\,\text{MHz} \ , \qquad \frac{\alpha_{\rm m}}{2\,\pi} = (1.663 \pm 0.002)\,\text{MHz} \ .$$

The mechanical mode is assumed to be in thermal equilibrium at ambient room temperature, $(295 \pm 3)\,\text{K}$, giving the cavity occupation

$$\bar{n}_{\rm m}(\omega_{\rm m}) \approx \frac{k_{\rm B}\,\mathbb{T}}{\hbar\,\omega_{\rm m}} = 2117 \pm 22 \ .$$

△.3.3 Optomechanical coupling

A weak phase modulated signal through the device has similar transmission properties to the thermal mechanical signal (see App. L) and can be used to normalize $\mathcal{A}$. Using the calibration in Sec. Σ.1.2,

$$\text{ϑ}_{\rm om} = \sqrt{\frac{\pi\,\mathcal{A}\,{f_\Phi}^2\,A_\Phi(P_\Phi)^2}{4\,\text{ϵ}_{\rm m}\,P_{f_\Phi}\,\bar{n}_{\rm m}(f_{\rm m})}} = (595 \pm 4)\,\text{kHz} \ .$$

3. Defining $\text{ϵ} = \alpha/(2\,\pi)$.

The cooperativity is

$$\mathcal{C}_{\mathrm{om}} = \frac{{g_{\mathrm{om}}}^2 \, |\bar{a}|^2}{\alpha_{\mathrm{o}} \, \alpha_{\mathrm{m}}} = 0.388 \pm 0.015 \; .$$

APPENDIX Θ

Classical input-output theory

This appendix covers the formulation of classical input-output theory and provides useful reference equations [148, 220, 230, 231, 305].

Θ.1 Zero port resonator

Let us begin with an unconnected resonator, shown in Fig. Θ.1, with only intrinsic losses to environment, and make the following definitions,

$a(t)$,	ω_0 ,	α ,	$\ell(t)$.
generalized amplitude	resonant angular frequency	amplitude decay rate	drive

The equation of motion for our system is

$$\frac{\mathrm{d}}{\mathrm{d}t}a(t) = -\mathrm{i}\,\omega_0\,a(t) - \alpha\,a(t) + \ell(t)\;, \tag{Θ.1}$$

which has solution

$$a(t) = a(t_0)\,\mathrm{e}^{-(\mathrm{i}\,\omega_0+\alpha)(t-t_0)} + \int_{t_0}^{t} \mathrm{e}^{-(\mathrm{i}\,\omega_0+\alpha)(t-t')}\,\ell(t')\,\mathrm{d}t'\;.$$

In this form we are assuming both $\omega_0 \in \mathbb{R}$ and $\alpha \in \mathbb{R}$. Alternatively we can have a complex frequency $\omega_0 \in \mathbb{C}$ where we identify $\alpha = -\Im[\omega_0]$.

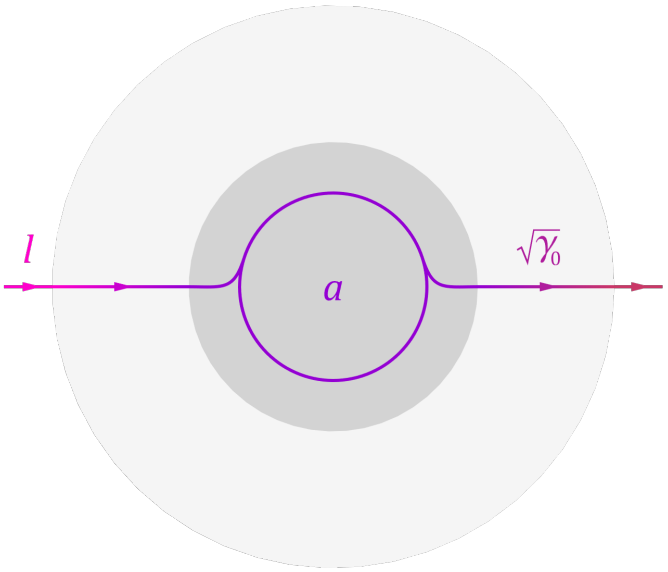

Figure Θ.1: Diagram of an isolated resonator with possible environmental drive.

Below are some additional definitions used when discussing resonance behaviour,

$$f = \frac{\omega}{2\pi}\,, \qquad \text{frequency}$$

$$T = \frac{1}{f}\,. \qquad \text{period}$$

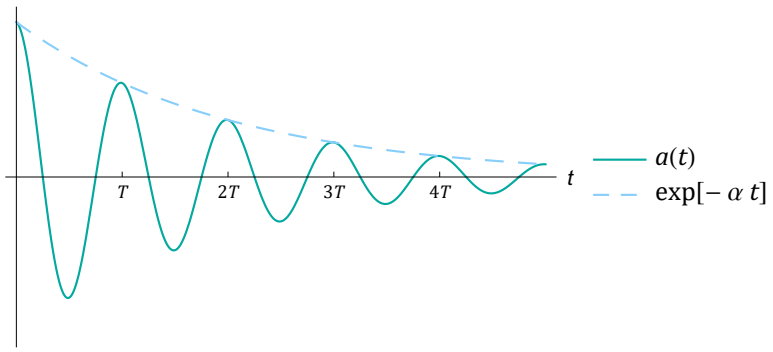

Figure Θ.2: Ring down of amplitude $a(t)$ with no drive.

Θ.1.1 No drive

If we have no driving term, our amplitude simply rings down as in Fig. Θ.2,

$$a(t) = a(t_0)\,\mathrm{e}^{-(\mathrm{i}\,\omega_0+\alpha)(t-t_0)}\ .$$

The energy stored in the resonator is proportional to the amplitude squared,

$$|a(t)|^2 = |a(t_0)|^2\,\mathrm{e}^{-2\,\alpha\,(t-t_0)}\ ,$$

and the power loss is thus

$$-\frac{\mathrm{d}}{\mathrm{d}t}\Big(|a(t)|^2\Big) = 2\,\alpha\,|a(t)|^2\ .$$

We can now determine the quality factor to be

$$Q = \omega_0\,\frac{\text{stored energy}}{\text{power loss}} = \frac{\omega_0}{2\,\alpha}\ .$$

Some additional definitions can also be made here,

$$\underset{\substack{\text{power}\\ \text{loss rate}}}{\gamma} = 2\,\alpha\ , \qquad \underset{\substack{\text{damping}\\ \text{ratio}}}{\zeta} = \frac{\alpha}{\omega_0}\ , \qquad \underset{\text{lifetime}}{\tau} = \frac{1}{\alpha}\ .$$

Θ.1.2 Fourier transform

Define the t_0 shifted Fourier transform on $a(t)$ as

$$a(\omega) = \frac{1}{\sqrt{2\,\pi}} \int_{-\infty}^{\infty} \mathrm{e}^{\mathrm{i}\,\omega\,(t-t_0)}\, a(t)\,\mathrm{d}t\ ,$$

and the inverse Fourier transform on $a(\omega)$ as

$$a(t) = \frac{1}{\sqrt{2\,\pi}} \int_{-\infty}^{\infty} \mathrm{e}^{-\mathrm{i}\,\omega\,(t-t_0)}\, a(\omega)\,\mathrm{d}\omega\ .$$

Applying this Fourier transform to (Θ.1), we get

$$-\mathrm{i}\,\omega\,a(\omega) = -\mathrm{i}\,\omega_0\,a(\omega) - \alpha\,a(\omega) + \ell(\omega)\ ,$$

$$\Rightarrow \quad a(\omega) = \frac{\ell(\omega)}{\alpha - \mathrm{i}\,(\omega - \omega_0)}\ ,$$

$$\Rightarrow \quad |a(\omega)|^2 = \frac{|\ell(\omega)|^2}{\alpha^2 + (\omega - \omega_0)^2}\ .$$

For a resonator with no input, the drive term is simply a thermal noise background and can be approximated (over a narrow range of frequencies) to be constant $\ell(\omega) = \ell$. For an

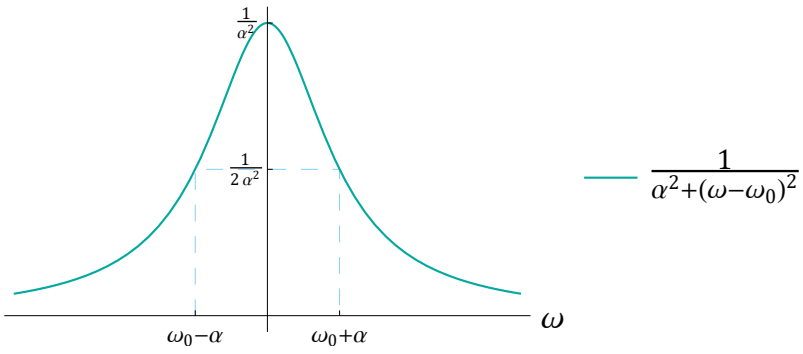

Figure Θ.3: Lorentz-like function.

isolated resonator with no drive,

$$-\mathrm{i}\,\omega\,a(\omega) = -\mathrm{i}\,\omega_0\,a(\omega) - \alpha\,a(\omega)\ ,$$

which has two solutions. The first solution is the trivial $a(\omega) = 0$ empty resonator steady state (after ringing down). The second solution is $\alpha = 0$ and $\omega = \omega_0$ corresponding to the idealized situation of the resonator being perfectly isolated from the environment and continuing to oscillate indefinitely precisely at the resonance frequency.

Note that the function, shown in Fig. Θ.3,

$$\omega \mapsto \frac{1}{\alpha^2 + (\omega - \omega_0)^2} = \frac{1}{\left(\frac{\gamma}{2}\right)^2 + (\omega - \omega_0)^2}\ ,$$

has a maximum value of $(1/\alpha)^2$ and full-width half-maximum of $2\,\alpha = \gamma$.

Θ.1.3 Equivalent circuit

Circuits featuring inductors, capacitors, and resistors exhibit resonant behaviour and can be used in modeling resonators. In this analysis we will be using complex voltages and currents.

Here we consider a series LCR circuit, shown in Fig. Θ.4, but the same results can be found

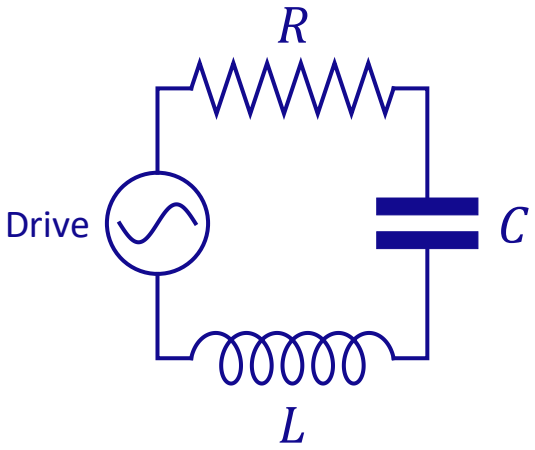

Figure Θ.4: Series LCR circuit.

for a parallel LCR circuit. The impedance of our series LCR is

$$Z = R + \mathrm{i}\,\omega\,L + \frac{1}{\mathrm{i}\,\omega\,C}\ ,$$

and resonant frequency for this circuit is found by

$$\mathrm{i}\,\omega_0\,L = \frac{\mathrm{i}}{\omega_0\,C} \quad \Rightarrow \quad \omega_0 = \frac{1}{\sqrt{L\,C}}\ .$$

The stored energy in inductor and capacitor are equal on resonance,

$$\text{stored energy} = \underbrace{\frac{1}{4}\,|I_L|^2\,L}_{\text{inductor}} + \underbrace{\frac{1}{4}\,|V_C|^2\,C}_{\text{capacitor}} \overset{\omega=\omega_0}{=} \frac{1}{2}\,|I|^2\,L\ ,$$

and the time averaged[1] power lost through the resistor is

$$\text{power loss} = \frac{1}{2}\,|I|^2\,R\ .$$

1. $|I_{\mathrm{RMS}}|^2 = |I_{\mathrm{peak}}|^2/2$.

Thus for a series LCR,

$$2\,\alpha = \gamma = \frac{R}{L}\,, \qquad\qquad Q = \frac{\omega_0}{\gamma} = \frac{\omega_0\,L}{R}\,.$$

The impedance of our series LCR circuit is then

$$Z = R + \mathrm{i}\,L\,\left(\omega - \frac{{\omega_0}^2}{\omega}\right)\,,$$

and for frequencies close to the resonance (enforced for high Q, low bandwidth resonators) we can series expand to

$$\begin{aligned} Z \overset{\omega\approx\omega_0}{=} R + \mathrm{i}\,L\,\left(2\,(\omega-\omega_0) + \mathcal{O}[\omega-\omega_0]^2\right) &\approx R + \mathrm{i}\,2\,L\,(\omega-\omega_0) \\ &= 2\,L\,\left(\alpha + \mathrm{i}\,(\omega-\omega_0)\right)\,. \end{aligned}$$

If the drive is an AC voltage V, we have

$$\begin{aligned} I &= V/Z \\ &= \frac{\frac{V}{2\,L}}{\alpha + \mathrm{i}\,(\omega-\omega_0)}\,, \end{aligned}$$

and thus we have a situation analogous to our zero port cavity resonator under $\omega \approx \omega_0$.

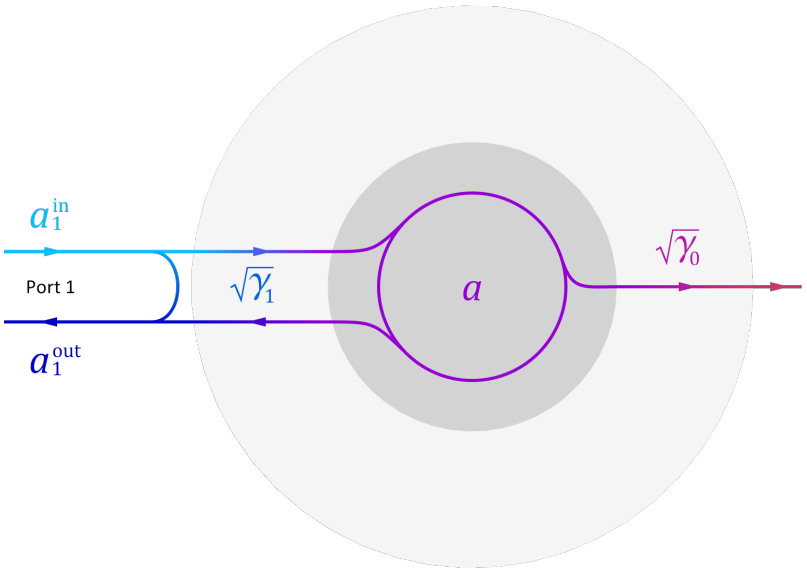

Figure Θ.5: Diagram of a resonator with one port and the various interactions.

Θ.2 One port resonator

In the case of a resonator with one port, as depicted in Fig. Θ.5, the equation of motion is

$$\frac{\mathrm{d}}{\mathrm{d}t}a(t) = -\mathrm{i}\,\omega_0\,a(t) - (\alpha_0+\alpha_1)\,a(t) + \lambda_1\,a_1^{\text{in}}(t)\ ,$$

$$a_1^{\text{out}}(t) = \mu_1\,a(t) + \nu_1\,a_1^{\text{in}}(t)\ .$$

This is similar to (Θ.1) with $\alpha = \alpha_0 + \alpha_1$ distinguishing the resonator loss channels, and with the drive now $\ell(t) = \lambda_1\,a_1^{\text{in}}(t)$. Here we are ignoring any background thermal drive

on the assumption that $\lambda_1 a_1^{\text{in}}(t)$ is much larger. We are also assuming a weak coupling regime where λ_1 is a constant, this is valid if the bandwidth is small enough and we can take $\lambda_1(\omega) \approx \lambda_1(\omega_0) = \lambda_1$.

In principle α_1 can be complex where the imaginary part corresponds to the port shifting the system's overall resonance frequency. As we're not concerned with dynamically changing the number of ports, we can make the following mapping for simplicity,

$$\omega_0 + \Im[\alpha_1] \mapsto \omega_0 \ ,$$
$$\Re[\alpha_1] \mapsto \alpha_1 \ ,$$

where ω_0 is now the full system (shifted) resonance frequency and α_1 always corresponds to the real part.

We can decompose the total loaded quality factor, Q_{L}, into an unloaded/intrinsic quality factor, Q_0, and coupling/extrinsic quality factor, Q_1, as

$$\frac{1}{Q_{\text{L}}} = \frac{1}{Q_0} + \frac{1}{Q_1} = \frac{1+\beta_1}{Q_0} \ ,$$

where we have also introduced the coupling coefficient, β_1, which obeys the following relations

$$\beta_1 = \frac{Q_0}{Q_1} = \frac{\alpha_1}{\alpha_0} \ , \qquad \frac{Q_1}{Q_{\text{L}}} = \frac{1+\beta_1}{\beta_1} \ , \qquad \frac{Q_0}{Q_{\text{L}}} = 1 + \beta_1 \ .$$

Θ.2.1 Isolated system

To determine the parameters λ_1, μ_1, ν_1, in relation to α_1 we need to carry out a series of thought experiments. In particular we consider the case of an isolated system, $\alpha_0 = 0$, where

power is conserved,

$$\frac{\mathrm{d}}{\mathrm{d}t}|a(t)|^2 = |a_1^{\mathrm{in}}(t)|^2 - |a_1^{\mathrm{out}}(t)|^2 \ . \tag{Θ.2}$$

No drive

If our system is isolated with no incoming drive, $a_1^{\mathrm{in}}(t) = 0$, the equations of motion become

$$\frac{\mathrm{d}}{\mathrm{d}t}a(t) = \ -\mathrm{i}\,\omega_0\,a(t) - \alpha_1\,a(t) \ , \tag{Θ.3}$$

$$a_1^{\mathrm{out}}(t) = \mu_1\,a(t) \ . \tag{Θ.4}$$

Solving (Θ.3) gives us

$$a(t) \propto \mathrm{e}^{-\mathrm{i}\,\omega_0\,t - \alpha_1\,t} \ ,$$

$$\Rightarrow \quad |a(t)|^2 \propto \mathrm{e}^{-2\,\alpha_1\,t} \ ,$$

$$\Rightarrow \quad \frac{\mathrm{d}}{\mathrm{d}t}|a(t)|^2 = \ -2\,\alpha_1\,|a(t)|^2 \ .$$

Combining this with (Θ.2) and (Θ.4) gives us

$$|a_1^{\mathrm{out}}(t)|^2 = |\mu_1|^2\,|a(t)|^2 = 2\,\alpha_1\,|a(t)|^2 \ ,$$

$$\Rightarrow \quad |\mu_1| = \sqrt{2\,\alpha_1} = \sqrt{\gamma_1} \ . \tag{Θ.5}$$

Uncoupled

If our resonator is uncoupled from the port, $\alpha_1 = \lambda_1 = 0$ then we essentially have two non-interacting systems,

$$\frac{\mathrm{d}}{\mathrm{d}t}a(t) = -\mathrm{i}\,\omega_0\,a(t)\;, \tag{Θ.6}$$

$$a_1^{\mathrm{out}}(t) = \nu_1\,a_1^{\mathrm{in}}(t)\;. \tag{Θ.7}$$

Equations (Θ.2) and (Θ.7) tell us

$$|a_1^{\mathrm{out}}(t)|^2 = |\nu_1|^2\,|a_1^{\mathrm{in}}(t)|^2 = |a_1^{\mathrm{in}}(t)|^2$$

$$\Rightarrow \quad |\nu_1| = 1\;. \tag{Θ.8}$$

General

We now turn to the general case for an isolated system,

$$\frac{\mathrm{d}}{\mathrm{d}t}a(t) = -\mathrm{i}\,\omega_0\,a(t) - \alpha_1\,a(t) + \lambda_1\,a_1^{\mathrm{in}}(t)\;, \tag{Θ.9}$$

$$a_1^{\mathrm{out}}(t) = \mu_1\,a(t) + \nu_1\,a_1^{\mathrm{in}}(t)\;. \tag{Θ.10}$$

Taking the complex conjugate of (Θ.9),

$$\frac{\mathrm{d}}{\mathrm{d}t}a(t)^* = \mathrm{i}\,\omega_0\,a(t)^* - \alpha_1\,a(t)^* + {\lambda_1}^*\,a_1^{\mathrm{in}}(t)^*\;, \tag{Θ.11}$$

allows us to expand the time derivative of $|a(t)|^2$,

$$\frac{\mathrm{d}}{\mathrm{d}t}|a(t)|^2 = \frac{\mathrm{d}}{\mathrm{d}t}\big(a(t)^*\, a(t)\big)$$

$$= \Big(\frac{\mathrm{d}}{\mathrm{d}t}a(t)^*\Big)\, a(t) + a(t)^*\, \Big(\frac{\mathrm{d}}{\mathrm{d}t}a(t)\Big)$$

$$\begin{aligned} &= \mathrm{i}\,\omega_0\,|a(t)|^2 - \alpha_1\,|a(t)|^2 + {\lambda_1}^*\, a(t)\, a_1^{\mathrm{in}}(t)^* \\ &\quad - \mathrm{i}\,\omega_0\,|a(t)|^2 - \alpha_1\,|a(t)|^2 + \lambda_1\, a(t)^*\, a_1^{\mathrm{in}}(t) \end{aligned}$$

$$= \; -2\,\alpha_1\,|a(t)|^2 + {\lambda_1}^*\, a(t)\, a_1^{\mathrm{in}}(t)^* + \lambda_1\, a(t)^*\, a_1^{\mathrm{in}}(t)\;. \qquad (\Theta.12)$$

Expanding (Θ.10) we have

$$|a_1^{\mathrm{out}}(t)|^2 = |\mu_1|^2\,|a(t)|^2 + |\nu_1|^2\,|a_1^{\mathrm{in}}(t)|^2 + \mu_1\,{\nu_1}^*\, a(t)\, a_1^{\mathrm{in}}(t)^* + {\mu_1}^*\,\nu_1\, a(t)^*\, a_1^{\mathrm{in}}(t)\;,$$

and substituting in (Θ.5), (Θ.8),

$$|a_1^{\mathrm{out}}(t)|^2 = 2\,\alpha_1\,|a(t)|^2 + |a_1^{\mathrm{in}}(t)|^2 + \mu_1\,{\nu_1}^*\, a(t)\, a_1^{\mathrm{in}}(t)^* + {\mu_1}^*\,\nu_1\, a(t)^*\, a_1^{\mathrm{in}}(t)\;. \qquad (\Theta.13)$$

Putting (Θ.12) and (Θ.13) into our power conservation equation (Θ.2), we get

$${\lambda_1}^*\, a(t)\, a_1^{\mathrm{in}}(t)^* + \lambda_1\, a(t)^*\, a_1^{\mathrm{in}}(t) = -\mu_1\,{\nu_1}^*\, a(t)\, a_1^{\mathrm{in}}(t)^* - {\mu_1}^*\,\nu_1\, a(t)^*\, a_1^{\mathrm{in}}(t)\;,$$

$$\Rightarrow \quad \lambda_1 = -{\mu_1}^*\,\nu_1 = -\sqrt{2\,\alpha_1}\,\mathrm{e}^{\,\mathrm{i}\,(\angle\nu_1 - \angle\mu_1)} \qquad (\Theta.14)$$

No escape

For consistency we can also consider the odd case of an isolated system with no outgoing power, $a_1^{\rm out}(t) = 0$, with equations of motion

$$\frac{\rm d}{{\rm d}t}a(t) = -{\rm i}\,\omega_0\,a(t) - \alpha_1\,a(t) + \lambda_1\,a_1^{\rm in}(t)\ , \tag{Θ.15}$$

$$0 = \mu_1\,a(t) + \nu_1\,a_1^{\rm in}(t)\ . \tag{Θ.16}$$

Substituting (Θ.16) into (Θ.15) gives

$$\frac{\rm d}{{\rm d}t}a(t) = -{\rm i}\,\omega_0\,a(t) - \alpha_1\,a(t) - \frac{\lambda_1\,\mu_1}{\nu_1}\,a(t)\ ,$$

which has solution

$$a(t) \propto {\rm e}^{(-{\rm i}\,\omega_0 - \alpha_1 - \lambda_1\,\mu_1/\nu_1)\,t}\ ,$$

$$\Rightarrow \quad |a(t)|^2 \propto {\rm e}^{-2\,\Re[\alpha_1 + \lambda_1\,\mu_1/\nu_1]\,t}\ ,$$

$$\Rightarrow \quad \frac{\rm d}{{\rm d}t}|a(t)|^2 = -\,2\,\Re\left[\alpha_1 + \frac{\lambda_1\,\mu_1}{\nu_1}\right]\,|a(t)|^2\ .$$

Combining this with (Θ.16) and (Θ.2) gives

$$|a_1^{\rm in}(t)|^2 = \frac{|\mu_1|^2}{|\nu_1|^2}\,|a(t)|^2 = -2\,\Re\left[\alpha_1 + \frac{\lambda_1\,\mu_1}{\nu_1}\right]\,|a(t)|^2\ ,$$

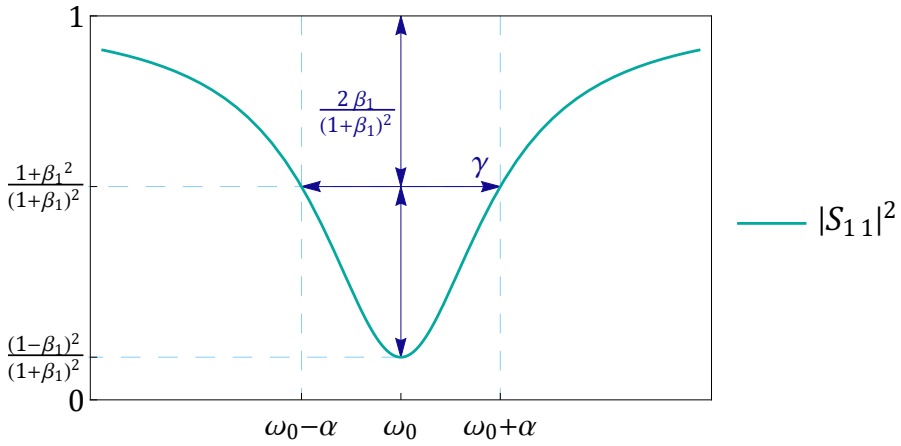

Figure Θ.6: Plot of $|S_{1\,1}|^2$ for a 1 port resonator, denoting $\alpha = \alpha_0 + \alpha_1$.

$$\Rightarrow \quad \frac{|\mu_1|^2}{|\nu_1|^2} = -2\,\Re\left[\alpha_1 + \frac{\lambda_1\,\mu_1}{\nu_1}\right] \ .$$

Substituting in our parameter solutions (Θ.5), (Θ.8), (Θ.14) leads to

$$2\,\alpha_1 = -2\,\Re\left[\alpha_1 - |\mu_1|^2\right] = -2\,(-\alpha_1) = 2\,\alpha_1 \ ,$$

providing a consistency check.

Θ.2.2 Full system Fourier transform

Returning to our full system with solved parameters,

$$\frac{\mathrm{d}}{\mathrm{d}t}a(t) = -\mathrm{i}\,\omega_0\,a(t) - (\alpha_0 + \alpha_1)\,a(t) - \sqrt{2\,\alpha_1}\,\mathrm{e}^{\mathrm{i}\,(\phi_1 - \theta_1)}\,a_1^{\mathrm{in}}(t) \ ,$$

$$a_1^{\mathrm{out}}(t) - \mathrm{e}^{\mathrm{i}\,\phi_1}\,a_1^{\mathrm{in}}(t) = \sqrt{2\,\alpha_1}\,\mathrm{e}^{\mathrm{i}\,\theta_1}\,a(t) \ ,$$

where ϕ_1 and θ_1 are some arbitrary phases.

Applying Fourier transforms as in the zero port resonator case,

$$a(\omega) = \frac{-\sqrt{2\,\alpha_1}\,\mathrm{e}^{\mathrm{i}\,(\phi_1-\theta_1)}\,a_1^{\mathrm{in}}(\omega)}{(\alpha_0+\alpha_1)-\mathrm{i}\,(\omega-\omega_0)}\ ,$$

$$a_1^{\mathrm{out}}(\omega) = \sqrt{2\,\alpha_1}\,\mathrm{e}^{\mathrm{i}\,\theta_1}\,a(\omega) + \mathrm{e}^{\mathrm{i}\,\phi_1}\,a_1^{\mathrm{in}}(\omega)\ .$$

Combining these two equations,

$$a_1^{\mathrm{out}}(\omega) = \left(\frac{-2\,\alpha_1}{(\alpha_0+\alpha_1)-\mathrm{i}\,(\omega-\omega_0)}+1\right)\mathrm{e}^{\mathrm{i}\,\phi_1}\,a_1^{\mathrm{in}}(\omega)\ .$$

Thus, the scattering element is

$$S_{1\,1}(\omega) = \frac{a_1^{\mathrm{out}}(\omega)}{a_1^{\mathrm{in}}(\omega)} = \mathrm{e}^{\mathrm{i}\,\phi_1}\,\left(1-\frac{2\,\alpha_1}{(\alpha_0+\alpha_1)-\mathrm{i}\,(\omega-\omega_0)}\right)\ ,$$

and

$$\begin{aligned}
|S_{1\,1}(\omega)| &= \left|1-\frac{2\,\alpha_1}{(\alpha_0+\alpha_1)-\mathrm{i}\,(\omega-\omega_0)}\right| \\
&= \left|\frac{(\alpha_0-\alpha_1)-\mathrm{i}\,(\omega-\omega_0)}{(\alpha_0+\alpha_1)-\mathrm{i}\,(\omega-\omega_0)}\right| \\
&= \left|1-\frac{2\,Q_0/Q_1}{\left(\frac{Q_0+Q_1}{Q_1}\right)-2\,\mathrm{i}\,Q_0\,\left(\frac{\omega-\omega_0}{\omega_0}\right)}\right| \\
&= \left|1-\frac{\frac{2\,\beta_1}{1+\beta_1}}{1-2\,\mathrm{i}\,Q_{\mathrm{L}}\,\left(\frac{\omega-\omega_0}{\omega_0}\right)}\right|\ ,
\end{aligned}$$

in various formats, some matching those used in Ref. [138], and Ref. [306], for example. The squared element is

$$|S_{1\,1}(\omega)|^2 = \frac{(\alpha_0 - \alpha_1)^2 + (\omega - \omega_0)^2}{(\alpha_0 + \alpha_1)^2 + (\omega - \omega_0)^2}$$

$$= 1 - \frac{4\,\alpha_0\,\alpha_1}{(\alpha_0 + \alpha_1)^2 + (\omega - \omega_0)^2}$$

$$= 1 - \frac{\frac{4\,\beta_1}{(1+\beta_1)^2}}{1 + 4\,{Q_{\rm L}}^2 \left(\frac{\omega-\omega_0}{\omega_0}\right)^2} \,.$$

The argument is

$$\angle\, S_{1\,1} = \arctan\left[\frac{(\omega - \omega_0)}{(\alpha_0 + \alpha_1) - \frac{(\alpha_0+\alpha_1)^2+(\omega-\omega_0)^2}{2\,\alpha_i}}\right]$$

$$= \arctan\left[\frac{2\,Q_{\rm L}\,\left(\frac{\omega-\omega_0}{\omega_0}\right)}{1 - \frac{Q_1}{2\,Q_{\rm L}} - 2\,Q_1\,Q_L\,\left(\frac{\omega-\omega_0}{\omega_0}\right)^2}\right] \,,$$

For critical coupling, $\beta_1 = 1$, and on resonance, $\omega = \omega_0$, we find that $|S_{1\,1}| = 0$. When off resonance, $|\omega - \omega_0| \to \infty$, we find $|S_{1\,1}| \to 1$.

Note that for the isolated system, $\alpha_0 = 0$, we find $|S_{1\,1}| = 1$, i.e. power is conserved. Likewise if the port becomes decoupled from the resonator, $\alpha_1 = \beta_1 = \lambda_1 = 0$, then $|S_{1\,1}| = 1$, and everything reflects back without interacting.

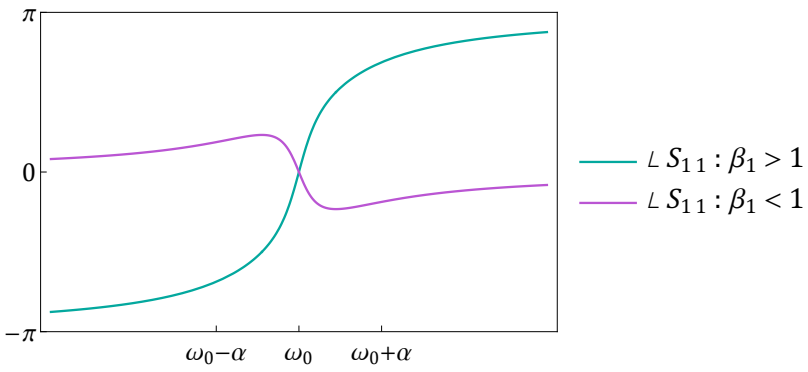

Figure Θ.7: Plots of $\angle S_{11}$.

Θ.2.3 Determining parameters

Fitting S_{11} to data allows extraction of the system parameters. The minimum of $|S_{11}|^2$ occurs at

$$|S_{11}(\omega = \omega_0)|^2 = \left(\frac{1-\beta_1}{1+\beta_1}\right)^2 ,$$

and the width halfway down the trough is $\omega_0/Q_\mathrm{L} = \gamma$, as plotted in Fig. Θ.6. There are two possible options for the coupling coefficient, however, as

$$|S_{11}(\beta_1, Q_\mathrm{L}, \omega_0; \omega)| = |S_{11}(1/\beta_1, Q_\mathrm{L}, \omega_0; \omega)| .$$

Looking at the argument of S_{11} allows us to determine if we are under-coupled, $\beta_1 < 1$, or over-coupled, $\beta_1 > 1$. The difference between these two cases, up to an arbitrary overall phase (constant offset in $\angle S_{11}$), is depicted in Fig. Θ.7.

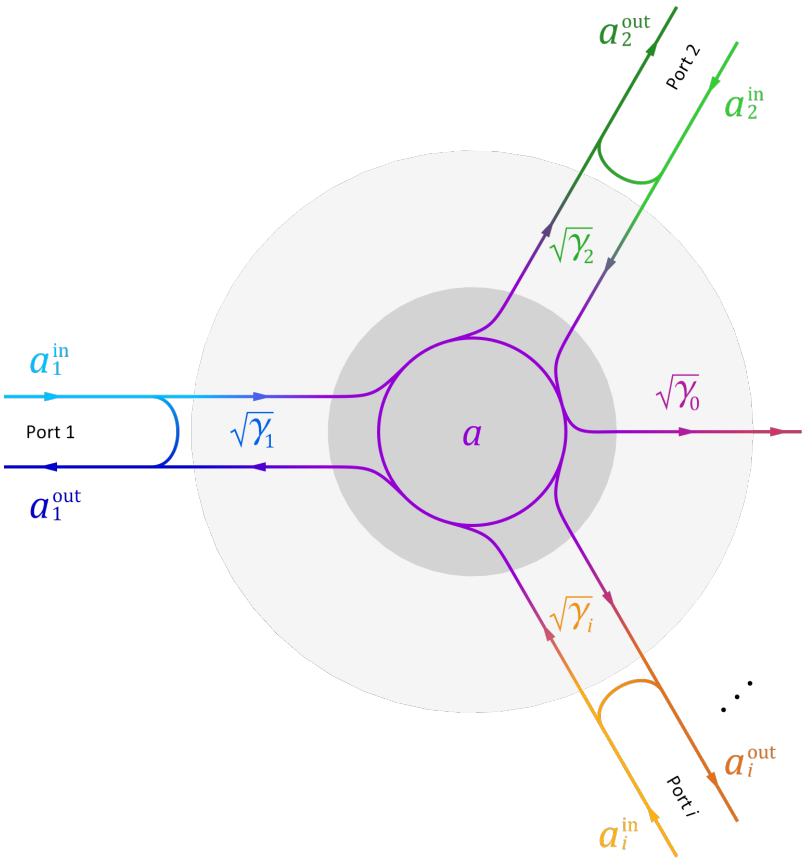

Figure Θ.8: Diagram of a resonator with multiple unconnected ports.

Θ.3 Multi port interposed resonator

We are now able to investigate a resonator with multiple ports that interact only via the central resonator as depicted in Fig. Θ.8, with the additional assumption that the ports act independently with no affect on each other. If we conduct more thought experiments, each set with only one $\alpha_i \neq 0$, we can use the results of our one port analysis to build up the

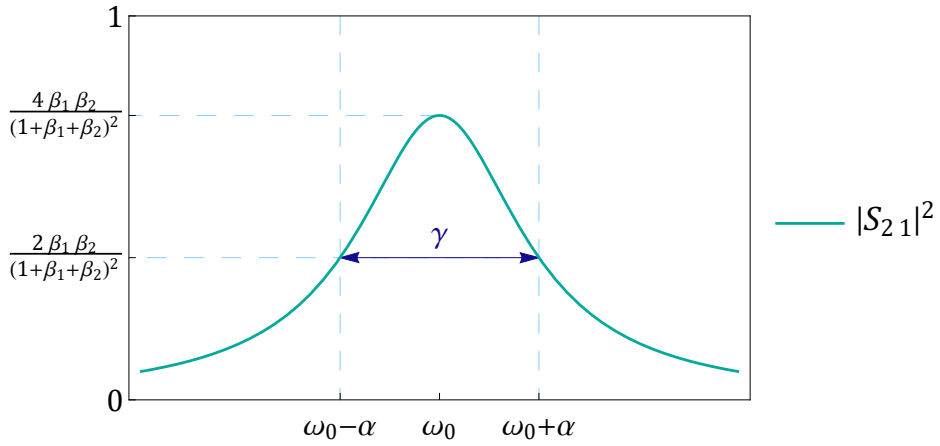

Figure Θ.9: Plot of $|S_{2\,1}|^2$ for a 2 port resonator, denoting $\alpha = \alpha_0 + \alpha_1 + \alpha_2$.

equation of motions. For an n port system,

$$\frac{\mathrm{d}}{\mathrm{d}t}a(t) = -\mathrm{i}\,\omega_0\,a(t) - \alpha_0\,a(t) - \sum_{i=1}^{n}\alpha_i\,a(t) - \sum_{i=1}^{n}\sqrt{2\,\alpha_i}\,\mathrm{e}^{\mathrm{i}\,(\phi_i-\theta_i)}\,a_i^{\mathrm{in}}(t)\;,$$

$$a_i^{\mathrm{out}}(t) - \mathrm{e}^{\mathrm{i}\,\phi_i}\,a_i^{\mathrm{in}}(t) = \sqrt{2\,\alpha_i}\,\mathrm{e}^{\mathrm{i}\,\theta_i}\,a(t)\;,$$

and we have the following relations,

$$\frac{1}{Q_{\mathrm{L}}} = \frac{1}{Q_0} + \sum_{i=1}^{n}\frac{1}{Q_i} = \frac{1+\sum_{i=1}^{n}\beta_i}{Q_0}\;, \qquad Q_i = \frac{\omega_0}{2\,\alpha_i}\;,$$

$$\beta_i = \frac{Q_0}{Q_i} = \frac{\alpha_i}{\alpha_0}\;, \qquad \frac{Q_i}{Q_{\mathrm{L}}} = \frac{1+\sum_{j=1}^{n}\beta_j}{\beta_i}\;, \qquad \frac{Q_0}{Q_{\mathrm{L}}} = 1 + \sum_{i=1}^{n}\beta_i\;.$$

The Fourier transform gives

$$a(\omega) = \frac{-\sum_{i=1}^{n} \sqrt{2\,\alpha_i}\, \mathrm{e}^{\mathrm{i}\,(\phi_i - \theta_i)}\, a_i^{\mathrm{in}}(\omega)}{(\alpha_0 + \sum_{i=1}^{n} \alpha_i) - \mathrm{i}\,(\omega - \omega_0)} \;,$$

$$a_i^{\mathrm{out}}(\omega) = \sqrt{2\,\alpha_i}\, \mathrm{e}^{\mathrm{i}\,\theta_i}\, a(\omega) + \mathrm{e}^{\mathrm{i}\,\phi_i}\, a_i^{\mathrm{in}}(\omega) \;.$$

The scattering matrix is defined as $a_i^{\mathrm{out}}(\omega) = \sum_{j=1}^{n} S_{i\,j}(\omega)\, a_j^{\mathrm{in}}(\omega)$, and we can determine individual elements by $S_{i\,j}(\omega) = a_i^{\mathrm{out}}(\omega)/a_j^{\mathrm{in}}(\omega)$ with $a_{k\neq j}^{\mathrm{in}}(\omega) = 0$,

$$S_{i\,j}(\omega) = \mathrm{e}^{\mathrm{i}\,(\theta_i - \theta_j + \phi_j)} \left(\delta_{i\,j} - \frac{2\,\sqrt{\alpha_i\,\alpha_j}}{\left(\sum_{k=0}^{n} \alpha_k\right) - \mathrm{i}\,(\omega - \omega_0)} \right) \;, \tag{Θ.17}$$

$$\Rightarrow \quad |S_{i\,j}(\omega)|^2 = \delta_{i\,j} - \frac{4\,\alpha_i \left(\delta_{i\,j} \left(\sum_{k=0}^{n} \alpha_k\right) - \alpha_j \right)}{\left(\sum_{k=0}^{n} \alpha_k\right)^2 + (\omega - \omega_0)^2} \;.$$

Some useful forms are

$$|S_{i\,i}(\omega)| = \left| 1 - \frac{2\,\alpha_i}{\left(\sum_{k=0}^{n} \alpha_k\right) - \mathrm{i}\,(\omega - \omega_0)} \right|$$

$$= \left| \frac{\left(\sum_{\substack{k=0 \\ k\neq i}}^{n} \alpha_k - \alpha_i\right) - \mathrm{i}\,(\omega - \omega_0)}{\left(\sum_{k=0}^{n} \alpha_k\right) - \mathrm{i}\,(\omega - \omega_0)} \right|$$

$$= \left| 1 - \frac{\frac{2\,\beta_i}{\sum_{k=0}^{n} \beta_k}}{1 - 2\,\mathrm{i}\,Q_{\mathrm{L}}\,\left(\frac{\omega - \omega_0}{\omega_0}\right)} \right| ,$$

$$|S_{i\,i}(\omega)|^2 = \frac{\left(\sum_{\substack{k=0 \\ k\neq i}}^{n} \alpha_k - \alpha_i\right)^2 + (\omega - \omega_0)^2}{\left(\sum_{k=0}^{n} \alpha_k\right)^2 + (\omega - \omega_0)^2}$$

$$= 1 - \frac{4\,\sum_{\substack{k=0 \\ k\neq i}}^{n} \alpha_k\,\alpha_i}{\left(\sum_{k=0}^{n} \alpha_k\right)^2 + (\omega - \omega_0)^2}$$

$$= 1 - \frac{\frac{4\,\sum_{\substack{k=0 \\ k\neq i}}^{n} \beta_k\,\beta_i}{\left(\sum_{k=0}^{n} \beta_k\right)^2}}{1 + 4\,{Q_{\mathrm{L}}}^2\,\left(\frac{\omega - \omega_0}{\omega_0}\right)^2} ,$$

$$\angle\, S_{i\,i} \;=\; \arctan\left[\frac{(\omega-\omega_0)}{\left(\sum_{k=0}^{n}\alpha_k\right)-\frac{\left(\sum_{k=0}^{n}\alpha_k\right)^2+(\omega-\omega_0)^2}{2\,\alpha_i}}\right]$$

$$=\; \arctan\left[\frac{2\,Q_{\mathrm{L}}\,\left(\frac{\omega-\omega_0}{\omega_0}\right)}{1-\frac{Q_i}{2\,Q_{\mathrm{L}}}-2\,Q_i\,Q_L\,\left(\frac{\omega-\omega_0}{\omega_0}\right)^2}\right]\;,$$

$$|S_{\substack{i\,j\\ i\neq j}}(\omega)| \;=\; \left|\frac{2\,\sqrt{\alpha_i\,\alpha_j}}{\left(\sum_{k=0}^{n}\alpha_k\right)-\mathrm{i}\,(\omega-\omega_0)}\right|$$

$$=\; \left|\frac{\frac{2\,\sqrt{\beta_i\,\beta_j}}{\left(\sum_{k=0}^{n}\beta_k\right)}}{1-2\,\mathrm{i}\,Q_{\mathrm{L}}\,\left(\frac{\omega-\omega_0}{\omega_0}\right)}\right|\;,$$

$$|S_{\substack{i\,j\\ i\neq j}}(\omega)|^2 \;=\; \frac{4\,\alpha_i\,\alpha_j}{\left(\sum_{k=0}^{n}\alpha_k\right)^2+(\omega-\omega_0)^2}$$

$$=\; \frac{\frac{4\,\beta_i\,\beta_j}{\left(\sum_{k=0}^{n}\beta_k\right)^2}}{1+4\,{Q_{\mathrm{L}}}^2\,\left(\frac{\omega-\omega_0}{\omega_0}\right)^2}\;,$$

$$\angle\, S_{\substack{i\,j\\ i\neq j}} \;=\; \arctan\left[\frac{(\omega-\omega_0)}{\sum_{k=0}^{n}\alpha_k}\right]$$

$$=\; \arctan\left[2\,Q_{\mathrm{L}}\,\left(\frac{\omega-\omega_0}{\omega_0}\right)\right]\;,$$

with $\beta_0 = 1$. Sample plots are given in Fig. Θ.6 and Fig. Θ.9.

Critical coupling occurs when

$$\sum_{i=1}^{n} \beta_i = 1 \quad \Rightarrow \quad \sum_{i=0}^{n} \beta_i = 2 \,,$$

and if the ports are all equally coupled, then $\beta_{i\neq 0} = \frac{1}{n}$. For this situation and on resonance, $\omega = \omega_0$, we find $|S_{i\,j}| = |\delta_{i\,j} - \frac{1}{n}|$. In the case of a two port symmetric system with critical coupling, $\beta_1 = \beta_2 = \frac{1}{2}$, on resonance, we have $|S_{i\,j}| = \frac{1}{2}$.

Θ.3.1 Stored energy

For a single input on resonance, power in $P_i^{\text{in}} \propto |a_i^{\text{in}}(\omega_0)|^2$, the stored energy, $E \propto |a(\omega_0)|^2$, is

$$E = \frac{2\,\alpha_i\,P_i^{\text{in}}}{\left(\sum_{k=0}^{n}\alpha_k\right)^2} = \frac{P_{j\neq i}^{\text{out}}}{2\,\alpha_{j\neq i}} \quad : \quad P_{l\neq i}^{\text{in}} = 0 \,.$$

Θ.3.2 Equivalent circuit

For an n-port electrical network with real input impedances, the scattering matrix is

$$\underline{\underline{S}} = \left(\sqrt{\underline{\underline{R_{\text{C}}}}}^{-1} \cdot \underline{\underline{Z}} \cdot \sqrt{\underline{\underline{R_{\text{C}}}}}^{-1} - \underline{\underline{\mathbb{I}_n}}\right) \cdot \left(\sqrt{\underline{\underline{R_{\text{C}}}}}^{-1} \cdot \underline{\underline{Z}} \cdot \sqrt{\underline{\underline{R_{\text{C}}}}}^{-1} + \underline{\underline{\mathbb{I}_n}}\right)^{-1} \,,$$

where

$$\underline{\underline{R_{\text{C}}}} = \text{Diag}\big[\{R_i\}_{i=1}^{n}\big]$$

is the diagonal matrix of real characteristic impedences, and $\underline{\underline{\mathbb{I}_n}}$ is the $n \times n$ identity matrix.

Using results from Sec. Θ.5.1,

$$S_{i\,j}(\omega) = \frac{2}{\sqrt{R_i\,R_j}}\,\frac{1}{\frac{1}{Z_0(\omega)} + \sum_{k=1}^{n}\frac{1}{R_k}} - \delta_{i\,j}\ , \qquad\qquad \beta_i = \frac{R_0}{R_i}\ ,$$

where $R_0 = \Re[Z_0(\omega_0)]$ is the series or parallel LCR resistor.

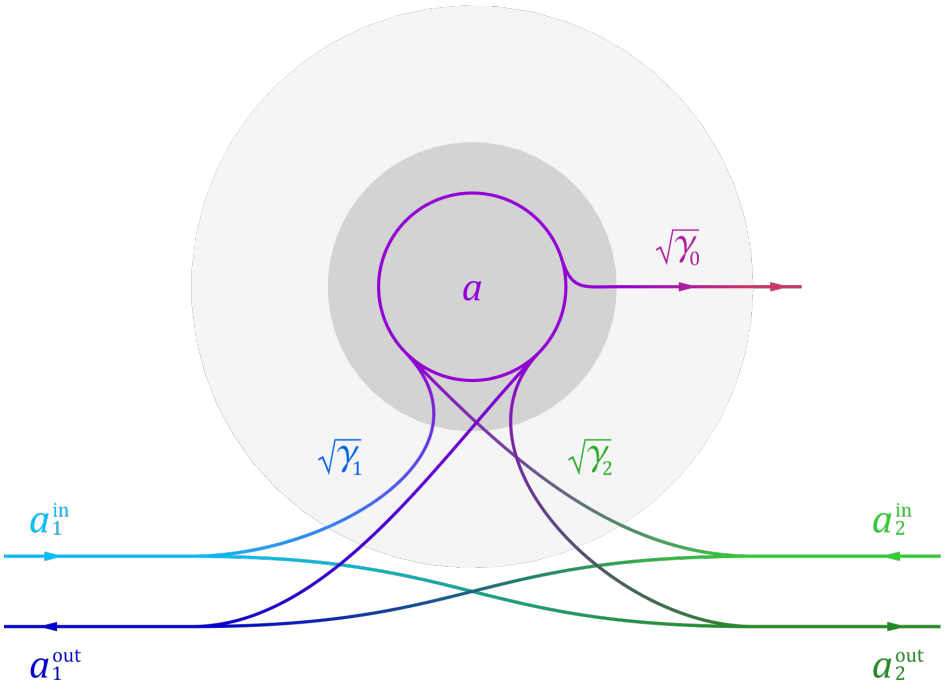

Figure Θ.10: Diagram of a resonator connected to a waveguide.

Θ.4 Two port waveguide resonator

For a resonator connected to a waveguide, Fig. Θ.10. we can't consider separate closed systems for each port individually and instead must also model the waveguide. Most generally we have

$$\begin{pmatrix} a_1^{\text{out}}(t) \\ a_2^{\text{out}}(t) \end{pmatrix} = \begin{pmatrix} \mu_1 \\ \mu_2 \end{pmatrix} a(t) + \begin{pmatrix} \nu_{1\,1} & \nu_{1\,2} \\ \nu_{2\,1} & \nu_{2\,2} \end{pmatrix} \begin{pmatrix} a_1^{\text{in}}(t) \\ a_2^{\text{in}}(t) \end{pmatrix},$$

and for an ideal waveguide (at least over the small the region interacting with the resonator) $\nu_{1\,1} = \nu_{2\,2} = 0$. The resonator equation of motion is the same as before,

$$\frac{\mathrm{d}}{\mathrm{d}t}a(t) = -\mathrm{i}\,\omega_0\,a(t) - (\alpha_0 + \alpha_{1\,2})\,a(t) + \lambda_1\,a_1^{\mathrm{in}}(t) + \lambda_2\,a_2^{\mathrm{in}}(t)\;, \tag{Θ.18}$$

with coupling and quality factor relations

$$Q_{1\,2} = \frac{\omega_0}{2\,\alpha_{1\,2}}\;, \qquad \beta_{1\,2} = \frac{\alpha_{1\,2}}{\alpha_0}\;, \qquad \frac{Q_0}{Q_{\mathrm{L}}} = 1 + \beta_{1\,2}\;.$$

If we consider an isolated system, $\alpha_0 = 0$, with no drive, $a_1^{\mathrm{in}}(t) = a_2^{\mathrm{in}}(t) = 0$, the power loss of the resonator into the waveguide gives us

$$2\,\alpha_{1\,2} = |\mu_1|^2 + |\mu_2|^2\;.$$

The uncoupled case, $\alpha_{1\,2} = \lambda_1 = \lambda_2 = 0$, enforces

$$|\nu_{1\,2}| = |\nu_{2\,1}| = 1\;,$$

which is equivalent to ν as a scattering matrix being unitary.

Using these results and working through the isolated system, $\alpha_0 = 0$ with either $a_1^{\mathrm{in}}(t) = 0$ or $a_2^{\mathrm{in}}(t) = 0$, and power conservation

$$\frac{\mathrm{d}}{\mathrm{d}t}|a(t)|^2 = |a_1^{\mathrm{in}}(t)|^2 + |a_2^{\mathrm{in}}(t)|^2 - |a_1^{\mathrm{out}}(t)|^2 - |a_2^{\mathrm{out}}(t)|^2\;,$$

we obtain

$$\lambda_1 = -{\mu_2}^* \, \nu_{2\,1} \; , \qquad\qquad \lambda_2 = -{\mu_1}^* \, \nu_{1\,2} \; .$$

With these results we can express the equations of motion of the two port waveguide resonator in terms of μ_1 and μ_2 as

$$\frac{\mathrm{d}}{\mathrm{d}t} a(t) = \; -\mathrm{i}\,\omega_0\, a(t) - \left(\alpha_0 + \frac{|\mu_1|^2 + |\mu_2|^2}{2} \right) a(t) - {\mu_2}^* \, \mathrm{e}^{\mathrm{i}\,\phi_{2\,1}} \; a_1^{\mathrm{in}}(t) - {\mu_1}^* \, \mathrm{e}^{\mathrm{i}\,\phi_{1\,2}} \, a_2^{\mathrm{in}}(t) \; ,$$

$$a_1^{\mathrm{out}}(t) = \mu_1 \, a(t) + \mathrm{e}^{\mathrm{i}\,\phi_{1\,2}} \, a_2^{\mathrm{in}}(t) \; ,$$

$$a_2^{\mathrm{out}}(t) = \mu_2 \, a(t) + \mathrm{e}^{\mathrm{i}\,\phi_{2\,1}} \, a_1^{\mathrm{in}}(t) \; .$$

The breakdown of $\alpha_{1\,2}$ into μ_1 and μ_2 will depend on the specifics of the waveguide and resonator interaction. Within a particular scheme, comparisons can be made to an independent two port resonator with

$$\begin{aligned} \alpha_{1\,2} &= \alpha_1 + \alpha_2 \; , \\ \mu_1 &= \sqrt{2\,\alpha_1} \, \mathrm{e}^{\mathrm{i}\,\theta_1} \; , \\ \mu_2 &= \sqrt{2\,\alpha_2} \, \mathrm{e}^{\mathrm{i}\,\theta_2} \; . \end{aligned}$$

Θ.4.1 Symmetric non-directional

If the resonator is symmetric and emits into each direction equally, we have

$$\begin{aligned}
\alpha_1 &= \alpha_2 = \alpha_{1\,2}/2 \,, \\
\mu_1 &= \mu_2 = \sqrt{\alpha_{1\,2}}\,\mathrm{e}^{\mathrm{i}\,\theta} \,, \\
\nu_{1\,2} &= \nu_{2\,1} = \mathrm{e}^{\mathrm{i}\,\phi} \,, \\
\lambda_1 &= \lambda_2 = -\sqrt{\alpha_{1\,2}}\,\mathrm{e}^{\mathrm{i}\,(\phi-\theta)} \,.
\end{aligned}$$

The full set of equations become

$$\frac{\mathrm{d}}{\mathrm{d}t}a(t) = -\,\mathrm{i}\,\omega_0\,a(t) - (\alpha_0 + \alpha_{1\,2})\;a(t) - \sqrt{\alpha_{1\,2}}\,\mathrm{e}^{\mathrm{i}\,(\phi-\theta)}\,a_1^{\mathrm{in}}(t) - \sqrt{\alpha_{1\,2}}\,\mathrm{e}^{\mathrm{i}\,(\phi-\theta)}\,a_2^{\mathrm{in}}(t) \,,$$

$$a_1^{\mathrm{out}}(t) = \sqrt{\alpha_{1\,2}}\,\mathrm{e}^{\mathrm{i}\,\theta}\,a(t) + \mathrm{e}^{\mathrm{i}\,\phi}\,a_2^{\mathrm{in}}(t) \,,$$

$$a_2^{\mathrm{out}}(t) = \sqrt{\alpha_{1\,2}}\,\mathrm{e}^{\mathrm{i}\,\theta}\,a(t) + \mathrm{e}^{\mathrm{i}\,\phi}\,a_1^{\mathrm{in}}(t) \,.$$

Taking the Fourier transform

$$a(\omega) = \frac{-\sqrt{\alpha_{1\,2}}\,\mathrm{e}^{\mathrm{i}\,(\phi-\theta)}\;\Big(a_1^{\mathrm{in}}(\omega) + a_2^{\mathrm{in}}(\omega)\Big)}{(\alpha_0 + \alpha_{1\,2}) - \mathrm{i}\,(\omega - \omega_0)} \,,$$

$$a_1^{\mathrm{out}}(\omega) = \sqrt{\alpha_{1\,2}}\,\mathrm{e}^{\mathrm{i}\,\theta}\,a(\omega) + \mathrm{e}^{\mathrm{i}\,\phi}\,a_2^{\mathrm{in}}(\omega) \,,$$

$$a_2^{\mathrm{out}}(\omega) = \sqrt{\alpha_{1\,2}}\,\mathrm{e}^{\mathrm{i}\,\theta}\,a(\omega) + \mathrm{e}^{\mathrm{i}\,\phi}\,a_1^{\mathrm{in}}(\omega) \,.$$

Thus

$$S_{1\,1}(\omega) = \mathrm{e}^{\mathrm{i}\,\phi}\,\left(\frac{-\alpha_{1\,2}}{(\alpha_0+\alpha_{1\,2})-\mathrm{i}\,(\omega-\omega_0)}\right)\ ,$$

$$S_{2\,1}(\omega) = \mathrm{e}^{\mathrm{i}\,\phi}\,\left(1-\frac{\alpha_{1\,2}}{(\alpha_0+\alpha_{1\,2})-\mathrm{i}\,(\omega-\omega_0)}\right)\ .$$

Defining $\beta_{1\,2} = \beta_1 + \beta_2 = \alpha_{1\,2}/\alpha_0$,

$$|S_{1\,1}(\omega)| = \left|\frac{\alpha_{1\,2}}{(\alpha_0+\alpha_{1\,2})-\mathrm{i}\,(\omega-\omega_0)}\right|$$

$$= \left|\frac{\frac{\beta_{1\,2}}{1+\beta_{1\,2}}}{1-2\,\mathrm{i}\,Q_{\mathrm{L}}\,\left(\frac{\omega-\omega_0}{\omega_0}\right)}\right|\ ,$$

$$|S_{1\,1}(\omega)|^2 = \frac{{\alpha_{1\,2}}^2}{(\alpha_0+\alpha_{1\,2})^2+(\omega-\omega_0)^2}$$

$$= \frac{\left(\frac{\beta_{1\,2}}{1+\beta_{1\,2}}\right)^2}{1+4\,{Q_{\mathrm{L}}}^2\,\left(\frac{\omega-\omega_0}{\omega_0}\right)^2}\ ,$$

$$|S_{2\,1}(\omega)| = \left| 1 - \frac{\alpha_{1\,2}}{(\alpha_0 + \alpha_{1\,2}) - \mathrm{i}\,(\omega - \omega_0)} \right|$$

$$= \left| \frac{\alpha_0 - \mathrm{i}\,(\omega - \omega_0)}{(\alpha_0 + \alpha_{1\,2}) - \mathrm{i}\,(\omega - \omega_0)} \right|$$

$$= \left| 1 - \frac{\frac{\beta_{1\,2}}{1+\beta_{1\,2}}}{1 - 2\,\mathrm{i}\,Q_{\mathrm{L}}\left(\frac{\omega-\omega_0}{\omega_0}\right)} \right| ,$$

$$|S_{2\,1}(\omega)|^2 = \frac{{\alpha_0}^2 + (\omega - \omega_0)^2}{(\alpha_0 + \alpha_{1\,2})^2 + (\omega - \omega_0)^2}$$

$$= 1 - \frac{2\,\alpha_0\,\alpha_{1\,2} + {\alpha_{1\,2}}^2}{(\alpha_0 + \alpha_{1\,2})^2 + (\omega - \omega_0)^2}$$

$$= 1 - \frac{1 - \frac{1}{(1+\beta_{1\,2})^2}}{1 + 4\,{Q_{\mathrm{L}}}^2\left(\frac{\omega-\omega_0}{\omega_0}\right)^2} .$$

Critical coupling occurs when $\beta_{1\,2} = 1$, and on resonance gives $|S_{1\,1}| = |S_{2\,1}| = \frac{1}{2}$.

Θ.4.2 Directional

For some systems, e.g. a ring resonator, the coupling is directional. For $1 \to 2$ with $a_2^{\mathrm{in}}(t) = 0$,

$$\begin{aligned}
\mu_1 &= \lambda_2 = \alpha_1 = 0 \,, \\
\alpha_2 &= \alpha_{1\,2} \,, \\
\mu_2 &= \sqrt{2\,\alpha_{1\,2}}\,\mathrm{e}^{\mathrm{i}\,\theta} \,, \\
\nu_{2\,1} &= \mathrm{e}^{\mathrm{i}\,\phi} \,, \\
\lambda_1 &= -\sqrt{2\,\alpha_{1\,2}}\,\mathrm{e}^{\mathrm{i}\,(\phi-\theta)} \,,
\end{aligned}$$

and our equations of motion look like that of a one port system.

Θ.4.3 Multiple identical resonators

In the case of n resonators all attached to the waveguide (at the same position) we can invoke additional amplitudes $a^i(t)$ and equations of motion,

$$\frac{\mathrm{d}}{\mathrm{d}t}a^i(t) = -\mathrm{i}\,\omega_0^i\,a(t) - \left(\alpha_0^i + \alpha_{1\,2}^i\right)\,a(t) + \lambda_1^i\,a_1^{\mathrm{in}}(t) + \lambda_2^i\,a_2^{\mathrm{in}}(t) \,,$$

with

$$\begin{pmatrix} a_1^{\mathrm{out}}(t) \\ a_2^{\mathrm{out}}(t) \end{pmatrix} = \sum_{i=1}^{n} \begin{pmatrix} \mu_1^i \\ \mu_2^i \end{pmatrix} a^i(t) + \begin{pmatrix} \nu_{1\,1} & \nu_{1\,2} \\ \nu_{2\,1} & \nu_{2\,2} \end{pmatrix} \begin{pmatrix} a_1^{\mathrm{in}}(t) \\ a_2^{\mathrm{in}}(t) \end{pmatrix} \,,$$

For identical symmetric resonators we find

$$\mu = \sqrt{\alpha_{1\,2}}\,\mathrm{e}^{\mathrm{i}\,\theta} \ ,$$

$$\lambda = -\frac{\sqrt{\alpha_{1\,2}}}{n}\,\mathrm{e}^{\mathrm{i}\,(\phi-\theta)} \ .$$

This leads to identical S-matrix equations. Despite there being more resonators, the loss rates α (individual and total) remain constant. In the equivalent circuit model, adding additional series or parallel resonators of identical parameters changes the overall impedance Z but keeps Q and ω_0 constant.

Θ.4.4 Equivalent systems

Different resonator systems share common forms of scattering matrix elements.

Symmetric interposed two-port		Symmetric non-directional waveguide
$S_{1\,1}$, $S_{2\,2}$	$\sim$	$S_{1\,2}$, $S_{2\,1}$
$S_{1\,2}$, $S_{2\,1}$	$\sim$	$S_{1\,1}$, $S_{2\,2}$

One-port		Directional waveguide
$S_{1\,1}$	$\sim$	$S_{1\,2}$, $S_{2\,1}$

Θ.5 Complex input-output theory

If we wish to consider complex couplings, i.e. frequency shifts induced by ports, or complex characteristic impedances, we can do so as follows. This formalism, as in Sec. Θ.3, assumes each port acts independently to induce a static frequency shift. Define the complex amplitude decay rate

$$\aleph_i = \alpha_i + \mathrm{i}\,\Delta\omega_i \ ,$$

with the special case

$$\aleph_0(\omega) = \alpha_0 + \mathrm{i}\,(\omega_0 - \omega) \qquad : \quad \Delta\omega_0(\omega) = \omega_0 - \omega \ ,$$

carrying the only frequency dependance. The multiport system of Sec. Θ.3 has Fourier transform equations

$$a(\omega) = \frac{-\sum_{i=1}^{n} \sqrt{2\,\Re[\aleph_i]}\,\mathrm{e}^{\mathrm{i}\,(\phi_i - \theta_i)}\,a_i^{\mathrm{in}}(\omega)}{\sum_{i=0}^{n} \aleph_i(\omega)} \ ,$$

$$a_i^{\mathrm{out}}(\omega) = \sqrt{2\,\Re[\aleph_i]}\,\mathrm{e}^{\mathrm{i}\,\theta_i}\,a(\omega) + \mathrm{e}^{\mathrm{i}\,\phi_i}\,a_i^{\mathrm{in}}(\omega) \ ,$$

and the scattering matrix elements are thus

$$S_{i\,j}(\omega) = \mathrm{e}^{\mathrm{i}\,(\theta_i - \theta_j + \phi_j)} \left(\delta_{i\,j} - \frac{\sqrt{2\,\Re[\aleph_i]}\,\sqrt{2\,\Re[\aleph_j]}}{\sum_{i=0}^{n} \aleph_i(\omega)} \right) . \tag{Θ.19}$$

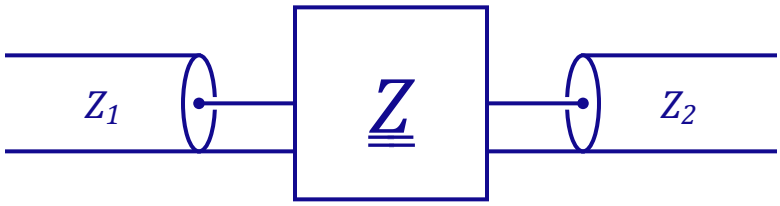

Figure Θ.11: Generic 2 port network described by an impedance matrix and transmission lines into each port.

The resonance frequency is given by the solution to

$$\sum_{i=1}^{n} \Im[\aleph_i(\omega_{\mathrm{res}})] = 0 \;, \qquad \Rightarrow \quad \omega_{\mathrm{res}} = \sum_{i=1}^{n} \Im[\aleph_i(0)] = \omega_0 + \sum_{i=1}^{n} \Delta\omega_i \;.$$

Hence the loaded quality factor is

$$Q_{\mathrm{L}} = \frac{\sum_{i=0}^{n} \Im[\aleph_i(0)]}{\sum_{i=0}^{n} 2\,\Re[\aleph_i]} \;.$$

With this definition, the complex resonance frequency is

$$\tilde{f}_{\mathrm{res}} = \frac{\omega_{\mathrm{res}} + \mathrm{i}\,\alpha}{2\,\pi} = \frac{\mathrm{i}}{2\,\pi} \sum_{i=0}^{n} \aleph_i(0)^* \;.$$

Θ.5.1 Equivalent circuit

The main motivation for complex input-output theory is its mapping to an equivalent circuit with complex characteristic impedances. For an n-port network, as depicted in Fig. Θ.11, with complex input impedances, the scattering matrix is [305]

$$\begin{aligned} \underline{\underline{S}} &= \underline{\underline{F}} \cdot \left(\underline{\underline{Z}} - \underline{\underline{Z_{\mathrm{C}}}}^*\right) \cdot \left(\underline{\underline{Z}} + \underline{\underline{Z_{\mathrm{C}}}}\right)^{-1} \cdot \underline{\underline{F}}^{-1} \\ &= \left(\underline{\underline{F}} \cdot \underline{\underline{Z}} \cdot \underline{\underline{F}}^{-1} - \underline{\underline{Z_{\mathrm{C}}}}^*\right) \cdot \left(\underline{\underline{F}} \cdot \underline{\underline{Z}} \cdot \underline{\underline{F}}^{-1} + \underline{\underline{Z_{\mathrm{C}}}}\right)^{-1} \;, \end{aligned} \tag{Θ.20}$$

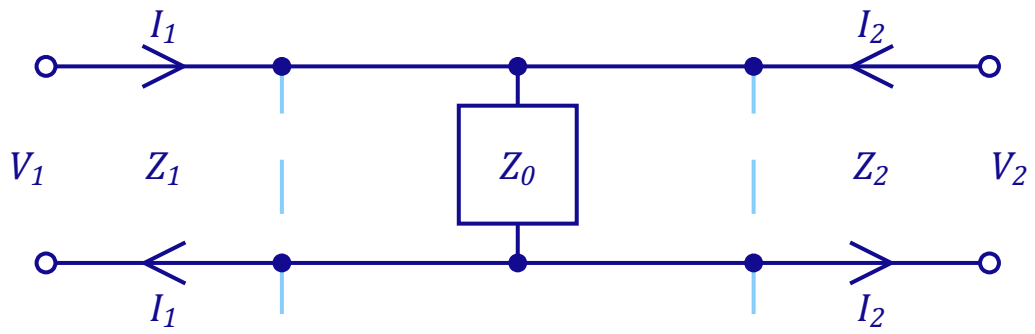

Figure Θ.12: Circuit model of two ports connected to a resonator Z_0.

where

$$\underline{\underline{Z_{\rm C}}} = \mathrm{Diag}\big[\{Z_i\}_{i=1}^{n}\big] \,, \qquad\qquad \underline{\underline{F}} = \left(2\sqrt{\Re\left[\underline{\underline{Z_{\rm C}}}\right]}\right)^{-1} \,.$$

The amplitude waves in and out are

$$a_i^{\rm in} = \frac{V_i + Z_i\, I_i}{2\sqrt{|\Re[Z_i]|}} \,, \qquad\qquad a_i^{\rm out} = \frac{V_i - Z_i^*\, I_i}{2\sqrt{|\Re[Z_i]|}} \,,$$

with powers

$$P_i^{\rm in} = \frac{|a_i^{\rm in}|^2}{2} \,, \qquad\qquad P_i^{\rm out} = \frac{|a_i^{\rm out}|^2}{2} \,.$$

For our model of multiple ports connected to a resonator, depicted in Fig. Θ.12, $\underline{\underline{Z}}$ is a constant matrix $Z_{i\,j} = Z_0$, thus

$$\left(\underline{\underline{F}} \cdot \underline{\underline{Z}} \cdot \underline{\underline{F}}^{-1}\right)_{i\,j} = Z_0\, \frac{2\sqrt{\Re[Z_j]}}{2\sqrt{\Re[Z_i]}} \,.$$

Defining

$$\mathfrak{a}_i = \frac{\sqrt{Z_0}}{2\sqrt{\Re[Z_i]}}\,, \qquad \mathfrak{b}_i = \sqrt{Z_0}\,2\sqrt{\Re[Z_i]}\,, \qquad \text{such that} \quad \underline{\underline{F}}\cdot\underline{\underline{Z}}\cdot\underline{\underline{F}}^{-1} = \underline{\mathfrak{a}}\otimes\underline{\mathfrak{b}} = \underline{\mathfrak{a}}\,\underline{\mathfrak{b}}^{\mathsf{T}}\,,$$

we have by the Sherman-Morrison formula,

$$\left(\underline{\mathfrak{a}}\,\underline{\mathfrak{b}}^{\mathsf{T}} + \underline{\underline{Z_{\mathrm{C}}}}\right)^{-1} = \underline{\underline{Z_{\mathrm{C}}}}^{-1} - \frac{\underline{\underline{Z_{\mathrm{C}}}}^{-1}\cdot\underline{\mathfrak{a}}\,\underline{\mathfrak{b}}^{\mathsf{T}}\cdot\underline{\underline{Z_{\mathrm{C}}}}^{-1}}{1+\underline{\mathfrak{b}}^{\mathsf{T}}\cdot\underline{\underline{Z_{\mathrm{C}}}}^{-1}\cdot\underline{\mathfrak{a}}}\,.$$

Putting this into (Λ.5), we find

$$S_{i\,j}(\omega) = Z_0\sqrt{\frac{\Re[Z_j]}{\Re[Z_i]}}\,\frac{1}{Z_j} - \frac{\frac{Z_0^{\,2}}{Z_j}\sqrt{\frac{\Re[Z_j]}{\Re[Z_i]}}\,\sum_{k=1}^{n}\frac{1}{Z_k}}{1+\sum_{k=1}^{n}\frac{Z_0}{Z_k}} - \delta_{i\,j}\,\frac{{Z_i}^*}{Z_i} + \frac{\frac{{Z_i}^*}{Z_i}\,\frac{Z_0}{Z_j}\sqrt{\frac{\Re[Z_j]}{\Re[Z_i]}}}{1+\sum_{k=1}^{n}\frac{Z_0}{Z_k}}$$

$$= \frac{\sqrt{2\,\Re[Z_i]}\,\sqrt{2\,\Re[Z_j]}}{Z_i\,Z_j\,\left(\sum_{k=0}^{n}\frac{1}{Z_k}\right)} - \delta_{i\,j}\,\frac{{Z_i}^*}{Z_i}$$

$$= \sqrt{\frac{{Z_i}^*}{Z_i}}\,\sqrt{\frac{{Z_j}^*}{Z_j}}\,\left(\frac{\sqrt{2\,\Re\left[\frac{1}{Z_i}\right]}\,\sqrt{2\,\Re\left[\frac{1}{Z_j}\right]}}{\sum_{k=0}^{n}\frac{1}{Z_k}} - \delta_{i\,j}\right).$$

Matching to $S_{i\,j}^{(*)}$ from (Θ.19), we can relate

$$\aleph_i^{(*)} \propto \frac{1}{Z_i}\,, \qquad \phi_i = 2\,\theta_i + \pi\,, \qquad \theta_i = \angle\,\aleph_i\,.$$

To explicitly map the decay parameters, we can look at the power loss at terminated ports for specific resonator models. Terminating a port with its characteristic impedance, Z_i, sets $V_i = -I_i\,Z_i$, and thus $P_i^{\mathrm{in}} = 0$, and $P_i^{\mathrm{out}} = \Re[Z_i]\,|I_i|^2/2$ i.e. resistor loss.

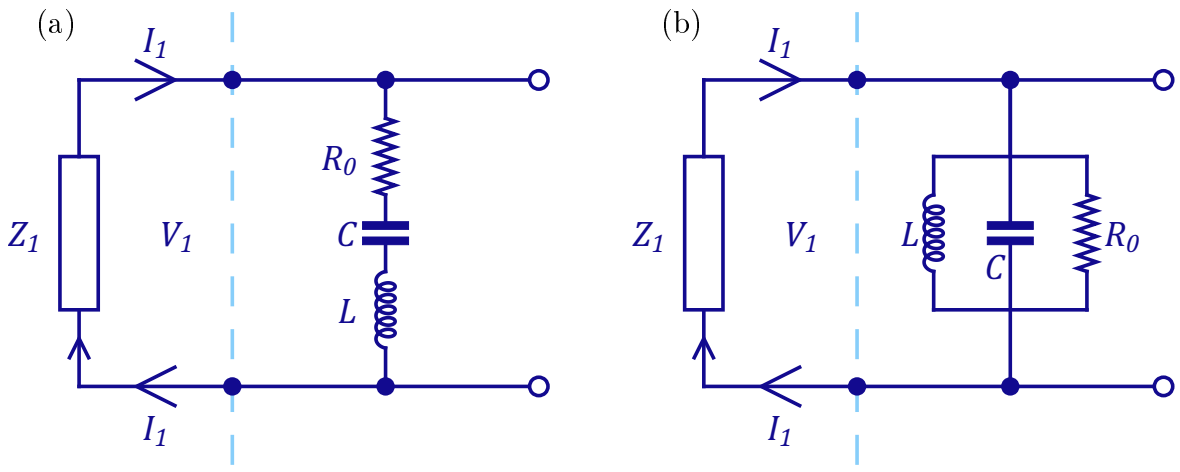

Figure Θ.13: LCR (a) series and (b) parallel resonator with terminated port.

For this mapping to work the characteristic impedances need to be (at least approximately) static in frequency. In reality the couplings may be capacitive and frequency dependent, violating the assumption that the ports operate independently, however if $C_i \ll C_0$ the impedance will be approximately constant around $\omega_{\text{res}} \approx \omega_0$.

Series LCR

A series LCR resonator, as shown in Fig. Θ.13(a), has impedance

$$Z_0 = R_0 + \mathrm{i}\,\omega\,L + \frac{1}{\mathrm{i}\,\omega\,C} \overset{\omega\approx\omega_0}{=} R_0 + \mathrm{i}\,2\,L\,(\omega - \omega_0) + \mathcal{O}[\omega - \omega_0]^2 \,,$$

with nominal resonance frequency

$$\omega_0 = \frac{1}{\sqrt{L\,C}} \,.$$

On resonance, the energy stored in the resonator is

$$E = \frac{1}{2}\,|I_0|^2\,L = \frac{1}{2}\,\frac{|Z_i|^2}{|Z_0|^2}\,|I_i|^2\,L \,,$$

and the power lost through the termination is

$$P_i = \frac{1}{2}\,\Re[V_i\,{I_i}^*] = \frac{1}{2}\,|I_i|^2\,\Re[Z_i]\;,$$

thus for a series LCR

$$2\,\Re[\aleph_i] = \frac{P_i}{E} = \frac{|Z_0|^2}{L}\,\frac{\Re[Z_i]}{|Z_i|^2} = \frac{|Z_0|^2}{L}\,\Re\Big[\frac{1}{Z_i}\Big]\;,$$

suggesting that

$$\aleph_i = \frac{|Z_0|^2}{2\,L}\,\frac{1}{Z_i} \quad : \quad \text{series LCR}\;.$$

Checking with $\aleph_0$,

$$\aleph_0 = \frac{{Z_0}^*}{2\,L} \approx \underbrace{\frac{R_0}{2\,L}}_{\alpha_0} + \mathrm{i}\,\underbrace{(\omega_0 - \omega)}_{\Delta\omega_0}\;.$$

The frequency dependence in $\aleph_i$ and problems when $R_0 = 0$ make the series LCR model often undesirable.

Parallel LCR

A parallel LCR resonator, as shown in Fig. Θ.13(b), has admittance

$$\frac{1}{Z_0} = \frac{1}{R_0} + \mathrm{i}\,\omega\,C + \frac{1}{\mathrm{i}\,\omega\,L} \overset{\omega\approx\omega_0}{=} \frac{1}{R_0} + \mathrm{i}\,2\,C\;(\omega - \omega_0) + \mathcal{O}[\omega - \omega_0]^2\;,$$

with nominal resonance frequency

$$\omega_0 = \frac{1}{\sqrt{L\,C}}\,.$$

On resonance, the energy stored in the resonator is

$$E = \frac{1}{2}\,|V_0|^2\,C = \frac{1}{2}\,|V_i|^2\,C\,,$$

and the power lost through the termination is

$$P_i = \frac{1}{2}\,\Re[V_i\,{I_i}^*] = \frac{1}{2}\,|V_i|^2\,\Re\Big[\frac{1}{{Z_i}^*}\Big]\,,$$

thus for a parallel LCR

$$2\,\Re[\aleph_i] = \frac{P_i}{E} = \frac{1}{C}\,\Re\Big[\frac{1}{{Z_i}^*}\Big]\,,$$

suggesting that

$$\aleph_i = \frac{1}{2\,C}\,\frac{1}{{Z_i}^*} \quad : \quad \text{parallel LCR}\,.$$

Checking with $\aleph_0$,

$$\aleph_0 = \frac{1}{2\,C\,{Z_0}^*} \approx \underbrace{\frac{1}{2\,C\,R_0}}_{\alpha_0} + \mathrm{i}\,\underbrace{(\omega_0 - \omega)}_{\Delta\omega_0}\,.$$

APPENDIX Λ

Signal analysis

A collection of equations and notes pertaining to signal analysis and measurement.

$\Lambda.1$ Spectral density

For an amplitude signal $X(t)$, which can be a random variable, the auto-correlation is defined as

$$R_{XX}(t_1, t_2) = \mathrm{E}\big[X(t_1)^* \, X(t_2)\big] \, .$$

If $X(t)$ is stationary, this will only depend on the delay $\tau = t_2 - t_1$,

$$R_{XX}(\tau) = \mathrm{E}\big[X(t)^* \, X(t+\tau)\big] = \big\langle X(t)^* \, X(t+\tau) \big\rangle_t \, ,$$

where the angled brackets are denoting time average.

For a real signal, the power spectral density is the Fourier transform of the auto-correlation,

$$S_{XX}(\omega) = \int_{-\infty}^{\infty} R_{XX}(\tau) \, \mathrm{e}^{\mathrm{i}\,\omega\,\tau} \, \mathrm{d}\tau \quad : \quad X \in \mathbb{R} \, , \tag{$\Lambda.1$}$$

with units of amplitude^2 $\times$ time, and runs over both negative and positive frequencies (two-sided). The amplitude spectral density is the square root of this and has units of amplitude $\times$ $\sqrt{\text{time}}$.

The power in some domain of this two-sided power spectrum is

$$P\big([\omega_1, \omega_2]\big) = \frac{1}{2\,\pi} \int_{\omega_1}^{\omega_2} S_{XX}(\omega)\,\mathrm{d}\omega \ ,$$

with units of amplitude^2 = power. However actual measurements typically take the one-sided power spectrum that includes both positive and negative frequencies for some bandwidth $[\omega_1, \omega_2]$,

$$P_1\big([\omega_1, \omega_2] \subset \mathbb{R}^+\big) = \frac{1}{2\,\pi} \int_{\omega_1}^{\omega_2} \Big(S_{XX}(\omega) + S_{XX}(-\omega)\Big)\,\mathrm{d}\omega \ .$$

The total power is

$$P = \frac{1}{2\,\pi} \int_{-\infty}^{\infty} S_{XX}(\omega)\,\mathrm{d}\omega = \big\langle X(t)^*\, X(t) \big\rangle_t \ ,$$

as expected from Parseval's theorem.

Alternatively, the amplitude spectral density can be defined as

$$\hat{X}_T(\omega) = \frac{1}{\sqrt{T}} \int_0^T X(t)\,\mathrm{e}^{\mathrm{i}\,\omega\,t}\,\mathrm{d}t \ ,$$

using a truncated Fourier transform over a finite collection period T. The power spectral density is then

$$\begin{aligned} S_{XX}(\omega) &= \lim_{T\to\infty} \mathrm{E}\big[\hat{X}_T(\omega)^*\, \hat{X}_T(\omega)\big] \quad : \quad X \in \mathbb{R} \\ &= \lim_{T\to\infty} \frac{1}{T} \int_0^T \int_0^T R_{XX}(t_1, t_2)\,\mathrm{e}^{\mathrm{i}\,\omega\,(t_2 - t_1)}\,\mathrm{d}t_1\,\mathrm{d}t_2 \ . \end{aligned} \tag{Λ.2}$$

The inverse from the Wiener–Khinchin theorem is

$$R_{XX}(\tau) = \frac{1}{2\,\pi} \int_{-\infty}^{\infty} S_{XX}(\omega)\, \mathrm{e}^{-\mathrm{i}\,\omega\,\tau} \mathrm{d}\omega \ .$$

Λ.1.1 Operator spectral density

For quantum operators [12, 140]

$$R_{\hat{X}\hat{X}}(\tau) = \left\langle \hat{X}^{\dagger}(t)\, \hat{X}(t+\tau) \right\rangle ,$$

$$S_{\hat{X}\hat{X}}(\omega) = \int_{-\infty}^{\infty} R_{\hat{X}\hat{X}}(\tau)\, \mathrm{e}^{\mathrm{i}\,\omega\,\tau}\, \mathrm{d}\tau = \lim_{T\to\infty} \left\langle \hat{X}_T^{\dagger}(-\omega)\, \hat{X}_T(\omega) \right\rangle , \tag{Λ.3}$$

and $\hat{X}(t)^{\dagger} = \hat{X}^{\dagger}(t)$, $\hat{X}(\omega)^{\dagger} = \hat{X}^{\dagger}(-\omega)$.

Thus

$$\hat{Y}(\omega) = f(\omega)\, \hat{X}(\omega) \quad \Rightarrow \quad S_{\hat{Y}\hat{Y}}(\omega) = |f(\omega)|^2\, S_{\hat{X}\hat{X}} \ .$$

As quantum spectral densities are not necessarily symmetric, we can define a symmetrized spectral density

$$\bar{S}_{\hat{X}\hat{X}}(\omega) = \frac{S_{\hat{X}\hat{X}}(\omega) + S_{\hat{X}\hat{X}}(-\omega)}{2} \ .$$

Harmonic operator

For a time harmonic operator,

$$\begin{aligned}
\hat{X}(t) &= \hat{x}\,\mathrm{e}^{-\mathrm{i}\,\Omega\,t}\ , \\
\hat{X}(\omega) &= \sqrt{2\,\pi}\,\hat{x}\,\delta(\omega-\Omega)\ , \\
R_{\hat{X}\hat{X}}(\tau) &= \hat{x}^{\dagger}\,\hat{x}\,\mathrm{e}^{-\mathrm{i}\,\Omega\,\tau}\ , \\
S_{\hat{X}\hat{X}}(\omega) &= 2\,\pi\,\hat{x}^{\dagger}\,\hat{x}\,\delta(\omega-\Omega)\ , \\
P &= \hat{x}^{\dagger}\,\hat{x}\ .
\end{aligned}$$

Λ.1.2 Real harmonic signal

For a harmonic signal $X(t) = x_{\mathrm{amp}}\,\cos[\Omega\,t]$, the time-averaged power is

$$\Rightarrow \quad \big\langle P \big\rangle = \big\langle X(t)^2 \big\rangle_t = \frac{{x_{\mathrm{amp}}}^2}{2}\ .$$

Obtaining this result through the spectral density,

$$\begin{aligned} R_{XX}(\tau) &= {x_{\text{amp}}}^2 \left\langle \cos\!\big[\Omega\, t\big]\, \cos\!\big[\Omega\,(t+\tau)\big] \right\rangle_t \\ &= {x_{\text{amp}}}^2 \left(\cos[\Omega\,\tau] \left\langle \cos[\Omega\, t]^2 \right\rangle_t - \sin[\Omega\,\tau] \left\langle \cos[\Omega\, t]\, \sin[\Omega\, t] \right\rangle_t \right) \\ &= \frac{{x_{\text{amp}}}^2\, \cos[\Omega\,\tau]}{2} \,, \end{aligned}$$

$$\begin{aligned} \Rightarrow \quad S_{XX}(\omega) &= \frac{{x_{\text{amp}}}^2}{4} \int_{-\infty}^{\infty} \left(\mathrm{e}^{\mathrm{i}\,(\Omega+\omega)\,\tau} + \mathrm{e}^{-\mathrm{i}\,(\Omega-\omega)\,\tau} \right) \mathrm{d}\tau \\ &= \frac{{x_{\text{amp}}}^2\, \pi}{2} \Big(\delta(\omega+\Omega) + \delta(\omega-\Omega) \Big) \,, \end{aligned}$$

$$\begin{aligned} \Rightarrow \quad P &= \frac{{x_{\text{amp}}}^2\, \pi}{4\,\pi} \int_{-\infty}^{\infty} \Big(\delta(\omega+\Omega) + \delta(\omega-\Omega) \Big) \,\mathrm{d}\omega \\ &= \frac{{x_{\text{amp}}}^2}{2} \,. \end{aligned}$$

Using the alternative definition (Λ.2) we need,

$$\begin{aligned} R_{XX}(t_1, t_2) &= \big\langle X(t_1 - t)^*\, X(t_2 - t) \big\rangle_t \\ &= \frac{{x_{\text{amp}}}^2}{2} \Big(\big\langle \cos[\Omega\,(t_2 - t_1)] \big\rangle_t + \big\langle \cos[\Omega\,(t_1 + t_2 + 2\,t)] \big\rangle_t \Big) \\ &= \frac{{x_{\text{amp}}}^2\, \cos[\Omega\,(t_2 - t_1)]}{2} \,. \end{aligned}$$

Equivalently we can think of our signal as having a random variable start phase

$$X(t) = x_{\text{amp}}\, \cos[\Omega\, t - \phi] \,, \qquad\qquad \phi \sim \text{Uniform}[0, 2\,\pi] \,,$$

$$\begin{aligned}
\Rightarrow \quad R_{XX}(t_1, t_2) &= \mathrm{E}\big[X(t_1)^*\, X(t_2)\big] \\
&= {x_{\mathrm{amp}}}^2 \int_0^{2\,\pi} \frac{1}{2\,\pi}\, \cos[\Omega\, t_1 - \phi]\, \cos[\Omega\, t_2 - \phi]\, \mathrm{d}\phi \\
&= \frac{{x_{\mathrm{amp}}}^2\, \cos[\Omega\, (t_2 - t_1)]}{2}\,.
\end{aligned}$$

Putting this into (Λ.2),

$$S_{XX}(\omega) = \lim_{T \to \infty} \frac{{x_{\mathrm{amp}}}^2}{4\,T} \int_0^T \int_0^T \left(\mathrm{e}^{\mathrm{i}\,\Omega\,(t_2 - t_1)} + \mathrm{e}^{-\mathrm{i}\,\Omega\,(t_2 - t_1)}\right) \mathrm{e}^{\mathrm{i}\,\omega\,(t_2 - t_1)}\, \mathrm{d}t_1\, \mathrm{d}t_2$$

$$\begin{aligned}
&= \frac{{x_{\mathrm{amp}}}^2}{4} \lim_{T \to \infty} \frac{1}{T} \left(\int_0^T \mathrm{e}^{-\mathrm{i}\,t_1\,(\Omega + \omega)}\, \mathrm{d}t_1 \int_0^T \mathrm{e}^{\mathrm{i}\,t_2\,(\Omega + \omega)}\, \mathrm{d}t_2 \right. \\
&\qquad \left. + \int_0^T \mathrm{e}^{-\mathrm{i}\,t_1\,(\Omega - \omega)}\, \mathrm{d}t_1 \int_0^T \mathrm{e}^{\mathrm{i}\,t_2\,(\Omega - \omega)}\, \mathrm{d}t_2 \right).
\end{aligned}$$

Applying L'Hôpital's rule and the fundamental theorem of calculus,

$$\begin{aligned}
S_{XX}(\omega) = \frac{{x_{\mathrm{amp}}}^2}{4} \lim_{T \to \infty} \Bigg(& \int_0^T \mathrm{e}^{\mathrm{i}\,(t_2 - T)\,(\Omega + \omega)}\, \mathrm{d}t_2 + \int_0^T \mathrm{e}^{\mathrm{i}\,(T - t_1)\,(\Omega + \omega)}\, \mathrm{d}t_1 \\
& + \int_0^T \mathrm{e}^{\mathrm{i}\,(t_2 - T)\,(\Omega - \omega)}\, \mathrm{d}t_2 + \int_0^T \mathrm{e}^{\mathrm{i}\,(T - t_1)\,(\Omega - \omega)}\, \mathrm{d}t_1 \Bigg)\,,
\end{aligned}$$

and making the substitutions $t_1 = T - t$, $t_2 = T + t$,

$$S_{XX}(\omega) = \frac{{x_{\text{amp}}}^2}{4} \lim_{T\to\infty} \left(\int_{-T}^{0} \mathrm{e}^{\mathrm{i}\, t\, (\Omega+\omega)}\, \mathrm{d}t - \int_{T}^{0} \mathrm{e}^{\mathrm{i}\, t\, (\Omega+\omega)}\, \mathrm{d}t \right.$$
$$\left. + \int_{-T}^{0} \mathrm{e}^{\mathrm{i}\, t\, (\Omega-\omega)}\, \mathrm{d}t - \int_{T}^{0} \mathrm{e}^{\mathrm{i}\, t\, (\Omega-\omega)}\, \mathrm{d}t \right)$$

$$= \frac{{x_{\text{amp}}}^2}{4} \left(\int_{-\infty}^{\infty} \mathrm{e}^{\mathrm{i}\, t\, (\Omega+\omega)}\, \mathrm{d}t + \int_{-\infty}^{\infty} \mathrm{e}^{\mathrm{i}\, t\, (\Omega-\omega)}\, \mathrm{d}t \right)$$

$$= \frac{{x_{\text{amp}}}^2\, \pi}{2} \Big(\delta(\omega + \Omega) + \delta(\omega - \Omega) \Big) \,,$$

we get the same as above.

Real multi-tone signal

For an amplitude of the form

$$X(t) = \sum_i x_i \, \cos[\Omega_i \, t - \phi_i] \,,$$

we find

$$R_{XX}(\tau) = \sum_i \sum_j x_i\, x_j \left\langle \cos[\Omega_i\, t - \phi_i]\, \cos[\Omega_j\, (t+\tau) - \phi_j] \right\rangle_t$$

$$= \sum_i \sum_j x_i\, x_j \left(\cos[\Omega_j\, \tau] \left\langle \cos[\Omega_i\, t - \phi_i]\, \cos[\Omega_j\, t - \phi_j] \right\rangle_t \right.$$
$$\left. - \sin[\Omega_j\, \tau] \left\langle \cos[\Omega_i\, t - \phi_i]\, \sin[\Omega_j\, t - \phi_j] \right\rangle_t \right)$$

$$= \sum_i \sum_j x_i\, x_j\, \delta_{\Omega_i\, \Omega_j}\, \frac{1}{2} \left(\cos[\Omega_j\, \tau]\, \cos[\phi_i - \phi_j] - \sin[\Omega_j\, \tau]\, \sin[\phi_i - \phi_j] \right) ,$$

$$S_{XX}(\omega) = \sum_i \sum_j x_i\, x_j\, \delta_{\Omega_i\, \Omega_j}\, \frac{\pi}{2} \left(\delta(\omega + \Omega_j) \left(\cos[\phi_i - \phi_j] - \sin[\phi_i - \phi_j] \right) \right.$$
$$\left. + \delta(\omega - \Omega_j) \left(\cos[\phi_i - \phi_j] + \sin[\phi_i - \phi_j] \right) \right) ,$$

$$P = \sum_i \sum_j \frac{x_i\, x_j}{2}\, \delta_{\Omega_i\, \Omega_j}\, \cos[\phi_i - \phi_j] \, .$$

If our amplitude is collected by frequency via

$$\sum_i x_i\, \cos[\Omega\, t - \phi_i] = \sqrt{\xi^2 + \zeta^2}\, \cos\big[\Omega\, t - \arctan[\zeta/\xi]\big] \quad : \quad \begin{cases} \xi = \sum_i x_i\, \cos[\phi_i] \\ \zeta = \sum_i x_i\, \sin[\phi_i] \end{cases} ,$$

such that

$$X(t) = \sum_{\Omega} x_{\Omega} \cos[\Omega\, t - \phi_{\Omega}] \,,$$

we find

$$R_{XX}(\tau) = \sum_{\Omega} \frac{{x_{\Omega}}^2}{2} \cos[\Omega\, \tau] \,,$$

$$S_{XX}(\omega) = \sum_{\Omega} \frac{\pi\, {x_{\Omega}}^2}{2} \Big(\delta(\omega + \Omega) + \delta(\omega - \Omega) \Big) \,,$$

$$P = \sum_{\Omega} \frac{{x_{\Omega}}^2}{2} \,.$$

Λ.1.3 Complex harmonic signal

When using a complex number as a proxy for a harmonic signal

$$\tilde{X}(t) = x_{\text{amp}}\, \mathrm{e}^{-\mathrm{i}\,\Omega\, t} \,, \qquad \Re\big[\tilde{X}(t)\big] = x_{\text{amp}} \cos[\Omega\, t] \,, \qquad x_{\text{RMS}} = \frac{x_{\text{amp}}}{\sqrt{2}} \,,$$

the average power is

$$P = \frac{|\tilde{X}|^2}{2} = \frac{{x_{\text{amp}}}^2}{2} \,,$$

and the power spectral density (Λ.1) needs to be likewise modified,

$$S_{\tilde{X}\tilde{X}}(\omega) = \frac{1}{2} \int_{-\infty}^{\infty} R_{\tilde{X}\tilde{X}}(\tau)\, \mathrm{e}^{\mathrm{i}\,\omega\,\tau}\, \mathrm{d}\tau \quad : \quad \tilde{X} \in \mathbb{C}\,.$$

Thus

$$R_{\tilde{X}\tilde{X}}(\tau) = {x_{\mathrm{amp}}}^2\, \mathrm{e}^{-\mathrm{i}\,\Omega\,\tau}\,,$$

$$\begin{aligned} \Rightarrow \quad S_{\tilde{X}\tilde{X}}(\omega) &= \frac{{x_{\mathrm{amp}}}^2}{2} \int_{-\infty}^{\infty} \mathrm{e}^{-\mathrm{i}\,(\Omega-\omega)\,\tau}\, \mathrm{d}\tau \\ &= {x_{\mathrm{amp}}}^2\, \pi\, \delta(\omega - \Omega)\,, \end{aligned}$$

$$\begin{aligned} \Rightarrow \quad P &= \frac{{x_{\mathrm{amp}}}^2\, \pi}{2\,\pi} \int_{-\infty}^{\infty} \delta(\omega - \Omega)\, \mathrm{d}\omega \\ &= \frac{{x_{\mathrm{amp}}}^2}{2}\,. \end{aligned}$$

Complex multi-tone signal

For an amplitude of the form

$$\tilde{X}(t) = \sum_i \tilde{x}_i\, \mathrm{e}^{-\mathrm{i}\,\Omega_i\,t} \quad : \quad \tilde{x}_i \in \mathbb{C}\,,$$

we find

$$\begin{aligned} R_{\tilde{X}\tilde{X}}(\tau) &= \sum_i \sum_j {x_i}^* \, x_j \left\langle \mathrm{e}^{\mathrm{i}\,\Omega_i\,t} \, \mathrm{e}^{-\mathrm{i}\,\Omega_j\,(t+\tau)} \right\rangle_t \\ &= \sum_i \sum_j {x_i}^* \, x_j \, \mathrm{e}^{-\mathrm{i}\,\Omega_j\,\tau} \left\langle \mathrm{e}^{\mathrm{i}\,(\Omega_i - \Omega_j)\,t} \right\rangle_t \\ &= \sum_i \sum_j {x_i}^* \, x_j \, \delta_{\Omega_i\,\Omega_j} \, \mathrm{e}^{-\mathrm{i}\,\Omega_j\,\tau} \ , \end{aligned}$$

$$S_{\tilde{X}\tilde{X}}(\omega) = \sum_i \sum_j \pi, {x_i}^* \, x_j \, \delta_{\Omega_i\,\Omega_j} \, \delta(\omega - \Omega_j) \ ,$$

$$P = \sum_i \sum_j \frac{{x_i}^* \, x_j}{2} \, \delta_{\Omega_i\,\Omega_j} \ .$$

If our amplitude is collected by frequency,

$$\tilde{X}(t) = \sum_\Omega \tilde{x}_\Omega \, \mathrm{e}^{-\mathrm{i}\,\Omega\,t}$$

we find

$$R_{\tilde{X}\tilde{X}}(\tau) = \sum_\Omega |x_\Omega|^2 \, \mathrm{e}^{-\mathrm{i}\,\Omega\,\tau} \ ,$$

$$S_{\tilde{X}\tilde{X}}(\omega) = \sum_\Omega \pi \, |x_\Omega|^2 \, \delta(\omega - \Omega) \ ,$$

$$P = \sum_{\Omega} \frac{|x_\Omega|^2}{2} \ .$$

Λ.1.4 Constant signal

For the trivial case of a constant signal,

$$\begin{aligned} X(t) &= x \ , \\ R_{XX}(\tau) &= x^2 \ , \\ S_{XX}(\omega) &= 2\,\pi\,\delta(\omega)\,x^2 \ , \\ P &= x^2 \ . \end{aligned}$$

Λ.1.5 White noise

For white noise our signal $X(t)$ is a random variable with no time dependence such that distributions at different times are uncorrelated. The signal at any particular time follows a normal distribution,

$$\begin{aligned} X(t) &\sim \text{Normal}\big[0, \sigma\big] \ , \\ \Rightarrow \quad X(t)^2 &\sim \text{Normal}\big[\sigma^2, \sqrt{2}\,\sigma^2\big] \ , \end{aligned}$$

and the auto-correlation is thus

$$\begin{aligned} R_{XX}(\tau) &= \text{E}\big[X(t)\,X(t+\tau)\big] \\ &= \delta(\tau)\ \text{E}\big[X(t)^2\big] + \big(1-\delta(\tau)\big)\ \text{E}\big[X(t)\big]\ \text{E}\big[X(t+\tau)\big] \\ &= \delta(\tau)\,\sigma^2 \ , \end{aligned}$$

giving power spectral density

$$S_{XX}(\omega) = \sigma^2 \, .$$

This gives the unphysical result of infinite power being emitted. In reality, however, there is some timescale involved in the noise generation leading to some upper frequency cut-off existing. Over small ranges of frequency where a flat power spectral density approximation holds, the power in some bandwidth is

$$P\big([\omega_1, \omega_2] \subset \mathbb{R}^+\big) = \frac{\omega_2 - \omega_1}{2\,\pi}\, 2\,\sigma^2 \, .$$

$\Lambda.2$ Thermal noise

Known as Johnson-Nyquist noise. If we model our heat bath as a continuous infinite set of harmonic oscillators $\{E_\omega\}_{\omega=0}^{\infty}$, at thermal equilibrium we can use the equipartition theorem to assert the energy in each is

$$S_{\mathrm{N}}(\omega > 0) = E(\omega) = k_{\mathrm{B}}\,\mathbb{T} \, .$$

Thus the one-sided power in some bandwidth is

$$P_{\mathrm{N}}\big([\omega_1, \omega_2] \subset \mathbb{R}^+\big) = \frac{\omega_2 - \omega_1}{2\,\pi}\, k_{\mathrm{B}}\,\mathbb{T} \, ,$$

$$P_{\mathrm{N}}(\Delta f) = \Delta f\, k_{\mathrm{B}}\,\mathbb{T} \, . \tag{$\Lambda.4$}$$

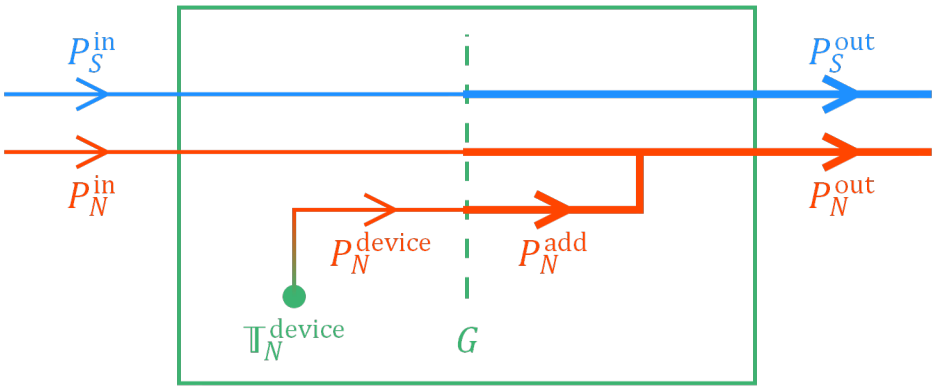

Figure Λ.1: Power flow diagram of a generic device with gain G and noise temperature $\mathbb{T}_{\mathrm{N}}^{\mathrm{device}}$.

Λ.3 Noise quantifiers

Λ.3.1 Signal to noise

The signal to noise ratio is defined as

$$\underset{\substack{\text{signal to}\\\text{noise ratio}}}{\mathrm{SNR}} = \underset{\substack{\text{signal}\\\text{power}}}{P_{\mathrm{S}}} \Big/ \underset{\substack{\text{noise}\\\text{power}}}{P_{\mathrm{N}}} \quad ,$$

where the powers are averaged appropriately and measured under the same conditions. The signal to noise ratio is therefore dependent on factors such as measurement bandwidth Δf. Following (Λ.4)

$$\underset{\substack{\text{noise}\\\text{power}}}{P_{\mathrm{N}}} = \underset{\text{bandwidth}}{\Delta f} \quad \underset{\substack{\text{Boltzmann}\\\text{constant}}}{k_{\mathrm{B}}} \quad \underset{\substack{\text{noise}\\\text{temperature}}}{\mathbb{T}_{\mathrm{N}}} \quad .$$

Λ.3.2 Device noise

For a generic device, as depicted in Fig. Λ.1, we have the following quantities and relations

$$\underset{\substack{\text{output signal}\\\text{power}}}{P_{\mathrm{S}}^{\mathrm{out}}} = \underset{\substack{\text{gain}}}{G}\ \underset{\substack{\text{input signal}\\\text{power}}}{P_{\mathrm{S}}^{\mathrm{in}}}\ ,$$

$$\underset{\substack{\text{added noise}\\\text{power}}}{P_{\mathrm{N}}^{\mathrm{add}}} = \underset{\substack{\text{gain}}}{G}\ \underset{\substack{\text{device (input)}\\\text{noise power}}}{P_{\mathrm{N}}^{\mathrm{device}}}\ ,$$

$$\underset{\substack{\text{output noise}\\\text{power}}}{P_{\mathrm{N}}^{\mathrm{out}}} = \underset{\substack{\text{gain}}}{G}\ \underset{\substack{\text{input noise}\\\text{power}}}{P_{\mathrm{N}}^{\mathrm{in}}} + \underset{\substack{\text{added noise}\\\text{power}}}{P_{\mathrm{N}}^{\mathrm{add}}}\ ,$$

$$\frac{\mathrm{SNR}^{\mathrm{in}}}{\mathrm{SNR}^{\mathrm{out}}} = 1 + \frac{P_{\mathrm{N}}^{\mathrm{add}}}{G\,P_{\mathrm{N}}^{\mathrm{in}}} = 1 + \frac{\mathbb{T}_{\mathrm{N}}^{\mathrm{device}}}{\mathbb{T}_{\mathrm{N}}^{\mathrm{in}}}\ ,$$

$$\underset{\substack{\text{noise factor}}}{F} = \frac{\mathrm{SNR}_0^{\mathrm{in}}}{\mathrm{SNR}^{\mathrm{out}}} = 1 + \frac{\mathbb{T}_{\mathrm{N}}^{\mathrm{device}}}{\mathbb{T}_0}\ ,$$

$$\underset{\substack{\text{noise figure}}}{\mathrm{NF}} = 10\,\log_{10}[F]\,\mathrm{dB}\ .$$

Noise factors are specified against a reference input temperature, typically $\mathbb{T}_0 = 290\,\mathrm{K}$.

Λ.3.3 Attenuator

Attenuators have

$$\underset{\text{attenuation}}{L} = \frac{1}{G}\,, \qquad \mathbb{T}_{\mathrm{N}}^{\mathrm{device}} = \big(L-1\big)\,\mathbb{T}_{\mathrm{env}}\,,$$

where $\mathbb{T}_{\mathrm{env}}$ is the physical temperature of the attenuator. If $\mathbb{T}_{\mathrm{env}} = \mathbb{T}_0$, then $F = L$.

Λ.3.4 Friis formula

The noise factor for a chain of devices can be computed using the Friis formula. For a series of devices with (internal) noise temperatures $\{\mathbb{T}_N^i\}_{i=1}^n$, the lumped device noise temperature is

$$\underset{\substack{\text{series lumped}\\ \text{device noise}\\ \text{temperature}}}{\mathbb{T}_N^{\rightarrow}} = \sum_{i=1}^{n} \frac{\mathbb{T}_{\mathrm{N}}^i}{\prod_{j=0}^{i-1} G_j} \qquad : \quad G_0 = 1\,.$$

Λ.3.5 Noise propagation

If there is no signal, the noise temperature can be propagated as

$$\mathbb{T}_{\mathrm{N}}^{\mathrm{out}} = F\,G\,\mathbb{T}_{\mathrm{N}}^{\mathrm{in}} \qquad : \; P_{\mathrm{S}}^{\mathrm{in}} = 0\,,$$

$$\mathbb{T}_{\mathrm{N}}^{\mathrm{out}} = \frac{\mathbb{T}_{\mathrm{N}}^{\mathrm{in}} - \mathbb{T}_{\mathrm{env}}}{L} + \mathbb{T}_{\mathrm{env}} \qquad : \; P_{\mathrm{S}}^{\mathrm{in}} = 0\,, \text{attenuator}\,.$$

Λ.4 Averaging

Λ.4.1 Noise amplitude

Averaging the amplitude suppresses random noise toward zero. For

$$X_i \sim \text{Normal}\big[0, \sigma\big] ,$$

the average is

$$M_X = \frac{\sum_{i=1}^{n} X_i}{n} ,$$

$$\Rightarrow \quad M_X \sim \text{Normal}\Big[0, \frac{\sigma}{\sqrt{n}}\Big] ,$$

$$\Rightarrow \quad \big(M_X\big)^2 \sim \text{Normal}\Big[\frac{\sigma^2}{n}, \frac{\sqrt{2}\,\sigma^2}{n}\Big] ,$$

$$\Rightarrow \quad S_{M_X\,M_X}(\omega) = \frac{\sigma^2}{n} .$$

Unfortunately the amplitude average of a harmonic signal is also zero. If the signal frequency is known, however, it can be mixed down and then measured.

Λ.4.2 Noise power

Averaging the power provides a more precise measurement of the the noise. For

$$\begin{aligned} X_i &\sim \text{Normal}\big[0, \sigma\big] \,, \\ {X_i}^2 &\sim \text{Normal}\big[\sigma^2, \sqrt{2}\,\sigma^2\big] \,, \end{aligned}$$

the average is

$$M_{X^2} = \frac{\sum_{i=1}^{n} {X_i}^2}{n} \,,$$

$$\Rightarrow \quad M_{X^2} \sim \text{Normal}\Big[\sigma^2, \frac{\sigma^2}{\sqrt{n}}\Big] \,,$$

$$\Rightarrow \quad S_{M_{X^2}\, M_{X^2}}(\omega) = \sigma^2 \,.$$

Λ.5 Decibels

Decibels are used to express ratios on a logarithmic scale, and are defined to put amplitudes and powers on the same scale.

$$\text{Amplitude level} = 20\, \log_{10}\Big[\frac{X}{X_0}\Big]\, \text{dB} \,,$$

$$P \propto X^2$$

$$\text{Power level} = 10\, \log_{10}\Big[\frac{P}{P_0}\Big]\, \text{dB} \,.$$

Named decibel units use an explicit reference level. For dBm, $P_0 = 1\,\text{mW}$.

Λ.6 Power formulas

Λ.6.1 Time average

The time average of a sinusoid is zero, whilst the time average of a squared sinusoid is

$$\big\langle \sin[\phi]^2 \big\rangle_\phi = \big\langle \cos[\phi]^2 \big\rangle_\phi = \frac{1}{2\,\pi} \int_0^{2\,\pi} \cos[\phi]^2 \, \mathrm{d}\phi = \frac{1}{2} \; .$$

Λ.6.2 Real harmonic signal

For a real harmonic voltage,

$$V(t) = V_{\text{amp}} \, \cos[\Omega \, t] \; ,$$

$$\Rightarrow \quad \big\langle V(t)^2 \big\rangle_t = \frac{{V_{\text{amp}}}^2}{2} \; ,$$

and we define the root-mean-squared voltage and peak-to-peak voltage as

$$V_{\text{RMS}} = \sqrt{\big\langle V(t)^2 \big\rangle_t} = \frac{V_{\text{amp}}}{\sqrt{2}} \; , \qquad\qquad V_{\text{peak-peak}} = 2 \, V_{\text{amp}} \; .$$

The power is

$$P(t) = V(t) \, I(t) = \frac{V(t)^2}{R}$$

$$\Rightarrow \quad \big\langle P \big\rangle = \frac{{V_{\text{amp}}}^2}{2 \, R} \; .$$

Λ.6.3 Complex harmonic signal

For a complex harmonic voltage

$$\tilde{V}(t) = V_{\text{amp}}\, \mathrm{e}^{\mathrm{i}\,\Omega\, t}\ , \qquad\qquad \Re\big[\tilde{V}(t)\big] = V_{\text{amp}}\, \cos[\Omega\, t]\ .$$

The average power is

$$\tilde{P} = \frac{\tilde{V}^*\, \tilde{I}}{2} = \frac{|\tilde{V}|^2}{2\, R}\ ,$$

$$\Rightarrow \quad \big\langle P \big\rangle = \Re[\tilde{P}] = \frac{{V_{\text{amp}}}^2}{2\, R}\ .$$

Λ.7 In-phase and quadrature

When making microwave voltage measurements it is common practice to do so with respect to a carrier frequency and separate in-phase and quadrature components. Mixing a controlled carrier frequency near the signal frequency produces a small difference frequency with a large oscillation period that is accessible to measurement electronics. Mathematically, this is

$$\underbrace{V(t)}_{\text{voltage}} = \underbrace{A(t)\, \sin\big[\omega_c\, t + \phi(t)\big]}_{\text{amplitude/phase form}} = \underbrace{A(t)\, \cos\big[\phi(t)\big]\, \sin\big[\omega_c\, t\big]}_{\text{in-phase}} + \underbrace{A(t)\, \sin\big[\phi(t)\big]\, \cos\big[\omega_c\, t\big]}_{\text{quadrature}}\ ,$$

where we have

$$\underset{\text{amplitude}}{A(t)} \quad \geqslant 0\ , \qquad\qquad \underset{\text{phase}}{\phi(t)} \quad \in S^1\ ,$$

and define

$$I(t) = A(t)\,\cos\big[\phi(t)\big]\ , \qquad\qquad Q(t) = A(t)\,\sin\big[\phi(t)\big]\ ,$$

giving

$$A(t) = \sqrt{I(t)^2 + Q(t)^2}\ , \qquad\qquad \phi(t) = \arctan\big[Q(t)/I(t)\big]\ .$$

The complex voltage is

$$\tilde{V}(t) = A(t)\,\mathrm{e}^{\mathrm{i}\,(\omega_c\,t + \phi(t) - \pi/2)}\ .$$

Λ.8 Quantum to classical signal

A quantum signal is often denoted having power

$$\big\langle P \big\rangle = \hat{a}_{\rm in}^{\dagger}\,\hat{a}_{\rm in}\,\hbar\,\omega_a\ ,$$

where $\hat{a}_{\rm in}$ has units of $\sqrt{\text{counts/s}}$. Thus

$$\tilde{a}_{\substack{\rm in\\ \rm RMS}}(t) = \sqrt{\hbar\,\omega_a}\,\hat{a}_{\rm in}(t) = \sqrt{P}\,\mathrm{e}^{-\mathrm{i}\,\omega_a\,t}$$

is a RMS complex signal. The real classical signal is therefore

$$a_{\rm in}(t) = \sqrt{2}\,\Re\big[\tilde{a}_{\substack{\rm in\\ \rm RMS}}(t)\big] \in \mathbb{R}\ .$$

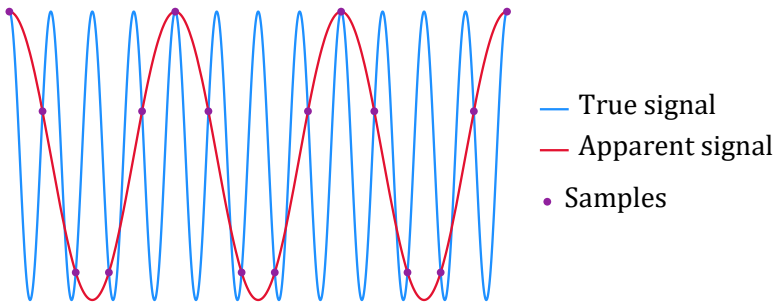

Figure Λ.2: A signal (blue) is undersampled at discrete points (purple) that look like a lower frequency signal (red).

Λ.9 Undersampling

Following the Nyquist-Shannon sampling theorem, a signal $X(t) \propto \cos[2\,\pi\,f_X\,t]$ needs to be sampled (discrete time measurements) at a rate $f_{\mathrm{Sa}} > 2\,f_X$ to be reconstructed. Signals above half the sampling rate will appear at lower frequencies according to[1]

$$f_X^{\text{apparent}} = \left| f_X \bmod_{-f_{\mathrm{Ny}}} f_{\mathrm{Sa}} \right| \qquad : \qquad \underbrace{f_{\mathrm{Ny}}}_{\substack{\text{Nyquist}\\ \text{frequency}}} = \underbrace{f_{\mathrm{Sa}}}_{\substack{\text{sampling}\\ \text{frequency}}} \Big/ 2\,.$$

A simple illustration is provided in Fig. Λ.2.

1. Offset modulo $a \bmod_c b = \big((a-c) \bmod b\big) + c$.

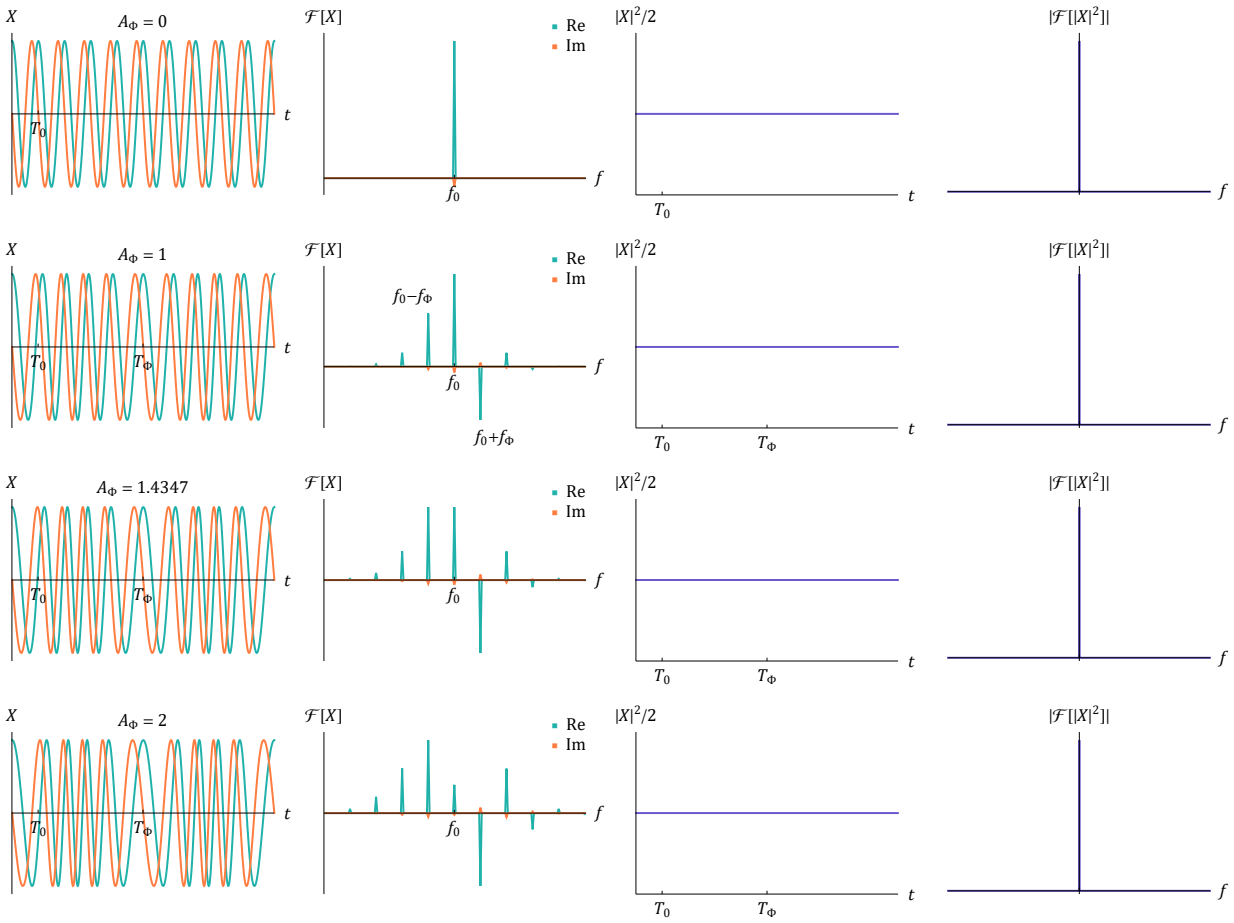

Figure Λ.3: Phase modulation of complex signals.

Λ.10 Modulation

Λ.10.1 Complex phase modulation

A phase modulated complex signal has the form

$$\tilde{X}(t) = x_{\text{amp}}\, \mathrm{e}^{-\mathrm{i}\left(\omega_0\, t - A_\Phi\, \sin[\omega_\Phi\, t]\right)}\ .$$

This looks like squeezing and stretching of the signal frequency over periods of $2\,\pi/\omega_\Phi$, creating side bands in Fourier space at intervals of f_Φ. Plots of various phase modulated

signals are shown in Fig. Λ.3. Importantly, phase modulation by itself does nothing to detected power. However, if a phase modulated signal is passed through an element with non-uniform transmission the spectral components will be affected differently, potentially creating side bands in the detected power spectral density.

The complex phase modulated signal can be expressed by the Jacobi-Anger expansion,

$$\mathrm{e}^{-\mathrm{i}\left(\omega_0 t - A_\Phi \sin[\omega_\Phi t]\right)} = \mathrm{e}^{-\mathrm{i}\,\omega_0 t} \sum_{j=-\infty}^{\infty} J_j[A_\Phi]\,\mathrm{e}^{-\mathrm{i}\,j\,\omega_\Phi t} \ ,$$

where J_j are Bessel functions of the first kind. This form allows us to determine the phase modulating amplitude that produces first-order side bands equal in strength to the carrier,

$$J_0[A_\Phi]^2 = J_1[A_\Phi]^2 \quad \Rightarrow \quad A_\Phi = 1.43469565 \quad : \text{ smallest solution} \ .$$

Λ.10.2 Complex intensity modulation

Consider an intensity attenuation modulation,

$$P(t) = P_0 \left(1 - \frac{A_\mathrm{I}}{2}\left(1 + \sin[\omega_\mathrm{I} t]\right)\right) \quad : \ A_\mathrm{I} \in [0, 1] \ ,$$

such that $A_\mathrm{I} = 0$ is no modulation and $A_\mathrm{I} = 1$ modulates to full extinction. The amplitude for this is

$$\tilde{X}(t) = x_\mathrm{amp} \sqrt{1 - \frac{A_\mathrm{I}}{2}\left(1 + \sin[\omega_\mathrm{I} t]\right)}\,\mathrm{e}^{-\mathrm{i}\,\omega_0 t} \ .$$

Plots of various intensity modulated signals are shown in Fig. Λ.4.

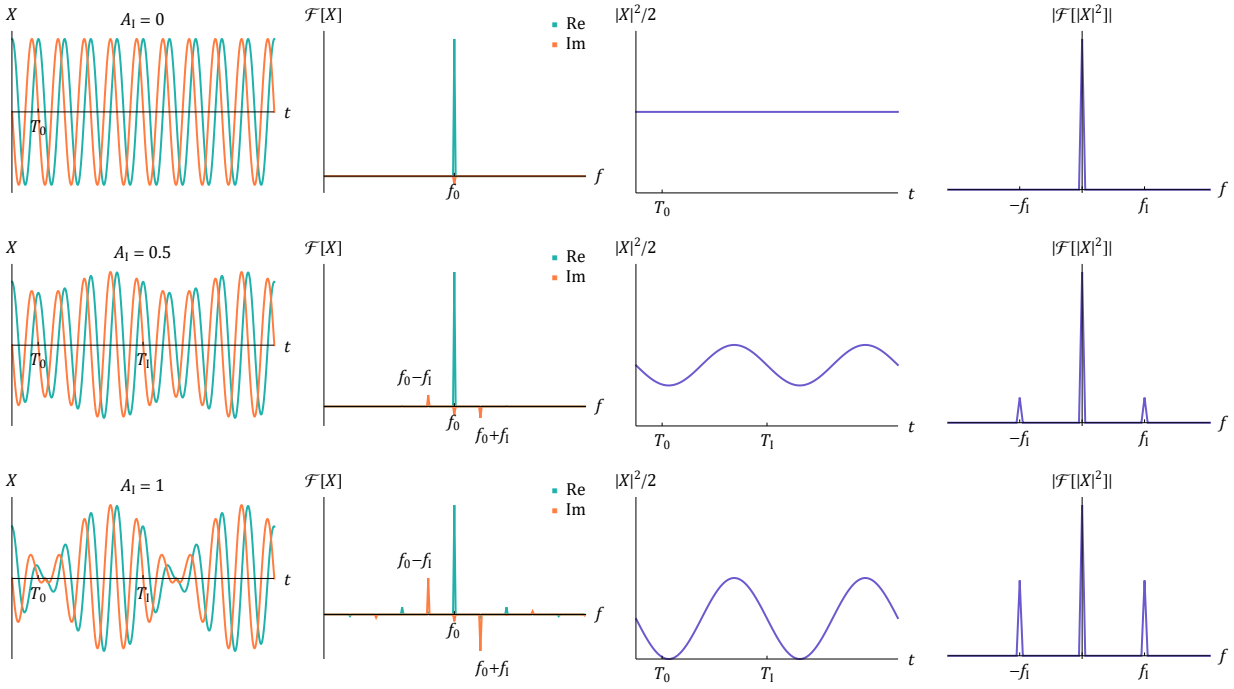

Figure Λ.4: Intensity modulation of complex signals.

Λ.10.3 Real signal modulation

We can also modulate real signals, $X(t)$ and examine $X(t)^2$. This situation needs some careful consideration of different time scales in use, in particular the bandwidth of a power detector, and interpretation of quantities. Typically we have the detector bandwidth much less than the carrier frequency, $f_{\text{det}} \ll f_0$. Plots of various phase modulated signals are shown in Fig. Λ.5 and intensity modulated signals in Fig. Λ.6.

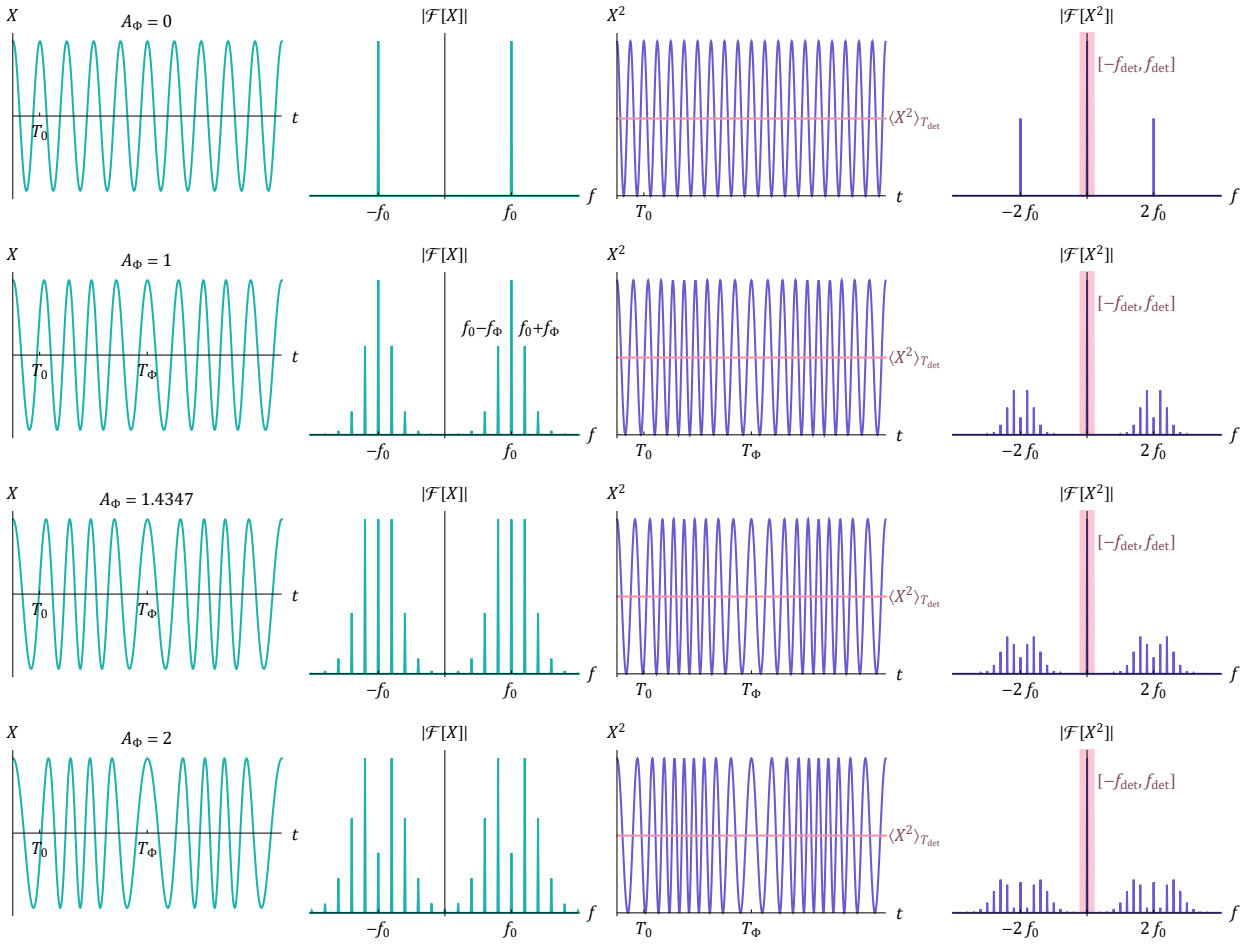

Figure Λ.5: Phase modulation of real signals.

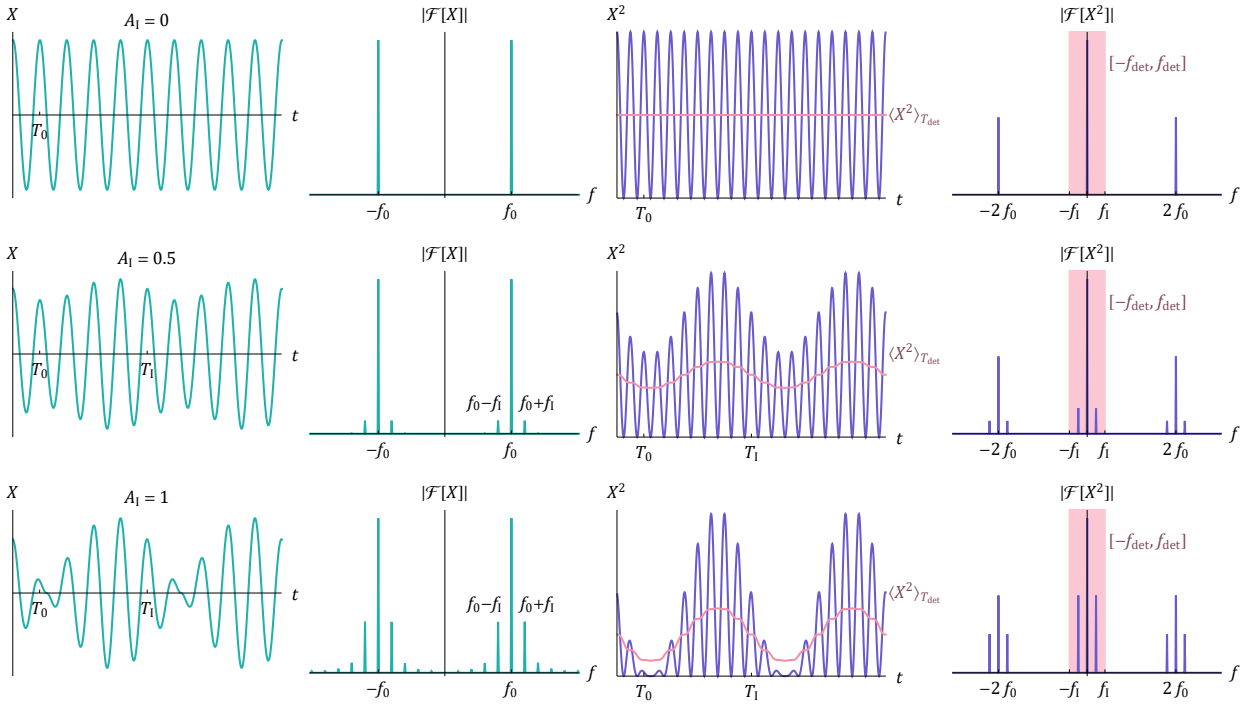

Figure Λ.6: Intensity modulation of real signals.

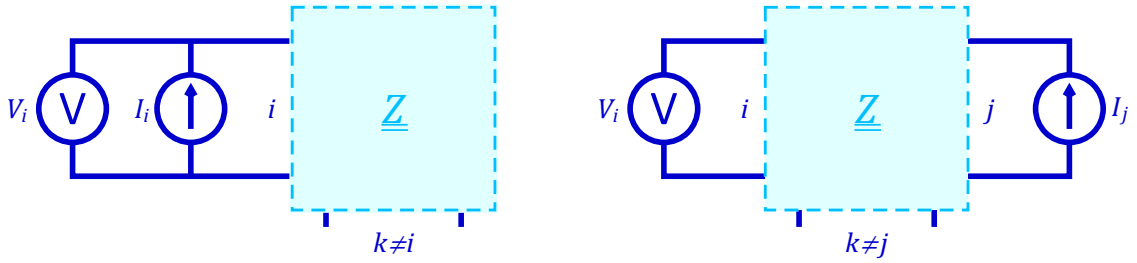

Figure Λ.7: Circuit diagrams for measuring $Z_{i\,i}$ (left) and $Z_{i\,j}$ (right) using current sources and open volt meters.

Λ.11 Electrical network

For an electrical network with multiple ports, the impedance matrix is defined as

$$Z_{i\,j} = \left.\frac{V_i}{I_j}\right|_{I_{k\neq j}=0} ,$$

and can be determined by considering the circuit diagrams given in Fig. Λ.7. The scattering matrix incorporates the characteristic line impedances, Z_i, of the ports and is given by [305]

$$\begin{aligned} \underline{\underline{S}} &= \underline{\underline{F}} \cdot \left(\underline{\underline{Z}} - \underline{\underline{Z_{\mathrm{C}}}}^*\right) \cdot \left(\underline{\underline{Z}} + \underline{\underline{Z_{\mathrm{C}}}}\right)^{-1} \cdot \underline{\underline{F}}^{-1} \\ &= \left(\underline{\underline{F}} \cdot \underline{\underline{Z}} \cdot \underline{\underline{F}}^{-1} - \underline{\underline{Z_{\mathrm{C}}}}^*\right) \cdot \left(\underline{\underline{F}} \cdot \underline{\underline{Z}} \cdot \underline{\underline{F}}^{-1} + \underline{\underline{Z_{\mathrm{C}}}}\right)^{-1} , \end{aligned} \tag{Λ.5}$$

where

$$\underline{\underline{Z_{\mathrm{C}}}} = \mathrm{Diag}\left[\{Z_i\}_{i=1}^n\right] , \qquad \underline{\underline{F}} = \left(2\sqrt{\Re\left[\underline{\underline{Z_{\mathrm{C}}}}\right]}\right)^{-1} .$$

The amplitude waves in and out are

$$a_i^{\mathrm{in}} = \frac{V_i + Z_i\, I_i}{2\sqrt{|\Re[Z_i]|}} , \qquad a_i^{\mathrm{out}} = \frac{V_i - Z_i^*\, I_i}{2\sqrt{|\Re[Z_i]|}} ,$$

with powers

$$P_i^{\text{in}} = \frac{|a_i^{\text{in}}|^2}{2} \,, \qquad\qquad P_i^{\text{out}} = \frac{|a_i^{\text{out}}|^2}{2} \,.$$

Λ.12 Spectrum analyzer

A spectrum analyzer is used to measure a power spectrum over some frequency span, f_{span}, at a certain number of points, n_{points}.

The resolution bandwidth, RBW, is the frequency width of each measurement,

$$P_{1\,\text{meas}}(f) \simeq P_1\big([f - \text{RBW}/2, f + \text{RBW}/2]\big) = \int_{f-\text{RBW}/2}^{f+\text{RBW}/2} \Big(S_{XX}(-f') + S_{XX}(f')\Big)\,\mathrm{d}f' \,.$$

The one-sided power spectral density is then approximately

$$\text{PSD}_1(f) = S_{XX}(f) + S_{XX}(-f) \simeq \frac{P_{1\,\text{meas}}(f)}{\text{RBW}} \,.$$

In reality the spectrum analyzer filter is not a perfect rectangular window, and care needs to be taken for any features at similar scales. For a detailed review of windows, see [307]. When measuring a particular feature, we need RBW $\ll$ feature width. To have no gaps in the spectrum, one should set RBW $\geqslant f_{\text{span}}/(n_{\text{points}} - 1)$. Decreasing RBW will lower the noise floor as less is collected in each bin.

The video bandwidth, VBW, provides time averaging of collection points over $\sim 1/\text{VBW}$. Typically VBW $\leqslant$ RBW. Decreasing VBW will reduce noise variance.

Trace averaging is performed after full scans have been completed. Averaging can be performed over the power, 'amplitude' ($\sqrt{\text{power}}$), or logarithmic power. Increasing averages will

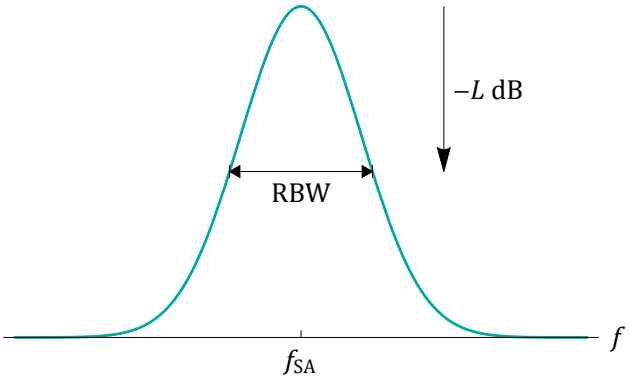

Figure Λ.8: Gaussian window.

reduce noise variance.

Λ.12.1 Gaussian window

A Gaussian window with level $-L\,\mathrm{dB}$, typically $-3\,\mathrm{dB}$, and resolution bandwidth RBW at frequency location f_{SA} has profile

$$w(f_{\mathrm{SA}}; f) = \sqrt{L}\sqrt{\frac{2\,\log[10]}{5\,\pi}}\,\exp\Big[-(f - f_{\mathrm{SA}})^2\,L\,\frac{2\,\log[10]}{5\,\mathrm{RBW}^2}\Big]\,,$$

as shown in Fig. Λ.8, such that the $-L\,\mathrm{dB}$ points are separated by RBW, and $\int w(f)\,\mathrm{d}f = \mathrm{RBW}$. Note that $w(f_{\mathrm{SA}}; f_{\mathrm{SA}}) < 1$.

Let us consider the case of measuring a monotone signal, power $P_\bullet$ at known frequency $f_\bullet$, with a spectrum analyzer using a Gaussian window. The true power spectral density is

$$\mathrm{PSD}_1(f) = P_\bullet\,\delta(f - f_\bullet) + \mathrm{bg}(f)\,.$$

The spectrum analyzer measurement at f_{SA} is then

$$P_{1\,\mathrm{meas}}(f_{\mathrm{SA}}) = \int_{-\infty}^{\infty} \mathrm{PSD}_1(f)\, w(f_{\mathrm{SA}}; f)\, \mathrm{d}f$$

$$= \int_{-\infty}^{\infty} P_\bullet\, \delta(f - f_\bullet)\, w(f_{\mathrm{SA}}; f)\, \mathrm{d}f + \int_{-\infty}^{\infty} \mathrm{bg}(f)\, w(f_{\mathrm{SA}}; f)\, \mathrm{d}f$$

$$= P_\bullet\, w(f_{\mathrm{SA}}; f_\bullet) + \underbrace{\mathrm{bg}(f_{\mathrm{SA}})\,\mathrm{RBW}}_{\text{for linear background}} \quad .$$

Thus, for a linear background,

$$P_\bullet = \frac{P_{1\,\mathrm{meas}}(f_{\mathrm{SA}}) - \mathrm{bg}(f_{\mathrm{SA}})\,\mathrm{RBW}}{w(f_{\mathrm{SA}}; f_\bullet)}$$

$$= \frac{P_{1\,\mathrm{meas}}(f_{\mathrm{SA}}) - \mathrm{bg}(f_{\mathrm{SA}})\,\mathrm{RBW}}{\sqrt{L}\sqrt{\frac{2\,\log[10]}{5\,\pi}}\,\exp\!\left[-(f_\bullet - f_{\mathrm{SA}})^2\, L\, \frac{2\,\log[10]}{5\,\mathrm{RBW}^2}\right]} \quad .$$

APPENDIX Ξ

Periodicity analysis

Whilst feature sizes can be highly variable with fabrication process and fluctuate significantly, the periodicity of objects is consistent. This makes measurements of periodicity a useful calibration tool when performing length measurements. In this appendix we outline two methods of measuring periodicity from an image.

Ξ.1 Fourier analysis

Without any other information, periodicity within an image can be uncovered by Fourier analysis. A gray scale image is effectively a rectangular array of real numbers, in Fourier analysis nomenclature this is a two-dimensional discrete time signal. The discrete time Fourier transform (DTFT) of this data is a continuous two-dimensional function, but is difficult to compute for arbitrary frequencies. Using fast Fourier transform (FFT) techniques, the discrete Fourier transform (DFT) samples the DTFT with the same number of points as the discrete time signal, and is quick to compute. For d-dimensional data, the discrete Fourier transform, with parameters a and b, is

$$\mathrm{DFT}_{a,b}\Big[\big\{u_{\vec{r}}\big\}_{\vec{r}}\Big] = \left\{ \nu_{\vec{s}} = \Pi[\vec{n}]^{\frac{a-1}{2}} \sum_{\vec{r}=\vec{1}}^{\vec{n}} \exp\Big[2\,\pi\,\mathrm{i}\,b\,\big(\vec{r}-\vec{1}\big)\cdot\big((\vec{s}-\vec{1})\oslash\vec{n}\big)\Big]\,u_{\vec{r}} \right\}_{\vec{s}}, \qquad (\Xi.1)$$

using some dubious vector notation[1] where $\vec{r} = \{r_i\}_{i=1}^{d}$ and $\vec{s} = \{s_i\}_{i=1}^{d}$, elements of $\oplus_{i=1}^{d}\mathbb{Z}_{n_i}^{+}$ indexing the data ($\mathbb{Z}_{n_i}^{+} = \{1, 2, \ldots, n_i\}$), and $\vec{n} = \{n_i\}_{i=1}^{d}$ is the number of data points along

1. $\oslash$ is Hadamard (element-wise) divide.

each dimension. The DFT is periodic in every dimension,

$$\nu_{\dots\, r_i + n_i \,\dots} = \nu_{\dots\, r_i \,\dots} \ .$$

Peaks in the DFT are often on the order of one pixel in size, and thus difficult to resolve. To fix this, we want to sample the DTFT at a higher resolution. A common method is zero-padding, where zeros are added to the original signal increasing the total number of points and hence points in the DFT. Another method involves 'zooming' in on the DTFT and sampling a smaller portion of it with the same number of points. Performing a Fourier zoom with magnification m about index $\vec{s}_\star$ we cover the index range

$$\vec{s} \in \left[\vec{s}_\star - \vec{\Delta}, \vec{s}_\star + \vec{\Delta}\right] \quad : \quad \vec{\Delta} = \frac{\vec{n} - \vec{1}}{2\,m} \ ,$$

with new index vector

$$\vec{s}\,' = \left(\vec{s} - \vec{s}_\star + \vec{\Delta}\right) \, m \quad \in \oplus_{i=1}^{d} \, \mathbb{Z}_{n_i}^{+} \ ,$$

which interpolates the original DFT corresponding to non-integer values of $\vec{s}$. Substituting this into (Ξ.1),

$$\nu[\vec{s}] = \Pi[\vec{n}]^{\frac{a-1}{2}} \sum_{\vec{r}=\vec{1}}^{\vec{n}} \exp\!\Big[2\,\pi\,\mathrm{i}\,\frac{b}{m}\,\big(\vec{r} - \vec{1}\big) \cdot \big((\vec{s}\,' - \vec{1}) \oslash \vec{n}\big)\Big] \\ \times \underbrace{u_{\vec{r}} \exp\!\Big[2\,\pi\,\mathrm{i}\,b\,\big(\vec{r} - \vec{1}\big) \cdot \big((\vec{s}_\star - \vec{1} - \vec{\Delta}) \oslash \vec{n}\big)\Big]}_{u'_{\vec{r}}} \ ,$$

which is a DFT from some modified signal data to a subregion of the DTFT,

$$\mathrm{DFT}_{a,b}\mathrm{Zoom}_{\vec{s}_\star,m}\Big[\big\{u_{\vec{r}}\big\}_{\vec{r}}\Big] = \mathrm{DFT}_{a,\frac{b}{m}}\Big[\big\{u'_{\vec{r}}\big\}_{\vec{r}}\Big] = \big\{\nu'_{\vec{s}\,'}\big\}_{\vec{s}\,'} \ ,$$

$$u'_{\vec{r}} = u_{\vec{r}} \exp\Big[2\,\pi\,\mathrm{i}\,b\,\big(\vec{r}-\vec{1}\big)\cdot\big((\vec{s}_\star-\vec{1}-\vec{\Delta})\oslash\vec{n}\big)\Big]\,, \qquad \nu'_{\vec{s}\,\prime} = \nu\Big[\vec{s}_\star-\vec{\Delta}+\frac{\vec{s}\,'}{m}\Big]\,.$$

By mapping our data $u_{\vec{r}} \mapsto u'_{\vec{r}}$ we can use the computational prowess of DFT to quickly sample the DTFT at higher resolutions.

The DFT assumes our signal is periodic, but this is often not the case and artifacts at frequencies corresponding to the size of the image appear in the DTFT. To remove these artifacts we can subtract off the equivalently zoomed DFT of a (non-zero) constant array rescaled to match the zero-frequency element. The cleaned DFT is

$$\begin{aligned}
&\mathrm{DFT}_{a,b}\mathrm{Zoom}^{\mathrm{clean}}_{\vec{s}_\star,m}\Big[\big\{u_{\vec{r}}\big\}_{\vec{r}}\Big] \\
&\quad = \mathrm{DFT}_{a,b}\mathrm{Zoom}_{\vec{s}_\star,m}\Big[\big\{u_{\vec{r}}\big\}_{\vec{r}}\Big] - \underbrace{\left(\frac{\mathrm{DFT}_{a,b}\Big[\big\{u_{\vec{r}}\big\}_{\vec{r}}\Big]\Big|_{\vec{s}=\vec{1}}}{\mathrm{DFT}_{a,b}\Big[\big\{1\big\}_{\vec{r}}\Big]\Big|_{\vec{s}=\vec{1}}}\right)}_{\nu_{\vec{1}}\,\Pi[\vec{n}]^{-\frac{a+1}{2}}} \mathrm{DFT}_{a,b}\mathrm{Zoom}_{\vec{s}_\star,m}\Big[\big\{1\big\}_{\vec{r}}\Big] \\
&\quad = \mathrm{DFT}_{a,b}\mathrm{Zoom}_{\vec{s}_\star,m}\Big[\big\{u_{\vec{r}}\big\}_{\vec{r}}\Big] - \mathrm{DFT}_{-1,b}\mathrm{Zoom}_{\vec{s}_\star,m}\Big[\big\{\nu_{\vec{1}}\big\}_{\vec{r}}\Big]\,.
\end{aligned}$$

An example zoomed and cleaned DFT is shown in Fig. Ξ.1.

Relevant frequencies can be found by looking for peaks in $|\nu|^2$. Locations in the zoomed DFT can be mapped back to the original DFT,

$$\vec{s}\,' \quad \mapsto \quad \vec{s} = \vec{s}_\star - \vec{\Delta} + \frac{\vec{s}\,'}{m}\,.$$

Using the definition (Ξ.1), positions in the DFT correspond to frequencies

$$\vec{f} = b\,(\vec{s}-\vec{1})\oslash\vec{n}\,.$$

If F is a square matrix of d reciprocal lattice vectors $\vec{f}$, the lattice vectors in the original time data are

$$T^{\mathsf{T}} = F^{-1} \, .$$

Mathematica code for performing Fourier zooms is available at `https://gitlab.com/rhyspovey/mathematica-fourier-plus`.

Ξ.2 Lattice fitting

If we know the form of the periodic lattice vectors, we can fit them to periodic sites extracted from an image. This is particularly useful for fitting a scaling parameter if we know what the lattice vectors should be. To perform the fit we need to create a bijection between spatial locations $\vec{y} \in \mathbb{R}^{d_2}$ and crystal lattice indices $\vec{x} \in \mathbb{Z}^{d_1}$,

$$\begin{gathered} X \subset \mathbb{Z}^{d_1} \xleftrightarrow[\text{bijection}]{} Y \subset \mathbb{R}^{d_2} \\ \text{lattice site index} \quad \vec{x} \xleftrightarrow{} \vec{y} \quad \text{spatial location} \, . \end{gathered}$$

Here d_2 is the spatial dimensions, 2 for a normal image, and $d_1 \leqslant d_2$ is the lattice dimensions.

The first step is extracting spatial positions of lattice sites from an image. For separated shapes, like snowflakes, we can do this by

1. Use edge detection to find pixels along an edge,
2. Search for sets of pixels forming closed loops,
3. Take the average of pixel locations in each set.

To associate each spatial location with a lattice index we'll need to approximately know the

lattice vectors prior. Using an approximate lattice we can search for spatial points near the estimated points and associate closest pairs.

We can now fit parameterized lattice vectors $\{\vec{a}_i[\theta]\}_{i=1}^{d_1}$ such that

$$\vec{y} = A[\theta] \cdot \vec{x} \,,$$

for associated pairs where A is the matrix of $\vec{a}$ column vectors. For n point-site pairs, we can assemble them into matrices to produce a multivariate fit problem,

$$\begin{aligned}
\textstyle\bigoplus_{k=1}^{n} \mathbb{R}^{d_1} &\longrightarrow \textstyle\bigoplus_{k=1}^{n} \mathbb{R}^{d_2} \\
X &\longmapsto Y = X \cdot A^{\mathsf{T}} \\
\{x_{k\,i}\}_{k=1,\,i=1}^{n,\,d_1} &\longmapsto \{y_{k\,j} = \textstyle\sum_{i=1}^{d_1} x_{k\,i}\, A_{j\,i}\}_{k=1,\,j=1}^{n,\,d_2} \,.
\end{aligned}$$

This problem can be flattened to a multivariable fit following App. Ψ

$$\begin{aligned}
\textstyle\bigoplus_{\alpha=1}^{n\times d_2} \mathbb{R}^{d_1\times d_2} &\longrightarrow \mathbb{R}^{n\times d_2} \\
X' &\longmapsto \vec{y}\,' = X' \cdot \vec{b}\,' \\
\{x'_{\alpha\,\beta}\}_{\alpha=1,\,\beta=1}^{n\times d_2,\,d_1\times d_2} &\longmapsto \{y'_\alpha = \textstyle\sum_{\beta=1}^{d_1\times d_2} x'_{\alpha\,\beta}\, b'_\beta\}_{\alpha=1}^{n\times d_2} \,,
\end{aligned}$$

with

$$\begin{aligned}
X'_{\alpha\,\beta} &= X_{(\alpha\,\mathrm{quot}_1\,d_2\,+1)\;(\beta\,\mathrm{mod}_1\,d_1)}\;\delta_{(\alpha\,\mathrm{mod}_1\,d_2)\;(\beta\,\mathrm{quot}_1\,d_1\,+1)} \,, \\
y'_\alpha &= Y_{(\alpha\,\mathrm{quot}_1\,d_2\,+1)\;(\alpha\,\mathrm{mod}_1\,d_2)} \,, \\
b'_\beta &= A^{\mathsf{T}}_{(\beta\,\mathrm{quot}_1\,d_2\,+1)\;(\beta\,\mathrm{mod}_1\,d_2)} \,.
\end{aligned}$$

In this format the fitting can be easily carried out by standard non-linear fitting algorithms where $\vec{b}\,'$ is a function of the fit parameters.

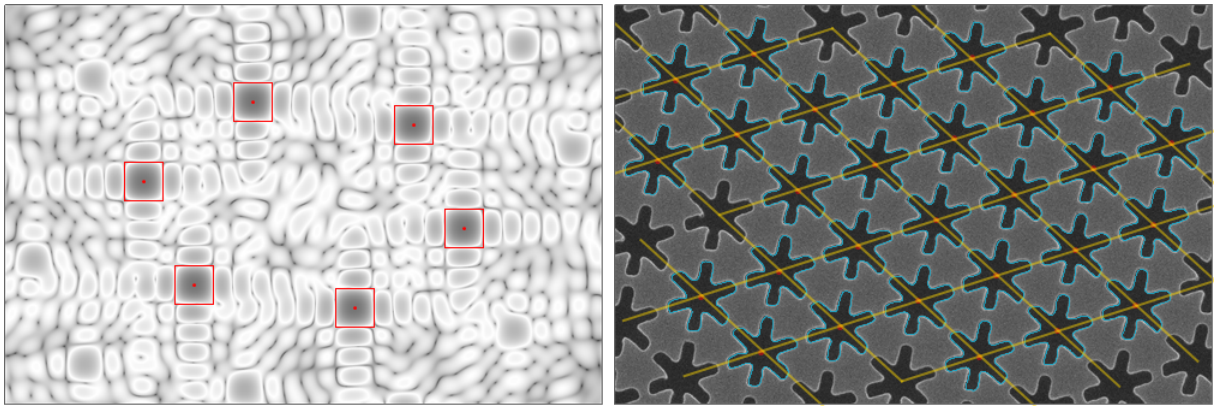

Figure Ξ.1: (Left) logarithm of the squared magnitude from a cleaned zoomed discrete Fourier transform, six major peaks are located corresponding to the snowflake crystal pattern. From their locations, lattice vectors of $\{(-173, 525), (372, 408)\}$ nm can be extracted. (Right) original image of the snowflakes, edge detection is shown in blue, shape centers used in the fit are red dots, and the fit result is depicted with yellow lines. Fitting only a global angle and scaling, the fit lattice vectors are $\{(-169, 527), (372, 409)\}$ nm.

Common fit parameters will be global angle, ϕ, and scaling, ξ,

$$A[\phi, \xi] = \xi \, R_\phi \cdot \bar{A} \ ,$$

where $\bar{A}$ are the expected lattice vectors, and R_ϕ is the rotation matrix. An example fit is shown in Fig. Ξ.1.

APPENDIX Π

Resonance fitting

Vector network analyzers (VNAs) are able to simultaneously measure the amplitude and phase of a signal transmitted through or reflected from an electrical network. With resonators in the network, one can fit the complex signal response to measure properties of the resonator.

Π.1 Scattering element

In general the scattering element for a resonator is

$$S(f) = \delta - \frac{A}{\text{~~}\alpha - \mathrm{i}\,(f - f_{\mathrm{res}})}\,, \tag{Π.1}$$

where δ and $A \in \mathbb{R}$ depend on the particular system according to Tab. Π.1 (See App. Θ). We will call the cases of $\delta = 0$ 'through' measurements, and $\delta = 1$ 'across' measurements. In through measurements the resonance appears as a peak above the ambient background, whilst for across measurements the resonance appears as dip in the transmitted signal.

	δ	A
interposed reflection, S_{11}	1	$2\,\text{~~}\alpha_1$
interposed transmission, S_{21}	0	$2\sqrt{\text{~~}\alpha_1\,\text{~~}\alpha_2}$
hanger reflection, S_{11}	0	$\text{~~}\alpha_{12}$
hanger transmission, S_{21}	1	$\text{~~}\alpha_{12}$
directional, S_{21}	1	$2\,\text{~~}\alpha_{12}$

Table Π.1: Parameters in (Π.1) depending on type of layout and measurement.

Π.2 Background terms

In general, one needs to determine the transmission function for their specific electrical network, here, we will consider the simplest cases. For an across measurement

$$t_{\mathrm{ac}}(f) = \mathfrak{X}(f)\left(1 - \frac{A}{\mathfrak{a} - \mathrm{i}\,(f - f_{\mathrm{res}})}\right) ,$$

where $\mathfrak{X}(f) \in \mathbb{C}$ is a transmission factor background.

For a through measurement

$$t_{\mathrm{th}}(f) = \mathfrak{X}(f)\left(C - \frac{A}{\mathfrak{a} - \mathrm{i}\,(f - f_{\mathrm{res}})}\right) ,$$

where $C \in \mathbb{C}$ is an ambient background. In this case there is redundancy between the parameters A, C, $\mathfrak{X}$, and they can not be fit independently. Given that $A \in \mathbb{R}$ we can make the redefinitions

$$t_{\mathrm{th}}(f) = \mathfrak{A}(f)\left(\mathfrak{c} - \frac{1}{\mathfrak{a} - \mathrm{i}\,(f - f_{\mathrm{res}})}\right) , \qquad \begin{aligned} \mathfrak{A} &= \mathfrak{X}\,A \\ \mathfrak{c} &= C/A \end{aligned} .$$

To capture a mild transmission landscape background we can expand $\mathfrak{X}$ (or $\mathfrak{A}$) to be a polynomial in the vicinity of our resonance,

$$\mathfrak{X}(f) = \sum_{i=0}^{n} \mathfrak{X}_i\,(f - f_{\mathrm{res}})^i .$$

Π.3 Fit functions

With data of the form ($f \in \mathbb{R}, t \in \mathbb{C}$) we need to split our transmission functions into real and imaginary parts. For the across measurement,

$$\begin{aligned}\Re[t_{\mathrm{ac}}(f)] = &\left(\sum_{i=0}^{n} \Re[\mathfrak{X}_i]\,(f-f_{\mathrm{res}})^i\right)\left(1-\frac{A\,\mathfrak{a}}{\mathfrak{a}^2+(f-f_{\mathrm{res}})^2}\right)\\ &-\left(\sum_{i=0}^{n} \Im[\mathfrak{X}_i]\,(f-f_{\mathrm{res}})^i\right)\frac{A\,(f-f_{\mathrm{res}})}{\mathfrak{a}^2+(f-f_{\mathrm{res}})^2}\ ,\end{aligned}$$

$$\begin{aligned}\Im[t_{\mathrm{ac}}(f)] = &\left(\sum_{i=0}^{n} \Im[\mathfrak{X}_i]\,(f-f_{\mathrm{res}})^i\right)\left(1-\frac{A\,\mathfrak{a}}{\mathfrak{a}^2+(f-f_{\mathrm{res}})^2}\right)\\ &+\left(\sum_{i=0}^{n} \Re[\mathfrak{X}_i]\,(f-f_{\mathrm{res}})^i\right)\frac{A\,(f-f_{\mathrm{res}})}{\mathfrak{a}^2+(f-f_{\mathrm{res}})^2}\ ,\end{aligned}$$

with fit parameters

$$\left\{f_{\mathrm{res}}, \mathfrak{a}, A\right\} \cup \left\{\Re[\mathfrak{X}_i], \Im[\mathfrak{X}_i]\right\}_{i=0}^{n}\ .$$

For the through measurement,

$$\begin{aligned}\Re[t_{\mathrm{th}}(f)] = &\left(\sum_{i=0}^{n} \Re[\mathfrak{A}_i]\,(f-f_{\mathrm{res}})^i\right)\left(\Re[\mathfrak{c}]-\frac{\mathfrak{a}}{\mathfrak{a}^2+(f-f_{\mathrm{res}})^2}\right)\\ &-\left(\sum_{i=0}^{n} \Im[\mathfrak{A}_i]\,(f-f_{\mathrm{res}})^i\right)\left(\Im[\mathfrak{c}]+\frac{(f-f_{\mathrm{res}})}{\mathfrak{a}^2+(f-f_{\mathrm{res}})^2}\right)\ ,\end{aligned}$$

$$\begin{aligned}\Im[t_{\mathrm{th}}(f)] = &\left(\sum_{i=0}^{n} \Im[\mathfrak{A}_i]\,(f-f_{\mathrm{res}})^i\right)\left(\Re[\mathfrak{c}]-\frac{\mathfrak{a}}{\mathfrak{a}^2+(f-f_{\mathrm{res}})^2}\right)\\ &+\left(\sum_{i=0}^{n} \Re[\mathfrak{A}_i]\,(f-f_{\mathrm{res}})^i\right)\left(\Im[\mathfrak{c}]+\frac{(f-f_{\mathrm{res}})}{\mathfrak{a}^2+(f-f_{\mathrm{res}})^2}\right)\ ,\end{aligned}$$

with fit parameters

$$\left\{f_{\mathrm{res}}, \text{ϝ}, \Re[\text{ϛ}], \Im[\text{ϛ}]\right\} \cup \left\{\Re[\mathfrak{A}_i], \Im[\mathfrak{A}_i]\right\}_{i=0}^{n} .$$

Π.4 Parameter estimates

To perform complicated non-linear fits, we need good parameter estimates.

Π.4.1 Magnitude

We can start by looking at the squared magnitude data $\left\{\left(f_k, |t_k|^2\right)\right\}_{k=1}^{d}$, where d is the number of data points.

We have

$$|t_{\mathrm{ac}}(f)|^2 = |\mathfrak{X}(f)|^2 \left(1 + \frac{A^2 - 2\,A\,\text{ϝ}}{\text{ϝ}^2 + (f - f_{\mathrm{res}})^2}\right) ,$$

$$\begin{aligned} |t_{\mathrm{th}}(f)|^2 &= |\mathfrak{X}(f)|^2 \left(|C|^2 + \frac{A^2 - 2\,A\,\text{ϝ}\,\Re[C] - 2\,A\,(f - f_{\mathrm{res}})\,\Im[C]}{\text{ϝ}^2 + (f - f_{\mathrm{res}})^2}\right) \\ &\overset{C \ll 1}{\approx} |\mathfrak{X}(f)|^2 \left(|C|^2 + \frac{A^2}{\text{ϝ}^2 + (f - f_{\mathrm{res}})^2}\right) , \end{aligned}$$

thus in general

$$|t(f)|^2 = \mathcal{C}(f) + \frac{\mathcal{A}}{\text{ϝ}^2 + (f - f_{\mathrm{res}})^2} ,$$

with

$$\mathcal{C}_{\rm ac} = |\mathfrak{X}|^2 \,, \qquad\qquad \mathcal{A}_{\rm ac} = |\mathfrak{X}|^2 \,\Big(A^2 - 2\,A\,\cancel{\alpha}\Big) < 0 \,,$$
$$\mathcal{C}_{\rm th} = |\mathfrak{X}|^2\,|C|^2 \,, \qquad\qquad \mathcal{A}_{\rm th} = |\mathfrak{X}|^2\,A^2 > 0 \,.$$

For a small data window around the resonance, and for the purpose of making estimates, we can assume $\mathcal{C}$ is linear,

$$\mathcal{C}(f) = \mathcal{C}_0 + \mathcal{C}_1\,(f - f_{\rm res}) \,.$$

We can start by estimating $\mathcal{C}_1$ using the edge data points,

$$\tilde{\mathcal{C}_1} = \frac{|t_d|^2 - |t_1|^2}{f_d - f_1} \,.$$

The resonance location can be estimated from the peak location

$$(\tilde{f}_{\rm res}, \tilde{t}_{\rm res}) \quad \text{by} \quad \max\left\{ \pm\Big(|t_k|^2 - \big(|t_1|^2 + \tilde{\mathcal{C}_1}\,(f_k - f_1)\big)\Big) \right\}_{k=1}^{d} \quad \begin{cases} + \;:\; \text{through} \\ \\ - \;:\; \text{across} \end{cases} \,.$$

Then

$$\tilde{\mathcal{C}_0} = |t_1|^2 + \tilde{\mathcal{C}_1}\,(\tilde{f}_{\rm res} - f_1) \,.$$

Next we can estimate $\cancel{\alpha}$ by the peak full-width-half-maximum. Explicitly, we want to find

the points

$$\left(\tilde{f}_{-\tilde{\alpha}}, \tilde{t}_{-\tilde{\alpha}}\right) \quad \text{by} \quad \min\left\{ |t_k|^2 - \left(\frac{\tilde{\mathcal{C}}_0 + |\tilde{t}_{\text{res}}|^2}{2} + \tilde{\mathcal{C}}_1 \left(f_k - \tilde{f}_{\text{res}} \right) \right) \ : \ f_k < \tilde{f}_{\text{res}} \right\}_{k=1}^{d} ,$$

$$\left(\tilde{f}_{+\tilde{\alpha}}, \tilde{t}_{+\tilde{\alpha}}\right) \quad \text{by} \quad \min\left\{ |t_k|^2 - \left(\frac{\tilde{\mathcal{C}}_0 + |\tilde{t}_{\text{res}}|^2}{2} + \tilde{\mathcal{C}}_1 \left(f_k - \tilde{f}_{\text{res}} \right) \right) \ : \ f_k > \tilde{f}_{\text{res}} \right\}_{k=1}^{d} ,$$

then

$$\tilde{\tilde{\alpha}} = \frac{\tilde{f}_{+\tilde{\alpha}} - \tilde{f}_{-\tilde{\alpha}}}{2} .$$

Π.4.2 Complex

Now that we have $\{\tilde{f}_{\text{res}}, \tilde{t}_{\text{res}}, \tilde{\tilde{\alpha}}\}$ we can use the complex data to guess the remaining fit parameters. We will guess only up to linear background terms, thus

$$\Re[\tilde{\mathfrak{X}}_i] = \Im[\tilde{\mathfrak{X}}_i] = \Re[\tilde{\mathfrak{A}}_i] = \Im[\tilde{\mathfrak{A}}_i] = 0 \quad : \quad i \geqslant 2 .$$

For accross measurements,

$$\Re[\tilde{\mathfrak{X}}_1] = \frac{\Re[t_d] - \Re[t_1]}{f_d - f_1} , \qquad \Im[\tilde{\mathfrak{X}}_1] = \frac{\Im[t_d] - \Im[t_1]}{f_d - f_1} .$$

then

$$\Re[\tilde{\mathfrak{X}}_0] = \Re[t_1] + \Re[\tilde{\mathfrak{X}}_1] \left(\tilde{f}_{\text{res}} - f_1 \right) , \qquad \Im[\tilde{\mathfrak{X}}_0] = \Im[t_1] + \Im[\tilde{\mathfrak{X}}_1] \left(\tilde{f}_{\text{res}} - f_1 \right) .$$

Enforcing A to be real, we can estimate it as

$$\tilde{A}_{\text{ac}} = \tilde{\alpha} \left(1 - \frac{\Re[\tilde{t}_{\text{res}}]\,\Re[\tilde{\mathfrak{X}}_0] + \Im[\tilde{t}_{\text{res}}]\,\Im[\tilde{\mathfrak{X}}_0]}{\Re[\tilde{\mathfrak{X}}_0]^2 + \Im[\tilde{\mathfrak{X}}_0]^2} \right)$$

For through measurements, first we compute

$$\Re[\tilde{\mathfrak{C}}_1] = \frac{\Re[t_d] - \Re[t_1]}{f_d - f_1} \,, \qquad \Im[\tilde{\mathfrak{C}}_1] = \frac{\Im[t_d] - \Im[t_1]}{f_d - f_1} \,,$$

$$\Re[\tilde{\mathfrak{C}_0}] = \Re[t_1] + \Re[\tilde{\mathfrak{C}}_1]\,(\tilde{f}_{\text{res}} - f_1) \,, \qquad \Im[\tilde{\mathfrak{C}_0}] = \Im[t_1] + \Im[\tilde{\mathfrak{C}}_1]\,(\tilde{f}_{\text{res}} - f_1) \,.$$

Then

$$\Re[\tilde{\mathfrak{A}}_0] = \frac{\Re[\tilde{\mathfrak{C}}_0] - \Re[\tilde{t}_{\text{res}}]}{\alpha} \,, \qquad \Im[\tilde{\mathfrak{A}}_0] = \frac{\Im[\tilde{\mathfrak{C}}_0] - \Im[\tilde{t}_{\text{res}}]}{\alpha} \,,$$

$$\Re[\tilde{\mathfrak{c}}] = \frac{\Re[\tilde{\mathfrak{C}}_0]\,\Re[\tilde{\mathfrak{A}}_0] + \Im[\tilde{\mathfrak{C}}_0]\,\Im[\tilde{\mathfrak{A}}_0]}{\Re[\tilde{\mathfrak{A}}_0]^2 + \Im[\tilde{\mathfrak{A}}_0]^2} \,, \qquad \Im[\tilde{\mathfrak{c}}] = \frac{\Im[\tilde{\mathfrak{C}}_0]\,\Re[\tilde{\mathfrak{A}}_0] - \Re[\tilde{\mathfrak{C}}_0]\,\Im[\tilde{\mathfrak{A}}_0]}{\Re[\tilde{\mathfrak{A}}_0]^2 + \Im[\tilde{\mathfrak{A}}_0]^2} \,,$$

$$\Re[\tilde{\mathfrak{A}}_1] = \frac{\Re[\tilde{\mathfrak{C}}_1]\,\Re[\tilde{\mathfrak{c}}] + \Im[\tilde{\mathfrak{C}}_1]\,\Im[\tilde{\mathfrak{c}}]}{\Re[\tilde{\mathfrak{c}}]^2 + \Im[\tilde{\mathfrak{c}}]^2} \,, \qquad \Im[\tilde{\mathfrak{A}}_1] = \frac{\Im[\tilde{\mathfrak{C}}_1]\,\Re[\tilde{\mathfrak{c}}] - \Re[\tilde{\mathfrak{C}}_1]\,\Im[\tilde{\mathfrak{c}}]}{\Re[\tilde{\mathfrak{c}}]^2 + \Im[\tilde{\mathfrak{c}}]^2} \,.$$

Π.5 Simultaneous fit

Armed with fit parameter estimates we are ready to perform the fit. Our fit function ($f \in \mathbb{R}) \mapsto (t \in \mathbb{C})$ is equivalent to a multivariate fit $\mathbb{R} \to \mathbb{R}^2$. To use standard fitting packages we can flatten this to a multivariable fit $\mathbb{R} \oplus \mathbb{R} \to \mathbb{R}$ following App. Ψ.

We can do this by expanding our data set $\{(f_k, t_k)\}_{k=1}^{d}$ to

$$\Big\{\big((1,0,f_k),\Re[t_k]\big)\Big\}_{k=1}^{d} \cup \Big\{\big((0,1,f_k),\Im[t_k]\big)\Big\}_{k=1}^{d} = \Big\{\big(\underbrace{(x_{1\,\kappa}, x_{2\,\kappa}, f_\kappa)}_{\vec{x}_\kappa}, y_\kappa\big)\Big\}_{\kappa=1}^{2\,d} ,$$

and using fit function

$$\hat{y} = x_1\,\Re\big[\hat{t}(f)\big] + x_2\,\Im\big[\hat{t}(f)\big] .$$

Alternatively we minimize the multivariate objective function and compute the covariance matrix ourselves (see App. Φ).

APPENDIX Σ

Optical measurement setup

The base optical measurement setup was inherited from previous experiments [120–122, 230, 304] studying optomechanics and transduction. Various improvements were made to control elements. At its core, the setup is a C band infra-red fiber optic based system with free space coupling to a chip in transmission and a high bandwidth photodetector that can resolve microwave frequencies. A complete diagram of the system is given in Fig. Σ.1.

From the laser, the optic signal first goes through optional phase modulation, and then a variable attenuator for power control, and a polarizer. It is directed onto the chip by a V-groove clamp that holds the fiber in place above the chip at an angle of 8° from normal. A second fiber is clamped 127 μm away to pick up the transmitted signal. A splitter takes a small amount of the signal for frequency locking whilst the rest goes through an amplifier and filter before hitting the fast photodetector.

Σ.1 Components

Σ.1.1 Laser

The laser is a New Focus TLB 6728 tunable laser diode with an operating range of 1520 nm to 1570 nm and power output up to 20 mW. Wavelength tuning is accomplished by an internal diffraction grating with a motor for coarse tuning and a piezoelectric transducer for fine tuning. The piezoelectric transducer has 0.3 nm of range and takes input $[-3, 3]$ V, such that the response is 0.05 nm/V. Diode lasers are prone to phase noise [230, 308] and are more stable when operating at constant current.

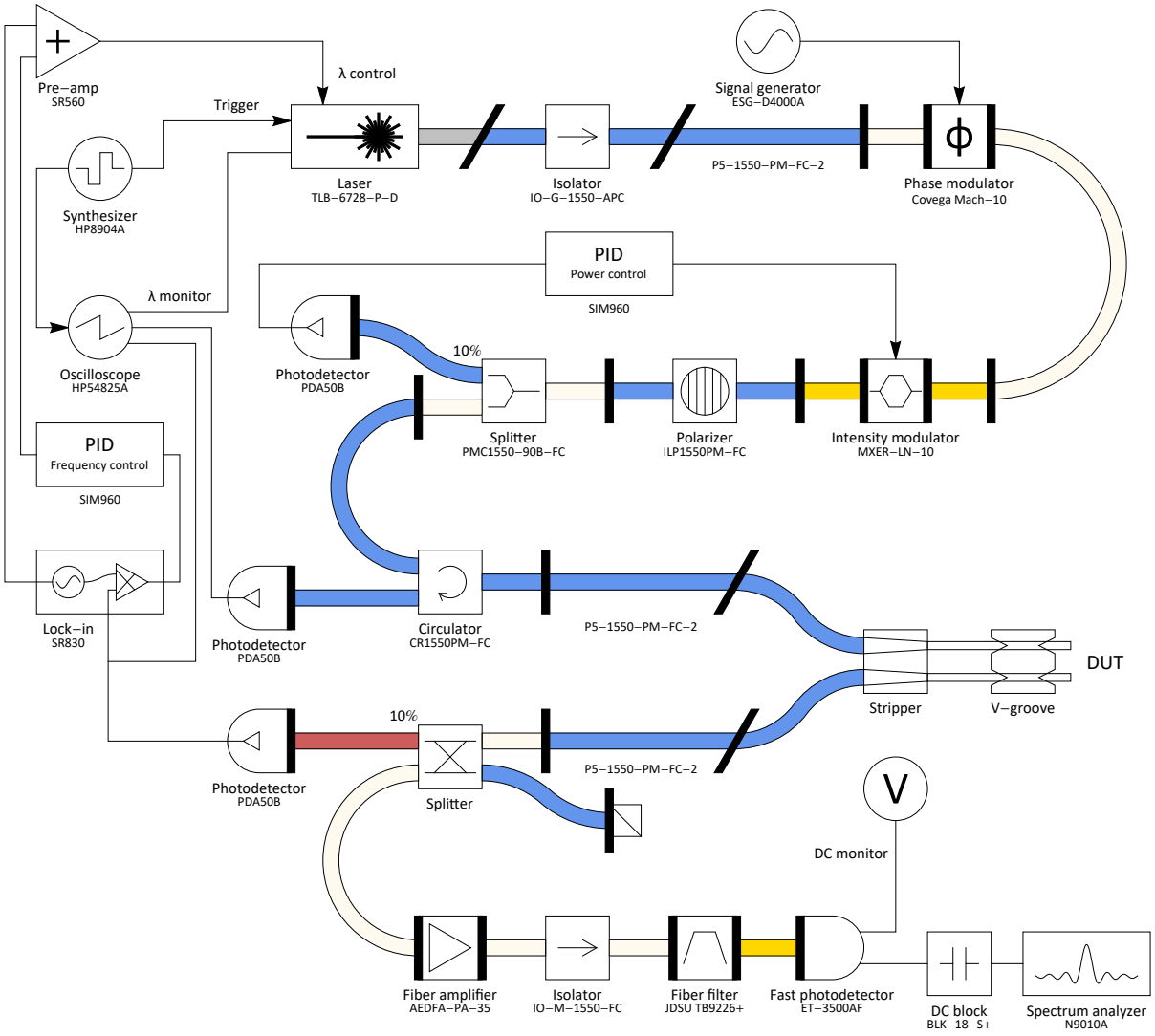

Figure Σ.1: Full diagram of the optical measurement setup. Thick vertical lines indicate flat physical contact (PC) connections, whilst thick angled lines indicate angled physical connections (APC). Fiber optic colours mimic their real-life colour, lengths are not to scale.

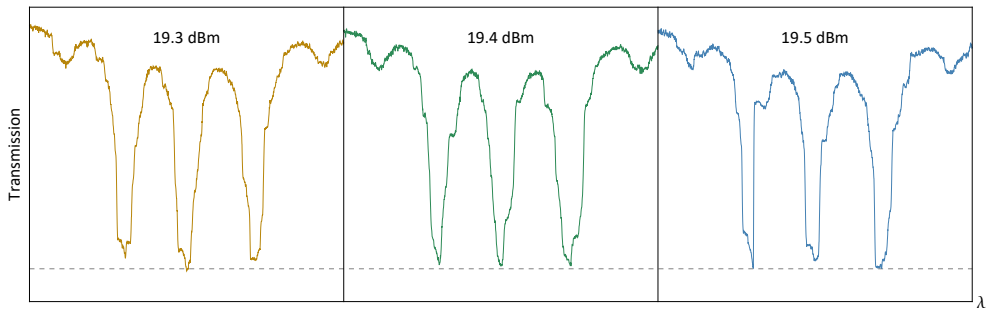

Figure Σ.2: Calibration of the phase modulator using a sharp ring resonator.

The laser offers a wavelength monitor voltage,

$$V_{\substack{\text{wavelength}\\\text{monitor}}} = 10\,\frac{\lambda - 1520\,\text{nm}}{1570\,\text{nm} - 1520\,\text{nm}}\,,$$

however the absolute accuracy is unclear.

Interfacing with the laser requires special drivers; instructions and a wrapper for using python is available at `https://gitlab.com/rhyspovey/python-tlb6700-laser`.

Σ.1.2 Phase modulator

A Covega Mach-10 phase modulator is used to create a sideband near the mechanical frequency for calibrating power transmission. It can handle drives up to 10 GHz and 5 V, although significantly lower drive powers should be used for 'weak' modulation.

Calibrating the phase modulator for a particular frequency can be performed by scanning over a narrow optical resonance ($\gamma < \omega_\Phi$). For a sufficiently large phase modulation drive, the resonance feature will appear three times, probed by the main carrier frequency and two closest sidebands. When the phase modulation drive is adjusted such that the three features have identical transmission, the response A_Φ can be determined. The average laser power

and photodetector current (see App. L) is

$$\langle P_D(t)\rangle_t = P_{\rm L} \sum_{j=-\infty}^{\infty} J_j[A_\Phi]^2 \, |S_{2\,1}(\omega_{\rm L} + j\,\omega_\Phi)|^2 \ ,$$

giving the background-removed response to the three spectral features

$$\begin{aligned} I_{\rm PD}(\omega_{\rm o}) &\propto J_0[A_\Phi]^2 \, |S_{2\,1}(\omega_{\rm o})|^2 \ , \\ I_{\rm PD}(\omega_{\rm o} - \omega_\Phi) &\propto J_1[A_\Phi]^2 \, |S_{2\,1}(\omega_{\rm o})|^2 \ , \\ I_{\rm PD}(\omega_{\rm o} + \omega_\Phi) &\propto J_{-1}[A_\Phi]^2 \, |S_{2\,1}(\omega_{\rm o})|^2 \ , \end{aligned}$$

with $J_{-1}[A_\Phi]^2 = J_1[A_\Phi]^2$. Thus

$$I_{\rm PD}(\omega_{\rm o}) = I_{\rm PD}(\omega_{\rm o} - \omega_\Phi) = I_{\rm PD}(\omega_{\rm o} + \omega_\Phi) \Rightarrow J_0[A_\Phi]^2 = J_1[A_\Phi]^2 \ .$$

The above equation has a countably infinite set of solutions but the smallest (positive) solution is $A_\Phi = 1.43469565$. If the phase modulation strength is linear with drive voltage then we can extrapolate to weak modulation.

In Fig. Σ.2 a ring resonator with narrow resonances is used for calibration. The even point occurs at $P_\Phi = (19.4 \pm 0.1)\,{\rm dBm} \Rightarrow V_{\Phi\,{\rm RMS}} = (2.087 \pm 0.024)\,{\rm V}$ giving $A_\Phi = (0.688 \pm 0.008)\,V_{\Phi\,{\rm RMS}}/{\rm V}$.

Σ.1.3 Intensity modulator

An iXblue MXER-LN-10 intensity modulator is used for power control. It can handle drives up to 10 GHz but it is used here in DC. The main operating range (with positive slope) is $[-5.5, 1]\,{\rm V}$. Fig. Σ.3 depicts the effective response to varying drive powers. The slope of

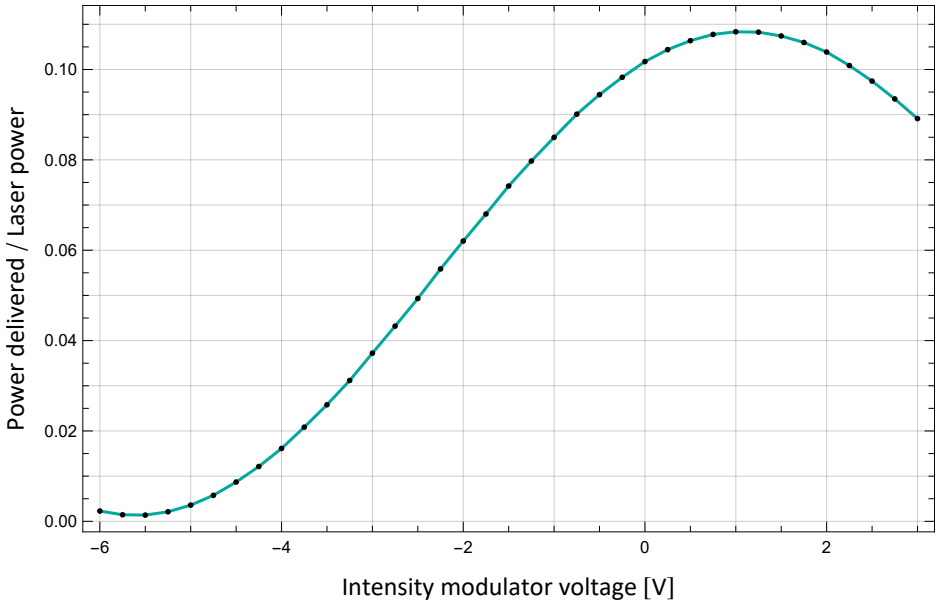

Figure Σ.3: Ratio of estimated power delivered to the device over laser power as a function of intensity modulator DC voltage bias. This includes constant losses from other optic elements.

the linear section (in terms of photodetector voltage) is used to set the proportional control parameter of the power feedback loop.

Σ.1.4 Photodetectors

Slow

Three Thor Labs PDA50B photodetectors are used at split-offs before and after the device under test. At 1550 nm they have a responsivity of $\approx 0.85\,\mathrm{A/W}$ and offer up to 70 dB of gain. When connected to a voltmeter, the measured voltage is

$$V_{\mathrm{PD}} = \underbrace{\left(0.85 \pm 0.03\right)\,\mathrm{A/W}}_{\text{responsivity}}\ \underbrace{1503 \times 10^{G/20}\,\mathrm{V/A}}_{\text{transimepdance gain}}\ \underbrace{\frac{R_{\mathrm{load}}}{R_{\mathrm{load}} + 50\,\Omega}}_{\text{scale factor}}\ P\ , \tag{Σ.1}$$

with $G \in \{0, 10, 20, 30, 40, 50, 60, 70\}\,\mathrm{dB}$. The photodetectors saturate at 10 V out.

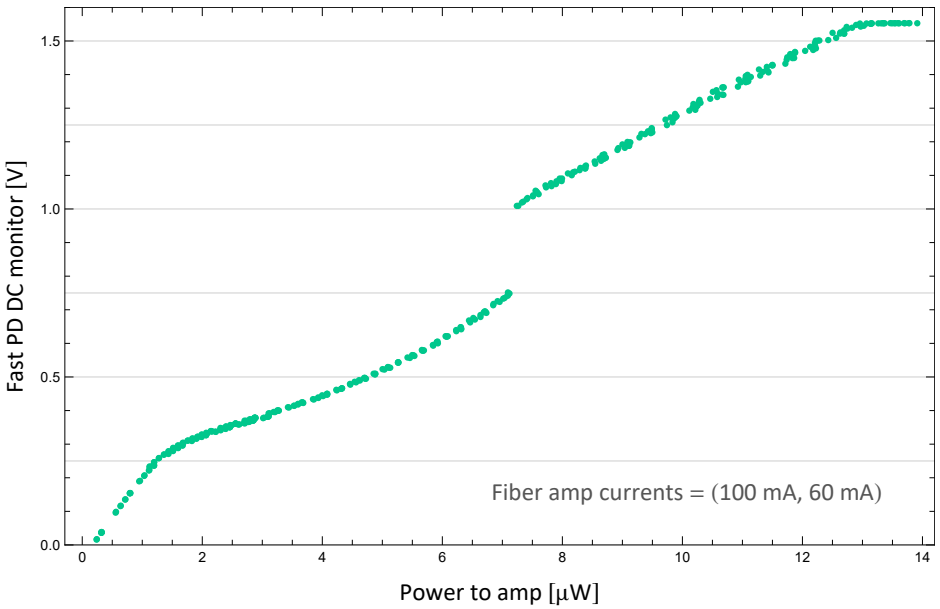

Figure Σ.4: Fast photodetector DC monitor readings for various input powers. Significant non-linearities make the photodetector unreliable as an absolute measure of power.

Fast

For optomechanical measurements, an EOT ET-3500AF amplified high speed photodetector is used, which can detect power fluctuations up to 10 GHz. In addition to its microwave frequency output, it has a DC monitor output

$$V_{\substack{\mathrm{DC}\\ \mathrm{monitor}}} = \bar{I}_{\mathrm{PD}}\,\mathrm{mV/\mu A}\ ,$$

however this is not very accurate. The maximum input is 10 mW, and the detector saturates with the DC monitor at $\sim 1.54\,\mathrm{V}$. Responsivity of the detector is unfortunately non-linear, plotted in Fig. Σ.4.

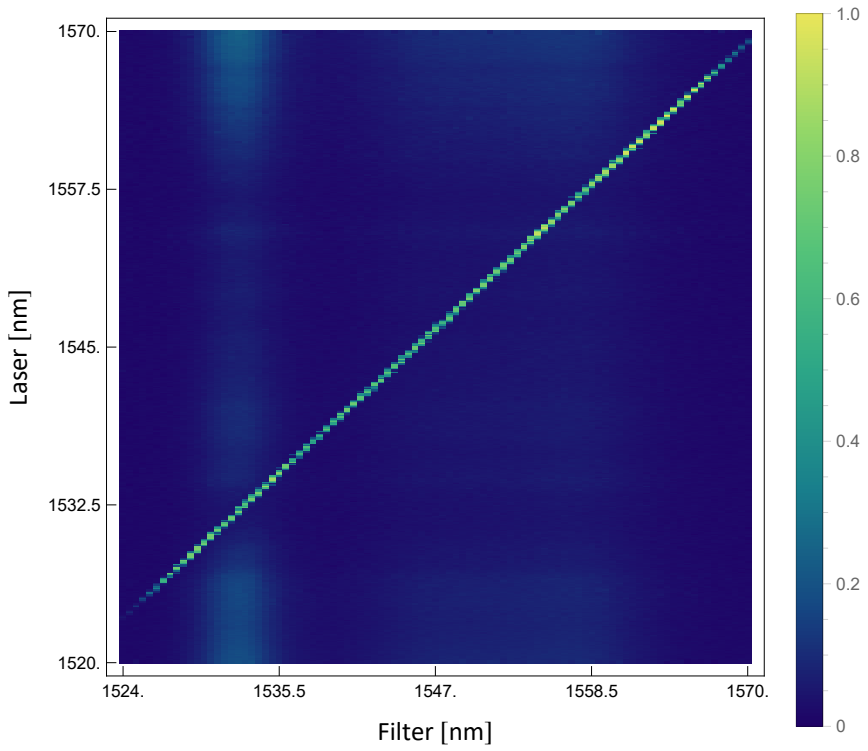

Figure Σ.5: Normalized transmission through the optical filter based on reported wavelengths.

Σ.1.5 Amplifier

Weak optical signals needs to be amplified before hitting the fast photodetector, for this an Amonics erbium doped fiber amplifier, AEDFA-PA-25, is used. The amplifier has two laser pumps and can provide up to 40 dB of gain for inputs of $[-40, -10]$ dBm. Care needs to be taken when setting the pumps as the fast photodetector can easily be saturated and potentially damaged. The optic amplifier produces amplified spontaneous emission (ASE) across its amplification range of $[1530, 1560]$ nm. Pump currents are typically set such that the fast photodetector is operating at $\sim 90\%$ of its range.

Σ.1.6 Filter

To reduce the ASE hitting the fast photodetector at non-signal frequencies, a band pass optical filter is needed. A JDS Uniphase tunable grating filter TB9226 is used which offers a $-3\,\mathrm{dB}$ pass band of $0.22\,\mathrm{nm} \sim 30\,\mathrm{GHz}$, and tuning in $[1530, 1565]\,\mathrm{nm}$. The filter utilizes a (non-uniform) fiber Bragg grating reflector [309, 310] which unfortunately does not have a closed-form expression for its transmission spectrum. Calibration between the purported filter wavelength and laser wavelength is shown in Fig. Σ.5, the offset was found to be $\lambda_{\mathrm{filter}} - \lambda_{\mathrm{laser}} = 0.61\,\mathrm{nm}$. Using the offset as a starting point, alignment of the optical filter is performed by maximizing the signal picked up by the fast photodetector.

Σ.1.7 Optic fibers

The fibers are all single mode C-band infra-red ($\sim 1550\,\mathrm{nm}$). For those which are polarization maintaining (which includes everything from the polarizer to the V-groove), the electric field is parallel to the slow axis, and the stripped fibers in the V-groove are aligned such that the slow axis is parallel to the plane of the V-groove. This ensures the light's electric field incident on the device chip (coming in on an angle) is parallel to the chip and aligned with the grating coupler.

Σ.1.8 V-groove and device mount

An OZ Optics V-groove clamp holds two parallel stripped fibers $127\,\mu\mathrm{m}$ apart, 8° from normal, and is positioned just above the sample as close as possible. The incident angle of 8° was chosen by previous experiments to optimize the efficiency of silicon on insulator grating couplers.

The device mount is a piece of acrylic with a hole drilled through to create a vacuum chuck, and attached to a two axis micrometer translation stage. Multiple devices patterned on a chip are oriented the same way such that they can easily be accessed by stage movements. Global rotational alignment has to be performed manually.

To assist with aligning, a microscope and lamp is suspended above the stage. From being lined up with the bottom edge of the V-groove clamp under the microscope, the device needs to be moved back $\approx 1050\,\mu\text{m}$ to be under the fibers.

$\Sigma.2$ Laser scans

The TLB 6700 laser is able to smoothly sweep its wavelength to produce optical transmission spectra picked up by the output split-off photodetector. A Hewlett Packard Infinium oscilloscope (HP54825A) captures the photodetector voltage and laser wavelength monitor voltage with a single scan matched to last the same duration as the laser's combined forward and backward sweep. To start both systems simultaneously, a Hewlett Packard multifunction synthesizer (HP8904A) is setup to send a square trigger pulse of 4 V to the laser and oscilloscope. Configuring the laser, oscilloscope, and trigger generator is all carried out from a connected computer.

Whilst the laser provides a wavelength estimate via a monitor voltage, the signal is rather noisy. To remove this noise the wavelength monitor is fit as a function of time to provide the smooth wavelength ramp and sweep and action. This is then used to pair photodetector voltage measurements with the appropriate wavelength based on the scan time. The laser scan function follows a quadratic ramp-up (duration τ_2), linear sweep (duration τ_1), then quadratic ramp-down (duration τ_2). From V_1 to V_2 (corresponding to start and end

wavelengths), the one-directional scan function is

$$V_{\substack{\text{wavelength}\\\text{monitor}}}(t) = \begin{cases} V_1 & : \; t < \tau_0 \\ V_1 + \frac{(t-\tau_0)^2\,(V_2-V_1)}{2\,\tau_2\,(\tau_1+\tau_2)} & : \; \tau_0 < t < \tau_0+\tau_2 \\ \frac{2\,\tau_1\,V_1+2\,(t-\tau_0)\,(V_2-V_1)+\tau_2\,(3\,V_1-V_2)}{2\,(\tau_1+\tau_2)} & : \; \tau_0+\tau_2 < t < \tau_0+\tau_2+\tau_1 \\ V_2 - \frac{(t-\tau_0-\tau_1-2\,\tau_2)^2\,(V_2-V_1)}{2\,\tau_2\,(\tau_1+\tau_2)} & : \; \tau_0+\tau_2+\tau_1 < t < \tau_0+2\,\tau_2+\tau_1 \\ V_2 & : \; \tau_0+2\,\tau_2+\tau_1 < t \end{cases} .$$

When fitting, V_1 and V_2 are given, and τ_0, τ_1, τ_2 are fit parameters.

The maximum laser sweep speed is 10 nm/s, however for reliable sweep timings should be kept to less than $L_{\text{sweep}}/(10\,\text{s})$. Due to ramps in the sweep speed, the sweep duration is not simply $2\,L_{\text{sweep}}/(\text{set speed})$. Found empirically, for a desired total (forward and backward) sweep duration τ_{total}, over sweep length L_{sweep} and back again, the set sweep speed should be

$$\text{set speed} = \frac{2\,L_{\text{sweep}}}{\tau_{\text{total}} - x + \sqrt{(\tau_{\text{total}}-x)\,(\tau_{\text{total}}+3\,x)}} \quad : \quad x = 6\,\text{s} + \frac{L_{\text{sweep}}}{5\,\text{nm/s}} .$$

Σ.3 Power estimates

Using the split-off input and output photodetectors along with (Σ.1) we can estimate optical powers in our set up. Voltage measurements need to be calibrated (offset) such that $V_{\text{PD}} = 0 \Leftrightarrow P_{\text{PD}} = 0$.

The power delivered to the device is

$$\begin{aligned} P_{\text{delivered}} &= (1-10\%)\, P_{\substack{\text{input}\\\text{PD}}}/10\% \\ &= \frac{0.9}{0.1}\, \frac{V_{\substack{\text{input}\\\text{PD}}}}{\left(0.85 \pm 0.03\right) \text{A/W}\ 1503 \times 10^{G/20}\,\text{V/A}\ \frac{1\,\text{M}\Omega}{1\,\text{M}\Omega + 50\,\Omega}} \,. \end{aligned}$$

Σ.3.1 Transmission

Comparing input and output powers, we can get the transmission through our device. For 10% splittings as labelled in Fig. Σ.1, we have

$$\eta_{\substack{\text{grating}\\\text{coupler}}}^{\ 2}\, T_{\text{DUT}} = \frac{P_{\text{out}}}{P_{\text{delivered}}} = \frac{P_{\substack{\text{output}\\\text{PD}}}/10\%}{P_{\substack{\text{input}\\\text{PD}}}\,(1-10\%)/10\%} = \frac{10^{(G_{\text{in}}-G_{\text{out}})/20}}{0.9}\, \frac{V_{\substack{\text{output}\\\text{PD}}}}{V_{\substack{\text{input}\\\text{PD}}}} \,.$$

Σ.3.2 Reflection

Assuming the circulator is 100% efficient,

$$\eta_{\substack{\text{grating}\\\text{coupler}}}^{\ 2}\, R_{\text{DUT}} = \frac{P_{\text{refl}}}{P_{\text{delivered}}} = \frac{P_{\substack{\text{refl}\\\text{PD}}}/100\%}{P_{\substack{\text{input}\\\text{PD}}}\,(1-10\%)/10\%} = \frac{10^{(G_{\text{in}}-G_{\text{refl}})/20}}{9}\, \frac{V_{\substack{\text{refl}\\\text{PD}}}}{V_{\substack{\text{input}\\\text{PD}}}} \,.$$

Σ.4 Frequency locking

Because the device is interrogated in open air, experiments are susceptible to temperature fluctuations causing drifts in resonant frequencies and overall transmission levels. To account for this we'd like our laser wavelength to be able to track the device resonance. For thermal mechanical spectrum measurements this means tracking the side of a resonance dip.

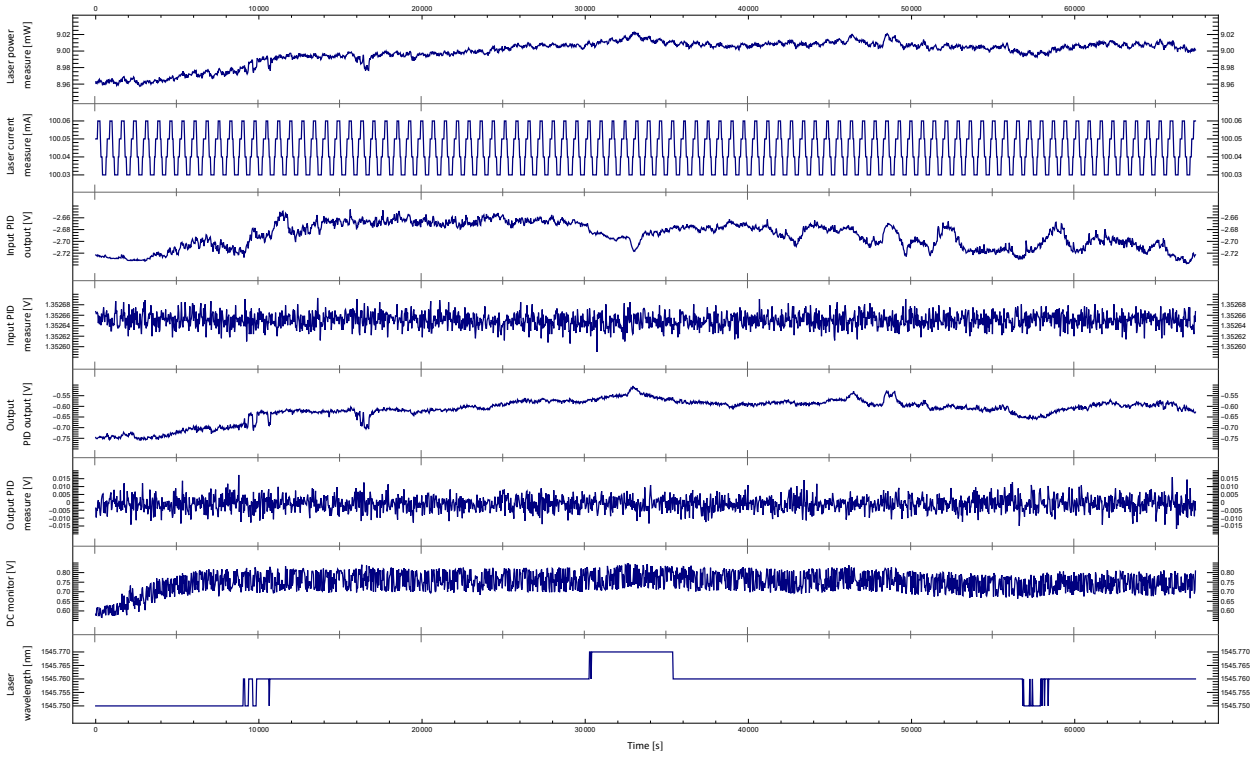

Figure Σ.6: Sample power and wavelength control monitoring data. Input side (power lock) PID output varies to compensate for laser power drift such that power to the device, PID measure, is held constant. Output side (wavelength lock) PID output varies to keep the dither signal, PID measure, zero. The laser's self measurement of wavelength is discretized to 0.01 nm. In this example a small drift in cavity resonance occurred over the first hour and was tracked by the locking system. As the optical filter is not dynamically adjusted this lead to a slight change in overall transmission as measured by the DC monitor.

The simplest way to do this is side-locking where a power control loop tries to keep a fixed transmission power corresponding to a point on the side of the resonance, and the gradient in the vicinity determines the proportional feedback parameter. This approach fails, however, if there is any change in the non-device transmission, such as a global fluctuation up or down. To track the side of the resonance through frequency and transmission drifts we employ second harmonic dither locking, described in App. Υ, to follow an inflection point (second derivative zero) of the transmission spectrum. Whilst fine tuning the laser's wavelength with the piezoelectric controller, it's own course tuning grating servo is disabled. An example of the locking systems in action is given in Fig. Σ.6.

APPENDIX ϒ

Dither locking

Dither locking is a laser frequency resonator tracking technique, similar to Pound-Drever-Hall stabilization [311–313] but simpler, slower, and working in transmission. By targeting a point on the optical resonance curve with zero derivative, dither locking is able to accommodate frequency and power shifts. The basic principle involves 'slowly' scanning the laser frequency back and forth, i.e. dithering, and using the signal in transmission, picked up by a photodetector, at this frequency to correct the laser output. Traditionally, dither locking is used to track the peak of an optical resonance where the first derivative is zero, but can be extended to inflection point tracking. Fig. ϒ.2 gives the basic experimental setup employed for a dither lock.

ϒ.1 Frequency dithering

For demonstration purposes, let's first consider the case of frequency dithering a resonance with flat background. In general the transmitted power can be expressed as (see App. Θ, Π)

$$T(\omega) = \mathcal{C} + \frac{\mathcal{A}}{\alpha^2 + (\omega - \omega_{\rm res})^2} \ .$$

It has derivatives

$$\frac{\rm d}{{\rm d}\omega} T(\omega) = \frac{-2\,\mathcal{A}}{\left(\alpha^2 + (\omega - \omega_{\rm res})^2\right)^2} \left(\omega - \omega_{\rm res}\right) ,$$

$$\frac{{\rm d}^2}{{\rm d}\omega^2} T(\omega) = \frac{6\,\mathcal{A}}{\left(\alpha^2 + (\omega - \omega_{\rm res})^2\right)^3} \left(\omega - \omega_{\rm res} - \frac{\alpha}{\sqrt{3}}\right) \left(\omega - \omega_{\rm res} + \frac{\alpha}{\sqrt{3}}\right) ,$$

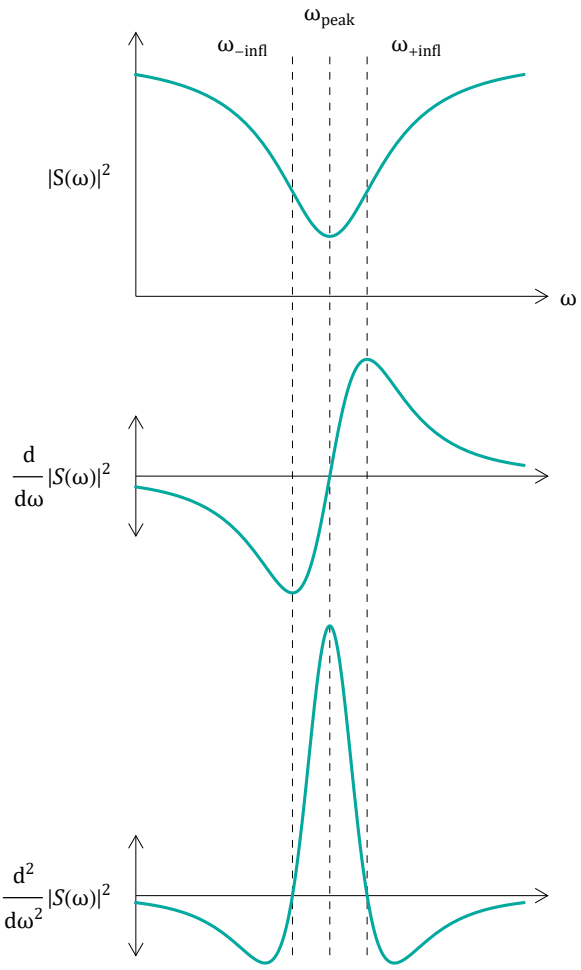

Figure ϒ.1: Plot of an 'across' resonator measurement and its derivatives. The first harmonic of the dither frequency probes the first derivative, whilst the second harmonic probes the second derivative.

as depicted in Fig. ϒ.1. The peak is located at

$$0 = \left(\frac{\mathrm{d}}{\mathrm{d}\omega}T(\omega)\right)_{\omega=\omega_{\mathrm{peak}}} \quad \Rightarrow \quad \omega_{\mathrm{peak}} = \omega_{\mathrm{res}} \ ,$$

and the inflection points are located at

$$0 = \left(\frac{\mathrm{d}^2}{\mathrm{d}\omega^{\,2}}T(\omega)\right)_{\omega=\omega_{\mathrm{infl}}} \quad \Rightarrow \quad \omega_{\mathrm{infl}} = \omega_{\mathrm{res}} \pm \frac{\alpha}{\sqrt{3}} \ .$$

In the presence of weak dithering,

$$\omega_{\rm laser}(t) = \omega_0 + \underset{\rm amp}{\omega_{\rm dither}}\, \sin[\omega_{\rm dither}\, t]\ ,$$

and

$$T(\omega_{\rm laser}; t) = T\Big(\omega_0 + \underset{\rm amp}{\omega_{\rm dither}}\, \sin[\omega_{\rm dither}\, t]\Big)$$

$$\overset{\omega_{\rm dither}\approx 0}{=} T(\omega_0) + \underset{\rm amp}{\omega_{\rm dither}}\, \sin[\omega_{\rm dither}\, t] \left(\frac{\rm d}{{\rm d}\omega} T(\omega)\right)_{\omega=\omega_0} + \frac{\left(\underset{\rm amp}{\omega_{\rm dither}}\, \sin[\omega_{\rm dither}\, t]\right)^2}{2} \left(\frac{{\rm d}^2}{{\rm d}\omega^{\,2}} T(\omega)\right)_{\omega=\omega_0} + \mathcal{O}[\omega_{\rm dither}]^3$$

$$= \mathcal{C} + \frac{\mathcal{A}}{\alpha^2 + (\omega_0 - \omega_{\rm res})^2} + \frac{-2\,\mathcal{A}}{\left(\alpha^2 + (\omega_0 - \omega_{\rm res})^2\right)^2}\, \underset{\rm amp}{\omega_{\rm dither}}\, (\omega_0 - \omega_{\rm peak})\, \sin[\omega_{\rm dither}\, t] + \frac{3\,\mathcal{A}}{\left(\alpha^2 + (\omega_0 - \omega_{\rm res})^2\right)^3}\, \underset{\rm amp}{\omega_{\rm dither}}^{\,2}\, (\omega_0 - \omega_{-\rm infl})\, (\omega_0 - \omega_{+\rm infl})\, \sin[\omega_{\rm dither}\, t]^2 + \mathcal{O}[\omega_{\rm dither}]^3\ .$$

If we want to lock ω_0 to $\omega_{\rm peak}$, we can use the signal oscillating at $\omega_{\rm dither}$ and feedback control it to zero. For $\omega_0 \approx \omega_{\rm peak}$ this signal is

$$\mathcal{F}\big[T\big]\big[\omega_{\rm dither}\big] \sim \frac{-2\,\mathcal{A}}{\alpha^4}\, \underset{\rm amp}{\omega_{\rm dither}}\, (\omega_0 - \omega_{\rm peak}) + \mathcal{O}[\omega_0 - \omega_{\rm peak}]^2 \to 0 \quad \Leftrightarrow \quad \omega_0 \to \omega_{\rm peak}\ .$$

If we want to lock ω_0 to $\omega_{\pm\rm infl}$, we note that $\sin[\theta]^2 = 1/2 - \cos[2\,\theta]/2$, and control the signal

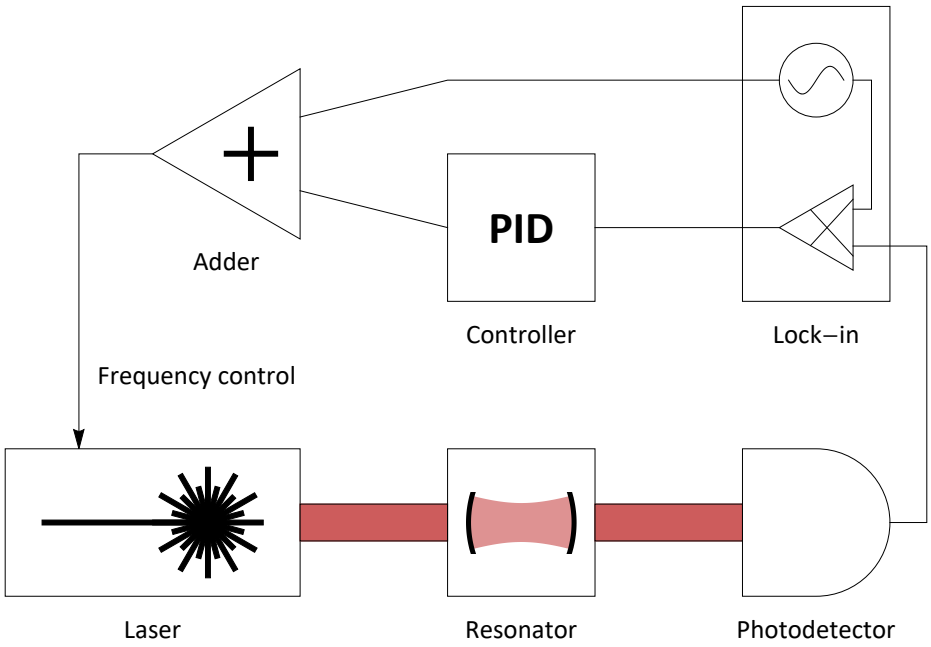

Figure ϒ.2: Diagram for a dither lock. The frequency of the laser is controlled by an incoming voltage that includes a 'static' shift provided by the controller and an oscillating term provided by the lock-in local drive. The detected signal at the lock-in frequency is passed to the controller which then decides what output voltage is required to appropriately shift the laser's center frequency.

oscillating at $2\,\omega_{\mathrm{dither}}$ to zero. For $\omega_0 \approx \omega_{\mathrm{infl}}$ this signal is

$$\mathcal{F}[T][2\,\omega_{\mathrm{dither}}] \sim \frac{27\sqrt{3}\,\mathcal{A}}{64\,\alpha^5}\,\underset{\mathrm{amp}}{\omega_{\mathrm{dither}}}^{2}\,(\omega_0 - \omega_{\mathrm{infl}}) + \mathcal{O}[\omega_0 - \omega_{\mathrm{infl}}]^2 \to 0 \quad \Leftrightarrow \quad \omega_0 \to \omega_{\mathrm{infl}}\,.$$

Sending these signals to zero is impervious to changes in ω_{res} or $\mathcal{C}$, allowing the lock to track drifts in power or resonant frequency.

ϒ.2 Laser wavelength system

Our setup uses a tunable diode laser with a motor for course wavelength tuning and a piezoelectric transducer that allows for fine wavelength tuning, and such we will need to use

wavelength, rather than frequency, for our locking system. Describing the setup with an equation we have,

$$\lambda_{\text{laser}} = \underbrace{\underbrace{\lambda_{\substack{\text{laser}\\\text{base}}}}_{\lambda_0} + \overbrace{\alpha\, V_{\substack{\text{piezo}\\\text{static}}}}^{\alpha\, V_{\text{piezo}}}}_{\lambda_0} + \underbrace{\underbrace{\alpha\, \overbrace{V_{\substack{\text{dither}\\\text{amp}}} \sin\big[\underbrace{2\,\pi\, f_{\text{dither}}}_{\omega_{\text{dither}}}\, t\big]}^{V_{\text{dither}}}}_{\lambda_{\substack{\text{dither}\\\text{amp}}}}}_{\lambda_{\text{dither}}}, \qquad f_{\substack{\text{dither}\\\text{amp}}} \approx \frac{c\,\lambda_{\substack{\text{dither}\\\text{amp}}}}{{\lambda_0}^2},$$

where $\alpha = 0.05\,\text{nm/V}$ is the piezoelectric actuation. To achieve dither locking, we need a hierarchy of frequencies,

$$f_{\text{dither}} \ll f_{\substack{\text{dither}\\\text{amp}}} \ll \gamma_{\text{res}}\,.$$

ϒ.2.1 Optical resonator

Dither locking (to zeroes) requires that the background transmission in the region of the resonator be sufficiently flat. In this case, in terms of wavelength, the power transmitted can be expressed generally as

$$T(\lambda) = \mathcal{C} + \frac{\mathcal{B}}{1 + 4\,Q^2\,\left(\frac{\lambda_{\text{res}}}{\lambda} - 1\right)^2}\,, \tag{ϒ.1}$$

where $\mathcal{B}$ and $\mathcal{C}$ depend on the particular resonator configuration.

ϒ.2.2 Equipment limitations

The (TLB-6700) laser's piezoelectric transducer has the following limitations,

$$V_{\text{piezo}} \in [-3,3]\,\text{V}\,, \qquad \begin{cases} f_{\text{dither}} \leqslant 2000\,\text{Hz} & : \quad V^{\text{dither}}_{\text{amp}} \leqslant 0.3\,\text{V} \\ f_{\text{dither}} \leqslant 700\,\text{Hz} & : \quad 0.3\,\text{V} < V^{\text{dither}}_{\text{amp}} \leqslant 3\,\text{V} \end{cases} .$$

Because we want to leave room for the static piezo shift, our dither amplitude voltage should be somewhat less than the maximal range.

The (PDA50B) photodetector has bandwidth limitations

$$\begin{cases} f_{\text{dither}} \leqslant 200\,\text{Hz} & : \quad 70\,\text{dB gain} \\ f_{\text{dither}} \leqslant 700\,\text{Hz} & : \quad 60\,\text{dB gain} \\ f_{\text{dither}} \leqslant 2000\,\text{Hz} & : \quad 50\,\text{dB gain} \end{cases} .$$

The (SR830) lock-in can put out $5\,\text{V}_{\text{RMS}}$ and frequencies up to 102 kHz, well beyond limitations imposed by the rest of the system.

Typical operating values were $V^{\text{dither}}_{\text{amp}} = 1\,\text{V}$ and $f_{\text{dither}} = 100\,\text{Hz}$.

ϒ.2.3 Resonance peak (first harmonic) locking

Locking to the resonance peak in wavelength is fairly straightforward and uses the first harmonic signal at the dither frequency. Taylor expanding the derivative of (ϒ.1) near

$\lambda \approx \lambda_{\rm res}$,

$$\frac{\mathrm{d}}{\mathrm{d}\lambda} T(\lambda) \overset{\lambda \approx \lambda_{\rm res}}{=} \frac{-8\,Q^2\,\mathcal{B}}{{\lambda_{\rm res}}^2}\,(\lambda - \lambda_{\rm res}) + \mathcal{O}[\lambda - \lambda_{\rm res}]^2\,. \tag{Υ.2}$$

We can also expand (Υ.1) for $\lambda_{\rm dither} \approx 0$,

$$\begin{aligned} T(\lambda_{\rm laser}; t) &= T\Big(\lambda_0 + \lambda_{\substack{\rm dither \\ \rm amp}} \sin[\omega_{\rm dither}\, t]\Big) \\ &\overset{\lambda_{\rm dither} \approx 0}{=} T(\lambda_0) + T'(\lambda_0)\, \lambda_{\substack{\rm dither \\ \rm amp}} \sin[\omega_{\rm dither}\, t] + \mathcal{O}[\lambda_{\rm dither}]^2 \\ &\overset{(\Upsilon.2)}{=} T(\lambda_0) + \underbrace{\frac{-8\,Q^2\,\mathcal{B}}{{\lambda_{\rm res}}^2}\,(\lambda_0 - \lambda_{\rm res})\,\alpha\,V_{\substack{\rm dither \\ \rm amp}}}_{T^{\rm 1st}_{\rm dither}} \sin[\omega_{\rm dither}\, t] + \dots\,, \end{aligned}$$

to realize a transmitted signal $T^{\rm 1st}_{\rm dither}$ at the dither frequency. Feedback controlling $T^{\rm 1st}_{\rm dither} \to 0$ will mean $\lambda_0 = \lambda_{\rm res}$, i.e. our laser will be centered at the resonance peak as desired.

Υ.2.4 Resonance inflection (second harmonic) locking

If we want to lock to one of the sides of the resonance, in particular at an inflection point where the second derivative is zero, we can use the second harmonic of the dither frequency. In wavelength, however, it is slightly more complicated,

$$0 = \frac{\mathrm{d}^2}{\mathrm{d}\lambda^2} \left(\mathcal{C} + \frac{\mathcal{B}}{1 + 4\,Q^2\,\left(\frac{\lambda_{\rm res}}{\lambda} - 1\right)^2} \right) \Bigg|_{\lambda = \lambda_{\rm infl}}$$

$$\Rightarrow \quad \lambda_{\text{infl}} = \lambda_{\text{res}} \left(\frac{1}{2} + \cos\Big[\frac{2}{3} \operatorname{arccot}\big[2\,Q\big] \pm \frac{\pi}{3} \Big] \right)$$

$$\overset{Q \approx \infty}{=} \lambda_{\text{res}} \left(1 \mp \frac{1}{2\sqrt{3}\,Q} + \mathcal{O}[Q]^{-2} \right) .$$

Expanding the second derivative of (Υ.1) near $\lambda \approx \lambda_{\text{infl}}$ gives

$$\frac{\mathrm{d}^2}{\mathrm{d}\lambda^2} T(\lambda) \overset{\lambda \approx \lambda_{\text{infl}}}{=} T^{(3)}(\lambda_{\text{infl}})\,(\lambda - \lambda_{\text{infl}}) + \mathcal{O}[\lambda - \lambda_{\text{infl}}]^2 , \tag{Υ.3}$$

where $T^{(3)}(\lambda_{\text{infl}}) = \frac{\mathrm{d}^3}{\mathrm{d}\lambda^3} T(\lambda)|_{\lambda=\lambda_{\text{infl}}}$ is a somewhat complicated expression. Importantly, we have a single term that goes to zero as $\lambda \to \lambda_{\text{infl}}$. Expanding ($\Upsilon$.1) for $\lambda_{\text{dither}} \approx 0$ now to second order,

$$T(\lambda_{\text{laser}}; t) = T\Big(\lambda_0 + \underset{\text{amp}}{\lambda_{\text{dither}}} \sin[\omega_{\text{dither}}\, t] \Big)$$

$$\overset{\lambda_{\text{dither}} \approx 0}{=} T(\lambda_0) + T'(\lambda_0)\, \underset{\text{amp}}{\lambda_{\text{dither}}} \sin[\omega_{\text{dither}}\, t] + T''(\lambda_0)\, \frac{\left(\underset{\text{amp}}{\lambda_{\text{dither}}} \sin[\omega_{\text{dither}}\, t] \right)^2}{2} + \mathcal{O}[\lambda_{\text{dither}}]^3 .$$

Using

$$\sin[\omega_{\text{dither}}\, t]^2 = \frac{1 - \cos[2\,\omega_{\text{dither}}\, t]}{2} ,$$

and substituting in (Υ.3), we get

$$T(\lambda_{\text{laser}}; t) \ni \underbrace{T^{(3)}(\lambda_{\text{infl}})\,(\lambda_0 - \lambda_{\text{infl}})\, \frac{\underset{\text{amp}}{\lambda_{\text{dither}}}^2}{4}}_{T^{\text{2nd}}_{\text{dither}}} \cos[2\,\omega_{\text{dither}}\, t] ,$$

realizing a signal $T^{\text{2nd}}_{\text{dither}}$ at double the dither frequency, $2\,f_{\text{dither}}$, which has the property

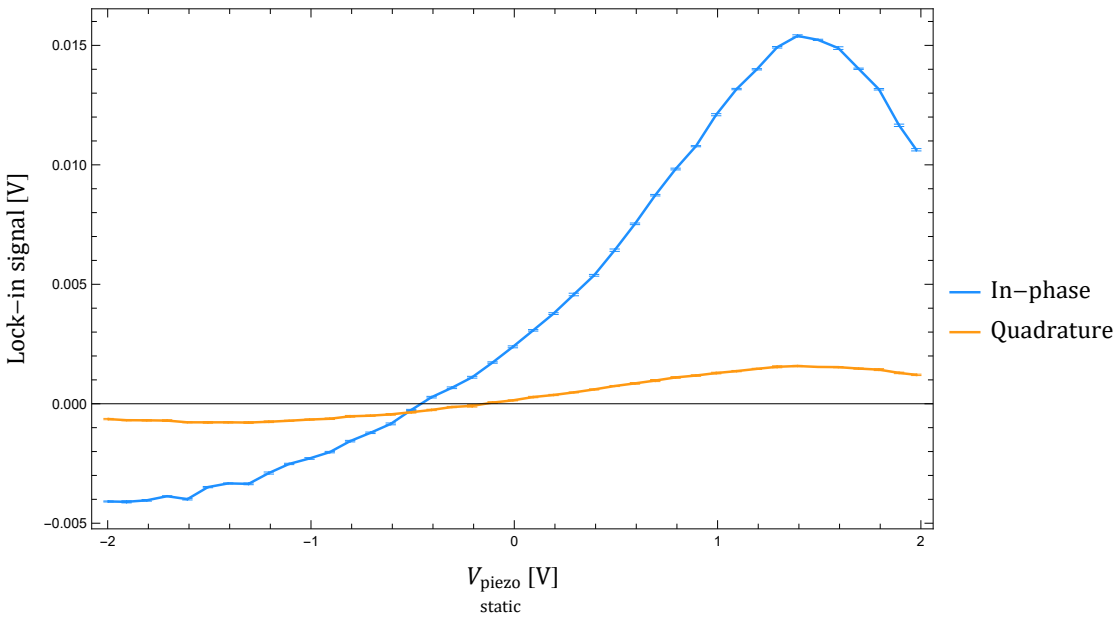

Figure ϒ.3: Example second harmonic dither lock-in response to scanning V_{piezo} near the inflection point. The crossing at zero is the desired resonance inflection point, and the slope in the vicinity provides the proportional control feedback parameter.

$T^{\text{2nd}}_{\text{dither}} \to 0 \Leftrightarrow \lambda_0 \to \lambda_{\text{infl}}$.

ϒ.2.5 PID calibration

To manage the feedback loop, a proportional-integral-derivative (PID) controller is used. With a set point of zero, the PID error signal is simply the T^{i}_{dither} signal. This signal as a function of λ_0 is dependent on the properties of the device being probed (Q, $\mathcal{B}$, $\mathcal{C}$) and thus the feedback control parameter (P) needs to be calibrated for any particular device and locking location. Fortunately, it is a simple task to map out the response by probing different static piezoelectric voltages V_{piezo}. From this the zero crossing can be used as the starting point, and the linear slope in the vicinity (halved to avoid overshoot) as P. A sample scan of the $T^{\text{2nd}}_{\text{dither}}$ response to varying V_{piezo} (and hence λ_0) for calibrating the feedback is given in Fig. ϒ.3.

APPENDIX Φ

Probability densities and uncertainties

In much of physics we are concerned with quantifying values in terms of probability densities. This appendix covers the theoretical basics of common uncertainties and their propagation.

Φ.1 Combining probability density functions

Φ.1.1 Bijections

If $\vec{X}$ is a vector random variable with probability density function $f_{\vec{X}}(\vec{x})$ and there is a bijection $\vec{X} \mapsto \vec{Y}$ then the probability density function for $\vec{Y}$ is given by

$$f_{\vec{Y}}(\vec{y}) = f_{\vec{X}}(\vec{x}) \left| \det \left[\frac{\mathrm{d}\vec{x}}{\mathrm{d}\vec{y}} \right] \right| , \tag{Φ.1}$$

where $\frac{\mathrm{d}\vec{x}}{\mathrm{d}\vec{y}}$ is the Jacobian. In particular if $\vec{Y} = \vec{g}(\vec{X})$, then

$$f_{\vec{Y}}(\vec{y}) = f_{\vec{X}}\left(\vec{g}^{\,-1}(\vec{y})\right) \left| \det \left[\frac{\mathrm{d}\,\vec{g}^{\,-1}(\vec{y})}{\mathrm{d}\vec{y}} \right] \right| .$$

Φ.1.2 Scalar function

If we are interested in combing quantities to a single scalar, such as $z = g(\vec{x})$, we can derive this as follows, starting with

$$f_Z(z) = \int_{-\infty}^{\infty} \mathrm{d}y_1 \, f_Z(y_1) \, \delta[z - y_1] \, .$$

Now if we let $Z = Y_1$, the first element of $\vec{Y}$, we can take it to be the marginal probability distribution

$$f_{Y_1}(y_1) = \left(\prod_{i=2}^{n} \int_{-\infty}^{\infty} \mathrm{d}y_i \right) f_{\vec{Y}}(\vec{y}) \; .$$

Then

$$\begin{aligned} f_Z(z) &= \left(\int_{-\infty}^{\infty} \mathrm{d}y_1 \right) \left(\prod_{i=2}^{n} \int_{-\infty}^{\infty} \mathrm{d}y_i \right) f_{\vec{Y}}(\vec{y}) \, \delta[z - y_1] \; , \\ &= \int \mathrm{d}^n \vec{y} \, f_{\vec{Y}}(\vec{y}) \, \delta[z - y_1] \; , \end{aligned}$$

and if we create an arbitrary bijection $\vec{X} \leftrightarrow \vec{Y}$ with $Y_1 = g(\vec{X})$, using (Φ.1),

$$f_Z(z) = \int \mathrm{d}^n \vec{y} \, \left| \det \left[\frac{\mathrm{d}\vec{x}}{\mathrm{d}\vec{y}} \right] \right| f_{\vec{X}}(\vec{x}) \, \delta[z - g(\vec{x})] \; ,$$

where we can do

$$\int \mathrm{d}^n \vec{y} \, \left| \det \left[\frac{\mathrm{d}\vec{x}}{\mathrm{d}\vec{y}} \right] \right| = \int \mathrm{d}^n \vec{x} \; .$$

Thus if we have $Z = g(\vec{X})$, then the probability distribution for Z is

$$f_Z(z) = \int \mathrm{d}^n \vec{x} \, f_{\vec{X}}(\vec{x}) \, \delta[z - g(\vec{x})] \; . \qquad (\Phi.2)$$

Φ.2 Expectation properties

For a random variable X, with continuous distribution f_X, the expectation of $g(X)$ is

$$\mathrm{E}[g(X)] = \int_{-\infty}^{\infty} g(x)\, f_X(x)\, \mathrm{d}x \ ,$$

and for a discrete distribution $\mathbb{P}(X)$ is

$$\mathrm{E}[g(X)] = \sum_i g(x_i)\, \mathbb{P}(X = x_i) \ .$$

The expectation operation is linear

$$\mathrm{E}[A + B] = \mathrm{E}[A] + \mathrm{E}[B] \ , \qquad\qquad \mathrm{E}[a\, A] = a\ \mathrm{E}[A] \ ,$$

where a is a scalar.

The mean and variance are

$$\mathrm{mean}[A] = \mathrm{E}[A] \ , \qquad\qquad \mathrm{var}[A] = \mathrm{E}\left[(A - \mathrm{E}[A])^2\right] = \mathrm{E}[A^2] - \mathrm{E}[A]^2 \ .$$

For two random variables the covariance is

$$\mathrm{cov}[A, B] = \mathrm{E}\left[(A - \mathrm{E}[A])\,(B - \mathrm{E}[B])\right] = \mathrm{E}[A\, B] - \mathrm{E}[A]\ \mathrm{E}[B] \ ,$$

with $\mathrm{var}[A] = \mathrm{cov}[A, A]$. If A and B are independent random variables then $\mathrm{cov}[A, B] = 0$

and $\mathrm{E}[A\,B] = \mathrm{E}[A]\ \mathrm{E}[B]$[1]. The variance distributes and scales as

$$\mathrm{var}[A+B] = \mathrm{var}[A] + \mathrm{var}[B] + 2\ \mathrm{cov}[A,B]\ , \qquad \mathrm{var}[a\,A] = a^2\ \mathrm{var}[A]\ ,$$

and more generally the covariance

$$\begin{aligned} \mathrm{cov}[A+B, C+D] &= \mathrm{cov}[A,C] + \mathrm{cov}[A,D] + \mathrm{cov}[B,C] + \mathrm{cov}[B,D]\ , \\ \mathrm{cov}[a\,A, b\,B] &= a\,b\ \mathrm{cov}[A,B]\ . \end{aligned}$$

Φ.2.1 Covariance matrix

Define the covariance matrix as

$$\mathrm{cov}[\vec{X}]_{i\,j} = \mathrm{cov}[X_i, X_j]\ , \quad \text{i.e.} \quad \mathrm{cov}[(A,B)] = \begin{pmatrix} \mathrm{var}[A] & \mathrm{cov}[A,B] \\ \mathrm{cov}[A,B] & \mathrm{var}[B] \end{pmatrix}\ .$$

Φ.2.2 Discrete sets

For a discrete set $\{x_i\}_{i=1}^n$ we can construct a random variable X with probability function $\mathbb{P}(X = x_i) = 1/n$. The distribution and expectation function is then

$$f_X(x) = \sum_{i=1}^{n} \frac{\delta(x - x_i)}{n}\ , \qquad \mathrm{E}[g(X)] = \sum_{i=1}^{n} \frac{g(x_i)}{n}\ .$$

1. The converse (no correlation implies independence) is not necessarily true.

The mean and variance are

$$\text{mean}[\{x_i\}_{i=1}^n] = \text{E}[X] = \sum_{i=1}^n \frac{x_i}{n} \,,$$

$$\text{var}[\{x_i\}_{i=1}^n] = \text{var}[X] = \sum_{i=1}^n \frac{(x_i - \text{mean}[\{x_i\}_{i=1}^n])^2}{n} = \sum_{i=1}^n \frac{{x_i}^2}{n} - \text{mean}[\{x_i\}_{i=1}^n]^2 \,.$$

Note that if $\{x_i\}_{i=1}^n$ is a sample from an unknown normal distribution, the variance computed this way is a biased estimate of the source variance. Following Sec. Φ.3.4, we define a sample variance

$$\text{var}_\text{s}[\{x_i\}_{i=1}^n] = \sum_{i=1}^n \frac{(x_i - \text{mean}[\{x_i\}_{i=1}^n])^2}{n-1} \,.$$

Φ.2.3 Weighted discrete sets

For a weighted discrete set $\{x_i, w_i\}_{i=1}^n$ with probability function $\mathbb{P}(X = x_i) = \frac{w_i}{\sum_{i=1}^n w_i}$, the distribution and expectation function is

$$f_X(x) = \frac{\sum_{i=1}^n w_i\, \delta(x - x_i)}{\sum_{i=1}^n w_i} \,, \qquad\qquad \text{E}[g(X)] = \frac{\sum_{i=1}^n w_i\, g(x_i)}{\sum_{i=1}^n w_i} \,.$$

The weighted mean and weighted variance are

$$\text{wmean}[\{x_i, w_i\}_{i=1}^n] = \text{E}[X] = \frac{\sum_{i=1}^n w_i\, x_i}{\sum_{i=1}^n w_i} \ ,$$

$$\begin{aligned} \text{wvar}[\{x_i, w_i\}_{i=1}^n] = \text{var}[X] &= \frac{\sum_{i=1}^n w_i\ (x_i - \text{wmean}[\{x_i, w_i\}_{i=1}^n])^2}{\sum_{i=1}^n w_i} \\ &= \frac{\sum_{i=1}^n w_i\, {x_i}^2}{\sum_{i=1}^n w_i} - \text{wmean}[\{x_i, w_i\}_{i=1}^n]^2 \ . \end{aligned}$$

Following Sec. Φ.3.4, we define a sample weighted variance

$$\text{wvar}_\text{s}[\{x_i, w_i\}_{i=1}^n] = \frac{n}{n-1}\ \text{wvar}[\{x_i, w_i\}_{i=1}^n] \ .$$

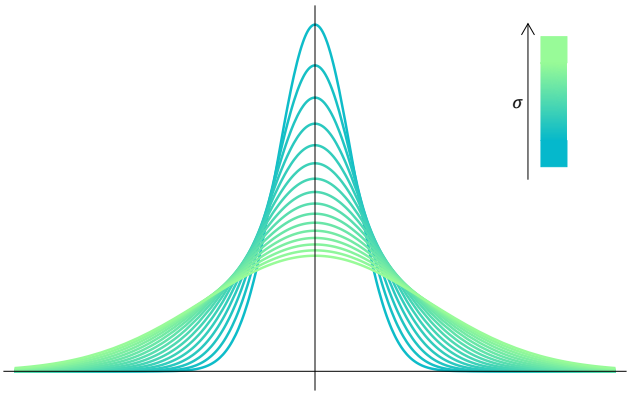

Figure Φ.1: Normal distribution probability density plots for varying standard deviation.

Φ.3 Normal distribution

As the outcome of the central limit theorem, the Normal distribution is particularly prevalent.

For a normally distributed random variable

$$X \sim \text{Normal}[\mu, \sigma] \quad : \quad \underbrace{\mu}_{\text{Mean}} \in \mathbb{R} \,, \quad \underbrace{\sigma}_{\substack{\text{Standard} \\ \text{deviation}}} > 0 \,,$$

the probability distribution function (examples depicted in Fig. Φ.1) is

$$f_{\text{Normal}}\left(x \,|\, \mu, \sigma\right) = \frac{1}{\sqrt{2\,\pi}\,\sigma} \exp\left[-\frac{(x-\mu)^2}{2\,\sigma^2}\right] \quad : \quad x \in \mathbb{R} \,.$$

Commonly the notation $\mu \pm \sigma$ refers to a normally distributed quantity.

Φ.3.1 Expectations

If X follows a normal distribution with mean μ and standard deviation σ, the raw moments are

$$\begin{aligned}
\mathrm{E}[X] &= \mu \,, \\
\mathrm{E}[X^2] &= \mu^2 + \sigma^2 \,, \\
\mathrm{E}[X^3] &= \mu^3 + 3\,\mu\,\sigma^2 \,, \\
\mathrm{E}[X^4] &= \mu^4 + 6\,\mu^2\,\sigma^2 + 3\,\sigma^4 \,,
\end{aligned}$$

with variance (second central moment)

$$\mathrm{var}[X] = \sigma^2 \,.$$

Φ.3.2 Combining independent normal variables

If we have a set of n normally distributed independent random variables, collectively denoted by $\vec{X}$, then their combined probability distribution function is

$$f_{\vec{X}}\left(\vec{x}\,|\,\vec{\mu},\vec{\sigma}\right) = \prod_{i=1}^{n} \frac{1}{\sqrt{2\,\pi}\,\sigma_i} \exp\left[-\frac{(x_i-\mu_i)^2}{2\,{\sigma_i}^2}\right] \,.$$

For a new variable $Z = g(\vec{X})$, using (Φ.2),

$$f_Z(z) = \left(\prod_{i=1}^{n} \int_{-\infty}^{\infty} \mathrm{d}x_i \, \frac{1}{\sqrt{2\,\pi}\,\sigma_i} \exp\left[-\frac{(x_i-\mu_i)^2}{2\,{\sigma_i}^2}\right]\right) \delta[z - g\,(\vec{x})] \,. \qquad (\Phi.3)$$

Expanding $g\left(\vec{x}\right)$ near $\vec{x} = \vec{\mu}$ to first order, we get

$$g\left(\vec{x}\right) \overset{\vec{x}=\vec{\mu}}{\approx} g\left(\vec{\mu}\right) + \sum_{i=1}^{n} \left(x_i - \mu_i\right) \left.\frac{\partial\, g(\vec{x})}{\partial x_i}\right|_{\vec{x}=\vec{\mu}} .$$

Making the substitutions

$$s_i = \left.\frac{\partial\, g(\vec{x})}{\partial x_i}\right|_{\vec{x}=\vec{\mu}} , \qquad\qquad u_i = \left(x_i - \mu_i\right) s_i = \left(x_i - \mu_i\right) \left.\frac{\partial\, g(\vec{x})}{\partial x_i}\right|_{\vec{x}=\vec{\mu}} ,$$

giving $\mathrm{d}x_i = \mathrm{d}u_i / s_i$ and putting this all into (Φ.3), we get

$$f_Z(z) = \left(\prod_{i=1}^{n} \int_{-\infty}^{\infty} \mathrm{d}u_i \, \frac{1}{\sqrt{2\,\pi}\left(s_i\,\sigma_i\right)} \, \exp\left[\frac{-\,{u_i}^2}{2\left(s_i\,\sigma_i\right)^2} \right] \right) \, \delta\left[z - g\left(\vec{\mu}\right) - \sum_{i=1}^{n} u_i \right] .$$

The delta function can be expanded according to

$$\delta[a] = \frac{1}{2\,\pi} \int_{-\infty}^{\infty} \mathrm{d}b \, \mathrm{e}^{\mathrm{i}\,a\,b} ,$$

to give

$$\begin{aligned} f_Z(z) = & \left(\prod_{i=1}^{n} \int_{-\infty}^{\infty} \mathrm{d}u_i \, \frac{1}{\sqrt{2\,\pi}\left(s_i\,\sigma_i\right)} \, \exp\left[\frac{-\,{u_i}^2}{2\left(s_i\,\sigma_i\right)^2} \right] \right) \\ & \times \frac{1}{2\,\pi} \int_{-\infty}^{\infty} \mathrm{d}v \, \exp\left[\mathrm{i}\,v \, \left(z - g\left(\vec{\mu}\right) - \sum_{i=1}^{n} u_i \right) \right] \end{aligned}$$

$$= \frac{1}{2\,\pi} \int_{-\infty}^{\infty} \mathrm{d}v \, \exp\left[\mathrm{i}\,v \, \left(z - g\left(\vec{\mu}\right)\right)\right] \left(\prod_{i=1}^{n} \int_{-\infty}^{\infty} \mathrm{d}u_i \, \frac{1}{\sqrt{2\,\pi}\left(s_i\,\sigma_i\right)} \, \exp\left[\frac{-\,{u_i}^2}{2\left(s_i\,\sigma_i\right)^2} - \mathrm{i}\,v\,u_i \right] \right) .$$

Using the integral identity

$$\int_{-\infty}^{\infty} \mathrm{d}c \, \mathrm{e}^{-a\,c^2 + \mathrm{i}\,b\,c} = \sqrt{\frac{\pi}{a}} \, \mathrm{e}^{\frac{-\,b^2}{4\,a}} \quad : \quad a > 0,\ b \in \mathbb{R} ,$$

we have

$$\int_{-\infty}^{\infty} \mathrm{d}u_i \, \frac{1}{\sqrt{2\,\pi}\,(s_i\,\sigma_i)} \, \exp\left[\frac{-\,{u_i}^2}{2\,(s_i\,\sigma_i)^2} - \mathrm{i}\,v\,u_i\right] = \exp\left[\frac{-\,v^2\,(s_i\,\sigma_i)^2}{2}\right] \,,$$

and thus

$$f_Z(z) = \frac{1}{2\,\pi}\int_{-\infty}^{\infty} \mathrm{d}v \, \exp\left[\mathrm{i}\,v\,\left(z - g\left(\vec{\mu}\right)\right)\right] \left(\prod_{i=1}^{n} \exp\left[\frac{-\,v^2\,(s_i\,\sigma_i)^2}{2}\right]\right)$$

$$= \frac{1}{2\,\pi}\int_{-\infty}^{\infty} \mathrm{d}v \, \exp\left[\frac{-1}{2}\,\left(\sum_{i=1}^{n}(s_i\,\sigma_i)^2\right)\,v^2 + \mathrm{i}\,v\,\left(z - g\left(\vec{\mu}\right)\right)\right] \,.$$

Using the same integral identity again,

$$f_Z(z) = \frac{1}{\sqrt{2\,\pi}\,\sqrt{\sum_{i=1}^{n}(s_i\,\sigma_i)^2}} \, \exp\left[-\frac{(z - g(\vec{\mu}))^2}{2\,\sum_{i=1}^{n}(s_i\,\sigma_i)^2}\right]$$

$$= f_{\mathrm{Normal}}\left(z \,|\, \mu_Z, \sigma_Z\right) \,,$$

with

$$\mu_Z = g(\vec{\mu}) \,, \qquad\qquad \sigma_Z = \sqrt{\sum_{i=1}^{n}\left(\sigma_i \,\left.\frac{\partial\, g(\vec{x})}{\partial x_i}\right|_{\vec{x}=\vec{\mu}}\right)^2} \,. \qquad\qquad (\Phi.4)$$

Thus to first order in g, a combination of independent normally distributed random variables generates a new normally distributed random variable. The formula (Φ.4) is the commonly used standard propagation of uncertainties.

Φ.3.3 Normal distribution with a normally distributed mean

If we have a normal distribution $X \sim \text{Normal}[M, \sigma]$ where the mean M is a random variable following a normal distribution $M \sim \text{Normal}[\mu_M, \sigma_M]$, the convoluted distribution is

$$f_X(x) = \int_{-\infty}^{\infty} f_{\text{Normal}}\left(x \,|\, m, \sigma\right)\ f_{\text{Normal}}\left(m \,|\, \mu_M, \sigma_M\right)\, \mathrm{d}m$$

$$= \int_{-\infty}^{\infty} \frac{1}{\sqrt{2\,\pi}\,\sigma}\ \exp\left[-\frac{(x-m)^2}{2\,\sigma^2}\right]\ \frac{1}{\sqrt{2\,\pi}\,\sigma_M}\ \exp\left[-\frac{(m-\mu_M)^2}{2\,{\sigma_M}^2}\right]\, \mathrm{d}m$$

$$= \frac{1}{2\,\pi\,\sigma\,\sigma_M} \times \int_{-\infty}^{\infty} \exp\left[\frac{-m^2\ \left(\sigma^2+{\sigma_M}^2\right)+2\,m\ \left(\mu_M\,\sigma^2+x\,{\sigma_M}^2\right)-{\mu_M}^2\,\sigma^2-x^2\,{\sigma_M}^2}{2\,\sigma^2\,{\sigma_M}^2}\right]\, \mathrm{d}m$$

$$= \frac{1}{2\,\pi\,\sigma\,\sigma_M}\ \exp\left[\frac{-\left(x-\mu_M\right)^2}{2\ \left(\sigma^2+{\sigma_M}^2\right)}\right] \times \int_{-\infty}^{\infty} \exp\left[-\left(\frac{\sigma^2+{\sigma_M}^2}{2\,\sigma^2\,{\sigma_M}^2}\right)\ \left(m-\frac{\mu_M\,\sigma^2+x\,{\sigma_M}^2}{\sigma^2+{\sigma_M}^2}\right)\right]\, \mathrm{d}m$$

$$= \frac{1}{\sqrt{2\,\pi}\,\sqrt{\sigma^2+{\sigma_M}^2}}\ \exp\left[\frac{-\left(x-\mu_M\right)^2}{2\ \left(\sigma^2+{\sigma_M}^2\right)}\right]$$

$$= f_{\text{Normal}}\left(x \,|\, \mu_M, \sqrt{\sigma^2+{\sigma_M}^2}\right)\ ,$$

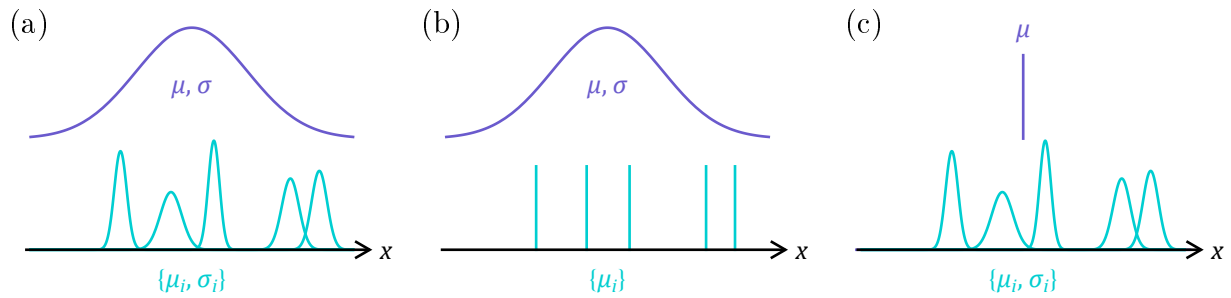

Figure Φ.2: Various measurement scenarios involving normal distributions. (a) General case of a normally distributed source with sample measurements that also have a normal distribution. (b) Normal distribution source that is sampled with precise measurements. (c) A constant with normally distributed measurement attempts.

also a normal distribution with standard deviation parameter $\sqrt{\sigma^2 + {\sigma_M}^2}$ that combines the spread in $\vec{x}$ with the uncertainty on m. Abusing notation,

$$\text{Normal}\big[\,\text{Normal}[\mu_M, \sigma_M], \sigma\,\big] = \text{Normal}[\mu_M, \sqrt{\sigma^2 + {\sigma_M}^2}]\,.$$

Φ.3.4 Normal distributions in measurements

In the most general case we have an unknown normal distribution source and a sample of known normal distribution measurements, where the goal is to determine the unknown source parameters μ, σ from our measurements $\{\mu_i, \sigma_i\}_{i=1}^n$. More particular cases, depicted in Fig. Φ.2, may have the measurements as exact values ($\sigma_i = 0$) or the source being a constant ($\sigma = 0$). We will carry out derivations in the general case and then consider the common special cases.

The combined probability distribution for n measurements μ_i with known standard deviation

σ_i from a source Normal$[\mu, \sigma]$ is

$$f\left(\{\mu_i\}_{i=1}^n \,|\, \mu, \sigma, \{\sigma_i\}_{i=1}^n\right) = \prod_{i=1}^n \left(\int_{-\infty}^{\infty} f_{\text{Normal}}\left(x_i \,|\, \mu, \sigma\right)\, f_{\text{Normal}}\left(\mu_i \,|\, x_i, \sigma_i\right)\, \mathrm{d}x_i \right)$$

$$= \prod_{i=1}^n f_{\text{Normal}}\left(\mu_i \,|\, \mu, \sqrt{\sigma^2 + {\sigma_i}^2}\right)$$

$$= \prod_{i=1}^n \frac{1}{\sqrt{2\,\pi}\,\sqrt{\sigma^2 + {\sigma_i}^2}}\, \exp\left[-\frac{(\mu_i - \mu)^2}{2\,(\sigma^2 + {\sigma_i}^2)}\right] \,.$$

Employing maximum likelihood methods, the likelihood function for μ, σ is

$$\mathcal{L}\left(\mu, \sigma \,|\, \{\mu_i, \sigma_i\}_{i=1}^n\right) = f\left(\{\mu_i\}_{i=1}^n \,|\, \mu, \sigma, \{\sigma_i\}_{i=1}^n\right) \,, \tag{Φ.5}$$

and maximizing the likelihood function is equivalent to maximizing the logarithm

$$\log \mathcal{L} = -\frac{1}{2} \sum_{i=1}^n \log\left[2\,\pi\,(\sigma^2 + {\sigma_i}^2)\right] - \frac{1}{2} \sum_{i=1}^n \frac{(\mu_i - \mu)^2}{(\sigma^2 + {\sigma_i}^2)} \,.$$

The derivatives are

$$\frac{\partial}{\partial \mu} \log \mathcal{L} = \sum_{i=1}^{n} \frac{\mu_i - \mu}{\sigma^2 + {\sigma_i}^2} \, ,$$

$$\frac{\partial}{\partial \sigma} \log \mathcal{L} = \sigma \sum_{i=1}^{n} \left(\left(\frac{\mu_i - \mu}{\sigma^2 + {\sigma_i}^2} \right)^2 - \frac{1}{\sigma^2 + {\sigma_i}^2} \right) \, ,$$

$$\frac{\partial}{\partial (\sigma^2)} \log \mathcal{L} = \frac{1}{2} \sum_{i=1}^{n} \left(\left(\frac{\mu_i - \mu}{\sigma^2 + {\sigma_i}^2} \right)^2 - \frac{1}{\sigma^2 + {\sigma_i}^2} \right) \, ,$$

$$\frac{\partial^2}{\partial \mu^2} \log \mathcal{L} = \sum_{i=1}^{n} \frac{-1}{\sigma^2 + {\sigma_i}^2} \, ,$$

$$\frac{\partial^2}{\partial \sigma^2} \log \mathcal{L} = \sum_{i=1}^{n} \left(- \left(\frac{\mu_i - \mu}{\sigma^2 + {\sigma_i}^2} \right)^2 \left(\frac{4\,\sigma^2}{\sigma^2 + {\sigma_i}^2} - 1 \right) + \frac{\sigma^2 - {\sigma_i}^2}{\left(\sigma^2 + {\sigma_i}^2 \right)^2} \right) \, ,$$

$$\frac{\partial^2}{\partial (\sigma^2)^2} \log \mathcal{L} = \frac{1}{2} \sum_{i=1}^{n} \left(-2 \, \frac{(\mu_i - \mu)^2}{\left(\sigma^2 + {\sigma_i}^2 \right)^3} + \frac{1}{\left(\sigma^2 + {\sigma_i}^2 \right)^2} \right) \, ,$$

$$\frac{\partial^2}{\partial \mu \, \partial \sigma} \log \mathcal{L} = \sum_{i=1}^{n} \frac{-2\,\sigma\,(\mu_i - \mu)}{\left(\sigma^2 + {\sigma_i}^2 \right)^2} \, ,$$

$$\frac{\partial^2}{\partial \mu \, \partial (\sigma^2)} \log \mathcal{L} = - \sum_{i=1}^{n} \frac{\mu_i - \mu}{\left(\sigma^2 + {\sigma_i}^2 \right)^2} \, .$$

Critical points with $\frac{\partial}{\partial\mu}\log\mathcal{L} = \frac{\partial}{\partial\sigma}\log\mathcal{L} = 0$ at $\mu = \hat{\mu}, \sigma = \hat{\sigma}$ generate the equations

$$\hat{\mu} = \frac{\sum_{i=1}^{n} \frac{\mu_i}{\hat{\sigma}^2 + {\sigma_i}^2}}{\sum_{i=1}^{n} \frac{1}{\hat{\sigma}^2 + {\sigma_i}^2}} \,, \tag{Φ.6}$$

$$\hat{\sigma} \sum_{i=1}^{n} \frac{1}{\hat{\sigma}^2 + {\sigma_i}^2} = \hat{\sigma} \sum_{i=1}^{n} \left(\frac{\mu_i - \hat{\mu}}{\hat{\sigma}^2 + {\sigma_i}^2} \right)^2 \,. \tag{Φ.7}$$

In general these may have multiple solutions and be computationally difficult to solve, particular special cases provide some simplifications however.

Computing the Fisher information matrix

$$\mathcal{I}(\mu,\sigma) = -E\left[\frac{\partial^2}{\partial\binom{\mu}{\sigma}\,\partial\binom{\mu}{\sigma}^{\mathrm{T}}} \log\!\left[f\left(\{\mu_i\}_{i=1}^n \,|\, \mu, \sigma, \{\sigma_i\}_{i=1}^n \right) \right] \right]$$

$$= -E\left[\begin{pmatrix} \frac{\partial^2}{\partial\mu^2}\log\mathcal{L} & \frac{\partial^2}{\partial\mu\,\partial\sigma}\log\mathcal{L} \\ \frac{\partial^2}{\partial\mu\,\partial\sigma}\log\mathcal{L} & \frac{\partial^2}{\partial\sigma^2}\log\mathcal{L} \end{pmatrix} \right]$$

$$= \begin{pmatrix} \sum_{i=1}^{n} \frac{1}{\sigma^2+{\sigma_i}^2} & 0 \\ 0 & \sum_{i=1}^{n} \frac{2\,\sigma^2}{(\sigma^2+{\sigma_i}^2)^2} \end{pmatrix} .$$

Alternatively

$$\mathcal{I}(\mu,\sigma^2) = \begin{pmatrix} \sum_{i=1}^{n} \frac{1}{\sigma^2+{\sigma_i}^2} & 0 \\ 0 & \frac{1}{2}\,\sum_{i=1}^{n} \frac{1}{(\sigma^2+{\sigma_i}^2)^2} \end{pmatrix} .$$

The covariance matrix Cramér-Rao lower bound is then

$$\mathrm{cov}\left[(\hat{\mu}, \hat{\sigma}_{\mathrm{s}})\right] \geqslant \mathcal{I}(\mu, \sigma)^{-1} \ ,$$

where $\hat{\mu}$ and $\hat{\sigma}_{\mathrm{s}}$ are unbiased.

In this general case we are essentially distinguishing source noise σ from measurement noise σ_i.

Expectations

Some expectation values,

$$\mathrm{E}[\mu_i] = \mu \ ,$$

$$\mathrm{E}[\mu_i \, \mu_j] = \mu^2 + \delta_{i\,j} \, \left(\sigma^2 + {\sigma_i}^2\right) \ .$$

Identical measurement variance

If all our measurements exhibit the same known standard deviation $\sigma_i = \sigma_0$ we can solve equations (Φ.6), (Φ.7) to obtain estimators

$$\hat{\mu} = \frac{\sum_{i=1}^{n} \mu_i}{n} \ ,$$

$$\hat{\sigma}^2 = \frac{\sum_{i=1}^{n} (\mu_i - \hat{\mu})^2}{n} - {\sigma_0}^2 \quad \text{or} \quad 0 \ .$$

The second derivatives

$$\frac{\partial^2}{\partial \mu^2} \log \mathcal{L}\Big|_{\substack{\mu=\hat{\mu} \\ \sigma=\hat{\sigma}}} = -\frac{n}{\hat{\sigma}^2 + {\sigma_0}^2} \quad < 0 \ ,$$

$$\frac{\partial^2}{\partial \sigma^2} \log \mathcal{L}\Big|_{\substack{\mu=\hat{\mu} \\ \sigma=\hat{\sigma}}} = -\frac{2\,n\,\hat{\sigma}^2}{\left(\hat{\sigma}^2 + {\sigma_0}^2\right)^2} \quad < 0 \ ,$$

$$\frac{\partial^2}{\partial \mu\, \partial \sigma} \log \mathcal{L}\Big|_{\substack{\mu=\hat{\mu} \\ \sigma=\hat{\sigma}}} = 0 \ ,$$

indicate this is indeed a maximum. Knowledge of our measurement variance ${\sigma_0}^2$ allows us to subtract it from sample variance to estimate the underlying source variance σ^2.

The expectations of our estimators are

$$\mathrm{E}[\hat{\mu}] = \mathrm{E}\left[\frac{1}{n}\sum_{i=1}^{n} \mu_i\right] = \mu \ ,$$

$$\begin{aligned}
\mathrm{E}[\hat{\sigma}^2] &= \mathrm{E}\left[\frac{1}{n}\sum_{i=1}^{n}\left(\mu_i - \frac{1}{n}\sum_{j=1}^{n}\mu_j\right)^2 - {\sigma_0}^2\right] \\
&= \frac{1}{n}\,\mathrm{E}\left[\sum_{i=1}^{n}{\mu_i}^2 - \frac{2}{n}\sum_{i=1}^{n}\sum_{j=1}^{n}\mu_i\,\mu_j + \frac{n}{n^2}\sum_{j=1}^{n}\sum_{k=1}^{n}\mu_j\,\mu_k\right] - {\sigma_0}^2 \\
&= \frac{1}{n}\left(\left(1-\frac{1}{n}\right)\sum_{i=1}^{n}\mathrm{E}[{\mu_i}^2] - \frac{1}{n}\sum_{i=1}^{n}\sum_{\substack{j=1 \\ j\neq i}}^{n}\mathrm{E}[\mu_i]\;\mathrm{E}[\mu_j]\right) - {\sigma_0}^2 \\
&= \frac{1}{n}\left(\left(\left(1-\frac{1}{n}\right)\,n\,\left(\mu^2 + \sigma^2 + {\sigma_0}^2\right) - \frac{1}{n}\,n\,(n-1)\,\mu^2\right) - {\sigma_0}^2\right. \\
&= \frac{n-1}{n}\,\sigma^2 - \frac{{\sigma_0}^2}{n} \ .
\end{aligned}$$

Thus whilst $\hat{\mu}$ is unbiased, $\hat{\sigma}^2$ is biased, but improving with increasing number of samples. This bias is often accounted for by using the sample variance

$$\hat{\sigma_{\rm s}}^2 = \frac{\sum_{i=1}^{n} (\mu_i - \hat{\mu})^2}{n-1} - {\sigma_0}^2 \ ,$$

so that $\mathrm{E}[\hat{\sigma_{\rm s}}^2] = \sigma^2$.

The variances of our estimators are

$$\mathrm{var}[\hat{\mu}] = \frac{\sigma^2 + {\sigma_0}^2}{n} \ ,$$

$$\mathrm{var}[\hat{\sigma}^2] = \frac{2\,(n-1)\,\left(\sigma^2 + {\sigma_0}^2\right)^2}{n^2} \ ,$$

$$\mathrm{var}[\hat{\sigma_{\rm s}}^2] = \frac{2\,\left(\sigma^2 + {\sigma_0}^2\right)^2}{n-1} \ .$$

Comparing this to the Cramér-Rao bounds,

$$\mathrm{var}[\hat{\mu}] \geqslant \frac{\sigma^2 + {\sigma_0}^2}{n} \ ,$$

$$\mathrm{var}[\hat{\sigma_{\rm s}}] \geqslant \frac{\left(\sigma^2 + {\sigma_0}^2\right)^2}{2\,n\,\sigma^2} \ ,$$

$$\mathrm{var}[\hat{\sigma_{\rm s}}^2] \geqslant \frac{2\,\left(\sigma^2 + {\sigma_0}^2\right)^2}{n} \ ,$$

can be made through normal distribution uncertainty propagation

$$\text{Normal}\left[\sigma, \frac{\sigma^2 + {\sigma_0}^2}{\sqrt{2\,n}\,\sigma}\right]^2 = \text{Normal}\left[\sigma^2, \frac{\sqrt{2}\,\left(\sigma^2 + {\sigma_0}^2\right)}{\sqrt{n}}\right] ,$$

$$\sqrt{\text{Normal}\left[\sigma^2, \frac{\sqrt{2}\,\left(\sigma^2 + {\sigma_0}^2\right)}{\sqrt{n-1}}\right]} = \text{Normal}\left[\sigma, \frac{\sigma^2 + {\sigma_0}^2}{\sqrt{2\,(n-1)}\,\sigma}\right] ,$$

to arrive at

$$\text{var}[\hat{\sigma_\text{s}}] = \frac{\left(\sigma^2 + {\sigma_0}^2\right)^2}{2\,(n-1)\,\sigma^2} > \frac{\left(\sigma^2 + {\sigma_0}^2\right)^2}{2\,n\,\sigma^2} ,$$

$$\text{var}[\hat{\sigma_\text{s}}^2] = \frac{2\,\left(\sigma^2 + {\sigma_0}^2\right)^2}{n-1} > \frac{2\,\left(\sigma^2 + {\sigma_0}^2\right)^2}{n} .$$

Thus whilst $\hat{\mu}$ is efficient, $\hat{\sigma_\text{s}}$ is inefficient, but improving with increasing number of samples. The variance calculated for the biased $\hat{\sigma}$ violates the Cramér-Rao inequality.

Using the set variance,

$$\hat{{\sigma_{(\text{s})}}}^2 = \text{var}_{(\text{s})}\left[\{\mu_i\}_{i=1}^n\right] - {\sigma_0}^2 , \tag{Φ.8}$$

$$\text{var}[\hat{\mu}] = \frac{\text{var}\left[\{\mu_i\}_{i=1}^n\right]}{n} .$$

It's worth addressing that for a low number of samples the above equation can estimate an invalid value of $\hat{\sigma}^2 < 0$, in this case the 0 estimate can be used. For increasing n, $\hat{\sigma}$ will tend toward its true (positive) value. This whole analysis, of course, is predicated upon σ_i actually being known, and not simply an estimate of the measurement uncertainty.

Exact measurements

For a source normal distribution with unknown parameters and a sample of outputs that we've precisely measured, as depicted in Fig. Φ.2 (b), we have $\sigma_i = 0$, and thus

$$\hat{\mu} = \frac{\sum_{i=1}^{n} \mu_i}{n} , \qquad \hat{\sigma}^2 = \frac{\sum_{i=1}^{n} (\mu_i - \hat{\mu})^2}{n} , \qquad \hat{\sigma_{\mathrm{s}}}^2 = \frac{\sum_{i=1}^{n} (\mu_i - \hat{\mu})^2}{n-1} .$$

Expectations and variances are

$$\mathrm{E}[\hat{\mu}] = \mu , \qquad \mathrm{E}[\hat{\sigma_{\mathrm{s}}}^2] = \sigma^2 ,$$

$$\mathrm{var}[\hat{\mu}] = \frac{\sigma^2}{n} , \qquad \mathrm{var}[\hat{\sigma_{\mathrm{s}}}^2] = \frac{2\,\sigma^4}{n-1} .$$

For the standard deviation we can use Eq. (Φ.4) to get

$$\sqrt{\mathrm{Normal}\left[\sigma^2, \frac{\sqrt{2}\,\sigma^2}{\sqrt{n-1}}\right]} \approx \mathrm{Normal}\left[\sigma, \frac{\sigma}{\sqrt{2\,(n-1)}}\right] .$$

Constant source

In this situation, depicted in Fig. Φ.2 (c), we are attempting to determine an exact value using measurements that have a known normal distribution. With $\sigma = 0$ we have

$$\hat{\mu} = \frac{\sum_{i=1}^{n} \frac{\mu_i}{{\sigma_i}^2}}{\sum_{i=1}^{n} \frac{1}{{\sigma_i}^2}} ,$$

often called the weighted mean where the weights are identified as $w_i = {\sigma_i}^{-2}$. The expectation and variance is

$$\mathrm{E}[\hat{\mu}] = \mu \,, \qquad\qquad \mathrm{var}[\hat{\mu}] = \frac{1}{\sum_{i=1}^{n} \frac{1}{{\sigma_i}^2}} \,.$$

Constant source with relative uncertainties

If we only know the relative uncertainties, κ_i, between our measurements, there is an unknown scaling parameter. We have $\sigma_i = \kappa_i \, k$, $\sigma = 0$, with likelihood function

$$\mathcal{L}\big(\mu, k \,|\, \{\mu_i, \kappa_i\}_{i=1}^n\big) = f\big(\{\mu_i\}_{i=1}^n \,|\, \mu, k, \{\kappa_i\}_{i=1}^n\big) = \prod_{i=1}^{n} f_{\mathrm{Normal}}\left(\mu_i \,|\, \mu, k\,\kappa_i\right) \,.$$

Our estimate for μ remains the same,

$$\hat{\mu} = \frac{\sum_{i=1}^{n} \frac{\mu_i}{k\,{\kappa_i}^2}}{\sum_{i=1}^{n} \frac{1}{k\,{\kappa_i}^2}} = \frac{\sum_{i=1}^{n} \frac{\mu_i}{{\kappa_i}^2}}{\sum_{i=1}^{n} \frac{1}{{\kappa_i}^2}} = \mathrm{wmean}\big[\{\mu_i, {\kappa_i}^{-2}\}_{i=1}^n\big] \,.$$

The scaling factor generates a new equation,

$$\frac{\partial}{\partial k} \log \mathcal{L} = \, -\frac{n}{k} + \sum_{i=1}^{n} \frac{(\mu_i - \mu)^2}{k^3\,{\kappa_i}^2} \,,$$

giving us the estimator

$$\hat{k}^2 = \frac{1}{n} \sum_{i=1}^{n} \frac{(\mu_i - \hat{\mu})^2}{{\kappa_i}^2} \,,$$

which is biased

$$\mathrm{E}[\hat{k}^2] = \frac{n-1}{n}\, k^2 \ ,$$

thus denote the unbiased estimate

$$\hat{k}_\mathrm{s}^2 = \frac{n}{n-1}\, \hat{k}^2 = \frac{1}{n-1} \sum_{i=1}^{n} \frac{(\mu_i - \hat{\mu})^2}{{\kappa_i}^2} \ .$$

The variance on $\hat{\mu}$ is thus

$$\mathrm{var}[\hat{\mu}] = \frac{1}{\sum_{i=1}^{n} \frac{1}{k^2\, {\kappa_i}^2}} \overset{\mathrm{s}}{\approx} \frac{\sum_{i=1}^{n} \frac{(\mu_i - \hat{\mu})^2}{{\kappa_i}^2}}{(n-1) \sum_{i=1}^{n} \frac{1}{{\kappa_i}^2}} = \frac{\mathrm{wvar}_\mathrm{s}\big[\{\mu_i, {\kappa_i}^{-2}\}_{i=1}^{n}\big]}{n} \ ,$$

where the set weighted variance provides compacted notation.

Similar measurement standard deviations

Returning to the more general case, (Φ.6) and (Φ.7) can be solved if all the measurement standard deviations are approximately equal, i.e.

$$\sigma_i = \sigma_0 + \delta_i \ , \qquad \sigma_0 = \sum_{i=1}^{n} \frac{\sigma_i}{n} \ , \qquad \sum_{i=1}^{n} \delta_i = 0 \ , \qquad \delta_i \ll \sigma_0 \ ,$$

then we can make a first order expansion and approximation. To carry this out we'll need the following series expansions,

$$(\mu_i - \hat{\mu})^2 \overset{\vec{\delta}=0}{\approx} (\mu_i - \mu_0)^2 + \sum_{j=1}^{n} \left(\frac{4\,\sigma_0\,\delta_j\ (\mu_i - \mu_0)\ (\mu_j - \mu_0)}{n\ \left(\hat{\sigma}^2 + {\sigma_0}^2\right)} + \mathcal{O}\left[{\delta_j}^2\right] \right) ,$$

$$\frac{1}{\hat{\sigma}^2 + {\sigma_i}^2} \overset{\vec{\delta}=0}{\approx} \frac{1}{\hat{\sigma}^2 + {\sigma_0}^2} - \frac{2\,\sigma_0\,\delta_i}{\left(\hat{\sigma}^2 + {\sigma_0}^2\right)^2} + \mathcal{O}\left[{\delta_i}^2\right] ,$$

$$\frac{1}{\left(\hat{\sigma}^2 + {\sigma_i}^2\right)^2} \overset{\vec{\delta}=0}{\approx} \frac{1}{\left(\hat{\sigma}^2 + {\sigma_0}^2\right)^2} - \frac{4\,\sigma_0\,\delta_i}{\left(\hat{\sigma}^2 + {\sigma_0}^2\right)^3} + \mathcal{O}\left[{\delta_i}^2\right] ,$$

with

$$\mu_0 = \sum_{i=1}^{n} \frac{\mu_i}{n} .$$

Putting these into (Φ.7) we get to first order in $\vec{\delta}$

$$\sum_{i=1}^{n} \left(\frac{1}{\hat{\sigma}^2 + {\sigma_0}^2} - \frac{2\,\sigma_0\,\delta_i}{\left(\hat{\sigma}^2 + {\sigma_0}^2\right)^2} \right) =$$
$$\sum_{i=1}^{n} \left(\frac{(\mu_i - \mu_0)^2}{\left(\hat{\sigma}^2 + {\sigma_0}^2\right)^2} - \frac{4\,\sigma_0\,\delta_i\ (\mu_i - \mu_0)^2)}{\left(\hat{\sigma}^2 + {\sigma_0}^2\right)^3} + \sum_{j=1}^{n} \left(\frac{4\,\sigma_0\,\delta_j\ (\mu_i - \mu_0)\ (\mu_j - \mu_0)}{n\ \left(\hat{\sigma}^2 + {\sigma_0}^2\right)^3} \right) \right) .$$

Distributing the summation and using $\sum_{i=1}^{n} \delta_i = 0$, $\sum_{i=1}^{n} \mu_i = n\,\mu_0$, we can obtain the quadratic equation

$$\Omega^2 - \Omega \sum_{i=1}^{n} \frac{(\mu_i - \mu_0)^2}{n} + 4\,\sigma_0 \sum_{i=1}^{n} \frac{\delta_i\ (\mu_i - \mu_0)^2}{n} = 0 , \qquad \Omega = \hat{\sigma}^2 + {\sigma_0}^2 ,$$

with solution

$$\hat{\sigma}^2 = \frac{\sum_{i=1}^{n} \frac{(\mu_i - \mu_0)^2}{n} \pm \sqrt{\left(\sum_{i=1}^{n} \frac{(\mu_i - \mu_0)^2}{n}\right)^2 - 4\,\sigma_0 \sum_{i=1}^{n} \frac{\delta_i\,(\mu_i - \mu_0)^2}{n}}}{2} - {\sigma_0}^2 \,.$$

The mean estimator $\hat{\mu}$ can then be determined from equation (Φ.6).

Similar measurement variances

Alternatively if the variances are similar,

$${\sigma_i}^2 = {\sigma_0}^2 + {\delta_i}^2 \,, \qquad {\sigma_0}^2 = \sum_{i=1}^{n} \frac{{\sigma_i}^2}{n} \,, \qquad \sum_{i=1}^{n} {\delta_i}^2 = 0 \,, \qquad {\delta_i}^2 \ll {\sigma_0}^2 \,,$$

then we can make a first order expansion and approximation. To carry this out we'll need the following series expansions,

$$(\mu_i - \hat{\mu})^2 \overset{\vec{\delta^2}=0}{\approx} (\mu_i - \mu_0)^2 + \sum_{j=1}^{n} \left(\frac{2\,{\delta_j}^2\,(\mu_i - \mu_0)\,(\mu_j - \mu_0)}{n\,\left(\hat{\sigma}^2 + {\sigma_0}^2\right)} + \mathcal{O}\left[{\delta_j}^4\right] \right) \,,$$

$$\frac{1}{\hat{\sigma}^2 + {\sigma_i}^2} \overset{\vec{\delta^2}=0}{\approx} \frac{1}{\hat{\sigma}^2 + {\sigma_0}^2} - \frac{{\delta_i}^2}{\left(\hat{\sigma}^2 + {\sigma_0}^2\right)^2} + \mathcal{O}\left[{\delta_i}^4\right] \,,$$

$$\frac{1}{\left(\hat{\sigma}^2 + {\sigma_i}^2\right)^2} \overset{\vec{\delta^2}=0}{\approx} \frac{1}{\left(\hat{\sigma}^2 + {\sigma_0}^2\right)^2} - \frac{2\,{\delta_i}^2}{\left(\hat{\sigma}^2 + {\sigma_0}^2\right)^3} + \mathcal{O}\left[{\delta_i}^4\right] \,,$$

with

$$\mu_0 = \sum_{i=1}^{n} \frac{\mu_i}{n} \,.$$

Putting these into (Φ.7) we get to first order in $\vec{\delta^2}$

$$\sum_{i=1}^{n}\left(\frac{1}{\hat{\sigma}^2+{\sigma_0}^2}-\frac{{\delta_i}^2}{\left(\hat{\sigma}^2+{\sigma_0}^2\right)^2}\right)= \sum_{i=1}^{n}\left(\frac{(\mu_i-\mu_0)^2}{\left(\hat{\sigma}^2+{\sigma_0}^2\right)^2}-\frac{2\,{\delta_i}^2\,(\mu_i-\mu_0)^2)}{\left(\hat{\sigma}^2+{\sigma_0}^2\right)^3}+\sum_{j=1}^{n}\left(\frac{2\,{\delta_j}^2\,(\mu_i-\mu_0)\,(\mu_j-\mu_0)}{n\,\left(\hat{\sigma}^2+{\sigma_0}^2\right)^3}\right)\right).$$

Distributing the summation and using $\sum_{i=1}^{n}{\delta_i}^2=0$, $\sum_{i=1}^{n}\mu_i=n\,\mu_0$, we can obtain the quadratic equation

$$\Omega^2-\Omega\sum_{i=1}^{n}\frac{(\mu_i-\mu_0)^2}{n}+2\sum_{i=1}^{n}\frac{{\delta_i}^2\,(\mu_i-\mu_0)^2}{n}=0\,,\qquad\qquad \Omega=\hat{\sigma}^2+{\sigma_0}^2\,,$$

with solution

$$\hat{\sigma}^2=\frac{\displaystyle\sum_{i=1}^{n}\frac{(\mu_i-\mu_0)^2}{n}\pm\sqrt{\left(\sum_{i=1}^{n}\frac{(\mu_i-\mu_0)^2}{n}\right)^2-2\sum_{i=1}^{n}\frac{{\delta_i}^2\,(\mu_i-\mu_0)^2}{n}}}{2}-{\sigma_0}^2\,.$$

The mean estimator $\hat{\mu}$ can then be determined from equation (Φ.6).

Uncertain measurements

Often we do not exactly know the precision σ_i of our measurements and instead make some guess on their uncertainty. In this case, a conservative guess on measurement uncertainty will cause us to underestimate the source parameter variance when subtracting the measurement variance in Eq. (Φ.8). Instead we can only estimate an upper bound on the source variance,

$$\hat{\sigma_{(\mathrm{s})}}^2\leqslant \mathrm{var}_{(\mathrm{s})}\left[\{\mu_i\}_{i=1}^{n}\right]\,.$$

One approach to include the measurement uncertainty is to take estimators of exact measurements in Sec. Φ.3.4 and propagate uncertainties using (to first order) Eq. (Φ.4). For measurements of $\mu_i \pm \sigma_i$ we obtain

$$\mathrm{unc}[\hat{\mu}]^2 = \frac{1}{n} \frac{\sum_{i=1}^n {\sigma_i}^2}{n} \,, \qquad \mathrm{unc}[\hat{\sigma_\mathrm{s}}^2]^2 = \frac{4}{n-1} \frac{\sum_{i=1}^n \left(\sigma_i \left(\mu_i - \hat{\mu}\right)\right)^2}{n-1}$$

which should be combined with the variances in Sec. Φ.3.4. If $\sigma_i = \sigma_0$, we get

$$\mathrm{var}[\hat{\mu}] + \mathrm{unc}[\hat{\mu}]^2 = \frac{\sigma^2 + {\sigma_0}^2}{n} \,, \qquad \mathrm{var}[\hat{\sigma_\mathrm{s}}^2] + \mathrm{unc}[\hat{\sigma_\mathrm{s}}^2]^2 = \frac{2\,\sigma^4 + 4\,{\sigma_0}^2\,{\hat{\sigma}_\mathrm{s}}^2}{n-1}$$

which is the same, to first order in ${\sigma_0}^2$, as the variances in Sec. Φ.3.4.

Bayesian likelihood

The likelihood function (Φ.5) can be determined using Bayesian methods. We start with

$$\mathbb{P}(X_i \,|\, \Theta) \sim f_\mathrm{Normal}(x_i \,|\, \mu, \sigma) \,, \qquad \mathbb{P}(X_i \,|\, M_i) \sim f_\mathrm{Normal}(x_i \,|\, \mu_i, \sigma_i) \,,$$

where X_i is a true sample value, $\Theta = \{\mu, \sigma\}$ is the source parameters, and $M_i = \{\mu_i, \sigma_i\}$ are measurement parameters. We want to compute

$$\begin{aligned}
\mathbb{P}(\Theta \,|\, \vec{M}) &= \frac{\mathbb{P}(\Theta \cap \vec{M})}{\mathbb{P}(\vec{M})} \\
&= \int^n \frac{\mathbb{P}(\Theta \cap \vec{M} \cap \vec{X})}{\mathbb{P}(\vec{M})} \, \mathrm{d}^n \vec{X} \\
&= \int^n \frac{\mathbb{P}(\Theta)\, \mathbb{P}(\vec{X} \,|\, \Theta)\, \mathbb{P}(\vec{M} \,|\, \Theta \cap \vec{X})}{\mathbb{P}(\vec{M})} \, \mathrm{d}^n \vec{X} \\
&\overset{(\Phi.9)}{=} \int^n \frac{\mathbb{P}(\Theta)\, \mathbb{P}(\vec{X} \,|\, \Theta)\, \mathbb{P}(\vec{M} \,|\, \vec{X})}{\mathbb{P}(\vec{M})} \, \mathrm{d}^n \vec{X} \\
&= \mathbb{P}(\Theta) \int^n \frac{\mathbb{P}(\vec{X} \,|\, \Theta)\, \mathbb{P}(\vec{X} \,|\, \vec{M})}{\mathbb{P}(\vec{X})} \, \mathrm{d}^n \vec{X} \ ,
\end{aligned}$$

where we have made the assertion that if X_i is known then the distribution for M_i doesn't care what Θ originally was

$$\mathbb{P}(\vec{M} \,|\, \Theta \cap \vec{X}) = \mathbb{P}(\vec{M} \,|\, \vec{X}) \ . \tag{$\Phi.9$}$$

With $\mathbb{P}(X_i)$ being an (infinitesimal) constant we identify the likelihood function as

$$\mathcal{L}(\Theta \,|\, \vec{M}) \sim \int^n \mathbb{P}(\vec{X} \,|\, \Theta)\, \mathbb{P}(\vec{X} \,|\, \vec{M}) \, \mathrm{d}^n \vec{X} \ .$$

Φ.3.5 Combining measurements

Restricting ourselves to situations with analytic forms, namely identical measurement variance (or exact) and constant source, separate subsets of measurements can be combined knowing only the resultant parameter estimates.

Identical measurement variance

For a single subset of measurements,

$$\widehat{\mu_J} = \frac{\sum\limits_{i\,\in J} \mu_i}{n_J} \,, \qquad\qquad \breve{\mu_J} = \sqrt{\frac{\widehat{\sigma_{J\,\mathrm{s}}}^2 + {\sigma_0}^2}{n_J}} \,,$$

$$\widehat{\sigma_{J\,\mathrm{s}}}^2 + {\sigma_0}^2 = \frac{\sum\limits_{i\,\in J} {\mu_i}^2 - n_J\,\widehat{\mu_J}^2}{n_J - 1} \,, \qquad \breve{\sigma_{J\,\mathrm{s}}}^2 = \sqrt{\frac{2}{n_J - 1}}\,\left(\widehat{\sigma_{J\,\mathrm{s}}}^2 + {\sigma_0}^2\right) \,,$$

$$\Rightarrow \quad n_J = \frac{\widehat{\sigma_{J\,\mathrm{s}}}^2 + {\sigma_0}^2}{\breve{\mu_J}^2} \,,$$

where $\breve{}$ is being used to denote standard deviation estimate. The combined estimates are

$$\widehat{\mu} = \frac{\sum_J n_J\,\widehat{\mu_J}}{\sum_J n_J} \,, \qquad\qquad \breve{\mu} = \sqrt{\frac{\hat{\sigma}_{\mathrm{s}}^2 + {\sigma_0}^2}{\sum_J n_J}} \,,$$

$$\hat{\sigma}_{\mathrm{s}}^2 + {\sigma_0}^2 = \frac{\sum_J (n_J - 1)\,\left(\widehat{\sigma_{J\,\mathrm{s}}}^2 + {\sigma_0}^2\right) + \sum_J n_J\,(\widehat{\mu_J} - \widehat{\mu})^2}{\sum_J n_J - 1} \,,$$

$$\breve{\sigma_{\mathrm{s}}}^2 = \sqrt{\frac{2}{\sum_J n_J - 1}}\,\left(\hat{\sigma}_{\mathrm{s}}^2 + {\sigma_0}^2\right) \,,$$

and $\hat{\sigma}_{\mathrm{s}}^2$ remains unbiased.

Constant source

For a single subset of measurements,

$$\widehat{\mu_J} = \frac{\sum\limits_{i\,\in J} \frac{\mu_i}{{\sigma_i}^2}}{\sum\limits_{i\,\in J} \frac{1}{{\sigma_i}^2}} \,, \qquad\qquad \widetilde{\mu_J} = \sqrt{\frac{1}{\sum\limits_{i\,\in J} \frac{1}{{\sigma_i}^2}}} \,,$$

and the combined estimate is

$$\widehat{\mu} = \frac{\sum\limits_{J} \frac{\widehat{\mu_J}}{\widetilde{\mu_J}^2}}{\sum\limits_{J} \frac{1}{\widetilde{\mu_J}^2}} \,, \qquad\qquad \breve{\mu} = \sqrt{\frac{1}{\sum\limits_{J} \frac{1}{\widetilde{\mu_J}^2}}} \,.$$

Bayesian inference

Similar results can be found using the previous estimates as a prior with the Bayesian likelihood, this effectively adds terms to the log likelihood function including that information.

Φ.3.6 Fitting

To perform a fit, the source mean becomes a function of some parameters in combination with an independent variable,

$$\mu = g\big(\underline{b}\,;\vec{x}\big) \,,$$
$$\mu_i = y_i \,,$$

where $\underline{b}$ is a set of m fit parameters, and the data is independent-dependent variable pairs $\{\vec{x}_i, y_i\}_{i=1}^{n}$.

Unweighted fit

An unweighted fit follows the situation of Sec. Φ.3.4,

$$\mathcal{L}\big(\underline{b},\sigma \,\big|\, \{\vec{x_i},y_i\}_{i=1}^n\big) = \prod_{i=1}^n f_{\text{Normal}}\Big(y_i \,\Big|\, g\big(\underline{b}\,;\vec{x_i}\big),\sigma\Big) \;,$$

$$\log\mathcal{L} = -\frac{n}{2}\log\big[2\,\pi\,\sigma^2\big] - \frac{1}{2\,\sigma^2}\sum_{i=1}^n \Big(y_i - g\big(\underline{b}\,;\vec{x_i}\big)\Big)^2 \;.$$

The likelihood is maximized by minimizing the sum of squared residuals,

$$\chi^2 = \sum_{i=1}^n \Big(y_i - g\big(\underline{b}\,;\vec{x_i}\big)\Big)^2 \;,$$

and we find

$$\hat{\sigma}^2 = \frac{\chi^2}{n} \quad \text{(biased)} \;,$$
$$\hat{\sigma}_{\text{s}}^2 = \frac{\chi^2}{n-m} \quad \text{(unbiased)} \;.$$

Taking the second derivatives of $\log\mathcal{L}$, the Fisher information matrix is

$$\mathcal{I}\big(\underline{b},\sigma\big) = \begin{pmatrix} \frac{1}{2\,\sigma^2}\,\frac{\partial}{\partial\underline{b}}\otimes\frac{\partial}{\partial\underline{b}}\,\chi^2 & 0 \\ 0 & \frac{n}{\sigma^2} - \frac{3}{\sigma^4}\,\chi^2 \end{pmatrix} \;,$$

using $\frac{\partial}{\partial\underline{b}}\,\chi^2 = 0$ when minimized, and we can get the fit parameter uncertainties

$$\underline{\underline{\Sigma}}_{\underline{b}} = \frac{2\,\chi^2}{n-m}\left(\frac{\partial}{\partial\underline{b}}\otimes\frac{\partial}{\partial\underline{b}}\,\chi^2\right)^{-1} \;.$$

Weighted fit

A weighted fit follows the situation of Sec. Φ.3.4,

$$\mathcal{L}\big(\underline{b}, \,\big|\, \{\vec{x_i}, y_i, \sigma_i\}_{i=1}^n\big) = \prod_{i=1}^n f_{\text{Normal}}\Big(y_i \,\Big|\, g\big(\underline{b}\,;\vec{x_i}\big), \sigma_i\Big) \;,$$

$$\log \mathcal{L} = -\frac{1}{2}\sum_{i=1}^n \log\big[2\,\pi\,{\sigma_i}^2\big] - \frac{1}{2}\sum_{i=1}^n \frac{1}{{\sigma_i}^2}\,\Big(y_i - g\big(\underline{b}\,;\vec{x_i}\big)\Big)^2 \;.$$

The likelihood is maximized by minimizing the weighted sum of squared residuals,

$$\chi^2 = \sum_{i=1}^n \frac{1}{{\sigma_i}^2}\,\Big(y_i - g\big(\underline{b}\,;\vec{x_i}\big)\Big)^2 \;,$$

where the weights are $w_i = {\sigma_i}^{-2}$. Taking the second derivatives of $\log \mathcal{L}$, the Fisher information matrix is

$$\mathcal{I}\big(\underline{b}\big) = \frac{1}{2}\,\frac{\partial}{\partial \underline{b}} \otimes \frac{\partial}{\partial \underline{b}}\,\chi^2 \;,$$

and we can get the fit parameter uncertainties

$$\underline{\underline{\Sigma}}_{\underline{b}} = 2\left(\frac{\partial}{\partial \underline{b}} \otimes \frac{\partial}{\partial \underline{b}}\,\chi^2\right)^{-1} \;.$$

Relatively weighted fit

An relatively weighted fit follows the situation of Sec. Φ.3.4,

$$\mathcal{L}\big(\underline{b}, k \,\big|\, \{\vec{x_i}, y_i, \kappa_i\}_{i=1}^n\big) = \prod_{i=1}^n f_{\text{Normal}}\Big(y_i \,\Big|\, g\big(\underline{b}\,;\vec{x_i}\big), k\,\kappa_i\Big) \;,$$

$$\log \mathcal{L} = -\frac{1}{2} \sum_{i=1}^{n} \log\left[2\,\pi\,k^2\,{\kappa_i}^2\right] - \frac{1}{2} \sum_{i=1}^{n} \frac{1}{k^2\,{\kappa_i}^2} \left(y_i - g\left(\underline{b}\,;\vec{x_i}\right)\right)^2 .$$

The likelihood is maximized by minimizing the weighted sum of squared residuals,

$$\chi^2 = \sum_{i=1}^{n} \frac{1}{{\kappa_i}^2} \left(y_i - g\left(\underline{b}\,;\vec{x_i}\right)\right)^2 ,$$

where the relative weights are $w_i = {\kappa_i}^{-2}$, and we find

$$\hat{k}^2 = \frac{\chi^2}{n} \quad \text{(biased)} ,$$
$$\hat{k}_{\mathrm{s}}^2 = \frac{\chi^2}{n-m} \quad \text{(unbiased)} .$$

Taking the second derivatives of $\log \mathcal{L}$, the Fisher information matrix is

$$\mathcal{I}\left(\underline{b}, k\right) = \begin{pmatrix} \frac{1}{2\,k^2}\,\frac{\partial}{\partial \underline{b}} \otimes \frac{\partial}{\partial \underline{b}}\,\chi^2 & 0 \\ 0 & \frac{n}{k^2} - \frac{3}{k^4}\,\chi^2 \end{pmatrix} ,$$

using $\frac{\partial}{\partial \underline{b}}\,\chi^2 = 0$ when minimized, and we can get the fit parameter uncertainties

$$\underline{\underline{\Sigma_b}} = \frac{2\,\chi^2}{n-m} \left(\frac{\partial}{\partial \underline{b}} \otimes \frac{\partial}{\partial \underline{b}}\,\chi^2\right)^{-1} .$$

Linear fit function

A linear fit function has the form

$$g\left(\underline{b}\,;\vec{x}_i\right) = \sum_k b_k\,g_k\left(\vec{x}\right) ,$$

allowing us to write

$$\chi^2 = \left(\underline{y} - \underline{\underline{X}} \cdot \underline{b}\right)^{\mathsf{T}} \cdot \underline{\underline{W}} \cdot \left(\underline{y} - \underline{\underline{X}} \cdot \underline{b}\right) ,$$

where $\underline{\underline{X}}$ is the design matrix, and $\underline{\underline{W}} = \mathrm{diag}\left[\{w_i\}_{i=1}^{n}\right]$ is a diagonal matrix of weights. In this form the minimization can be performed analytically to give solution

$$\hat{\underline{b}} = \left(\underline{\underline{X}}^{\mathsf{T}} \cdot \underline{\underline{W}} \cdot \underline{\underline{X}}\right)^{-1} \cdot \underline{\underline{X}}^{\mathsf{T}} \cdot \underline{\underline{W}} \cdot \underline{y} ,$$

and the second derivatives are

$$\frac{\partial}{\partial \underline{b}} \otimes \frac{\partial}{\partial \underline{b}} \chi^2 = 2\, \underline{\underline{X}}^{\mathsf{T}} \cdot \underline{\underline{W}} \cdot \underline{\underline{X}} .$$

For the weighted fit, this allows us to write[2]

$$\underline{\underline{\Sigma}}_{\underline{b}} = \left(\underline{\underline{X}}^{\mathsf{T}} \cdot \underline{\underline{W}} \cdot \underline{\underline{X}}\right)^{-1} = \frac{\partial \underline{b}}{\partial \underline{y}} \cdot \underline{\underline{W}} \cdot \frac{\partial \underline{b}}{\partial \underline{y}}^{\mathsf{T}} .$$

For the unweighted fit we can also compute the bias in $\hat{\sigma}$,

$$\begin{aligned}
\mathrm{E}\left[\hat{\sigma}^2\right] &= \mathrm{E}\left[\frac{1}{n}\left(\underline{y} - \underline{\underline{X}} \cdot \hat{\underline{b}}\right)^{\mathsf{T}} \cdot \left(\underline{y} - \underline{\underline{X}} \cdot \hat{\underline{b}}\right)\right] \\
&= \mathrm{E}\left[\frac{1}{n}\, \underline{y}^{\mathsf{T}} \cdot \left(\underline{\underline{\mathbb{I}}}_n - \underline{\underline{X}} \cdot \left(\underline{\underline{X}}^{\mathsf{T}} \cdot \underline{\underline{X}}\right)^{-1} \cdot \underline{\underline{X}}^{\mathsf{T}}\right)^{\mathsf{T}} \cdot \left(\underline{\underline{\mathbb{I}}}_n - \underline{\underline{X}} \cdot \left(\underline{\underline{X}}^{\mathsf{T}} \cdot \underline{\underline{X}}\right)^{-1} \cdot \underline{\underline{X}}^{\mathsf{T}}\right) \cdot \underline{y}\right] \\
&= \mathrm{E}\left[\frac{1}{n}\, \underline{y}^{\mathsf{T}} \cdot \left(\underline{\underline{\mathbb{I}}}_n - \underline{\underline{X}} \cdot \left(\underline{\underline{X}}^{\mathsf{T}} \cdot \underline{\underline{X}}\right)^{-1} \cdot \underline{\underline{X}}^{\mathsf{T}}\right) \cdot \underline{y}\right] .
\end{aligned}$$

2. Using notation $\frac{\partial \underline{a}}{\partial \underline{\underline{b}}} = \left(\frac{\partial}{\partial \underline{b}}^{\mathsf{T}} \cdot \underline{a}^{\mathsf{T}}\right)^{\mathsf{T}}$ such that $\left(\frac{\partial \underline{a}}{\partial \underline{\underline{b}}}\right)_{i\,j} = \frac{\partial a_i}{\partial b_j}$.

Letting $\underline{\underline{M}} = \underline{\underline{\mathbb{I}_n}} - \underline{\underline{X}} \cdot \left(\underline{\underline{X}}^{\mathsf{T}} \cdot \underline{\underline{X}}\right)^{-1} \cdot \underline{\underline{X}}^{\mathsf{T}}$,

$$\begin{aligned}
\mathrm{E}\big[\hat{\sigma}^2\big] &= \frac{1}{n}\,\mathrm{E}\Big[\underline{y}^{\mathsf{T}} \cdot \underline{\underline{M}} \cdot \underline{y}\Big] \\
&= \frac{1}{n}\,\mathrm{E}\Big[\sum_{i=1}^{n}\sum_{j=1}^{n} y_i\, y_j\, M_{i\,j}\Big] \\
&= \frac{1}{n}\,\sum_{i=1}^{n}\mathrm{E}\big[{y_i}^2\big]\, M_{i\,i} + \frac{1}{n}\,\sum_{i=1}^{n}\sum_{\substack{j=1\\ j\neq i}}^{n}\mathrm{E}[y_i]\;\mathrm{E}[y_j]\, M_{i\,j} \\
&= \frac{1}{n}\,\sum_{i=1}^{n}\left(\left(\sum_{k=1}^{m} X_{i\,k}\, b_k\right)^2 + \sigma^2\right) M_{i\,i} + \frac{1}{n}\,\sum_{i=1}^{n}\sum_{\substack{j=1\\ j\neq i}}^{n}\left(\sum_{k=1}^{m} X_{i\,k}\, b_k\right)\left(\sum_{l=1}^{m} X_{j\,l}\, b_l\right) M_{i\,j} \\
&= \frac{\sigma^2}{n}\,\sum_{i=1}^{n} M_{i\,i} + \frac{1}{n}\,\sum_{i=1}^{n}\sum_{j=1}^{n}\sum_{k=1}^{m}\sum_{l=1}^{m} b_k\, X_{i\,k}\, M_{i\,j}\, X_{j\,l}\, b_l \\
&= \frac{\sigma^2}{n}\,\mathrm{tr}\Big[\underline{\underline{M}}\Big] + \frac{1}{n}\,\underline{b}^{\mathsf{T}} \cdot \underline{\underline{X}}^{\mathsf{T}} \cdot \underline{\underline{M}} \cdot \underline{\underline{X}} \cdot \underline{b}\,.
\end{aligned}$$

Now, $\underline{\underline{X}}^{\mathsf{T}} \cdot \underline{\underline{M}} \cdot \underline{\underline{X}} = \underline{\underline{X}}^{\mathsf{T}} \cdot \underline{\underline{X}} - \underline{\underline{X}}^{\mathsf{T}} \cdot \underline{\underline{X}} = 0$, and

$$\begin{aligned}
\mathrm{tr}\Big[\underline{\underline{M}}\Big] &= \mathrm{tr}\Big[\underline{\underline{\mathbb{I}_n}} - \underline{\underline{X}} \cdot \left(\underline{\underline{X}}^{\mathsf{T}} \cdot \underline{\underline{X}}\right)^{-1} \cdot \underline{\underline{X}}^{\mathsf{T}}\Big] \\
&= \mathrm{tr}\Big[\underline{\underline{\mathbb{I}_n}}\Big] - \mathrm{tr}\Big[\underline{\underline{X}} \cdot \left(\underline{\underline{X}}^{\mathsf{T}} \cdot \underline{\underline{X}}\right)^{-1} \cdot \underline{\underline{X}}^{\mathsf{T}}\Big] \\
&= \mathrm{tr}\Big[\underline{\underline{\mathbb{I}_n}}\Big] - \mathrm{tr}\Big[\underline{\underline{X}}^{\mathsf{T}} \cdot \underline{\underline{X}} \cdot \left(\underline{\underline{X}}^{\mathsf{T}} \cdot \underline{\underline{X}}\right)^{-1}\Big] \\
&= \mathrm{tr}\Big[\underline{\underline{\mathbb{I}_n}}\Big] - \mathrm{tr}\Big[\underline{\underline{\mathbb{I}_m}}\Big] \\
&= n - m\,,
\end{aligned}$$

giving

$$\mathrm{E}\big[\hat{\sigma}^2\big] = \frac{n-m}{n}\,\sigma^2\,,$$

where n is the number of data points and m is the number of parameters (length of $\underline{b}$). Thus,

define the unbiased sample estimated variance (also called the reduced χ^2)

$$\hat{\sigma_{\mathrm{s}}}^2 = \frac{\chi^2}{n-m} \ .$$

The unweighted fit parameter uncertainties are then

$$\underline{\underline{\Sigma_b}} = \hat{\sigma_{\mathrm{s}}}^2 \left(\underline{\underline{X}}^{\mathsf{T}} \cdot \underline{\underline{X}} \right)^{-1} = \hat{\sigma_{\mathrm{s}}}^2 \, \frac{\partial \underline{b}}{\partial \underline{y}} \cdot \frac{\partial \underline{b}}{\partial \underline{y}}^{\mathsf{T}} \ .$$

For a relatively weighted fit with $\underline{\underline{W}} = \mathrm{diag}\big[\{{\kappa_i}^{-2}\}_{i=1}^{n}\big]$,

$$\underline{\underline{\Sigma_b}} = \hat{k_{\mathrm{s}}}^2 \left(\underline{\underline{X}}^{\mathsf{T}} \cdot \underline{\underline{W}} \cdot \underline{\underline{X}} \right)^{-1} = \hat{k_{\mathrm{s}}}^2 \, \frac{\partial \underline{b}}{\partial \underline{y}} \cdot \underline{\underline{W}} \cdot \frac{\partial \underline{b}}{\partial \underline{y}}^{\mathsf{T}} \ .$$

Transformed fits

It may be desirable to transform data and the fit function (e.g. so that it's linear). For transform function h,

$$h\Big(y_i \sim \mathrm{Normal}\big[g(\underline{b}; \vec{x_i}), \ \sigma_i\big] \Big) \approx \Big(h(y_i) \sim \mathrm{Normal}\big[h \circ g(\underline{b}; \vec{x_i}), \ \sigma_i \, h'(y_i)\big] \Big) \ .$$

This will re-weight a weighted fit and transform an unweighted fit to a relatively weighted fit.

In the new fit, it often useful to relabel the parameters $\underline{c}(\underline{b})$, which will have uncertainties

related to the original fit parameters via[3]

$$\underline{c}\left(\text{Normal}\left[\underline{b},\ \underline{\underline{\Sigma}}_{\underline{b}}\right]\right) \approx \text{Normal}\left[\underline{c}(\underline{b}),\ \underline{c}'(\underline{b}) \cdot \underline{\underline{\Sigma}}_{\underline{b}} \cdot \underline{c}'(\underline{b})^{\mathsf{T}}\right] .$$

3. Using notation $\underline{f}'(\underline{x}) = \frac{\partial \underline{f}(\underline{z})}{\partial \underline{z}}\Big|_{\underline{z}=\underline{x}}$.

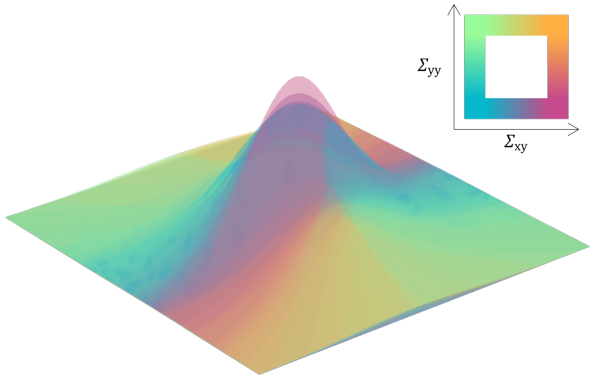

Figure Φ.3: Multinormal distribution probability density plots for varying covariance.

Φ.4 Multinormal distribution

For a vector of possibly correlated normal variables, we have the Multinormal distribution

$$\vec{X} \sim \text{Normal}[\vec{\mu}, \Sigma] \quad : \quad \underbrace{\vec{\mu}}_{\substack{\text{Mean} \\ \text{vector}}} \in \mathbb{R}^d \,, \quad \underbrace{\Sigma}_{\substack{\text{Covariance} \\ \text{matrix}}} : \begin{cases} \det[\Sigma] > 0 \\ \Sigma \text{ symmetric} \end{cases} ,$$

with probability distribution function (examples depicted in Fig. Φ.3)

$$f_{\text{Normal}}\left(\vec{x} \,|\, \vec{\mu}, \Sigma\right) = \frac{1}{\sqrt{(2\,\pi)^d \, \det[\Sigma]}} \exp\left[-\frac{1}{2}\,(\vec{x} - \vec{\mu})^{\mathsf{T}} \cdot \Sigma^{-1} \cdot (\vec{x} - \vec{\mu})\right] \quad : \quad x \in \mathbb{R}^d \,.$$

If the covariance matrix is diagonal (uncorrelated variables), the multinormal distribution reduces to a product of normal distributions.

Φ.4.1 Expectations

Some moments are

$$\mathrm{E}\left[\vec{X}\right] = \vec{\mu}\ , \qquad \mathrm{cov}\left[\vec{X}, \vec{X}^{\mathsf{T}}\right] = \Sigma\ , \qquad \mathrm{E}\left[\vec{X}^{\otimes 2}\right] = \vec{\mu}^{\otimes 2} + \Sigma\ .$$

For individual variates,

$$\mathrm{E}[X_i] = \mu_i\ , \qquad \mathrm{var}[X_i] = {\sigma_i}^2 \qquad \mathrm{E}[{X_i}^2] = {\mu_i}^2 + {\sigma_i}^2\ ,$$

where $\sigma_i = \sqrt{\Sigma_{i\,i}}$.

Φ.4.2 Standard deviation hyperellipsoid

In $\mathbb{R}^d$, the k-standard deviation hyperellipsoid is given by

$$(\vec{x} - \vec{\mu})^{\mathsf{T}} \cdot \Sigma^{-1} \cdot (\vec{x} - \vec{\mu}) = k^2\ .$$

The value of the multinormal distribution on the k-standard deviation hyperellipsoid is thus

$$f_{\mathrm{Normal}}\left(\vec{x} \in k\text{-}\sigma \,|\, \vec{\mu}, \Sigma\right) = \frac{f_{\mathrm{Normal}}\left(\vec{\mu} \,|\, \vec{\mu}, \Sigma\right)}{\sqrt{\mathrm{e}^{k^2}}}\ ,$$

where

$$f_{\mathrm{Normal}}\left(\vec{\mu} \,|\, \vec{\mu}, \Sigma\right) = \frac{1}{\sqrt{(2\,\pi)^d\ \det[\Sigma]}}\ ,$$

d \ k	1	2	3	4	5	6	7
1	0.6827	0.9545	0.9973	0.9999	1.0000	1.0000	1.0000
2	0.3935	0.8647	0.9889	0.9997	1.0000	1.0000	1.0000
3	0.1987	0.7385	0.9707	0.9989	1.0000	1.0000	1.0000
4	0.0902	0.5940	0.9389	0.9970	0.9999	1.0000	1.0000
5	0.0374	0.4506	0.8909	0.9932	0.9999	1.0000	1.0000
6	0.0144	0.3233	0.8264	0.9862	0.9997	1.0000	1.0000
7	0.0052	0.2202	0.7473	0.9749	0.9992	1.0000	1.0000
8	0.0018	0.1429	0.6577	0.9576	0.9984	1.0000	1.0000
9	0.0006	0.0886	0.5627	0.9331	0.9970	1.0000	1.0000
10	0.0002	0.0527	0.4679	0.9004	0.9947	0.9999	1.0000

Figure Φ.4: Confidence levels of k-standard deviation hyperellipsoids for multinormal distributions of dimension d.

is the distribution peak value. Under a logarithm, for use with log likelihoods,

$$\log \mathcal{L}(k\text{-}\sigma) = \log \mathcal{L}(\text{peak}) - k^2/2 \ .$$

The confidence level of the standard deviation hyperellipsoid varies with dimension d and can be calculated numerically via [314]

$$\mathbb{P}_{d=1}(x < k\text{-}\sigma) = \ \text{erf}\left[k/\sqrt{2}\right] \ ,$$

$$\mathbb{P}_{d=2}(x < k\text{-}\sigma) = \ 1 - \exp\left[-k^2/2\right] \ ,$$

$$\mathbb{P}_{d>2}(x < k\text{-}\sigma) = \ \mathbb{P}_{d-2}(x < k\text{-}\sigma) - \left(\frac{k}{\sqrt{2}}\right)^{d-2} \frac{\exp\left[-k^2/2\right]}{\Gamma\left[d/2\right]} \ .$$

A table of values is given in Fig. Φ.4.

Φ.4.3 Vector combinations of normal variables

Not proved here. If $\vec{X}$ is a vector of normally distributed random variables with covariance matrix $\Sigma_{\vec{X}}$, then for an arbitrary vector combination $\vec{g}(\vec{X})$, to first order, we have

$$\vec{Y} = \vec{g}(\vec{X}) \quad \Rightarrow \quad \Sigma_{\vec{Y}} = J \cdot \Sigma_{\vec{X}} \cdot J^{\mathsf{T}} \ ,$$

where J is the evaluated Jacobian[4],

$$J = \left.\frac{\partial\, \vec{g}(\vec{x})}{\partial \vec{x}}\right|_{\vec{x}=\vec{\mu}} \ , \qquad\qquad J_{i\,j} = \left.\frac{\partial\, g_i(\vec{x})}{\partial x_j}\right|_{\vec{x}=\vec{\mu}}$$

If $\vec{g}(\vec{X}) = G \cdot \vec{X}$, i.e. $\vec{g}$ is linear, then $J = G$.

Abusing notation, we can write

$$\vec{g}\Big(\text{ Normal}[\vec{\mu}, \Sigma]\Big) \approx \text{Normal}\big[\vec{g}(\vec{\mu}), J \cdot \Sigma \cdot J^{\mathsf{T}}\big] \ .$$

Φ.4.4 Scalar combination of normal variables

If $\vec{Y}$ has only one component, i.e. $Z = g(\vec{X})$,

$$\mu_Z = g(\vec{\mu}) \ , \qquad\qquad \sigma_Z = \sqrt{\sum_{i=1}^{d}\sum_{j=1}^{d} \Sigma_{i\,j} \left.\frac{\partial\, g(\vec{x})}{\partial x_i}\right|_{\vec{x}=\vec{\mu}} \left.\frac{\partial\, g(\vec{x})}{\partial x_j}\right|_{\vec{x}=\vec{\mu}}} \ .$$

4. Using notation where $\frac{\partial}{\partial \vec{x}}$ is a row vector.

Φ.4.5 Marginalizing normal variables

Not proved here. A multinormal distribution Normal$[\vec{\mu}, \Sigma]$, with mean vector $\vec{\mu}$ and covariance matrix Σ, marginalizes to a single normal distribution,

$$\left(\prod_{i=2}^{d} \int_{-\infty}^{\infty} \mathrm{d}x_i \right) f_{\text{Normal}}\left(\vec{x} \,|\, \vec{\mu}, \Sigma\right) = f_{\text{Normal}}\left(x_1 \,|\, \mu_1, \sigma_1\right) \ .$$

Φ.4.6 Correlation matrix

The correlation matrix is defined as

$$C = \sqrt{\text{diag}[\Sigma]^{-1}} \cdot \Sigma \cdot \sqrt{\text{diag}[\Sigma]^{-1}} \ , \qquad\qquad C_{i\,j} = \frac{\Sigma_{i\,j}}{\sqrt{\Sigma_{i\,i}\,\Sigma_{j\,j}}} \ ,$$

where diag$[\Sigma]$ takes only the diagonal components of Σ whilst leaving the rest zero.

If two multinormal distributions, Normal$[\vec{\mu_A}, \Sigma_A]$ and Normal$[\vec{\mu_B}, \Sigma_B]$, are full correlated, their combined covariance matrix is[5]

$$\Sigma = \begin{pmatrix} \Sigma_A & \sqrt[\odot]{\Sigma_A} \odot \sqrt[\odot]{\Sigma_B} \\ \sqrt[\odot]{\Sigma_A} \odot \sqrt[\odot]{\Sigma_B} & \Sigma_B \end{pmatrix} ,$$

such that the combined correlation matrix has 1s across the diagonal of each block.

5. $\odot$ is the Hadamard (element-wise) product.

Φ.4.7 Normal distribution with correlated measurements

Extending Sec. Φ.3.4 to a set of correlated measurements we have

$$f\left(\vec{\mu}\,|\,\mu,\sigma,\Sigma\right) = \prod_{i=1}^{n}\left(\int_{-\infty}^{\infty}\mathrm{d}x_i\;\underbrace{f_{\mathrm{Normal}}\left(x_i\,|\,\mu,\sigma\right)}_{\mathrm{Source}}\right)\;\underbrace{f_{\mathrm{Normal}}\left(\vec{\mu}\,|\,\vec{x},\Sigma\right)}_{\mathrm{Measurements}}$$

$$= f_{\mathrm{Normal}}\left(\vec{\mu}\,|\,\vec{1}_n\,\mu,\Sigma+\mathbb{I}_n\,\sigma^2\right)$$

$$= \mathcal{L}\left(\begin{matrix}\mu,\sigma\\ \mathrm{Source}\end{matrix}\,\middle|\,\begin{matrix}\vec{\mu},\Sigma\\ \mathrm{Measurements}\end{matrix}\right)\;.$$

If we have a set of measurements with correlation matrix C and individual variances ${\sigma_i}^2$,

$$\Sigma = \mathrm{diag}[\vec{\sigma}]\cdot C\cdot\mathrm{diag}[\vec{\sigma}]\;,$$

where $\mathrm{diag}[\vec{\sigma}]$ is assembling a diagonal matrix with elements given by $\vec{\sigma}=(\sigma_1,\ldots,\sigma_n)$.

The log likelihood function is

$$\log\mathcal{L} = -\frac{n}{2}\,\log\left[2\,\pi\right] - \frac{1}{2}\,\log\Big[\det[\Sigma+\mathbb{I}_n\,\sigma^2]\Big] - \frac{1}{2}\sum_{i=1}^{n}\sum_{j=1}^{n}\left(\mu-\mu_i\right)\left(\mu-\mu_j\right)\,\left(\Sigma+\mathbb{I}_n\,\sigma^2\right)^{-1}_{i\,j}\;,$$

with derivatives

$$\frac{\partial}{\partial\mu}\log\mathcal{L} = \sum_{i=1}^{n}\sum_{j=1}^{n}\left(\mu_i-\mu\right)\,\left(\Sigma+\mathbb{I}_n\,\sigma^2\right)^{-1}_{i\,j}\;,$$

$$\frac{\partial}{\partial\sigma}\log\mathcal{L} = \sigma\sum_{i=1}^{n}\sum_{j=1}^{n}\left(\mu_i-\mu\right)\left(\mu_j-\mu\right)\,\left(\Sigma+\mathbb{I}_n\,\sigma^2\right)^{-2}_{i\,j} - \sigma\sum_{i=1}^{n}\,\left(\Sigma+\mathbb{I}_n\,\sigma^2\right)^{-1}_{i\,i}\;,$$

which requires numerics to find the roots.

Expectations

Some expectation values,

$$\mathrm{E}[\mu_i] = \mu \ ,$$

$$\mathrm{E}[\mu_i \, \mu_j] = \mu^2 + \Sigma_{i\,j} + \delta_{i\,j} \, \sigma^2 \ .$$

Fully correlated measurements

If our measurements are maximally correlated (with the same uncertainty), perhaps from a systematic, we have $\Sigma = {\sigma_0}^2 \, 1_n$ constant matrix. Using (Φ.14),

$$\frac{\partial}{\partial \mu} \log \mathcal{L} = \sum_{i=1}^{n} \sum_{j=1}^{n} (\mu_i - \mu) \, \frac{1}{\sigma^2} \left(\delta_{i\,j} - \frac{1}{n + \frac{\sigma^2}{{\sigma_0}^2}} \right) ,$$

$$\frac{\partial}{\partial \sigma} \log \mathcal{L} = \frac{1}{\sigma^3} \sum_{i=1}^{n} \sum_{j=1}^{n} (\mu_i - \mu) \, (\mu_j - \mu) \left(\delta_{i\,j} + \frac{1}{n + \frac{\sigma^2}{{\sigma_0}^2}} \left(\frac{n}{n + \frac{\sigma^2}{{\sigma_0}^2}} - 2 \right) \right) - \frac{1}{\sigma} \sum_{i=1}^{n} \left(1 - \frac{1}{n + \frac{\sigma^2}{{\sigma_0}^2}} \right) .$$

Solving for the critical points,

$$\hat{\mu} = \frac{\sum_{i=1}^{n} \sum_{j=1}^{n} \mu_i \left(\delta_{i\,j} - \frac{1}{n + \frac{\hat{\sigma}^2}{{\sigma_0}^2}} \right)}{n - \frac{n^2}{n + \frac{\hat{\sigma}^2}{{\sigma_0}^2}}} = \frac{\sum_{i=1}^{n} \mu_i}{n} \,,$$

$$\hat{\sigma}^2 \left(1 - \frac{1}{n + \frac{\hat{\sigma}^2}{{\sigma_0}^2}} \right) = \frac{\sum_{i=1}^{n} \left(\mu_i - \hat{\mu} \right)^2}{n} = \mathrm{var}\big[\{\mu_i\}_{i=1}^{n} \big] \,.$$

The second equation has solution

$$\hat{\sigma}^2 = \left(\frac{\mathrm{var}\big[\{\mu_i\}_{i=1}^{n} \big] - (n-1)\,{\sigma_0}^2}{2} \right) \pm \sqrt{\left(\frac{\mathrm{var}\big[\{\mu_i\}_{i=1}^{n} \big] - (n-1)\,{\sigma_0}^2}{2} \right)^2 + \mathrm{var}\big[\{\mu_i\}_{i=1}^{n} \big]\, n\, {\sigma_0}^2} \,,$$

where we take the positive square root to ensure $\hat{\sigma}^2 \geqslant 0$ via $x + \sqrt{x^2 + y^2} \geqslant x + |x| \geqslant 0$. If $\sigma_0 = 0$ we obtain the familiar result

$$\hat{\sigma}^2 = \mathrm{var}\big[\{\mu_i\}_{i=1}^{n} \big] \quad : \; \sigma_0 = 0 \,.$$

For large n,

$$\begin{aligned} \hat{\sigma}^2 &\overset{n \approx \infty}{\approx} \frac{n+1}{n}\ \mathrm{var}\big[\{\mu_i\}_{i=1}^{n} \big] + \mathcal{O}\left[\frac{1}{n^2} \right] \\ \hat{\sigma}^2 &\overset{n \approx \infty}{\approx}\ \mathrm{var}\big[\{\mu_i\}_{i=1}^{n} \big] + \mathcal{O}\left[\frac{1}{n} \right] \,, \end{aligned}$$

notably independent of σ_0.

We have

$$\mathrm{E}[\hat{\mu}] = \mathrm{E}\left[\frac{1}{n}\sum_{i=1}^{n}\mu_i\right] = \mu \ ,$$

$$\mathrm{E}[\hat{\mu}^2] = \mathrm{E}\left[\frac{1}{n^2}\sum_{i=1}^{n}\sum_{j=1}^{n}\mu_i\,\mu_j\right] = \mu^2 + {\sigma_0}^2 + \frac{\sigma^2}{n} \ ,$$

$$\begin{aligned}
\mathrm{E}\Big[\mathrm{var}\big[\{\mu_i\}_{i=1}^{n}\big]\Big] &= \mathrm{E}\left[\frac{1}{n}\sum_{i=1}^{n}\left(\mu_i - \frac{1}{n}\sum_{j=1}^{n}\mu_j\right)^2\right] \\
&= \frac{1}{n}\,\mathrm{E}\left[\sum_{i=1}^{n}{\mu_i}^2 - \frac{2}{n}\sum_{i=1}^{n}\sum_{j=1}^{n}\mu_i\,\mu_j + \frac{n}{n^2}\sum_{j=1}^{n}\sum_{k=1}^{n}\mu_j\,\mu_k\right] \\
&= \frac{1}{n}\left(\left(1-\frac{1}{n}\right)\sum_{i=1}^{n}\mathrm{E}[{\mu_i}^2] - \frac{1}{n}\sum_{i=1}^{n}\sum_{\substack{j=1\\ j\neq i}}^{n}\mathrm{E}[\mu_i\,\mu_j]\right) \\
&= \frac{1}{n}\left(\left(1-\frac{1}{n}\right)\,n\,\left(\mu^2+\sigma^2+{\sigma_0}^2\right) - \frac{1}{n}\,n\,(n-1)\,\left(\mu^2+{\sigma_0}^2\right)\right) \\
&= \frac{n-1}{n}\,\sigma^2 \ .
\end{aligned}$$

Such that

$$\mathrm{var}[\hat{\mu}] = {\sigma_0}^2 + \frac{\sigma^2}{n} \ ,$$

as one might expect with the global measurement systematic affecting our uncertainty in the mean position.

Constant source

If our source is an unknown constant, $\sigma = 0$, we can solve for

$$\hat{\mu} = \frac{\sum_{i=1}^{n} \sum_{j=1}^{n} \mu_i \, \Sigma^{-1}_{i\,j}}{\sum_{i=1}^{n} \sum_{j=1}^{n} \Sigma^{-1}_{i\,j}} \ ,$$

in the form of a correlated weighted mean.

Φ.4.8 Multinormal distribution with independent measurements

For an unknown multinormal distribution source with a set of independent multinormal distribution measurements the probability distribution function is

$$f\big(\{\vec{\mu_i}\}_{i=1}^{n} \,\big|\, \vec{\mu}, \Sigma, \{\Sigma_i\}_{i=1}^{n}\big) = \prod_{i=1}^{n} \left(\int_{-\vec{\infty}}^{\vec{\infty}} f_{\text{Normal}}\left(\vec{x_i} \,|\, \vec{\mu}, \Sigma\right) \, f_{\text{Normal}}\left(\vec{\mu_i} \,|\, \vec{x_i}, \Sigma_i\right) \, \mathrm{d}^d \vec{x_i} \right)$$

$$= \prod_{i=1}^{n} f_{\text{Normal}}\big(\vec{\mu_i} \,\big|\, \vec{\mu}, \Sigma + \Sigma_i\big)$$

$$= \mathcal{L}\big(\vec{\mu}, \Sigma \,\big|\, \{\vec{\mu_i}, \Sigma_i\}_{i=1}^{n}\big) \ ,$$

and hence the log likelihood function is

$$\log \mathcal{L} = \ -\frac{n\,d}{2} \, \log\left[2\,\pi\right] - \frac{1}{2} \sum_{i=1}^{n} \log\big[\det[\Sigma + \Sigma_i]\big] - \frac{1}{2} \sum_{i=1}^{n} \left(\vec{\mu_i} - \vec{\mu}\right)^{\mathsf{T}} \cdot \left(\Sigma + \Sigma_i\right)^{-1} \cdot \left(\vec{\mu_i} - \vec{\mu}\right) \ .$$

In total there are

$$\underbrace{d}_{\vec{\mu}} + \underbrace{\frac{d^2+d}{2}}_{\Sigma} = \frac{d^2+3\,d}{2}$$

parameters to find, where d is the length of the multinormal variate vector.

Clarifying some notation,

- $\vec{\mu}$ source distribution parameter list,
- μ_a source distribution parameter a,
- Σ source covariance matrix,
- $\vec{\mu_i}$ measurement i parameter list,
- $\mu_{i\,a}$ measurement i parameter a,
- Σ_i measurement i covariance matrix.

To compute the derivatives we'll need the matrix formulas (Φ.12), (Φ.13), and note that our symmetric covariance matrix Σ has $\frac{d^2+d}{2}$ unique entries, giving us

$$\frac{\partial}{\partial \Sigma_{a\,b}} \Sigma_{j\,k} = \frac{\delta_{a\,j}\,\delta_{b\,k} + \delta_{a\,k}\,\delta_{b\,j}}{1+\delta_{a\,b}} \ .$$

In component notation, the derivatives are

$$\frac{\partial}{\partial \mu_a} \log \mathcal{L} = \sum_{i=1}^{n} \sum_{j=1}^{d} \left(\mu_{i\,j} - \mu_j\right) \, (\Sigma + \Sigma_i)^{-1}_{j\,a} \ ,$$

$$\frac{\partial}{\partial \Sigma_{a\,b}} \log \mathcal{L} = \frac{1}{1 + \delta_{a\,b}} \sum_{i=1}^{n} \Bigg(- (\Sigma + \Sigma_i)^{-1}_{a\,b} + \left(\sum_{j=1}^{d} \left(\mu_{i\,j} - \mu_j\right) \, (\Sigma + \Sigma_i)^{-1}_{j\,a} \right) \left(\sum_{j=1}^{d} \left(\mu_{i\,j} - \mu_j\right) \, (\Sigma + \Sigma_i)^{-1}_{j\,b} \right) \Bigg)$$

$$\frac{\partial^2}{\partial \mu_a \, \partial \mu_b} \log \mathcal{L} = - \sum_{i=1}^{n} (\Sigma + \Sigma_i)^{-1}_{a\,b} \ ,$$

$$\begin{aligned} \frac{\partial^2}{\partial \Sigma_{a\,b} \, \partial \Sigma_{c\,d}} \log \mathcal{L} &= \frac{1}{(1 + \delta_{a\,b}) \, (1 + \delta_{c\,d})} \\ &\times \sum_{i=1}^{n} \Bigg((\Sigma + \Sigma_i)^{-1}_{a\,c} \, (\Sigma + \Sigma_i)^{-1}_{b\,d} + (\Sigma + \Sigma_i)^{-1}_{a\,d} \, (\Sigma + \Sigma_i)^{-1}_{b\,c} \\ &- \left(\sum_{j=1}^{d} \left(\mu_{i\,j} - \mu_j\right) \, (\Sigma + \Sigma_i)^{-1}_{j\,b} \right) \left(\sum_{j=1}^{d} \left(\mu_{i\,j} - \mu_j\right) \, (\Sigma + \Sigma_i)^{-1}_{j\,d} \right) (\Sigma + \Sigma_i)^{-1}_{a\,c} \\ &- \left(\sum_{j=1}^{d} \left(\mu_{i\,j} - \mu_j\right) \, (\Sigma + \Sigma_i)^{-1}_{j\,b} \right) \left(\sum_{j=1}^{d} \left(\mu_{i\,j} - \mu_j\right) \, (\Sigma + \Sigma_i)^{-1}_{j\,c} \right) (\Sigma + \Sigma_i)^{-1}_{a\,d} \\ &- \left(\sum_{j=1}^{d} \left(\mu_{i\,j} - \mu_j\right) \, (\Sigma + \Sigma_i)^{-1}_{j\,a} \right) \left(\sum_{j=1}^{d} \left(\mu_{i\,j} - \mu_j\right) \, (\Sigma + \Sigma_i)^{-1}_{j\,d} \right) (\Sigma + \Sigma_i)^{-1}_{b\,c} \\ &- \left(\sum_{j=1}^{d} \left(\mu_{i\,j} - \mu_j\right) \, (\Sigma + \Sigma_i)^{-1}_{j\,a} \right) \left(\sum_{j=1}^{d} \left(\mu_{i\,j} - \mu_j\right) \, (\Sigma + \Sigma_i)^{-1}_{j\,c} \right) (\Sigma + \Sigma_i)^{-1}_{b\,d} \Bigg) \ , \end{aligned}$$

$$\frac{\partial^2}{\partial\Sigma_{a\,b}\,\partial\mu_c}\log\mathcal{L} = \frac{-1}{1+\delta_{a\,b}}\sum_{i=1}^{n}\left(\left(\sum_{j=1}^{d}\left(\mu_{i\,j}-\mu_j\right)\left(\Sigma+\Sigma_i\right)^{-1}_{j\,a}\right)\left(\Sigma+\Sigma_i\right)^{-1}_{b\,c} + \left(\sum_{j=1}^{d}\left(\mu_{i\,j}-\mu_j\right)\left(\Sigma+\Sigma_i\right)^{-1}_{j\,b}\right)\left(\Sigma+\Sigma_i\right)^{-1}_{a\,c}\right) ,$$

or in vector notation where convenient,

$$\frac{\partial}{\partial\vec{\mu}}\log\mathcal{L} = \sum_{i=1}^{n}\left(\vec{\mu_i}-\vec{\mu}\right)^{\mathsf{T}}\cdot\left(\Sigma+\Sigma_i\right)^{-1} ,$$

$$\frac{\partial}{\partial\Sigma}\log\mathcal{L} = \sum_{i=1}^{n}\left(1-\frac{\mathrm{diag}}{2}\right)\left(\left(\left(\Sigma+\Sigma_i\right)^{-1}\cdot\left(\vec{\mu_i}-\vec{\mu}\right)\right)^{\otimes 2}-\left(\Sigma+\Sigma_i\right)^{-1}\right) .$$

The critical point occurs at

$$\hat{\vec{\mu}} = \left(\sum_{i=1}^{n}\left(\hat{\Sigma}+\Sigma_i\right)^{-1}\right)^{-1}\cdot\left(\sum_{i=1}^{n}\left(\hat{\Sigma}+\Sigma_i\right)^{-1}\cdot\vec{\mu_i}\right) ,$$

$$\sum_{i=1}^{n}\left(\hat{\Sigma}+\Sigma_i\right)^{-1} = \sum_{i=1}^{n}\left(\left(\hat{\Sigma}+\Sigma_i\right)^{-1}\cdot\left(\vec{\mu_i}-\hat{\vec{\mu}}\right)\right)^{\otimes 2} .$$

In the completely general case, the best approach is likely numerical maximization techniques on $\log\mathcal{L}$ using starting points from the next subsection.

The Fisher information matrix is going to be a $\frac{d^2+3\,d}{2}$ symmetric square matrix constructed from all the different pairwise parameter combinations. First computing

$$\mathrm{E}\left[\sum_{j=1}^{d}\sum_{k=1}^{d}\left(\mu_{i\,j}-\mu_j\right)\left(\mu_{i\,k}-\mu_k\right)\left(\Sigma+\Sigma_i\right)^{-1}_{j\,a}\left(\Sigma+\Sigma_i\right)^{-1}_{k\,b}\right] = \left(\Sigma+\Sigma_i\right)^{-1}_{a\,b} ,$$

we have

$$-\,\mathrm{E}\left[\frac{\partial^2}{\partial\mu_a\,\partial\mu_b}\log\mathcal{L}\right] \;=\; \sum_{i=1}^{n}\,(\Sigma+\Sigma_i)^{-1}_{a\,b}\;,$$

$$-\,\mathrm{E}\left[\frac{\partial^2}{\partial\Sigma_{a\,b}\,\partial\Sigma_{c\,d}}\log\mathcal{L}\right] = \frac{\sum_{i=1}^{n}\left((\Sigma+\Sigma_i)^{-1}_{a\,c}\,(\Sigma+\Sigma_i)^{-1}_{b\,d}+(\Sigma+\Sigma_i)^{-1}_{a\,d}\,(\Sigma+\Sigma_i)^{-1}_{b\,c}\right)}{(1+\delta_{a\,b})\,(1+\delta_{c\,d})}\;,$$

$$-\,\mathrm{E}\left[\frac{\partial^2}{\partial\Sigma_{a\,b}\,\partial\mu_c}\log\mathcal{L}\right] = 0\;.$$

The Cramér-Rao lower bound for unbiased estimators is

$$\mathrm{cov}\big[(\hat{\mu}_1,\ldots,\hat{\mu}_d,(\hat{\Sigma_{\mathrm{s}}})_{1\,1},\ldots,(\hat{\Sigma_{\mathrm{s}}})_{d\,d},(\hat{\Sigma_{\mathrm{s}}})_{1\,2},\ldots)\big] \geqslant \mathcal{I}(\mu_1,\ldots,\mu_d,\Sigma_{1\,1},\ldots,\Sigma_{d\,d},\Sigma_{1\,2},\ldots)^{-1}\;.$$

Applying (Φ.10) to the general measurement variance case, we can make a guess at an unbiased covariance estimator from a numerically calculated one as

$$\hat{\Sigma_{\mathrm{s}}} = \frac{n}{n-1}\,\hat{\Sigma} + \frac{\sum_{i=1}^{n}\Sigma_i}{n\,(n-1)}\;.$$

Expectations

Extending Sec. Φ.4.1 to higher order moments [315] within the context of many independent multinormal distributions,

$$\mathrm{E}[\mu_{i\,a}] = \mu_a \ ,$$

$$\mathrm{E}[\mu_{i\,a}\,\mu_{j\,b}] = \mu_a\,\mu_b + \delta_{i\,j}\,(\Sigma + \Sigma_i)_{a\,b} \ ,$$

$$\mathrm{E}[\mu_{i\,a}\,\mu_{j\,b}\,\mu_{k\,c}] = \mu_a\,\mu_b\,\mu_c + \delta_{i\,j}\,\mu_c\,(\Sigma + \Sigma_i)_{a\,b} + \delta_{j\,k}\,\mu_a\,(\Sigma + \Sigma_j)_{b\,c} + \delta_{i\,k}\,\mu_b\,(\Sigma + \Sigma_i)_{a\,c} \ ,$$

$$\begin{aligned}\mathrm{E}[\mu_{i\,a}\,\mu_{j\,b}\,\mu_{k\,c}\,\mu_{l\,d}] = {} & \mu_a\,\mu_b\,\mu_c\,\mu_d + \delta_{i\,j}\,\mu_c\,\mu_d\,(\Sigma + \Sigma_i)_{a\,b} + \delta_{j\,k}\,\mu_a\,\mu_d\,(\Sigma + \Sigma_j)_{b\,c} \\ & + \delta_{k\,l}\,\mu_a\,\mu_b\,(\Sigma + \Sigma_k)_{c\,d} + \delta_{i\,l}\,\mu_b\,\mu_c\,(\Sigma + \Sigma_i)_{a\,d} + \delta_{i\,k}\,\mu_b\,\mu_d\,(\Sigma + \Sigma_i)_{a\,c} \\ & + \delta_{j\,l}\,\mu_a\,\mu_c\,(\Sigma + \Sigma_j)_{b\,d} + \delta_{i\,j}\,\delta_{k\,l}\,(\Sigma + \Sigma_i)_{a\,b}\,(\Sigma + \Sigma_k)_{c\,d} \\ & + \delta_{i\,k}\,\delta_{j\,l}\,(\Sigma + \Sigma_i)_{a\,c}\,(\Sigma + \Sigma_j)_{b\,d} + \delta_{i\,l}\,\delta_{j\,k}\,(\Sigma + \Sigma_i)_{a\,d}\,(\Sigma + \Sigma_j)_{b\,c} \ .\end{aligned}$$

Some in vector notation,

$$\mathrm{E}[\vec{\mu_i}] = \vec{\mu} \ ,$$

$$\mathrm{E}[\vec{\mu_i} \otimes \vec{\mu_j}] = \vec{\mu} \otimes \vec{\mu} + \delta_{i\,j}\,(\Sigma + \Sigma_i) \ .$$

Identical measurement variance

If all our measurements exhibit the same known covariance $\Sigma_i = \Sigma_0$, we can solve the estimator equations to obtain

$$\hat{\vec{\mu}} = \frac{\sum_{i=1}^{n} \vec{\mu_i}}{n} \,,$$

$$\hat{\Sigma} = \frac{\sum_{i=1}^{n} \left(\vec{\mu_i} - \hat{\vec{\mu}}\right)^{\otimes 2}}{n} - \Sigma_0 \,.$$

Following similar calculations to Sec. Φ.3.4,

$$\mathrm{E}\big[\hat{\vec{\mu}}\big] = \vec{\mu} \,,$$

$$\begin{aligned}
\mathrm{E}\big[\hat{\Sigma} + \Sigma_0\big] &= \frac{1}{n} \sum_{i=1}^{n} \mathrm{E}\left[\vec{\mu_i} \otimes \vec{\mu_i} + \frac{1}{n^2} \sum_{j=1}^{n} \sum_{k=1}^{n} \vec{\mu_j} \otimes \vec{\mu_k} - \frac{1}{n} \sum_{j=1}^{n} \left(\vec{\mu_i} \otimes \vec{\mu_j} + \vec{\mu_j} \otimes \vec{\mu_i}\right)\right] , \\
&= \frac{1}{n} \sum_{i=1}^{n} \left(\vec{\mu} \otimes \vec{\mu} + \left(\Sigma + \Sigma_0\right) + \vec{\mu} \otimes \vec{\mu} + \frac{1}{n}\left(\Sigma + \Sigma_0\right) - 2\,\vec{\mu} \otimes \vec{\mu} - \frac{2}{n}\left(\Sigma + \Sigma_0\right)\right) , \\
&= \frac{n-1}{n}\left(\Sigma + \Sigma_0\right) \,,
\end{aligned}$$

we derive an unbiased sample covariance estimator

$$\left(\hat{\Sigma_{\mathrm{s}}} + \Sigma_0\right) = \frac{n}{n-1}\left(\hat{\Sigma} + \Sigma_0\right) \tag{Φ.10}$$

$$\Rightarrow \quad \hat{\Sigma_{\mathrm{s}}} = \frac{\sum_{i=1}^{n} \left(\vec{\mu_i} - \hat{\vec{\mu}}\right)^{\otimes 2}}{n-1} - \Sigma_0 \,.$$

The covariance matrix for $\hat{\vec{\mu}}$ is

$$\operatorname{cov}\left[\hat{\vec{\mu}}\right] = \frac{\Sigma + \Sigma_0}{n} \,, \qquad\qquad \operatorname{cov}\left[\hat{\mu}_a, \hat{\mu}_b\right] = \frac{(\Sigma + \Sigma_0)_{a\,b}}{n} \,,$$

and the element-wise covariance for $\hat{\Sigma}_\mathrm{s}$ is

$$\operatorname{cov}\left[(\hat{\Sigma}_\mathrm{s})_{a\,b}, (\hat{\Sigma}_\mathrm{s})_{c\,d}\right] = \frac{(\Sigma + \Sigma_0)_{a\,c}\,(\Sigma + \Sigma_0)_{b\,d} + (\Sigma + \Sigma_0)_{a\,d}\,(\Sigma + \Sigma_0)_{b\,c}}{n-1} \,.$$

Constant source

For $\Sigma = 0$, we find the weighted mean

$$\hat{\vec{\mu}} = \left(\sum_{i=1}^{n} \Sigma_i^{-1}\right)^{-1} \cdot \left(\sum_{i=1}^{n} \Sigma_i^{-1} \cdot \vec{\mu_i}\right) \,,$$

with covariance matrix

$$\operatorname{cov}\left[\hat{\vec{\mu}}\right] = \left(\sum_{i=1}^{n} \Sigma_i^{-1}\right)^{-1} \,.$$

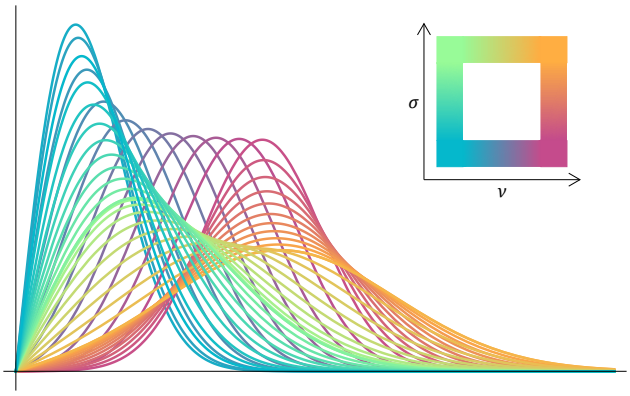

Figure Φ.5: Rice distribution probability density plots for varying amplitude and standard deviation.

Φ.5 Rice distribution

The Rice distribution is a positive only distribution for the radius within a two-dimensional normal distribution. For a Rician distributed variable

$$R \sim \text{Rice}[\nu, \sigma] \quad : \quad \underbrace{\nu}_{\text{Amplitude}} > 0 \,, \quad \underbrace{\sigma}_{\substack{\text{Standard} \\ \text{deviation}}} > 0 \,,$$

the probability distribution function (depicted in Fig. Φ.5) is

$$f_{\text{Rice}}\left(r \,|\, \nu, \sigma\right) = \frac{r}{\sigma^2} \, \exp\left[-\frac{\left(r^2 + \nu^2\right)}{2\,\sigma^2}\right] \, I_0\left[\frac{r\,\nu}{\sigma^2}\right] \quad : \quad r > 0 \,,$$

where I is the modified Bessel function of the first kind.

Φ.5.1 I/Q measurements

When measuring in-phase, $I(t)$, and quadrature, $Q(t)$, signals, it's often the amplitude $A(t)$ we actually care about. If there is normally distributed noise in the voltage signal $V(t)$, this will carry over to the in-phase $I(t)$ and quadrature $Q(t)$ measurements. The amplitude

however, being restricted to positive reals, will only be normally distributed when the mean is several standard deviations away from zero, i.e. large amplitudes or asymptotically infinite samples. When taking a series of small amplitude measurements they need to be analyzed using a Rice distribution[6].

Φ.5.2 Derivation

The Rice distribution can be derived from a two-dimensional Normal distribution situated at (μ_x, μ_y) with uniform standard deviation σ,

$$\begin{aligned} f\left(x, y \,|\, \mu_x, \mu_y, \sigma\right) &= f_{\text{Normal}}\left(x \,|\, \mu_x, \sigma\right)\ f_{\text{Normal}}\left(y \,|\, \mu_y, \sigma\right) \\ &= \frac{1}{2\,\pi\,\sigma^2}\ \exp\left[-\frac{(x-\mu_x)^2}{2\,\sigma^2} - \frac{(y-\mu_y)^2}{2\,\sigma^2}\right] . \end{aligned}$$

Switching to polar coordinates,

$$\begin{aligned} x &= r\ \cos[\phi] , & \mu_x &= \nu\ \cos[\theta] , \\ y &= r\ \sin[\phi] , & \mu_y &= \nu\ \sin[\theta] , \end{aligned}$$

we get

$$f\left(r, \phi \,|\, \nu, \theta, \sigma\right) = \frac{1}{2\,\pi\,\sigma^2}\ \exp\left[-\frac{\left(r^2+\nu^2\right)}{2\,\sigma^2}\right]\ \exp\Big[-2\,r\,\nu\ \cos[\theta-\phi]\Big] .$$

6. If the series of measurements have constant phase ϕ, then $I(t)$ and $Q(t)$ are perfectly correlated, and can be analyzed separately according to normal distributions with the results being combined to give an amplitude $A(t)$.

Marginalizing out the phase with $\int_0^{2\,\pi} r\,\mathrm{d}\phi$ and using

$$\int_0^{2\,\pi} \exp\Big[-2\,r\,\nu\,\cos[\theta-\phi]\Big]\,\mathrm{d}\phi = 2\,\pi\,I_0\left[\frac{r\,\nu}{\sigma^2}\right]\ ,$$

where I is the modified Bessel function of the first kind, gives us the Rice probability distribution function

$$f\underset{\text{Rice}}{(r\,|\,\nu,\sigma)} = \frac{r}{\sigma^2}\,\exp\left[-\frac{\left(r^2+\nu^2\right)}{2\,\sigma^2}\right]\,I_0\left[\frac{r\,\nu}{\sigma^2}\right]\ .$$

Φ.5.3 Expectations

Computing some expectation values for $R \sim \text{Rice}[\nu,\sigma]$,

$$\begin{aligned}
\mathrm{E}\left[R\right] &= \frac{\sqrt{\pi/2}}{2\,\sigma}\,\exp\left[\frac{-\nu^2}{4\,\sigma^2}\right]\left(\nu^2\,I_1\left[\frac{\nu^2}{4\,\sigma^2}\right]+(\nu^2+2\,\sigma^2)\,I_0\left[\frac{\nu^2}{4\,\sigma^2}\right]\right)\ ,\\
\mathrm{E}\left[R^2\right] &= \nu^2+2\,\sigma^2\ ,\\
\mathrm{E}\left[R\,\frac{I_1\left[\frac{R\,\nu}{\sigma^2}\right]}{I_0\left[\frac{R\,\nu}{\sigma^2}\right]}\right] &= \nu\ ,\\
\mathrm{E}\left[\left(R\,\frac{I_1\left[\frac{R\,\nu}{\sigma^2}\right]}{I_0\left[\frac{R\,\nu}{\sigma^2}\right]}\right)^2\right] &= \int_0^\infty \frac{r^3}{\sigma^2}\,\exp\left[-\frac{\left(r^2+\nu^2\right)}{2\,\sigma^2}\right]\,\frac{I_1\left[\frac{r\,\nu}{\sigma^2}\right]^2}{I_0\left[\frac{r\,\nu}{\sigma^2}\right]}\,\mathrm{d}r = \zeta(\nu,\sigma)^2\ ,
\end{aligned}$$

where $\zeta(\nu,\sigma)$ has to be computed numerically for a particular ν and σ, or approximated with $\zeta(\hat{\nu},\hat{\sigma}) \approx \hat{\gamma}$ defined in (Φ.11).

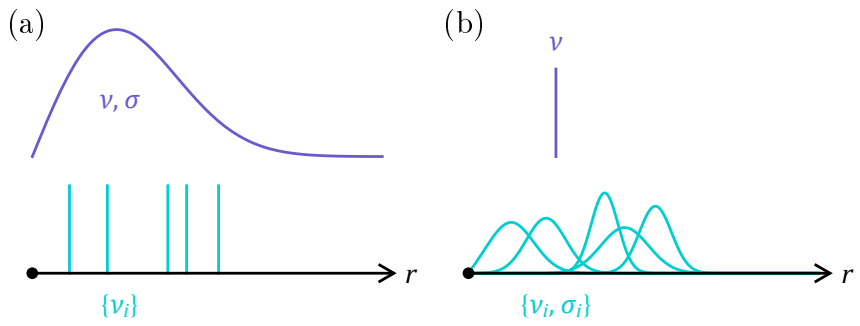

Figure Φ.6: Considered measurement scenarios involving Rice distributions. (a) Rice distribution source that is sampled with precise measurements. (b) A constant with Rician distributed measurement attempts.

Φ.5.4 Rice distribution in measurements

The convolution of two Rician distributions is not easily computable so we will stick with the cases of exact measurements or constant source, as shown in Fig. Φ.6.

Exact measurements

The combined probability distribution for n precise measurements of a source Rice$[\nu, \sigma]$, as depicted in Fig. Φ.6 (a), is

$$f\left(\{\nu_i\}_{i=1}^n \,|\, \nu, \sigma\right) = \prod_{i=1}^{n} \frac{\nu_i}{\sigma^2} \exp\left[-\frac{\left(\nu_i^2 + \nu^2\right)}{2\,\sigma^2}\right] I_0\left[\frac{\nu_i\,\nu}{\sigma^2}\right] \,.$$

Employing maximum likelihood methods, the likelihood function for μ, σ is

$$\mathcal{L}\big(\nu, \sigma \,|\, \{\nu_i\}_{i=1}^n\big) = f\big(\{\nu_i\}_{i=1}^n \,|\, \nu, \sigma\big) \,,$$

and maximizing the likelihood function is equivalent to maximizing the logarithm

$$\log \mathcal{L} = -2\,n\,\log\left[\sigma\right] + \sum_{i=1}^{n} \log\left[\nu_i\right] - \frac{1}{2\,\sigma^2}\,\sum_{i=1}^{n} \nu_i^2 - \frac{n\,\nu^2}{2\,\sigma^2} + \sum_{i=1}^{n} \log\left[I_0\left[\frac{\nu_i\,\nu}{\sigma^2}\right]\right] .$$

The derivatives are

$$\frac{\partial}{\partial \nu} \log \mathcal{L} = \; - \frac{n\,\nu}{\sigma^2} + \frac{1}{\sigma^2}\,\sum_{i=1}^{n} \nu_i\,\frac{I_1\left[\frac{\nu_i\,\nu}{\sigma^2}\right]}{I_0\left[\frac{\nu_i\,\nu}{\sigma^2}\right]} ,$$

$$\frac{\partial}{\partial \sigma} \log \mathcal{L} = \; - \frac{2\,n}{\sigma} + \frac{1}{\sigma^3}\,\sum_{i=1}^{n} \nu_i^2 + \frac{n\,\nu^2}{\sigma^3} - \frac{2\,\nu}{\sigma^3}\,\sum_{i=1}^{n} \nu_i\,\frac{I_1\left[\frac{\nu_i\,\nu}{\sigma^2}\right]}{I_0\left[\frac{\nu_i\,\nu}{\sigma^2}\right]} ,$$

$$\frac{\partial^2}{\partial \nu^2} \log \mathcal{L} = \; - \frac{n}{\sigma^2} + \frac{1}{\sigma^4}\,\sum_{i=1}^{n} {\nu_i}^2 - \frac{1}{\nu\,\sigma^2}\,\sum_{i=1}^{n} \nu_i\,\frac{I_1\left[\frac{\nu_i\,\nu}{\sigma^2}\right]}{I_0\left[\frac{\nu_i\,\nu}{\sigma^2}\right]} - \frac{1}{\sigma^4}\,\sum_{i=1}^{n} \left(\nu_i\,\frac{I_1\left[\frac{\nu_i\,\nu}{\sigma^2}\right]}{I_0\left[\frac{\nu_i\,\nu}{\sigma^2}\right]}\right)^2 ,$$

$$\begin{aligned}\frac{\partial^2}{\partial \sigma^2} \log \mathcal{L} = \frac{2\,n}{\sigma^2} - \frac{3}{\sigma^4}\,\sum_{i=1}^{n} {\nu_i}^2 - \frac{3\,n\,\nu^2}{\sigma^4} + \frac{4\,\nu^2}{\sigma^6}\,\sum_{i=1}^{n} {\nu_i}^2 + \frac{2\,\nu}{\sigma^4}\,\sum_{i=1}^{n} \nu_i\,\frac{I_1\left[\frac{\nu_i\,\nu}{\sigma^2}\right]}{I_0\left[\frac{\nu_i\,\nu}{\sigma^2}\right]} \\ - \frac{4\,\nu^2}{\sigma^6}\,\sum_{i=1}^{n} \left(\nu_i\,\frac{I_1\left[\frac{\nu_i\,\nu}{\sigma^2}\right]}{I_0\left[\frac{\nu_i\,\nu}{\sigma^2}\right]}\right)^2 ,\end{aligned}$$

$$\frac{\partial^2}{\partial \mu\,\partial \sigma} \log \mathcal{L} = \frac{2\,n\,\nu}{\sigma^3} - \frac{2\,\nu}{\sigma^5}\,\sum_{i=1}^{n} {\nu_i}^2 + \frac{2\,\nu}{\sigma^5}\,\sum_{i=1}^{n} \left(\nu_i\,\frac{I_1\left[\frac{\nu_i\,\nu}{\sigma^2}\right]}{I_0\left[\frac{\nu_i\,\nu}{\sigma^2}\right]}\right)^2 ,$$

where we have made use of

$$\frac{\partial}{\partial x} I_a[x] = \frac{1}{2}\Big(I_{a-1}[x] + I_{a+1}[x]\Big) , \qquad \frac{a}{x}\,I_a[x] = \frac{1}{2}\Big(I_{a-1}[x] - I_{a+1}[x]\Big) .$$

Taking $\frac{\partial}{\partial\nu}\log\mathcal{L} = \frac{\partial}{\partial\sigma}\log\mathcal{L} = 0$, the critical point at $\hat{\nu},\hat{\sigma}$ satisfies

$$\frac{1}{n}\sum_{i=1}^{n}\nu_i\,\frac{I_1\left[\frac{\nu_i\,\hat{\nu}}{\hat{\sigma}^2}\right]}{I_0\left[\frac{\nu_i\,\hat{\nu}}{\hat{\sigma}^2}\right]} = \hat{\nu}\;, \qquad\qquad \frac{1}{n}\sum_{i=1}^{n}{\nu_i}^2 = \hat{\nu}^2 + 2\,\hat{\sigma}^2\;.$$

To check this is a maximum we can look at the second derivatives,

$$\frac{\partial^2}{\partial\nu^2}\log\mathcal{L}\Big|_{\substack{\nu=\hat{\nu}\\ \sigma=\hat{\sigma}}} = \frac{n}{\hat{\sigma}^4}\,\left(\hat{\nu}^2 - \hat{\gamma}^2\right)\;,$$

$$\frac{\partial^2}{\partial\sigma^2}\log\mathcal{L}\Big|_{\substack{\nu=\hat{\nu}\\ \sigma=\hat{\sigma}}} = \frac{4\,\hat{\nu}^2\,n}{\hat{\sigma}^6}\,\left(\hat{\nu}^2 + \hat{\sigma}^2 - \hat{\gamma}^2 - \frac{\hat{\sigma}^4}{\hat{\nu}^2}\right)\;,$$

$$\frac{\partial^2}{\partial\mu\,\partial\sigma}\log\mathcal{L}\Big|_{\substack{\nu=\hat{\nu}\\ \sigma=\hat{\sigma}}} = \frac{2\,\hat{\nu}\,n}{\hat{\sigma}^5}\,\left(\hat{\gamma}^2 - \hat{\nu}^2 - \hat{\sigma}^2\right)\;,$$

where we have defined

$$\hat{\gamma}^2 = \frac{1}{n}\sum_{i=1}^{n}\left(\nu_i\,\frac{I_1\left[\frac{\nu_i\,\hat{\nu}}{\hat{\sigma}^2}\right]}{I_0\left[\frac{\nu_i\,\hat{\nu}}{\hat{\sigma}^2}\right]}\right)^2\;. \tag{Φ.11}$$

Computing the determinant of the Hessian,

$$\det[\hat{\mathcal{H}}] = \left(\frac{\partial^2}{\partial\nu^2}\log\mathcal{L}\right)\left(\frac{\partial^2}{\partial\sigma^2}\log\mathcal{L}\right) - \left(\frac{\partial^2}{\partial\mu\,\partial\sigma}\log\mathcal{L}\right)^2\Bigg|_{\substack{\nu=\hat{\nu}\\ \sigma=\hat{\sigma}}}$$

$$= \frac{4\,\hat{\nu}^2\,n^2}{\hat{\sigma}^8}\,\left(\hat{\gamma}^2 - \hat{\nu}^2 - 2\,\hat{\sigma}^2 + \frac{\hat{\gamma}^2\,\hat{\sigma}^2}{\hat{\nu}^2}\right)\;,$$

appears to require a numeric approach to confirm that $\det[\mathcal{H}] > 0$, indicating $\hat{\nu},\hat{\sigma}$ is an

extrema (not a saddle point). By Cauchy-Schwarz,

$$\underbrace{\left(\sum_{i=1}^{n}\frac{\nu_i}{n}\frac{I_1\left[\frac{\nu_i\,\hat{\nu}}{\hat{\sigma}^2}\right]}{I_0\left[\frac{\nu_i\,\hat{\nu}}{\hat{\sigma}^2}\right]}\right)^2}_{\hat{\nu}^2} \leqslant \underbrace{\left(\sum_{i=1}^{n}1^2\right)}_{n}\underbrace{\left(\sum_{i=1}^{n}\left(\frac{\nu_i}{n}\frac{I_1\left[\frac{\nu_i\,\hat{\nu}}{\hat{\sigma}^2}\right]}{I_0\left[\frac{\nu_i\,\hat{\nu}}{\hat{\sigma}^2}\right]}\right)^2\right)}_{\hat{\gamma}^2/n} \quad \Rightarrow \quad \hat{\nu}^2 < \hat{\gamma}^2\,,$$

we can easily check that $\frac{\partial^2}{\partial\nu^2}\log\mathcal{L} < 0$, indicating a maximum (assuming $\det[\mathcal{H}] > 0$).

To find the estimators $\hat{\nu}, \hat{\sigma}$ from our data set $\{r_i\}_{i=1}^n$ we start by finding the second raw moment

$$\mu_2' = \frac{1}{n}\sum_{i=1}^{n}{\nu_i}^2\,,$$

and numerically solve the equation for $\hat{\nu}$

$$\sum_{i=1}^{n}\nu_i\frac{I_1\left[\frac{2\,\nu_i\,\hat{\nu}}{\mu_2'-\hat{\nu}^2}\right]}{I_0\left[\frac{2\,\nu_i\,\hat{\nu}}{\mu_2'-\hat{\nu}^2}\right]} - n\,\hat{\nu} = 0\,.$$

Then

$$\hat{\sigma} = \sqrt{\frac{\mu_2'-\hat{\nu}^2}{2}}\,.$$

Using expectations given earlier and the second derivatives at the critical point, the Fisher information matrix is

$$\mathcal{I}(\mu,\sigma) = -\,\mathrm{E}\left[\hat{\mathcal{H}}\right] = \begin{pmatrix} -\frac{n}{\sigma^4}\,\left(\nu^2-\zeta(\nu,\sigma)^2\right) & -\frac{2\,\nu\,n}{\sigma^5}\,\left(\zeta(\nu,\sigma)^2-\nu^2-\sigma^2\right) \\ -\frac{2\,\nu\,n}{\sigma^5}\,\left(\zeta(\nu,\sigma)^2-\nu^2-\sigma^2\right) & -\frac{4\,\nu^2\,n}{\sigma^6}\,\left(\nu^2+\sigma^2-\zeta(\nu,\sigma)^2-\frac{\sigma^4}{\nu^2}\right) \end{pmatrix}.$$

The covariance matrix Cramér-Rao lower bound is then

$$\begin{aligned}\operatorname{cov}\left[(\hat{\mu},\hat{\sigma})\right] &\geqslant \mathcal{I}(\mu,\sigma)^{-1} \\ &= \frac{\sigma^2}{4\,n}\,\frac{\begin{pmatrix} -4\,\nu^2\,\left(\nu^2+\sigma^2-\zeta(\nu,\sigma)^2-\frac{\sigma^4}{\nu^2}\right) & 2\,\nu\,\sigma\,\left(\zeta(\nu,\sigma)^2-\nu^2-\sigma^2\right) \\ 2\,\nu\,\sigma\,\left(\zeta(\nu,\sigma)^2-\nu^2-\sigma^2\right) & -\sigma^2\,\left(\nu^2-\zeta(\nu,\sigma)^2\right) \end{pmatrix}}{\nu^2\,\zeta(\nu,\sigma)^2-\nu^4-2\,\nu^2\,\sigma^2+\sigma^2\,\zeta(\nu,\sigma)^2}\,,\end{aligned}$$

if $\hat{\nu}$ and $\hat{\sigma}$ are unbiased.

Unfortunately, because $\hat{\nu}$ is found from a transcendental equation, estimating the bias is not straight-forward. The bias on $\hat{\sigma}^2$ depends on the $\hat{\nu}^2$ bias as

$$\mathrm{E}\left[\hat{\sigma}^2\right]-\sigma^2=-\frac{1}{2}\,\left(\mathrm{E}\left[\hat{\nu}^2\right]-\nu^2\right)\,.$$

If $\hat{\nu}$ is close to zero then the estimator pair of equations become degenerate to

$$\frac{1}{n}\,\sum_{i=1}^{n}{\nu_i}^2=2\,\hat{\sigma}^2\,,$$

and we lose information about $\hat{\nu}$, also seen by $\mathcal{I}$ becoming singular. In this case the likelihood function can not be approximated by a Gaussian near its maximum (due to $\nu>0$ condition) and the Fisher Information matrix is not usable, instead direct interrogation of the likelihood function is needed.

Constant source

For a constant source of unknown amplitude ν, and n measurements with distribution Rice$[\nu_i,\sigma_i]$, as depicted in Fig. Φ.6 (b), the combined probability distribution and likeli-

hood function is

$$f\left(\{\nu_i\}_{i=1}^n \,|\, \nu, \{\sigma_i\}_{i=1}^n\right) = \prod_{i=1}^n \frac{\nu_i}{{\sigma_i}^2} \exp\left[-\frac{\left({\nu_i}^2+\nu^2\right)}{2\,{\sigma_i}^2}\right] I_0\left[\frac{\nu_i\,\nu}{{\sigma_i}^2}\right] = \mathcal{L}\big(\nu \,|\, \{\nu_i, \sigma_i\}_{i=1}^n\big) \,.$$

The derivatives are

$$\frac{\partial}{\partial\nu}\log\mathcal{L} = -\sum_{i=1}^n \frac{\nu}{{\sigma_i}^2} + \sum_{i=1}^n \frac{\nu_i}{{\sigma_i}^2} \frac{I_1\left[\frac{\nu_i\,\nu}{{\sigma_i}^2}\right]}{I_0\left[\frac{\nu_i\,\nu}{{\sigma_i}^2}\right]} \,,$$

$$\frac{\partial^2}{\partial\nu^2}\log\mathcal{L} = -\sum_{i=1}^n \frac{1}{{\sigma_i}^2} + \sum_{i=1}^n \frac{{\nu_i}^2}{{\sigma_i}^4} - \frac{1}{\nu}\sum_{i=1}^n \frac{\nu_i}{{\sigma_i}^2} \frac{I_1\left[\frac{\nu_i\,\nu}{{\sigma_i}^2}\right]}{I_0\left[\frac{\nu_i\,\nu}{{\sigma_i}^2}\right]} - \sum_{i=1}^n \left(\frac{\nu_i}{{\sigma_i}^2} \frac{I_1\left[\frac{\nu_i\,\nu}{{\sigma_i}^2}\right]}{I_0\left[\frac{\nu_i\,\nu}{{\sigma_i}^2}\right]}\right)^2 \,.$$

At the critical point, $\frac{\partial}{\partial\nu}\log\mathcal{L} = 0$, we have

$$\hat{\nu} = \frac{\displaystyle\sum_{i=1}^n \frac{\nu_i}{{\sigma_i}^2} \frac{I_1\left[\frac{\nu_i\,\hat{\nu}}{{\sigma_i}^2}\right]}{I_0\left[\frac{\nu_i\,\hat{\nu}}{{\sigma_i}^2}\right]}}{\displaystyle\sum_{i=1}^n \frac{1}{{\sigma_i}^2}} \,,$$

a weighted Rician amplitude.

The second derivative at this point is

$$\frac{\partial^2}{\partial\nu^2}\log\mathcal{L}\Big|_{\substack{\nu=\hat{\nu}\\ \sigma=\hat{\sigma}}} = \sum_{i=1}^n \frac{{\nu_i}^2 - 2\,{\sigma_i}^2 - \left(\nu_i \dfrac{I_1\left[\frac{\nu_i\,\hat{\nu}}{{\sigma_i}^2}\right]}{I_0\left[\frac{\nu_i\,\hat{\nu}}{{\sigma_i}^2}\right]}\right)^2}{{\sigma_i}^4} \,,$$

which requires numerics to check if less than zero away from asymptotic limits $\nu_i \lesseqgtr \sigma_i$. The

Fisher information is

$$\mathcal{I}(\nu) = -\,\mathrm{E}\left[\frac{\partial^2}{\partial \nu^2}\log \mathcal{L}\right] = -\sum_{i=1}^{n} \frac{\nu^2 - \zeta(\nu,\sigma_i)^2}{{\sigma_i}^4}\ ,$$

which gives the Cramér-Rao lower bound

$$\mathrm{var}[\hat{\nu}] \geqslant \mathcal{I}(\nu)^{-1} = \frac{1}{\sum\limits_{i=1}^{n} \dfrac{\zeta(\nu,\sigma_i)^2 - \nu^2}{{\sigma_i}^4}}\ ,$$

if $\hat{\nu}$ is unbiased.

Φ.5.5 Normal limit

If the amplitude is significantly far from zero, $\nu \gg \sigma$, the distribution can be approximated by a normal. Within various parts of the measurement analysis this can be observed by applying [316]

$$\lim_{x\to\infty} \frac{I_1[x]}{I_0[x]} = 1\ .$$

For the distribution function we can use

$$I_0[x] \overset{x\sim\infty}{\approx} \frac{\mathrm{e}^x}{\sqrt{2\,\pi\,x}}\ ,$$

to get

$$f_{\text{Rice}}\left(r \,|\, \nu, \sigma\right) \overset{\nu \gg \sigma}{\approx} \frac{r}{\sigma^2} \exp\left[-\frac{\left(r^2+\nu^2\right)}{2\,\sigma^2}\right] \frac{\sigma}{\sqrt{2\,\pi\,\nu\,r}} \exp\left[\frac{r\,\nu}{\sigma^2}\right]$$
$$= \sqrt{\frac{r}{\nu}} \frac{1}{\sqrt{2\,\pi}\,\sigma} \exp\left[-\frac{(r-\nu)^2}{2\,\sigma^2}\right] ,$$

which is resemblant of the normal distribution if $r \approx \nu$.

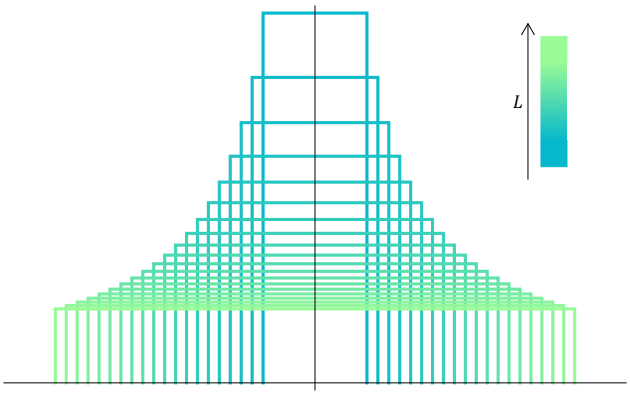

Figure Φ.7: Uniform distribution probability density plots for varying length.

Φ.6 Uniform distribution

Often, when dealing with discrete measurements, our uncertainty is best modelled by a uniform distribution, a simple example is pixels in image.

A uniform random variable has

$$X \sim \text{Uniform}[\mu - L/2, \mu + L/2] \quad : \quad \underbrace{\mu}_{\text{Center}} \in \mathbb{R}\,, \quad \underbrace{L}_{\text{Length}} > 0\,,$$

and probability distribution function[7] (depicted in Fig. Φ.7)

$$\begin{aligned} f_{\text{Uniform}}(x \,|\, \mu, L) &= \frac{\Theta[x - (\mu - L/2)] - \Theta[x - (\mu + L/2)]}{L} \\ &= \begin{cases} 1/L & : \ \mu - L/2 < x < \mu + L/2 \\ 0 & : \ \big(x < \mu - L/2\big) \vee \big(x > \mu + L/2\big) \end{cases}, \end{aligned}$$

and for consistency with other functions is $1/(2\,L)$ for exactly $x = \mu \pm L/2$.

7. Where Θ is Heaviside Theta.

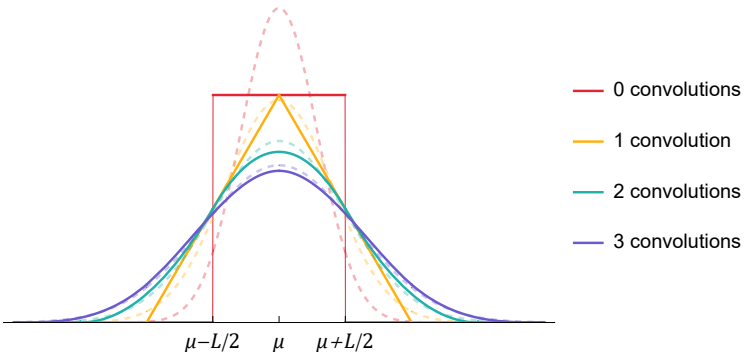

Figure Φ.8: Convolutions of uniform distributions with length L and the approximate normal distribution equivalent dashed.

Φ.6.1 Expectations

The uniform distribution has

$$\mathrm{E}[X] = \mu \,, \qquad\qquad \mathrm{var}[X] = \frac{L^2}{12} \,.$$

Φ.6.2 Convolutions

When we start using uniform distributions we inevitably start convolving them together. The convolution of two uniform distributions is a triangular or trapezium distribution, and thanks to the central limit theorem, after a few more tends toward the normal distribution [317–319]. In particular, if all the uniform distributions have equal length this happens within three to four convolutions, as depcited in Fig. Φ.8. Thus, we can arrive at the same results by approximating our uniform distributions as normal distributions with equal variance,

$$\mathrm{Uniform}[\mu - L/2, \mu + L/2] \approx \mathrm{Normal}[\mu, L/\sqrt{12}]$$

after a few convolutions.

Equivalently, in 'plus/minus' notation, we can write

$$x \underset{\text{Uniform}}{\pm} a \qquad \approx \qquad x \underset{\text{Normal}}{\pm} \frac{a}{\sqrt{3}} \,,$$

where $L = 2\,a$.

$\Phi.7$ Formulas

Some formulas used in derivations.

Derivative of matrix inverse,

$$\frac{\mathrm{d}}{\mathrm{d}x}\, \underline{\underline{A}}(x)^{-1} = -\underline{\underline{A}}(x)^{-1} \cdot \frac{\mathrm{d}}{\mathrm{d}x}\, \underline{\underline{A}}(x) \cdot \underline{\underline{A}}(x)^{-1} \,. \tag{Φ.12}$$

Jacobi's Formula,

$$\frac{\mathrm{d}}{\mathrm{d}x}\, \det\left[\underline{\underline{A}}(x)\right] = \det\left[\underline{\underline{A}}(x)\right]\, \mathrm{tr}\left[\underline{\underline{A}}(x)^{-1} \cdot \frac{\mathrm{d}}{\mathrm{d}x}\, \underline{\underline{A}}(x)\right] \,, \tag{Φ.13}$$

if $\underline{\underline{A}}(x)$ is invertible.

Inverse of constant plus identity matrix,

$$\left(a\, \underline{\underline{1_n}} + b\, \underline{\underline{\mathbb{I}_n}}\right)^{-1} = \frac{-1}{n\, b + \frac{b^2}{a}}\, \underline{\underline{1_n}} + \frac{1}{b}\, \underline{\underline{\mathbb{I}_n}} \,, \tag{Φ.14}$$

where $\underline{\underline{1_n}}$ is a $n \times n$ matrix of ones. Proof via ansatz and $\underline{\underline{1_n}}^2 = n\, \underline{\underline{1_n}}$.

APPENDIX Ψ

Multivariate fitting

Given a multivariate function of the form

$$\begin{aligned}
\hat{\vec{y}} : \mathbb{R}^{d_1} &\longrightarrow \mathbb{R}^{d_2} \\
\vec{x} &\longmapsto \vec{y} = \underline{\underline{B^{\mathsf{T}}}} \cdot \vec{x} \\
\{x_i\}_{i=1}^{d_1} &\longmapsto \{y_j = \textstyle\sum_{i=1}^{d_1} B^{\mathsf{T}}{}_{j\,i}\, x_i\}_{j=1}^{d_2}
\end{aligned}$$

the fit with a set of data points (independent-dependent variable pairs) $\{\vec{x}_k, \vec{y}_k\}$ can be flattened to a multivariable fit as follows

$$\begin{aligned}
\hat{\underline{\underline{Y}}} : \textstyle\bigoplus_{k=1}^{n} \mathbb{R}^{d_1} &\longrightarrow \textstyle\bigoplus_{k=1}^{n} \mathbb{R}^{d_2} \\
\underline{\underline{X}} &\longmapsto \underline{\underline{Y}} = \underline{\underline{X}} \cdot \underline{\underline{B}} \\
\{x_{k\,i}\}_{k=1,\,i=1}^{n,\,d_1} &\longmapsto \{y_{k\,j} = \textstyle\sum_{i=1}^{d_1} x_{k\,i}\, B_{i\,j}\}_{k=1,\,j=1}^{n,\,d_2} \\
&\Big\downarrow \mathcal{F} \\
\hat{\underline{y}}\,' : \textstyle\bigoplus_{\alpha=1}^{n\times d_2} \mathbb{R}^{d_1\times d_2} &\longrightarrow \mathbb{R}^{n\times d_2} \\
\underline{\underline{X}}\,' &\longmapsto \underline{y}\,' = \underline{\underline{X}}\,' \cdot \underline{b}\,' \\
\{x'_{\alpha\,\beta}\}_{\alpha=1,\,\beta=1}^{n\times d_2,\,d_1\times d_2} &\longmapsto \{y'_\alpha = \textstyle\sum_{\beta=1}^{d_1\times d_2} x'_{\alpha\,\beta}\, b'_\beta\}_{\alpha=1}^{n\times d_2}
\end{aligned}$$

If $\underline{b}\,'$ is the list of parameters, then this is a linear model with design matrix $\underline{\underline{X}}\,'$ and response $\underline{y}\,'$.

The new vectors and matrix are obtained by flattening or rearranging,

$$
\begin{aligned}
X'_{\alpha\,\beta} &= x_{\,(\alpha\,\mathrm{quot}_1\,d_2\,+1)\;(\beta\,\mathrm{mod}_1\,d_1)}\;\delta_{\,(\alpha\,\mathrm{mod}_1\,d_2)\;(\beta\,\mathrm{quot}_1\,d_1\,+1)}\;, \\
y'_{\alpha} &= y_{\,(\alpha\,\mathrm{quot}_1\,d_2\,+1)\;(\alpha\,\mathrm{mod}_1\,d_2)}\;, \\
b'_{\beta} &= B_{\,(\beta\,\mathrm{quot}_1\,d_2\,+1)\;(\beta\,\mathrm{mod}_1\,d_2)}\;,
\end{aligned}
$$

where $m\,\mathrm{quot}_w\,n$ is quotient operator with offset w such that it returns $z\;:\;w \leqslant m - n\,z < w + n$, and $m\,\mathrm{mod}_w\,n$ is modulus operator with offset w such that it returns $z\;:\;w \leqslant z < w + n$.

For consistency, the indices follow

$$
\begin{aligned}
i\;&\in [1, d_1] \subset \mathbb{Z} && \text{coordinate in } \mathbb{R}^{d_1}\;, \\
j\;&\in [1, d_2] \subset \mathbb{Z} && \text{coordinate in } \mathbb{R}^{d_2}\;, \\
k\;&\in [1, n] \subset \mathbb{Z} && \text{data point number}\;, \\
\alpha\;&\in [1, n \times d_2] \subset \mathbb{Z}\;, \\
\beta\;&\in [1, d_1 \times d_2] \subset \mathbb{Z}\;.
\end{aligned}
$$

Mathematica code for flattening a multivariate fit is available at `https://gitlab.com/rhyspovey/mathematica-multivariate-fitting`.

APPENDIX Ω

Cleanroom process

In Figs. Ω.2, Ω.3, Ω.4, Ω.5 (with legend Fig. Ω.1) step by step procedures in the cleanroom for fabrication described in Ch. 4 are given.

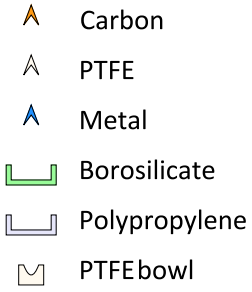

Figure Ω.1: Cleanroom process legend.

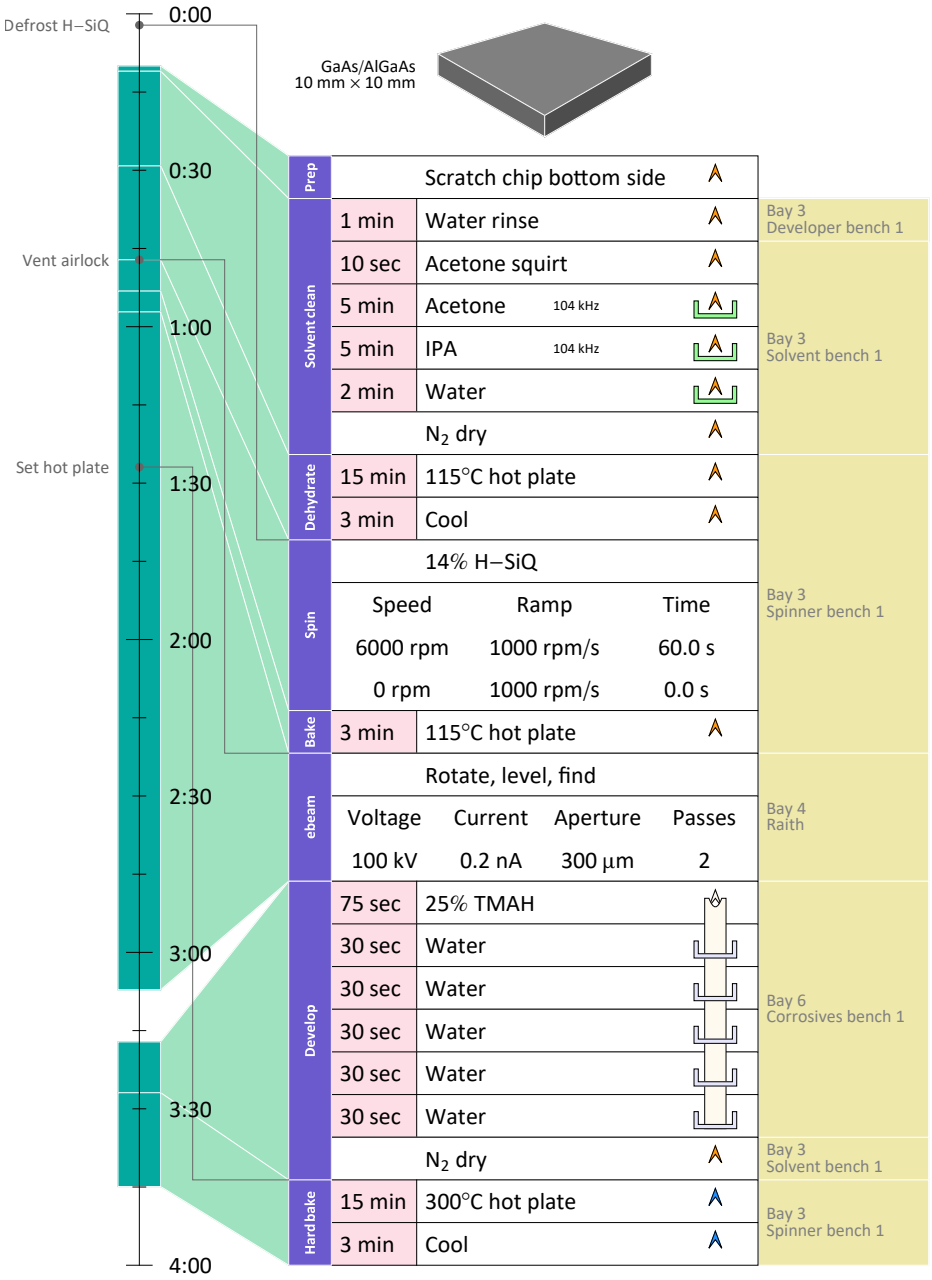

Figure Ω.2: Electron beam lithography process.

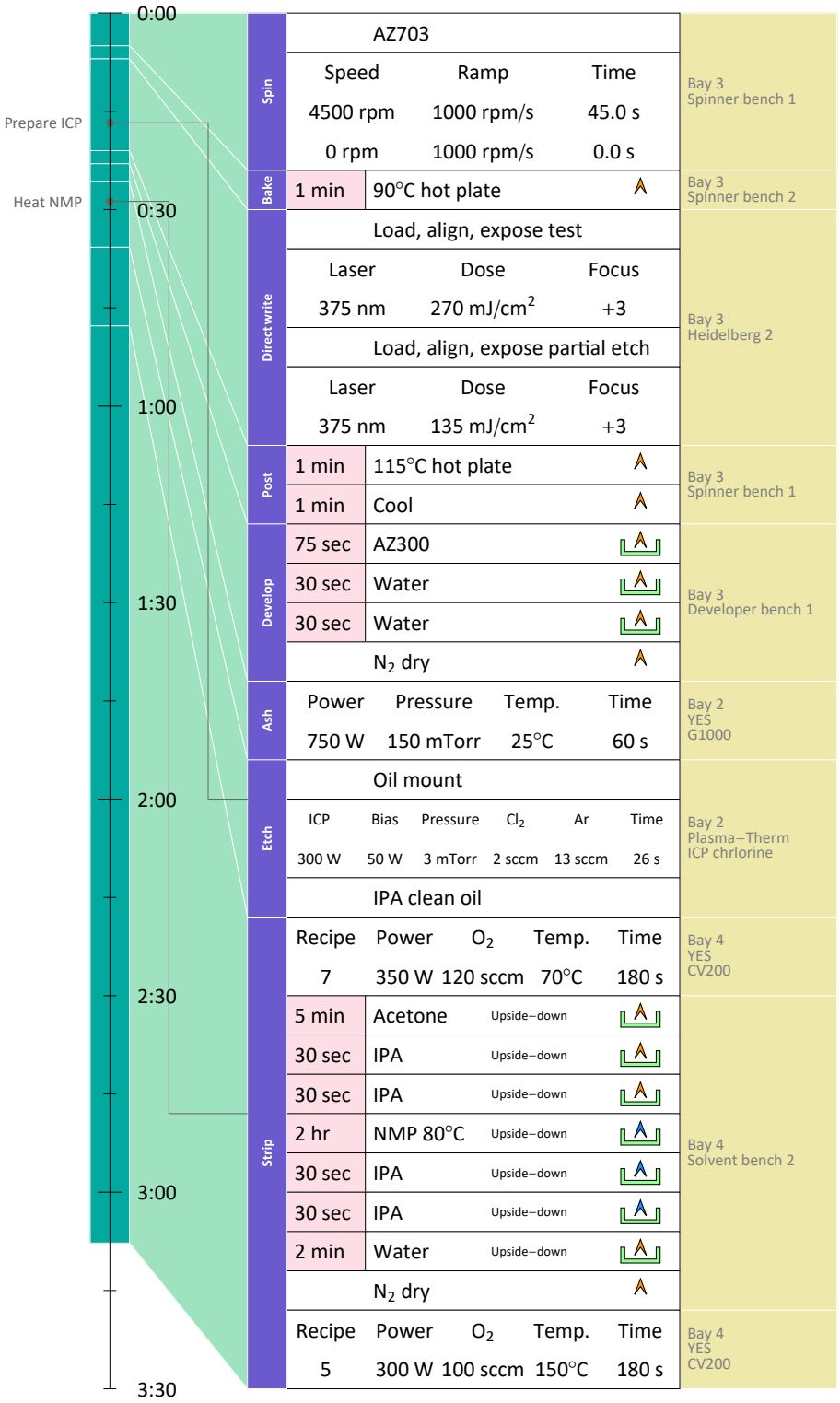

Figure Ω.3: Partial etch process.

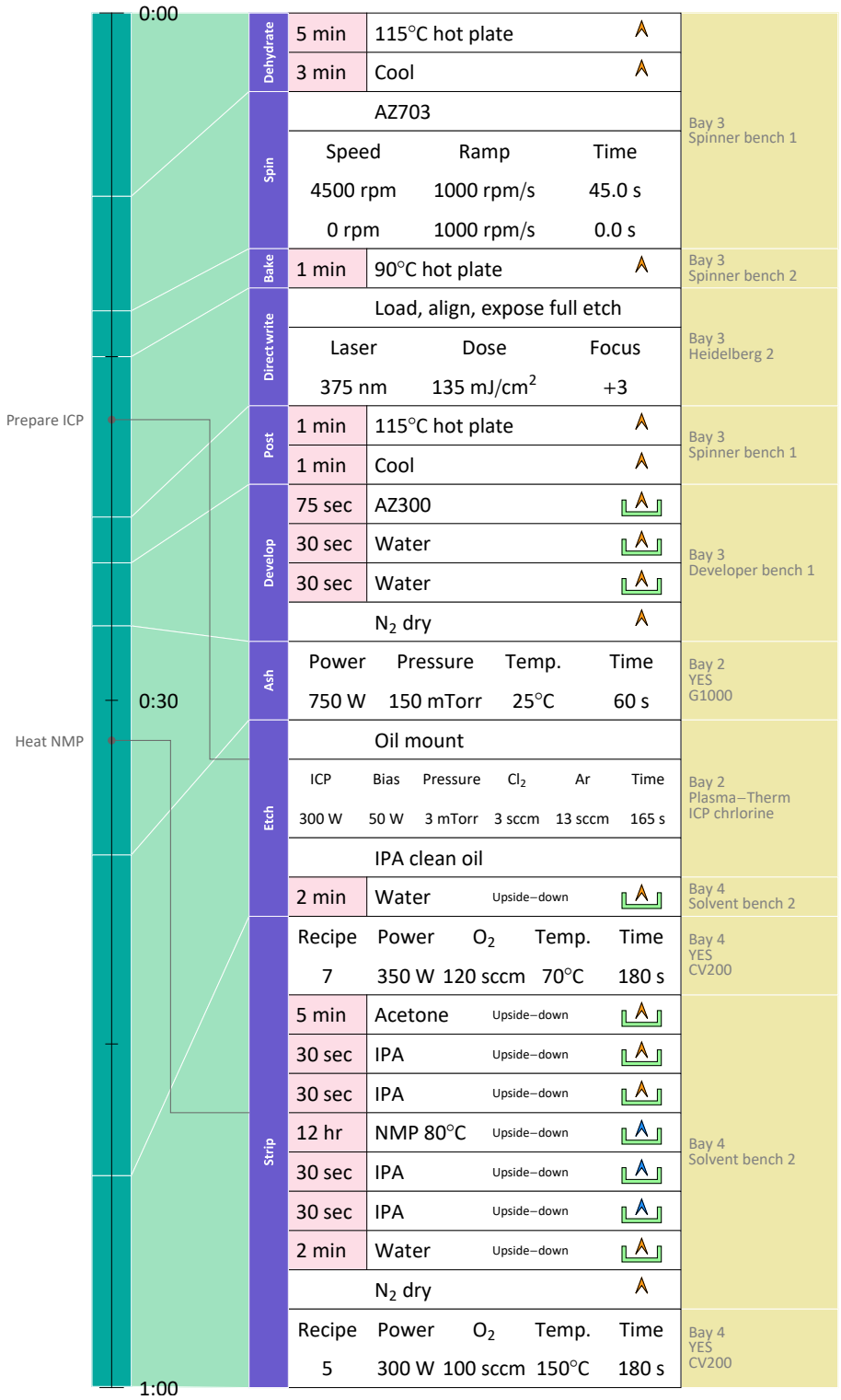

Figure Ω.4: Full etch process.

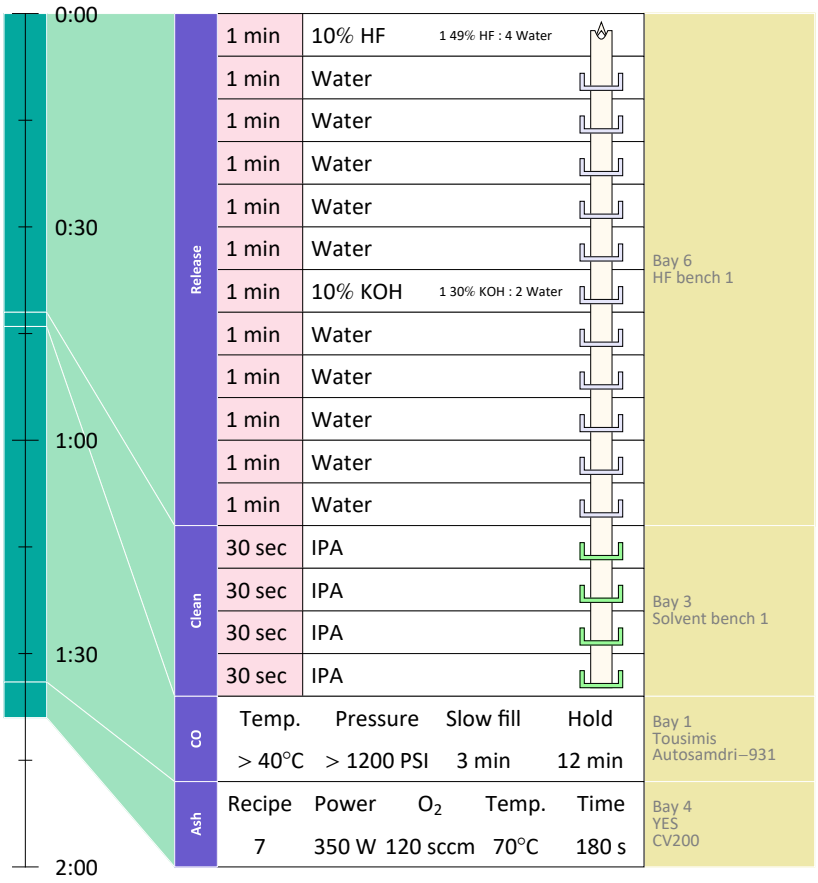

Figure Ω.5: Release process.

APPENDIX D

PTFE bowl

In order to carry out various cleanroom fabrication procedures, custom polytetrafluoroethylene (PTFE) bowls were constructed. Both are catered toward 1 cm square chips. The bowls were made in the University of Chicago student machine shops under the guidance of Luigi Mazzenga.

The first bowl, Fig. D.1, is primarily for transferring chips in acid to water during the release step, and then into isopropyl alcohol for critical point drying. During these steps the chip must remain submerged in liquid, hence the need for a transfer bowl. A lathe with a curved tool is used to create the bowl. The handle is made from a PTFE rod with a screw die, and the bowl is given a screw tapped hole.

The second bowl, Fig. D.2, is used to hold the chip upside-down whilst in some liquid. Drainage is essential for use in the critical point dryer where the liquid needs to be fully replaced. The channels underneath are made using a mill, and conveniently allow the bowl to be picked up using a pair of angled tweezers on opposing sides.

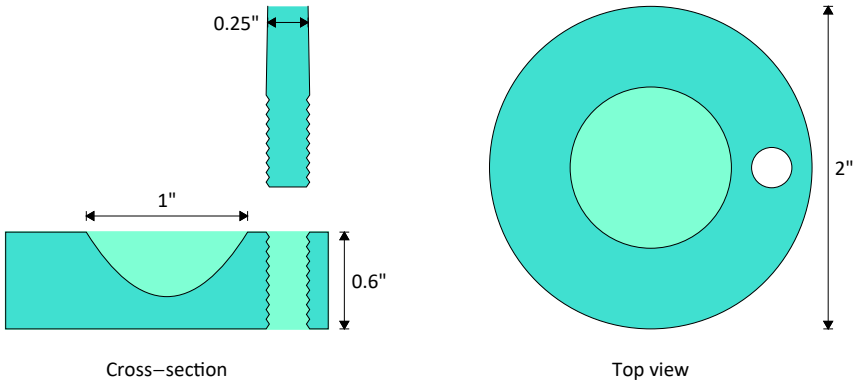

Figure D.1: PTFE transfer bowl design.

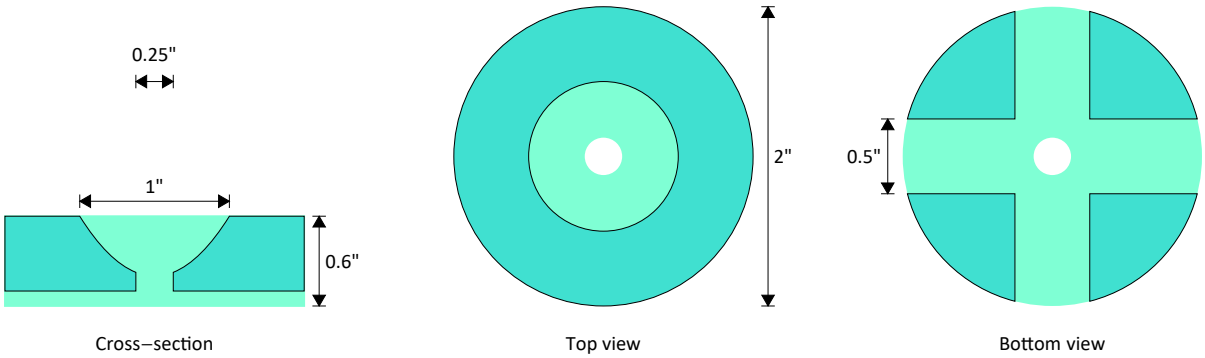

Figure D.2: PTFE drainage bowl design.

References

[1] A. Steane, "Quantum computing," *Reports on Progress in Physics* **61** no. 2, (Feb, 1998) 117–173. https://iopscience.iop.org/article/10.1088/0034-4885/61/2/002/meta.

[2] J. Preskill, "Quantum computing in the NISQ era and beyond," *Quantum* **2** (Aug, 2018) 79. https://quantum-journal.org/papers/q-2018-08-06-79/.

[3] N. Gisin and R. Thew, "Quantum communication," *Nature Photonics* **1** no. 3, (Mar, 2007) 165–171. https://www.nature.com/articles/nphoton.2007.22.

[4] A. Singh, K. Dev, H. Siljak, H. D. Joshi, and M. Magarini, "Quantum internet—applications, functionalities, enabling technologies, challenges, and research directions," *IEEE Communications Surveys: Tutorials* **23** no. 4, (2021) 2218–2247, arxiv:2101.04427 [quant-ph]. https://ieeexplore.ieee.org/abstract/document/9528843.

[5] A. D. O'Connell, M. Hofheinz, M. Ansmann, R. C. Bialczak, M. Lenander, E. Lucero, M. Neeley, D. Sank, H. Wang, M. Weides, J. Wenner, J. M. Martinis, and A. N. Cleland, "Quantum ground state and single-phonon control of a mechanical resonator," *Nature* **464** no. 7289, (Mar, 2010) 697–703. https://www.nature.com/articles/nature08967.

[6] S. Kotler, G. A. Peterson, E. Shojaee, F. Lecocq, K. Cicak, A. Kwiatkowski, S. Geller, S. Glancy, E. Knill, R. W. Simmonds, J. Aumentado, and J. D. Teufel, "Direct observation of deterministic macroscopic entanglement," *Science* **372** no. 6542, (May, 2021) 622–625. https://science.sciencemag.org/content/372/6542/622.

[7] D. Cattiaux, I. Golokolenov, S. Kumar, M. Sillanpää, L. M. de Lépinay, R. R. Gazizulin, X. Zhou, A. D. Armour, O. Bourgeois, A. Fefferman, and E. Collin, "A macroscopic object passively cooled into its quantum ground state of motion beyond single-mode cooling," *Nature Communications* **12** no. 1, (Oct, 2021) 6182, arxiv:2104.09541 [quant-ph]. https://www.nature.com/articles/s41467-021-26457-8.

[8] V. Giovannetti, S. Lloyd, and L. Maccone, "Quantum-enhanced measurements: Beating the standard quantum limit," *Science* **306** no. 5700, (Nov, 2004) 1330–1336. https://www.science.org/doi/full/10.1126/science.1104149.

[9] C. B. Møller, R. A. Thomas, G. Vasilakis, E. Zeuthen, Y. Tsaturyan, M. Balabas, K. Jensen, A. Schliesser, K. Hammerer, and E. S. Polzik, "Quantum back-action-evading measurement of motion in a negative mass reference frame," *Nature* **547** no. 7662, (Jul, 2017) 191–195. https://www.nature.com/articles/nature22980.

[10] R. D. Delaney, A. P. Reed, R. W. Andrews, and K. W. Lehnert, "Measurement of motion beyond the quantum limit by transient amplification," *Physical Review Letters* **123** no. 18, (Oct, 2019) 183603. https://journals.aps.org/prl/abstract/10.1103/PhysRevLett.123.183603.

[11] A. A. Clerk, F. Marquardt, and K. Jacobs, "Back-action evasion and squeezing of a mechanical resonator using a cavity detector," *New Journal of Physics* **10** no. 9, (Sep, 2008) 095010. https://iopscience.iop.org/article/10.1088/1367-2630/10/9/095010/meta.

[12] A. A. Clerk, M. H. Devoret, S. M. Girvin, F. Marquardt, and R. J. Schoelkopf, "Introduction to quantum noise, measurement, and amplification," *Reviews of Modern Physics* **82** no. 2, (Apr, 2010) 1155–1208. https://journals.aps.org/rmp/abstract/10.1103/RevModPhys.82.1155.

[13] M. A. Taylor, J. Janousek, V. Daria, J. Knittel, B. Hage, H.-A. Bachor, and W. P. Bowen, "Biological measurement beyond the quantum limit," *Nature Photonics* **7** no. 3, (Feb, 2013) 229–233. https://www.nature.com/articles/nphoton.2012.346.

[14] C. Degen, F. Reinhard, and P. Cappellaro, "Quantum sensing," *Reviews of Modern Physics* **89** no. 3, (Jul, 2017) 035002. https://journals.aps.org/rmp/abstract/10.1103/RevModPhys.89.035002.

[15] P. A. M. Dirac, "The fundamental equations of quantum mechanics," *Proceedings of the Royal Society of London. Series A, Containing Papers of a Mathematical and Physical Character* **109** no. 752, (Dec, 1925) 642–653. https://royalsocietypublishing.org/doi/abs/10.1098/rspa.1925.0150.

[16] R. Shankar, *Principles of Quantum Mechanics*. Springer, 2012.

[17] R. LaPierre, *Introduction to Quantum Computing*. Springer International Publishing, 2021. https://link.springer.com/book/10.1007/978-3-030-69318-3.

[18] P. W. Shor, "Algorithms for quantum computation: discrete logarithms and factoring," in *Proceedings 35th Annual Symposium on Foundations of Computer Science*. IEEE Comput. Soc. Press, 1994. https://ieeexplore.ieee.org/abstract/document/365700.

[19] R. L. Rivest, A. Shamir, and L. Adleman, "A method for obtaining digital signatures and public-key cryptosystems," *Communications of the ACM* **21** no. 2, (Feb, 1978) 120–126. https://dl.acm.org/doi/10.1145/359340.359342.

[20] I. Georgescu, S. Ashhab, and F. Nori, "Quantum simulation," *Reviews of Modern Physics* **86** no. 1, (Mar, 2014) 153–185. https://journals.aps.org/rmp/abstract/10.1103/RevModPhys.86.153.

[21] B. Bauer, S. Bravyi, M. Motta, and G. K.-L. Chan, "Quantum algorithms for quantum chemistry and quantum materials science," *Chemical Reviews* **120** no. 22, (Oct, 2020) 12685–12717. https://pubs.acs.org/doi/full/10.1021/acs.chemrev.9b00829.

[22] K. Bharti, A. Cervera-Lierta, T. H. Kyaw, T. Haug, S. Alperin-Lea, A. Anand, M. Degroote, H. Heimonen, J. S. Kottmann, T. Menke, W.-K. Mok, S. Sim, L.-C. Kwek, and A. Aspuru-Guzik, "Noisy intermediate-scale quantum algorithms," *Reviews of Modern Physics* **94** no. 1, (Feb, 2022) 015004. https://journals.aps.org/rmp/abstract/10.1103/RevModPhys.94.015004.

[23] D. Kielpinski, C. Monroe, and D. J. Wineland, "Architecture for a large-scale ion-trap quantum computer," *Nature* **417** no. 6890, (Jun, 2002) 709–711. https://www.nature.com/articles/nature00784.

[24] H. Haffner, C. Roos, and R. Blatt, "Quantum computing with trapped ions," *Physics Reports* **469** no. 4, (Dec, 2008) 155–203. https://www.sciencedirect.com/science/article/pii/S0370157308003463.

[25] I. H. Deutsch, G. K. Brennen, and P. S. Jessen, "Quantum computing with neutral atoms in an optical lattice," *Fortschritte der Physik* **48** no. 9-11, (Sep, 2000) 925–943. https://onlinelibrary.wiley.com/doi/10.1002/1521-3978(200009)48:9/11<925::AID-PROP925>3.0.CO;2-A.

[26] H.-J. Briegel, T. Calarco, D. Jaksch, J. I. Cirac, and P. Zoller, "Quantum computing with neutral atoms," *Journal of Modern Optics* **47** no. 2-3, (Feb, 2000) 415–451. https://www.tandfonline.com/doi/abs/10.1080/09500340008244052.

[27] M. Saffman, "Quantum computing with neutral atoms," *National Science Review* **6** no. 1, (Sep, 2018) 24–25. https://academic.oup.com/nsr/article/6/1/24/5094563.

[28] T. M. Graham, Y. Song, J. Scott, C. Poole, L. Phuttitarn, K. Jooya, P. Eichler, X. Jiang, A. Marra, B. Grinkemeyer, M. Kwon, M. Ebert, J. Cherek, M. T. Lichtman, M. Gillette, J. Gilbert, D. Bowman, T. Ballance, C. Campbell, E. D. Dahl, O. Crawford, N. S. Blunt, B. Rogers, T. Noel, and M. Saffman, "Multi-qubit entanglement and algorithms on a neutral-atom quantum computer," *Nature* **604** no. 7906, (Apr, 2022) 457–462. https://www.nature.com/articles/s41586-022-04603-6.

[29] T. D. Ladd, J. R. Goldman, F. Yamaguchi, Y. Yamamoto, E. Abe, and K. M. Itoh, "All-silicon quantum computer," *Physical Review Letters* **89** no. 1, (Jun, 2002) 017901. https://journals.aps.org/prl/abstract/10.1103/PhysRevLett.89.017901.

[30] R. G. Clark, R. Brenner, T. M. Buehler, V. Chan, N. J. Curson, A. S. Dzurak, E. Gauja, H. S. Goan, A. D. Greentree, T. Hallam, A. R. Hamilton, L. C. L. Hollenberg, D. N. Jamieson, J. C. McCallum, G. J. Milburn, J. L. O'Brien, L. Oberbeck, C. I. Pakes, S. D. Prawer, D. J. Reilly, F. J. Ruess, S. R. Schofield, M. Y. Simmons, F. E. Stanley, R. P. Starrett, C. Wellard, and C. Yang, "Progress in silicon-based quantum computing," *Philosophical Transactions of the Royal Society of London. Series A: Mathematical, Physical and Engineering Sciences* **361** no. 1808, (Jul, 2003) 1451–1471. https://royalsocietypublishing.org/doi/abs/10.1098/rsta.2003.1221.

[31] M. A. Eriksson, M. Friesen, S. N. Coppersmith, R. Joynt, L. J. Klein, K. Slinker, C. Tahan, P. M. Mooney, J. O. Chu, and S. J. Koester, "Spin-based quantum dot quantum computing in silicon," *Quantum Information Processing* **3** no. 1-5, (Oct, 2004) 133–146. https://link.springer.com/article/10.1007/s11128-004-2224-z.

[32] J. J. L. Morton, D. R. McCamey, M. A. Eriksson, and S. A. Lyon, "Embracing the quantum limit in silicon computing," *Nature* **479** no. 7373, (Nov, 2011) 345–353. https://www.nature.com/articles/nature10681.

[33] F. A. Zwanenburg, A. S. Dzurak, A. Morello, M. Y. Simmons, L. C. L. Hollenberg, G. Klimeck, S. Rogge, S. N. Coppersmith, and M. A. Eriksson, "Silicon quantum electronics," *Reviews of Modern Physics* **85** no. 3, (Jul, 2013) 961–1019. https://journals.aps.org/rmp/abstract/10.1103/RevModPhys.85.961.

[34] T. F. Watson, S. G. J. Philips, E. Kawakami, D. R. Ward, P. Scarlino, M. Veldhorst, D. E. Savage, M. G. Lagally, M. Friesen, S. N. Coppersmith, M. A. Eriksson, and L. M. K. Vandersypen, "A programmable two-qubit quantum processor in silicon," *Nature* **555** no. 7698, (Feb, 2018) 633–637. https://www.nature.com/articles/nature25766.

[35] C. H. Yang, R. C. C. Leon, J. C. C. Hwang, A. Saraiva, T. Tanttu, W. Huang, J. C. Lemyre, K. W. Chan, K. Y. Tan, F. E. Hudson, K. M. Itoh, A. Morello, M. Pioro-Ladrière, A. Laucht, and A. S. Dzurak, "Operation of a silicon quantum processor unit cell above one kelvin," *Nature* **580** no. 7803, (Apr, 2020) 350–354. https://www.nature.com/articles/s41586-020-2171-6.

[36] M. F. Gonzalez-Zalba, S. de Franceschi, E. Charbon, T. Meunier, M. Vinet, and A. S. Dzurak, "Scaling silicon-based quantum computing using CMOS technology," *Nature Electronics* **4** no. 12, (Dec, 2021) 872–884. https://www.nature.com/articles/s41928-021-00681-y.

[37] P. M. Platzman and M. I. Dykman, "Quantum computing with electrons floating on liquid helium," *Science* **284** no. 5422, (Jun, 1999) 1967–1969. https://www.science.org/doi/full/10.1126/science.284.5422.1967.

[38] S. A. Lyon, "Spin-based quantum computing using electrons on liquid helium," *Physical Review A* **74** no. 5, (Nov, 2006) 052338. https://journals.aps.org/pra/abstract/10.1103/PhysRevA.74.052338.

[39] X. Zhou, G. Koolstra, X. Zhang, G. Yang, X. Han, B. Dizdar, X. Li, R. Divan, W. Guo, K. W. Murch, D. I. Schuster, and D. Jin, "Single electrons on solid neon as a solid-state qubit platform," *Nature* **605** no. 7908, (May, 2022) 46–50. https://www.nature.com/articles/s41586-022-04539-x.

[40] M. Freedman, A. Kitaev, M. Larsen, and Z. Wang, "Topological quantum computation," *Bulletin of the American Mathematical Society* **40** no. 1, (Oct, 2002) 31–38. https://www.ams.org/journals/bull/2003-40-01/S0273-0979-02-00964-3/.

[41] A. Stern and N. H. Lindner, "Topological quantum computation—from basic concepts to first experiments," *Science* **339** no. 6124, (Mar, 2013) 1179–1184. https://www.science.org/doi/full/10.1126/science.1231473.

[42] Y. Nakamura, Y. A. Pashkin, and J. S. Tsai, "Coherent control of macroscopic quantum states in a single-Cooper-pair box," *Nature* **398** no. 6730, (Apr, 1999) 786–788. https://www.nature.com/articles/19718.

[43] J. Q. You and F. Nori, "Quantum information processing with superconducting qubits in a microwave field," *Physical Review B* **68** no. 6, (Aug, 2003) 064509. https://journals.aps.org/prb/abstract/10.1103/PhysRevB.68.064509.

[44] A. Blais, R.-S. Huang, A. Wallraff, S. M. Girvin, and R. J. Schoelkopf, "Cavity quantum electrodynamics for superconducting electrical circuits: An architecture for quantum computation," *Physical Review A* **69** no. 6, (Jun, 2004) 062320. https://journals.aps.org/pra/abstract/10.1103/PhysRevA.69.062320.

[45] L. Frunzio, A. Wallraff, D. Schuster, J. Majer, and R. Schoelkopf, "Fabrication and characterization of superconducting circuit QED devices for quantum computation," *IEEE Transactions on Appiled Superconductivity* **15** no. 2, (Jun, 2005) 860–863. https://ieeexplore.ieee.org/abstract/document/1439774.

[46] G. Wendin, "Quantum information processing with superconducting circuits: a review," *Reports on Progress in Physics* **80** no. 10, (Sep, 2017) 106001. https://iopscience.iop.org/article/10.1088/1361-6633/aa7e1a.

[47] S. Kwon, A. Tomonaga, G. L. Bhai, S. J. Devitt, and J.-S. Tsai, "Gate-based superconducting quantum computing," *Journal of Applied Physics* **129** no. 4, (Jan, 2021) 041102, arxiv:2009.08021 [quant-ph]. https://aip.scitation.org/doi/full/10.1063/5.0029735.

[48] Y. Y. Gao, M. A. Rol, S. Touzard, and C. Wang, "Practical guide for building superconducting quantum devices," *PRX Quantum* **2** no. 4, (Nov, 2021) 040202, arxiv:2106.06173 [quant-ph]. https://journals.aps.org/prxquantum/abstract/10.1103/PRXQuantum.2.040202.

[49] F. Arute, K. Arya, R. Babbush, D. Bacon, J. C. Bardin, R. Barends, R. Biswas, S. Boixo, F. G. S. L. Brandao, D. A. Buell, B. Burkett, Y. Chen, Z. Chen, B. Chiaro, R. Collins, W. Courtney, A. Dunsworth, E. Farhi, B. Foxen, A. Fowler, C. Gidney, M. Giustina, R. Graff, K. Guerin, S. Habegger, M. P. Harrigan, M. J. Hartmann, A. Ho, M. Hoffmann, T. Huang, T. S. Humble, S. V. Isakov, E. Jeffrey, Z. Jiang, D. Kafri, K. Kechedzhi, J. Kelly, P. V. Klimov, S. Knysh, A. Korotkov, F. Kostritsa, D. Landhuis, M. Lindmark, E. Lucero, D. Lyakh, S. Mandrà, J. R. McClean, M. McEwen, A. Megrant, X. Mi, K. Michielsen, M. Mohseni, J. Mutus, O. Naaman, M. Neeley, C. Neill, M. Y. Niu, E. Ostby, A. Petukhov, J. C. Platt, C. Quintana, E. G. Rieffel, P. Roushan, N. C. Rubin, D. Sank, K. J. Satzinger, V. Smelyanskiy, K. J. Sung, M. D. Trevithick, A. Vainsencher, B. Villalonga, T. White, Z. J. Yao, P. Yeh, A. Zalcman, H. Neven, and J. M. Martinis, "Quantum supremacy using a programmable superconducting processor," *Nature* **574** no. 7779, (Oct, 2019) 505–510. https://www.nature.com/articles/s4158601916665.

[50] "Google Quantum AI." https://quantumai.google/.

[51] "IBM Quantum." https://www.ibm.com/quantum.

[52] "Amazon Braket." https://aws.amazon.com/braket/.

[53] B. D. Josephson, "Coupled superconductors," *Reviews of Modern Physics* **36** no. 1, (Jan, 1964) 216–220. https://journals.aps.org/rmp/abstract/10.1103/RevModPhys.36.216.

[54] B. D. Josephson, "Supercurrents through barriers," *Advances in Physics* **14** no. 56, (Oct, 1965) 419–451. https://www.tandfonline.com/doi/abs/10.1080/00018736500101091.

[55] A. A. Golubov, M. Y. Kupriyanov, and E. Il'ichev, "The current-phase relation in Josephson junctions," *Reviews of Modern Physics* **76** no. 2, (Apr, 2004) 411–469. https://journals.aps.org/rmp/abstract/10.1103/RevModPhys.76.411.

[56] P. Krantz, M. Kjaergaard, F. Yan, T. P. Orlando, S. Gustavsson, and W. D. Oliver, "A quantum engineer's guide to superconducting qubits," *Applied Physics Reviews* **6** no. 2, (Jun, 2019) 021318. https://aip.scitation.org/doi/full/10.1063/1.5089550.

[57] S. E. Rasmussen, K. S. Christensen, S. P. Pedersen, L. B. Kristensen, T. Bækkegaard, N. J. S. Loft, and N. T. Zinner, "Superconducting circuit companion—an introduction with worked examples," *PRX Quantum* **2** no. 4, (Dec,

2021) 040204, arxiv:2103.01225 [quant-ph]. https://journals.aps.org/prxquantum/abstract/10.1103/PRXQuantum.2.040204.

[58] N. J. Lambert, A. Rueda, F. Sedlmeir, and H. G. L. Schwefel, "Coherent conversion between microwave and optical photons: An overview of physical implementations," *Advanced Quantum Technologies* **3** no. 1, (Jan, 2020) 1900077. https://onlinelibrary.wiley.com/doi/full/10.1002/qute.201900077.

[59] N. Lauk, N. Sinclair, S. Barzanjeh, J. P. Covey, M. Saffman, M. Spiropulu, and C. Simon, "Perspectives on quantum transduction," *Quantum Science and Technology* **5** no. 2, (Mar, 2020) 020501. https://iopscience.iop.org/article/10.1088/2058-9565/ab788a.

[60] Y. Chu and S. Gröblacher, "A perspective on hybrid quantum opto- and electromechanical systems," *Applied Physics Letters* **117** no. 15, (Oct, 2020) 150503, arxiv:2007.03360 [quant-ph]. https://aip.scitation.org/doi/full/10.1063/5.0021088.

[61] G. Moody, V. J. Sorger, D. J. Blumenthal, P. W. Juodawlkis, W. Loh, C. Sorace-Agaskar, A. E. Jones, K. C. Balram, J. C. F. Matthews, A. Laing, M. Davanco, L. Chang, J. E. Bowers, N. Quack, C. Galland, I. Aharonovich, M. A. Wolff, C. Schuck, N. Sinclair, M. Lončar, T. Komljenovic, D. Weld, S. Mookherjea, S. Buckley, M. Radulaski, S. Reitzenstein, B. Pingault, B. Machielse, D. Mukhopadhyay, A. Akimov, A. Zheltikov, G. S. Agarwal, K. Srinivasan, J. Lu, H. X. Tang, W. Jiang, T. P. McKenna, A. H. Safavi-Naeini, S. Steinhauer, A. W. Elshaari, V. Zwiller, P. S. Davids, N. Martinez, M. Gehl, J. Chiaverini, K. K. Mehta, J. Romero, N. B. Lingaraju, A. M. Weiner, D. Peace, R. Cernansky, M. Lobino, E. Diamanti, L. T. Vidarte, and R. M. Camacho, "2022 roadmap on integrated quantum photonics," *Journal of Physics: Photonics* **4** no. 1, (Jan, 2022) 012501. https://iopscience.iop.org/article/10.1088/2515-7647/ac1ef4.

[62] M. Soltani, M. Zhang, C. Ryan, G. J. Ribeill, C. Wang, and M. Lončar, "Efficient quantum microwave-to-optical conversion using electro-optic nanophotonic coupled resonators," *Physical Review A* **96** no. 4, (Oct, 2017) 043808. https://journals.aps.org/pra/abstract/10.1103/PhysRevA.96.043808.

[63] J. D. Witmer, J. A. Valery, P. Arrangoiz-Arriola, C. J. Sarabalis, J. T. Hill, and A. H. Safavi-Naeini, "High-Q photonic resonators and electro-optic coupling using silicon-on-lithium-niobate," *Scientific Reports* **7** no. 1, (Apr, 2017) 46313. https://www.nature.com/articles/srep46313.

[64] J. Holzgrafe, N. Sinclair, D. Zhu, A. Shams-Ansari, M. Colangelo, Y. Hu, M. Zhang, K. K. Berggren, and M. Lončar, "Cavity electro-optics in thin-film lithium niobate for efficient microwave-to-optical transduction," *Optica* **7** no. 12, (Dec, 2020) 1714, arxiv:2005.00939 [quant-ph].

[65] T. P. McKenna, J. D. Witmer, R. N. Patel, W. Jiang, R. V. Laer, P. Arrangoiz-Arriola, E. A. Wollack, J. F. Herrmann, and A. H. Safavi-Naeini, "Cryogenic microwave-to-optical conversion using a triply resonant lithium-niobate-on-sapphire transducer," *Optica* **7** no. 12, (Dec, 2020) 1737, arxiv:2005.00897 [quant-ph].

[66] W. Hease, A. Rueda, R. Sahu, M. Wulf, G. Arnold, H. G. L. Schwefel, and J. M. Fink, "Bidirectional electro-optic wavelength conversion in the quantum ground state," *PRX Quantum* **1** no. 2, (Nov, 2020) 020315. https://journals.aps.org/prxquantum/abstract/10.1103/PRXQuantum.1.020315.

[67] R. Sahu, W. Hease, A. Rueda, G. Arnold, L. Qiu, and J. M. Fink, "Quantum-enabled operation of a microwave-optical interface," *Nature Communications* **13** no. 1, (Mar, 2022) . https://www.nature.com/articles/s41467-022-28924-2.

[68] R. Sahu, L. Qiu, W. Hease, G. Arnold, Y. Minoguchi, P. Rabl, and J. M. Fink, "Entangling microwaves with light," *Science* **380** no. 6646, (May, 2023) 718–721. https://www.science.org/doi/full/10.1126/science.adg3812.

[69] Y. Xu, A. A. Sayem, L. Fan, C. Zou, and H. X. Tang, "Bidirectional electro-optic conversion reaching 1% efficiency with thin film lithium niobate," in *Conference on Lasers and Electro-Optics*. Optica Publishing Group, 2021. arxiv:2012.14909 [physics.optics].

[70] W. Fu, M. Xu, X. Liu, C.-L. Zou, C. Zhong, X. Han, M. Shen, Y. Xu, R. Cheng, S. Wang, L. Jiang, and H. X. Tang, "Cavity electro-optic circuit for microwave-to-optical conversion in the quantum ground state," *Physical Review A* **103** no. 5, (May, 2021) 053504, arxiv:2010.11392 [quant-ph]. https://journals.aps.org/pra/abstract/10.1103/PhysRevA.103.053504.

[71] A. M. Jayich, J. C. Sankey, B. M. Zwickl, C. Yang, J. D. Thompson, S. M. Girvin, A. A. Clerk, F. Marquardt, and J. G. E. Harris, "Dispersive optomechanics: a membrane inside a cavity," *New Journal of Physics* **10** no. 9, (Sep, 2008) 095008. https://iopscience.iop.org/article/10.1088/1367-2630/10/9/095008.

[72] R. W. Andrews, R. W. Peterson, T. P. Purdy, K. Cicak, R. W. Simmonds, C. A. Regal, and K. W. Lehnert, "Bidirectional and efficient conversion between microwave and optical light," *Nature Physics* **10** no. 4, (Mar, 2014) 321–326. https://www.nature.com/articles/nphys2911.

[73] M. Kalaee, T. K. Paraïso, H. Pfeifer, and O. Painter, "Design of a quasi-2D photonic crystal optomechanical cavity with tunable, large x^2-coupling," *Optics Express* **24** no. 19, (Sep, 2016) 21308. https://www.osapublishing.org/oe/abstract.cfm?uri=oe-24-19-21308.

[74] A. Okada, F. Oguro, A. Noguchi, Y. Tabuchi, R. Yamazaki, K. Usami, and Y. Nakamura, "Cavity enhancement of anti-stokes scattering via optomechanical

coupling with surface acoustic waves," *Physical Review Applied* **10** no. 2, (Aug, 2018) 024002. https://journals.aps.org/prapplied/abstract/10.1103/PhysRevApplied.10.024002.

[75] X. Han, W. Fu, C. Zhong, C.-L. Zou, Y. Xu, A. A. Sayem, M. Xu, S. Wang, R. Cheng, L. Jiang, and H. X. Tang, "Cavity piezo-mechanics for superconducting-nanophotonic quantum interface," *Nature Communications* **11** no. 1, (Jun, 2020) 3237. https://www.nature.com/articles/s41467-020-17053-3.

[76] X. Gao, Z.-Q. Yin, and T. Li, "High-speed quantum transducer with a single-photon emitter in a 2D resonator," *Annalen der Physik* (Aug, 2020) 2000233. https://onlinelibrary.wiley.com/doi/abs/10.1002/andp.202000233.

[77] S. K. Manjeshwar, K. Elkhouly, J. M. Fitzgerald, M. Ekman, Y. Zhang, F. Zhang, S. M. Wang, P. Tassin, and W. Wieczorek, "Suspended photonic crystal membranes in AlGaAs heterostructures for integrated multi-element optomechanics," *Applied Physics Letters* **116** no. 26, (Jun, 2020) 264001. https://aip.scitation.org/doi/10.1063/5.0012667.

[78] J. Li and S. Gröblacher, "Stationary quantum entanglement between a massive mechanical membrane and a low frequency LC circuit," *New Journal of Physics* **22** no. 6, (Jun, 2020) 063041. https://iopscience.iop.org/article/10.1088/1367-2630/ab90d2.

[79] T. M. Karg, B. Gouraud, C. T. Ngai, G.-L. Schmid, K. Hammerer, and P. Treutlein, "Light-mediated strong coupling between a mechanical oscillator and atomic spins 1 meter apart," *Science* **369** no. 6500, (May, 2020) 174–179. https://science.sciencemag.org/content/369/6500/174.

[80] Y. Tominaga, A. Mikami, A. Iwamura, K. Usami, and K. Takeda, "Heating-free, room-temperature operation of a radiofrequency-to-light signal transducer with a membrane oscillator and a built-in metasurface mirror," *Applied Physics Express* **15** no. 1, (Dec, 2021) 012003. https://iopscience.iop.org/article/10.35848/1882-0786/ac3e15.

[81] M. H. J. de Jong, J. Li, C. Gärtner, R. A. Norte, and S. Gröblacher, "Coherent mechanical noise cancellation and cooperativity competition in optomechanical arrays," *Optica* **9** no. 2, (Feb, 2022) 170, arxiv:2012.11733 [physics.optics].

[82] B. M. Brubaker, J. M. Kindem, M. D. Urmey, S. Mittal, R. D. Delaney, P. S. Burns, M. R. Vissers, K. W. Lehnert, and C. A. Regal, "Optomechanical ground-state cooling in a continuous and efficient electro-optic transducer," *Physical Review X* **12** no. 2, (Dec., 2022) 021062, arXiv:2112.13429 [quant-ph]. https://arxiv.org/abs/2112.13429.

[83] M. Rudd, P. Kim, C. Potts, C. Doolin, H. Ramp, B. Hauer, and J. Davis, "Coherent magneto-optomechanical signal transduction and long-distance phase-shift keying,"

Physical Review Applied **12** no. 3, (Sep, 2019) 034042. https://journals.aps.org/prapplied/abstract/10.1103/PhysRevApplied.12.034042.

[84] Z.-Y. Fan, H. Qian, and J. Li, "Stationary optomagnonic entanglement and magnon-to-optics quantum state transfer via opto-magnomechanics," *Quantum Science and Technology* **8** no. 1, (Nov, 2022) 015014, arXiv:2206.05688 [quant-ph]. https://iopscience.iop.org/article/10.1088/2058-9565/aca3cf.

[85] Z.-Y. Fan, L. Qiu, S. Gröblacher, and J. Li, "Microwave-optics entanglement via cavity optomagnomechanics," arXiv:2208.10703 [quant-ph]. https://arxiv.org/abs/2208.10703.

[86] Z. Shen, G.-T. Xu, M. Zhang, Y.-L. Zhang, Y. Wang, C.-Z. Chai, C.-L. Zou, G.-C. Guo, and C.-H. Dong, "Coherent coupling between phonons, magnons, and photons," *Physical Review Letters* **129** no. 24, (Dec, 2022) 243601. https://journals.aps.org/prl/abstract/10.1103/PhysRevLett.129.243601.

[87] Y.-T. Yan, C. Zhao, Z. Yang, D.-W. Wang, and L. Zhou, "Quantum state transfer with cavity-magnonics nodes," *Journal of Physics B: Atomic, Molecular and Optical Physics* **55** no. 19, (Sep, 2022) 195502. https://iopscience.iop.org/article/10.1088/1361-6455/ac86b1/meta.

[88] M. J. A. Schuetz, E. M. Kessler, G. Giedke, L. M. K. Vandersypen, M. D. Lukin, and J. I. Cirac, "Universal quantum transducers based on surface acoustic waves," *Physical Review X* **5** no. 3, (Sep, 2015) 031031. https://journals.aps.org/prx/abstract/10.1103/PhysRevX.5.031031.

[89] M. Weiß and H. J. Krenner, "Interfacing quantum emitters with propagating surface acoustic waves," *Journal of Physics D: Applied Physics* **51** no. 37, (Aug, 2018) 373001. https://iopscience.iop.org/article/10.1088/1361-6463/aace3c.

[90] M. Weiß, D. Wigger, M. Nägele, K. Müller, J. J. Finley, T. Kuhn, P. Machnikowski, and H. J. Krenner, "Optomechanical wave mixing by a single quantum dot," *Optica* **8** no. 3, (Mar, 2021) 291. https://www.osapublishing.org/optica/fulltext.cfm?uri=optica-8-3-291&id=448648.

[91] R. A. DeCrescent, Z. Wang, P. Imany, R. C. Boutelle, C. A. McDonald, T. Autry, J. D. Teufel, S. W. Nam, R. P. Mirin, and K. L. Silverman, "Large single-phonon optomechanical coupling between quantum dots and tightly confined surface acoustic waves in the quantum regime," *Physical Review Applied* **18** no. 3, (Sep, 2022) 034067. https://journals.aps.org/prapplied/abstract/10.1103/PhysRevApplied.18.034067.

[92] D. D. Bühler, M. Weiß, A. Crespo-Poveda, E. D. S. Nysten, J. J. Finley, K. Müller, P. V. Santos, M. M. de Lima, and H. J. Krenner, "On-chip generation and dynamic piezo-optomechanical rotation of single photons," *Nature Communications* **13** no. 1, (Nov, 2022) 6998. https://www.nature.com/articles/s41467-022-34372-9.

[93] Y. Tsuchimoto, P. Knüppel, A. Delteil, Z. Sun, M. Kroner, and A. Imamoğlu, "Proposal for a quantum interface between photonic and superconducting qubits," *Physical Review B* **96** no. 16, (Oct, 2017) 165312. https://journals.aps.org/prb/abstract/10.1103/PhysRevB.96.165312.

[94] Y. Tsuchimoto, Z. Sun, E. Togan, S. Fält, W. Wegscheider, A. Wallraff, K. Ensslin, A. İmamoğlu, and M. Kroner, "Large-bandwidth transduction between an optical single quantum dot molecule and a superconducting resonator," *PRX Quantum* **3** no. 3, (Sep, 2022) 030336, arxiv:2110.03230 [quant-ph]. https://journals.aps.org/prxquantum/abstract/10.1103/PRXQuantum.3.030336.

[95] P. Sesin, A. S. Kuznetsov, G. Rozas, S. Anguiano, A. E. Bruchhausen, A. Lemaître, K. Biermann, P. V. Santos, and A. Fainstein, "Giant optomechanical coupling and dephasing protection with cavity exciton-polaritons," arXiv:2212.08269 [cond-mat.mes-hall]. https://arxiv.org/abs/2212.08269.

[96] Y. Chu, P. Kharel, W. H. Renninger, L. D. Burkhart, L. Frunzio, P. T. Rakich, and R. J. Schoelkopf, "Quantum acoustics with superconducting qubits," *Science* **358** no. 6360, (Sep, 2017) 199–202. https://science.sciencemag.org/content/358/6360/199.abstract.

[97] W. H. Renninger, P. Kharel, R. O. Behunin, and P. T. Rakich, "Bulk crystalline optomechanics," *Nature Physics* **14** no. 6, (Apr, 2018) 601–607. https://www.nature.com/articles/s41567-018-0090-3.

[98] H. Tian, J. Liu, B. Dong, J. C. Skehan, M. Zervas, T. J. Kippenberg, and S. A. Bhave, "Hybrid integrated photonics using bulk acoustic resonators," *Nature Communications* **11** no. 1, (Jun, 2020) 3073. https://www.nature.com/articles/s41467-020-16812-6.

[99] T. Blésin, H. Tian, S. A. Bhave, and T. J. Kippenberg, "Quantum coherent microwave-optical transduction using high-overtone bulk acoustic resonances," *Physical Review A* **104** no. 5, (Nov, 2021) 052601, arxiv:2103.00471 [quant-ph]. https://journals.aps.org/pra/abstract/10.1103/PhysRevA.104.052601.

[100] H. M. Doeleman, T. Schatteburg, R. Benevides, S. Vollenweider, D. Macri, and Y. Chu, "Brillouin optomechanics in the quantum ground state," arXiv:2303.04677 [quant-ph]. https://arxiv.org/abs/2303.04677.

[101] T. Liu, J.-L. Zhao, B.-Q. Guo, Q.-C. Wu, Y.-H. Zhou, and C.-P. Yang, "One-step implementation of a coherent conversion between microwave and optical cavities via an ensemble of nitrogen-vacancy centers," *Physical Review A* **103** no. 2, (Feb, 2021) 023706. https://journals.aps.org/pra/abstract/10.1103/PhysRevA.103.023706.

[102] P. K. Shandilya, D. P. Lake, M. J. Mitchell, D. D. Sukachev, and P. E. Barclay, "Optomechanical interface between telecom photons and spin quantum memory,"

Nature Physics **17** no. 12, (Oct, 2021) 1420–1425, arxiv:2102.04597 [quant-ph]. https://www.nature.com/articles/s41567-021-01364-3.

[103] D. B. Higginbottom, F. K. Asadi, C. Chartrand, J.-W. Ji, L. Bergeron, M. L. Thewalt, C. Simon, and S. Simmons, "Memory and transduction prospects for silicon t center devices," *PRX Quantum* **4** no. 2, (Apr., 2023) 020308. https://journals.aps.org/prxquantum/abstract/10.1103/PRXQuantum.4.020308.

[104] B. Kim, H. Kurokawa, H. Kosaka, and M. Nomura, "Design of a diamond optomechanical cavity with a color center for microwave-to-optical quantum interfaces," arXiv:2305.08306 [quant-ph]. https://arxiv.org/abs/2305.08306.

[105] R. Ohta, L. Herpin, V. M. Bastidas, T. Tawara, H. Yamaguchi, and H. Okamoto, "Rare-earth-mediated optomechanical system in the reversed dissipation regime," *Physical Review Letters* **126** no. 4, (Jan, 2021) 047404, arxiv:2006.14133 [physics.optics].

[106] F. K. Asadi, J.-W. Ji, and C. Simon, "Proposal for transduction between microwave and optical photons using ^{167}Er-doped yttrium orthosilicate," *Physical Review A* **105** no. 6, (Jun, 2022) 062608. https://journals.aps.org/pra/abstract/10.1103/PhysRevA.105.062608.

[107] J. Rochman, T. Xie, J. G. Bartholomew, K. C. Schwab, and A. Faraon, "Microwave-to-optical transduction with erbium ions coupled to planar photonic and superconducting resonators," *Nature Communications* **14** no. 1, (Mar, 2023) 1153. https://www.nature.com/articles/s41467-023-36799-0.

[108] Y. Yu, D. Oser, G. Da Prato, E. Urbinati, J. C. Ávila, Y. Zhang, P. Remy, S. Marzban, S. Gröblacher, and W. Tittel, "Frequency tunable, cavity-enhanced single erbium quantum emitter in the telecom band," arXiv:2304.14685 [quant-ph]. https://arxiv.org/abs/2304.14685.

[109] R. V. Laer, R. N. Patel, T. P. McKenna, J. D. Witmer, and A. H. Safavi-Naeini, "Electrical driving of X-band mechanical waves in a silicon photonic circuit," *APL Photonics* **3** no. 8, (Aug, 2018) 086102. https://aip.scitation.org/doi/full/10.1063/1.5042428.

[110] G. Enzian, M. Szczykulska, J. Silver, L. D. Bino, S. Zhang, I. A. Walmsley, P. Del'Haye, and M. R. Vanner, "Observation of Brillouin optomechanical strong coupling with an 11 GHz mechanical mode," *Optica* **6** no. 1, (Dec, 2018) 7. https://www.osapublishing.org/optica/abstract.cfm?uri=optica-6-1-7.

[111] L. Shao, M. Yu, S. Maity, N. Sinclair, L. Zheng, C. Chia, A. Shams-Ansari, C. Wang, M. Zhang, K. Lai, and M. Lončar, "Microwave-to-optical conversion using lithium niobate thin-film acoustic resonators," *Optica* **6** no. 12, (Dec, 2019) 1498. https://www.osapublishing.org/optica/fulltext.cfm?uri=optica-6-12-1498.

[112] M. Shen, J. Xie, C.-L. Zou, Y. Xu, W. Fu, and H. X. Tang, "High frequency lithium niobate film-thickness-mode optomechanical resonator," *Applied Physics Letters* **117** no. 13, (Sep, 2020) 131104. https://aip.scitation.org/doi/10.1063/5.0020019.

[113] M. Cheng, K. Wang, and J. Sun, "Efficient Brillouin optomechanical interaction assisted by piezomechanics on the SOI platform," *IEEE Photonics Journal* (2021) 1–1. https://ieeexplore.ieee.org/abstract/document/9424382.

[114] N. C. Carvalho, R. Benevides, M. Ménard, G. S. Wiederhecker, N. C. Frateschi, and T. P. M. Alegre, "High-frequency GaAs optomechanical bullseye resonator," *APL Photonics* **6** no. 1, (Jan, 2021) 016104. https://pubs.aip.org/aip/app/article/6/1/016104/123347/High-frequency-GaAs-optomechanical-bullseye.

[115] M. Eichenfield, J. Chan, R. M. Camacho, K. J. Vahala, and O. Painter, "Optomechanical crystals," *Nature* **462** no. 7269, (Oct, 2009) 78–82. https://www.nature.com/articles/nature08524.

[116] K. Fang, M. H. Matheny, X. Luan, and O. Painter, "Optical transduction and routing of microwave phonons in cavity-optomechanical circuits," *Nature Photonics* **10** no. 7, (Jun, 2016) 489–496. https://www.nature.com/articles/nphoton.2016.107.

[117] M. Mirhosseini, A. Sipahigil, M. Kalaee, and O. Painter, "Superconducting qubit to optical photon transduction," *Nature* **588** no. 7839, (Dec, 2020) 599–603, arxiv:2004.04838 [quant-ph]. https://www.nature.com/articles/s41586-020-3038-6.

[118] P. Chiappina, J. Banker, S. Meesala, D. Lake, S. Wood, and O. Painter, "Design of an ultra-low mode volume piezo-optomechanical quantum transducer," arXiv:2303.03664 [quant-ph]. https://arxiv.org/abs/2303.03664.

[119] S. Meesala, S. Wood, D. Lake, P. Chiappina, C. Zhong, A. D. Beyer, M. D. Shaw, L. Jiang, and O. Painter, "Non-classical microwave-optical photon pair generation with a chip-scale transducer," arXiv:2303.17684 [quant-ph].

[120] J. Bochmann, A. Vainsencher, D. D. Awschalom, and A. N. Cleland, "Nanomechanical coupling between microwave and optical photons," *Nature Physics* **9** no. 11, (Sep, 2013) 712–716. https://www.nature.com/articles/nphys2748.

[121] A. Vainsencher, K. J. Satzinger, G. A. Peairs, and A. N. Cleland, "Bi-directional conversion between microwave and optical frequencies in a piezoelectric optomechanical device," *Applied Physics Letters* **109** no. 3, (Jul, 2016) 033107. https://aip.scitation.org/doi/10.1063/1.4955408.

[122] G. A. Peairs, M.-H. Chou, A. Bienfait, H.-S. Chang, C. R. Conner, É. Dumur, J. Grebel, R. G. Povey, E. Şahin, K. J. Satzinger, Y. Zhong, and A. N. Cleland, "Continuous and time-domain coherent signal conversion between optical and microwave frequencies," *Physical Review Applied* **14** no. 6, (Dec, 2020) 061001.

https://journals.aps.org/prapplied/abstract/10.1103/PhysRevApplied.14.061001.

[123] K. C. Balram, M. I. Davanço, J. D. Song, and K. Srinivasan, "Coherent coupling between radiofrequency, optical and acoustic waves in piezo-optomechanical circuits," *Nature Photonics* **10** no. 5, (Mar, 2016) 346–352. https://www.nature.com/articles/nphoton.2016.46.

[124] M. Wu, E. Zeuthen, K. C. Balram, and K. Srinivasan, "Microwave-to-optical transduction using a mechanical supermode for coupling piezoelectric and optomechanical resonators," *Physical Review Applied* **13** no. 1, (Jan, 2020) 014027. https://journals.aps.org/prapplied/abstract/10.1103/PhysRevApplied.13.014027.

[125] K. C. Balram and K. Srinivasan, "Piezoelectric optomechanical approaches for efficient quantum microwave-to-optical signal transduction: the need for co-design," *Advanced Quantum Technologies* **5** no. 3, (Jan, 2022) 2100095, arxiv:2108.11797 [physics.optics]. https://onlinelibrary.wiley.com/doi/full/10.1002/qute.202100095.

[126] R. Riedinger, A. Wallucks, I. Marinković, C. Löschnauer, M. Aspelmeyer, S. Hong, and S. Gröblacher, "Remote quantum entanglement between two micromechanical oscillators," *Nature* **556** no. 7702, (Apr, 2018) 473–477. https://www.nature.com/articles/s41586-018-0036-z.

[127] I. Marinković, A. Wallucks, R. Riedinger, S. Hong, M. Aspelmeyer, and S. Gröblacher, "Optomechanical Bell test," *Physical Review Letters* **121** no. 22, (Nov, 2018) 220404. https://journals.aps.org/prl/abstract/10.1103/PhysRevLett.121.220404.

[128] M. Forsch, R. Stockill, A. Wallucks, I. Marinković, C. Gärtner, R. A. Norte, F. van Otten, A. Fiore, K. Srinivasan, and S. Gröblacher, "Microwave-to-optics conversion using a mechanical oscillator in its quantum ground state," *Nature Physics* **16** no. 1, (Oct, 2019) 69–74. https://www.nature.com/articles/s41567-019-0673-7.

[129] R. Stockill, M. Forsch, F. Hijazi, G. Beaudoin, K. Pantzas, I. Sagnes, R. Braive, and S. Gröblacher, "Ultra-low-noise microwave to optics conversion in gallium phosphide," *Nature Communications* **13** no. 1, (Nov, 2022) 6583, arxiv:2107.04433 [quant-ph]. https://www.nature.com/articles/s41467-022-34338-x.

[130] M. J. Weaver, P. Duivestein, A. C. Bernasconi, S. Scharmer, M. Lemang, T. C. van Thiel, F. Hijazi, B. Hensen, S. Gröblacher, and R. Stockill, "An integrated microwave-to-optics interface for scalable quantum computing," arXiv:2210.15702 [quant-ph]. https://arxiv.org/abs/2210.15702.

[131] W. Jiang, R. N. Patel, F. M. Mayor, T. P. McKenna, P. Arrangoiz-Arriola, C. J. Sarabalis, J. D. Witmer, R. V. Laer, and A. H. Safavi-Naeini, "Lithium niobate

piezo-optomechanical crystals," *Optica* **6** no. 7, (Jul, 2019) 845. https://www.osapublishing.org/optica/abstract.cfm?uri=optica-6-7-845.

[132] W. Jiang, C. J. Sarabalis, Y. D. Dahmani, R. N. Patel, F. M. Mayor, T. P. McKenna, R. V. Laer, and A. H. Safavi-Naeini, "Efficient bidirectional piezo-optomechanical transduction between microwave and optical frequency," *Nature Communications* **11** no. 1, (Mar, 2020) 1166. https://www.nature.com/articles/s41467-020-14863-3.

[133] W. Jiang, F. M. Mayor, S. Malik, R. V. Laer, T. P. McKenna, R. N. Patel, J. D. Witmer, and A. H. Safavi-Naeini, "Optically heralded microwave photons," arXiv:2210.10739 [quant-ph]. https://arxiv.org/abs/2210.10739.

[134] L. Qiu, I. Shomroni, P. Seidler, and T. J. Kippenberg, "Laser cooling of a nanomechanical oscillator to its zero-point energy," *Physical Review Letters* **124** no. 17, (Apr, 2020) 173601. https://journals.aps.org/prl/abstract/10.1103/PhysRevLett.124.173601.

[135] S. Hönl, Y. Popoff, D. Caimi, A. Beccari, T. J. Kippenberg, and P. Seidler, "Microwave-to-optical conversion with a gallium phosphide photonic crystal cavity," *Nature Communications* **13** no. 1, (Apr, 2022) 2065, arxiv:2105.13242 [physics.optics]. https://www.nature.com/articles/s41467-022-28670-5.

[136] G. Arnold, M. Wulf, S. Barzanjeh, E. S. Redchenko, A. Rueda, W. J. Hease, F. Hassani, and J. M. Fink, "Converting microwave and telecom photons with a silicon photonic nanomechanical interface," *Nature Communications* **11** no. 1, (Sep, 2020) 4460, arxiv:2002.11628 [quant-ph]. https://www.nature.com/articles/s41467-020-18269-z.

[137] A. G. Primo, P. V. Pinho, R. Benevides, S. Gröblacher, G. S. Wiederhecker, and T. P. M. Alegre, "Waveguide-cavity scattering in high-frequency dissipative optomechanics," arXiv:2212.14533 [physics.optics]. https://arxiv.org/abs/2212.14533.

[138] M. Aspelmeyer, T. J. Kippenberg, and F. Marquardt, "Cavity optomechanics," *Reviews of Modern Physics* **86** no. 4, (Dec, 2014) 1391–1452. https://journals.aps.org/rmp/abstract/10.1103/RevModPhys.86.1391.

[139] M. Aspelmeyer, T. J. Kippenberg, and F. Marquardt, eds., *Cavity optomechanics*. Quantum Science and Technology. Springer Berlin Heidelberg, 2014. https://link.springer.com/book/10.1007/978-3-642-55312-7.

[140] W. P. Bowen and G. J. Milburn, *Quantum optomechanics*. CRC Press, 2015.

[141] Z. Shen, *Experimental Research of Cavity Optomechanics*. Springer Singapore, 2021.

[142] S. Barzanjeh, A. Xuereb, S. Gröblacher, M. Paternostro, C. A. Regal, and E. M. Weig, "Optomechanics for quantum technologies," *Nature Physics* **18** no. 1, (Nov.,

2021) 15–24, arXiv:2111.14715 [quant-ph]. https://www.nature.com/articles/s41567-021-01402-0.

[143] S. M. Meenehan, J. D. Cohen, G. S. MacCabe, F. Marsili, M. D. Shaw, and O. Painter, "Pulsed excitation dynamics of an optomechanical crystal resonator near its quantum ground state of motion," *Physical Review X* **5** no. 4, (Oct, 2015) 041002. https://journals.aps.org/prx/abstract/10.1103/PhysRevX.5.041002.

[144] S. G. Hofer, W. Wieczorek, M. Aspelmeyer, and K. Hammerer, "Quantum entanglement and teleportation in pulsed cavity optomechanics," *Physical Review A* **84** no. 5, (Nov, 2011) 052327. https://journals.aps.org/pra/abstract/10.1103/PhysRevA.84.052327.

[145] S.-S. Chen, H. Zhang, Q. Ai, and G.-J. Yang, "Phononic entanglement concentration via optomechanical interactions," *Physical Review A* **100** no. 5, (Nov, 2019) 052306. https://journals.aps.org/pra/abstract/10.1103/PhysRevA.100.052306.

[146] S. Krastanov, H. Raniwala, J. Holzgrafe, K. Jacobs, M. Lončar, M. J. Reagor, and D. R. Englund, "Optically heralded entanglement of superconducting systems in quantum networks," *Physical Review Letters* **127** no. 4, (Jul, 2021) 040503, arxiv:2012.13408 [quant-ph]. https://journals.aps.org/prl/abstract/10.1103/PhysRevLett.127.040503.

[147] C. Zhong, X. Han, and L. Jiang, "Microwave and optical entanglement for quantum transduction with electro-optomechanics," *Physical Review Applied* **18** no. 5, (Nov, 2022) 054061. https://journals.aps.org/prapplied/abstract/10.1103/PhysRevApplied.18.054061.

[148] J. D. Joannopoulos, S. G. Johnson, J. N. Winn, and R. D. Meade, *Photonic crystals: molding the flow of light*. Princeton University Press, 2011.

[149] H. Benisty, C. Weisbuch, D. Labilloy, M. Rattier, C. J. M. Smith, T. F. Krauss, R. M. de la Rue, R. Houdré, U. Oesterle, C. Jouanin, and D. Cassagne, "Optical and confinement properties of two-dimensional photonic crystals," *Journal of Lightwave Technology* **17** no. 11, (1999) 2063–2077. https://ieeexplore.ieee.org/document/802996/.

[150] S. Olivier, H. Benisty, M. Rattier, C. Weisbuch, M. Qiu, A. Karlsson, C. J. M. Smith, R. Houdré, and U. Oesterle, "Resonant and nonresonant transmission through waveguide bends in a planar photonic crystal," *Applied Physics Letters* **79** no. 16, (Oct, 2001) 2514–2516. https://aip.scitation.org/doi/10.1063/1.1410338.

[151] M. Qiu, K. Azizi, A. Karlsson, M. Swillo, and B. Jaskorzynska, "Numerical studies of mode gaps and coupling efficiency for line-defect waveguides in two-dimensional photonic crystals," *Physical Review B* **64** no. 15, (Sep, 2001) 155113. https://journals.aps.org/prb/abstract/10.1103/PhysRevB.64.155113.

[152] H. Ren, M. H. Matheny, G. S. MacCabe, J. Luo, H. Pfeifer, M. Mirhosseini, and O. Painter, "Two-dimensional optomechanical crystal cavity with high quantum cooperativity," *Nature Communications* **11** no. 1, (Jul, 2020) 3373. https://www.nature.com/articles/s41467-020-17182-9.

[153] A. Andronico, I. Favero, and G. Leo, "Difference frequency generation in GaAs microdisks," *Optics Letters* **33** no. 18, (Sep, 2008) 2026. https://www.osapublishing.org/ol/abstract.cfm?uri=ol-33-18-2026.

[154] L. Ding, C. Baker, P. Senellart, A. Lemaitre, S. Ducci, G. Leo, and I. Favero, "High frequency GaAs nano-optomechanical disk resonator," *Physical Review Letters* **105** no. 26, (Dec, 2010) 263903. https://journals.aps.org/prl/abstract/10.1103/PhysRevLett.105.263903.

[155] L. Ding, C. Baker, P. Senellart, A. Lemaitre, S. Ducci, G. Leo, and I. Favero, "Wavelength-sized GaAs optomechanical resonators with gigahertz frequency," *Applied Physics Letters* **98** no. 11, (Mar, 2011) 113108. https://aip.scitation.org/doi/10.1063/1.3563711.

[156] C. Baker, W. Hease, D.-T. Nguyen, A. Andronico, S. Ducci, G. Leo, and I. Favero, "Photoelastic coupling in gallium arsenide optomechanical disk resonators," *Optics Express* **22** no. 12, (Jun, 2014) 14072. https://www.osapublishing.org/oe/abstract.cfm?uri=oe-22-12-14072.

[157] K. C. Balram, M. Davanço, J. Y. Lim, J. D. Song, and K. Srinivasan, "Moving boundary and photoelastic coupling in GaAs optomechanical resonators," *Optica* **1** no. 6, (Dec, 2014) 414. https://www.osapublishing.org/optica/abstract.cfm?uri=optica-1-6-414.

[158] H. Ramp, B. Hauer, K. Balram, T. Clark, K. Srinivasan, and J. Davis, "Elimination of thermomechanical noise in piezoelectric optomechanical crystals," *Physical Review Letters* **123** no. 9, (Aug, 2019) 093603. https://journals.aps.org/prl/abstract/10.1103/PhysRevLett.123.093603.

[159] K. Srinivasan and O. Painter, "Momentum space design of high-Q photonic crystal optical cavities," *Optics Express* **10** no. 15, (Jul, 2002) 670. https://www.osapublishing.org/oe/abstract.cfm?uri=oe-10-15-670.

[160] Y. Akahane, T. Asano, B.-S. Song, and S. Noda, "High-Q photonic nanocavity in a two-dimensional photonic crystal," *Nature* **425** no. 6961, (Oct, 2003) 944–947. https://www.nature.com/articles/nature02063.

[161] U. K. Khankhoje, S.-H. Kim, B. C. Richards, J. Hendrickson, J. Sweet, J. D. Olitzky, G. Khitrova, H. M. Gibbs, and A. Scherer, "Modelling and fabrication of GaAs photonic-crystal cavities for cavity quantum electrodynamics," *Nanotechnology* **21** no. 6, (Jan, 2010) 065202. https://iopscience.iop.org/article/10.1088/0957-4484/21/6/065202.

[162] J. Riedrich-Möller, L. Kipfstuhl, C. Hepp, E. Neu, C. Pauly, F. Mücklich, A. Baur, M. Wandt, S. Wolff, M. Fischer, S. Gsell, M. Schreck, and C. Becher, "One- and two-dimensional photonic crystal microcavities in single crystal diamond," *Nature Nanotechnology* **7** no. 1, (Nov, 2011) 69–74. https://www.nature.com/articles/nnano.2011.190.

[163] Y. Zhang, C. Zeng, D. Li, G. Gao, Z. Huang, J. Yu, and J. Xia, "High-quality-factor photonic crystal ring resonator," *Optics Letters* **39** no. 5, (Feb, 2014) 1282. https://opg.optica.org/ol/fulltext.cfm?uri=ol-39-5-1282.

[164] M. Li, H. Liang, R. Luo, Y. He, and Q. Lin, "High-quality two-dimensional lithium niobate photonic crystal slab nanoresonators,". https://www.osapublishing.org/abstract.cfm?uri=FiO-2018-FTu4E.4.

[165] M. Eichenfield, J. Chan, A. H. Safavi-Naeini, K. J. Vahala, and O. Painter, "Modeling dispersive coupling and losses of localized optical and mechanical modes in optomechanical crystals," *Optics Express* **17** no. 22, (Oct, 2009) 20078. https://www.osapublishing.org/oe/abstract.cfm?uri=oe-17-22-20078.

[166] E. Gavartin, R. Braive, I. Sagnes, O. Arcizet, A. Beveratos, T. J. Kippenberg, and I. Robert-Philip, "Optomechanical coupling in a two-dimensional photonic crystal defect cavity," *Physical Review Letters* **106** no. 20, (May, 2011) 203902. https://journals.aps.org/prl/abstract/10.1103/PhysRevLett.106.203902.

[167] S. El-Jallal, M. Oudich, Y. Pennec, B. Djafari-Rouhani, V. Laude, J.-C. Beugnot, A. Martínez, J. M. Escalante, and A. Makhoute, "Analysis of optomechanical coupling in two-dimensional square lattice phoxonic crystal slab cavities," *Physical Review B* **88** no. 20, (Nov, 2013) 205410. https://journals.aps.org/prb/abstract/10.1103/PhysRevB.88.205410.

[168] M. Maldovan and E. L. Thomas, "Simultaneous localization of photons and phonons in two-dimensional periodic structures," *Applied Physics Letters* **88** no. 25, (Jun, 2006) 251907. https://aip.scitation.org/doi/10.1063/1.2216885.

[169] S. Mohammadi, A. A. Eftekhar, A. Khelif, and A. Adibi, "Simultaneous two-dimensional phononic and photonic band gaps in opto-mechanical crystal slabs," *Optics Express* **18** no. 9, (Apr, 2010) 9164. https://www.osapublishing.org/oe/abstract.cfm?uri=oe-18-9-9164.

[170] T. P. M. Alegre, A. Safavi-Naeini, M. Winger, and O. Painter, "Quasi-two-dimensional optomechanical crystals with a complete phononic bandgap," *Optics Express* **19** no. 6, (Mar, 2011) 5658. https://opg.optica.org/oe/fulltext.cfm?uri=oe-19-6-5658.

[171] H. Sekoguchi, Y. Takahashi, T. Asano, and S. Noda, "Photonic crystal nanocavity with a Q-factor of ~ 9 million," *Optics Express* **22** no. 1, (Jan, 2014) 916. https://opg.optica.org/oe/fulltext.cfm?uri=oe-22-1-916.

[172] K. Makles, T. Antoni, A. G. Kuhn, S. Deléglise, T. Briant, P.-F. Cohadon, R. Braive, G. Beaudoin, L. Pinard, C. Michel, V. Dolique, R. Flaminio, G. Cagnoli, I. Robert-Philip, and A. Heidmann, "2D photonic-crystal optomechanical nanoresonator," *Optics Letters* **40** no. 2, (Jan, 2015) 174. https://www.osapublishing.org/ol/abstract.cfm?uri=ol-40-2-174.

[173] R. Benevides, F. G. S. Santos, G. O. Luiz, G. S. Wiederhecker, and T. P. M. Alegre, "Ultrahigh-Q optomechanical crystal cavities fabricated in a CMOS foundry," *Scientific Reports* **7** no. 1, (May, 2017) 2491. https://www.nature.com/articles/s41598-017-02515-4.

[174] A. H. Safavi-Naeini, T. P. M. Alegre, M. Winger, and O. Painter, "Optomechanics in an ultrahigh-Q two-dimensional photonic crystal cavity," *Applied Physics Letters* **97** no. 18, (Nov, 2010) 181106. https://aip.scitation.org/doi/10.1063/1.3507288.

[175] A. Pitanti, J. M. Fink, A. H. Safavi-Naeini, J. T. Hill, C. U. Lei, A. Tredicucci, and O. Painter, "Strong opto-electro-mechanical coupling in a silicon photonic crystal cavity," *Optics Express* **23** no. 3, (Feb, 2015) 3196. https://www.osapublishing.org/oe/abstract.cfm?uri=oe-23-3-3196.

[176] A. H. Safavi-Naeini and O. Painter, "Design of optomechanical cavities and waveguides on a simultaneous bandgap phononic-photonic crystal slab," *Optics Express* **18** no. 14, (Jun, 2010) 14926. https://www.osapublishing.org/oe/abstract.cfm?uri=oe-18-14-14926.

[177] A. H. Safavi-Naeini, J. T. Hill, S. Meenehan, J. Chan, S. Gröblacher, and O. Painter, "Two-dimensional phononic-photonic band gap optomechanical crystal cavity," *Physical Review Letters* **112** no. 15, (Apr, 2014) 153603. https://journals.aps.org/prl/abstract/10.1103/PhysRevLett.112.153603.

[178] C. M. Kersul, R. Benevides, F. Moraes, G. H. M. de Aguiar, A. Wallucks, S. Gröblacher, G. S. Wiederhecker, and T. P. M. Alegre, "Silicon anisotropy in a bi-dimensional optomechanical cavity," *APL Photonics* **8** no. 5, (May, 2023) 056112, arXiv:2211.10573 [quant-ph]. https://pubs.aip.org/aip/app/article/8/5/056112/2892992.

[179] G. S. MacCabe, H. Ren, J. Luo, J. D. Cohen, H. Zhou, A. Sipahigil, M. Mirhosseini, and O. Painter, "Nano-acoustic resonator with ultralong phonon lifetime," *Science* **370** no. 6518, (Nov, 2020) 840–843, arxiv:1901.04129 [cond-mat.mes-hall].

[180] O. Florez, G. Arregui, M. Albrechtsen, R. C. Ng, J. Gomis-Bresco, S. Stobbe, C. M. Sotomayor-Torres, and P. D. García, "Engineering nanoscale hypersonic phonon transport," *Nature Nanotechnology* **17** no. 9, (Aug, 2022) 947–951. https://www.nature.com/articles/s41565-022-01178-1.

[181] COMSOL AB, "COMSOL Multiphysics®." http://www.comsol.com.

[182] The MathWorks Inc., "MATLAB®." https://www.mathworks.com/products/matlab.html.

[183] G. S. MacCabe, *Phonon dynamics and damping in three-dimensional acoustic bandgap cavity-optomechanical resonators*. PhD thesis, California Institute of Technology, 2019. https://thesis.library.caltech.edu/11417/.

[184] D. Morgan, *Surface Acoustic Wave Filters With Applications to Electronic Communications and Signal Processing*. Elsevier Science & Technology Books, 2010. https://www.elsevier.com/books/surface-acoustic-wave-filters/morgan/978-0-12-372537-0.

[185] Y. Takagaki, E. Wiebicke, P. V. Santos, R. Hey, and K. H. Ploog, "Propagation of surface acoustic waves in a GaAs/AlAs/GaAs heterostructure and micro-beams," *Semiconductor Science and Technology* **17** no. 9, (Aug, 2002) 1008–1012. https://iopscience.iop.org/article/10.1088/0268-1242/17/9/319.

[186] M. M. de Lima, F. Alsina, W. Seidel, and P. V. Santos, "Focusing of surface-acoustic-wave fields on (100) GaAs surfaces," *Journal of Applied Physics* **94** no. 12, (2003) 7848. https://aip.scitation.org/doi/abs/10.1063/1.1625419.

[187] M. M. de Lima, W. Seidel, H. Kostial, and P. V. Santos, "Embedded interdigital transducers for high-frequency surface acoustic waves on GaAs," *Journal of Applied Physics* **96** no. 6, (Sep, 2004) 3494–3500. https://aip.scitation.org/doi/10.1063/1.1782961.

[188] T.-T. Wu, H.-T. Tang, Y.-Y. Chen, and P.-L. Liu, "Analysis and design of focused interdigital transducers," *IEEE Transactions on Ultrasonics, Ferroelectrics and Frequency Control* **52** no. 8, (Aug, 2005) 1384–1392. https://ieeexplore.ieee.org/abstract/document/1509798.

[189] V. Laude, D. Gérard, N. Khelfaoui, C. F. Jerez-Hanckes, S. Benchabane, and A. Khelif, "Subwavelength focusing of surface acoustic waves generated by an annular interdigital transducer," *Applied Physics Letters* **92** no. 9, (Mar, 2008) 094104. https://aip.scitation.org/doi/10.1063/1.2891055.

[190] M. K. Ekström, T. Aref, A. Ask, G. Andersson, B. Suri, H. Sanada, G. Johansson, and P. Delsing, "Towards phonon routing: controlling propagating acoustic waves in the quantum regime," *New Journal of Physics* **21** no. 12, (Dec, 2019) 123013. https://iopscience.iop.org/article/10.1088/1367-2630/ab5ca5.

[191] A. Siddiqui, R. H. Olsson, and M. Eichenfield, "Lamb wave focusing transducer for efficient coupling to wavelength-scale structures in thin piezoelectric films," *Journal of Microelectromechanical Systems* **27** no. 6, (Dec, 2018) 1054–1070. https://ieeexplore.ieee.org/abstract/document/8456611.

[192] P. Arrangoiz-Arriola, E. A. Wollack, M. Pechal, J. D. Witmer, J. T. Hill, and A. H. Safavi-Naeini, "Coupling a superconducting quantum circuit to a phononic crystal defect cavity," *Physical Review X* **8** no. 3, (Jul, 2018) 031007. https://journals.aps.org/prx/abstract/10.1103/PhysRevX.8.031007.

[193] Y. D. Dahmani, C. J. Sarabalis, W. Jiang, F. M. Mayor, and A. H. Safavi-Naeini, "Piezoelectric transduction of a wavelength-scale mechanical waveguide," *Physical Review Applied* **13** no. 2, (Feb, 2020) 024069. https://journals.aps.org/prapplied/abstract/10.1103/PhysRevApplied.13.024069.

[194] E. A. Wollack, A. Y. Cleland, R. G. Gruenke, Z. Wang, P. Arrangoiz-Arriola, and A. H. Safavi-Naeini, "Quantum state preparation and tomography of entangled mechanical resonators," *Nature* **604** no. 7906, (Apr, 2022) 463–467, arXiv:2110.07561 [quant-ph]. https://www.nature.com/articles/s41586-022-04500-y.

[195] N. Clark, "Hydrogen silsesquioxane (HSQ) for use in nano imprint lithography," Master's thesis, Henry M. Rowan College of Engineering, 2009. https://rdw.rowan.edu/etd/370/.

[196] X. Chen, T. Zhang, V. Constantoudis, S.-L. Zhang, and Z. Zhang, "Aged hydrogen silsesquioxane for sub-10nm line patterns," *Microelectronic Engineering* **163** (Sep, 2016) 105–109. https://www.sciencedirect.com/science/article/abs/pii/S0167931716303343.

[197] Genisys, "TRACER." https://www.genisys-gmbh.com/tracer.html.

[198] D. Drouin, A. R. Couture, D. Joly, X. Tastet, V. Aimez, and R. Gauvin, "CASINO v2.42—a fast and easy-to-use modeling tool for scanning electron microscopy and microanalysis users," *Scanning* **29** no. 3, (2007) 92–101. https://onlinelibrary.wiley.com/doi/abs/10.1002/sca.20000.

[199] B. A. Nilsson, "Experimental evaluation method of point spread functions used for proximity effects correction in electron beam lithography," *Journal of Vacuum Science & Technology B, Nanotechnology and Microelectronics: Materials, Processing, Measurement, and Phenomena* **29** no. 6, (Nov, 2011) 06F311. https://avs.scitation.org/doi/10.1116/1.3656343.

[200] S. Babin, S. Borisov, A. Ivanchikov, and I. Ruzavin, "CHARIOT: Software tool for modeling SEM signal and e-beam lithography," *Physics procedia* **1** no. 1, (Aug, 2008) 305–313. https://www.sciencedirect.com/science/article/pii/S187538920800120X.

[201] Genisys, "BEAMER." https://www.genisys-gmbh.com/beamer.html.

[202] M. Konagai, M. Sugimoto, and K. Takahashi, "High efficiency GaAs thin film solar cells by peeled film technology," *Journal of Crystal Growth* **45** (Dec, 1978) 277–280. http://www.sciencedirect.com/science/article/pii/0022024878904499.

[203] X. S. Wu, L. A. Coldren, and J. L. Merz, "Selective etching characteristics of HF for AlxGa1-xAs/GaAs," *Electronics Letters* **21** no. 13, (1985) 558. https://ieeexplore.ieee.org/abstract/document/4251323.

[204] M. M. A. J. Voncken, J. J. Schermer, A. T. J. van Niftrik, G. J. Bauhuis, P. Mulder, P. K. Larsen, T. P. J. Peters, B. de Bruin, A. Klaassen, and J. J. Kelly, "Etching AlAs with HF for epitaxial lift-off applications," *Journal of The Electrochemical Society* **151** no. 5, (2004) G347. https://iopscience.iop.org/article/10.1149/1.1690293.

[205] P. Kumar, S. Kanakaraju, and D. L. DeVoe, "Sacrificial etching of AlxGa1-xAs for III-V MEMS surface micromachining," *Applied Physics A* **88** no. 4, (May, 2007) 711–714. https://link.springer.com/article/10.1007/s00339-007-4032-7.

[206] J. Sweet, B. C. Richards, J. D. Olitzky, J. Hendrickson, G. Khitrova, H. M. Gibbs, D. Litvinov, D. Gerthsen, D. Z. Hu, D. M. Schaadt, M. Wegener, U. Khankhoje, and A. Scherer, "GaAs photonic crystal slab nanocavities: Growth, fabrication, and quality factor," *Photonics and Nanostructures - Fundamentals and Applications* **8** no. 1, (Jan, 2010) 1–6. https://www.sciencedirect.com/science/article/pii/S1569441009000558.

[207] S. K. Manjeshwar, *Free-space cavity optomechanical systems on a chip with III-V heterostructures*. PhD thesis, Chalmers University of Technology, 2023. https://research.chalmers.se/en/publication/534269.

[208] G. C. DeSalvo, C. A. Bozada, J. L. Ebel, D. C. Look, J. P. Barrette, C. L. A. Cerny, R. W. Dettmer, J. K. Gillespie, C. K. Havasy, T. J. Jenkins, K. Nakano, C. I. Pettiford, T. K. Quach, J. S. Sewell, and G. D. Via, "Wet chemical digital etching of GaAs at room temperature," *Journal of The Electrochemical Society* **143** no. 11, (Nov, 1996) 3652–3656. https://iopscience.iop.org/article/10.1149/1.1837266.

[209] L. Midolo, T. Pregnolato, G. Kiršanskė, and S. Stobbe, "Soft-mask fabrication of gallium arsenide nanomembranes for integrated quantum photonics," *Nanotechnology* **26** no. 48, (Nov, 2015) 484002, 1506.00376. https://iopscience.iop.org/article/10.1088/0957-4484/26/48/484002.

[210] L. Glasser, "Equations of state and phase diagrams," *Journal of Chemical Education* **79** no. 7, (Jul, 2002) 874. https://pubs.acs.org/doi/abs/10.1021/ed079p874.

[211] A. N. Cleland, *Foundations of nanomechanics*. Springer Berlin Heidelberg, 2003. https://link.springer.com/book/10.1007/978-3-662-05287-7.

[212] M.-H. Chou, É. Dumur, Y. P. Zhong, G. A. Peairs, A. Bienfait, H.-S. Chang, C. R. Conner, J. Grebel, R. G. Povey, K. J. Satzinger, and A. N. Cleland, "Measurements of a quantum bulk acoustic resonator using a superconducting qubit," *Applied Physics*

Letters **117** no. 25, (Dec, 2020) 254001. https://pubs.aip.org/aip/apl/article/117/25/254001/39297/Measurements-of-a-quantum-bulk-acoustic-resonator.

[213] S. M. Meenehan, J. D. Cohen, S. Gröblacher, J. T. Hill, A. H. Safavi-Naeini, M. Aspelmeyer, and O. Painter, "Silicon optomechanical crystal resonator at millikelvin temperatures," *Physical Review A* **90** no. 1, (Jul, 2014) 011803. https://journals.aps.org/pra/abstract/10.1103/PhysRevA.90.011803.

[214] K. J. Satzinger, C. R. Conner, A. Bienfait, H.-S. Chang, M.-H. Chou, A. Y. Cleland, É. Dumur, J. Grebel, G. A. Peairs, R. G. Povey, S. J. Whiteley, Y. P. Zhong, D. D. Awschalom, D. I. Schuster, and A. N. Cleland, "Simple non-galvanic flip-chip integration method for hybrid quantum systems," *Applied Physics Letters* **114** no. 17, (Apr, 2019) 173501. https://pubs.aip.org/aip/apl/article/114/17/173501/36631/Simple-non-galvanic-flip-chip-integration-method.

[215] P. Piergentili, L. Catalini, M. Bawaj, S. Zippilli, N. Malossi, R. Natali, D. Vitali, and G. D. Giuseppe, "Two-membrane cavity optomechanics," *New Journal of Physics* **20** no. 8, (Aug, 2018) 083024. https://iopscience.iop.org/article/10.1088/1367-2630/aad85f/meta.

[216] P. Piergentili, W. Li, R. Natali, N. Malossi, D. Vitali, and G. D. Giuseppe, "Two-membrane cavity optomechanics: non-linear dynamics," *New Journal of Physics* **23** no. 7, (Jul, 2021) 073013. https://iopscience.iop.org/article/10.1088/1367-2630/abdd6a/meta.

[217] J. del Pino, J. J. Slim, and E. Verhagen, "Non-hermitian chiral phononics through optomechanically induced squeezing," *Nature* **606** no. 7912, (Jun, 2022) 82–87, arXiv:2110.14710 [cond-mat.mes-hall]. https://www.nature.com/articles/s41586-022-04609-0.

[218] J. Guo and S. Gröblacher, "Coherent feedback in optomechanical systems in the sideband-unresolved regime," *Quantum* **6** (June, 2022) 848, arXiv:2206.13917 [quant-ph]. https://quantum-journal.org/papers/q-2022-11-03-848/.

[219] P. Piergentili, W. Li, R. Natali, D. Vitali, and G. D. Giuseppe, "Absolute determination of the single-photon optomechanical coupling rate via a Hopf bifurcation," *Physical Review Applied* **15** no. 3, (Mar, 2021) 034012, arxiv:2012.05886 [quant-ph]. https://journals.aps.org/prapplied/abstract/10.1103/PhysRevApplied.15.034012.

[220] K. Zhang and D. Li, *Electromagnetic theory for microwaves and optoelectronics*. Springer, 2008.

[221] W. Heywang, K. Lubitz, and W. Wersing, eds., *Piezoelectricity*. Springer Series in Materials Science. Springer Berlin Heidelberg, 2008. https://www.springer.com/us/book/9783540686804.

[222] B. A. Auld, *Acoustic fields and waves in solids*. Wiley, 1973.

[223] R. F. Harrington, *Time-harmonic electromagnetic fields*. McGraw-Hill, 1961.

[224] A. Yariv and P. Yeh, *Optical waves in crystal*. Wiley, 1984.

[225] J. Chan, *Laser cooling of an optomechanical crystal resonator to its quantum ground state of motion*. PhD thesis, California Institute of Technology, 2012. https://thesis.library.caltech.edu/7098/.

[226] J. Chan, A. H. Safavi-Naeini, J. T. Hill, S. Meenehan, and O. Painter, "Optimized optomechanical crystal cavity with acoustic radiation shield," *Applied Physics Letters* **101** no. 8, (Aug, 2012) 081115. https://aip.scitation.org/doi/10.1063/1.4747726.

[227] W. Zhou, Z. Yu, J. Ma, B. Zhu, H. K. Tsang, and X. Sun, "Ultraviolet optomechanical crystal cavities with ultrasmall modal mass and high optomechanical coupling rate," *Scientific Reports* **6** no. 1, (Nov, 2016) 37134. https://www.nature.com/articles/srep37134.

[228] P. Helnwein, "Some remarks on the compressed matrix representation of symmetric second-order and fourth-order tensors," *Computer Methods in Applied Mechanics and Engineering* **190** no. 22-23, (Feb, 2001) 2753–2770. https://www.sciencedirect.com/science/article/pii/S0045782500002632.

[229] C. W. Gardiner and M. J. Collett, "Input and output in damped quantum systems: Quantum stochastic differential equations and the master equation," *Physical Review A* **31** no. 6, (Jun, 1985) 3761–3774. https://journals.aps.org/pra/abstract/10.1103/PhysRevA.31.3761.

[230] A. S. Vainsencher, *Building an optomechanical interface for superconducting qubits*. PhD thesis, University of California, Santa Barbara, 2016. https://alexandria.ucsb.edu/lib/ark:/48907/f31c1wqf.

[231] D. F. Walls and G. J. Milburn, *Quantum optics*. Springer, 2008.

[232] C. Gardiner and P. Zoller, *Quantum noise: a handbook of Markovian and non-Markovian quantum stochastic methods with applications to quantum optics*. Springer Series in Synergetics. Springer, 2004.

[233] R. Kubo, "The fluctuation-dissipation theorem," *Reports on Progress in Physics* **29** no. 1, (Jan, 1966) 255–284. https://iopscience.iop.org/article/10.1088/0034-4885/29/1/306/meta.

[234] F. Marquardt, J. P. Chen, A. A. Clerk, and S. M. Girvin, "Quantum theory of cavity-assisted sideband cooling of mechanical motion," *Physical Review Letters* **99** no. 9, (Aug, 2007) 093902. https://journals.aps.org/prl/abstract/10.1103/PhysRevLett.99.093902.

[235] A. H. Safavi-Naeini, *Quantum optomechanics with silicon nanostructures*. PhD thesis, California Institute of Technology, 2013. https://thesis.library.caltech.edu/7797/.

[236] X. Han, C.-L. Zou, and H. X. Tang, "Multimode strong coupling in superconducting cavity piezoelectromechanics," *Physical Review Letters* **117** no. 12, (Sep, 2016) 123603. https://journals.aps.org/prl/abstract/10.1103/PhysRevLett.117.123603.

[237] M. L. Gorodetsky, A. Schliesser, G. Anetsberger, S. Deleglise, and T. J. Kippenberg, "Determination of the vacuum optomechanical coupling rate using frequency noise calibration," *Optics Express* **18** no. 22, (Oct, 2010) 23236. https://www.osapublishing.org/oe/abstract.cfm?uri=oe-18-22-23236.

[238] J. S. Blakemore, "Semiconducting and other major properties of gallium arsenide," *Journal of Applied Physics* **53** no. 10, (Oct, 1982) R123–R181. https://aip.scitation.org/doi/10.1063/1.331665.

[239] A. Dargys and J. Kundrotas, *Handbook on physical properties of Ge, Si, GaAs and InP*. Science and Encyclopedia Publishers, 1994. https://books.google.com/books?id=_VtnQgAACAAJ.

[240] M. R. Brozel and G. E. Stillman, eds., *Properties of gallium arsenide*. An INSPEC publication. INSPEC, 1996. https://books.google.com/books?id=JDiPI-s1SPEC.

[241] S. Adachi, *Properties of group-IV, III-V and II-VI semiconductors*. Wiley Series in Materials for Electronic & Optoelectronic Applications. John Wiley & Sons, 2005. https://books.google.com/books?id=J6W5n5Z1EQIC.

[242] R. I. Cottam and G. A. Saunders, "The elastic constants of GaAs from 2 K to 320 K," *Journal of Physics C: Solid State Physics* **6** no. 13, (Jul, 1973) 2105–2118. https://iopscience.iop.org/article/10.1088/0022-3719/6/13/011.

[243] G. Arlt and P. Quadflieg, "Piezoelectricity in III-V compounds with a phenomenological analysis of the piezoelectric effect," *Physica Status Solidi (b)* **25** no. 1, (1968) 323–330. https://onlinelibrary.wiley.com/doi/abs/10.1002/pssb.19680250131.

[244] J. F. Nye, *Physical Properties of Crystals*. Clarendon Press, 1985. https://books.google.com/books?id=ugwql-uVB44C.

[245] R. W. Dixon, "Photoelastic properties of selected materials and their relevance for applications to acoustic light modulators and scanners," *Journal of Applied Physics* **38** no. 13, (Dec, 1967) 5149–5153. https://aip.scitation.org/doi/10.1063/1.1709293.

[246] N. Suzuki and K. Tada, "Elastooptic and electrooptic properties of GaAs," *Japanese Journal of Applied Physics* **23** no. Part 1, No. 8, (Aug, 1984) 1011–1016. https://iopscience.iop.org/article/10.1143/JJAP.23.1011.

[247] J. S. Blakemore, "Mid-infrared dispersion of the refractive index and reflectivity for GaAs," *Journal of Applied Physics* **62** no. 11, (Dec, 1987) 4528–4532. https://aip.scitation.org/doi/10.1063/1.339044.

[248] W. Sellmeier, "Zur erkarung der abnormen farbenfolge im spectrum einiger. substanzen," *Annalen der Physik und Chemie* **219** (1871) 272–282.

[249] T. Skauli, P. S. Kuo, K. L. Vodopyanov, T. J. Pinguet, O. Levi, L. A. Eyres, J. S. Harris, M. M. Fejer, B. Gerard, L. Becouarn, and E. Lallier, "Improved dispersion relations for GaAs and applications to nonlinear optics," *Journal of Applied Physics* **94** no. 10, (Nov, 2003) 6447–6455. https://aip.scitation.org/doi/10.1063/1.1621740.

[250] A. N. Pikhtin and A. D. Yas'kov, "Dispersion of the refractive index in semiconductors with diamond and zinc-blend structures," *Soviet Physics: Semiconductors* **12** no. 6, (1978) 622–626.

[251] B. D. Lichter and P. Sommelet, "Thermal properties of a^{III} b^{V} compounds: II. high-temperature heat contents and heats of fusion of InAs and GaAs," *Transition Metal Society AIME* **245** (1969) 1021–1027.

[252] T. C. Cetas, C. R. Tilford, and C. A. Swenson, "Specific heats of Cu, GaAs, GaSb, InAs, and InSb from 1 to 30°K," *Physical Review* **174** no. 3, (Oct, 1968) 835–844. https://journals.aps.org/pr/abstract/10.1103/PhysRev.174.835.

[253] U. Piesbergen, "Die durchschnittlichen atomwärmen der $\mathrm{A^{III}}$ $\mathrm{B^{V}}$-halbleiter AlSb, GaAs, GaSb, InP, InAs, lnSb und die atomwärme des elements germanium zwischen 12 und 273°K," *Zeitschrift für Naturforschung A* **18** no. 2, (Feb, 1963) 141–147. https://www.degruyter.com/view/j/zna.1963.18.issue-2/zna-1963-0206/zna-1963-0206.xml.

[254] M. G. Holland, "Phonon scattering in semiconductors from thermal conductivity studies," *Physical Review* **134** no. 2A, (Apr, 1964) A471–A480. https://journals.aps.org/pr/abstract/10.1103/PhysRev.134.A471.

[255] S. I. Novikova, "Investigation of thermal expansion of GaAs and ZnSe," *Soviet Physics: Solid State* **3** no. 1, (1961) .

[256] P. W. Sparks and C. A. Swenson, "Thermal expansions from 2 to 40°K of Ge, Si, and four III-V compounds," *Physical Review* **163** no. 3, (Nov, 1967) 779–790. https://journals.aps.org/pr/abstract/10.1103/PhysRev.163.779.

[257] R. Feder and T. Light, "Precision thermal expansion measurements of semi-insulating GaAs," *Journal of Applied Physics* **39** no. 10, (Sep, 1968) 4870–4871. https://aip.scitation.org/doi/10.1063/1.1655870.

[258] T. F. Smith and G. K. White, "The low-temperature thermal expansion and Gruneisen parameters of some tetrahedrally bonded solids," *Journal of Physics C: Solid State Physics* **8** no. 13, (Jul, 1975) 2031–2042. https://iopscience.iop.org/article/10.1088/0022-3719/8/13/012.

[259] D. F. Edwards and E. Ochoa, "Infrared refractive index of silicon," *Applied Optics* **19** no. 24, (Dec, 1980) 4130. https://opg.optica.org/ao/fulltext.cfm?uri=ao-19-24-4130&id=164769.

[260] T. R. Figueiro, *Process modeling for proximity effect correction in electron beam lithography*. PhD thesis, Université Grenoble Alpes, 2015. https://tel.archives-ouvertes.fr/tel-01206934.

[261] V. Jain, M. C. Biesinger, and M. R. Linford, "The Gaussian-Lorentzian sum, product, and convolution (Voigt) functions in the context of peak fitting X-ray photoelectron spectroscopy (XPS) narrow scans," *Applied Surface Science* **447** (Jul, 2018) 548–553. https://www.sciencedirect.com/science/article/abs/pii/S0169433218308766.

[262] J. D. Jackson, *Classical Electrodynamics*. Wiley, 1998.

[263] C. Brendel, V. Peano, O. Painter, and F. Marquardt, "Snowflake phononic topological insulator at the nanoscale," *Physical Review B* **97** no. 2, (Jan, 2018) 020102. https://journals.aps.org/prb/abstract/10.1103/PhysRevB.97.020102.

[264] Q. V. Tran, S. Combrié, P. Colman, and A. D. Rossi, "Photonic crystal membrane waveguides with low insertion losses," *Applied Physics Letters* **95** no. 6, (Aug, 2009) 061105. https://aip.scitation.org/doi/10.1063/1.3205452.

[265] N. Ikeda, H. Kawashima, Y. Sugimoto, T. Hasama, K. Asakawa, and H. Ishikawa, "Coupling characteristic of micro planar lens for 2D photonic crystal waveguides," in *19th International Conference on Indium Phosphide & Related Materials*. IEEE, May, 2007. https://ieeexplore.ieee.org/abstract/document/4265989.

[266] T. Shoji, T. Tsuchizawa, T. Watanabe, K. Yamada, and H. Morita, "Low loss mode size converter from 0.3 μm square Si wire waveguides to singlemode fibres," *Electronics Letters* **38** no. 25, (2002) 1669. https://digital-library.theiet.org/content/journals/10.1049/el_20021185.

[267] S. McNab, N. Moll, and Y. Vlasov, "Ultra-low loss photonic integrated circuit with membrane-type photonic crystal waveguides," *Optics Express* **11** no. 22, (Nov, 2003) 2927. https://www.osapublishing.org/oe/abstract.cfm?uri=oe-11-22-2927.

[268] M. Cai, O. Painter, and K. J. Vahala, "Observation of critical coupling in a fiber taper to a silica-microsphere whispering-gallery mode system," *Physical Review Letters* **85** no. 1, (Jul, 2000) 74–77. https://journals.aps.org/prl/abstract/10.1103/PhysRevLett.85.74.

[269] W. Kuang, C. Kim, A. Stapleton, and J. D. O'Brien, "Grating assisted coupling of optical fibers and photonic crystal waveguides," in *Summaries of Papers Presented at the Lasers and Electro-Optics. CLEO '02*. Opt. Soc. America, 2002. https://ieeexplore.ieee.org/abstract/document/1033371.

[270] C. P. Michael, M. Borselli, T. J. Johnson, C. Chrystal, and O. Painter, "An optical fiber-taper probe for wafer-scale microphotonic device characterization," *Optics Express* **15** no. 8, (2007) 4745. https://www.osapublishing.org/oe/abstract.cfm?uri=oe-15-8-4745.

[271] L. Ding, C. Belacel, S. Ducci, G. Leo, and I. Favero, "Ultralow loss single-mode silica tapers manufactured by a microheater," *Applied Optics* **49** no. 13, (Apr, 2010) 2441. https://www.osapublishing.org/ao/abstract.cfm?uri=ao-49-13-2441.

[272] D. Taillaert, F. V. Laere, M. Ayre, W. Bogaerts, D. V. Thourhout, P. Bienstman, and R. Baets, "Grating couplers for coupling between optical fibers and nanophotonic waveguides," *Japanese Journal of Applied Physics* **45** no. 8A, (Aug, 2006) 6071–6077. https://iopscience.iop.org/article/10.1143/JJAP.45.6071.

[273] A. Faraon, I. Fushman, D. Englund, N. Stoltz, P. Petroff, and J. Vuckovic, "Dipole induced transparency in waveguide coupled photonic crystal cavities," *Optics Express* **16** no. 16, (Jul, 2008) 12154. https://www.osapublishing.org/oe/abstract.cfm?uri=oe-16-16-12154.

[274] A. Mekis, S. Gloeckner, G. Masini, A. Narasimha, T. Pinguet, S. Sahni, and P. D. Dobbelaere, "A grating-coupler-enabled CMOS photonics platform," *IEEE Journal of Selected Topics in Quantum Electronics* **17** no. 3, (May, 2011) 597–608. https://ieeexplore.ieee.org/abstract/document/5645652.

[275] R. Halir, P. Cheben, S. Janz, D.-X. Xu, Íñigo Molina-Fernández, and J. G. Wangüemert-Pérez, "Waveguide grating coupler with subwavelength microstructures," *Optics Letters* **34** no. 9, (Apr, 2009) 1408. https://www.osapublishing.org/ol/abstract.cfm?uri=ol-34-9-1408.

[276] D. Benedikovic, P. Cheben, J. H. Schmid, D.-X. Xu, J. Lapointe, S. Wang, R. Halir, A. Ortega-Moñux, S. Janz, and M. Dado, "High-efficiency single etch step apodized surface grating coupler using subwavelength structure," *Laser & Photonics Reviews* **8** no. 6, (Oct, 2014) L93–L97. https://onlinelibrary.wiley.com/doi/full/10.1002/lpor.201400113.

[277] L. Liu, M. Pu, K. Yvind, and J. M. Hvam, "High-efficiency, large-bandwidth silicon-on-insulator grating coupler based on a fully-etched photonic crystal

structure," *Applied Physics Letters* **96** no. 5, (Feb, 2010) 051126. https://aip.scitation.org/doi/10.1063/1.3304791.

[278] D. Taillaert, *Grating couplers as interface between optical fibres and nanophotonic waveguides*. PhD thesis, Ghent University, 2005. https://lib.ugent.be/en/catalog/rug01:000857054. Roosterkoppelaars voor koppeling tussen optische vezels en nanofotonische golfgeleiders.

[279] J. C. Wirth, "Silicon grating couplers for low loss coupling between optical fiber and silicon nanowires," Master's thesis, Purdue University, 2011. https://docs.lib.purdue.edu/dissertations/AAI1510029/.

[280] J. D. Cohen, *Fiber-optic integration and efficient detection schemes for optomechanical resonators*. PhD thesis, California Institute of Technology, 2015. https://thesis.library.caltech.edu/8808/.

[281] N. H. Asmar, *Partial Differential Equations with Fourier Series and Boundary Value Problems*. Pearson Prentice Hall, 2005. https://books.google.com/books?id=2FonAQAAIAAJ.

[282] R. G. Povey, J. G. Hartnett, and M. E. Tobar, "Microwave cavity light shining through a wall optimization and experiment," *Physical Review D* **82** no. 5, (Sep, 2010) 052003. https://doi.org/10.1103/PhysRevD.82.052003.

[283] D. L. Creedon, Y. Reshitnyk, W. Farr, J. M. Martinis, T. L. Duty, and M. E. Tobar, "High Q-factor sapphire whispering gallery mode microwave resonator at single photon energies and millikelvin temperatures," *Applied Physics Letters* **98** no. 22, (May, 2011) 222903.

[284] M. Eichenfield, R. Camacho, J. Chan, K. J. Vahala, and O. Painter, "A picogram- and nanometre-scale photonic-crystal optomechanical cavity," *Nature* **459** no. 7246, (May, 2009) 550–555. https://www.nature.com/articles/nature08061.

[285] A. H. Safavi-Naeini, T. P. M. Alegre, J. Chan, M. Eichenfield, M. Winger, Q. Lin, J. T. Hill, D. E. Chang, and O. Painter, "Electromagnetically induced transparency and slow light with optomechanics," *Nature* **472** no. 7341, (Mar, 2011) 69–73. https://www.nature.com/articles/nature09933.

[286] J. Chan, T. P. M. Alegre, A. H. Safavi-Naeini, J. T. Hill, A. Krause, S. Gröblacher, M. Aspelmeyer, and O. Painter, "Laser cooling of a nanomechanical oscillator into its quantum ground state," *Nature* **478** no. 7367, (Oct, 2011) 89–92. https://www.nature.com/articles/nature10461.

[287] J. T. Hill, A. H. Safavi-Naeini, J. Chan, and O. Painter, "Coherent optical wavelength conversion via cavity optomechanics," *Nature Communications* **3** no. 1, (Jan, 2012) 1196. https://www.nature.com/articles/ncomms2201.

[288] J. Gomis-Bresco, D. Navarro-Urrios, M. Oudich, S. El-Jallal, A. Griol, D. Puerto, E. Chavez, Y. Pennec, B. Djafari-Rouhani, F. Alzina, A. Martínez, and C. M. S. Torres, "A one-dimensional optomechanical crystal with a complete phononic band gap," *Nature Communications* **5** no. 1, (Jul, 2014) 4452. https://www.nature.com/articles/ncomms5452.

[289] J. D. Cohen, S. M. Meenehan, G. S. MacCabe, S. Gröblacher, A. H. Safavi-Naeini, F. Marsili, M. D. Shaw, and O. Painter, "Phonon counting and intensity interferometry of a nanomechanical resonator," *Nature* **520** no. 7548, (Apr, 2015) 522–525. https://www.nature.com/articles/nature14349.

[290] R. Riedinger, S. Hong, R. A. Norte, J. A. Slater, J. Shang, A. G. Krause, V. Anant, M. Aspelmeyer, and S. Gröblacher, "Non-classical correlations between single photons and phonons from a mechanical oscillator," *Nature* **530** no. 7590, (Jan, 2016) 313–316. https://www.nature.com/articles/nature16536.

[291] S. Hong, R. Riedinger, I. Marinković, A. Wallucks, S. G. Hofer, R. A. Norte, M. Aspelmeyer, and S. Gröblacher, "Hanbury Brown and Twiss interferometry of single phonons from an optomechanical resonator," *Science* **358** no. 6360, (Sep, 2017) 203–206. https://science.sciencemag.org/content/358/6360/203.

[292] R. N. Patel, C. J. Sarabalis, W. Jiang, J. T. Hill, and A. H. Safavi-Naeini, "Engineering phonon leakage in nanomechanical resonators," *Physical Review Applied* **8** no. 4, (Oct, 2017) 041001. https://journals.aps.org/prapplied/abstract/10.1103/PhysRevApplied.8.041001.

[293] M. H. Matheny, "Enhanced photon-phonon coupling via dimerization in one-dimensional optomechanical crystals," *Applied Physics Letters* **112** no. 25, (Jun, 2018) 253104. https://aip.scitation.org/doi/full/10.1063/1.5030659.

[294] M. Kalaee, M. Mirhosseini, P. B. Dieterle, M. Peruzzo, J. M. Fink, and O. Painter, "Quantum electromechanics of a hypersonic crystal," *Nature Nanotechnology* **14** no. 4, (Feb, 2019) 334–339. https://www.nature.com/articles/s41565-019-0377-2.

[295] N. Fiaschi, B. Hensen, A. Wallucks, R. Benevides, J. Li, T. P. M. Alegre, and S. Gröblacher, "Optomechanical quantum teleportation," *Nature Photonics* **15** no. 11, (Oct, 2021) 817–821, arxiv:2104.02080 [quant-ph]. https://www.nature.com/articles/s41566-021-00866-z.

[296] A. Zivari, N. Fiaschi, R. Burgwal, E. Verhagen, R. Stockill, and S. Gröblacher, "On-chip distribution of quantum information using traveling phonons," arXiv:2204.05066 [quant-ph]. https://arxiv.org/abs/2204.05066.

[297] J. M. Fink, M. Kalaee, A. Pitanti, R. Norte, L. Heinzle, M. Davanço, K. Srinivasan, and O. Painter, "Quantum electromechanics on silicon nitride nanomembranes," *Nature Communications* **7** no. 1, (Aug, 2016) 12396. https://www.nature.com/articles/ncomms12396.

[298] T. P. Purdy, K. E. Grutter, K. Srinivasan, and J. M. Taylor, "Quantum correlations from a room-temperature optomechanical cavity," *Science* **356** no. 6344, (Jun, 2017) 1265–1268. https://science.sciencemag.org/content/356/6344/1265.

[299] A. H. Ghadimi, S. A. Fedorov, N. J. Engelsen, M. J. Bereyhi, R. Schilling, D. J. Wilson, and T. J. Kippenberg, "Elastic strain engineering for ultralow mechanical dissipation," *Science* **360** no. 6390, (Apr, 2018) 764–768. https://science.sciencemag.org/content/360/6390/764.

[300] J. Guo, R. Norte, and S. Gröblacher, "Feedback cooling of a room temperature mechanical oscillator close to its motional ground state," *Physical Review Letters* **123** no. 22, (Nov, 2019) 223602. https://journals.aps.org/prl/abstract/10.1103/PhysRevLett.123.223602.

[301] J. Olthaus, P. P. J. Schrinner, D. E. Reiter, and C. Schuck, "Optimal photonic crystal cavities for coupling nanoemitters to photonic integrated circuits," *Advanced Quantum Technologies* **3** no. 2, (Oct, 2019) 1900084. https://onlinelibrary.wiley.com/doi/full/10.1002/qute.201900084.

[302] D. Bothner, S. Yanai, A. Iniguez-Rabago, M. Yuan, Y. M. Blanter, and G. A. Steele, "Cavity electromechanics with parametric mechanical driving," *Nature Communications* **11** no. 1, (Mar, 2020) 1589. https://www.nature.com/articles/s41467-020-15389-4.

[303] P. Arrangoiz-Arriola, E. A. Wollack, Z. Wang, M. Pechal, W. Jiang, T. P. McKenna, J. D. Witmer, R. V. Laer, and A. H. Safavi-Naeini, "Resolving the energy levels of a nanomechanical oscillator," *Nature* **571** no. 7766, (Jul, 2019) 537–540. https://www.nature.com/articles/s41586-019-1386-x.

[304] G. Peairs, *Fast and efficient transducers for microwave-optical quantum communication*. PhD thesis, University of California, Santa Barbara, 2019. https://escholarship.org/uc/item/0dd4s9s4.

[305] D. M. Pozar, *Microwave engineering*. Wiley, 2011.

[306] E. B. Magnusson, B. H. Williams, R. Manenti, M.-S. Nam, A. Nersisyan, M. J. Peterer, A. Ardavan, and P. J. Leek, "Surface acoustic wave devices on bulk ZnO crystals at low temperature," *Applied Physics Letters* **106** no. 6, (Feb, 2015) 063509. https://aip.scitation.org/doi/10.1063/1.4908248.

[307] G. Heinzel, A. Rüdiger, and R. Schilling, "Spectrum and spectral density estimation by the discrete Fourier transform (DFT), including a comprehensive list of window functions and some new at-top windows," *Max Planck Society* (2002) . http://hdl.handle.net/11858/00-001M-0000-0013-557A-5.

[308] A. H. Safavi-Naeini, J. Chan, J. T. Hill, S. Gröblacher, H. Miao, Y. Chen, M. Aspelmeyer, and O. Painter, "Laser noise in cavity-optomechanical cooling and

thermometry," *New Journal of Physics* **15** no. 3, (Mar, 2013) 035007. https://iopscience.iop.org/article/10.1088/1367-2630/15/3/035007/meta.

[309] K. O. Hill and G. Meltz, "Fiber Bragg grating technology fundamentals and overview," *Journal of Lightwave Technology* **15** no. 8, (1997) 1263–1276. https://ieeexplore.ieee.org/document/618320.

[310] R. Kashyap, *Fiber Bragg Gratings*. Academic Press, second ed., Oct., 2009. https://www.ebook.de/de/product/15172845/raman_kashyap_fiber_bragg_gratings.html.

[311] R. V. Pound, "Electronic frequency stabilization of microwave oscillators," *Review of Scientific Instruments* **17** no. 11, (Nov, 1946) 490–505. https://aip.scitation.org/doi/abs/10.1063/1.1770414.

[312] R. W. P. Drever, J. L. Hall, F. V. Kowalski, J. Hough, G. M. Ford, A. J. Munley, and H. Ward, "Laser phase and frequency stabilization using an optical resonator," *Applied Physics B Photophysics and Laser Chemistry* **31** no. 2, (Jun, 1983) 97–105. https://link.springer.com/article/10.1007/BF00702605.

[313] E. D. Black, "An introduction to Pound–Drever–Hall laser frequency stabilization,". https://aapt.scitation.org/doi/10.1119/1.1286663.

[314] B. Wang, W. Shi, and Z. Miao, "Confidence analysis of standard deviational ellipse and its extension into higher dimensional euclidean space," *PLOS ONE* **10** no. 3, (Mar, 2015) e0118537. https://journals.plos.org/plosone/article?id=10.1371/journal.pone.0118537.

[315] B. Holmquist, "Moments and cumulants of the multivariate normal distribution," *Stochastic Analysis and Applications* **6** no. 3, (Jan, 1988) 273–278. https://www.tandfonline.com/doi/abs/10.1080/07362998808809148.

[316] D. E. Amos, "Computation of modified Bessel functions and their ratios," *Mathematics of Computation* **28** no. 125, (Jan, 1974) 239–239. https://www.ams.org/journals/mcom/1974-28-125/S0025-5718-1974-0333287-7/.

[317] M. Loève, "Fundamental limit theorems of probability theory," *The Annals of Mathematical Statistics* **21** no. 3, (1950) 321–338. https://www.jstor.org/stable/2236489.

[318] E. G. Olds, "A note on the convolution of uniform distributions," *The Annals of Mathematical Statistics* **23** no. 2, (1952) 282–285. https://www.jstor.org/stable/2236455.

[319] F. Killmann and E. von Collani, "A note on the convolution of the uniform and related distributions and their use in quality control," *Economic Quality Control* **16** no. 1, (Jan., 2001) 17–41. https://www.degruyter.com/document/doi/10.1515/EQC.2001.17.